

**DIRECT DESIGN OF REINFORCED CONCRETE STRUCTURES
USING NONELASTIC STRESS FIELDS**

By

**Abdelmadjid Bensalem
Ingenieur d' Etat en Genie Civil**

**A thesis Submitted for Degree of
Doctor of Philosophy**

**Department of Civil Engineering
University of Glasgow**

January 1993

© Abdelmadjid Bensalem 1993

ProQuest Number: 13834022

All rights reserved

INFORMATION TO ALL USERS

The quality of this reproduction is dependent upon the quality of the copy submitted.

In the unlikely event that the author did not send a complete manuscript and there are missing pages, these will be noted. Also, if material had to be removed, a note will indicate the deletion.



ProQuest 13834022

Published by ProQuest LLC (2019). Copyright of the Dissertation is held by the Author.

All rights reserved.

This work is protected against unauthorized copying under Title 17, United States Code
Microform Edition © ProQuest LLC.

ProQuest LLC.
789 East Eisenhower Parkway
P.O. Box 1346
Ann Arbor, MI 48106 – 1346

Thesis
9456
Copy 1

By the name of God, the Compassionate, the merciful

ACKNOWLEDGEMENTS

The work described in this thesis was carried out in the Department of Civil Engineering at the University of Glasgow, under the general guidance of Professor A. Coull whose interest and encouragement are gratefully acknowledged.

The author is indebted to Dr. P. Bhatt for his valuable supervision, patience, encouragement and advice throughout the course of this study.

I wish also to express my thanks to Professor D. R. Green and Professor D. Muirwood, past and present heads of Department of Civil Engineering for making the facilities available.

Grateful thanks are due to:

Dr. D. V. Phillips, Dr. T. J. A. Agar and Dr. P. D. Arthur for their interest and useful discussions.

The structural laboratory staff, especially Mr A. Burnett, Mr. R. McCaskie, Mr. R. Thornton, Mr. B. Thomson, Mr. A. Yuill, Mr R. Hawthorn, Mr. I. Gardner, I. Dickson and Mr. Ken Ryan for their valuable assistance in preparing and testing the Models.

The research staff and students of Civil Engineering Department, especially Dr. B. Zhang, Dr. B. Famiyesin, Dr. H. Musavi, Mr S. D. Djellab, Mr. M. Abdelkader and Mr. B. Khaled for their useful discussions.

To my wife and lovely son Mouatassim for their patience and moral support and for my parents for their valuable encouragement throughout the years.

This study was made possible by the award of a scholarship by the ministry of Higher Education and research in cooperation with the British Council in Algeria. I am grateful to these bodies.

Summary

This research work is mainly concerned with the service and ultimate load behaviour of reinforced concrete slabs and deep beams designed using nonelastic stress fields. The nonelastic stress fields, at design ultimate load were determined using a finite element procedure using uncracked stiffness, along with von Mises yield criteria. The orthogonal reinforcement was provided based on Wood—Armer and Nielsen—Clark yield criteria, respectively for slabs and deep beams.

The experimental study consisted of six simply supported slabs, two of which were additionally supported by a column in the middle and two simply supported deep beams with different span depth ratios. The first and the third slab were designed using 70 and 30% of plasticity stress distribution whereas the rest of the models were designed using 100% plasticity stress distribution. The major parameter varied was the levels of plasticity to observe their effect on the behaviour of the structures studied.

A nonlinear finite element program based on plate bending layer approach for slabs and inplane formulation for deep beams was used to study the behaviour of the designed models. The steel is modelled as embedded and smeared and assumed to be elastic perfectly plastic or with allowance for strain hardening. Kupfer—Hilsdrof criterion was adopted as the failure criterion for concrete. Smeared crack approach was used to account for the development of concrete cracks. Good agreement between experimental and numerical results was obtained.

Results indicate that all the models designed by this method showed, when tested, satisfactory behaviour both at service load and ultimate load. Both deflections for slabs and crack width for slabs and deep beams were within acceptable limits at service loads. All the models failed in a ductile manner with cracks spread over the structure. For all the models the failure load was above the design ultimate load.

It is concluded that the proposed design procedure produces a natural smoothing out of the stress peaks, leading to a reasonably uniform steel distribution over the slab avoiding congestion in the critical areas of slabs, which is desirable in practice. For simply supported deep beams it appears that no significant redistribution of stresses takes place and the use of elastic stress field in the design is sufficient.

A nonlinear procedure which treats reinforced concrete as an elasto—plastic material is developed. This is applied to the analysis of inplane and plate bending problems. The results appear encouraging.

Acknowledgement

Summary

Contents

Notations

Chapter 1:

Introduction	1
---------------------	----------

Chapter 2:

Analysis and Design of Slabs and Deep Beams

2.1 Introduction	3
2.2 Elastic Methods of Analysis	3
2.2.1 Elastic Methods of Analysis for Slabs	4
2.2.2 Elastic Methods of Analysis for Deep Beams	7
2.3 Plastic Methods of Analysis and Design	11
2.3.1 Plastic Methods for Slabs	11
2.3.1.1 Upper Bound Analysis (Yield Line Theory for Slabs)	11
2.3.1.2 Lower Bound Analysis (Hillerborg Strip Method for Slabs)	12
2.3.2 Plastic Methods for Deep beams	13
2.3.2.1 Upper Bound Analysis	14
2.3.2.1 Lower Bound Solution	17
2.4 Current Simplified Methods of Design and Analysis	21
2.4.1 Simplified Methods for Slabs	21
2.4.2 Simplified Methods for Deep Beams, CIRIA Guide 2	22
2.5 Numerical Methods	26
2.5.1 Finite Element Method	26

Chapter 3:

Direct Design of Reinforced Concrete

3.1 Introduction	28
3.2 Direct Design Approach	29
Equilibrium condition	30
Yield condition	30
Mechanism condition	30
Ductility demand	30
3.2.1 Assumptions and Definitions	31

3.2.2 Plate Bending	31
3.2.2.1 Derivation of Yield Criteria	32
3.2.2.2 Design Equations	38
3.2.2.3 Rules for Placing Reinforcement	40
3.2.3 Inplane Problems	41
3.2.3.1 Derivation of the Yield Criterion	42
3.2.3.2 Derivation of Design Equations	44
3.2.3.2 Derivation of Boundary curves	51
3.3 Multiple Load Cases	52

Chapter 4:

The Finite Element Method

4.1 Introduction	55
4.2 Finite Element Concept and Formulation	55
4.2.1 Discretisation by Finite Element	55
4.2.2 Layer Approach	58
4.2.2.1 Basic Assumptions	59
4.2.2.2 Displacement Representation	59
4.2.3 Shape Function	62
4.2.4 Strain Displacement Relationship	63
4.2.5 Cartesian Derivatives of Shape Functions	64
4.2.6 Element Stiffness Matrix and Force Vector	66
4.3 Nonlinear Solution Techniques	67
4.3.1 Incremental Procedure	68
4.3.2 Iterative Procedure	69
4.3.3 Mixed Procedure	70
4.4 Convergence Criteria	70
4.5 Basic Steps in the Nonlinear Program	71

Chapter 5:

Material Modelling and Numerical Applications

5.1 Introduction	75
5.2 Mechanical Behaviour of Concrete	76
5.2.1 Uniaxial Compressive Stress–Strain Response	76
5.2.2 Uniaxial Tensile Stress–Strain Response	77
5.2.3 Biaxial Concrete Behaviour	78
5.3 Constitutive Formulation of Concrete Modelling	78

5.3.1 Elasticity Based Models	83
5.3.2 Plasticity Based Models	84
5.3.3 Plastic— Fracturing Models	84
5.3.4 Endochronic Models	85
5.4 Cracking Models	85
5.4.1 Smeared Cracking Model	86
5.4.2 Discrete Cracking Model	86
5.4.3 Fracture Mechanics Model	87
5.5 Present Model For Concrete	88
5.5.1 Yield Criterion	88
5.5.1.1 Compression Yielding	89
5.5.2.2 Tension— Compression	90
5.5.2.3 Tension— Tension	90
5.6 Concrete Nonlinearity	90
5.6.1 Concrete under Compression	90
5.6.2 Concrete in Tension	94
5.6.2.1 Singly Cracked Concrete	94
5.6.2.2 Doubly Cracked Concrete	96
5.6.2.3 Shear Transfer	97
5.6.2.4 Tension Stiffening	99
5.7 Modelling of Steel	101
5.7.1 Finite Element Representation of Steel Bars	103
5.7.1.1 Smeared Model	103
5.6.3.2 Embedded Model	104
5.6.3.3 Discrete Model	105
5.8 Numerical Applications	107
5.8.1 HAGO's Slabs	108
a— Simply Supported Slab (Model N. 4)	108
b— Two Adjacent Edges Simply Supported and one Corner Slab (Model N.4)	113
5.8.2 McNEICE Corner Supported Slab	118
5.8.3 VICCHIO and COLLINS Panels	120
5.8.4 CERVENKA Panel W2	131
5.8.5 KHASKHELI Transfer Girders	137
5.8.6 GIJESBERS and SMIT'S Beam	150
5.9 Conclusions	154

Chapter 6:

Experimental Set— up and Instrumentation

6.1 Introduction	156
6.2 Description of Experimental Parameters	159
6.3 Loading Rig	159
6.3.1 Slabs	159
6.3.1.1 Support System	160
6.3.1.2 Loading System	160
6.3.1.2.1 Direct Point Load System	161
6.3.1.2.1 Indirect Point Load System	161
6.3.2 Deep Beams	161
6.3.2.1 Support Girders	168
6.3.2.2 Support Bearings	168
6.3.2.3 Loading Point System	168
6.3.2.4 Losenhausen Machine Platen	168
6.4 Formwork	169
6.5 Material	169
6.5.1 Concrete	169
6.5.2 Reinforcing Steel	170
6.6 Instrumentation	171
6.6.1 Deflections	171
6.6.2 Steel Strains	171
6.7 Test Procedure	175

Chapter 7:

Nonelastic Stress Fields and Design of Experimental Models

7.1 Introduction	180
7.2 Design Procedure for Slabs	181
7.3 Slab Models Design and Discussion	182
7.3.1 Models S.1, S.2 and S.3	182
7.3.2 Model S.5	194
7.3.3 Model S.4 and S.6	203
7.4 Design of Deep Beam	214
7.4.1 Design of Support Bearings	215
7.4.2 Bond and Anchorage	216
7.4.3 Beam Models Design and Discussion	216

Chapter 8:

Experimental and Numerical Analysis of Slabs and Deep Beams

8.1 Introduction	240
------------------	-----

8.2 Slab Models	241
8.2.1 Simply Supported Slabs	241
8.2.1.1 Model S.1	241
8.2.1.2 Model S.2	261
8.2.1.3 Model S.3	278
8.2.1.4 Comparison of Models (S.1, S.2 and S.3)	296
8.2.1.5 Model S.5	300
8.2.2 Simply Supported Slabs with a Column Support in the Middle	315
8.2.2.1 Model S.4	315
8.2.2.2 Model S.6	326
8.3 Deep Beams Models	342
8.3.1 Model B.1	342
8.3.2 Model B.2	350

Chapter 9:

Analysis of Reinforced Concrete Slabs and Deep Beams Assuming Reinforced Concrete as an Elasto— plastic Material.

9.1 Introduction	362
9.2 Programs Content	362
9.2.1 Mathematical Formulation of the Yield Criteria	363
9.2.2 Yield Criteria for Reinforced Concrete Plates	366
9.2.3 Yield Criteria for Reinforced Concrete Inplane Problems	368
9.2.4 Yielding Condition and Stress Reduction Factor	372
9.2.5 Yielding and Plastic Flow	374
9.3 Numerical Applications and Comparisons	376
9.3.1 Plate Bending	376
9.3.2 Inplane	389

Chapter 10

Conclusions and Suggestions for Further Work

10.1 Conclusions	396
10.2 Suggestions	398
References	400

Notations

Major symbols used in the text are listed below. Others are defined when they first appear.

$\{a\}$	Flow vector.
$\{a_b\}$	Flow vector for positive yield surface.
$\{a_t\}$	Flow vector for negative yield surface.
A_c	Area of concrete section.
A_i	The equivalent area of steel of i^{th} layer.
A_s	Area of steel in the longitudinal direction.
A_x, A_y	Area of steel in x and y directions respectively.
b	Section breath.
b_s	Body forces.
$[B]$	Strain matrix
$[B_f]$	Strain matrix associated with flexural deformation.
$[B_p]$	Strain matrix associated with inplane deformation.
$[B_s]$	Strain matrix associated with shear deformation.
C_1, C_2	Coefficient for tension stiffening.
D	Flexural stiffness per unit width.
$[D]$	Elasticity matrix for any material.
$[D']$	Instantaneous elasticity matrix.
$[D_{cr}]$	Rigidity inplane matrix for cracked concrete.
$[D_{ep}]$	Elasto-plastic stress-strain matrix.
d	Effective depth.
d_n	Depth of neutral axis.
$\{d_i\}$	displacement vector.
E	Young's modulus.
E_c	Young's modulus of concrete.
E_i	Instantaneous Young's modulus for concrete.
E_s	Young's modulus of steel.

E_x, E_y	Young's modulus in X and Y directions respectively.
f_c'	Cylinder compressive strength of concrete.
f_{cc}	Intermediate yield surface strength of concrete.
f_{cu}	Cube strength of concrete.
f_d	Equivalent biaxial compressive strength of concrete.
f_t	Tensile strength of concrete.
f_y	Yield strength of steel.
$\{F\}$	Vector of nodal forces in the cartesian coordinate system.
$\{F'\}$	Vector of nodal forces in the local coordinate system (n,t).
G	Shear modulus.
H	Strain hardening parameter for steel.
I_{cr}	Second moment of area of a cracked section.
I_{eff}	Effective second moment of area of a section.
I_g	Second moment of area of gross concrete section (steel neglected)
$[K]$	Stiffness matrix.
L_x	Length of the member in X direction.
L_y	Length of the member in Y direction.
m	Ratio of tensile to compressive strengths of concrete.
M	Bending moment at any stage of loading.
M_{cr}	Cracking moment.
M_n, M_t, M_{nt}	Applied moment components at a point in the local coordinate system (n,t).
M_x, M_y, M_{xy}	Applied moment components at a point in the cartesian coordinate system.
M_x^*, M_y^*	Design moments in X and Y directions respectively.
M_p	Plastic moment.
M_1, M_2	Principal moments.
N	total number of node points.
N_i	Shape function associated with node i.
N_x, N_y, N_{xy}	Applied inplane forces at a point in the cartesian

coordinate system.

P	Applied load.
P_{cr}	First cracking load.
P_d	Design load.
P_{scr}	Load at a crack width of 0.3 mm.
P_{sd}	Load at the limit service deflection.
P_u	Ultimate load.
P_y	Load at first yield of steel.
q	Intensity of the uniform distributed load.
Q_x, Q_y	Shear force components in cartesian coordinate.
S	Loaded surface area.
S_x, S_y	Effective shear moduli in the x and y directions.
$[T]$	Transformation matrix for cracks.
t	Plate thickness.
ΔU	The total internal strain energy.
ΔV	The total external energy.
u, v, w	Displacements at a point in X,Y,Z directions respectively.
u_0, v_0, w_0	Displacements at a point in a reference plane of a plate.
X, Y, Z	Rectangular cartesian coordinates.
x, y, z	coordinates at a point in X, Y, Z system.
z_i	Distance from the reference plane to centre of the i^{th} layer.
β	Shear retention factor.
B	Shear retention factor at cracking strain of concrete.
$d\lambda$	Plastic multiplier.
γ	Area shear factor.
γ_{xz}, γ_{yz}	Shear strain components in the cartesian coordinates.
$\{\delta\}$	Nodal displacement vector in the cartesian coordinates.
ϵ_{cr}	Crack strain of concrete.
ϵ_e	Elastic strain.

ϵ_p	Plastic strain.
ϵ_{pk}	Peak strain.
$\{\epsilon_f\}$	Strain vector associated with flexural deformations.
$\{\epsilon_s\}$	Strain vector associated with shear deformations.
$\epsilon_x, \epsilon_y, \gamma_{xy}$	Strain components in the cartesian coordinates.
ϵ_{ys}	Yield strain of steel.
ξ, η	Local coordinate system.
θ	Angle of the principal plane.
θ_{cr}	Angle of crack with respect to X axis.
θ_x, θ_y	Rotations about x and y axis respectively.
θ_n, θ_t	Rotations about n and t axis respectively.
ν	Poisson's ratio.
$\{\sigma\}$	Stress vector.
$\{\sigma_0\}$	Initial stress vector.
σ	Stress at a point.
$\Delta\sigma_i$	The i^{th} incremental stress at a point.
σ_{oct}	The octahedral stress at a point.
σ_n	Normal stress.
σ_p	The peak stress.
$\sigma_x, \sigma_y, \sigma_{xy}$	Stress components in a cartesian coordinates.
σ_1, σ_2	The principal stresses.
$\tau_{xy}, \tau_{xz}, \tau_{yz}$	The shear stresses in xy, xz, yz planes respectively.
δ	Curvature ratio defining ductility demand.
ϵ_y, ϵ_u	Curvature at yield and at ultimate capacity of the slab respectively.
ρ_x, ρ_y	Steel ratios in X and Y direction.
Φ	Reinforcement bar diameter.
Φ_x, Φ_y	Transversal shear rotations in the XZ and YZ planes respectively.
Φ_1, Φ_2	Reduction factor related to l_g and l_{cr} respectively.

Chapter 1

Introduction

Reinforced concrete slabs and deep beams find extensive applications in engineering practice. Slabs are used as floors and roofs of buildings, and as bridge decks to carry traffic loads. Their main function is to transmit loading acting normal to their plane. Deep beams appear frequently in complex structures in the form of transfer girders, foundation walls etc. They are loaded in their plane in which shear is a dominant feature.

Present design procedure of reinforced concrete structures is based on limit state concepts. These concepts ensure that a structure has a suitable factor of safety against failure, and in addition, it is serviceable when subjected to its design working load. According to limit analysis, it is generally difficult to calculate the exact value of limit load of a reinforced concrete structure. The methods in use give either:

i— a stress distribution not violating the yield criterion and satisfying equilibrium with the external load and the prescribed boundary conditions. A stress distribution such as this is denoted safe and statically admissible stress distribution. The load corresponding to this stress distribution will always be less than or equal to the true collapse load of the structure, hence the name lower bound solution. Hillerborg's strip method and direct design method are of this nature.

ii— a valid collapse mechanism compatible with the boundary conditions of the

structure so that the internal dissipation of energy on yield lines must be equal to the work done by the external loads. The load corresponding to this collapse mechanism will always be greater than or equal to the true collapse load, thus the name of upper bound solution. The true collapse load corresponds to the collapse mechanism giving the least load. Yield line methods for slabs and deep beams fall in to this category. Further details of the methods is the subject of the next chapter.

Modern limit state design specifications require designers to consider the behaviour of a structure as it reaches its limit of resistance, which includes nonelastic response in most cases. To produce designs that account for this behaviour requires the use of either conventional elastic analysis supplemented by semi-empirical or judgemental allowances for nonlinearity, or more advanced methods of analysis.

The object of the present study is to explore the possibility of using nonelastic stress fields in the direct design of reinforced concrete slabs and deep beams. The direct design method is described in chapter three. The finite element method, which is the object of chapter four, was used to design and analyse the models. Nonlinear analysis of reinforced concrete slabs and deep beams was carried out using a layer approach by considering material nonlinearities as presented in chapter five. The details of the test set-up and material properties for the tested models are given in chapter six. Generation of nonelastic stress fields and design of slab and deep beam models tested are described in chapter seven. The behaviour of the models, at service and ultimate load, both experimentally and numerically based on nonlinear finite element analysis, are examined in chapter eight. The possibility of treating reinforced concrete as an elasto-plastic material obeying Wood-Armer and Nielsen-Clarck yield criteria for both plate bending and inplane problems, respectively, is the object of chapter nine.

Chapter 2

Analysis and Design of Slabs and Deep Beams

2.1 Introduction:

In practice, loads to which a structure will be normally subjected to, with in certain bounds, are normally known. Design consists of finding the stress distribution in the structure for the concrete section and calculating the required reinforcement steel area. The stress distribution in any structure is dependent upon the geometry, loading, boundary condition and the state of the material in the structure, whether elastic or plastic. Accordingly the analysis and design methods can be classified into two main categories, viz: elastic and plastic methods of analysis and design.

The purpose of this chapter is to discuss the basis of the methods used for the analysis and design reinforced concrete slabs and deep beams.

2.2 Elastic Methods of Analysis:

In these methods, classical elasticity theory is used to obtain the stress distribution.

2.2.1 Elastic Methods of Analysis for Slabs:

The behaviour of linearly elastic thin plates loaded normal to their plane was investigated by Lagrange(90). In developing a satisfactory approximate theory of bending, the following assumptions are made:

- i- During bending, middle plane of the plate remains unstretched.
- ii- Stresses perpendicular to the plane of the plate are ignored.
- iii- Plane section remain plane before and after bending, figure 2.2.
- iv- The deflections of the slab are small in comparison with its thickness.

By considering the equilibrium of forces acting on the slab element in figure 2.1 with dimensions dx and dy in the x and y directions respectively, the following equation can be derived:

$$\frac{\partial^2 M_x}{\partial x^2} + 2.0 \frac{\partial^2 M_{xy}}{\partial x \partial y} + \frac{\partial^2 M_y}{\partial y^2} = -q \quad 2.1$$

This equation 2.1 is known as the plate equilibrium equation. If the plane sections remain plane before and after bending, the strain due to the displacement at any level Z are given by:

$$\epsilon_x = -Z \frac{\partial \theta_x}{\partial x} \quad ; \quad \epsilon_y = -Z \frac{\partial \theta_y}{\partial y}$$

and

$$\gamma_{xy} = -Z \left(\frac{\partial \theta_x}{\partial y} + \frac{\partial \theta_y}{\partial x} \right) \quad 2.2$$

where ϵ_x , ϵ_y and γ_{xy} are the inplane strains at level Z from the neutral plane of a given point in x,y cartesian system coordinates. θ_x and θ_y are the rotations of normals to neutral axis and can be written in Mindlin plate theory as:

$$\theta_x = \frac{\partial w}{\partial x} + \Psi_x \quad ; \quad \theta_y = \frac{\partial w}{\partial y} + \Psi_y \quad 2.3$$

Where w is the deflection in Z direction.

In the classical plate theory Ψ_x and Ψ_y , which are average rotations due to the transverse shear effects in x and y respectively, are neglected. Thus, by replacing equations 2.3 in equations 2.2 the normal and shearing strain at level Z can be written, in terms of deflection w as follows:

$$\epsilon_x = -Z \frac{\partial^2 w}{\partial x^2} \quad ; \quad \epsilon_y = -Z \frac{\partial^2 w}{\partial y^2}$$

and $\gamma_{xy} = -2.0 Z \frac{\partial^2 w}{\partial y \partial x}$ 2.4

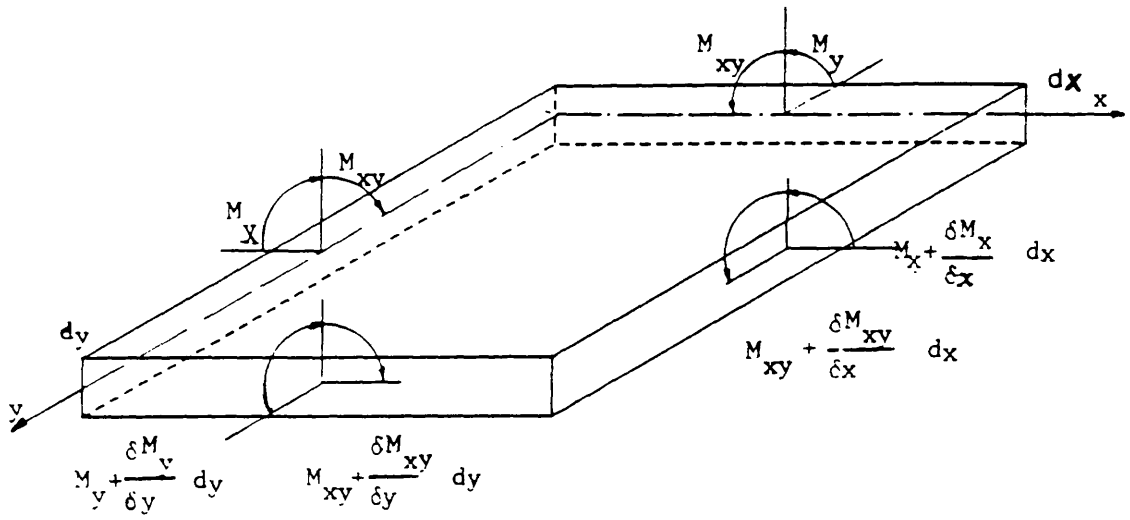
Using Hooke's law for isotropic material, the stresses are related to the strains by:

$$\begin{Bmatrix} \sigma_x \\ \sigma_y \\ \tau_{xy} \end{Bmatrix} = \begin{bmatrix} E & \nu E & 0 \\ \nu E & E & 0 \\ 0 & 0 & G \end{bmatrix} \begin{Bmatrix} \epsilon_x \\ \epsilon_y \\ \gamma_{xy} \end{Bmatrix} \quad 2.5$$

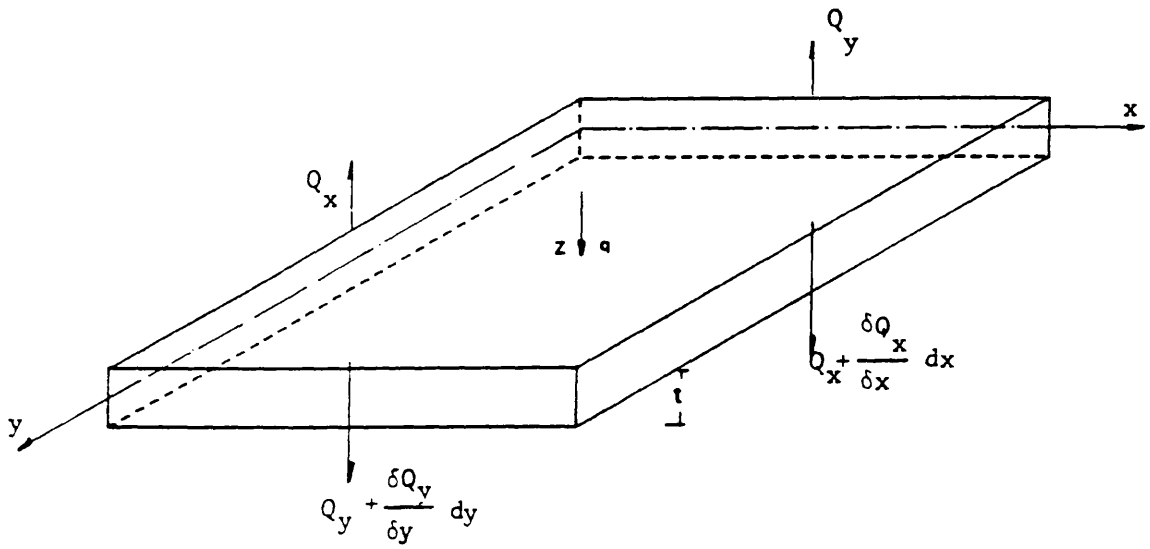
where E and G are the independent material constants defining the elastic properties of the plate and ν is the Poisson's ratio. The moments are given, by integrating the stress over the thickness of the plate t .

$$M_x = \int_{-t/2}^{t/2} \sigma_x Z \, dZ = \int_{-t/2}^{t/2} (E \epsilon_x + \nu E \epsilon_y) Z \, dZ$$

$$\text{Thus } M_x = - \int_{-t/2}^{t/2} \left(E \frac{\partial^2 w}{\partial x^2} + \nu E \frac{\partial^2 w}{\partial y^2} \right) Z^2 \, dZ$$



a- Moment per Unit Length



b- Shear Force per Unit Length

Fig. 2.1 Equilibrium of Slab Element

$$= - \left(D \frac{\partial^2 w}{\partial x^2} + \nu D \frac{\partial^2 w}{\partial y^2} \right) \quad 2.6a$$

Similarly:

$$M_y = - \left(D \frac{\partial^2 w}{\partial y^2} + \nu D \frac{\partial^2 w}{\partial x^2} \right) \quad 2.6b$$

$$M_{xy} = 2.0 D_{xy} \frac{\partial^2 w}{\partial x \partial y}$$

Where

$$D = \frac{E}{1 - \nu^2} \frac{t^3}{12}$$

$$D_{xy} = \frac{E}{2(1 + \nu)} \frac{t^3}{12}$$

Substituting expressions 2.6 in the equilibrium equation 2.1 we obtain the following expression:

$$\frac{\partial^4 w}{\partial x^4} + 2.0 \frac{\partial^4 w}{\partial x^2 \partial y^2} + \frac{\partial^4 w}{\partial y^4} = \frac{q}{D} \quad 2.7$$

where $D = \frac{E t^3}{12(1 - \nu^2)}$

and q is the normal loading intensity per unit area.

In the analytical procedures, the deflected surface of the plate is represented by either a double infinite Fourier Series (Navier Solution) or by a single infinite trigonometric series (Levy's solution). Detailed accounts of such methods can be found in text books on plate theory(90).

2.2.2 Elastic Analysis Methods for Deep Beams:

Deep beam members in structural frame have always presented structural

analysts and designers an interesting dilemma. On the one hand, design codes usually require the designers to account for the deep beam action and, on the other hand, there are no available general solutions for the deep beam problem. However, two types of solutions to the deep beam problems are available in literature, i.e., elasticity and finite element solutions. Timonshenko and Goodier(91) presented elasticity solutions for inplane problems with different loading and boundary conditions. A rigorous theory of elasticity solutions for the case of the deep beam that is either simply supported or is resting on infinite number of equally spaced support have been given for gravity as well as for surface loading(92). Later Bhatt(93) presented a general solution procedure to any statistically indeterminate support of continuous deep beams. In the following, the description of inplane solution development is discussed.

Consider the equilibrium of a small rectangular element in figure 2.3 and by neglecting the body forces, the equations of equilibrium for two dimensional problems are:

$$\frac{\partial \sigma_x}{\partial x} + \frac{\partial \tau_{xy}}{\partial y} = 0 \quad 2.8a$$

$$\frac{\partial \sigma_y}{\partial y} + \frac{\partial \tau_{xy}}{\partial x} = 0 \quad 2.8b$$

These equations are not sufficient for determination of the three stress component σ_x , σ_y and σ_{xy} . Therefore the problem is statistically indeterminate. In order to obtain the solution, the elastic deformation of the body must also be considered by using the condition of compatibility of strain distribution with the deformations u and v . For two dimensional problems this is presented as follows:

$$\epsilon_x = \frac{\partial u}{\partial x} \quad ; \quad \epsilon_y = \frac{\partial v}{\partial y}$$

and
$$\gamma_{xy} = \frac{\partial u}{\partial y} + \frac{\partial v}{\partial x}$$

Eliminating γ_{xy} from the above equations,

$$\frac{\partial^2 \epsilon_x}{\partial x^2} + \frac{\partial^2 \epsilon_y}{\partial y^2} = \frac{\partial^2 \gamma_{xy}}{\partial x \partial y} \quad 2.9$$

The above equation is called condition of compatibility which must be satisfied by the strain components. By using Hooke's law for isotropic materials and equations 2.8, equation 2.9 can be written in terms of stress as follows:

$$\left(\frac{\partial^2}{\partial x^2} + \frac{\partial^2}{\partial y^2} \right) (\sigma_x + \sigma_y) = 0 \quad 2.10$$

Equations 2.8a, 2.8b and 2.10 are sufficient to solve for the stress components. The solution must be compatible with the boundary conditions. To solve these equations, usually a so called Airy's stress function ϕ is used from which the stress components can be calculated as follows:

$$\sigma_x = \frac{\partial^2 \phi}{\partial y^2} ; \sigma_y = \frac{\partial^2 \phi}{\partial x^2} \text{ and } \tau_{xy} = - \frac{\partial^2 \phi}{\partial x \partial y} \quad 2.11$$

Substituting expressions 2.11 into equation of 2.9, thus the stress function ϕ must satisfy the equation:

$$\frac{\partial^4 \phi}{\partial x^4} + 2.0 \frac{\partial^4 \phi}{\partial x^2 \partial y^2} + \frac{\partial^4 \phi}{\partial y^4} = 0.0 \quad 2.12$$

A number of practical two dimensional problems can be solved using equation 2.12, for more details reference can be made to reference (91).

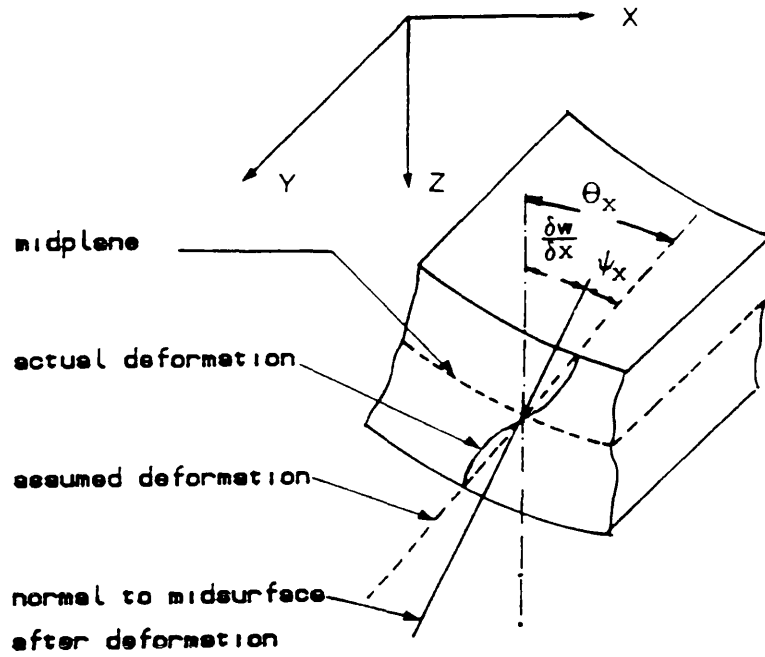


Fig. 2.2 Cross-Section Deformation of Mindlin Plate

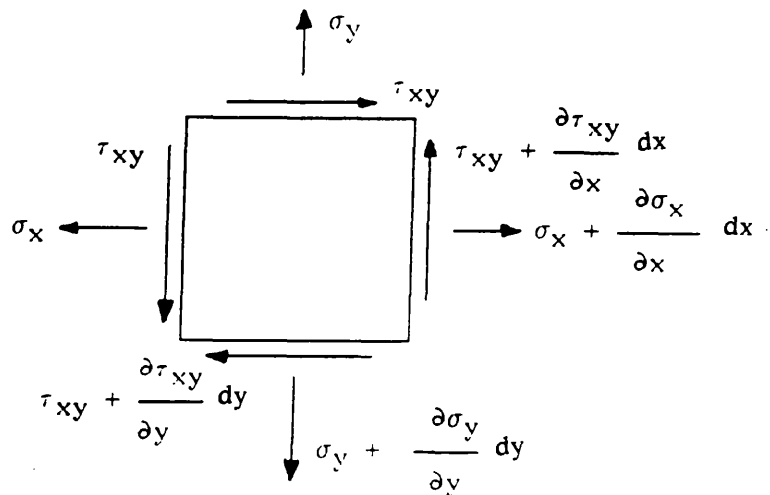


Fig. 2.3 Equilibrium of an Element Under Inplane Stress

2.3 Plastic Methods of Analysis and Design:

Concrete is a brittle material in tension, but exhibits a little ductility in compression. However, stress redistribution occurs in most reinforced concrete structures. This means that the member sections are sufficiently ductile so that the yielded sections continue to deform at constant strength, but the available ductility, unlike steel section, is limited. This section discusses some of the plastic methods applied to the analysis and design of reinforced concrete slabs and deep beams.

2.3.1 Plastic Methods for Slabs:

2.3.1.1 Upper Bound Analysis (Yield line Theory of Slabs):

Yield line theory is an upper bound method, introduced by Johansen(99). The method determines upper bound load based on an assumed failure mechanism. It is assumed that all the reinforcement crossing the yield line, defining the postulated mechanism, yields. The moment at plastic 'hinges' (yield line) is equal to the ultimate moment of resistance of the section and the collapse mechanism is compatible with the boundary conditions. To design by yield line theory a layout of reinforcement must be selected and then various collapse mechanisms are examined to find the one which corresponds to the lowest load. The shape of the assumed mechanism depends on the slab geometry, support conditions and the type of loading. If the collapse mechanism is incorrectly chosen this can lead to unsafe design. Thus the designer is forced to seek all possible modes, for correct analysis. This would create some difficulties for slabs with uncommon shapes.

The main advantage of the yield line theory for slab is that it requires relatively simple calculation. The method can be applied to any shape of slab, any load and any edge condition but is restricted in practice to slabs of constant thickness, uniformly reinforced in each of the two orthogonal or skew directions. The

method suffers from some disadvantages. It does not give any information on the best steel distribution within the slab, load distribution to supports and stress distribution inside rigid regions. Moreover, the method provides no information on the slab deflections or crack width at any stage of the loading. For slabs of complex shape, it is difficult for the designer to find an appropriate collapse mechanism, therefore the application of this method requires considerable experience.

2.3.1.2 Lower Bound Analysis (Hillerborg Strip Method for Slabs):

Other plastic methods of slab analysis are used, like strip method presented by Hillerborg(59). Based on the lower bound approach, Hillerborg made use of the strip action in slab, and choose his solution to equation 2.1 so that the torsional moment M_{xy} is equal to zero, everywhere in the slab. Thus equation 2.1 reduces to:

$$\frac{\partial^2 M_x}{\partial x^2} + \frac{\partial^2 M_y}{\partial y^2} = -q \quad 2.13$$

The load q is divided into a component αq carried in x direction and $(1-\alpha)q$ in y direction, so that equation 2.20 can be split into two equilibrium equations:

$$\frac{\partial^2 M_x}{\partial x^2} = -\alpha q \quad \text{and} \quad \frac{\partial^2 M_y}{\partial y^2} = -(1-\alpha)q \quad 2.14$$

It is usual to choose α between zero and unity ($0 \leq \alpha \leq 1$). The load is thus carried by bending action created by parallel strips spanning in two direction x and y . One important drawback of the strip method is that, in pursuit of simple solution, the designer may choose stress distributions which might depart far from those required for a good serviceability behaviour. This may seriously impair the function of the slab at early stages of loading.

2.3.2 Plastic Method for Deep Beams:

The solution of deep beam type problems using plasticity concepts was developed by Nielsen. He derived some solutions for deep beams considered as wall elements. An extensive work on the method was presented by Nielsen(74), Jensen(57) and Braestrup(58). The authors assumed that concrete has no resistance in tension and introduced an effectiveness factor λ to account for limited ductility of concrete in compression, so that $f_c^* = \lambda f_c'$. Where f_c^* is the concrete effectiveness strength and f_c' is concrete cylinder strength. The strength of reinforcement under compression was neglected.

Consider an yield line in a plane concrete element separating two rigid parts of the body figure 2.6. The relative displacement rate of the rigid part is δ , inclined at an angle α to the yield line figure 2.6. In the local displacement zone Δ we have:

$$\epsilon_t = 0, \quad \epsilon_n = \frac{\delta}{\Delta} \sin\alpha, \quad \gamma_{nt} = \frac{\delta}{\Delta} \cos\alpha \quad 2.15$$

Thus the principal strain rates are as follows:

$$\epsilon_1 = \frac{\delta}{2\Delta} (1 + \sin\alpha), \quad \epsilon_2 = - \frac{\delta}{2\Delta} (1 - \sin\alpha) \quad 2.16$$

For $-\pi/2 \leq \alpha \leq \pi/2$ it can be seen that $\epsilon_1 \geq 0$ and $\epsilon_2 \leq 0$. According to the associated flow rule, the only state of stress in concrete for which such deformations can occur is when $\sigma_1 = 0$ and $\sigma_2 = -f_c^* = -\lambda f_c'$, figure 2.7, where λ is the effectiveness factor accounting for limited ductility of concrete. The internal work per unit length of the yield line of plain concrete and over the element of thickness b is:

$$W_{ci} = \Delta \int_b (\sigma_1 \epsilon_1 + \sigma_2 \epsilon_2) db \quad 2.17$$

$$W_{ci} = \Delta b \left[0 + f_c^* \frac{\delta}{2\Delta} (1 - \sin\alpha) \right] \quad 2.18$$

$$\therefore W_{ci} = \frac{1}{2} b f_c^* \delta (1 - \sin\alpha) \quad 2.19$$

It is clear that if the relative displacement δ is perpendicular to the yield line, that is $\alpha = \pi/2$, the work $W_{ci} = 0$. This reflects the assumption of zero tensile concrete strength. However as soon as δ has a tangential component that is $\alpha < \pi/2$ the resistance increases. If $\alpha = 0$, that means pure shear where $\tau = f_c^*/2$. For pure crushing $\alpha = -\pi/2$, the compressive resistance σ is equal to the factored concrete strength f_c^* .

The total rate of internal work dissipated in the plain concrete along the yield line of length L is:

$$W_{ci} = \frac{1}{2} L b \delta f_c^* (1 - \sin\alpha) \quad 2.20$$

For a reinforced bar crossing an yield line at an angle γ figure 2.6, the contribution of steel to the internal work rate is:

$$W_{si} = T_y \cos(\gamma - \alpha) \delta \quad 2.21$$

T_y is the longitudinal reinforcement yield force.

In the following, both upper and lower bound solutions are discussed.

2.3.2.1 Upper Bound Analysis:

Figure 2.7 shows an admissible failure mechanism of a deep beam with an yield line running at an inclination β from the edge of the load platen. The

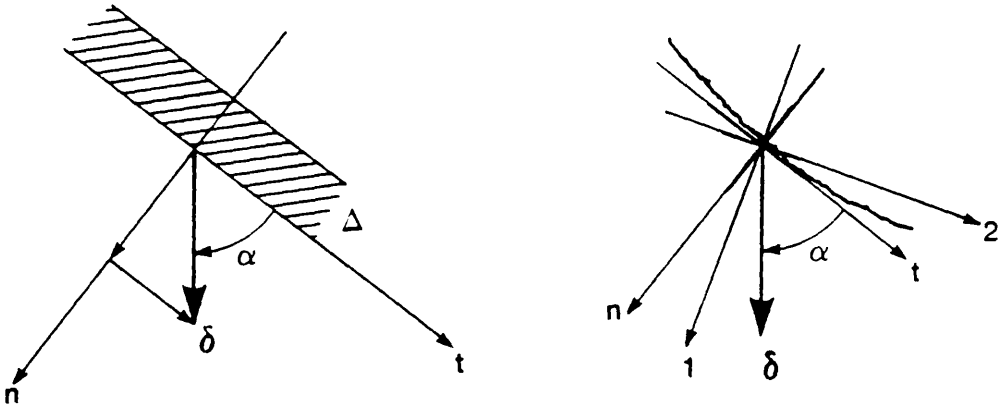


Fig. 2.4 Yield Line in Plain Concrete

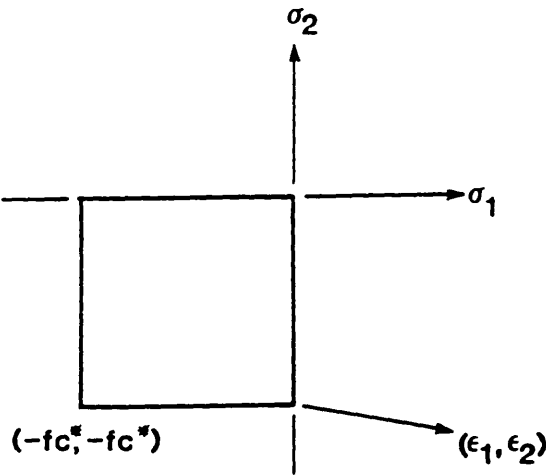


Fig. 2.5 Square Yield Locus for Concrete

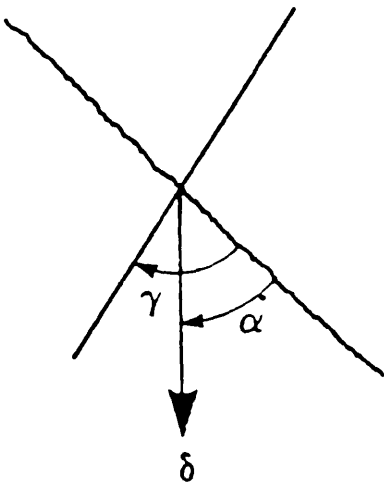


Fig. 2.6 Yield Line Crossed by Reinforcing Bar

relative displacement rate is δ inclined at an angle α to the yield line. The rate of the work done by the load V is:

$$W_e = V \sin(\alpha+\beta) \delta$$

With reference to equation 2.20 the internal work dissipated in the plain concrete, along the yield line $L = h/\sin\beta$ is:

$$W_{ci} = \frac{1}{2} \frac{h}{\sin\beta} b \delta f_c^* (1 - \sin\alpha)$$

The reinforced bar is assumed to yield in tension so that in figure 2.7 $\alpha + \beta \geq \pi/2$. The contribution of reinforced bar, crossing the yield line, of longitudinal yield force T_y , is:

$$W_{si} = - T_y \cos(\alpha+\beta) \delta$$

Thus the total internal work is calculated as follows:

$$W_i = W_{ci} + W_{si} = \frac{1}{2} \frac{h}{\sin\beta} b \delta f_c^* (1 - \sin\alpha) - T_y \cos(\alpha+\beta) \delta \quad 2.22$$

The upper bound solution is given by the work equation of external and internal work: $W_i = W_e$ which gives the upper bound solution:

$$V = \frac{h b f_c^* (1 - \sin\alpha) - 2 T_y \cos(\alpha+\beta) \sin\beta}{2 \sin(\alpha+\beta) \sin\beta} \quad 2.22$$

The lowest upper bound solution is found by minimising equation 2.22 with respect to the variable α . A minimum is found for $dV/d\alpha = 0.0$, which gives:

$$b h f_c^* \cos(\alpha+\beta) = - (b h f_c^* - 2 T_y) \sin\beta \quad 2.23$$

With longitudinal reinforcement under tension, thus $\alpha + \beta \geq \pi/2$. This means that

$(bhf_c^* - 2T_y)$ in equation 2.23 must be greater than zero. That is $2T_y/bh \leq f_c^*$, thus: $\Phi \leq \lambda/2$, where Φ is the ratio of longitudinal reinforcement force to concrete compressive force $\Phi = T_y/bhf_c'$ and $\lambda = f_c^*/f_c'$.

By replacing the resulting value of α and $\cot\beta = a/h$ in equation 2.22, the minimum is:

$$V = 1/2 b \lambda f_c' \{ \sqrt{a^2 + 4h^2\Phi(\lambda-\Phi)/\lambda^2} - a \} \quad 2.24$$

valid for $\Phi \leq \lambda/2$.

If reinforced bar is under compression, thus $\alpha + \beta \leq \pi/2$ for which $dV/d\alpha \leq 0$.

The lowest upper bound solution is obtained when: $\alpha + \beta = \pi/2$, thus :

$$V = 1/2 b \lambda f_c' [\sqrt{a^2 + h^2} - a] \quad 2.25$$

valid for $\Phi \geq \lambda/2$.

2.3.2.2 Lower bound Analysis:

Nielsen and Braestrup(57) assumed the stress distribution in the shear span as shown in figure 2.8. The load was assumed to be running along the compressive strut between the load and the support, and inclined at an angle θ . The triangular shaded area^{was} considered to be under biaxial hydrostatic compression. The force in the tensile reinforcement is T . The stress state is statistically admissible in the sense that it satisfies the equilibrium equations and the statical boundary conditions on the upper and lower face. The anchored reinforcement at the support transmits a compressive force on concrete of intensity T distributed over the depth Y as shown in figure 2.8. The width of x and y , defining the region in biaxial compression under the point load and on the support area figure 2.8, are determined by considering vertical and horizontal equilibrium:

$$V = b \times \sigma \quad 2.26$$

$$T = b y \sigma \quad 2.27$$

where σ is the compressive stress of concrete. In general the length of the load platen t is equal to x . The dimension s is determined so that equilibrium condition at the support is guaranteed, that is:

$$V (s/2 - x) = T (y/2 - c) \quad 2.28$$

From figure 2.8, the inclination θ satisfies the geometrical relation:

$$\cot \theta = y/x = (a + x)/(h-y) \quad 2.29$$

and using equation 2.26 and 2.27, the lower bound solution can be written as:

$$V = 1/2 \{ \sqrt{[(b\sigma)^2 + 4T(bh\sigma - T)]} - b\sigma \} \quad 2.30$$

The highest lower bound is determined by maximising equation 2.30 with respect to the statical parameters σ and T . It appears that:

$$\frac{\partial V}{\partial \sigma} \geq 0 \text{ always.}$$

$$\frac{\partial V}{\partial T} \geq 0 \text{ for } T \leq bh\sigma/2$$

Therefore the highest lower bound is obtained with the maximum concrete stress.

i.e. $\sigma = f_c^* = \lambda f_c'$.

For $T < 1/2 bhf_c^*$ the highest lower bound is obtained with the maximum reinforcement force ($T = T_y$). Thus, by introducing the same constants as defined for the upper bound solution; the highest lower bound solution is given by the following equation:

$$V = 1/2 b \lambda f_c' \{ \sqrt{[a^2 + 4h^2\Phi(\lambda - \Phi)/\lambda^2]} - a \} \quad 2.31$$

valid for $\Phi \leq \lambda/2$.

For $T \geq 1/2 bhf_c^*$ the highest lower bound is obtained with $T = 1/2 bhf_c^*$, thus:

$$V = 1/2 b \lambda f_c' [\sqrt{(a^2 + h^2)} - a] \quad 2.32$$

valid for $\Phi \geq \lambda/2$.

In general the methods are used to find the ultimate load of an existing beam. For more detailed explanation of the methods and their practical applications reference should be made to references (77,74,58).

It is clear that the lower bound solution equations 2.31 and 2.32 are identical with the upper bound solution, equations 2.24 and 2.25. Thus the method is an exact plastic solution for deep beams subjected to point loading.

The problem with this method is finding the effectiveness parameters λ , which at first instance was taken to reflect the limited ductility of concrete which depends on the strength f_c' . However this factor must account for other neglected features, notably the size effect, the tensile concrete strength, and the state of stresses at failure(58). Many workers have compared the plastic solution to the existing published test results. An attempt to find relationships between certain parameters of the tested beam and the effectiveness factor λ was carried out by Stewart and Watt(118). They concluded that more results should be analysed from different sources. By analysing nearly a hundred beams, Bhatt(60) concluded that the results appear very promising with $\lambda = 0.44$. Braestrup(58) reported that a comprehensive investigation of published test results has been carried out by Chen(61) and yielded the following formula of λ , for rectangular non—prestressed beams.

$$\lambda = (1-0.25)(2-0.25h)(2-0.4a/h)(2+100\rho) 0.60/\sqrt{f_c'} \quad 2.33$$

with $h \leq 1m$; $h/a \leq 2.5$ and the steel percentage $\rho \leq 0.02$.

Nielsen and Braestrup(57) reported a series of five rectangular simply supported

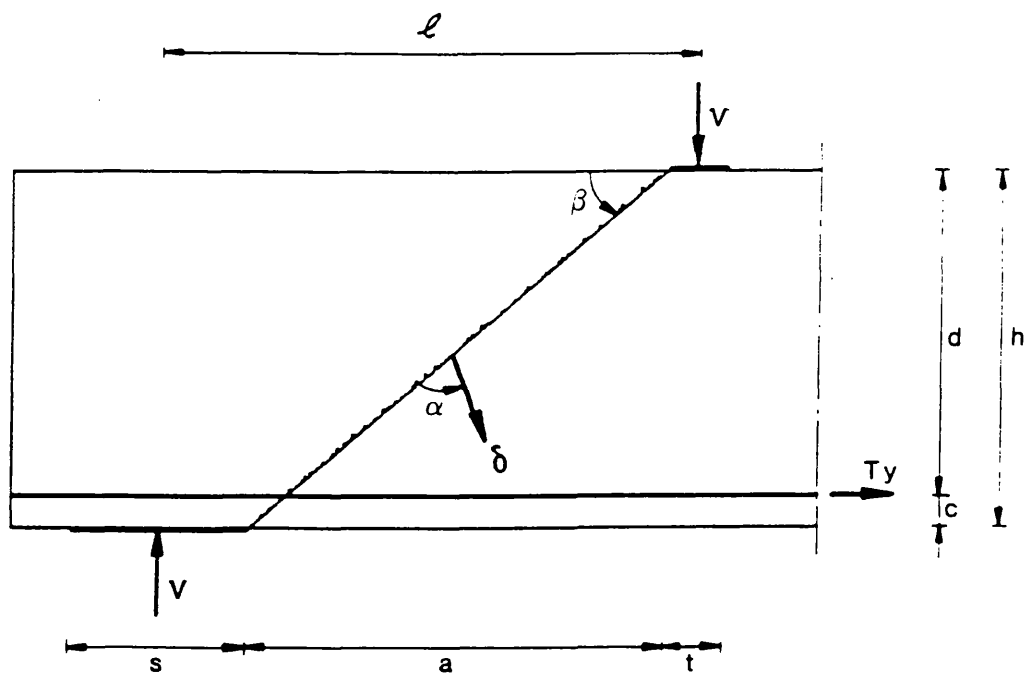


Fig. 2.7 Failure Mechanism for Beam with Point Loading

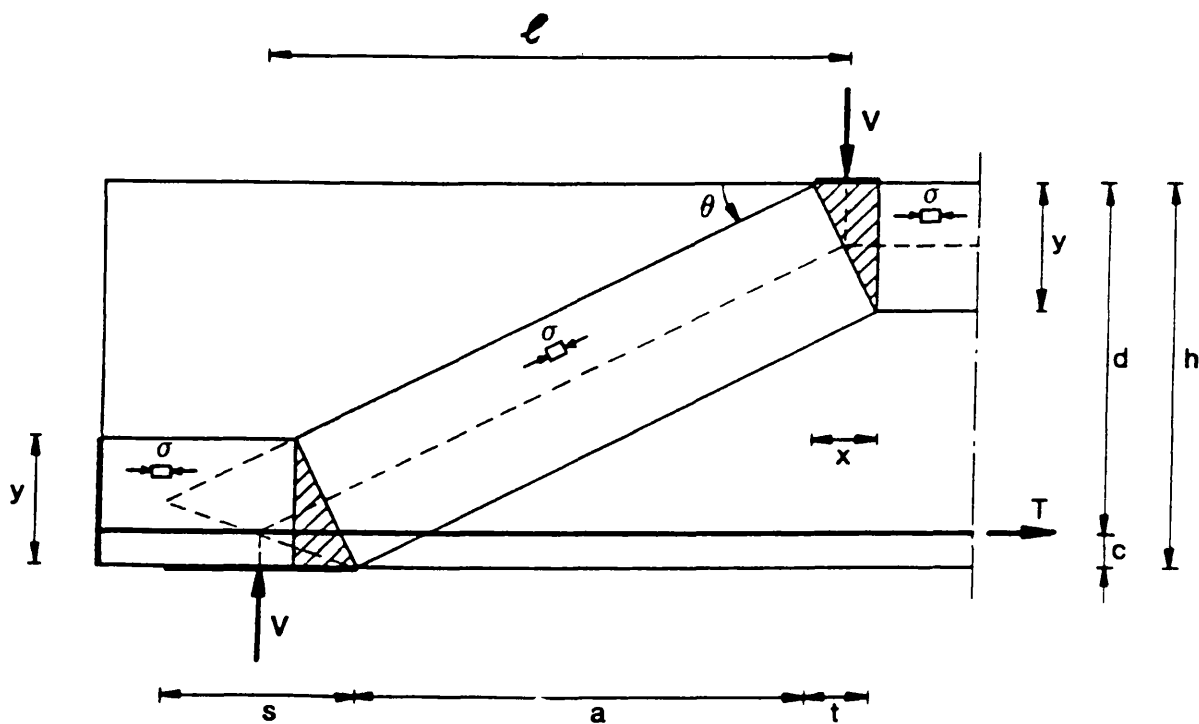


Fig. 2.8 Stress Distribution for Beam with Point Loading

prestressed beams under two point loading. The beams had different shear span ratio a/h . The authors concluded that the results were in excellent agreement with the solution, with an effective factor $\lambda = 0.46$.

For design engineers, all the methods described above are not design orientated, and simplified methods have always been employed, unless of course design tables and charts are available.

2.4 Current Simplified Methods of Design and Analysis:

2.4.1 Simplified Method for Slabs:

For slabs Rankine–Grashof method, which generally approximates the slab to a set of parallel beams resisting the load by bending actions and where torsional moments are ignored, is used. The condition of compatibility is only approximately satisfied. For a given uniform load q , the proportion of the load carried by orthogonal strips in x and y directions are such that

$$q_x + q_y = q. \quad 2.34$$

The value of q_x and q_y are determined from the condition of deflection compatibility at the centre strips. Thus using simple beam deflections:

$$\frac{5q_x l^4}{384E_x I_x} = \frac{5q_y l^4}{384E_y I_y} \quad 2.35$$

By assuming equal rigidities in the two strips, and solving for q_x and q_y using equations 2.34 and 2.35, it results in:

$$q_x = \frac{L_y^4}{L_x^4 + L_y^4} q \quad 2.36$$

$$q_y = \frac{L_x^4}{L_x^4 + L_y^4} q \quad 2.37$$

Thus the maximum bending moments in x and y directions can be obtained as:

$$M_x = \frac{L_y^4}{L_x^4 + L_y^4} \frac{qL_x^2}{8} = \alpha_{sx} qL_x^2 \quad 2.38$$

$$M_y = \frac{L_x^2 L_y^2}{L_x^4 + L_y^4} \frac{qL_x^2}{8} = \alpha_{sy} qL_x^2 \quad 2.39$$

Coefficient α_{sx} and α_{sy} depend on aspect side ratio, and are given in table 3.14 of BS8110(1). This method applies for rectangular simply supported slabs under uniform load.

2.4.2 Simplified Method for Deep Beam, CIRIA Guide 2:

For a shallow beam subjected to concentrated loading, the capacity is governed by either the strength in flexure of the maximum moment section or the strength in shear of the span. However, for a deep beam, the ultimate load is determined by transfer of forces between load and support. Usually for shallow beams, bending, shear and axial forces are considered separately. This becomes less appropriate in beams with span/depth ratio less than 2.5, because of the interdependence and interaction of vertical and horizontal stresses. It was Kaar(94) who concluded, by testing homogenous and isotropic materials, that when the span to depth ratio was less than 1.5 the use of flexural formula for measuring the stresses was seriously in error. By using elastic stress distribution in deep beams CIRIA Guide 2(98) revealed that:

- i- Plane sections of the beam do not remain plane after deformation.
- ii- Areas over the supports are highly stressed. Therefore splitting forces arise more frequently in deep beams.
- iii- The distance between the centroids of the tensile zones varies along the

length of the beam and is greatest at mid span.

iv— In deep beams vertical and shear strains are largely comparable with bending strains.

CIRIA Guide 2 report(98) was intended to provide designers guidance on the design of reinforced concrete deep beams. Its rules were mainly based on the published information which had been assessed critically and presented in a form suitable for application(97). The guide applies to beams having an effective span/depth ratio l/h less than 2 for single span and 2.5 for continuous beams. This guide was intended to be used in conjunction with British code CP110(95). However Kong et al.(96) concluded that CIRIA Guide could safely be used with BS8110(1). Of all the currently used main design documents, CIRIA Guide gives the most comprehensive recommendations(85). In the following some sections of the Guide are discussed, in conjunction with the reinforced concrete code of practice BS8110(1).

The effective span length l and the active height h_a are determined with reference to figure 2.9 as follows:

$$l = l_0 + [\text{lesser of } (c_1/2 \text{ and } 0.1l_0) + \text{lesser of } (c_2/2 \text{ and } 0.1l_0)] \quad 2.40$$

$$h_a = \text{minimum of } (h, l) \quad 2.41$$

The part of the beam which is above this active height h_a acts as a load-bearing wall.

The flexural and shear strength of the beams are determined as follows:

a— flexural strength:

i— Calculate the ultimate moment capacity of concrete section:

$$M_u = 0.12 f_{cu} b h_a^2 \quad 2.42$$

where f_{cu} is the concrete characteristic strength and b is the beam thickness.

- ii- If $l/h_a > 1.5$, the applied moment must not exceed M_u .
- iii- Calculate the area of the main longitudinal reinforcement:

$$A_s = \frac{M}{0.87 f_y Z} \quad 2.43$$

f_y is the steel characteristic strength and Z the lever arm calculated as follows:

For single span beams;

$$Z = 0.2 l + 0.4 h_a \quad 2.44a$$

For continuous beams;

$$Z = 0.2 l + 0.3 h_a \quad 2.44b$$

- iv- The calculated reinforcement area A_s must be distributed over a depth of $0.2 h_a$ and appropriately anchored at the end.

b- Shear strength:

For a given beam under concentrated load and with reinforcement A_r (horizontal and vertical), the applied shear force must not exceed the limit imposed by equation 2.45 ie:

$$\frac{V}{bh_a} < \lambda_1 \left[1.0 - 0.35 \frac{x_e}{h_a} \right] \sqrt{f_{cu}} + \lambda_2 \sum 100.0 \frac{A_r y_r \sin^2 \theta_r}{bh_a} \quad 2.45$$

where x_e is the clear shear span of the point load (in figure 2.10 $x_e = x$).

$\lambda_1 = 0.44$ and 0.32 for normal and light weight concrete respectively. $\lambda_2 = 1.95$ and 0.58 N/mm² for deformed and plain bars respectively. y_r is the depth at which the typical web bar intersects the critical diagonal crack Y-Y in figure 2.10. θ_r is the angle between the bar being considered and the line Y-Y in figure 2.10. The rest of the parameters in equation 2.45 are as defined

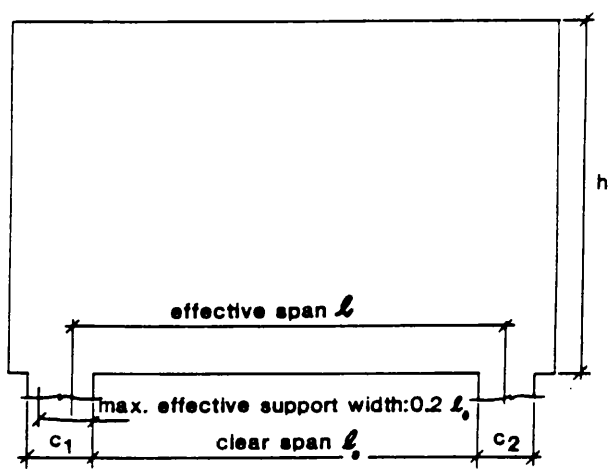


Fig. 2.9 Meanings of Symbols c_1 , c_2 , h , l and l_0

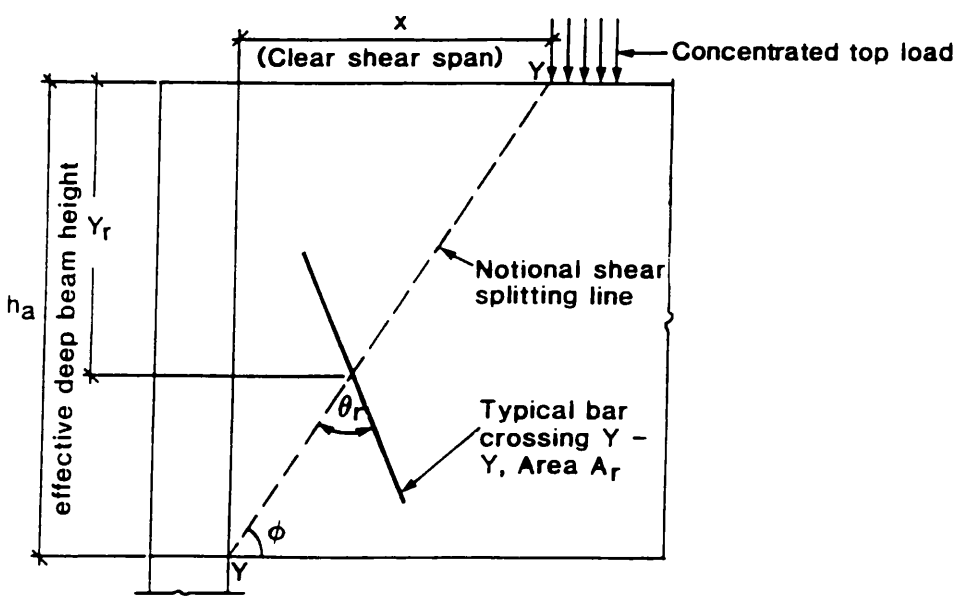


Fig. 2.10 Meaning of Symbols A_t , h_a , Y_r , θ_r

previously.

Equation 2.45 is essentially the Kong et al.(97) equation where λ_1 , λ_2 are modified to introduce the necessary safety factors for design purposes. According to CIRIA Guide2(98) this equation applies only for x_e/h_a over the range 0.23 to 0.7. However later Kong et al.(96) concluded that equation 2.45 can be applied to an extended range of x_e/h_a from 0 to 0.70. In equation 2.45 the first factor of the right side is the concrete contribution to the shear capacity. The second term is the steel contribution to the shear capacity. The total contribution of the steel reinforcement must not be less than 0.2 V. If it is less than this value, the web reinforcement must be increased up to 0.2 V. The shear force also must not be greater than the shear capacity of concrete defined in section 3.4.2 of CIRIA Guide 2(98) as:

$$\frac{V}{bh_a} < 1.3 \lambda_1 \sqrt{f_{cu}} \quad 2.46$$

All these methods of analysis and design, whether plastic, elastic or based on experimental test results, fail to be general and independent of the shape, boundary and loading conditions. However numerical methods have been found to be more convenient to overcome most of these limitations. In these methods stress distribution, deflections and other informations on slabs and deep beams can be calculated easily.

2.5 Numerical Methods:

2.5.1 Finite Element Method:

The finite element method is the most versatile method used, in the design and analysis of slabs and deep beams. The method can be used to analyse variable thickness slabs and deep beams with curved, stepped or inclined edges. Edge stiffening, openings and loading at any location can be easily dealt with,

and different material properties of the constituent materials, concrete and steel can be included. The continuum is replaced by an equivalent idealized structure composed of discrete elements connected together at a finite number of nodes. The conditions of equilibrium are applied at every node of the idealized structure and the solution of the set of equilibrium equations yields nodal displacements, which in turn are used to calculate the internal strains and stresses. Further details of the method are given in chapter 4. The method is extensively used in the present work both for the analysis and design of slabs and deep beams. The direct design method, which is a lower bond method and described in the next chapter, is used in the design of the present models using a nonelastic stress fields generated by finite element procedures.

Chapter 3

Direct Design of Reinforced Concrete

3.1 Introduction:

In chapter two, various methods for the design of concrete slabs and deep beams were described. Most of these methods concentrated on the calculation of the ultimate loads, and no other information is given. It is desirable that the method of design itself must not be a complicated task for the designer and capable of handling any geometry, boundary and loading conditions with minimum difficulties. The direct design method is one attractive method which is design orientated and in addition pays attention to serviceability limit states as well. The method will be described in the following sections for both plate bending and inplane problems.

Currently, the recommendations in British practice for reinforced concrete are based on limit state design and are given in British Standard Code of Practice BS 8110(1). In practice any structure must satisfy the following two limit states:

a— Ultimate limit state (ULS):

This state is associated with the maximum load carrying capacity of the

structure. The collapse of the structure or part of it, may arise from rupture of one or more critical sections, from the loss of static equilibrium (transformation into mechanism) or from buckling due to elastic or plastic instability. In practice the designed structure must have a security margin, assured by an appropriate load factor.

b– Serviceability limit state (SLS):

This condition requires that the structure should not exceed certain limitations in terms of deflections, crack widths, steel strains and for some structures vibration under service loads.

In general, reinforced concrete structures are designed for the ultimate limit state and checked for the serviceability limit state.

3.2 Direct Design Approach:

The speed of developments in computer technology have diverted the attention of the designers from using conventional design methods in conjunction with code prescribed rules to a more highly sophisticated computer aided design (CAD) procedures. The advances in finite element techniques has also increased the need to find an automatic design procedure. In other words a computer design orientated method, so that a structure can be designed with minimum intervention by the designer. 'Direct Design' is one attractive method. This method combines analysis and design into a single continuous operation.

The direct design method satisfies theoretically all the basic classical plasticity theory requirements, viz equilibrium, yield condition, mechanism and ductility demand.

Equilibrium condition:

In classical approaches, the distribution of stress in reinforced concrete structures are determined using elastic theory. In fact any stress distribution, in equilibrium with the applied loads, can be used. In this study the stress fields are obtained using finite elements of the unreinforced concrete structure with the uncracked properties of concrete, so the equilibrium condition is automatically satisfied.

Yield condition:

Using direct design procedure, the steel of reinforced concrete structure is determined directly from yield criteria so that the resistance provided by concrete and the steel, at each point, must be equal to, or greater than the applied stresses. In ^{the} direct design technique, the resistance of the structure at each point is matched as closely as possible to the applied stress. This will let all points of the structure, theoretically, yield simultaneously.

Mechanism condition:

Since the steel area, at any point of the structure, is obtained directly by satisfying the yield condition, thus at ultimate load all the points attain their ultimate strength with a minimum of redistribution of stresses converting the structure into mechanism.

Ductility demand:

It is assumed, in the classical plasticity theory, that the material possesses unlimited ductility. This means that the early yielded region in the structure will continue to deform without any reduction in their strength. However, this requirement can be avoided if the difference between the load at first yielding and the ultimate load of the whole structure is made as small as possible, so that the early yielded points or regions can deform at constant stress before reaching

the descending branch of stress-strain of material. Theoretically using this method, this condition will be satisfied automatically as the required steel is determined directly from the yield criterion, thus all the points of the slab will yield simultaneously.

3.2.1 Assumptions and Definitions:

Simplifying assumptions are further made and can be summarized as follows:

- i— The reinforcing bars carry only uniaxial stress in their original directions. So kinking and dowel actions are neglected.
- ii— For inplane problems the reinforcement is taken to be positioned symmetrically with respect to the middle surface of the section and to be in two orthogonal directions (fig. 3.2 and 3.8).
- iii— The reinforcing bars are assumed to be elastic perfectly plastic with yield stress f_s in tension and f_s' in compression (fig. 3.5).
- iv— The bars are considered in terms of area per unit length rather than as individual bars, because it is assumed that the bar spacing is small in comparison with the overall dimensions of the structure.
- v— The concrete is assumed to have no resistance in tension, to satisfy a square yield criterion in inplane stress (fig. 3.6) and to be perfectly plastic. This last assumption obviously does not reflect the true behaviour of the concrete.
- vi— Instability failure and bond failure are assumed to not happen, by proper choice of the section and reinforcement.

3.2.2 Plate Bending:

It was Hillerborg(65) who first proposed a method for the reinforcement of slabs and shells designed according to the theory of elasticity. This method was

later reconsidered by Kemp(82) and finally Wood(71) reexamined and enlarged the idea of Hillerborg by establishing simple rules and equations for the optimum steel in slab elements subjected to the moment field (M_x, M_y, M_{xy}) without membrane forces. Wood's equations for the design of orthogonal steel of slab elements at the top and bottom faces have been extended by Armer(72) to cover skew reinforcement.

In the following sections, the derivation of the yield criterion and design equations of reinforced concrete slabs, will be briefly described.

3.2.2.1 Derivation of the yield criteria:

The yield criterion for any material is a mathematical relationship between a set of applied stress and strength of the material. The yield condition is satisfied if the strength of the material at any point is equal to the applied stress.

Consider an element of a slab subjected to bending moments M_x , M_y and torsional moment M_{xy} as shown in figure 3.1. The slab element can provide a flexural strength of M_x^* , M_y^* in x and y directions (fig. 3.4). The yield criterion can be written as:

$$F(M_x, M_y, M_{xy}, M_x^*, M_y^*) = 0.0 \quad 3.1$$

Consider as shown in figure 3.3, at any point in the slab element, a line with a normal n and tangent t . The normal applied moment M_n must not exceed the value of the moment of resistance that the reinforced section in the slab could develop in direction n . This is called a normal moment criterion.

Taking the normal to the yield line at an angle θ to the x axis and considering the equilibrium of the element shown in figure 3.3 we have :

$$M_n = M_x \cos^2 \theta + M_y \sin^2 \theta - 2.0 M_{xy} \sin \theta \cos \theta \quad 3.2$$

$$M_t = M_x \sin^2 \theta + M_y \cos^2 \theta + 2.0 M_{xy} \sin \theta \cos \theta \quad 3.3$$

$$M_{nt} = (M_x - M_y) \sin \theta \cos \theta + M_{xy} (\cos^2 \theta - \sin^2 \theta) \quad 3.4$$

The resisting normal moment at the yield line can be expressed as:

$$M_n^* = M_x^* \cos^2 \theta + M_y^* \sin^2 \theta \quad 3.5$$

The value of M_n^* in equation 3.5 must always be greater than that for M_n calculated from equation 3.2, that is:

$$M_n^* - M_n \geq 0.0 \quad 3.6$$

Substituting equation 3.2 and 3.5 in 3.6, thus:

$$(M_x^* - M_x) \cos^2 \theta + (M_y^* - M_y) \sin^2 \theta + 2.0 M_{xy} \sin \theta \cos \theta \geq 0.0 \quad 3.7$$

If we take:

$$A = M_x^* - M_x \quad 3.8$$

$$B = M_y^* - M_y \quad 3.9$$

$$C = M_{xy} \quad 3.10$$

equation 3.7 will be in the form:

$$A \cos^2 \theta + B \sin^2 \theta + 2.0 C \cos \theta \sin \theta \geq 0.0 \quad 3.11$$

Dividing by $\cos^2 \theta$, equation 3.11 reduces to:

$$F(\theta) = A + B \tan^2 \theta + 2.0 C \tan \theta \geq 0.0 \quad 3.12$$

For optimum steel, excess strength must be a minimum, that is to say:

$$\frac{dF(\theta)}{d \tan \theta} = 0.0 \quad 3.13$$

$$\frac{d^2 F(\theta)}{d \tan^2 \theta} > 0.0 \quad 3.14$$

$$\therefore \frac{dF(\theta)}{d \tan \theta} = B \tan \theta + C = 0.0 \Rightarrow \tan \theta = - \frac{C}{B} \quad 3.15$$

$$\tan \theta = - \frac{M_{xy}}{M_y^* - M_y} \quad 3.16$$

$$\therefore \frac{d^2 F(\theta)}{d \tan^2 \theta} = B > 0.0 \Rightarrow M_y^* > M_y \quad 3.17$$

Substituting equation 3.15 in equation 3.11 then:

$$A + B \left(- \frac{C}{B} \right)^2 + 2.0 C \left(- \frac{C}{B} \right) = 0.0 \quad 3.18$$

$$\text{or} \quad A B - C^2 = 0.0 \quad 3.19$$

Replacing A, B and C by their values, one gets:

$$- (M_x^* - M_x) (M_y^* - M_y) + M_{xy}^2 = 0.0 \quad 3.20$$

This is the yield criterion for reinforced concrete slabs, known as Wood criterion(71). Armer(72) extended the work of Wood to take account of skew reinforcement.

For the yield criterion in the negative steel at the top of the slab, similar

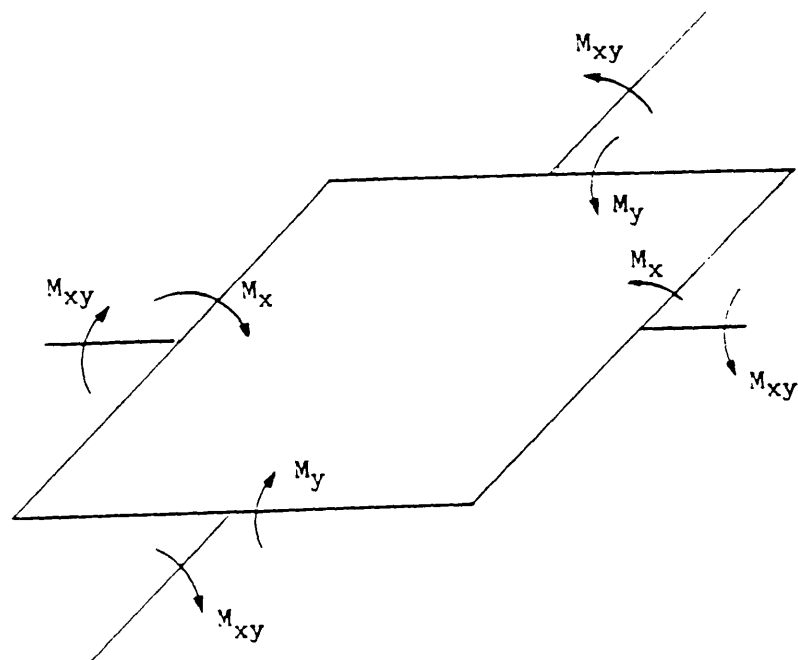


Fig. 3.1 Moments on a Slab Element (Positive)

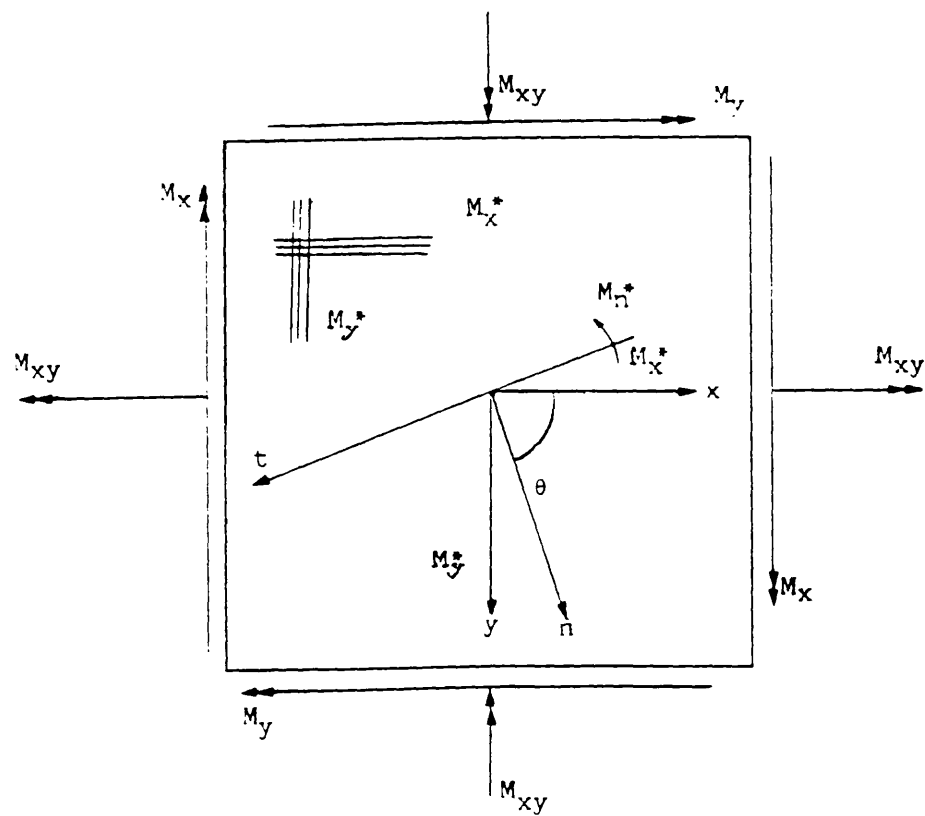


Fig. 3.2 Applied and Resistant Moments on an Element

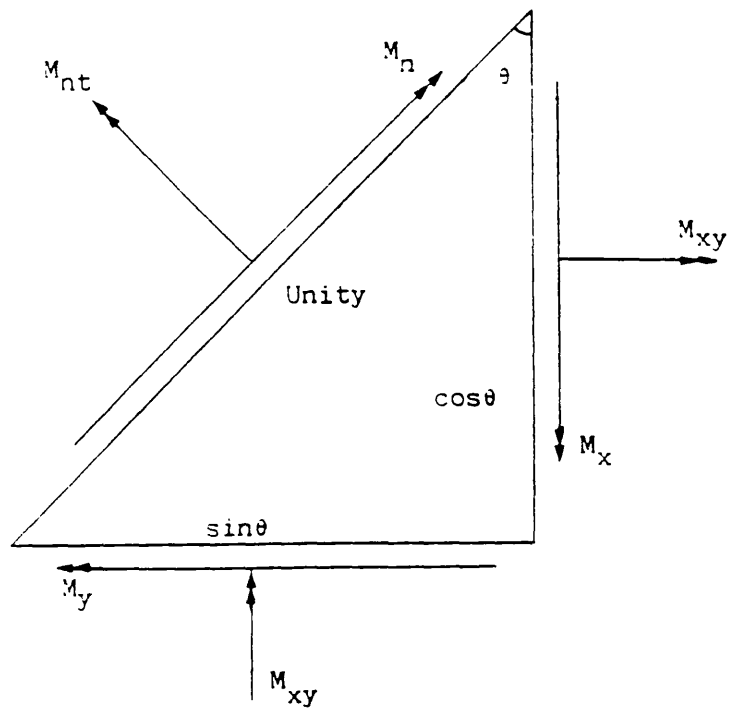


Fig. 3.3 Equilibrium of a slab Element under a Moment Field.

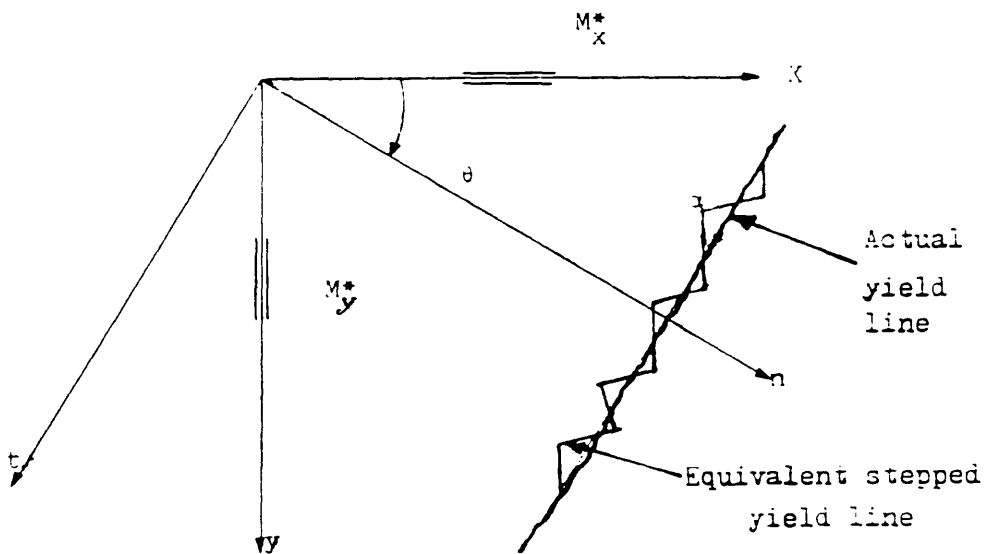


Fig. 3.4 Johanson's Stepped Yield Criterion.

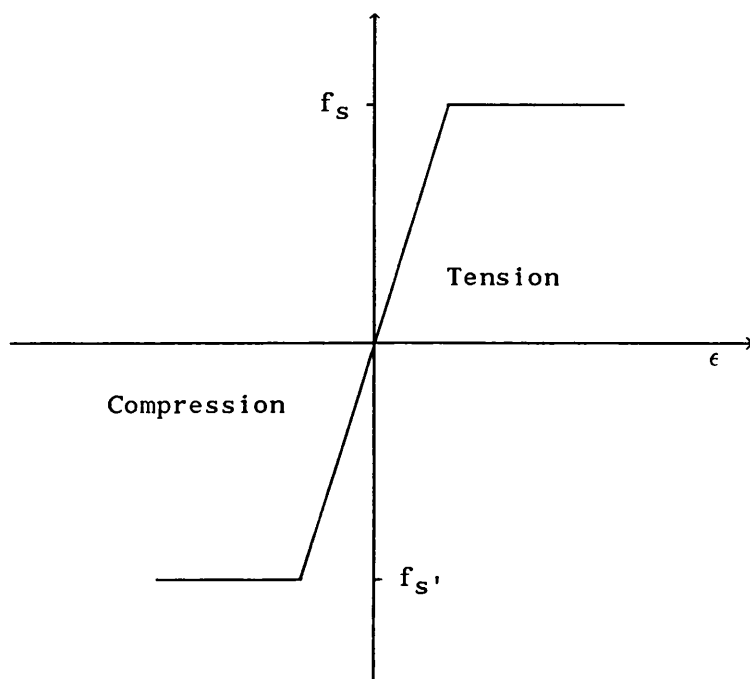


Fig. 3.5 Assumed Reinforcing Steel Stress-Strain Response.

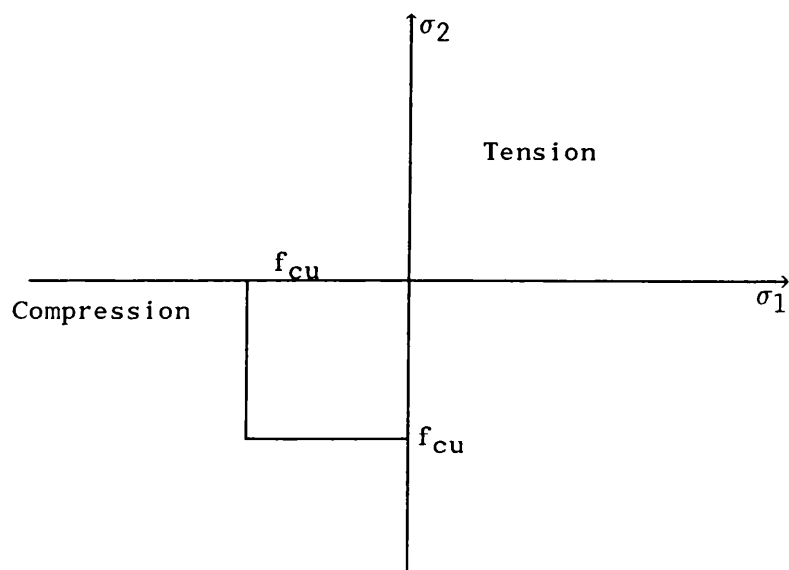


Fig. 3.6 Square Yield Criteria for Concrete.

procedure can be adopted. The yield condition for negative steel (top steel) can be written as:

$$- (M_x^{*t} + M_x) (M_y^{*t} + M_y) + M_{xy}^2 = 0.0 \quad 3.21$$

The validity of the criterion was confirmed for the case of orthogonal steel by extensive experimental work carried out by many research workers such as Lenschow and Sozen(66), Cardenas and Sozen(67) and Jain et al(68). Cardenas and Sozen(67) concluded from an extensive experimental investigation that in nonisotropically reinforced slabs, the yield lines do not necessarily coincide with the principal direction of either the applied or resisting moments. Consequently, twisting moments do exist at the yield line in addition to the flexural moments. Later Hago and Bhatt(69), and Bhatt et al.(70) used elastic stress field, in conjunction with Wood—Armer yield criterion, for the design of slabs with orthogonal and skew reinforcement and concluded that it is a highly practical design procedure which leads to lower bound solution of reinforced slabs. Bhatt and Benredouane(13,14) also investigated theoretically the possibility of using nonelastic stress fields in the design of reinforced concrete slabs in conjunction with the above yield criterion.

3.2.2.2 Design Equations:

From the yield condition derived previously, the following equation can be used for the design of slabs.

a— Positive moment field: (Bottom steel)

Referring to equation 3.20:

$$M_x^{*} = \frac{M_{xy}^2}{M_y^{*} - M_y} + M_x$$

The total amount of bottom steel $M_x^{*} + M_y^{*}$ at any point, is presented by the

following equation:

$$M_x^* + M_y^* = \frac{M_{xy}^2}{M_y^* - M_y} + M_x + M_y^*$$

$$\text{So that for minimum steel } \frac{d(M_x^* + M_y^*)}{d M_y^*} = 0$$

Hence

$$M_y^* = M_y + M_{xy}$$

Since in equation 3.17 $M_y^* > M_y$

$$M_y^* = M_y + |M_{xy}| \quad 3.22$$

By substituting equation 3.22 in 3.20 we get:

$$M_x^* = M_x + |M_{xy}| \quad 3.23$$

b- Negative moments fields:(Top Steel)

Similar procedure can be adopted to the negative yield criterion, equation 3.21, to get the following equations:

$$M_x^{*t} = M_x - |M_{xy}| \quad 3.24$$

$$M_y^{*t} = M_y - |M_{xy}| \quad 3.25$$

c- Mixed moment fields:

When calculating with the previous equations 3.22 and 3.23 if:

$M_y^* \leq 0.0$; M_y^* is considered to be equal to zero and from the yield condition 3.20 the following expression can be obtained:

$$M_x^* = M_x + \left| \frac{M_{xy}^2}{M_y} \right| \quad 3.26a$$

and if $M_x^* \leq 0.0$, from equation 3.20 the following equation can be written as:

$$M_y^* = M_y + \left| \frac{M_{xy}^2}{M_x} \right| \quad 3.26b$$

The same procedures can be adopted for the negative moment fields, and the corresponding expressions are:

$$M_x^{*t} = M_x - \left| \frac{M_{xy}^2}{M_y} \right| \quad 3.27a$$

$$M_y^{*t} = M_y - \left| \frac{M_{xy}^2}{M_x} \right| \quad 3.27b$$

3.2.2.3 Rules for Placing Reinforcement:

At any point of the slab, given the trial stress field (M_x , M_y , M_{xy}) the reinforcement in x and y directions will be placed according to the following rules:

a– Bottom steel:

- i– Compute the design moment M_x^* and M_y^* from equation 3.23 and 3.22 respectively.
- ii– If both M_x^* and M_y^* are negative, then no reinforcement is needed at the bottom.
- iii– If both M_x^* and M_y^* are positive, the calculated values are adopted as the resistant moments.
- iv– If $M_x^* < 0.0$ then set $M_x^* = 0.0$ and compute M_y^* from equation 3.26b.

v- If $M_y^* < 0.0$ then set $M_y^* = 0.0$ and compute M_x^* from equation 3.26a.

b- Top steel:

The same procedure is adopted for top steel by changing negative sign to positive.

i- Compute the design moment M_x^{*t} and M_y^{*t} from equation 3.24 and 3.25 respectively.

ii- If both M_x^{*t} and M_y^{*t} are positive, then no reinforcement is needed at the top.

iii- If both M_x^{*t} and M_y^{*t} are negative, the calculated values are adopted as the resistant moments.

iv- If $M_x^{*t} > 0.0$ then set $M_x^{*t} = 0.0$ and compute M_y^{*t} from equation 3.27b.

v- If $M_y^{*t} > 0.0$ then set $M_y^{*t} = 0.0$ and compute M_x^{*t} from equation 3.27a.

3.2.3 Inplane Problems:

With regard to the problem of inplane forces, Nielsen(73) has presented the yield criterion for a section having known orthogonal isotropic or orthotropic reinforcement which can carry either tension or compression and is symmetrically placed with respect to the middle surface of the section. He derived the equations for the determination of the orthogonal tension reinforcement to resist a particular inplane force triad. Nielsen(75) has also considered the case of skew tension reinforcement. In his work he assumed that the concrete has sufficient compressive strength such that no compression reinforcement is required. If the compressive strength of the concrete section is violated, ^{the} concrete section must be increased. Subedi(76) presented a graphical approach to design compression reinforcement. It was Clark(78) who finally presented equations for proportioning skew or orthogonal tension and/or compression reinforcement to resist a triad of

inplane forces. Using elastic stress field, Clark's equations were used by Lin(79), Memon(80) and Khaskheli(81) for the design of deep beams, perforated deep beams and transfer girders respectively.

3.2.3.1 Derivation of Yield Criteria:

Let the principal stresses in the concrete element be σ_1 and σ_2 (fig. 3.8) with the major principal stress at θ to the x axis. Let the area of reinforcement, per unit length in the x and y direction, be A_x and A_y and their associated stresses f_x and f_y . From equilibrium of the reinforced concrete element, (fig. 3.8), of thickness t under the external inplane normal and shear forces per unit length n_x n_y n_{xy} (fig. 3.7) the three following equations can be written for orthogonal reinforcement as:

$$n_x = A_x f_x + \sigma_1 t \cos^2 \theta + \sigma_2 t \sin^2 \theta \quad 3.28$$

$$n_y = A_y f_y + \sigma_1 t \sin^2 \theta + \sigma_2 t \cos^2 \theta \quad 3.29$$

$$n_{xy} = - \sigma_1 t \cos \theta \sin \theta + \sigma_2 t \cos \theta \sin \theta \quad 3.30$$

If we take:

$$\sigma_x = \frac{n_x}{t}, \quad \sigma_y = \frac{n_y}{t}, \quad \tau_{xy} = \frac{n_{xy}}{t}$$

and
$$\sigma_x^* = \frac{A_x f_x}{t}, \quad \sigma_y^* = \frac{A_y f_y}{t}$$

Where σ_x , σ_y and τ_{xy} are the normal and shear stresses.

σ_x^* , σ_y^* are the resistant stresses provided by steel

reinforcement in x and y directions respectively.

Equations 3.28 to 3.29 can be presented as follows:

$$\sigma_x = \sigma_1 \cos^2 \theta + \sigma_2 \sin^2 \theta + \sigma_x^* \quad 3.31$$

$$\sigma_y = \sigma_1 \sin^2 \theta + \sigma_2 \cos^2 \theta + \sigma_y^* \quad 3.32$$

$$\tau_{xy} = (\sigma_2 - \sigma_1) \cos \theta \sin \theta \quad 3.33$$

Now if tensile steel is to be provided, then $\sigma_1 = 0.0$, hence the above equations become:

$$\sigma_x = \sigma_2 \sin^2 \theta + \sigma_x^* \quad 3.34$$

$$\sigma_y = \sigma_2 \cos^2 \theta + \sigma_y^* \quad 3.35$$

$$\tau_{xy} = \sigma_2 \cos \theta \sin \theta \quad 3.36$$

thus:

$$\sigma_x^* - \sigma_x = \sigma_2 \sin^2 \theta$$

$$\sigma_y^* - \sigma_y = \sigma_2 \cos^2 \theta$$

$$\tau_{xy} = \sigma_2 \cos \theta \sin \theta$$

Eliminating σ_2 and θ from the above equations we have:

$$(\sigma_x^* - \sigma_x)(\sigma_y^* - \sigma_y) - \tau_{xy}^2 = 0.0 \quad 3.37$$

This is the yield criterion derived by Nielsen(73) for a section having known orthogonal isotropic or orthotropic reinforcement carrying tension forces and symmetrically placed with respect to the middle surface of the section. Nielsen assumed that the concrete had sufficient compressive strength so as not to require compression reinforcement. Nielsen also developed design equations for four different cases of reinforcement design. Later Clark(78) introduced the compressive reinforcement by extending these later four cases to nine cases for different combination of stresses. Table 3.1 shows the possible combination of reinforcement. From this table it can be noticed that all the cases can be solved by direct solution except for cases 1 and 4 where the minimisation of the total reinforcement in both directions of the member is necessary. The principal stress

σ_1 is considered equal to zero when tension reinforcement is required and σ_2 equal to the concrete compressive strength f_c when the compressive reinforcement is required. The way, the design equations were developed, is presented in the following section.

3.2.3.2 Derivation of Design Equations:

a- Cases where tensile steel is to be provided:

Case 1: $\sigma_x^* > 0$ and $\sigma_y^* > 0$

Since in equation 3.37, $\sigma_y^* = \sigma_y + \frac{\tau_{xy}^2}{(\sigma_x^* - \sigma_x)}$

The total provided steel in x direction is minimum when:

$$\frac{d}{d\sigma_x^*} (\sigma_x^* + \sigma_y^*) = 0$$

$$\text{Thus: } \frac{d}{d\sigma_x^*} \left(\sigma_x^* + \sigma_y + \frac{\tau_{xy}^2}{(\sigma_x^* - \sigma_x)} \right) = 1 - \frac{\tau_{xy}^2}{(\sigma_x^* - \sigma_x)^2} = 0$$

$$\therefore \text{ Since } \sigma_x^* > \sigma_x, \sigma_x^* = \sigma_x + |\tau_{xy}|$$

$$\text{The steel ratio is: } \rho_x = 1/f_s (\sigma_x + |\tau_{xy}|)$$

$$\text{Similarly } \rho_y = 1/f_s (\sigma_y + |\tau_{xy}|)$$

Case 2: $\sigma_x^* = 0$ and $\sigma_y^* > 0$

$$\text{Directly from equation 3.37 we get } \sigma_y^* = \sigma_y - \frac{\tau_{xy}^2}{\sigma_x}$$

Hence

$$\rho_x = 0$$

$$\rho_y = 1/f_s \left(\sigma_y - \frac{\tau_{xy}^2}{\sigma_x} \right)$$

Case 3: $\sigma_x^* > 0$ and $\sigma_y^* = 0$

Similar to case 2: $\rho_x = 1/f_s \left(\sigma_x - \frac{\tau_{xy}^2}{\sigma_y} \right)$

$$\rho_x = 0$$

b- Cases where compression steel is to be provided:

In this case the minor principal stress in the concrete reaches the concrete strength, thus $\sigma_2 = -f_{cu}$ and $\sigma_1 < 0.0$. Equations 3.31 to 3.33 can be written as follows:

$$\sigma_x = \sigma_1 \cos^2 \theta - f_{cu} \sin^2 \theta + \sigma_x^* \quad 3.38$$

$$\sigma_y = \sigma_1 \sin^2 \theta - f_{cu} \cos^2 \theta + \sigma_y^* \quad 3.39$$

$$\tau_{xy} = (-f_{cu} - \sigma_1) \cos \theta \sin \theta \quad 3.40$$

thus:

$$\sigma_x + f_{cu} = \sigma_1 \cos^2 \theta + f_{cu} \cos^2 \theta + \sigma_x^* \quad 3.41$$

$$\sigma_y + f_{cu} = \sigma_1 \sin^2 \theta + f_{cu} \sin^2 \theta + \sigma_y^* \quad 3.42$$

$$\tau_{xy} = (-f_{cu} - \sigma_1) \cos \theta \sin \theta \quad 3.43$$

hence:

$$\sigma_x + f_{cu} - \sigma_x^* = (\sigma_1 + f_{cu}) \cos^2 \theta$$

$$\sigma_y + f_{cu} - \sigma_y^* = (\sigma_1 + f_{cu}) \sin^2 \theta$$

$$\tau_{xy} = -(\sigma_1 + f_{cu}) \cos \theta \sin \theta$$

$$\therefore -(\sigma_x + f_c - \sigma_x^*)(\sigma_y + f_c - \sigma_y^*) + \tau_{xy}^2 = 0.0 \quad 3.44$$

In the following: $\sigma_{xf} = \sigma_x + f_c$ and $\sigma_{yf} = \sigma_y + f_c$

Case 4: $\sigma_x^* < 0$ and $\sigma_y^* < 0$

$$\text{From equation 3.44, } \sigma_y^* = + \sigma_{yf} - \frac{\tau_{xy}^2}{(\sigma_{xf} - \sigma_x^*)}$$

Case 3: $\sigma_x^* > 0$ and $\sigma_y^* = 0$

Similar to case 2:
$$\rho_x = 1/f_s \left(\sigma_x - \frac{\tau_{xy}^2}{\sigma_y} \right)$$

$$\rho_x = 0$$

b- Cases where compression steel is to be provided:

In this case the minor principal stress in the concrete reaches the concrete strength, thus $\sigma_2 = -f_{cu}$ and $\sigma_1 < 0.0$. Equations 3.31 to 3.33 can be written as follows:

$$\sigma_x = \sigma_1 \cos^2 \theta - f_{cu} \sin^2 \theta + \sigma_x^* \quad 3.38$$

$$\sigma_y = \sigma_1 \sin^2 \theta - f_{cu} \cos^2 \theta + \sigma_y^* \quad 3.39$$

$$\tau_{xy} = (-f_{cu} - \sigma_1) \cos \theta \sin \theta \quad 3.40$$

thus:

$$\sigma_x + f_{cu} = \sigma_1 \cos^2 \theta + f_{cu} \cos^2 \theta + \sigma_x^* \quad 3.41$$

$$\sigma_y + f_{cu} = \sigma_1 \sin^2 \theta + f_{cu} \sin^2 \theta + \sigma_y^* \quad 3.42$$

$$\tau_{xy} = (-f_{cu} - \sigma_1) \cos \theta \sin \theta \quad 3.43$$

hence:

$$\sigma_x + f_{cu} - \sigma_x^* = (\sigma_1 + f_{cu}) \cos^2 \theta$$

$$\sigma_y + f_{cu} - \sigma_y^* = (\sigma_1 + f_{cu}) \sin^2 \theta$$

$$\tau_{xy} = -(\sigma_1 + f_{cu}) \cos \theta \sin \theta$$

$$\therefore -(\sigma_x + f_c - \sigma_x^*)(\sigma_y + f_c - \sigma_y^*) + \tau_{xy}^2 = 0.0 \quad 3.44$$

In the following: $\sigma_{xf} = \sigma_x + f_c$ and $\sigma_{yf} = \sigma_y + f_c$

Case 4: $\sigma_x^* < 0$ and $\sigma_y^* < 0$

From equation 3.44,
$$\sigma_y^* = + \sigma_{yf} - \frac{\tau_{xy}^2}{(\sigma_{xf} - \sigma_x^*)}$$

Minimum provided steel when: $\frac{d}{d\sigma_x^*} (\sigma_x^* + \sigma_y^*) = 0$

Thus: $1 - \frac{\tau_{xy}^2}{(\sigma_{xf} - \sigma_x^*)^2} = 0$

∴ Since $\sigma_x^* < \sigma_{xf}$, $\sigma_x^* = \sigma_{xf} - |\tau_{xy}|$

The steel ratio is: $\rho_x = 1/f_s' (\sigma_{xf} - |\tau_{xy}|)$

Similarly $\rho_y = 1/f_s' (\sigma_{yf} - |\tau_{xy}|)$

Case 5: $\sigma_x^* = 0$ and $\sigma_y^* < 0$

Directly from equation 3.44 we get $\sigma_y^* = \sigma_{yf} - \frac{\tau_{xy}^2}{\sigma_{xf}}$

Hence

$$\rho_x = 0$$

$$\rho_y = 1/f_s' \left(\sigma_{yf} - \frac{\tau_{xy}^2}{\sigma_{xf}} \right)$$

Case 6: $\sigma_x^* < 0$ and $\sigma_y^* = 0$

Same as case 5: $\rho_x = 1/f_s' \left(\sigma_{xf} - \frac{\tau_{xy}^2}{\sigma_{yf}} \right)$

$$\rho_y = 0$$

c- Mixed cases: σ_x^* and σ_y^* are of different signs:

Case 7: $\sigma_x^* > 0$ and $\sigma_y^* < 0$

$\sigma_1 = 0$ and $\sigma_2 = f_c$ thus equations 3.31 to 3.33 become:

$$\sigma_x = f_c \sin^2 \theta + \sigma_x^* = [f_c/2.0] (1 - \cos 2\theta) + \sigma_x^* \quad 3.45$$

$$\sigma_y = f_c \cos^2 \theta + \sigma_y^* = [f_c/2.0] (1 + \cos 2\theta) + \sigma_y^* \quad 3.46$$

$$\tau_{xy} = f_c \sin \theta \cos \theta = [f_c/2.0] \sin 2\theta \quad 3.47$$

From equation 3.41 $\beta = \cos 2\theta = \sqrt{1 - \frac{2\tau_{xy}^2}{f_c}}$.

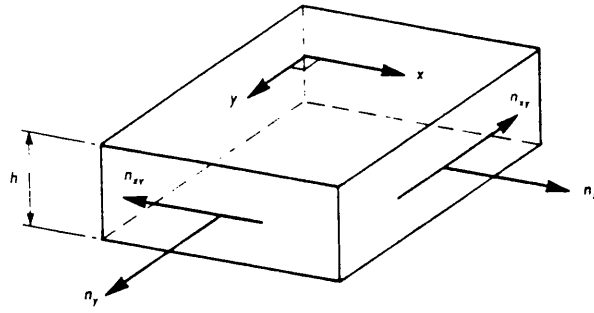


Fig. 3.7 Sign Convention for Inplane Normal and Shear Forces per Unit Length

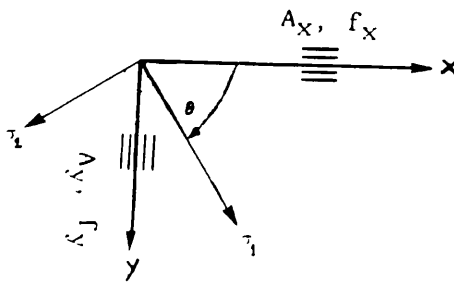


Fig. 3.8 Principal Concrete Stresses and Reinforcement Directions.

Case	Reinforcement description	Known values	Method of solution
1	Both tension	$f_x = f_\alpha = f_s, \sigma_1 = 0$	Minimization of $(\rho_x + \rho_\alpha)$
2	No x α tension	$f_\alpha = f_s, \rho_x = 0, \sigma_1 = 0$	Direct solution
3	No α x tension	$f_x = f_s, \rho_\alpha = 0, \sigma_1 = 0$	Direct solution
4	Both compression	$f_x = f_\alpha = f'_s, \sigma_2 = f_c$	Minimization of $(\rho_x + \rho_\alpha)$
5	No x α compression	$f_\alpha = f'_s, \rho_x = 0, \sigma_2 = f_c$	Direct solution
6	No α x compression	$f_x = f'_s, \rho_\alpha = 0, \sigma_2 = f_c$	Direct solution
7	x tension α compression	$f_x = f_s, f = f'_s, \sigma_1 = 0, \sigma_2 = f_c$	Direct solution
8	x compression α tension	$f_x = f'_s, f = f_s, \sigma_1 = 0, \sigma_2 = f_c$	Direct solution
9	No reinforcement	$\rho_x = \rho_\alpha = 0$	Direct solution

Table 3.1 Possible Combinations of Reinforcement.

Curve	Equation	Curve	Equation
1	$\frac{\sigma_y}{ \tau_{xy} } = +\infty$	7	$\frac{\sigma_x}{ \tau_{xy} } = \frac{1}{2} \left(\frac{f_c}{ \tau_{xy} } - \sqrt{\left(\frac{f_c}{ \tau_{xy} } \right)^2 - 4} \right)$
2	$\frac{\sigma_x}{ \tau_{xy} } = \frac{1}{2} \left(\frac{f_c}{ \tau_{xy} } + \sqrt{\left(\frac{f_c}{ \tau_{xy} } \right)^2 - 4} \right)$	8	$\frac{\sigma_x}{ \tau_{xy} } = -1$
3	$\frac{\sigma_y}{ \tau_{xy} } = -1$	9	$\frac{\sigma_x f}{ \tau_{xy} } \frac{\sigma_y f}{ \tau_{xy} } = 1$
4	$\frac{\sigma_y}{ \tau_{xy} } = \frac{f_c}{ \tau_{xy} } + 1$	10	$\frac{\sigma_x}{ \tau_{xy} } \frac{\sigma_y}{ \tau_{xy} } = 1$
5	$\frac{\sigma_y}{ \tau_{xy} } = \frac{1}{2} \left(\frac{f_c}{ \tau_{xy} } - \sqrt{\left(\frac{f_c}{ \tau_{xy} } \right)^2 - 4} \right)$	11	$\frac{\sigma_x}{ \tau_{xy} } = \frac{f_c}{ \tau_{xy} } + 1$
6	$\frac{\sigma_y}{ \tau_{xy} } = -\infty$	12	$\frac{\sigma_x}{ \tau_{xy} } = \frac{1}{2} \left(\frac{f_c}{ \tau_{xy} } + \sqrt{\left(\frac{f_c}{ \tau_{xy} } \right)^2 - 4} \right)$

Table 3.2 Boundary Curve Equations for Orthogonal Reinforcement.

Table 3.3 Design Equations for Orthogonal reinforcement .

Case	ρ_x	ρ_y	σ_1	σ_2	$\tan \theta$
1	$\frac{1}{f_s}(\sigma_x + \tau_{xy})$	$\frac{1}{f_s}(\sigma_y + \tau_{xy})$	0	$-2 \tau_{xy} $	$-\frac{\tau_{xy}}{ \tau_{xy} }$
2	0	$\frac{1}{f_s}\left(\sigma_y - \frac{\tau_{xy}^2}{\sigma_x}\right)$	0	$\sigma_x + \frac{\tau_{xy}^2}{\sigma_x}$	$\frac{\sigma_x}{\tau_{xy}}$
3	$\frac{1}{f_s}\left(\sigma_x - \frac{\tau_{xy}^2}{\sigma_y}\right)$	0	0	$\sigma_y + \frac{\tau_{xy}^2}{\sigma_y}$	$\frac{\tau_{xy}}{\sigma_y}$
4	$\frac{1}{f_s'}(\sigma_{xf} - \tau_{xy})$	$\frac{1}{f_s'}(\sigma_{yf} - \tau_{xy})$	$f_c + 2 \tau_{xy} $	f_c	$-\frac{\tau_{xy}}{ \tau_{xy} }$
5	0	$\frac{1}{f_s'}\left(\sigma_{yf} - \frac{\tau_{xy}^2}{\sigma_{xf}}\right)$	$\sigma_x + \frac{\tau_{xy}^2}{\sigma_{xf}}$	f_c	$-\frac{\tau_{xy}}{\sigma_{xf}}$
6	$\frac{1}{f_s'}\left(\sigma_{xf} - \frac{\tau_{xy}^2}{\sigma_{yf}}\right)$	0	$\sigma_y + \frac{\tau_{xy}^2}{\sigma_{yf}}$	f_c	$-\frac{\sigma_{yf}}{\tau_{xy}}$
7	$\frac{1}{f_s}\left[\sigma_x - \frac{f_c}{2}(1 - \beta)\right]$	$\frac{1}{f_s'}\left[\sigma_y - \frac{f_c}{2}(1 + \beta)\right]$	0	f_c	$\frac{2\tau_{xy}}{f_c(1 + \beta)}$
8	$\frac{1}{f_s'}\left[\sigma_x - \frac{f_c}{2}(1 + \beta)\right]$	$\frac{1}{f_s}\left[\sigma_y - \frac{f_c}{2}(1 - \beta)\right]$	0	f_c	$\frac{2\tau_{xy}}{f_c(1 - \beta)}$
9	0	0	$\frac{\sigma_x + \sigma_y + \sqrt{(\sigma_x - \sigma_y)^2 + 4\tau_{xy}^2}}{2}$	$\frac{\sigma_x + \sigma_y - \sqrt{(\sigma_x - \sigma_y)^2 + 4\tau_{xy}^2}}{2}$	$\frac{\sigma_x - \sigma_y - \sqrt{(\sigma_x - \sigma_y)^2 + 4\tau_{xy}^2}}{2\tau_{xy}}$

Eliminating θ from equations 3.45 and 3.46 we get:

$$\sigma_x^* = \sigma_x - (f_c/2.0)(1 - \beta)$$

$$\sigma_y^* = \sigma_y - (f_c/2.0)(1 + \beta)$$

The steel ratios are : $\rho_x = 1/f_s [\sigma_x - (f_c/2)(1 - \beta)]$

$$\rho_y = 1/f'_s [\sigma_y - (f_c/2)(1 + \beta)]$$

Case 8: $\sigma_x^* < 0$ and $\sigma_y^* > 0$

Similarly to case 7: $\rho_x = 1/f'_s [\sigma_x - (f_c/2)(1 + \beta)]$

$$\rho_y = 1/f_s [\sigma_y - (f_c/2)(1 - \beta)]$$

Case 9: No steel is needed. $\rho_x = \rho_y = 0$

3.2.3.3 Derivation of the boundary curves:

To know which set of equations in table 3.3 is to be used in design, knowing the stresses (σ_x , σ_y , τ_{xy}) at any point, it is necessary to establish the equations of the boundary between the different case surfaces in stress space of horizontal axis $\sigma_x/|\tau_{xy}|$ and vertical axis $\sigma_y/|\tau_{xy}|$. Figure 3.9 shows the different case surfaces. The circled numbers in the figure represent the cases numbers. All the boundary curves were derived by equating the design equations of two considered cases. Example: for curve separating case 1 and 2 :

All points belonging to the curve between case 1 and 2 must have equal values in these two correspondent equations. Thus:

$$\rho_{x1} = \rho_{x2} \implies \sigma_x = -|\tau_{xy}| \implies \frac{\sigma_x}{|\tau_{xy}|} = -1.0$$

The same equation can be obtained by equating the expressions steel ratios of the other direction:

$$\rho_{y1} = \rho_{y2} \implies \sigma_y + |\tau_{xy}| = \sigma_y - \frac{\tau_{xy}^2}{\sigma_x} \implies \frac{\sigma_x}{|\tau_{xy}|} = -1.0$$

which is the equation of a straight line marked as number s in figure 3.9. In this way all the cases intersection boundaries were determined. Table 3.2 shows the boundary equations for orthogonal reinforcement.

For the general case of combinations of moment and inplane forces, a sandwich method of design was proposed by Brøndum—Nielsen(84), where the Nielsen's equations are applied separately to the two layers of a sandwich model of the real slab element. Morley and Gulvanessian(83) presented a general filled sandwich method for optimum design of reinforcement in a concrete slab element required to resist given combinations of membrane forces and bending moments. The method allows for concrete of the filling between the outer layers of a sandwich to resist compressive forces.

3.3 Multiple Load Cases:

The previous design equations for both plate bending and inplane problems apply only when the structure is subjected to a stress field resulting from a single load case. In practice structures are subjected to multiple load cases. An advantage of direct design method is that it can also handle multiple load cases easily. Here, the method is presented in general for plate bending and inplane problems:

- 1— For any load case i with the applied stresses S_{xi} , S_{yi} and S_{xyi} , (with $i = 1, n$ and n is the total number of loading cases), compute the corresponding resistant stress S_{xi}^* and S_{yi}^* using the appropriate equations. S_{xi}^* , S_{yi}^* can be resistant moments (bottom or top) for plate bending problems or resistant inplane stress for inplane problems, in x and y direction respectively.
- 2— At each point compute the maximum of all S_{xi}^* and S_{yi}^* for $i = 1, n$. Let these be S_{x-max}^* , S_{y-max}^* . Obviously if we use these values as the design

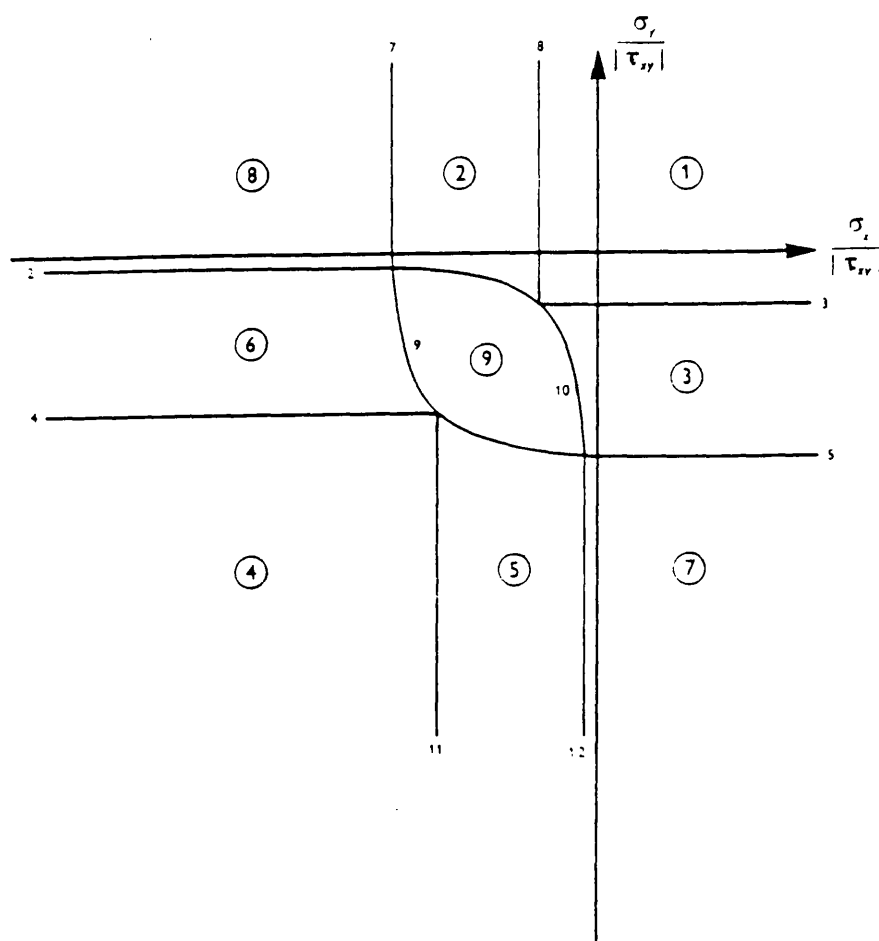


Fig. 3.9 Different Case Surfaces in Stress Space for Orthogonal Reinforcement. $f_{cu} = -4 |\tau_{xy}|$

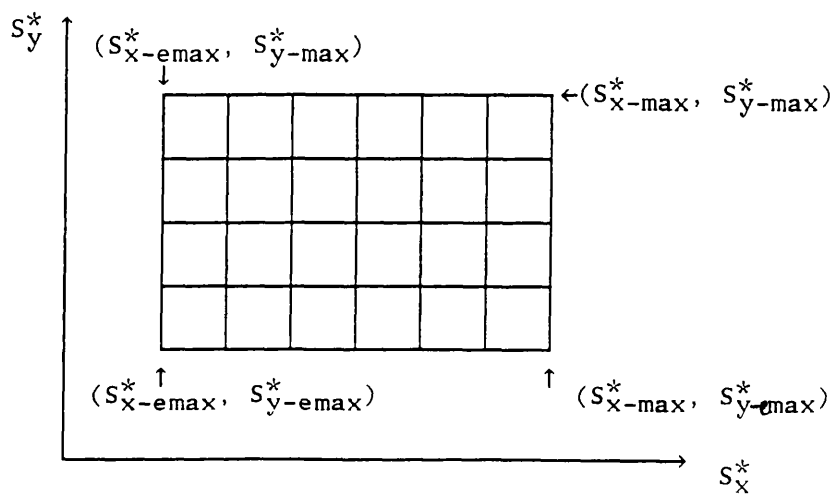


Fig. 3.10 Simple Search Technique

stresses, then we will get a safe design but not necessarily an economic one. So to move to an optimum design the following procedure can be adopted.

3- Assume that in x direction we provide $S_{x-\max}^*$, but in y direction we provide S_y^* so to satisfy the corresponding yield criterion in each case. For example for bottom steel of plate bending problems the yield criterion to be used is equation 3.20.

Calculate the maximum of all these S_{yi}^* , let it be $S_{y-\max}^*$. Evidently a safe design is produced if we use $S_{x-\max}^*$ in conjunction with $S_{y-\max}^*$.

4- The same procedure as (3) can be adopted for $S_{y-\max}^*$ to calculate the corresponding maximum $S_{x-\max}^*$ so to satisfy the appropriate yield criterion, for each load case. Therefore a better design is to choose a set of design moment where the sum $(S_x^* + S_y^*)$ is the smallest.

We can stop at this stage but if need be we can improve on this by assuming that other possible combinations are possible and use a simple search technique by examining the feasible design region as shown in figure 3.10.

For each load case, we see if the design stress at the grid points is a better minimum. If it is not, we reject it. If it is check to see if it violates the yield criteria. If it does, reject it, if not we see at which grid point in figure 3.10 is better minimum of $(S_x^* + S_y^*)$. This definitely gives us the optimum design steel volume.

Chapter 4

The Finite Element Method

4.1 Introduction:

In the previous chapter, rules have been established for designing of reinforced concrete plate bending and beam inplane problems for a given stress triad. The stress triad is obtained using a finite element program. In this chapter the finite element method will be described. Nowadays there are numerous texts (2,3,4,5,6,7), which describe finite element methods and their applications. For reinforced concrete in particular, the phenomena of cracking, nonlinear multiaxial behaviour and other effects can now be considered more rationally. In this work, the method is used not only for designing of slabs and deep beams but also to carryout a detailed nonlinear analysis of the experimental models.

4.2 Finite Element Concept and Formulation:

As the standard procedure of finite element analysis is well known only a brief review of the method is presented.

4.2.1 Discretisation by Finite Element:

In any numerical approach an approximate solution is attempted by assuming

that the continuum can be represented by finite number of element of simple geometric shapes. The elements are connected at a finite number of points. This process is known as discretisation. In the finite element displacement approach, the displacements at any point within an element are dependent only upon the unknown nodal displacements as follows:

$$\{\delta\} = [N] \{\delta^e\} \quad 4.1$$

$[N]$ denotes a rectangular matrix containing the shape functions that relate displacements $\{\delta\}$ at any point within an element to its nodal displacements $\{\delta^e\}$.

For structural applications, the governing equilibrium equations can be obtained by minimizing the total energy of the system. The total potential energy can be expressed as:

$$\begin{aligned} \Pi_S = & \frac{1}{2} \int_V \{\sigma\}^T \{\epsilon\} dv - \int_V \{\delta\}^T \{b\} dv - \int_S \{\delta\}^T \{q\} ds \\ & - \{\delta\}^T \{p\} \end{aligned} \quad 4.2$$

where $\{\sigma\}$ and $\{\epsilon\}$ are the stress and strain vectors respectively, $\{b\}$ is the body forces per unit volume, $\{q\}$ is the applied surface load and $\{p\}$ are concentrated forces. v and s stands for volume and surface respectively. Π_S represent the total potential energy.

The first term of the right hand side of equation 4.2 represents the strain energy of internal stresses, the second, the third and the fourth are the loss of potential of body forces, distributed surface load and concentrated loads respectively. Integrations are taken over the whole structure and will be the energy contribution of each individual element, thus:

$$\Pi_S = \sum_{i=1}^n \Pi_e \quad 4.3$$

π_e represents the total potential energy of the i^{th} element which can be written as:

$$\begin{aligned} \pi_e = & \frac{1}{2} \int_{ve} \{\delta^e\}^T [B]^T [D] [B] \{\delta^e\} dv - \int_{ve} \{\delta^e\}^T [N]^T \{b\} dv \\ & - \int_{se} \{\delta^e\}^T [N]^T \{q\} ds - \{\delta^e\}^T \{P\} \end{aligned} \quad 4.4$$

where ve and se are volume and surface of element respectively. $[B]$ is the strain matrix generally composed of derivatives of shape functions. $[D]$ is linear elastic or elasto-plastic material stress strain matrix.

Minimizing the potential energy results in:

$$\begin{aligned} \frac{\partial \pi_e}{\partial \delta^e} = & \int_{ve} [B]^T [D] [B] \{\delta^e\} dv - \int_{ve} [N]^T \{b\} dv \\ & - \int_{se} [N]^T \{q\} ds - \{P\} \end{aligned} \quad 4.5$$

The total potential energy π_s of the system is minimum, when:

$$\frac{\partial \pi_s}{\partial \delta} = 0.0 \quad 4.6$$

The equivalent nodal forces for the element are:

$$\{F_e\} = + \int_{ve} [N]^T \{b\} dv + \int_{se} [N]^T \{q\} ds + \{P\} \quad 4.7$$

and the element stiffness matrix is:

$$[K_e] = \int_{ve} [B]^T [D] [B] dv \quad 4.8$$

The summation of the terms in equation 4.5 over all elements results in:

$$\frac{\partial \pi_s}{\partial \delta} = [K_s] \{\delta\} - \{F_s\} \quad 4.9$$

where $\{F_s\}$ and $[K_s]$ are the global loading vector and structural stiffness matrix respectively.

Equating the right side of equations 4.6 and 4.9, gives the following expression:

$$[K_s] \{\delta\} - [F_s] = 0.0 \quad 4.10$$

After the insertion of the necessary boundary conditions, equation 4.10 is then solved by any standard technique to yield the nodal displacements.

$$\{\delta\} = [K_s]^{-1} \{F_s\} \quad 4.11$$

Once the displacement are determined, the strain and thereafter the stress in each element can be evaluated using the following equations:

$$\{\epsilon\} = [B] \{\delta\} \quad 4.12a$$

$$\{\sigma\} = [D] \{\epsilon\} \quad 4.12b$$

4.2.2 Layer Approach:

For flexural deformation, material property variation through the thickness must be taken into account. This can be accomplished in a discretized fashion via a layering approach, where the plate thickness is divided into a finite number of layers parallel to the middle plane of the plate fig. 4.1, or by the introduction of numerical integration points through the thickness.

The layer concept was adopted in the literature by many research workers, Johnarry(42), Hago and Bhatt(69) using a rectangular element with five degrees of

freedom $(u, v, w, \theta_x, \theta_y)$. Later Abdel Hafez(43) used an isotropic eight noded element with five degree of freedom. All reported good agreement with experimental results. So the last model was adopted in this present study.

4.2.2.1 Basic Assumptions:

In this model, each layer is supposed to be in a state of plane stress condition, and a linear strain variation with the depth is assumed based on the small deflection theory. The layers are allowed to resist the transverse shear stress fig 4.2. The variation of the stress through the thickness of a layer is ignored. Each layer can be of a different material, thus for a reinforced concrete element, each constituent material is assigned a different layer. Perfect bond between all layers is normally assumed.

For plate bending cases these assumptions are made:

- i- Displacement are small compared to the dimension of the plates.
- ii- The stress normal to the plate are negligible.
- iii- The Normal to the reference surface deformation remains straight but not necessarily normal to the reference surface after deformation fig. 4.3.

4.2.2.2 Displacement Representation:

Using the above assumptions, displacements u, v, w at any point in the structure with coordinates (x, y, z) can be expressed as:

$$\begin{Bmatrix} u \\ v \\ w \end{Bmatrix} = \begin{Bmatrix} u_0(x, y) - z \theta_x(x, y) \\ v_0(x, y) - z \theta_y(x, y) \\ w_0(x, y) \end{Bmatrix} \quad 4.13$$

where u_0, v_0, w_0 are the displacement at the plate reference surface, figure 4.3. in the x, y, z directions respectively. θ_x, θ_y are the rotations of the normal in

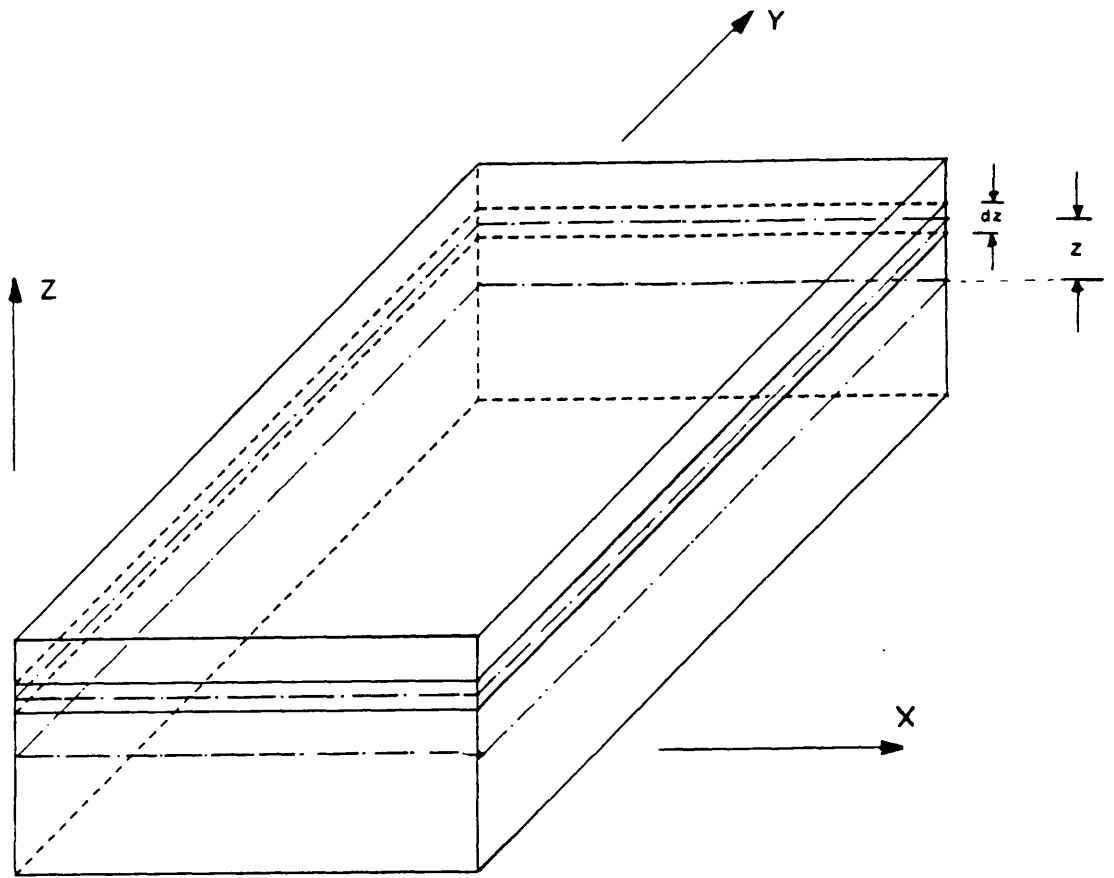


Fig. 4.1 Layer Idealization.

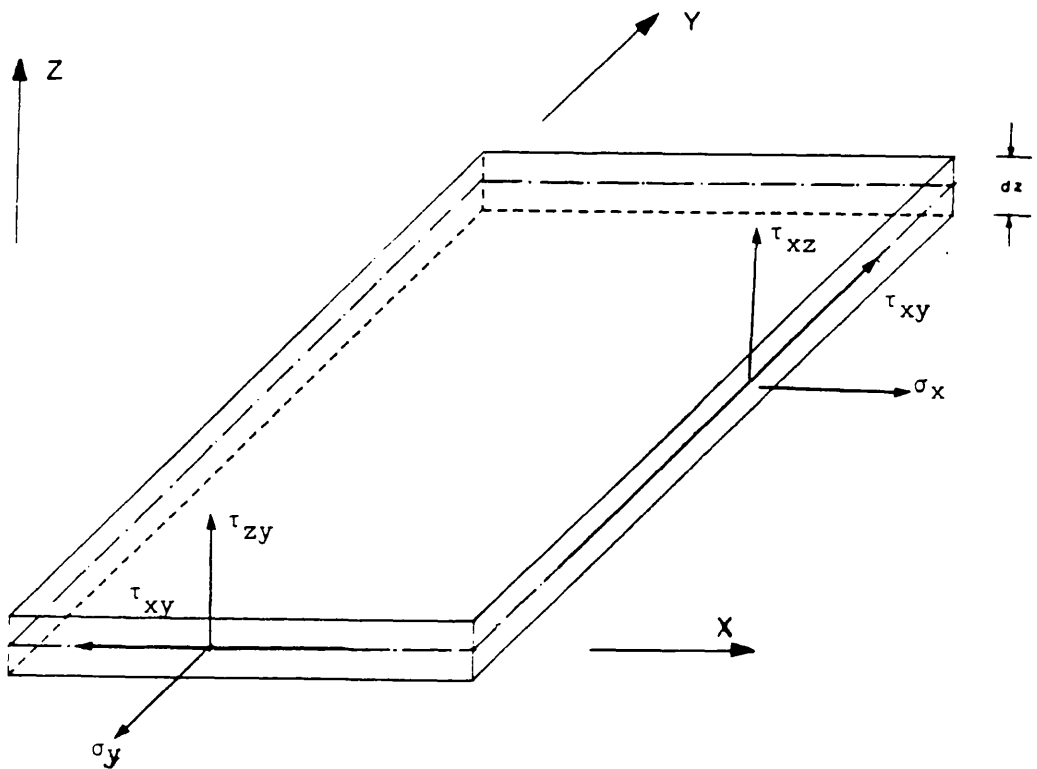


Fig. 4.2 Layer Plate Model, Stress Sign Convention.

(Positive as shown).

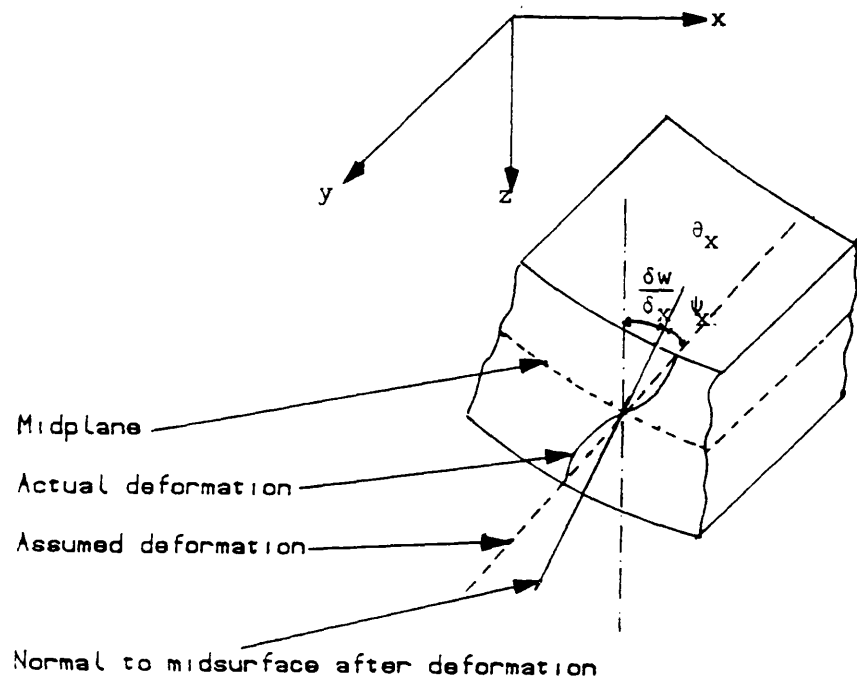


Fig. 4.3 Cross Section Deformation of Mindlin Plate.

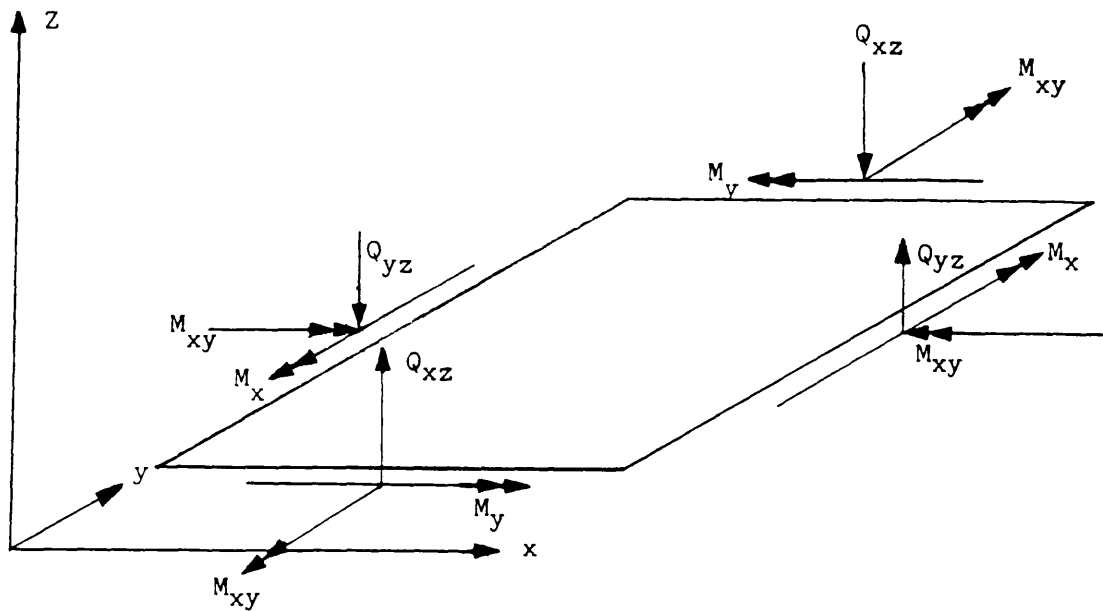


Fig. 4.4 A Typical Mindlin Plate (Positive as shown).

xz and yz plane respectively. z is the distance from the reference surface to the mid-plane of the layer under consideration.

The rotations are determined as follows:

$$\begin{bmatrix} \theta_x \\ \theta_y \end{bmatrix} = \begin{bmatrix} \frac{\partial w(x,y)}{\partial x} + \Phi_x(x,y) \\ \frac{\partial w(x,y)}{\partial y} + \Phi_y(x,y) \end{bmatrix} \quad 4.14$$

Φ_x and Φ_y denote the shear deformations, figure 4.3.

Since in this study the same finite element program was adopted for both plate bending and inplane nonlinear analysis problems, the displacement vector, for inplane problems, is composed only of u and v with z kept equal to zero.

4.2.3 Shape Functions:

Using the finite element idealization, the displacement vector at any point in an eight node isoparametric element is given by the expression:

$$\delta = \sum_{i=1}^8 N_i \delta_i \quad 4.15$$

Where N_i is the shape function of node i and δ_i is the vector of the nodal displacements at node i . The shape functions are given in terms of the local coordinates (ξ, η) , where on the edges of an isoparametric element the values of ξ and η are ± 1 , figure 4.5. Therefore the displacement δ at any point within the element can be expressed as follow:

$$\delta(\xi, \eta) = \sum_{i=1}^8 N_i(\xi, \eta) \delta_i \quad 4.16$$

4.2.4 Strain Displacement Relationship:

Once the nodal displacement are expressed in terms of shape functions, the strain within the element can be expressed in terms of displacements or their derivatives. In the two dimensional analysis based on the Mindlin plate bending and plane stress assumption, the strain displacement relationship may be written as:

$$\begin{Bmatrix} \epsilon_x \\ \epsilon_y \\ \gamma_{xy} \\ \gamma_{xz} \\ \gamma_{yz} \end{Bmatrix} = \begin{bmatrix} \frac{\partial N_i}{\partial x} & 0 & 0 & -Z \frac{\partial N_i}{\partial x} & 0 \\ 0 & \frac{\partial N_i}{\partial y} & 0 & 0 & -Z \frac{\partial N_i}{\partial y} \\ \frac{\partial N_i}{\partial y} & \frac{\partial N_i}{\partial x} & 0 & \frac{\partial N_i}{\partial y} & \frac{\partial N_i}{\partial x} \\ \hline 0 & 0 & C \frac{\partial N_i}{\partial x} & -CN_i & 0 \\ 0 & 0 & C \frac{\partial N_i}{\partial y} & 0 & -CN_i \end{bmatrix} \begin{Bmatrix} u_i \\ v_i \\ \theta_{xi} \\ \theta_{yi} \end{Bmatrix} \quad 4.17$$

in which ϵ_x , ϵ_y and γ_{xy} are the inplane strains components. γ_{xz} and γ_{yz} are the transversal shear strain components. Z is the distance from the reference plane to the layer centre, as shown in figure 4.1. C is the shear strain coefficient which depends on the shape of the cross section(5), and assumed to be equal to 1.0. Strain displacement can be presented in a simple form:

$$\{\epsilon\} = \sum_{i=1}^n B_i \{\delta_i\} \quad 4.18$$

where B_i is the 5x5 matrix which contains cartesian derivatives of the shape functions. B_i can be written as:

$$B_i = \begin{bmatrix} B_{pi} & B_{fi} \\ \hline 0 & B_{si} \end{bmatrix} \quad 4.19$$

B_{pi} is the strain matrix associated with plane stress deformation. It is the one

which is used for plate bending and inplane problems. B_{fi} is the strain matrix associated with the flexural deformation. B_{si} is the strain matrix associated with the shear deformation. The two strain matrices B_{fi} and B_{si} are used for plate bending only.

4.2.5 Cartesian Derivatives of Shape Functions:

Since the shape function N_i are defined in terms of local coordinates ξ and η of the element, transformation from local to global coordinates is required to obtain the strain matrix $[B]$. This is done by using the chain rule for differentiation to give Jacobian transformation as follows:

$$\frac{\partial N_i}{\partial \xi} = \frac{\partial N_i}{\partial x} \frac{\partial x}{\partial \xi} + \frac{\partial N_i}{\partial y} \frac{\partial y}{\partial \xi} \quad 4.20$$

$$\frac{\partial N_i}{\partial \eta} = \frac{\partial N_i}{\partial x} \frac{\partial x}{\partial \eta} + \frac{\partial N_i}{\partial y} \frac{\partial y}{\partial \eta} \quad 4.21$$

in matrix form:

$$\begin{aligned} \begin{Bmatrix} \frac{\partial N_i}{\partial \xi} \\ \frac{\partial N_i}{\partial \eta} \end{Bmatrix} &= \begin{bmatrix} \frac{\partial x}{\partial \xi} & \frac{\partial y}{\partial \xi} \\ \frac{\partial x}{\partial \eta} & \frac{\partial y}{\partial \eta} \end{bmatrix} \begin{Bmatrix} \frac{\partial N_i}{\partial x} \\ \frac{\partial N_i}{\partial y} \end{Bmatrix} = \\ &= [J] \begin{Bmatrix} \frac{\partial N_i}{\partial x} \\ \frac{\partial N_i}{\partial y} \end{Bmatrix} \quad 4.22 \end{aligned}$$

$$\therefore \begin{Bmatrix} \frac{\partial N_i}{\partial x} \\ \frac{\partial N_i}{\partial y} \end{Bmatrix} = [J]^{-1} \begin{Bmatrix} \frac{\partial N_i}{\partial \xi} \\ \frac{\partial N_i}{\partial \eta} \end{Bmatrix} \quad 4.23$$

where $[J]$ is:

$$[J] = \begin{bmatrix} \frac{\partial x}{\partial \xi} & \frac{\partial y}{\partial \xi} \\ \frac{\partial x}{\partial \eta} & \frac{\partial y}{\partial \eta} \end{bmatrix} \quad 4.24$$

Since we are following isoparametric formulation,

$$x = \sum N_i x_i \text{ and } y = \sum N_i y_i$$

$$\therefore \frac{\partial x}{\partial \xi} = \sum_{i=1}^8 \frac{\partial N_i}{\partial \xi} x_i, \quad \frac{\partial x}{\partial \eta} = \sum_{i=1}^8 \frac{\partial N_i}{\partial \eta} x_i$$

$$\therefore \frac{\partial y}{\partial \xi} = \sum_{i=1}^8 \frac{\partial N_i}{\partial \xi} y_i, \quad \frac{\partial y}{\partial \eta} = \sum_{i=1}^8 \frac{\partial N_i}{\partial \eta} y_i \quad 4.25$$

$$\text{Thus } [J] = \sum_{i=1}^8 \begin{bmatrix} \frac{\partial N_i}{\partial \xi} x_i & \frac{\partial N_i}{\partial \xi} y_i \\ \frac{\partial N_i}{\partial \eta} x_i & \frac{\partial N_i}{\partial \eta} y_i \end{bmatrix} \quad 4.26$$

where x_i and y_i are the nodal coordinates.

The inverse of Jacobian matrix is:

$$[J]^{-1} = \begin{bmatrix} \frac{\partial \xi}{\partial x} & \frac{\partial \eta}{\partial x} \\ \frac{\partial \xi}{\partial y} & \frac{\partial \eta}{\partial y} \end{bmatrix} = \frac{1}{\det J} \begin{bmatrix} \frac{\partial y}{\partial \eta} & -\frac{\partial y}{\partial \xi} \\ -\frac{\partial x}{\partial \eta} & \frac{\partial x}{\partial \xi} \end{bmatrix} \quad 4.27$$

The cartesian derivatives of the shape functions can thus be calculated from equation 4.23. They are used for the computation of the strain matrix [B] as shown in equation 4.17.

4.2.6 Stress Strain Relationship:

Using the basic theory of elasticity, the stress strain relationship, for each layer may be written in the form:

$$\{\sigma\} = [D] \{\epsilon\} \quad 4.28$$

where [D] is the elasticity matrix given by:

$$[D] = \frac{E}{1-\nu^2} \begin{bmatrix} 1 & \nu & 0 & 0 & 0 \\ \nu & 1 & 0 & 0 & 0 \\ 0 & 0 & \frac{1-\nu}{2} & 0 & 0 \\ \hline 0 & 0 & 0 & \frac{5(1-\nu)}{12} & 0 \\ 0 & 0 & 0 & 0 & \frac{5(1-\nu)}{12} \end{bmatrix} \quad 4.29$$

E and ν represent young's modulus and poisson's ratio of the concrete.

[D] matrix can also be written in the form:

$$[D] = \begin{bmatrix} D_{pi} & 0 \\ \hline 0 & D_{sj} \end{bmatrix} \quad 4.30$$

where D_{pi} is related to plane stresses and D_{sj} is related to the transverse shear stresses.

Reinforcing steel layer is assumed to be smeared into a thin layer of thickness equivalent to its total area. This smeared layer of steel is assumed to have unidirectional stiffness corresponding to the direction of its physical layout. $[D]$ matrix is given by:

$$[D] = E_s \begin{bmatrix} 1 & 0 & 0 \\ 0 & 0 & 0 \\ 0 & 0 & 0 \end{bmatrix} \quad 4.31$$

If the steel is disposed at an angle α counter clockwise, from the x -axis, the local modulus matrix is transformed to the global cartesian axis.

4.2.7 Element Stiffness Matrix and Force Vector:

For elastic material behaviour, all the information required to evaluate the element stiffness matrix $[K]$ has been given previously so that it will be as follows:

$$[K] = \sum_{i=1}^n \int \int [B]^T [D] [B] \, dx \, dy \, t_i \quad 4.32$$

where t_i is the thickness of the i^{th} layer, n is the total number of layers, $[B]$ is the strain matrix and $[D]$ is the material constitutive matrix depending on the type of the material (concrete or steel) and the state of the stress (elastic, cracked, plastic etc...). In the next chapter the material constitutive matrix in the nonlinear range will be described.

Numerical integration is used to evaluate the stiffness matrix given by the above expression and Gauss integration rules are chosen to carryout the integration over the element area as follows:

$$[K] = \sum_{i=1}^n \int_{-1}^1 \int_{-1}^1 [B]^T [D] [B] \det J \, d\xi \, d\eta \, t_i \quad 4.33$$

and numerically can be written as:

$$[K] = \sum_{i=1}^n \sum_{j=1}^m \sum_{k=1}^m W_j W_k [B]^T [D] [B] \det J \, t_i \quad 4.34$$

m is the number of Gauss point in each direction, n is the number of layer.

W_j, W_k are the weight coefficient corresponding to the specified Gauss point with local coordinates (ξ, η) .

The equivalent load vector at the nodes due to the effect of uniformly distributed element surface load is :

$$\{F\} = \int_S [N]^T \{q\} \, ds \quad 4.35$$

which can be written in the form:

$$\{F\} = \sum_{j=1}^m \sum_{i=1}^m W_j W_i [N]^T \{q\} \det J \quad 4.36$$

4.3 Nonlinear Solution Techniques:

If the applied loading is small compared with the ultimate load, it may be assumed that the structure behaves elastically and a linear elastic analysis can be performed to give the stress distribution in different part of the structure. If nearly full ultimate loading is considered then it is necessary to establish a full nonlinear analysis. Three procedures are usually used namely incremental, iterative and mixed.

4.3.1 Incremental Procedure:

In this procedure the load is divided into a number of equal or unequal load increment. At each step only one increment of load is added to the structure. At each stage of loading the stiffness of the structure may have a different value depending on the deformation reached and constitutive law adopted for the material as well as the method for estimating the stiffness at that stage.

The total load and displacement at any stage is given by the sum of the increments of all the loads and displacements of the previous stages. The process is repeated until the ultimate or the total load is reached. This method has the advantage that it is simple to apply but the accuracy is rather low unless the load increments are very small. The method has a serious drawback that at each step the stiffness matrix has to be assembled and the solution procedure for the linear equation has to be performed at each time. This is uneconomical in terms of computational efforts.

4.3.2 Iterative Procedure:

In the iterative procedure, the load is applied to the structure and then the displacement is adjusted in accordance with the constitutive laws until equilibrium is attained. In this method either the stiffness matrix remains constant or varies throughout a solution. One distinct advantage of this method is that the same stiffness matrix can be used at each step of iteration which involves a small amount of computing effort in each subsequent iteration step for the determination of the corresponding displacement. Other methods with variable stiffness matrix $[K]$ such as the secant method and Newton–Raphson method may have a faster convergence rate but only at the expense of having to reassemble and solve a new system of linear equations at each iteration.

4.3.3 Mixed Procedure:

In practice, usually a combination of both the incremental and iterative procedures is used. The total load is divided into a number of load increments. At every increment of load, iterative procedure is applied until convergence is obtained under that load increment. The constant stiffness procedure can be used. For nonlinear analysis of reinforced concrete structures, experience seems to indicate that relatively small load increments with fairly frequent updating of the stiffness for just a few iteration steps are required to produce the best results(36,89). In this work the modified Newton–Raphson(2) approach is used to evaluate the stiffness matrix by updating the stiffness at some chosen iteration. This algorithm gives satisfactory results for reasonable computational effort. Developments in numerical analysis and applied mathematics can be used to further improve the efficiency of solution techniques at low additional cost. Recently, a number of techniques have been introduced in order to accelerate the rate of convergence, such as the accelerated method and arc length methods(86,87,88).

4.4 Convergence Criteria:

Since in a numerical process, equilibrium conditions are unlikely to be satisfied exactly, criteria to determine convergence have to be established for objective analysis. The main purpose for reliable convergence criterion is to monitor the gradual elimination of the out-of-balance residual forces until the desired accuracy has been achieved. The convergence criteria, usually used, is based on displacement or out-of-balance forces norm and sometimes on internal strain energy. In the present work, convergence is based on out-of-balance force norms. They indicate directly how well equilibrium requirements are met(36). Since it is difficult and expensive to check the decay of residual forces for every degree of freedom, an overall evaluation of convergence is preferable. This is achieved by

using norms as follows:

$$\frac{\Delta R_i^*}{F_i^*} * 100 \leq T_c \quad 4.41$$

where :

T_c : A user prescribed convergence tolerance.

ΔR_i^* : Norm of the residuals

$$\Delta R_i^* = \sqrt{\{R_i\}^T \{R_i\}}$$

$\{R_i\}$ is the residual force vector at i^{th} iteration given by equation 4.40.

F_i^* : Norm of the total applied load.

$$= \sqrt{\{F_i\}^T \{F_i\}}$$

$\{F_i\}$ is the total applied load vector.

Fine tolerances are theoretically desirable but can be very expensive to obtain because they quite often require a large number of iterations. Steep discontinuities in material laws (cracks, yielding ...) can cause large residuals and these residuals need to be distributed. However this redistribution will cause more discontinuities in other parts of the structure and hence residuals in subsequent iterations. In such cases the rate of accumulation of residuals can be higher than the rate of distributing them. An intermediate solution is to choose a tolerance value at initial stages and increase it towards the later part of the load history. In the present study, the load increment is reduced in the cracking stages.

4.5 Basic Steps in the Nonlinear Program:

The major steps in the linear and the nonlinear analysis of a typical finite element program are:

- 1— Subdivision of the structure and representing different parts by appropriate types of finite elements.
- 2— Generation and assembly of the load vector $\{F\}$.
- 3— Generation of the element stiffness $[K_e]$.
- 4— Assembly of the structure stiffness $[K]$.
- 5— Solution for the nodal displacements $\{\delta_i\} = [K]^{-1} \{F_i\}$ and hence the strain:

$$\{\epsilon\} = \int [B]^T \{\delta_i\}$$
- 6— Determination of element stresses $\{\sigma\} = [D] \{\epsilon\}$

For nonlinear analysis:

- 7— Check for cracking, yielding, and failure.
- 8— Determination of unbalanced nodal forces.
- 9— Check for convergence.
- 10— (a) If not converged apply the unbalanced nodal forces again to the structure and go to step 3 if the stiffness is to be updated and to 5 if constant stiffness solution is adopted.
- (b) If converged apply the next load increment and go to step 2.
- 11— Stop when failure occurs or when full loading has been applied.

Figure 4.6 shows the main steps of the finite element nonlinear analysis procedure.

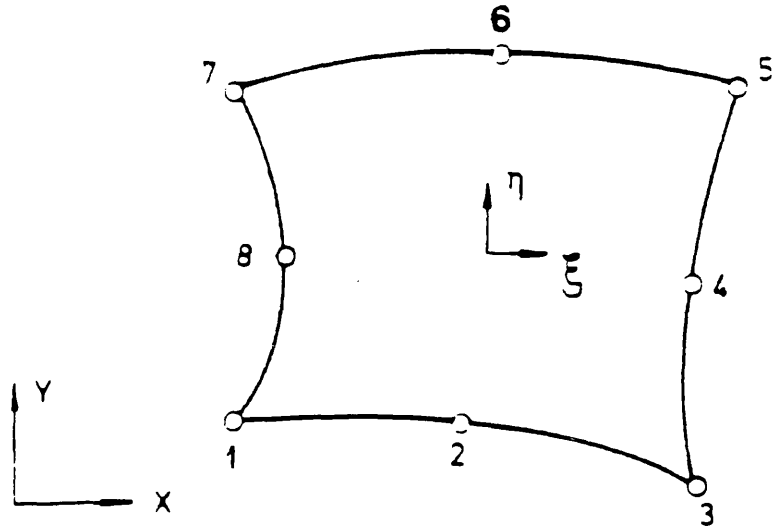


Fig. 4.5 Parabolic Isoparametric Finite Element.

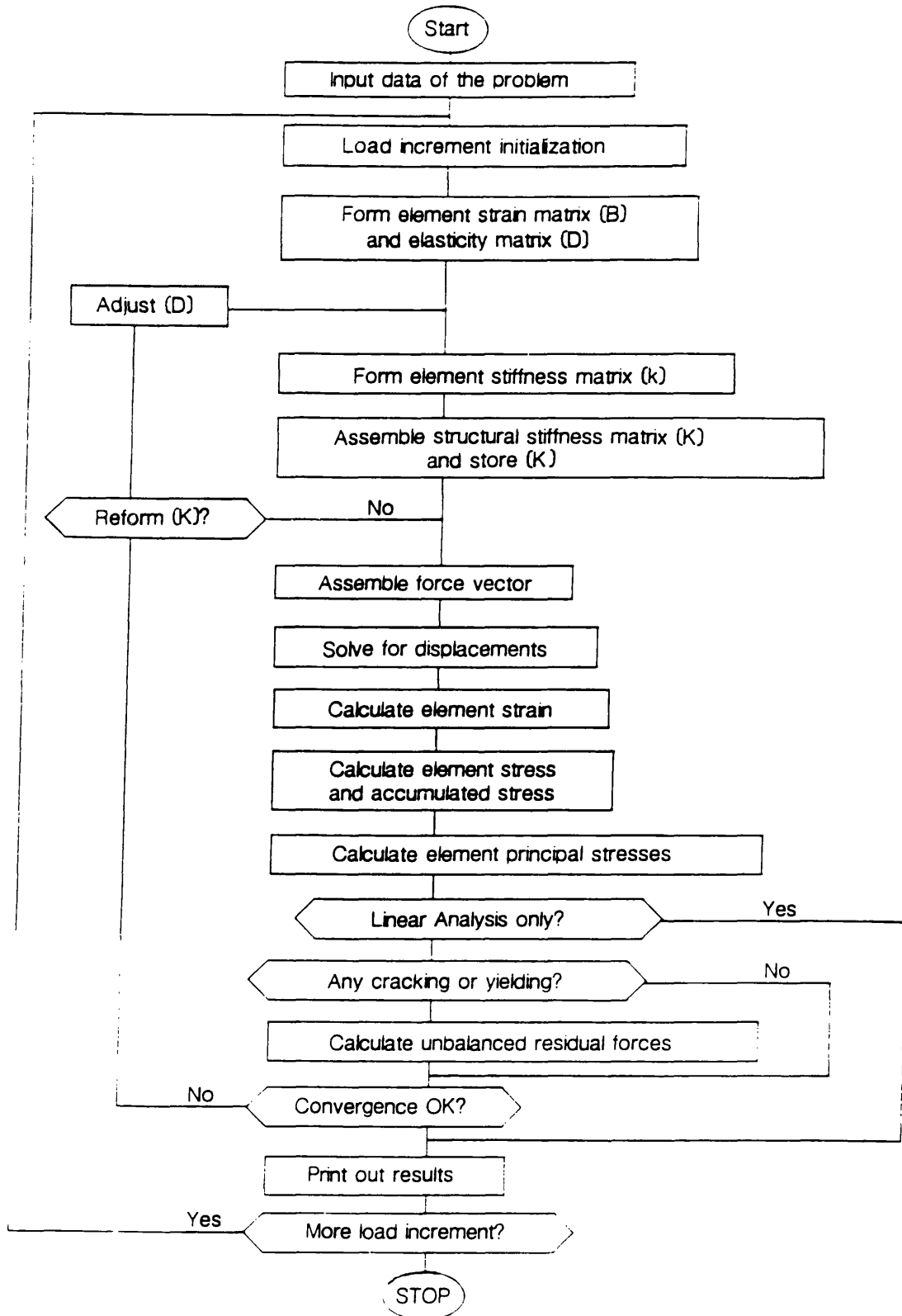


Fig. 4.6 Flow Chart for Linear and Nonlinear Reinforced Concrete Analysis.

Chapter 5

Material Modelling and Numerical Applications

5.1 Introduction:

In the present state of development of finite element computer programs, the problem of modelling the mechanical behaviour of concrete for use for analytical studies of reinforced concrete structures remains one of the most difficult challenges in the field of structural concrete. The analysis of the complete response of structural systems of steel and concrete requires consideration of a number of nonlinear effects. The most important effects include tensile cracking, yielding of steel, nonlinear material behaviour, compressive crushing of concrete, aggregate interlock, bond between concrete and steel and dowel action of reinforcing bars.

The basic information required is the multidimensional stress–strain relationships describing adequately the characteristics of reinforced concrete materials. These are called constitutive laws which describe mathematically the behaviour of constituent materials approximating closely the real behaviour. These laws are based on experimental data and allow the formulation of relationship between applied multiaxial stress state and the resulting strains. Currently the constitutive properties of concrete have not yet been universally defined and there is no generally

accepted material law which fully describes the concrete behaviour in combined stress conditions(8). The scatter of the results can be attributed to variations in three principle factors namely: i— materials tested. ii— the test method it self and iii— the loading systems.

In the following sections, the behaviour of concrete and steel is described as well as the model adopted and its applications to experimental tests for both plate bending and inplane problems.

5.2 Mechanical Behaviour of Concrete:

This section summarizes some of the facts of the experimental behaviour of plain concrete under uniaxial and biaxial states of stress.

5.2.1 Uniaxial Compressive Stress—Strain Response:

The comprehension of the behaviour of plain concrete under uniaxial stress—strain response is a useful starting point for a discussion of more complex conditions. A typical stress strain relationship for concrete under uniaxial compression is shown in figure 5.1a. The main experimental observations can be summarized as follows:

- i— The concrete has nearly linear behaviour up to 30 percent of its maximum compressive strength f'_c .
- ii— Stress above $0.3 f'_c$ shows a gradual increase in deformation up to about $0.75 f'_c$ to $0.90 f'_c$, whereupon it bends more sharply when approaching the peak strength f'_c .
- iii— Beyond the peak strength f'_c , the stress strain curve has a descending branch until crushing failure occurs at some ultimate strain (ϵ_u). This strain is in the

range of 0.003 and 0.004 approximately.

Figure 5.1b shows that the initial modulus of elasticity of concrete is highly dependent on the compressive strength. Also a high strength concrete behaves in a linear fashion to a relatively higher stress level than low strength concrete, but all peak points are located close to 0.002 strain. On the descending portion of the stress–strain curve, high strength concretes tend to behave in a more brittle manner, and the stress dropping off more sharply than it does for concrete with low strength.

Numerous mathematical expressions based on the above experimental data have been used to predict uniaxial compressive stress–strain response using curve fitting techniques. An excellent and comprehensive summary of these efforts have been presented by Popvics(10).

5.2.2 Uniaxial Tensile Stress–Strain Response:

Figure 5.2 shows the stress strain relationship for different concrete specimens tested in uniaxial tension(11). The curves are relatively linear up to a high percentage of its ultimate tensile strength f_t . Three testing methods are generally used to measure the tensile strength. They are direct, flexural and indirect, figure 5.3. Of all the indirect methods used, cylinder splitting test, figure 5.3, is the most commonly used. In this test, a concrete cylinder is laid horizontally between the loading platens of a testing machine and compressed until the specimen splits along a vertical diametrical plane.

In general the effective tensile strength of concrete is difficult to determine, despite its importance in tracing the history and the behaviour of reinforced concrete structures. It is considered as the most important criterion for the onset of cracking and the development of constitutive models.

5.2.3 Biaxial Concrete Behaviour:

Many important classes of structures can be approximated as being in a state of biaxial plane stress, such as beams, panels, and thin shells. Concrete, under different combinations of biaxial loading, exhibits stress and strain behaviour different from that under uniaxial conditions. A large amount of research has been done in recent years regarding determination of mechanical properties of concrete in biaxial loading. At present, considerable experimental data are available regarding the strength, deformational characteristics, and microcracking behaviour of concrete under biaxial stresses(15,16,17).

Figure 5.4 illustrates a typical biaxial strength envelop for concrete subjected to proportional biaxial loading. In general the maximum concrete compressive strength increases for the biaxial compression stress state fig. 5.5a. Also for biaxial compression, concrete exhibits an increased initial stiffness that may be due to Poisson's effect. Under biaxial tension, concrete exhibits a constant(17) perhaps a slightly increased(16), tensile strength, compared with values obtained under uniaxial. Under combination of compression and tension state, concrete exhibits a noticeably reduced strength. The compressive strength decreases almost linearly as the tensile strength is increased, figures 5.4 and 5.5b.

5.3 Constitutive Formulations of Concrete Modelling:

To date, procedures for the analysis and design of reinforced concrete structures have been based mainly on empirical expressions, or on some simplified rules of material properties. Constitutive laws for reinforced concrete are simple analytical formulations to fit numerically the complicated behaviour and relations between stress and strain in concrete. A large number of numerical models and techniques has been developed in an attempt to analyse different reinforced concrete structures (22,23,24,25). The state of the art ASCE 1982(22) classified the present constitutive models into the following models:

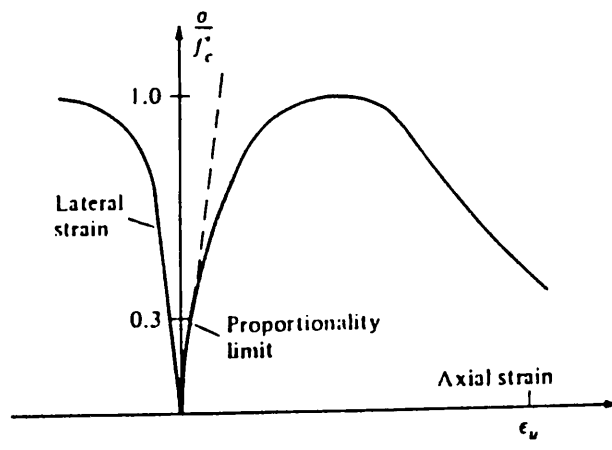


Fig. 5.1a Typical compressive stress axial and lateral strain for concrete.

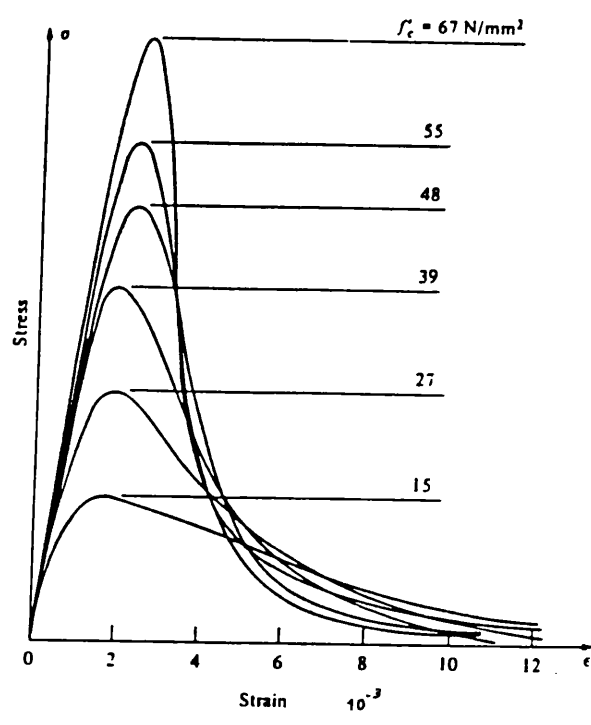


Fig. 5.1b Complete compressive stress strain curve for different compressive strengths.

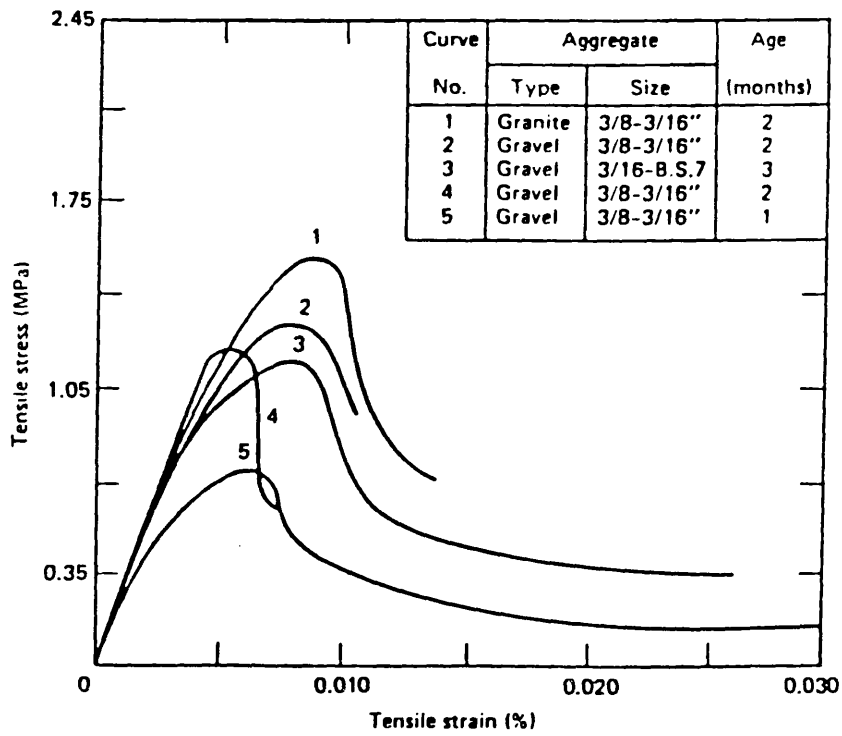


Fig. 5.2 Tensile stress-strain curves for concrete.

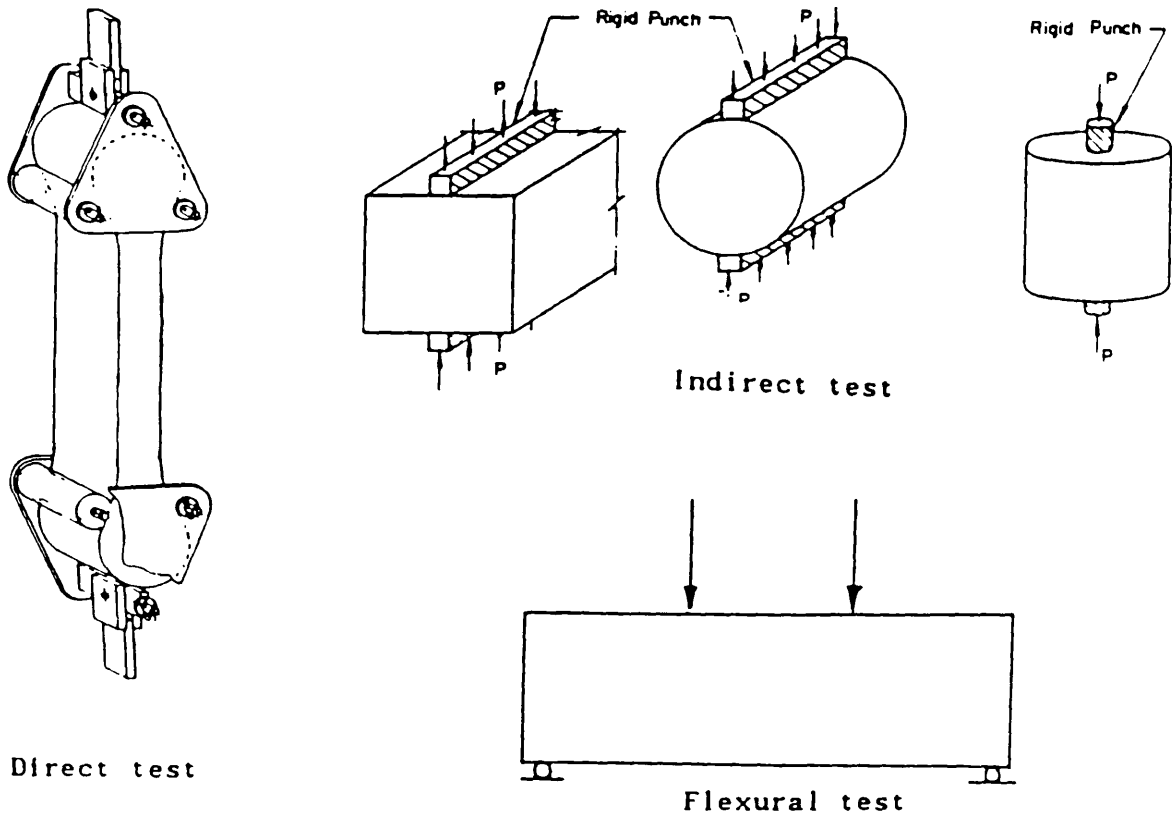


Fig. 5.3 Concrete direct, Indirect and flexural tensile strength tests.

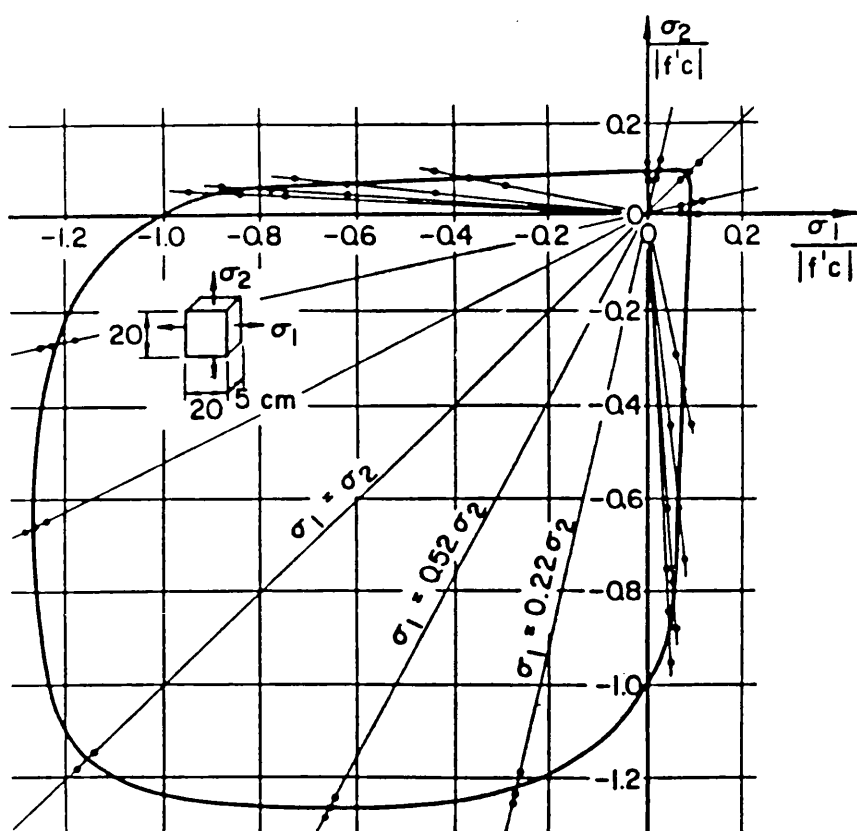
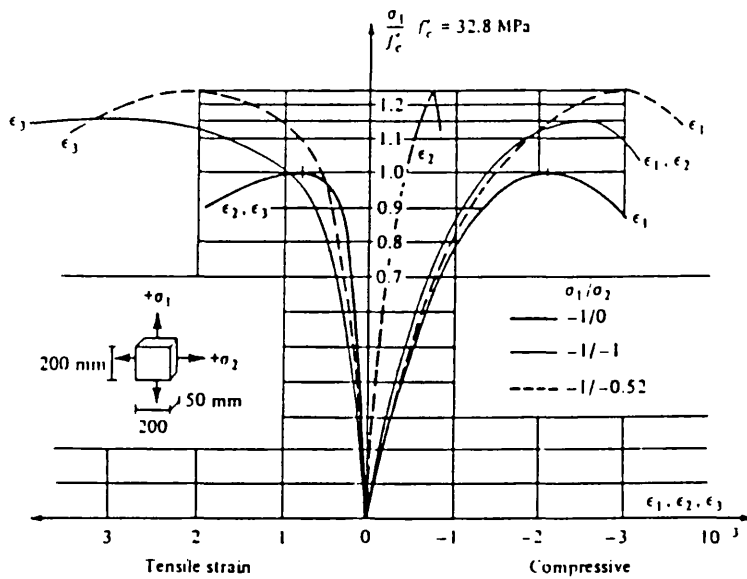
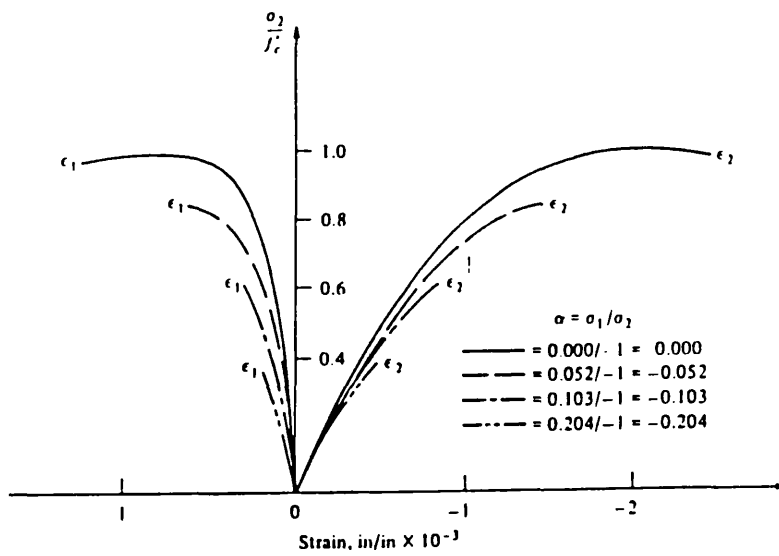


Fig. 5.4 Biaxial strength of concrete.



a- Compression-compression



b- Compression-tension

Fig. 5.5 Stress strain relationships of concrete under biaxial stress states.

- i— Elasticity based models (linear/nonlinear).
- ii— Plasticity based models.
- iii— Plastic—Fracture type models.
- iv— Endochronic models.

A brief description of the above models will be given in the following:

5.3.1 Elasticity based models:

During the past three decades, a relatively large number of elasticity—based constitutive models have been developed to represent the behaviour of concrete under general types of loading. In this model the stress strain behaviour can be expressed as either

$$\{\sigma\} = [D] \{\epsilon\} \quad 5.1$$

$$\text{or } \{d\sigma\} = [D] \{d\epsilon\} \quad 5.2$$

Where $[D]$ represents either the secant or tangential constitutive matrix. $\{\sigma\}$ and $\{\epsilon\}$ are the stress and the strain vectors, respectively.

From a purely formal point of view there is no basic difference between elasticity based models and the other models. They all result in variable increment material stiffness matrix. In the elasticity—based models, the tangential constitutive matrix is obtained or induced directly by intuitive or approximate considerations that do not use more sophisticated concepts such as flow rules, intrinsic time, etc. In general, two different approaches are employed in the formulation of the nonlinear elastic models for characterizing the degradation of concrete stiffness under loading. They are: i— finite or total material characterization in the form of secant stress—strain formulation, where the current state of stress is assumed to be uniquely determined as a function of the current state of strain. ii— Incremental or different material description in the form of tangential stress—strain models. It is often used to describe the behaviour of materials in which the state of stress depends on the current state of strain as well as on the stress path followed to reach that state.

In the present work, the elasticity—based model was adopted.

5.3.2 Plasticity based models:

Initially, the theory of plasticity was developed for metals. It has been extended recently to predict the behaviour of reinforced concrete structures. In general, models based on the theory of plasticity describe concrete as an elastic–perfectly plastic material or with allowance for some hardening as an elasto–plastic hardening material. The elastoplastic matrix is determined by specifying a yield function F , a flow rule (associated or non–associated) and a hardening rule (isotropic, kinematic or mixed). The yield function specifies the state of stresses corresponding to the beginning of plastic flow. This method has been used by many researchers by altering the von Mises criterion (26,27). Later new failure theories were therefore developed with specific application to concrete (28). It was demonstrated that the use of non–associated flow rule is necessary (29). The application of non–associated flow rule has been introduced and showed to be successful in controlling the main aspects affecting the behaviour of concrete structures(30).

5.3.3 Plastic–Fracturing Models:

The application of normality flow rule used for plastic flow of concrete does not reflect the observed behaviour in the case of fractured concrete (32). This conclusion by Andenaes (32) led to constitutive models based on the plastic–fracturing theory. This theory requires two loading surfaces depending on both stresses and strains (33). It combines plastic strain increments and fracturing stress decrements, which reflect microcracking and accounts for the degradation of elastic moduli, internal friction etc.. The disadvantage of the method is that it requires six inelastic parameters. The theory was verified (34) and gives good agreement with the experimental results.

5.3.4 Endochronic Modelling:

The endochronic theory was proposed by Valinas (18) and applied to predict the mechanical response of metals under complex strains histories. The basic concept underlying the endochronic formulations is the characterisation of the material strain state in terms of an intrinsic time. Valinas termed the materials for which the stress is a function of the strain history with respect to an intrinsic time scale as endochronic (Greek: end = inner, chronic = time). The intrinsic time is a non-decreasing scalar variable used to measure the extent of the irreversible damage of the internal structure of the concrete material, when subjected to deformation histories.

The endochronic theory was first applied to concrete by Bazant and Bhat (19,20) by extending the formulation of metals, developed by Valinas (18), to include many nonlinear features of concrete. Reddy and Gopal (21) stated that, the endochronic theory is the only constitutive theory which can model most of the nonlinear features of concrete at the present time. However Al-Manaseer(36) concluded that the method is complicated and simplifications need to be introduced so that the theory becomes more accessible.

5.4 Cracking Models:

As is well known, concrete has a low strength in tension, resulting in a cracking type of failure at early stages of loading before steel starts yielding. Therefore, the brittleness of concrete in tension and the formation of the cracks is the most important nonlinear phenomena which governs the behaviour of concrete. In the finite element analysis of concrete structures, three different crack models have been employed by researchers, depending on the purpose of the analysis:

- 1- Smeared cracking models.
- 2- Discrete cracking models.

3- Fracture mechanics models.

In this study the smeared crack approach was adopted. Most structural engineers adopt this model for its simplicity. In general, if overall load deflection behaviour is desired, without regard to completely realistic crack patterns and local stresses, the smeared crack model is probably the best choice. For special problems in which fracture mechanics is the appropriate tool, a specialised fracture model might be necessary.

5.4.1 Smeared Cracking Model:

In this model the cracked solid is imagined to be a continuum fig. 5.6a. The behaviour of cracked concrete can then be described in terms of stress-strain relationship and it is sufficient to switch from the initial isotropic to an orthotropic stress-strain relationship after cracking. In this model the topology of the original finite element mesh remains preserved which is computationally convenient. It is for this reason that this model is widely used and quickly replaced the early discrete crack model. This model was first introduced by Rashid (35).

Smeared crack concepts can be modelled as either fixed or rotating cracks. With the fixed crack concept the orientation of the crack is fixed during the entire computational process, whereas a rotating concept allows the orientation of the crack to co-rotate with the axes of principal strains. To account for aggregate interlock on the cracked concrete plane interface, a reduced shear modulus can be assumed. For stiffness calculation it is necessary to transform the local material stiffness matrix into global coordinates, by using the well known transformation matrix relating crack direction to global direction.

5.4.2 Discrete Cracking Model:

The discrete cracking model was introduced by Ngo and Scordellis(7) in 1967

when analysing the behaviour of beams with predefined cracks. The discrete crack is modelled by disconnecting the nodes for adjoining elements along the length of the crack. Almahaidi (37) improved the model by introducing a new definition, so that at a single point, continuity is preserved by two or four nodes tied together by stiff linkage elements until cracking occurs in one or two directions respectively, figure 5.6b. In general the crack directions and locations are not known in advance and with geometrical restrictions imposed by the preselected finite element mesh it is obvious that this approach suffers difficulties, so that the crack is constrained to follow a predefined path along the element edges. The second disadvantage is that, after cracking there is a continuous change in nodal connectivity which does not fit the nature of finite element method which requires a narrow band width on the structural stiffness matrix. Because of its lack of generality in a possible crack direction and redefinition of element nodes, this concept has resulted in very limited acceptance in structural application. Only in very special problems involving a few dominant cracks or predefined cracks, is the discrete crack model a realistic choice.

To date, there is not yet a consensus on the question of which type of approach should be preferred for a given problem (38). Crisfield(39) concluded that there is a danger of spurious mechanisms which can blow up the entire iterative procedure in smeared model. To sum up, both approaches presently seen to have their own merits and demerits.

5.4.3 Fracture Mechanics Model:

This model is used in solving various types of cracking problems in metals, ceramics and rocks. Chen(23) concluded that, the use of fracture mechanics model for reinforced concrete is still questionable and much remains to be done. In its current state of development, the practical applicability of fracture mechanics to reinforced concrete materials is still under investigation by several researchers(40).

5.5 Present Model for Concrete:

An international competition putting into test the different theories, described previously, organised by Collins and Vecchio(41) concluded that there is no correlation between the complexity of the analytical models and the accuracy of the resulting predictions. Very simple models can produce predictions that are just as good or just as bad as those arrived at by very complex models.

The model used in this study is simple but capable of simulating the nonlinear behaviour of slabs and deep beams. This model was used by Johansen(42) and Adel-Hafez(43) in the analysis of reinforced concrete slabs.

5.5.1 Yield Criterion:

There have been a number of failure theories proposed and used by various investigators. Recently, investigations have been made towards developing a consistent failure theory for concrete(22,24). In any well designed reinforced concrete structure, the cracking of concrete in tension, and compressive and tensile yielding of steel are the major source of nonlinearity. In this study the octahedral shear stress, linearised in term of the octahedral normal stress, is used, to fit the yield surfaces for concrete under biaxial stress states fig. 5.7, in the form:

$$\tau_{oct} = a + b \sigma_{oct} \quad 5.3$$

Where τ_{oct} is the octahedral shear stress given by:

$$\tau_{oct} = \frac{\sqrt{2}}{3} (\sigma_x^2 + \sigma_y^2 - \sigma_x \sigma_y + 3 \tau_{xy}^2)^{1/2} \quad 5.4$$

and σ_{oct} is the octahedral stress given as:

$$\sigma_{\text{oct}} = \frac{1}{3} (\sigma_x + \sigma_y) \quad 5.5$$

Taking f'_c as the uniaxial compressive strength of concrete, f_d as the equivalent compressive strength under biaxial compression, assumed to be $1.16 f'_c$ and $m = f_t/f'_c$, constants a and b in equation 5.3 are determined as follows:

5.5.1.1 Compression yielding:

i- For uniaxial compression: $\sigma_x = -f'_c$, $\sigma_y = \tau_{xy} = 0.0$

$$\tau_{\text{oct}} = \frac{\sqrt{2}}{3} f'_c \quad \text{and} \quad \sigma_{\text{oct}} = \frac{f'_c}{3}$$

Substituting in equation 5.3 we get:

$$\frac{\sqrt{2} f'_c}{3} = -\frac{b f'_c}{3} + a \quad 5.6$$

ii- For biaxial compression: $\sigma_x = \sigma_y = -f_d = -1.16 f'_c$, $\tau_{xy} = 0.0$

$$\tau_{\text{oct}} = 1.16 \frac{\sqrt{2}}{3} f'_c \quad \text{and} \quad \sigma_{\text{oct}} = 1.16 \frac{f'_c}{3}$$

Thus equation 5.3 can be written as:

$$1.16 \frac{\sqrt{2} f'_c}{3} = -1.16 \frac{b f'_c}{3} + a \quad 5.7$$

Solving for a and b , the biaxial compression yield criterion is given by:

$$\frac{\tau_{\text{oct}}}{f'_c} + (0.1714 \frac{\sigma_{\text{oct}}}{f'_c} - 0.4143) = 0.0 \quad 5.8$$

5.5.1.2 Tension— Compression:

$$\sigma_x = -f'_c, \quad \sigma_y = f_t = m f_c$$

Using the same procedure, it results:

$$\frac{\tau_{oct}}{f'_c} + \sqrt{2} \frac{1-m}{1+m} \frac{\sigma_{oct}}{f'_c} - \frac{2\sqrt{2}}{3} \frac{m}{1+m} = 0.0 \quad 5.9$$

5.5.1.3 Tension— Tension:

For biaxial tension the simple circular criterion is adopted.

$$\left[\frac{\sigma_1}{f_t} \right]^2 + \left[\frac{\sigma_2}{f_t} \right]^2 - 1.0 = 0.0 \quad 5.10$$

where σ_1 and σ_2 are the standard principal stresses.

5.6 Concrete Nonlinearity:

5.6.1 Concrete under Compression:

To account for nonlinear stress—strain relationship of concrete in the principal stress direction, equation describing concrete in elastic stage ($\sigma = D \epsilon$) is adopted as proposed by Saenz(45) and modified by Liu et al.(46), to account for biaxial effects. It takes the form:

$$\sigma = \frac{A + B E_C \epsilon}{(1 - \nu \alpha)(1 + C \epsilon + D \epsilon^2)} \quad 5.11$$

where α is the ratio of the principal stresses. $\alpha = \sigma_1 / \sigma_2$, ν is the Poisson's ratio and A, B, C and D are parameters which depend on the shape of the

stress-strain curve. They were calculated from the following conditions:

i- At the initiation of loading, that is $\epsilon = 0.0$:

$$\frac{d\sigma}{d\epsilon} = E_c / (1 - \nu\alpha) \quad \text{and} \quad \sigma = 0.0$$

ii- At the peak stress of concrete σ_p the corresponding strain is ϵ_p and the slope of the stress-strain curve become zero, thus at $\epsilon = \epsilon_p$ we have:

$$\frac{d\sigma}{d\epsilon} = 0.0 \quad \text{and} \quad \sigma = \sigma_p$$

The above conditions provide four equations sufficient to define the unknown parameters A, B, C and D of equation 5.11. After solving for the constants we have:

$$\sigma = \frac{E_c \epsilon}{(1 - \nu\alpha) \left[1 + \left(\frac{1}{1 - \nu\alpha} \frac{E_c}{E_{se}} - 2 \right) \frac{\epsilon}{\epsilon_p} + \left[\frac{\epsilon}{\epsilon_p} \right]^2 \right]} \quad \dots 5.12$$

where:

σ_p is the ultimate strength of concrete in compression, equal to f'_c .

ϵ_p is the strain at maximum concrete compression stress, taken as equal to 0.0025.

E_c is the initial modulus of elasticity of concrete for uniaxial loading.

E_{se} is the secant modulus of elasticity at the peak stress and given by the expression $E_{se} = \sigma_p / \epsilon_p$.

α is the ratio of the principal stresses. $\alpha = \sigma_1 / \sigma_2$

ν Poisson's ratio.

σ and ϵ are stress and strain in biaxial loading.

Equation 5.12 is used to generate the stress-strain behaviour of concrete in biaxial compression up to peak strain ϵ_p , after which this equation ceases to be valid due

to the strain softening deformation. In this work softening is neglected by assuming perfectly plastic behaviour up to the ultimate strain ϵ_u .

To accommodate the early changes in stiffness of concrete, equation 5.12 is incrementally linearized during loading by assuming intermediate surfaces similar to that used by Bell and Elms(47) and Chen et al.(48). Such surfaces are shown in figure 5.7. The first loading surface corresponds to the initial discontinuity in the stress-strain diagram. The subsequent loading surfaces are assumed to have the same shape of limiting yield surface. Accordingly, the intermediate surfaces will be represented by equation 5.3 but with an intermediate concrete strength f_{cc} replacing the ultimate strength f'_c . Johari(42) proposed the following equation:

$$f_{cc} = f_{co} - f_t + \frac{E_c}{E_i} f_t \quad 5.13$$

Where :

$$f_{co} = 0.5 f'_c$$

f_t : Tensile strength of concrete.

E_c : Modulus of elasticity of concrete.

Abdel-Hafez(43) used the above equation and concluded that it is a useful proposition.

Up to the peak strain ϵ_p , the concrete instantaneous modulus is computed using equation 5.12 and for strain above this value the following expression was used up to the assumed crushing strain (0.0035).

$$E_i = \frac{f'_c}{\epsilon_i} \quad 5.14$$

The concrete is considered to be crushed if one of the two conditions are violated:

- i- if the failure criteria of equation 5.8 is violated or,
- ii- if the principal compressive strain exceeds the ultimate compressive strain $\epsilon_u = 0.0035$.

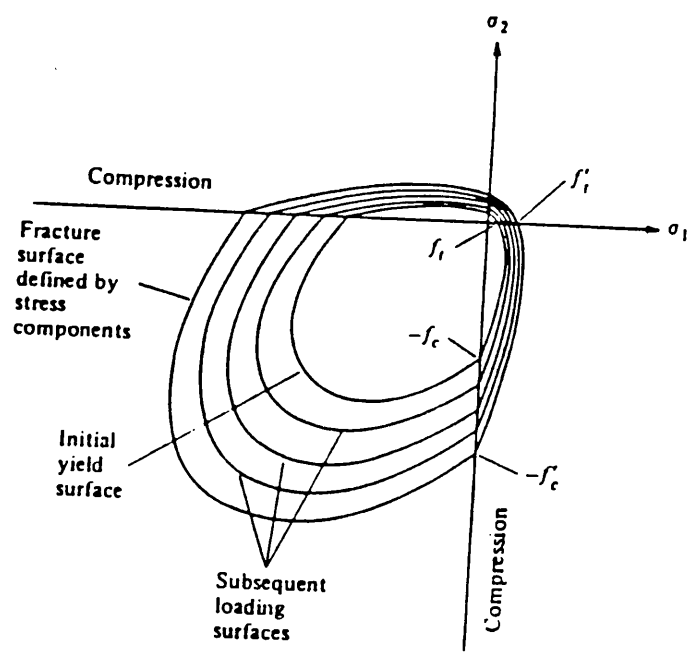


Fig. 5.7 Yield surface zones, initial, intermediate and failure envelop.

5.6.2 Concrete in Tension:

Cracking of concrete, under tension is the major source of nonlinearity in reinforced concrete structures . The main features, accounted for concrete in tension, are summarized:

- i— Cracking in one or two directions is allowed.
- ii— Cracks are allowed to transmit the shear to account for aggregate interlock.
- iii— Different crack direction is allowed for each layer.
- iv— Tension stiffening is included.

5.6.2.1 Singly cracked Concrete:

The crack is supposed to open, if one of the yield criterion of equations 5.9 and 5.10 are violated, depending on the state of stress is in tension—compression or in tension—tension state. The direction of the crack is taken as normal to the major principal tensile stress. For fixed crack direction analysis, the direction of the first crack is fixed. The stiffness perpendicular to the crack is assumed to be equal to zero (if tension stiffening is neglected). However, material parallel to the crack, is still capable of carrying stress prevailing at the crack, and some shear force can be transferred along the rough surfaces of a crack. Accordingly the material stiffness of concrete, in the local coordinate system (n,t) fig. 5.6a, is given as:

$$[D']_{Cr} = \begin{bmatrix} E_c & 0 & 0 \\ 0 & 0 & 0 \\ 0 & 0 & \beta G \end{bmatrix} \quad 5.15$$

A reduced shear modulus βG is assumed to account for aggregate interlock ($0 \leq \beta \leq 1$). G is the shear modulus. The Poisson's effect is neglected due to the assumption that there is no interaction between the two principal directions after concrete cracking.

i- Calculate the principal stress using the following standard expression:

$$\sigma_{1,2} = \frac{\sigma_x + \sigma_y}{2} \pm \left[\left[\frac{\sigma_x - \sigma_y}{2} \right]^2 + \tau_{xy}^2 \right]^{\frac{1}{2}} \quad 5.16$$

ii- Compute the principal angle θ , with report to x axis, in the form:

$$\tan 2\theta = - \frac{2\tau_{xy}}{\sigma_x - \sigma_y} \quad 5.17$$

The angle θ given in the above equation lies between -45° and $+45^\circ$ therefore it can lead to confusion on the principal direction. To determine the correct principal angle, the following step is used.

iii- Calculate the normal stress associated with the angle θ using the following expression:

$$\sigma_n = \sigma_x \cos^2\theta + \sigma_y \sin^2\theta + 2 \tau_{xy} \sin\theta \cos\theta \quad 5.18$$

iv- Compare the values of σ_1 and σ_2 with the above normal stress σ_n :

- If $\sigma_n = \sigma_2$, then σ_1 is inclined at $\theta + 90^\circ$ to x axis. Therefore the crack angle is at θ to x axis.

- If $\sigma_n = \sigma_1$, then the crack is normal to σ_1 . Hence the crack angle is $\theta + 90^\circ$.

5.6.2.2 Doubly Cracked Concrete:

The presence of shear retention and tension stiffening if not neglected at the previously formed crack will cause subsequent cracking and effectively produces changes in the crack orientation. In fact, accounting for aggregate interlock implies that the primary crack direction does not coincide with the principal direction and consequently the second cracks may not be necessarily orthogonal to the previous crack. Thus the orthogonal fixed crack approach results in conflict with the assumption of the principal planes. It has been confirmed experimentally by Vecchio and Collins(49) that changes in crack orientation takes place especially for panels not equally reinforced.

For the previously uncracked concrete, smeared cracks occur in two orthogonal directions when both the principal stresses exceed the tensile strength of concrete f_t . In this case, the material stiffness matrix in the local coordinates (n,t) becomes:

$$[D']_{cr} = \begin{bmatrix} 0 & 0 & 0 \\ 0 & 0 & 0 \\ 0 & 0 & \beta G \end{bmatrix} \quad 5.19$$

The first two diagonal terms in the above matrix may be updated if tension stiffening is considered.

Since the material stiffness matrix $[D']_{cr}$ is expressed in local coordinates system (n,t), it is, therefore, transformed to the global coordinates system (x,y) using the standard transformation matrix $[T]$ as follows:

$$[D]_{cr} = [T]^T [D']_{cr} [T] \quad 5.20$$

$$\text{Where } [T] = \begin{bmatrix} C^2 & S^2 & CS \\ S^2 & C^2 & -CS \\ -2CS & 2CS & C^2 - S^2 \end{bmatrix} \quad 5.21$$

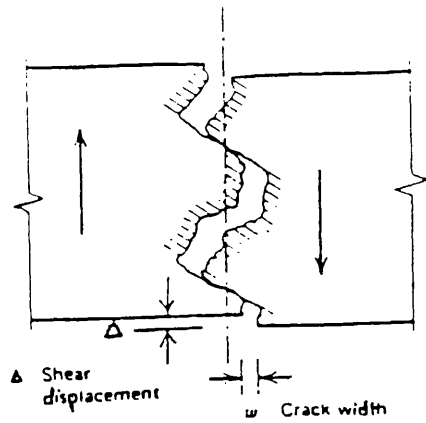
Where $C = \cos \theta_{cr}$ and $S = \sin \theta_{cr}$

5.6.2.3 Shear Transfer:

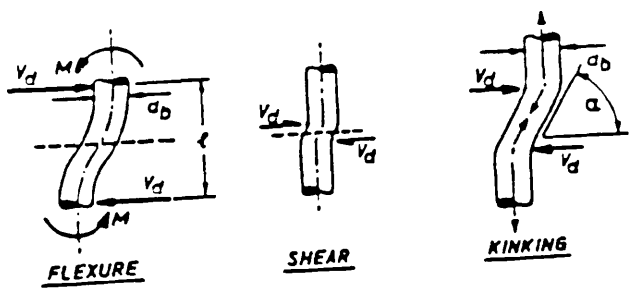
Along reinforced concrete crack interfaces, aggregate interlock (fig. 5.8a) and to some extent dowel action (fig. 5.8b) are the main mechanisms of load transfer(50). The aggregate interlock is caused by the nature of the concrete crack roughness, where as dowel action occurs due to steel bars crossing cracks. These bars tend to resist sliding shear movement and resist opening of the crack. Experimental results have shown that the aggregate interlock resist more shear than dowel action(51,52). Because large amount of deformation is required to develop significant dowel action, and to reach that amount the concrete surrounding the bars may have already deteriorated.

Based on many experimental studies, various analytical models of shear transfer have been developed, figure 5.8. Hand et al.(53) proposed the shear modulus approach to overcome some numerical difficulties, where they used a constant value of β after cracking of concrete. A variable shear retention factor, which decreases linearly with a fictitious strain normal to the crack, was later introduced by Cedolin and Deipoli(54). Al-Mahaidi(37) has also suggested a hyperbolic variation of shear stiffness G with the fictitious strain normal to the crack fig. 5.8c. In this work the Al-Mahaidi's model was used with a value of reduced shear modulus as follows:

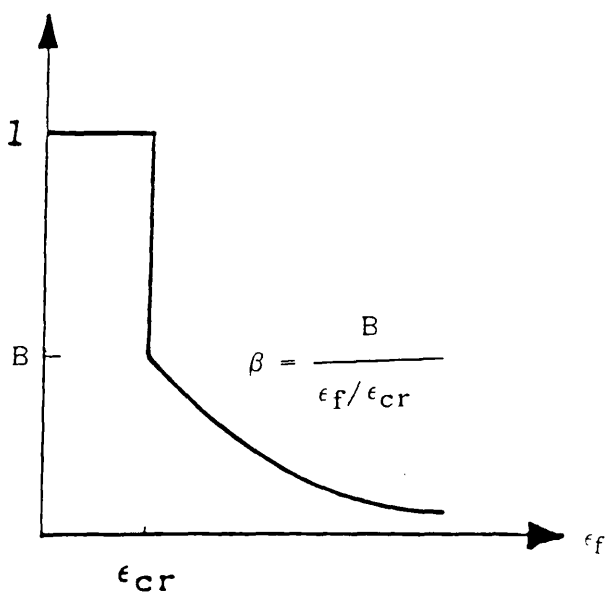
$$\beta = \frac{B}{\epsilon_f / \epsilon_{cr}} \quad 5.22$$



a- Aggregate interlock along a cracked plane.



b- Dowel action mechanisms across a crack interfaces.



c- Hyperbolic shear retention.

Fig. 5.8 Mechanism of shear transfer and model adopted.

Where:

$0 \leq B \leq 1$ and ϵ_f is the fictitious strain normal to the crack and expressed as:

$$\epsilon_f = \epsilon_x \sin^2 \theta_{cr} + \epsilon_y \cos^2 \theta_{cr} - \gamma_{xy} \sin \theta_{cr} \cos \theta_{cr} \quad 5.23$$

ϵ_{cr} is the concrete cracking strain, $\epsilon_{cr} = f_t/E_c$

ϵ_x , ϵ_y and γ_{xy} are the inplane strains.

θ_{cr} is the angle of the crack to x axis figure 5.6a.

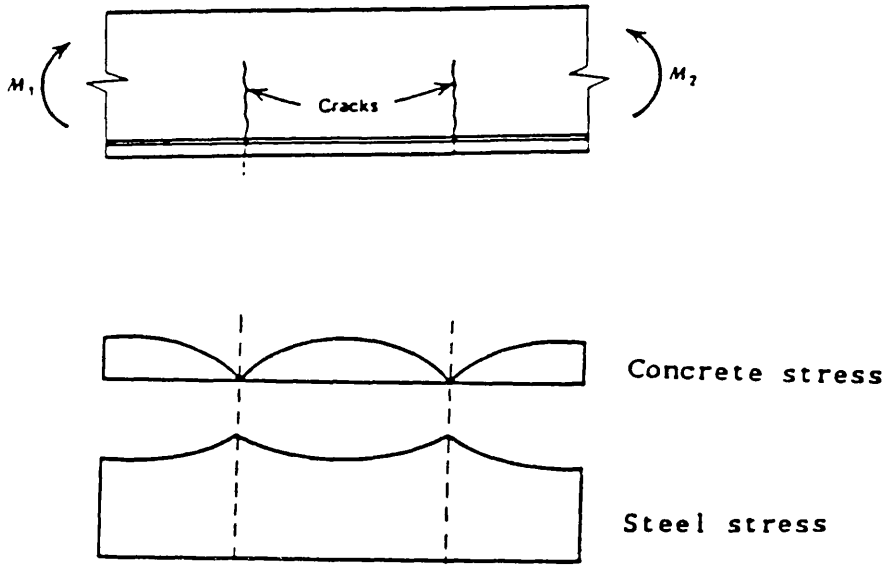
In this work dowel action of the bars, crossing crack interfaces, was neglected.

5.6.2.4 Tension Stiffening:

As the cracks form, the tensile strength of that particular region drops to zero and the residual stresses are transferred to steel, figure 5.9a. However, between cracks, load is shared between steel and concrete due mainly to bond between steel and the surrounding concrete. Tension stiffening is introduced to model the ability of concrete between two adjacent cracks, to assist steel in carrying tensile stress.

The use of tension stiffening is not only more realistic, but tensile forces released from cracked zones are gradually redistributed into the structure. It was Scanlon and Murray(55) who introduced a descending branch, for the stress strain curve, beyond the cracking strain. Later Clark and Speirs(56) showed, from the results for beams and one way spanning slabs with different steel ratios, that the effect of tension stiffening decreases with an increase in the steel ratios and steel strain. The results suggest that tension stiffening can be ignored for steel ratio above 1.5% and for steel strains greater than about 0.0016. A simple form of tension stiffening was adopted in the present work, figure 5.9b, as follows:

$$\text{If } \epsilon_i < \epsilon_{cr} \quad \sigma = E_i \epsilon_i$$



Stress distribution in a cracked reinforced concrete.
(a)

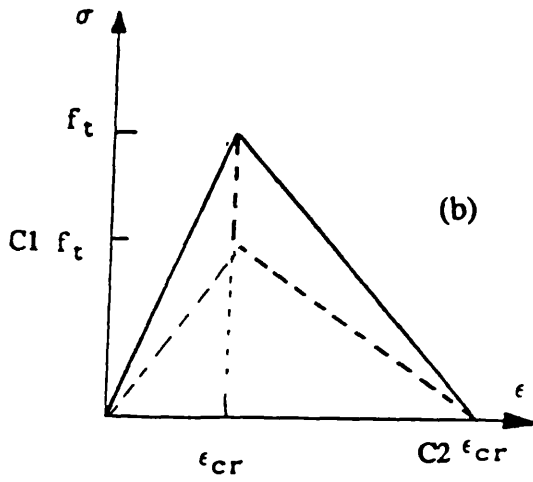


Fig. 5.9 Tension stiffening idealization.

$$\begin{aligned} \text{If } \epsilon_{cr} \leq \epsilon_i \leq C2 \epsilon_{cr} \quad \sigma &= C1 f_t \frac{(C2 \epsilon_{cr} - \epsilon_i)}{\epsilon_{cr}(C2 - 1)} \\ \text{If } C2 \epsilon_i > C2 \epsilon_{cr} \quad \sigma &= 0 \end{aligned}$$

where ϵ_{cr} is the concrete cracking strain ($\epsilon_{cr} = f_t/E_c$), σ and ϵ_i are local stress and strain orthogonal to the crack, f_t is the tensile strength of concrete. The coefficients $C1$ and $C2$ are taken as: $0.5 \leq C1 \leq 1.0$ and $10.0 \leq C2 \leq 20.0$. Discussion on the values chosen for $C1$ and $C2$ in the present work will be presented later.

5.7 Modelling of steel:

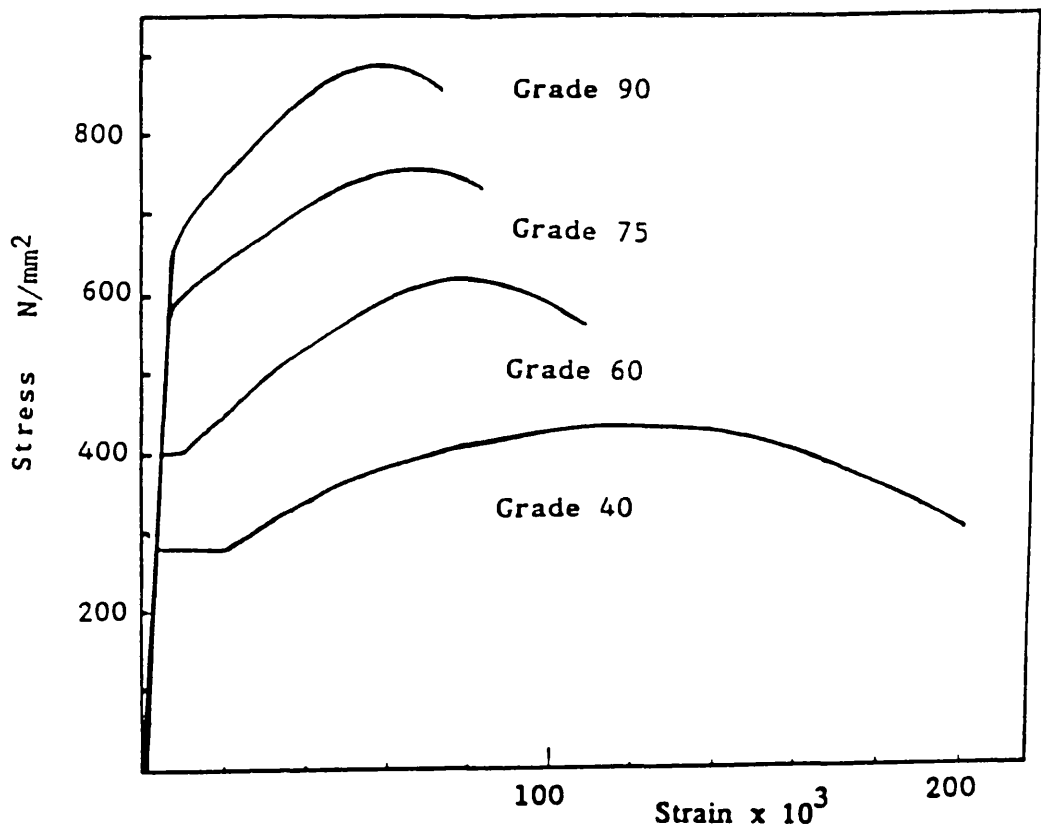
In contrast to concrete, steel bar behaviour is comparatively well understood, and since, steel reinforcement elements in concrete construction are mostly one dimensional, it is generally not necessary to introduce a complex multiaxial constitutive relationships. Generally steel bars exhibit an initial elastic portion, a yield plateau at which the strain increases with a little or no increase in stress, a strain hardening range in which stress again increases with strain, and finally a range in which stress drops until fracture occurs. In the present study a simple bilinear idealisation of figure 5.10 is incorporated, simulating the behaviour of reinforcing steel as elastic perfectly plastic or with allowance of some hardening as follows:

i— At elastic stage, the incremental stress strain is given by:

$$\Delta\sigma = E_s \Delta\epsilon \quad 5.24$$

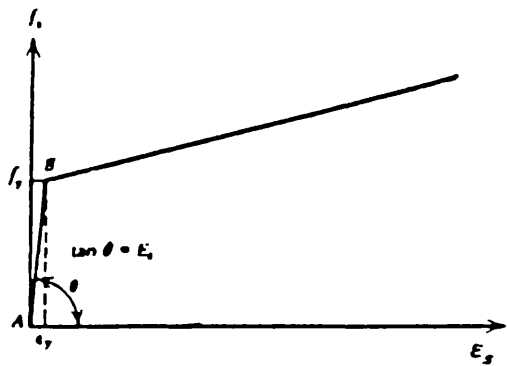
ii— When the stress in the steel bar reaches its yield value f_y , the incremental elastic— plastic stress relationship takes the form:

$$\Delta\sigma = E_s (1 - E_s / (E_s + H)) \Delta\epsilon \quad 5.25$$

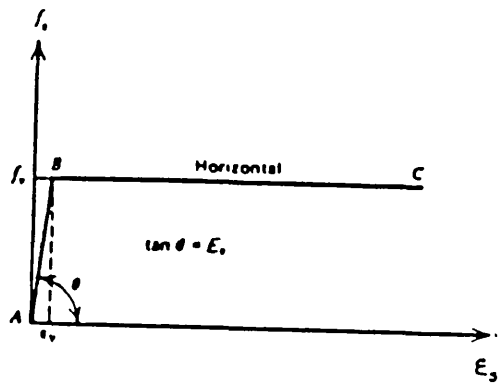


STRESS-STRAIN CURVES FOR REINFORCING BARS.

(a)



Bilinear approximation



Elastic perfectly plastic

(b)

Fig. 5.10 Stress- strain curves for reinforced bars and idealized model.
under tension or compression

Where H is the hardening parameter and E_s is the Young's modulus of steel.

Generally for mild steel an elastic–perfectly plastic model is quite adequate, whereas for high yield steel bars, the strain hardening effect, may be important.

5.7.1 Finite Element Representation of Steel Bars:

To account for the effect of steel reinforcements in stiffness calculations, three alternative approaches can be used namely smeared, embedded and discrete.

5.7.1.1 Smeared Model:

In the smeared model, reinforcements are assumed to be distributed over the element, figure 5.11. This model is convenient for structures where a large number of reinforcing bars are placed. Due to this feature it is rather difficult to model each reinforcing bar individually. This model is widely used in reinforced concrete plate and shell structures, in which the structure is divided into layers. This approach was first adopted by Wegmuller in 1974(100) and improved by others(101,102). In this model the stress strain relationship for each layer is given by:

$$\{\sigma\} = [D'_s] \{\epsilon\} \quad 5.26$$

where D'_s is the constitutive relationship for steel.

For steel layer the behaviour is first described in the local coordinate direction of the steel so that the bar can be orientated at any angle to the global axes (x,y) , then the constitutive relationship is transformed from the local to the global axes in terms of the angle θ_s between the local axes and the global axes.

5.7.1.2 Embedded Model:

Over the past decade, a number of embedded representation for reinforcement have been published. Phillips and Zeinkiewicz(103) developed embedded representation in which virtual work integration is performed along the reinforcing bar. In their formulation, the reinforcement was restricted to lie along one of the local coordinate lines, figure 11b.

Chang et al.(104) recently published the embedded representations that allows for a reinforcing bar to be placed at an angle to the local isoparametric element axes but restricted to problems having straight reinforcing and rectilinear meshes. Elwi and Hruday(105), and Phillips and Wu(106) developed a formulation presenting a general oriented and curved embedded reinforcement.

The advantage of using embedded model is that the geometry of the finite element mesh can be constructed independently of the reinforcement layout and every bar is modelled in its correct position. Since we are following the usual procedure for isoparametric mapping, and full compatibility between the bar and basic element is assumed, the displacements $\{u,v\}$ of any point on the bar are obtained from the displacement field of the basic element as:

$$\begin{Bmatrix} u \\ v \end{Bmatrix} = [N(\xi, \eta)] \{\delta\}^e$$

For bars only one component of strain contributes to the strain energy and is defined locally as:

$$\epsilon_p = \partial u' / \partial x'$$

where x' and y' are the local coordinate system at any point on the bar with y' being normal to the bar, and u' , v' are the corresponding displacements.

In this work, only reinforced bars laying parallel to the coordinate lines x or y are considered. If a bar is laying along ξ , all points of the bar have a constant $\eta = \eta_c$ and vise versa.

The element stiffness matrix of steel reinforcement has the following form:

$$[K_s] = A_s \int_1 [B]^T [D] [B] dl \quad 5.27$$

Where A_s is the cross sectional area of reinforcement. $[D]$ is the elasticity matrix determined as follows:

If the bar is laying in x direction: $D(1,1) = E_s$

While in y direction $D(2,2) = E_s$.

$[B]$ is the nodal displacement-strain matrix for isoparametric element but accounting only for one degree of freedom in the direction of the reinforced bar.

dl is the segment along the reinforcement.

The integration in equation 5.27 is performed over the whole bar length crossing the element. A two Gauss point system was used.

Both smeared and embedded formulations are adopted in the present work by assuming perfect bond between steel and concrete. Thus the overall constitutive relationship is simply evaluated by adding the material matrices for concrete and steel together, as follows:

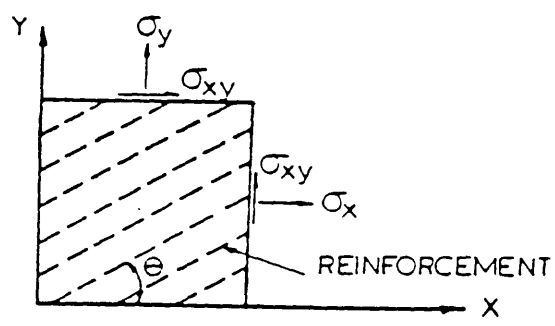
$$[K_e] = [K_c] + [K_s] \quad 5.28$$

In which $[K_e]$ is the stiffness matrix of the composite element, $[K_c]$ and $[K_s]$ are the element concrete and steel stiffness matrices respectively.

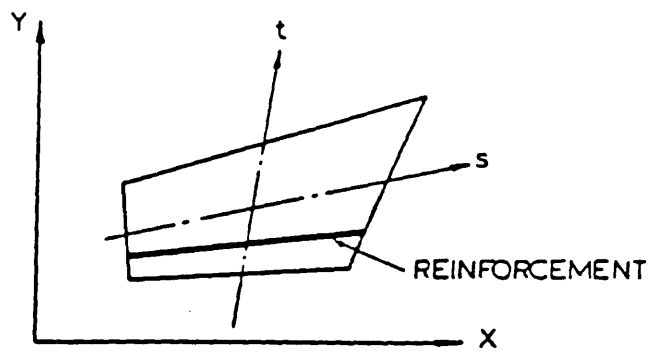
In fact the name embedded can be given for all models when full bound between steel and concrete is assumed. The so called embedded model could be better named as partially discrete model, since the strains of steel are calculated in their exact position on the bar, whereas its stiffness is distributed between the nodal points of the parent element, depending on the position of the bar within the element.

5.7.1.3 Discrete model:

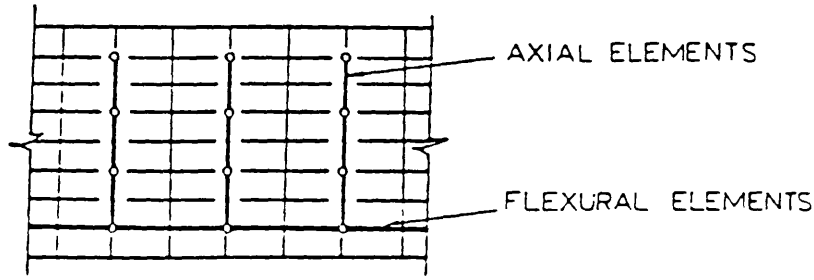
In the discrete model, figure 5.11c, a one dimensional bar element is superimposed on the two dimensional parent element by assuming that the bar is



a- Smeared model



b-Embedded model



c- Discrete model

Fig. 5.11 Finite element representations of steel.

pin connected with two degrees of freedom at nodal points. Alternatively, discrete beam elements can be used, in which the steel is assumed to be capable of resisting axial force, shear force and bending moment. The use of the beam elements, with three degrees of freedom per node, may be suitable and necessary in the case of heavy bars for which bending is a significant effect. The discrete model was first used by Ngo and Scordelis(7) in the analysis of beams.

In either case, bar or beam element, steel–concrete interaction can be represented by linkage element to account for possible relative displacement of the reinforcement to the surrounding concrete. In this model the stiffness and the strains are calculated exactly on the bar position. In spite of its simplicity, the discrete model has one major disadvantage in that the finite element mesh patterns are restricted by the locations of the reinforcement, which leads to an increase in the size of the stiffness matrix.

5.8 Numerical Applications:

In this section some practical application of the model adopted are presented. The main purpose is to verify the applicability and the accuracy of the numerical model, for reinforced concrete structures classified as plate bending and inplane problems. This is done by testing the model against various carefully conducted experimental tests involving different types of reinforced concrete structures exhibiting various modes of failure. The load deformation response, cracking history and crack locations and directions, steel yielding, ultimate load were recorded as well as the mode of failure. In the nonlinear solution, the combined algorithm is adopted in which the stiffness is updated at 2nd, 5th, 10th iterations and so on until convergence or collapse of the structure is obtained. A convergence force tolerance of 4% was adopted for the analysis, the maximum number of iteration of 30 and 50 were fixed for the analysis of slabs and deep beams respectively. The reason for increasing the number of iteration for beams is that, they show a slow rate of redistribution of the residual stress, at the first stages of cracking of the

structure, but, unlike slabs, with a small increase in deformations. Also in order to keep costs down, small load increments are applied only for highly nonlinear parts of the solution. It was concluded(43) that there is not much difference in results using different load increment sizes. By analysing slabs, Abdel-Hafez(43) also showed that the results and the cost of the analysis are only slightly influenced by the number of layers used. A total of 10 layers, including steel layers, were fixed for slab analysis.

5.8.1 HAGO's slabs:

Two slabs with different types of support conditions were chosen from the six slabs tested by Hago (115). The analysis of these slabs, with various degrees of orthotropy of reinforcement, allows the effect of the amount of steel reinforcement to be tested as well as different types of support conditions.

a- Simply supported slab (Model N. 3)

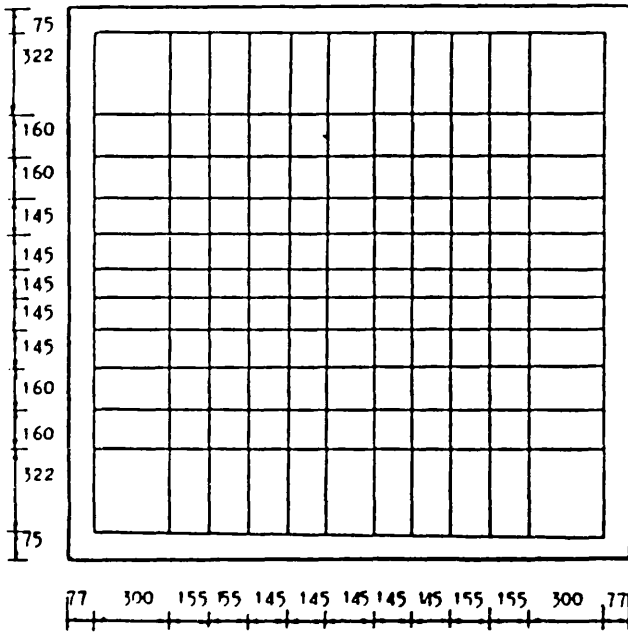
This example is a square simply supported slab, designed for a total load of 210 KN, applied as four point loads. The thickness of the slab is 100 mm, with orthotropic reinforcement as shown in figure 5.12. The material properties used are as follows:

$$f_{cu} = 44.2 \text{ N/mm}^2 \quad ; \quad f_y = 460.0 \text{ N/mm}^2$$

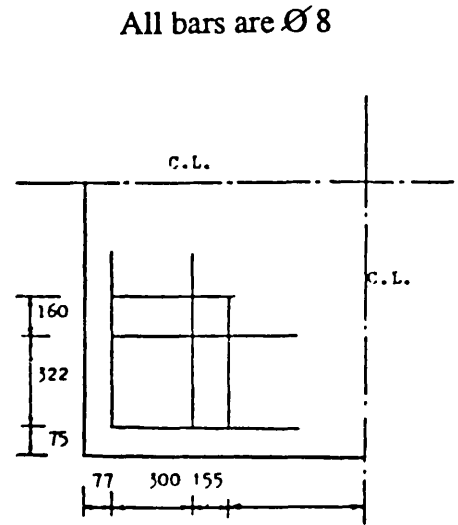
$$E_c = 21500.0 \text{ N/mm}^2 \quad ; \quad E_s = 214000.0 \text{ N/mm}^2$$

$$f_t = 3.4 \text{ N/mm}^2$$

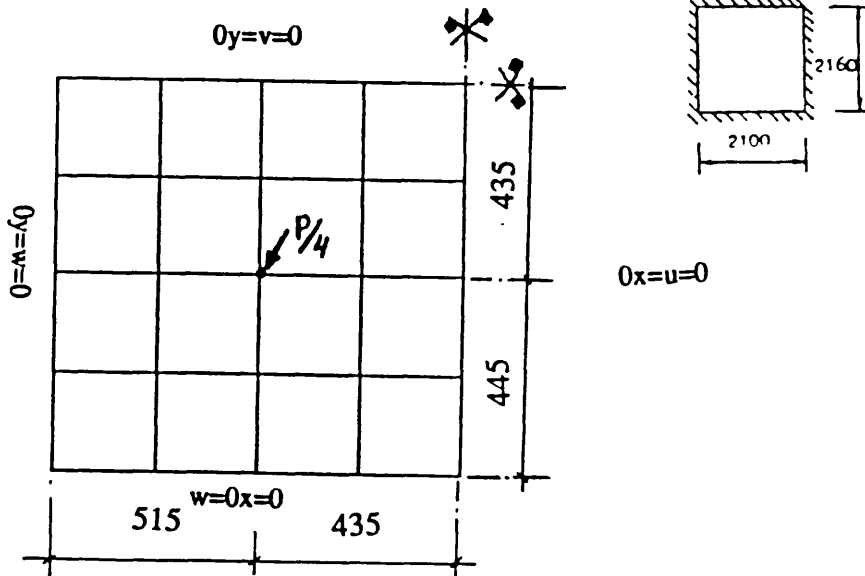
A quarter of the slab was analysed as shown in figure 5.12a. To study the effect of the finite element mesh size, different mesh arrangements were used. Figure 5.13 shows that a more flexible deformation was obtained when a larger number of elements were used. The time cost of the analysis was significantly



a- Bottom Steel



b- Top steel



c- Finite element idealization

Fig. 5.12 Details of Hago's model N. 3

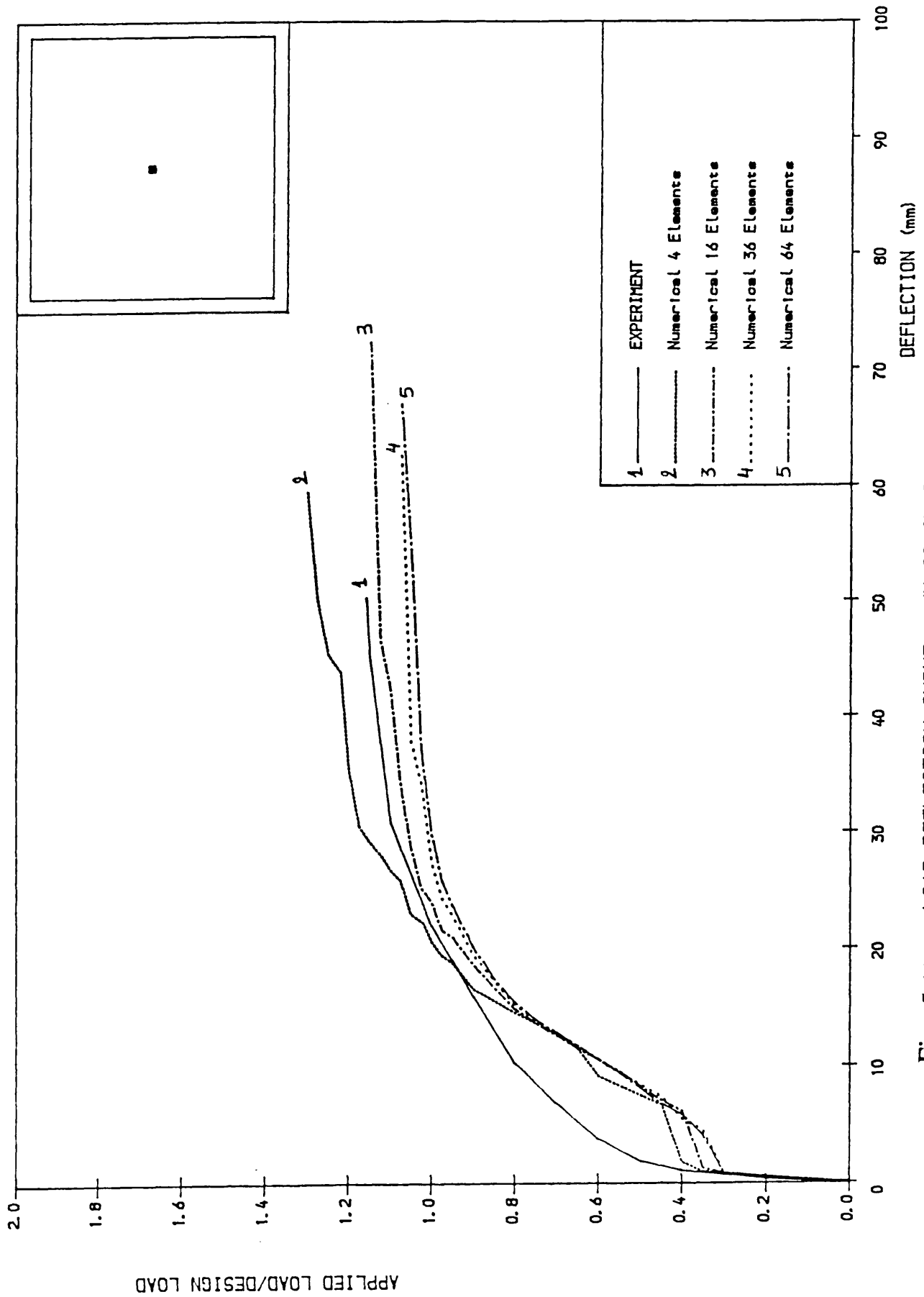


Fig. 5.13 LOAD-DEFLECTION CURVE (HAGO SLAB N. 3)
Different Number of Elements in the Finite Element Mesh

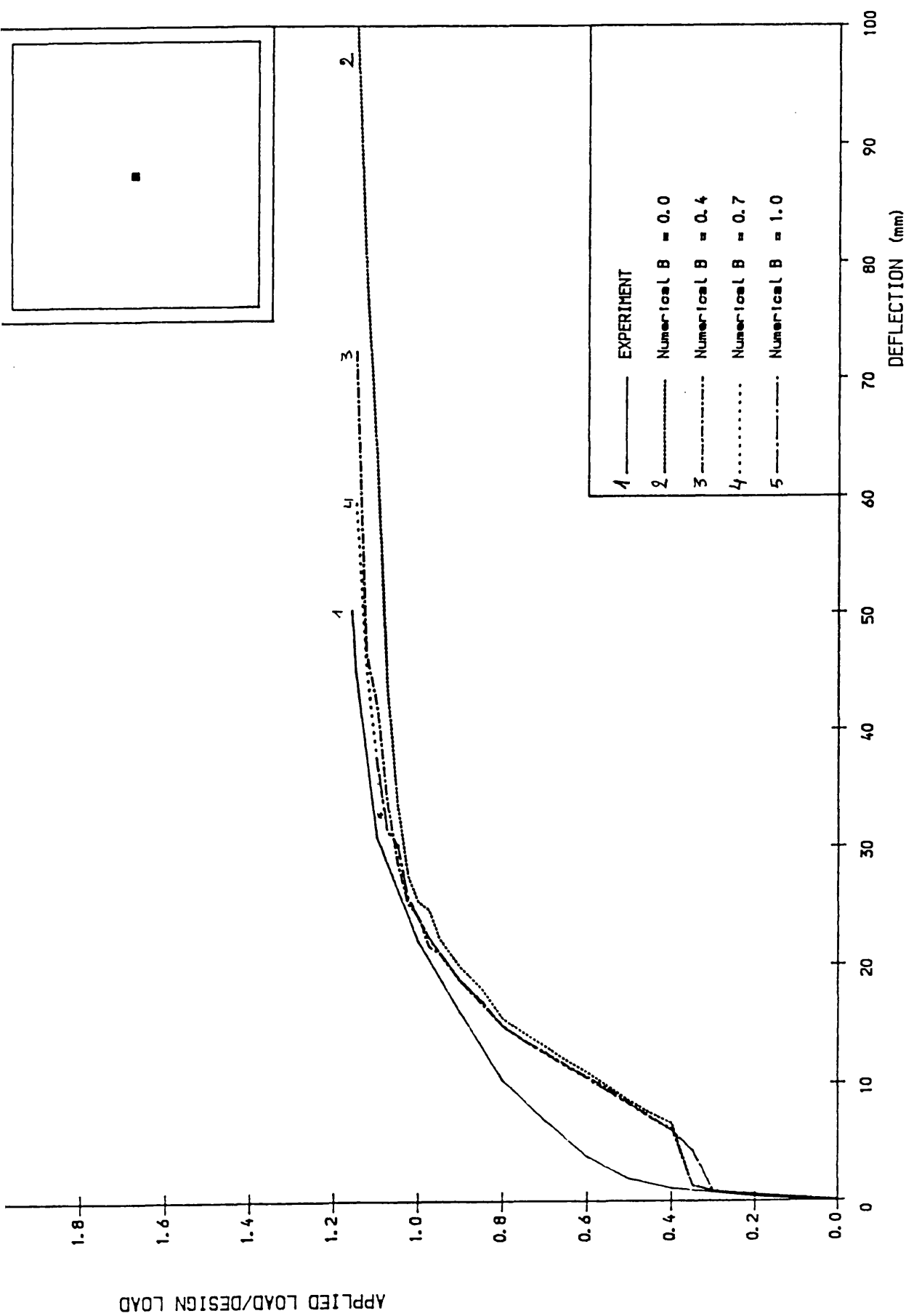


Fig. 5.14 LOAD-DEFLECTION CURVE (HAGO SLAB N. 3)

Different shear retention factors

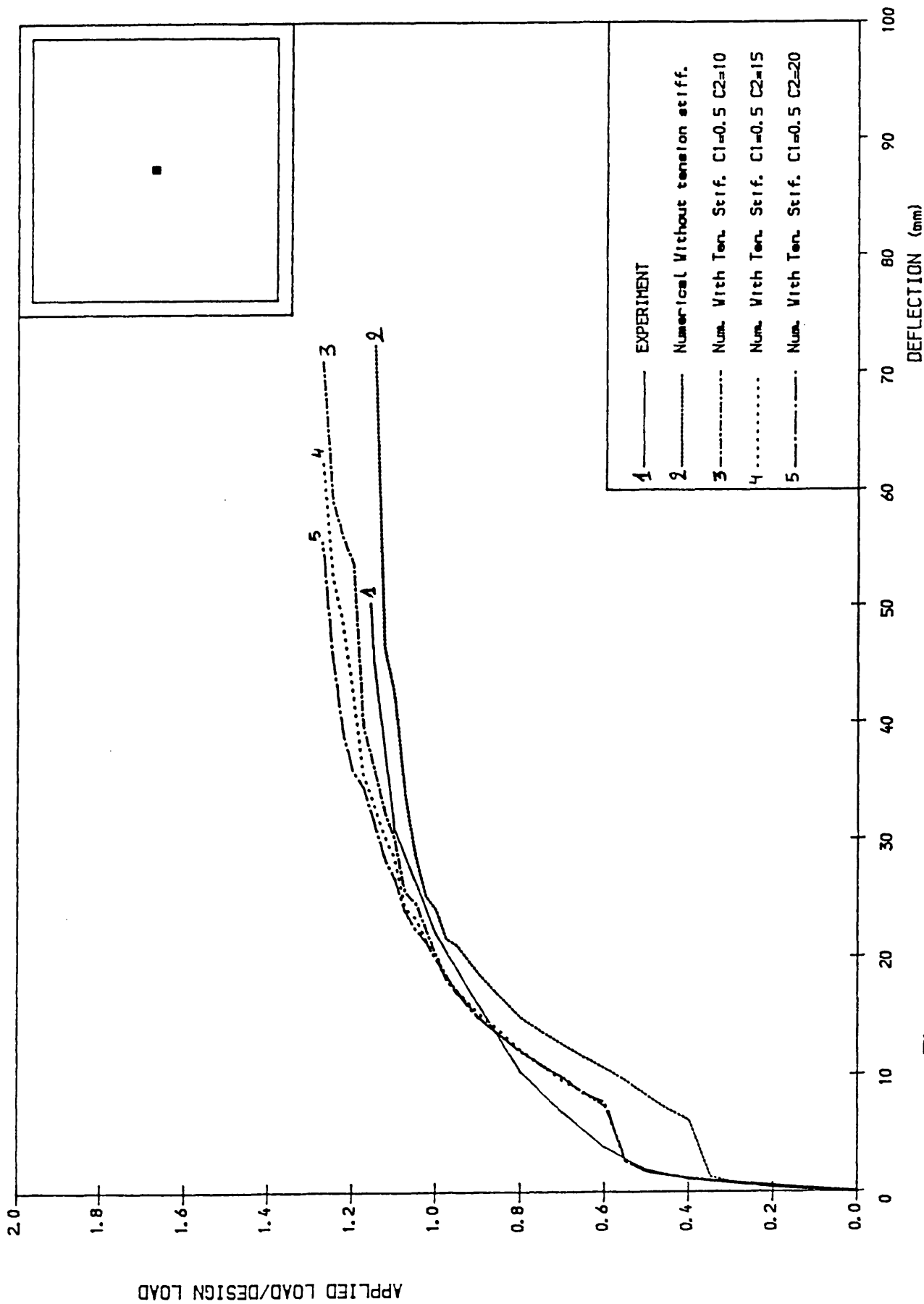


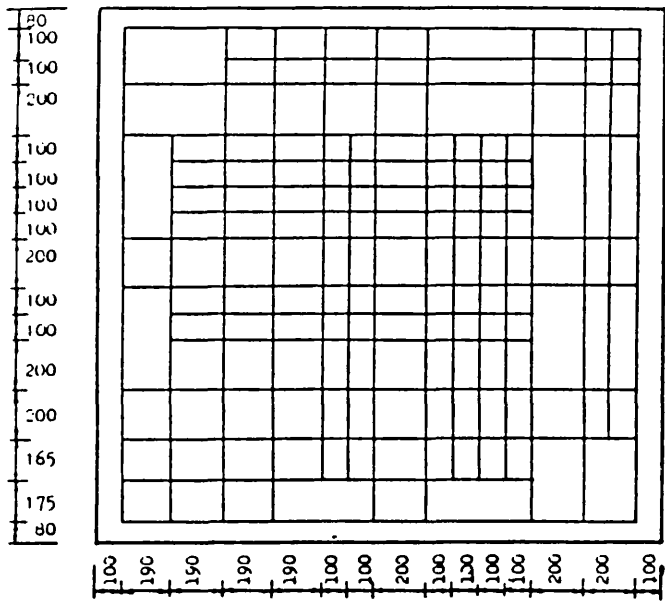
Fig. 5.15 LOAD-DEFLECTION CURVE (HAGO SALB N. 3)
Tension Stiffening

influenced by the number of element used. A 4x4 finite element mesh gives an acceptable solution at a reasonable cost. The time increases by almost four times when using 8x8 element mesh instead of 4x4. The slab was loaded using 0.2 Pd for the first increment, where Pd is the design ultimate load, and a load increment of 0.05 Pd was adopted in the first stage where cracking starts. A load increment of 0.1 Pd was fixed beyond this last stage until design load was reached after which it was reduced to 0.05 Pd.

Generally slabs, failing flexurally, start cracking in the range of 20 to 35% of their ultimate strength. A maximum of 18 iteration was recorded, during the analysis, at the early stages of cracking. Different value of the shear retention factor ($B = 0.0, 0.4, 0.7$ and 1.0) have been used to study the effect of shear transfer to simulate variations from very smooth to very rough concrete crack faces. Load deflection curves of the central point of the slab are illustrated in figure 5.14. From the results only small difference can be noticed between the deflections for the different values of B chosen. A little improvement in the ultimate load can be seen when B was increased to the value of 0.4, while above this value there is no difference in the ultimate load. A simple model for tension stiffening was used with values of C2 equal to 10.0, 15.0 and 20.0 (the factor C2 determines the descending branch in figure 5.10b). Figure 5.15 shows that deflection values are sensitive to the tension stiffening especially at service load, where predictions are better predictions. In terms of ultimate load, using high values of C2 leads to higher ultimate load.

b— Hago's two adjacent edges simply supported and one corner supported slab N.4:

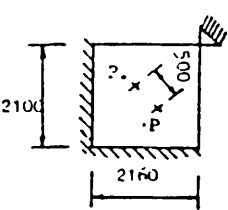
This is a 2100 x 2160 mm square slab with two adjacent sides simply supported and one corner on column support. The thickness of the slab is 100mm with orthotropic reinforcement as shown in figure 5.16. The slab had the following material properties:



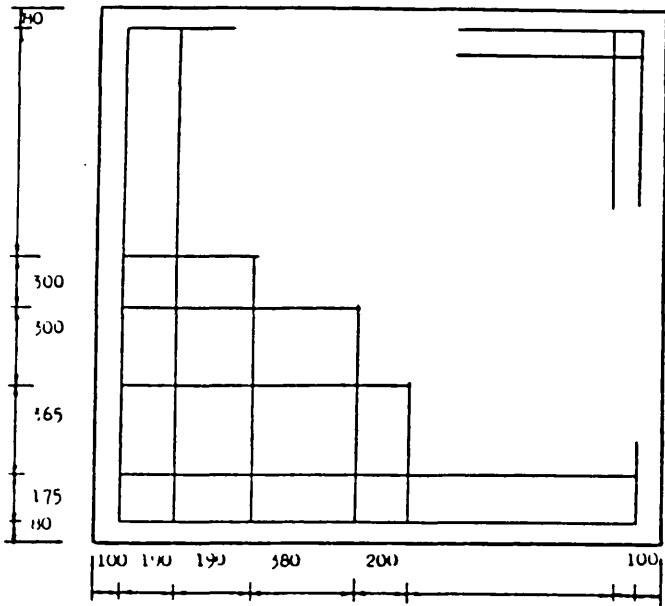
a- Bottom steel reinforcement

LEGEND

All Bars Are ϕ 8



c- Loading system



b- Top steel reinforcement

Fig. 5.16 Details of Hago's model N. 4

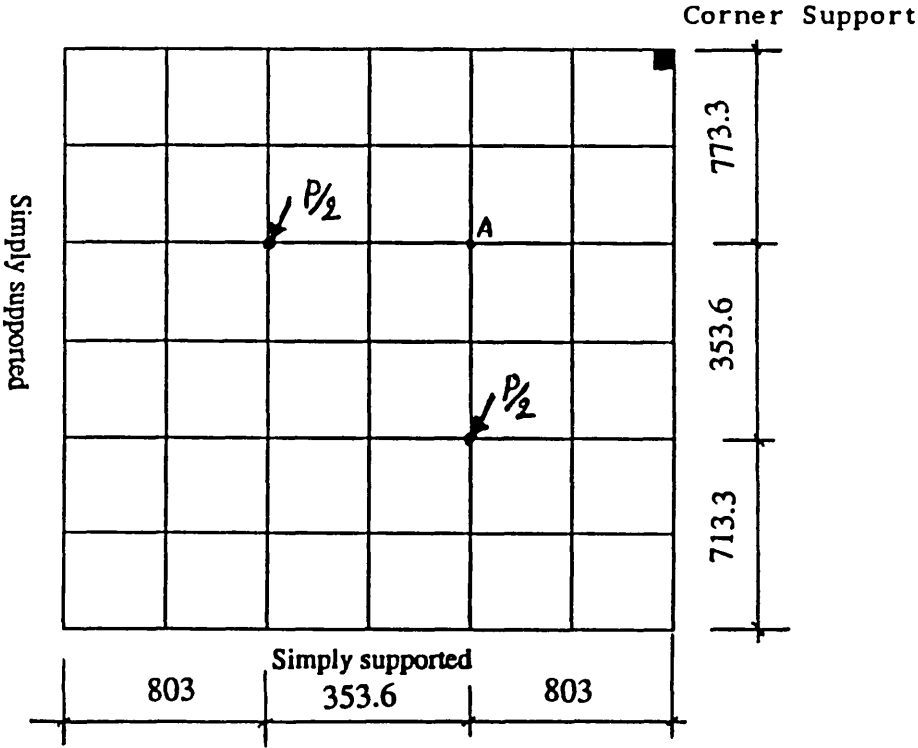


Fig. 5.17 Finite element idealization of Hago's model N. 4

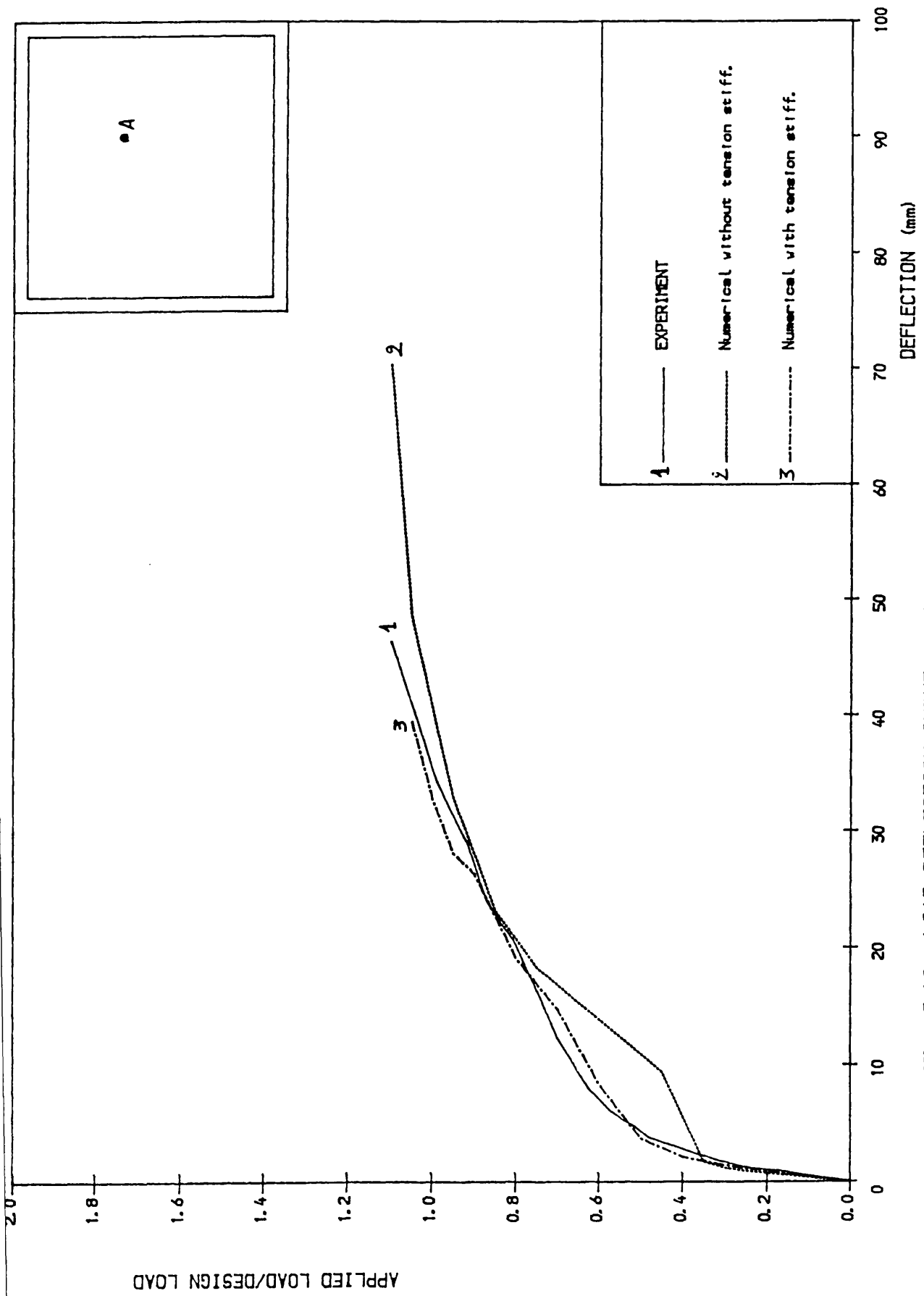
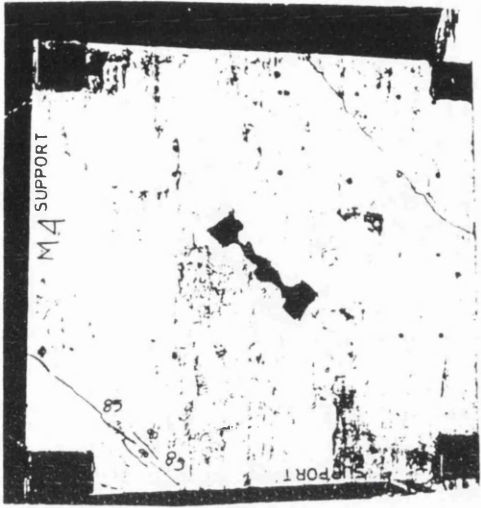
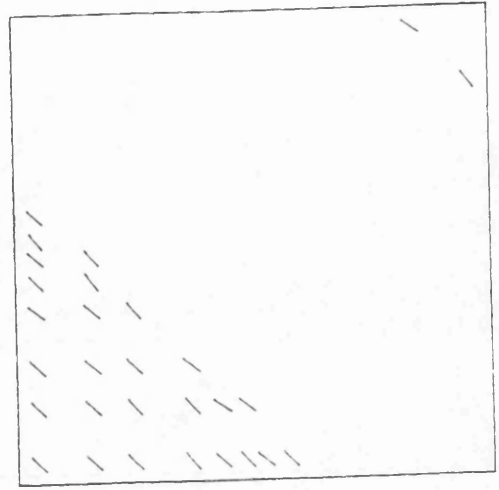


Fig. 5.18 LOAD-DEFLECTION CURVE (HAGO SALB N. 4)



Experimental



Numerical

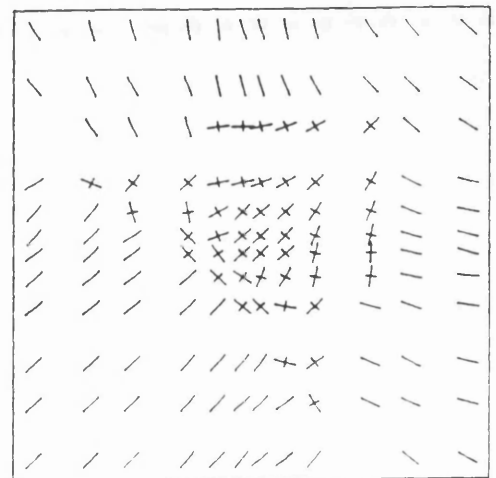
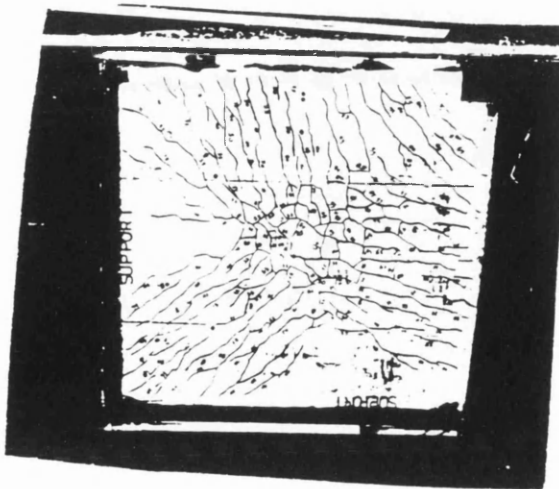


Fig. 5.19 Crack pattern comparison at failure load.
Hago's model N. 4

$$\begin{aligned}
 f_{cu} &= 37.3 \text{ KN/mm}^2 & ; & & f_y &= 473 \text{ KN/mm}^2 \\
 f_t &= 2.97 \text{ KN/mm}^2 & ; & & E_s &= 214000 \text{ KN/mm}^2 \\
 E_c &= 20400 \text{ KN/mm}^2
 \end{aligned}$$

Since the slab was not symmetric, a 6x6 finite element mesh is used over the whole plate as shown in figure 5.17. The cross section of the slab was divided into six concrete layers and four steel layers when top and bottom steel were present. Figure 5.18 compares the load–deflection curve obtained by experimental and numerical results. The numerical results were obtained using a shear retention factor B of 0.4. A better correlation between the experimental and the numerical deflection was obtained using tension stiffening, where as in term of ultimate load there is no difference, figure 5.18.

Tension stiffening had a significant influence on the convergence rate of the solution at working load. Taking tension stiffening into consideration, a maximum of 9 iterations was required at the first stages of cracking, while analysis without tension stiffening increases the maximum number of iterations to 24.

The incremental load size was reduced to 2.5 % of the design load near the ultimate load. Figure 5.19 shows crack pattern comparison between the experimental results and the numerical, for both top and bottom concrete faces, at ultimate load.

The bottom steel yielded numerically at 0.9 Pd, in both analysis with or without tension stiffening, where as experimentally the steel yielded at the design load. Numerical failure took place at 98 % of the experimental ultimate load. The predicted mode of failure was flexural as was the experimental.

5.8.2 McNeice corner support slab(116):

This example was a 914.0 mm square corner supported slab, loaded with a central concentrated force. This slab was chosen to assess the present model for the two–way bending and corner supported slabs. Material properties are given as

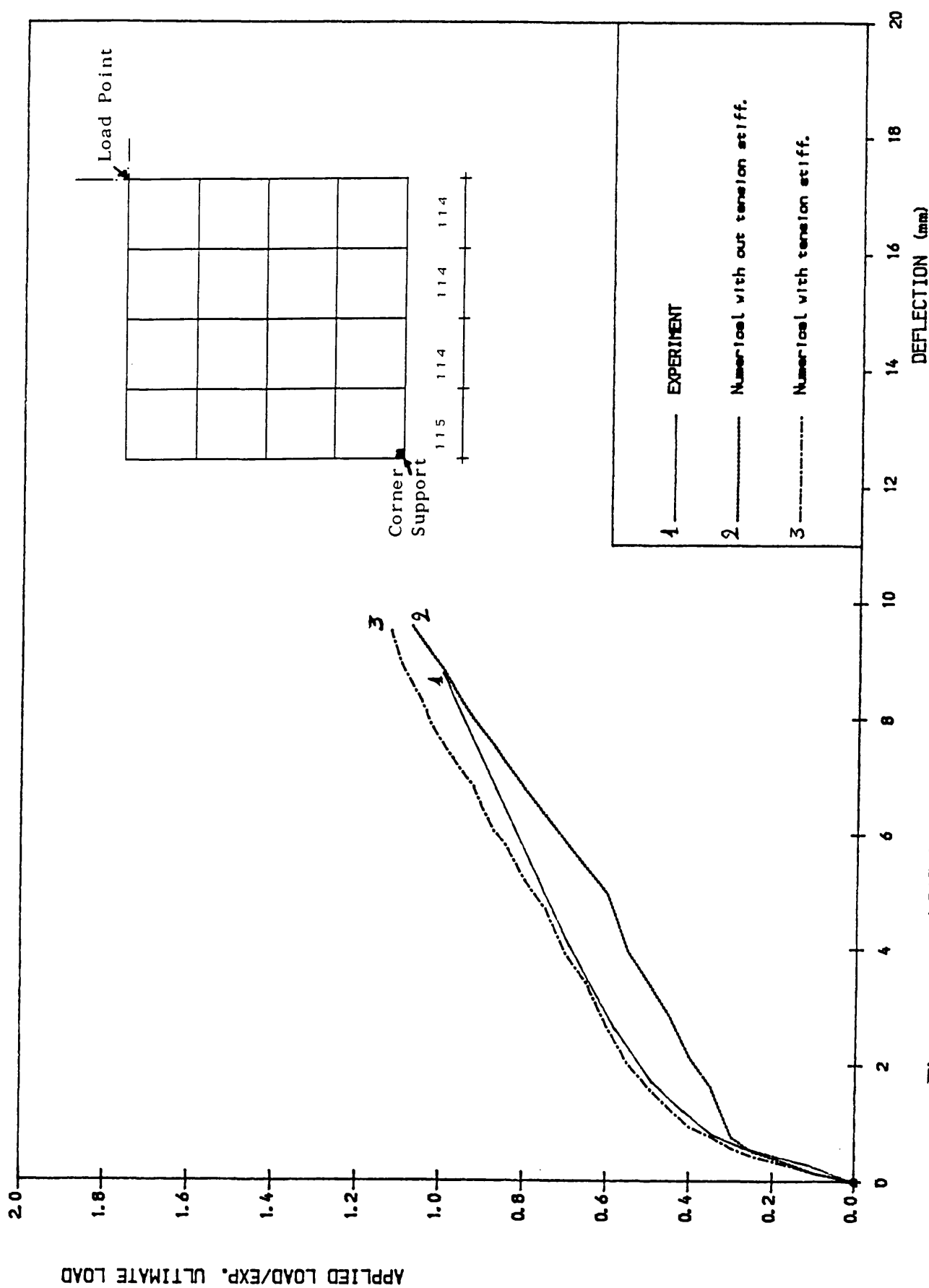


Fig. 5.20 LOAD-DEFLECTION CURVE (McNeice's slab corner supported)

follows:

$$\begin{aligned} f_{cu} &= 32.4 \text{ N/mm}^2 & ; & \quad f_y = 345 \text{ N/mm}^2 \\ f_t &= 3.2 \text{ N/mm}^2 & ; & \quad E_s = 200000 \text{ N/mm}^2 \\ E_c &= 29000 \text{ N/mm}^2 \\ \nu &= 0.15 \end{aligned}$$

A mesh of 4x4 elements over a symmetric quadrant was used as shown in figure 5.20. The experimental failure load was at 14.3 KN. Two results of analysis are given here, one considering tension stiffening (with $C1 = 0.5$ and $C2 = 10.0$) and the other without tension stiffening. The agreement, between analytic with tension stiffening and experiment, is good at working load of the slab but the numerical results are stiffer beyond 0.7 of the ultimate load. Results without tension stiffening gives large deflection at working load range. The slab failed at 1.10 and 1.125 of the experimental ultimate load excluding and including tension stiffening, respectively.

5.8.3 VICCHIO and COLLINS Panels:

Two panels were chosen from an experimental research program, conducted by Vicchio and Collins(111). The program involved testing reinforced concrete panels under a variety of well-defined and uniform stresses in a specially designed test rig, figure 5.21. These two panels were part of an international competition(41) organised to compare analytical methods for predicting the response of reinforced concrete elements subjected to general two dimensional stress states. Twenty seven predictions from thirteen contries were submitted. The predictions were concerned with the ultimate strength and deformation using different analytical methods. This competition was organized to highlight the difficulties in assessing numerically the behaviour of reinforced concrete structures. Figure 5.23 shows the scatter in the predicted ultimate strengths of the panels.

The panels have the same dimensions as shown in figure 5.22, 890mm square and 70mm thickness. They are reinforced by two layers of isotropic reinforcement ($\rho_x = \rho_y$) and parallel to the edges.

Panel A was loaded under pure shear, whereas panel B was subjected to combined biaxial compression and shear. The panels were heavily reinforced and hence failure could be expected by concrete crushing. Material properties, reinforcement ratio, and loading details are summarized in table 5.1 and the remaining parameters are adopted as given by Chang et al.(104). The concrete elastic modulus and the tensile strength were taken as 0.2×10^5 MPa and $0.1 f'_c$ respectively. The steel reinforcement was assumed to be perfectly elastic-plastic material with $E_s = 0.2 \times 10^6$ MPa.

The panels were analysed using 4x4 finite element mesh as shown in figure 5.22. The response of the panels A and B in terms of the applied shear stress V versus shear strain γ_{xy} is shown in figures 5.24 and 5.25 respectively. Figure 5.24a and 5.25a show that the variation of the shear retention factor had no effect on the panels behaviour both at working load and at ultimate load of the panels. Taking tension stiffening into account, for panel A, made no difference in the shear deformation obtained at cracking load, figure 5.24b. This is mainly due to the uniformly sudden cracking of the panels. In contrast, panel B shows higher stiffening when tension stiffening constant C_2 increased, figure 5.25b. This is may be explained by the presence of compressive forces. In term of ultimate load tension stiffening had no effect for both panels.

The presence of the compressive forces in the second panel increased the cracking load of the panel.

Panel B was designed to answer the question, if a panel is failing in crushing of the concrete, will the addition of biaxial compression weaken the panel or strengthen the panel?. Both the experimental and numerical results show that the presence of biaxial compression increase the ultimate shear strength of the panel, so that the failure shear strength in panel B was increased by almost 50% experimentally and by 15% numerically over that of panel A. Comparisons also,

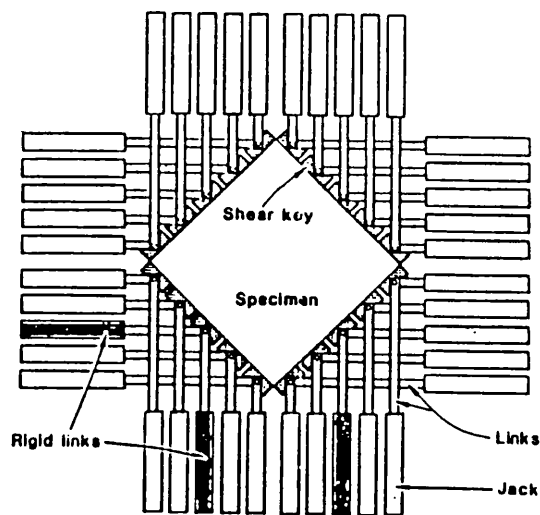


Fig. 5.21 Details of loading rig.(Vecchio and Collins)

Specimen	Concrete	Reinforcement		Loading
	f_c' MPa	Ratio	f_y MPa	
Panel A	20.5	$\rho_x = \rho_y =$ 0.01785	442	$0 \leq \tau \leq \tau_u$ $\sigma_x = \sigma_y = 0$
Panel B	19.2	$\rho_x = \rho_y =$ 0.01785	446	$0 \leq \tau \leq \tau_u$ $\sigma_x = \sigma_y =$ $0.7 \tau_u$

$1 \text{ MPa} = 1 \text{ N/mm}^2$

Table 5.1 Material properties, reinforcement ratio and loading details.

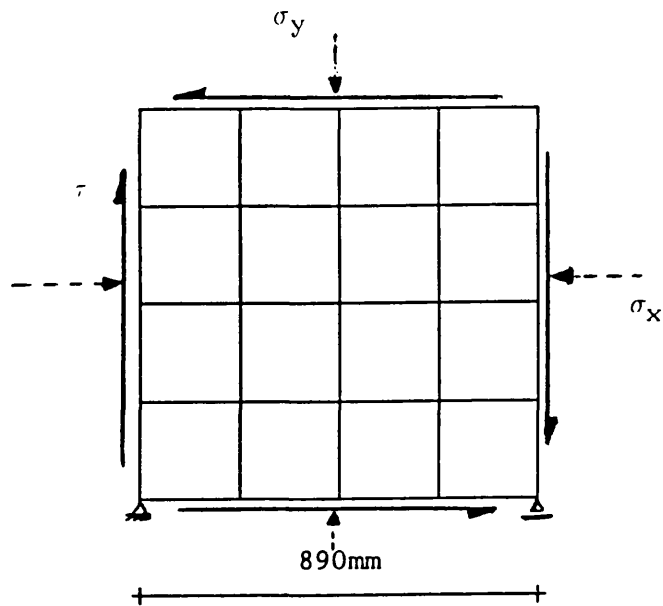


Fig. 5.22 Finite element idealization.

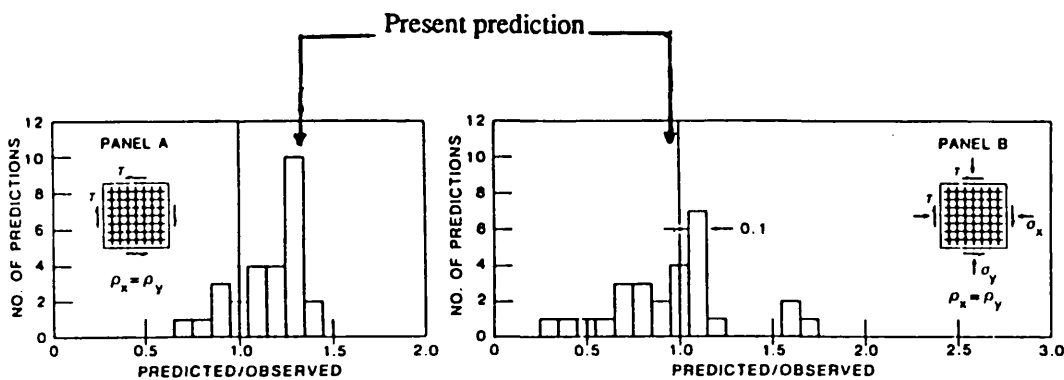


Fig. 5.23 Panels predicted strengths scatter and present prediction.

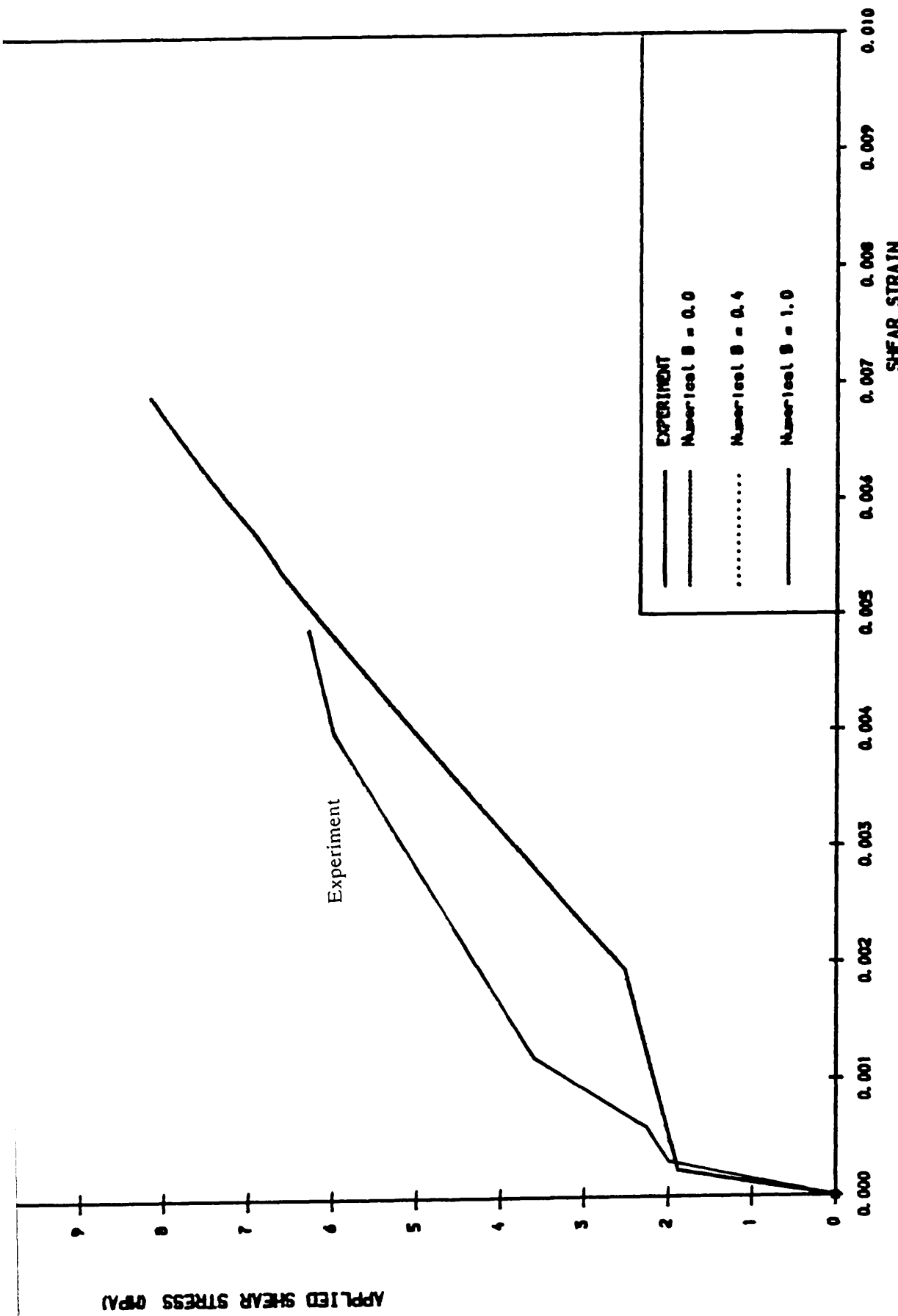


Fig. 5.24a APPLIED SHEAR STRESS-SHEAR STRAIN CURVE VICHIO & COLLIN
Panel A Under Pure Shear. Different shear retention factors

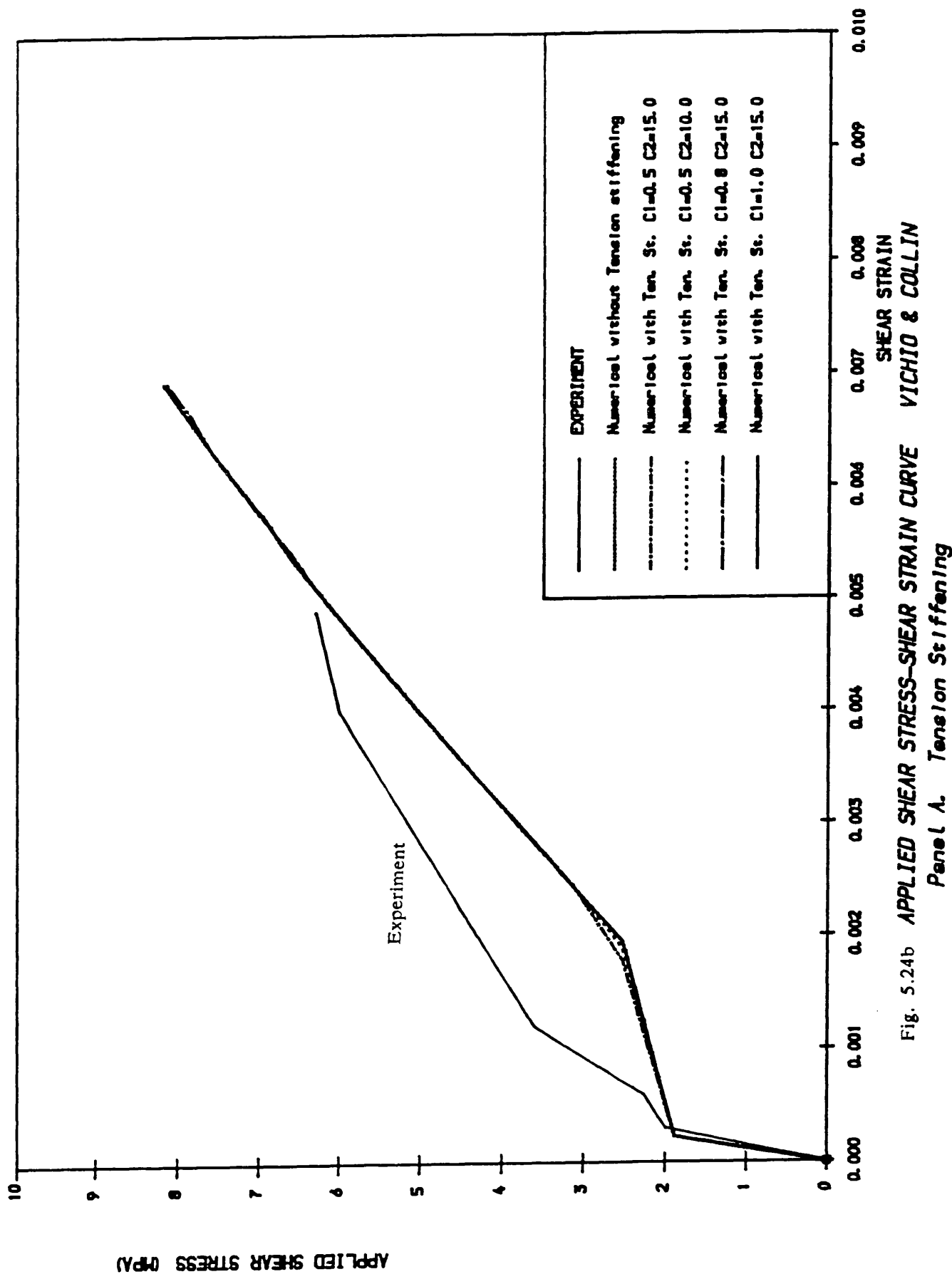
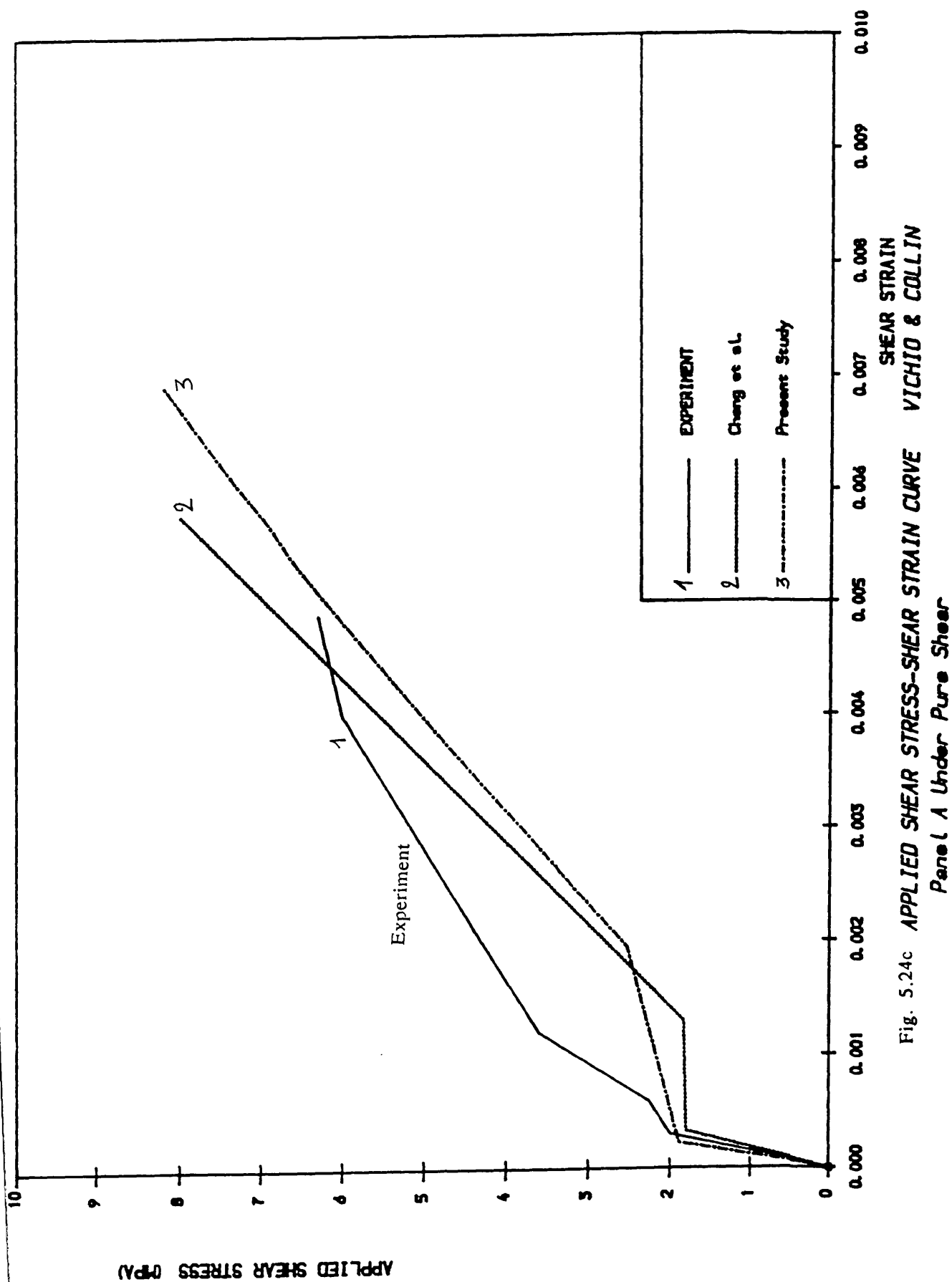


Fig. 5.24b APPLIED SHEAR STRESS-SHEAR STRAIN CURVE VICHIO & COLLIN
Panel A. Tension Stiffening



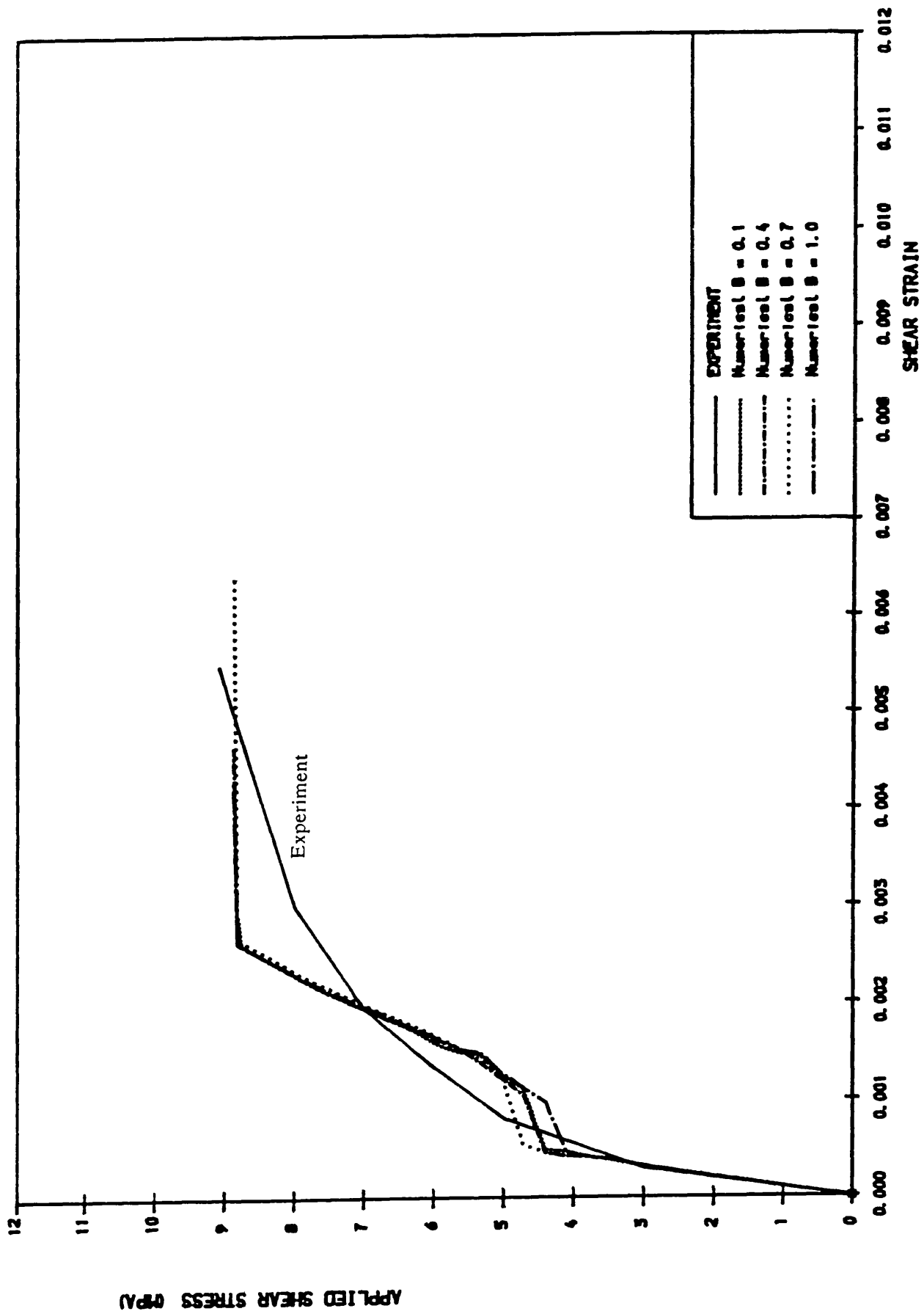


Fig. 5.25a APPLIED SHEAR STRESS-SHEAR STRAIN CURVE VICHIO & COLLIN
Panel B. Different Shear Retention factors

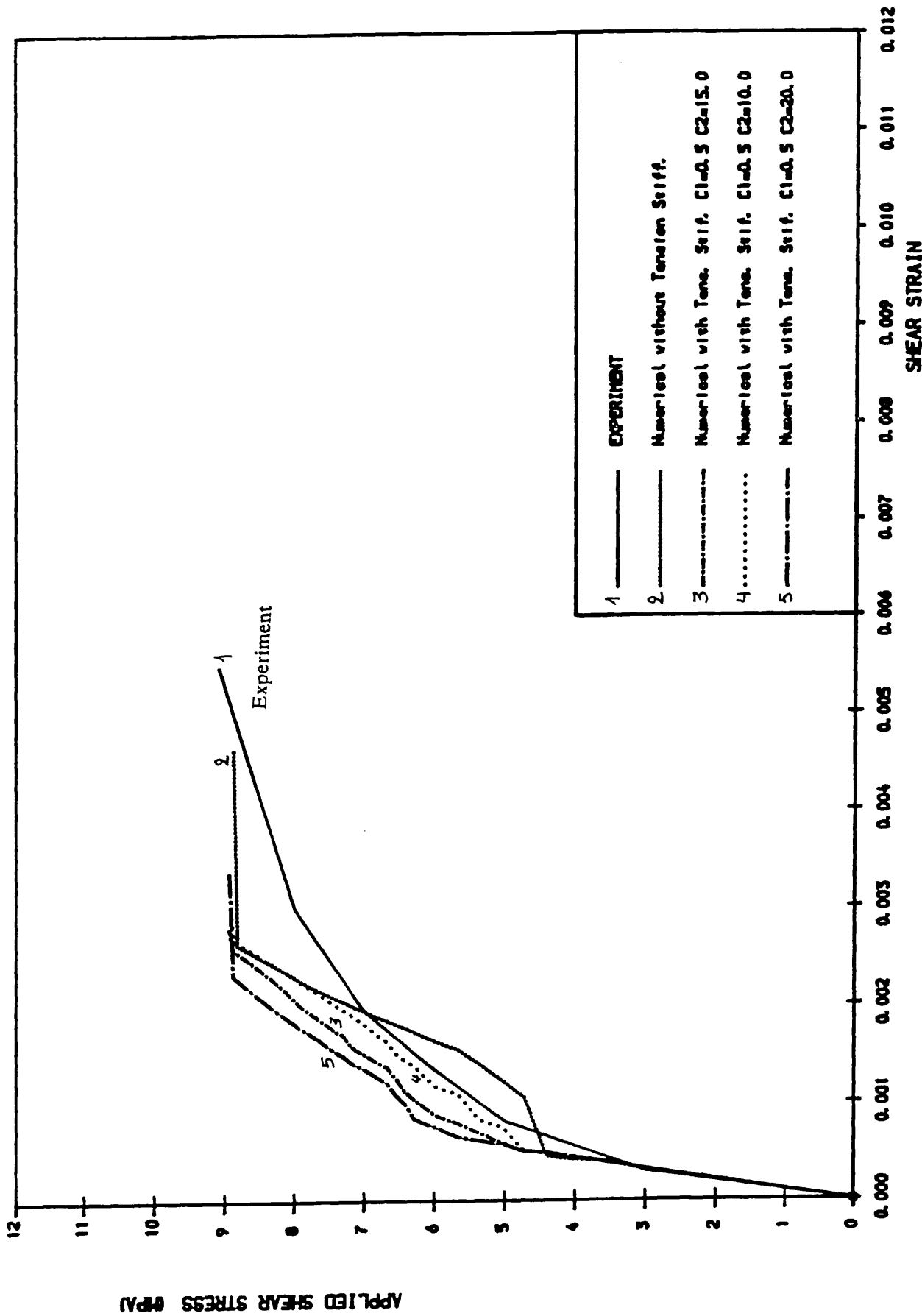


Fig. 5.25b APPLIED SHEAR STRESS-SHEAR STRAIN CURVE VICHIO & COLLIN
Panel B. Tension stiffening

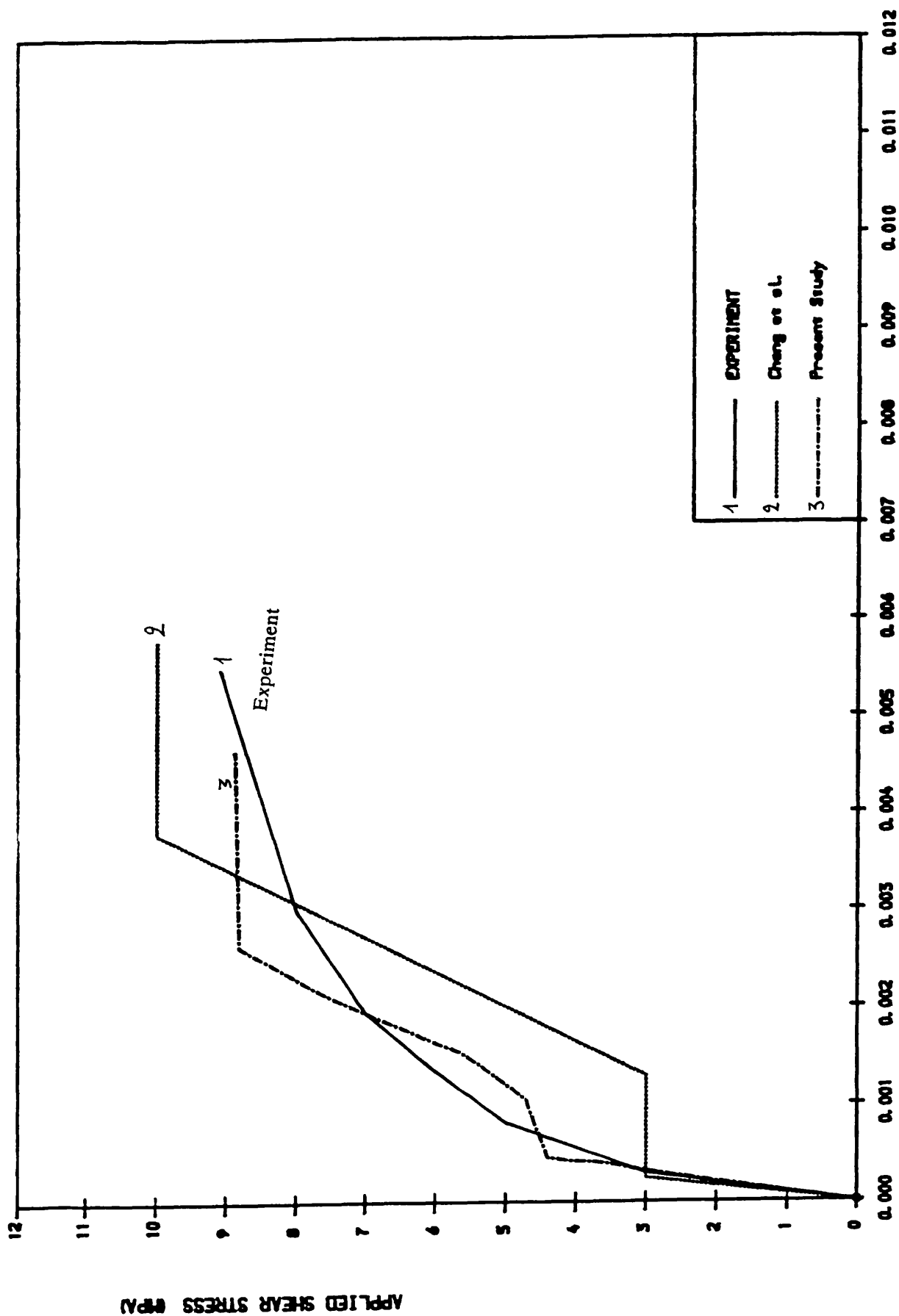
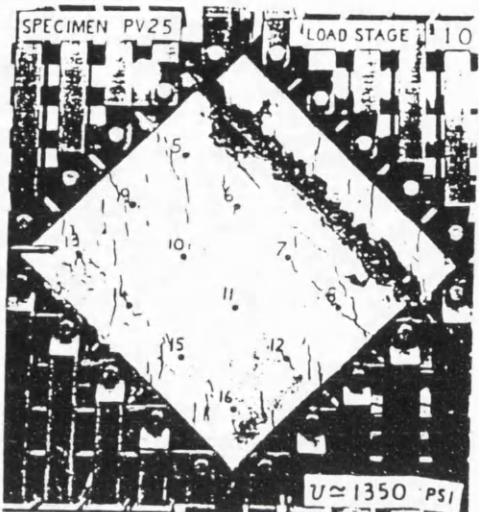


Fig. 5.25c APPLIED SHEAR STRESS-SHEAR STRAIN CURVE VICHIO & COLLIN
Panel B.



Panel A



Panel B

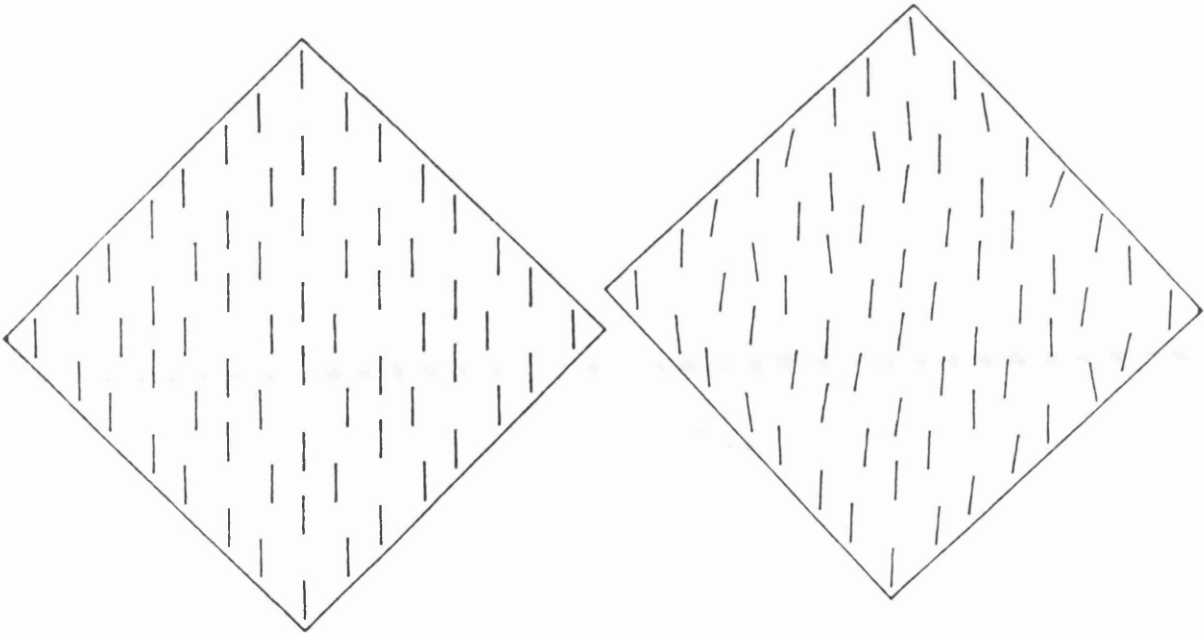


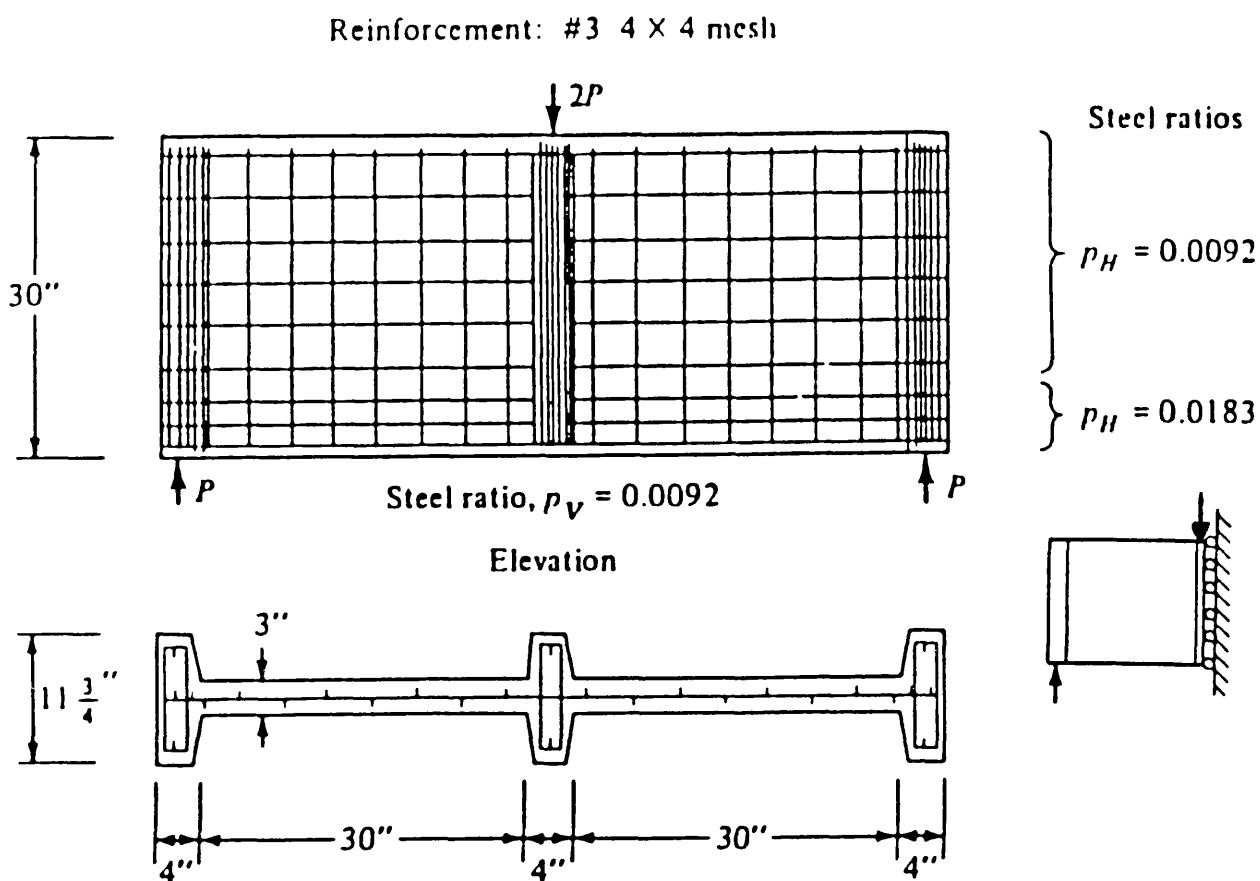
Figure 5.26 Experimental and Numerical crack pattern comparison.

were made with Chang et al.(104) numerical results and show good agreement in the predictions for panel A, figure 5.24c, while the present prediction for panel B are better both at working load and at ultimate load, figure 5.25c. Figure 5.23 a and b show that the present results are in the scatter range, where most competitors (41) predicted the ultimate strength of the panels. The crack pattern at collapse load are presented in figure 5.26. In both the panels steel did not yield in the experiment and this was true in the case of numerical results also. The crushing of the concrete was noted on the last increment and convergence could not be attained at this level.

5.8.4 CERVENKA Panel W2:

The panel was chosen from finite element investigation(26) of several shear panels which Cervenka had tested experimentally. The panels were studied numerically by many investigators(102,110). Dimensions, loading, reinforcing scheme and method of loading are shown in figure 5.27. The experimental failure load took place at $P_u = 230 \text{ KN}$.

Different finite element meshes, of 4x4, 6x6 and 8x7, were used in the numerical analysis. Figure 5.28a shows that as the number of element decreased the stiffness of the panel increased especially as approaching the failure load of the 4x4 mesh analysis. The predicted ultimate load was almost the same for all the meshes used. Both smeared and embedded representation of steel reinforcement give good correlation with the experimental results, figure 5.28b. When taking into account tension stiffening, the panel stiffened at working load, while the ultimate load was almost the same as the one given excluding tension stiffening. Shear retention factor variation, simulating smooth to rough concrete crack interface, seems to have little influence on the behaviour of the panel as well as its ultimate load, figure 5.28c. This may be due to the flexural behaviour of the panel and the presence of important vertical steel reinforcement. Crack patterns, both experimental and numerical at failure load, are presented in figure 5.29 and shows the ability of this



Concrete: $f'_c = 26.8 \text{ MPa}$ $f_t = 3.6 \text{ MPa}$

$$E_c = 2.0 \times 10^4 \text{ MPa}$$

Steel: $f_y = 353 \text{ MPa}$ $E_s = 1.9 \times 10^5 \text{ MPa}$

Fig. 5.27 Dimensions, reinforcement, loading and material properties.
Cervenka Panel W2.

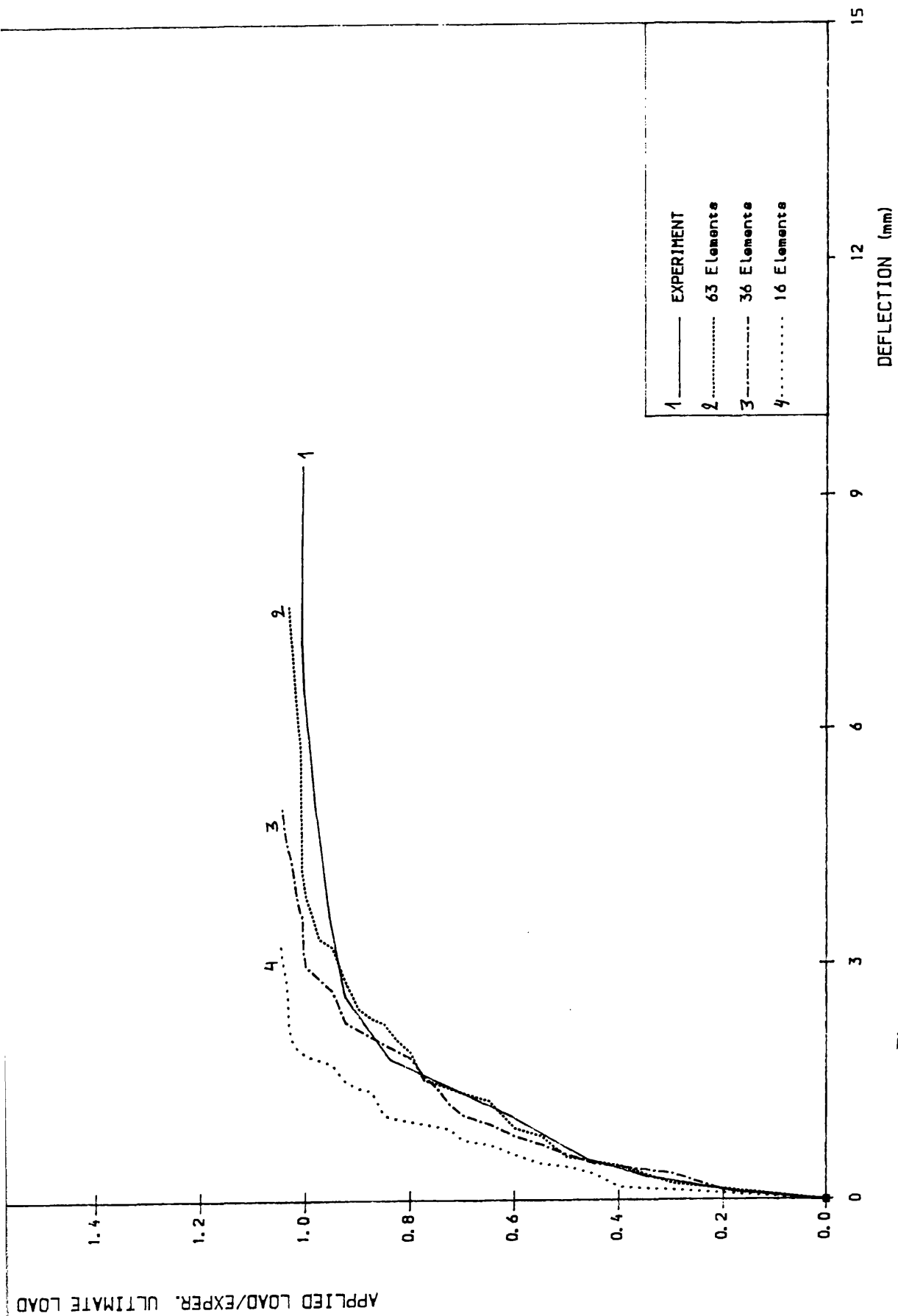


Fig. 5.28a LOAD-DEFLECTION CURVE CERVENKA WALL PANEL
Finite Element Mesh Size

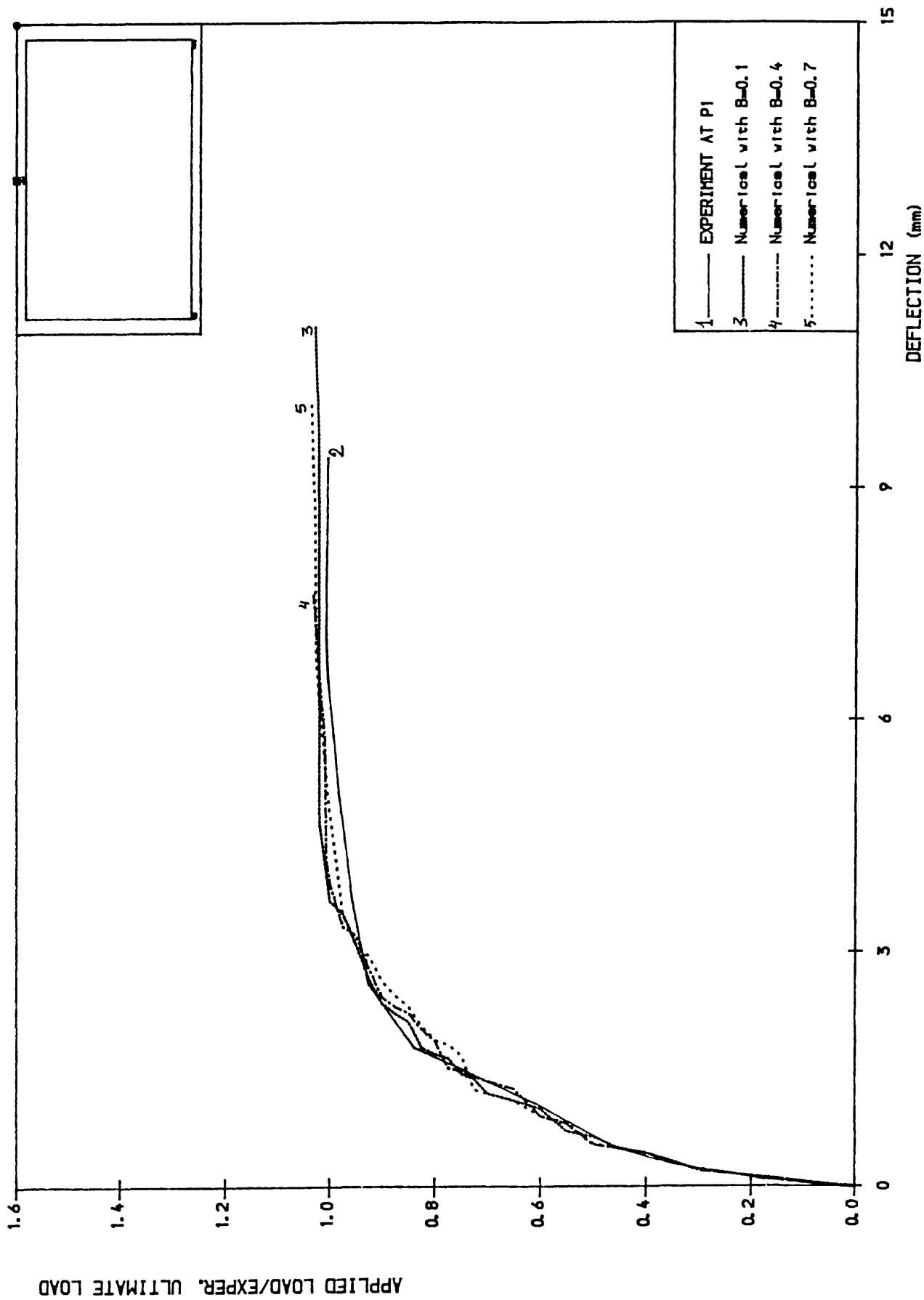


Fig. 5.28b LOAD-DEFLECTION CURVE CERVENKA WALL PANEL
SHEAR RETENSION FACTOR

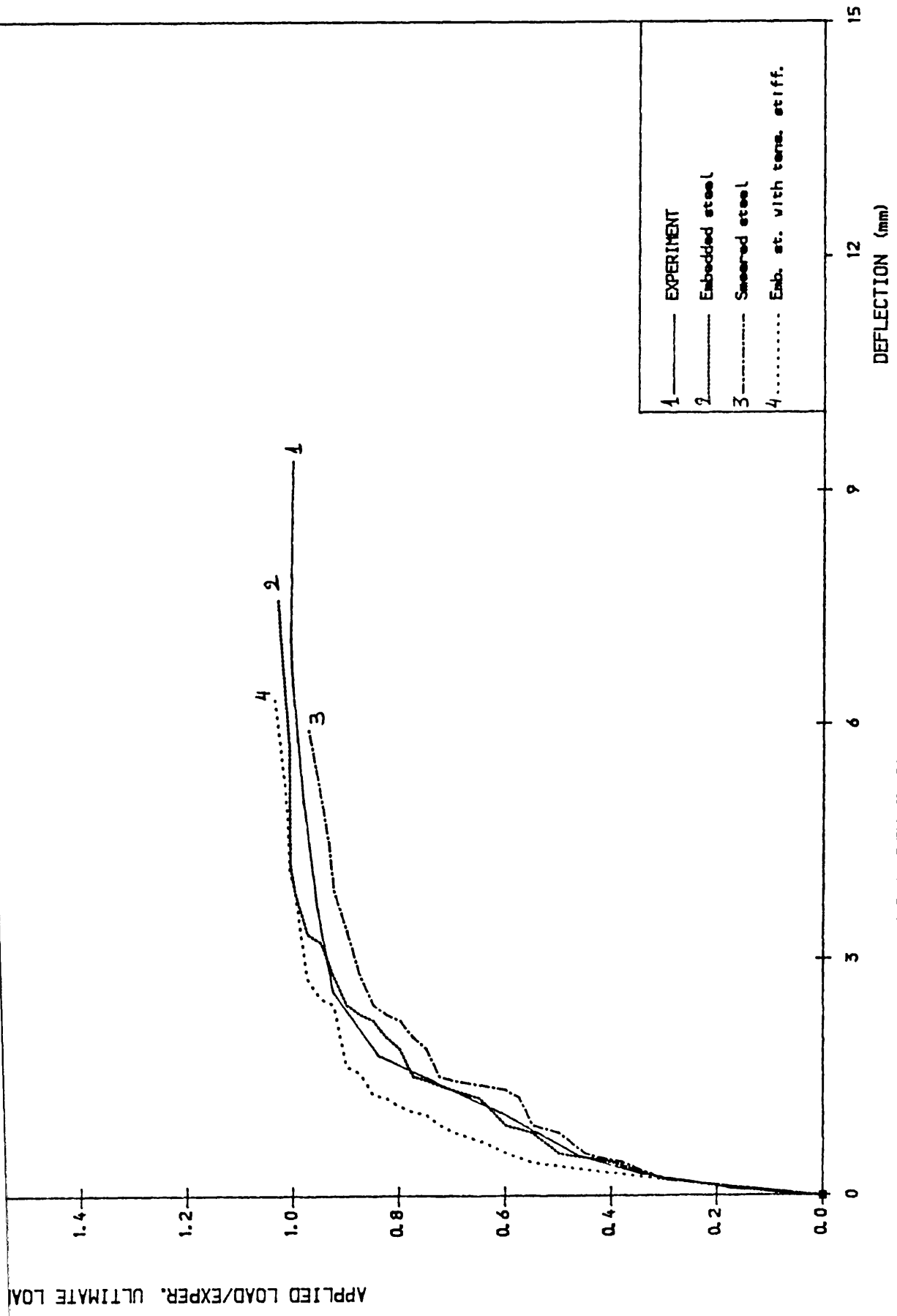


Fig. 5.28c LOAD-DEFLECTION CURVE CERVENKA WALL PANEL

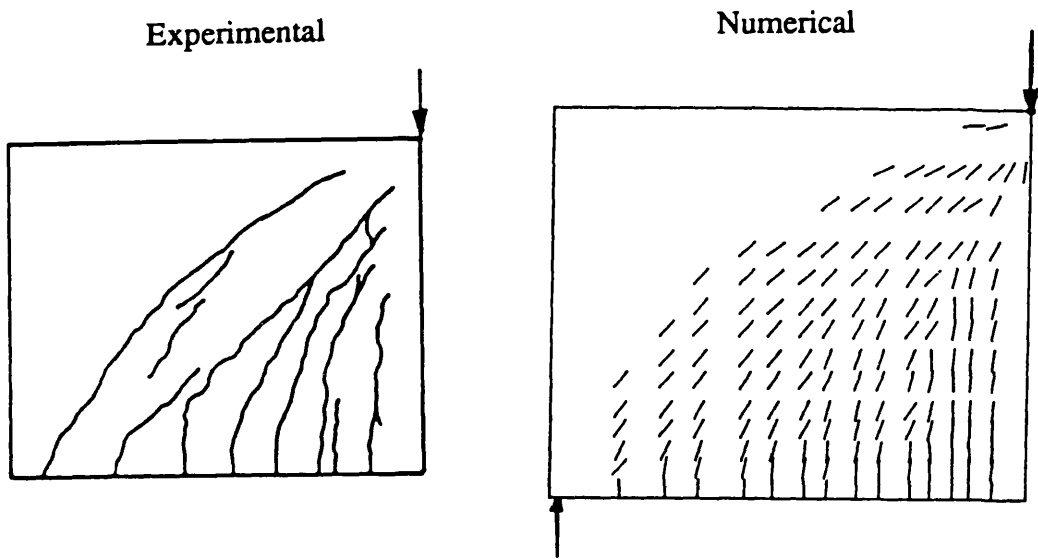


Fig. 5.29 Experimental and numerical crack patterns comparison.

model to duplicate the experimental crack patterns. The panel failed flexurally by yielding of longitudinal steel corresponding with experimental mode of failure.

5.8.5 Khaskheli Transfer Girder:

Four two span continuous deep beams TRGRAS1, TRGRAS2, TRGRAS3 and TRGRAS4 were chosen from the test program carried out by Khaskheli(81). The purpose of the experimental work was mainly to validate the direct design procedures for designing deep beams in general and continuous deep girders in particular, for serviceability and ultimate conditions.

The aim of analysing these beams was to check the performance of the present analytical model, both at service and ultimate loads, in predicting the behaviour of such structures, which had different reinforcement distribution and span depth ratio. The geometry of the first three beams were the same with span to depth ratio of 1.07. The span to depth ratio of the fourth beam TRGRAS4 was 1.61. All the beams were designed according to direct design rules. The difference between beams TRGRAS1 and TRGRAS2 was in the amount of shear reinforcement provided, which was greater in TRGRAS1, while the main reinforcement was the same. The analysis of these two beams will evaluate the effect of the shear reinforcement on the ultimate load of the beams. The difference between the beam TRGRAS2 and beam TRGRAS3 was in the longitudinal reinforcement, while the shear reinforcement was the same. The design load, $P_d = 1100\text{KN}$, of TRGRAS3 was higher than that of TRGRAS2. The design ultimate load of TRGRAS4 was the same as that of the first two girders and was equal to 810KN . The overall depth and the thickness of all the beams was kept constant equal to 900mm and 100mm respectively. The span between the centres of the support bearings was 960mm for the first three beams whereas for the forth beam it was increased to 1450mm . Figures 5.30 show the steel layout and the dimensions of the beams. The material properties of the beams are presented in table 5.2.

	Concrete Properties			Span-Depth Ratio	Shear Span-Depth Ratio	Design Load Pd KN
	E_c KN/mm ²	f_{cu} KN/mm ²	f_t KN/mm ²			
TRGRAS1	19.3	63.0	3.2	1.07	0.42	810
TRGRAS2	23.2	61.0	3.7	1.07	0.42	810
TRGRAS3	20.8	61.0	3.4	1.07	0.42	1100
TRGRAS4	19.2	52.0	2.6	1.61	0.69	810
Steel diam. 6mm $f_y = 513 \text{ N/mm}^2$, $E_s = 199000 \text{ N/mm}^2$ Steel diam. 8mm $f_y = 520 \text{ N/mm}^2$, $E_s = 195000 \text{ N/mm}^2$						

Table 5.2 Khaskheli Beams properties

Taking advantage of symmetry, only one span of the beams was analysed using 8x7 finite element mesh. Beam TRGRAS1 was analysed using both smeared and embedded steel formulations. The first crack opened in the two numerical analysis at the same level of loading (0.4 Pd) while experimentally, it was reported to have appeared at 0.3 Pd in the same location as in the numerical analysis, at the soffit of the beam in the mid-span. The first yielding of longitudinal steel, in the middle span of the beam soffit, was experimentally recorded at 1.30 Pd, whereas numerically it was at 1.0 Pd. A little enhancement in the ultimate load, using embedded bar analysis, was recorded as presented in figure 5.31. Closer examination of the load displacement curve reveals an important loss of stiffness of the beam at 1.075 Pd caused by a sudden shear cracks. It is instructive to plot

the crack pattern just before this irregularity (at 1.05 Pd) and after (at 1.075 Pd), figures 5.32a and 5.32b. Note that this load level roughly coincide with the experimental load of the inclined shear cracks which opened in the internal shear span of the beam at 1.16 Pd. It can be seen that no inclined shear cracks in the interior span of the beam opened at 1.05 Pd (figure 5.32a), while suddenly at 1.075 all the interior span was covered by cracks. Notice that there is almost no difference in crack pattern at this level and the one where failure load was considered, figure 5.32b and 5.32c. This explains that the cracks opened at 1.075 Pd had an important effect on the ultimate behaviour of the beam.

Figure 5.31c shows different load deflection curves corresponding to different shear retention factor B ranging from 0.1 to 1.0. Using low value of B (0.1) gives low ultimate load and equal to the load where the shear cracks opened in the interior span of the beam. This confirms that the cracks opened at 1.075 Pd were caused by high shear stresses. The other values of B gives almost the same ultimate load, although $B = 0.4$ resulted in higher ultimate load. For steel strain of the longitudinal bar at the soffit of the beam, a reasonable agreement can be seen between the numerical and the experimental results, figure 5.31b. The curves show that no significant strain prior cracking of concrete was recorded. Numerically the steel yielded at 1.075 Pd. At failure, good agreement between experimental and numerical crack patterns was obtained as shown in figure 5.32c. The experimental failure load (P_u) took place at 1.56 Pd. The Numerical failure load was of 0.92 of the experimental one, using embedded formulation, while using smeared the ultimate load was of 0.87 P_u . No vertical steel yielded both experimentally and numerically.

The load deflection curves for beam TRGRAS2 and TRGRAS3 are shown in figures 5.33a and 5.33b respectively and are similar to beam TRGRAS1. The difference was in the load where the inclined cracks of the interior shear span opened. For TRGRAS2 this crack opened at 0.975 Pd (828.5 KN) lower than the corresponding load of the first beam, which was at 1.075 Pd (914 KN). The failure took place numerically at 1.375 Pd (1164 KN) and at 1.43 Pd (1216 KN)

experimentally. Both numerical and experimental results gave a lower ultimate load for this beam TRGRAS2 than the one of the previous beam. For TRGRAS3 the load corresponding to the shear cracking of the interior shear span of the beam, was at $0.8 P_d$ (880 KN). The failure load took place numerically at $1.275 P_d$ (1402.5 KN) while experimentally it was at $1.36 P_d$ (1500 KN). Beam TRGRAS4 was chosen to ascertain the effect of the span—depth ratio on the beam behaviour and failure mechanism, since its span—depth ratio was greater than that of the previous beams. The design load was the same as for the first and the second beam ($P_d = 850$ KN). The beam was loaded using the same load increments as for the previous beams. The first crack was detected at 0.3 of the design load at the soffit of the beam, whereas experimentally it opened at $0.12 P_d$. As the load increased the cracks propagate towards the loading point. The cracks opened at the top of the intermediate support at $0.65 P_d$ numerically and at $0.70 P_d$ experimentally. Up to this level of loading the load deflection relationship was almost linear, figure 5.34. As for previous beams, at $0.725 P_d$ a large number of cracks, in the interior span of the beam, opened (compare figure 5.35a and 5.35b). A maximum of 43 iteration require to achieve convergence at this load increment. The inclined shear crack was reported experimentally at $1.05 P_d$. The steel yielded earlier numerically ($0.80 P_d$) than experimentally ($0.92 P_d$). The failure took place at $1.15 P_d$ and 1.34 in the numerical and experimental results, respectively. The load deflection and load strain curves, both numerical and experimental, show that the beam behaved more flexurally than the previous beams, although failure took place experimentally in shear. In this beam the strain in horizontal steel was several time of its yield strain. It is unfortunate that in the the experiment, the strain gage was failed before the ultimate load of the beam was reached, thus providing no comparison with experimental values. At failure no vertical steel had yielded both experimentally and numerically.

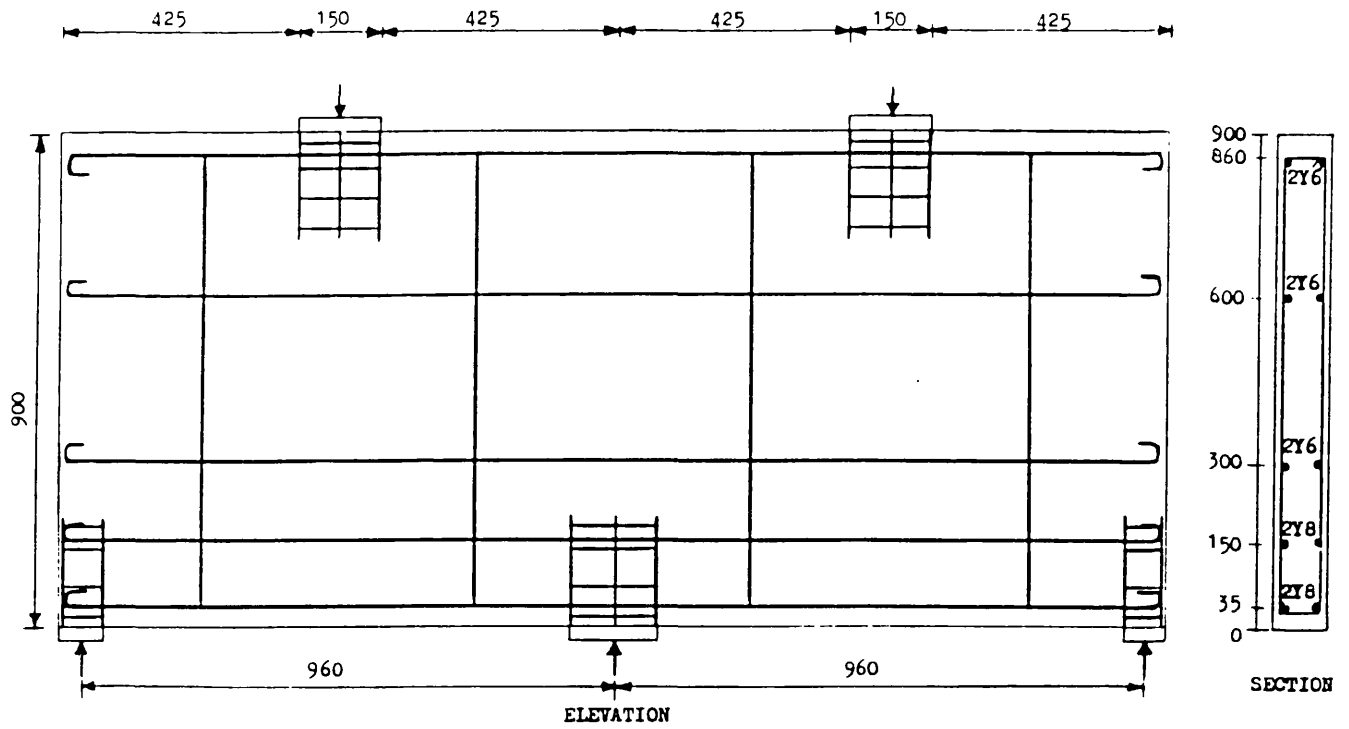


Fig. 5.30a Dimensions and reinforcing details of girder TRGRAS3

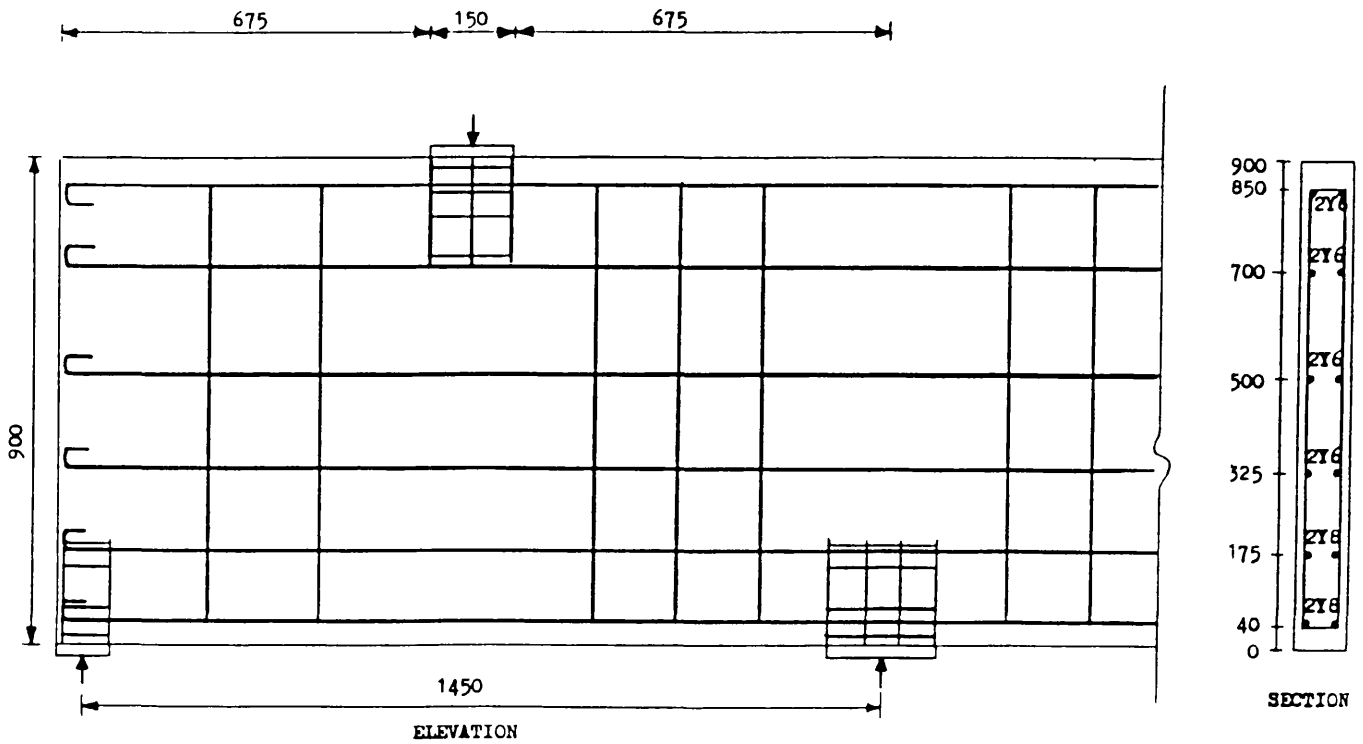


Fig. 5.30b Dimensions and reinforcing details of girder TRGRAS4

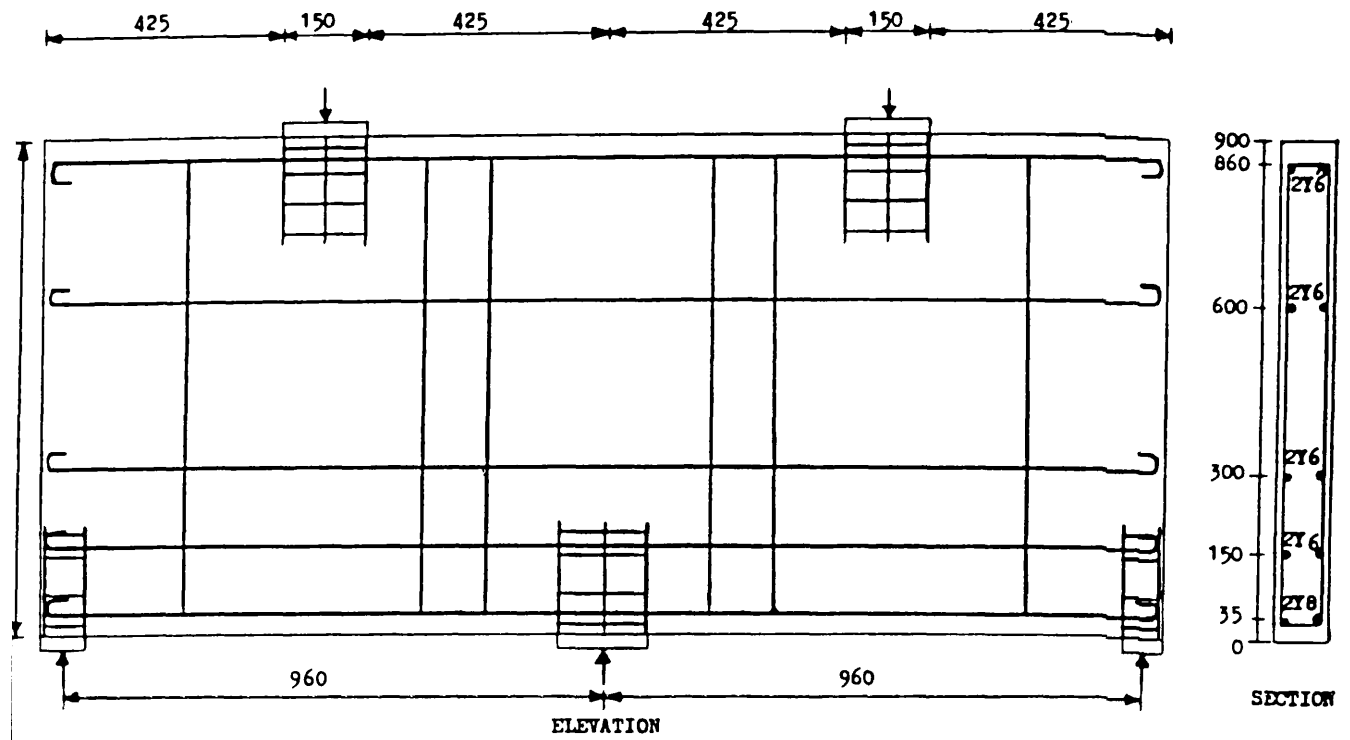


Fig. 5.30c Dimensions and reinforcing details of girder TRGRAS1

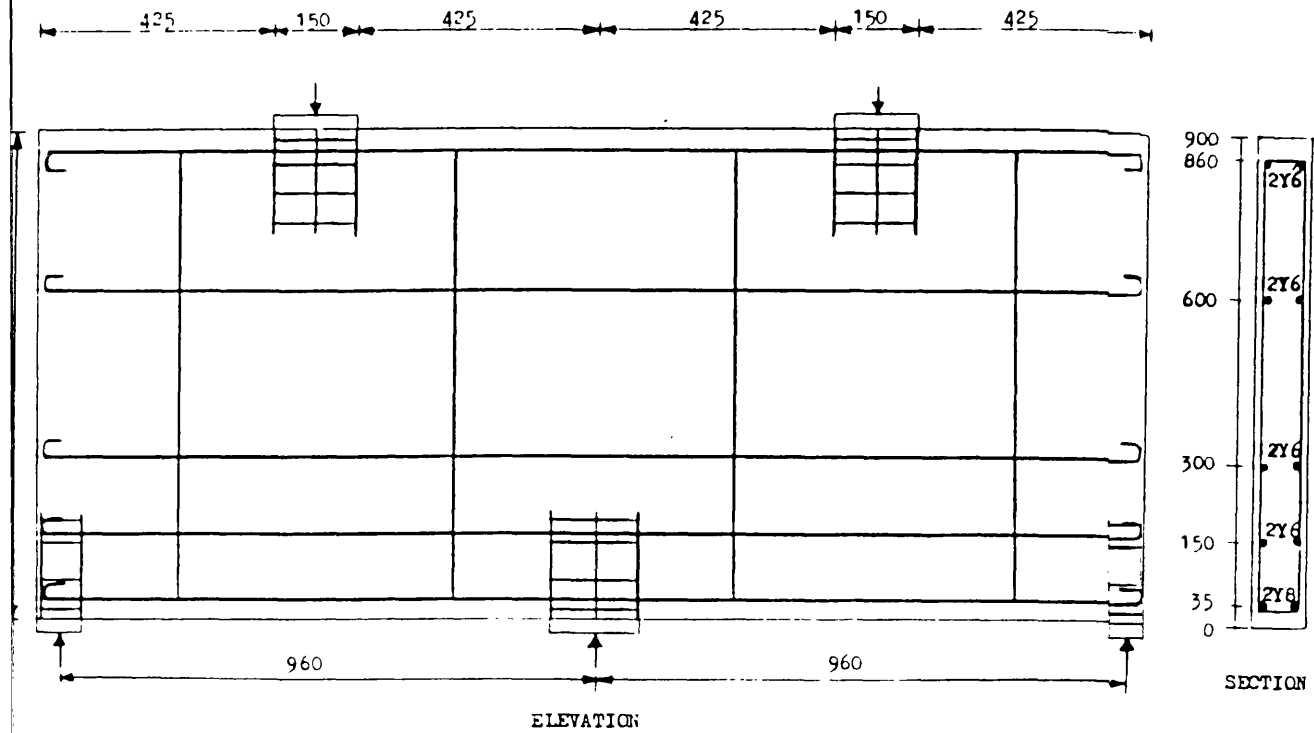


Fig. 5.30d Dimensions and reinforcing details of girder TRGRAS2

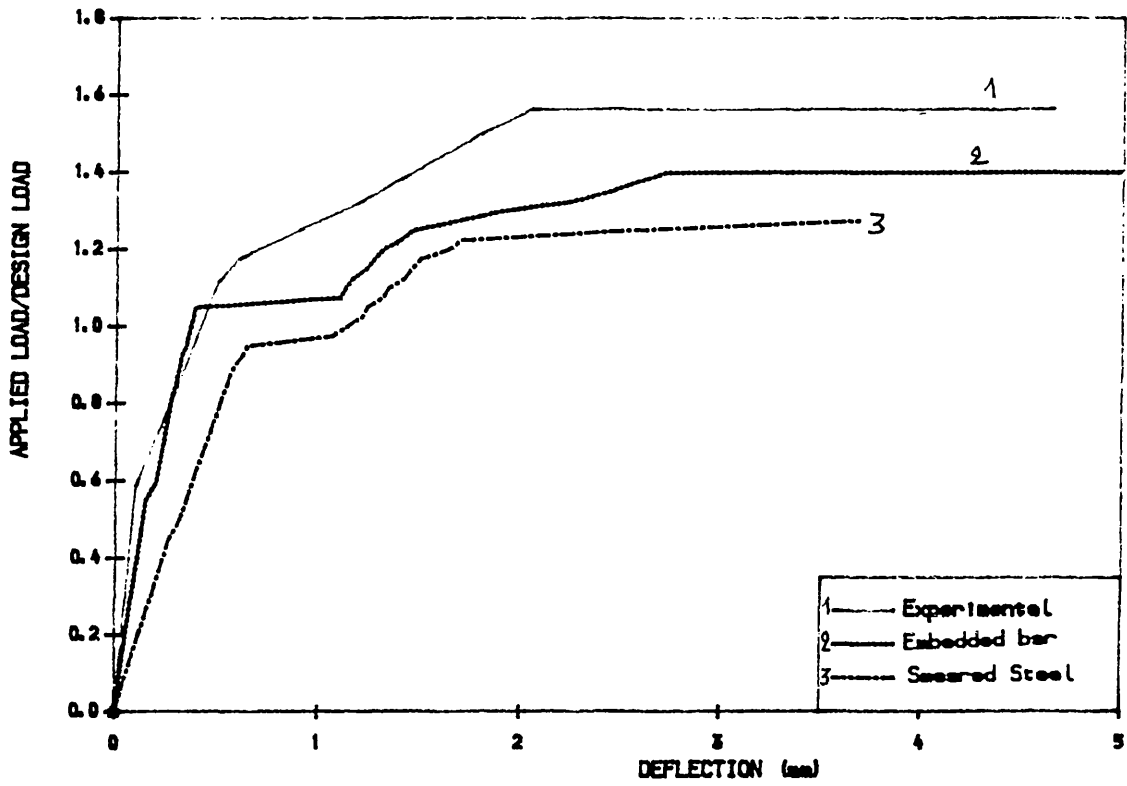


Fig. 5.31a Load- Deflection Curve. Khaskheli Beam TRGRAS1.

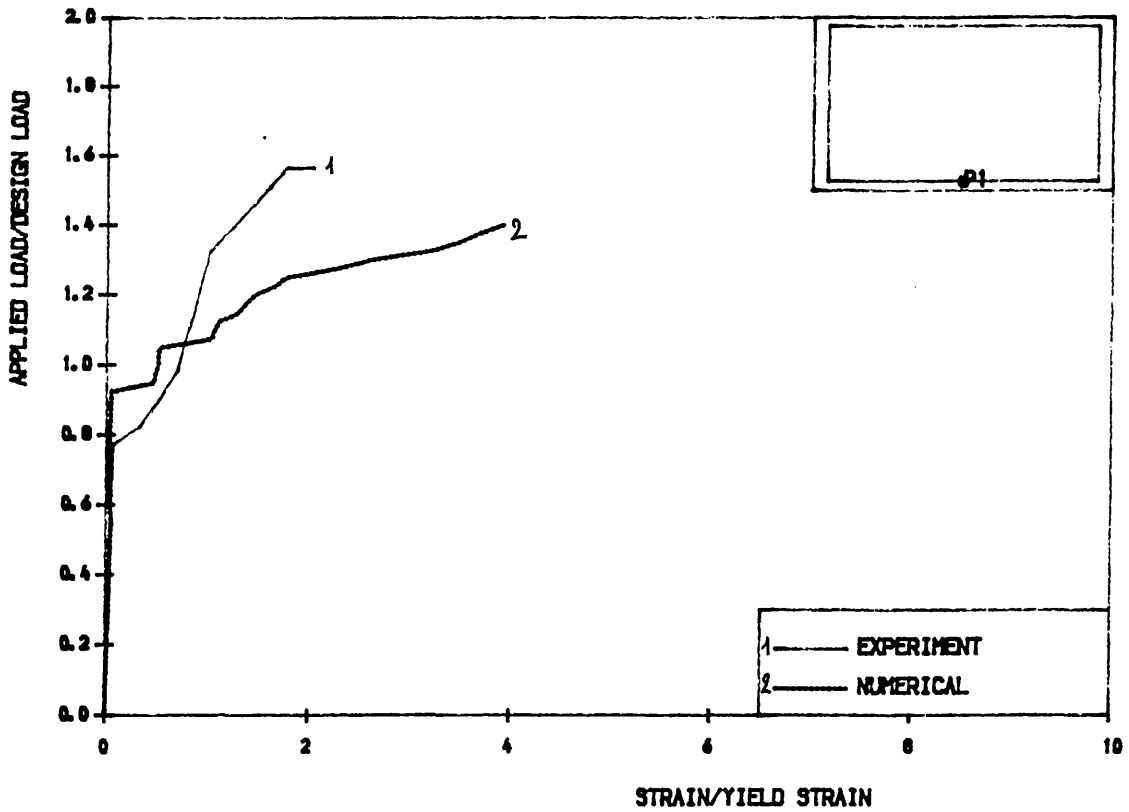


Fig. 5.31b Load-Steel Strain curve. Khaskheli Beam TRGRAS1.

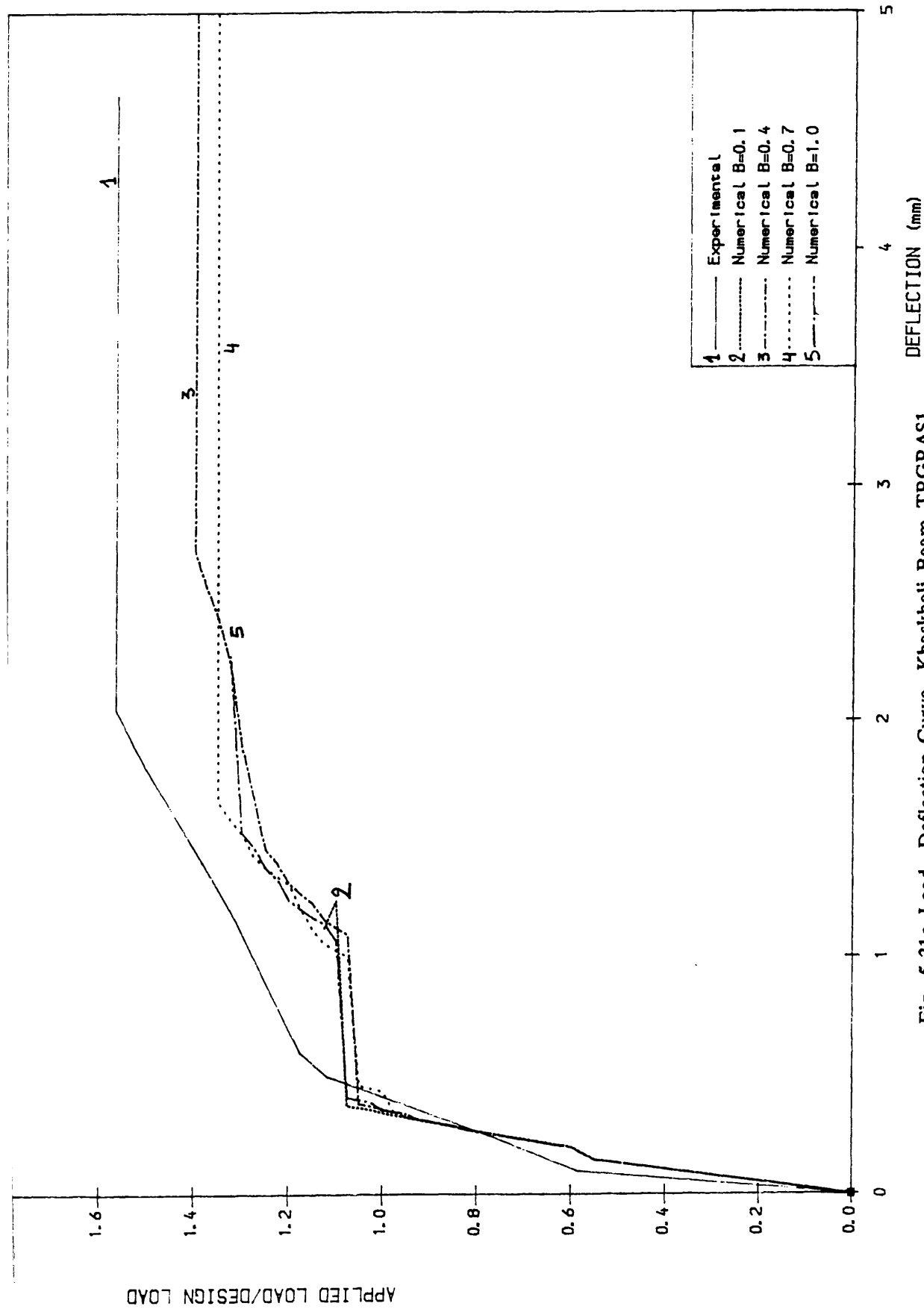


Fig. 5.31c Load-Deflection Curve, Khaskheli Beam TRGRAS1.

Different Shear Retention Factors.

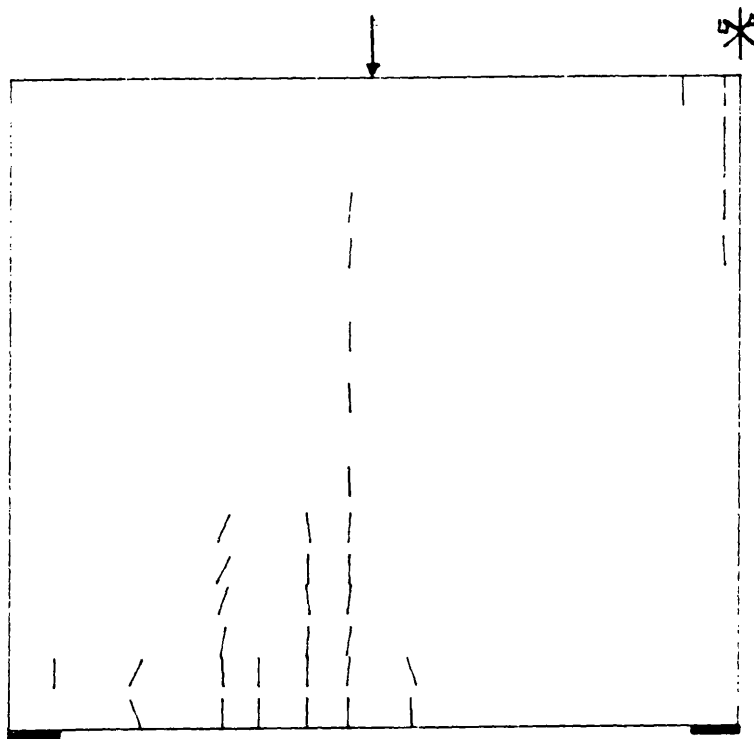


Fig. 5.32a Crack pattern at 1.05 Pd. Beam TRGRAS1

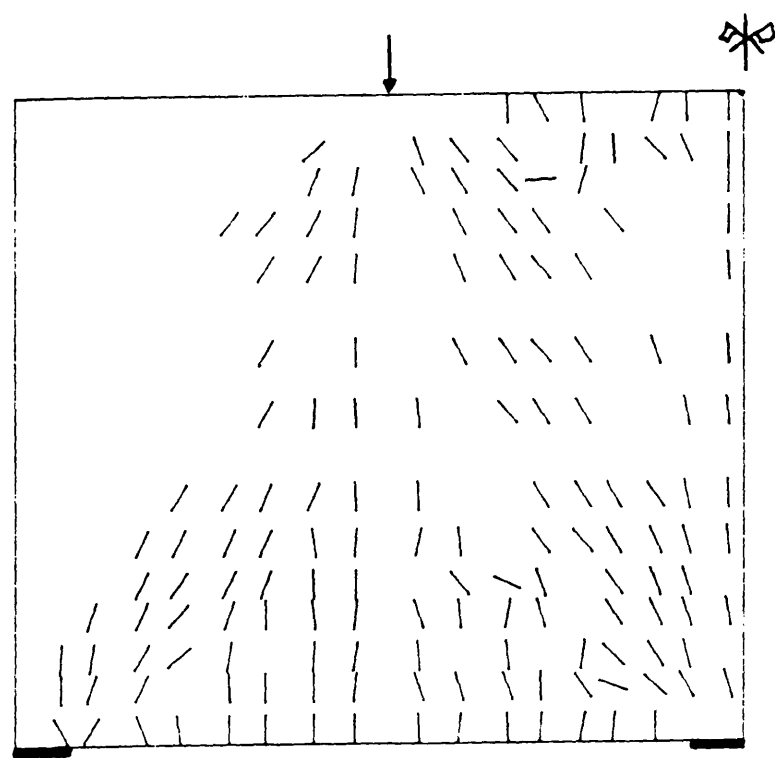
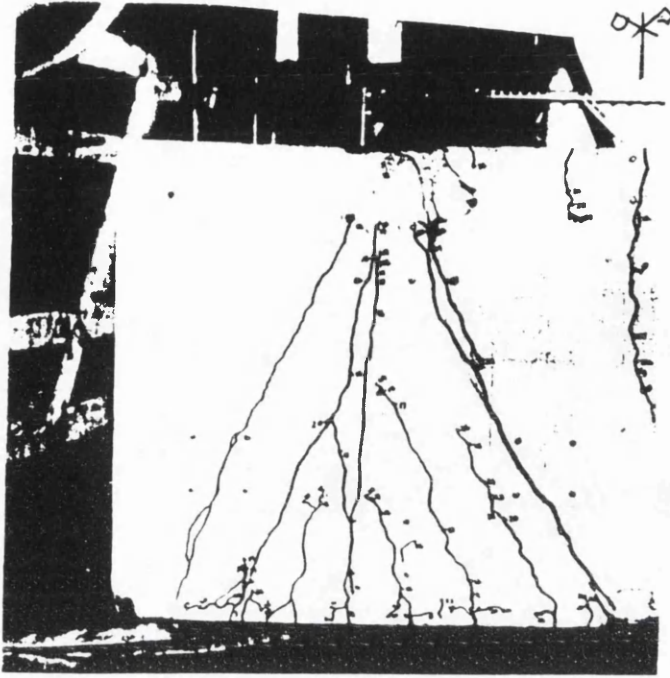
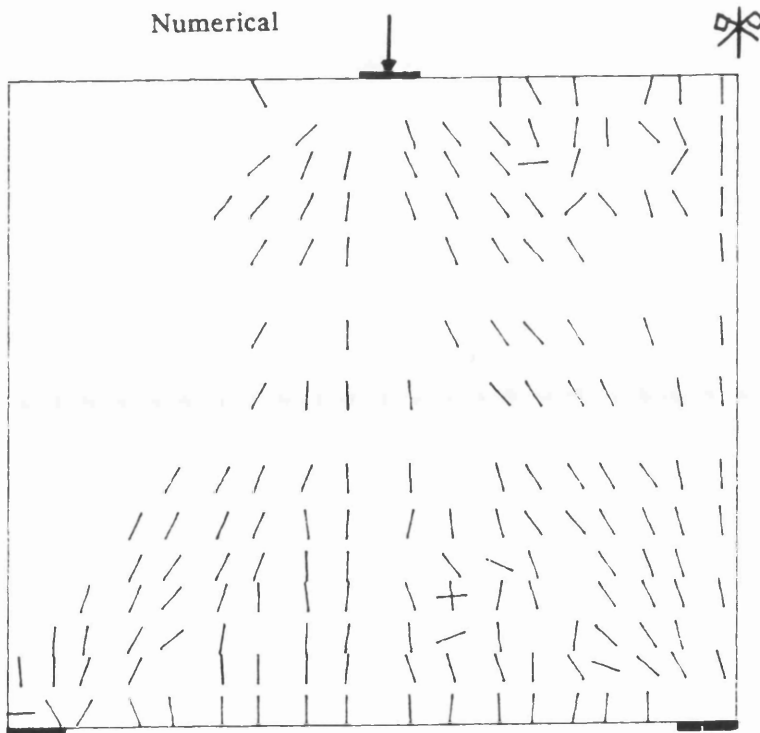


Fig. 5.32b Crack pattern at 1.075 Pd. Beam TRGRAS1



Experimental



Numerical

Fig. 5.32c Crack pattern at Collapse Load. 1/2 Beam TRGRAS1.

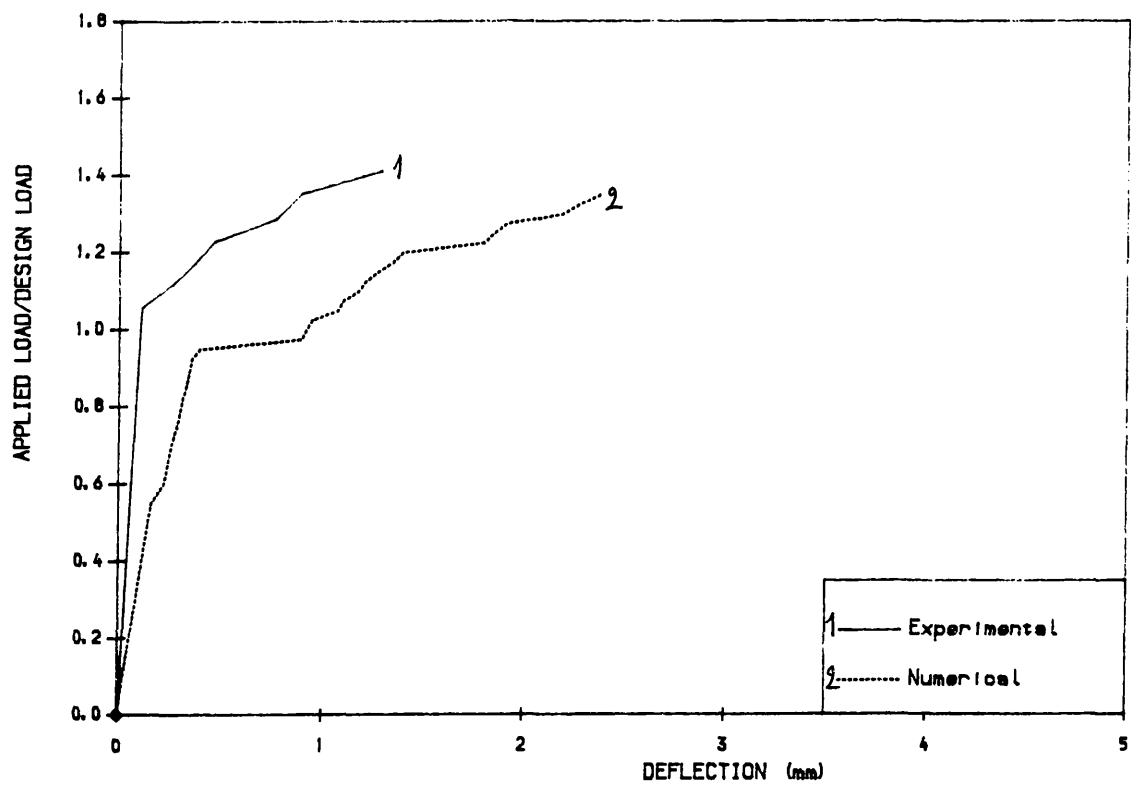


Fig. 5.33a Load— Deflection Curve. Khaskheli Beam TRGRAS2

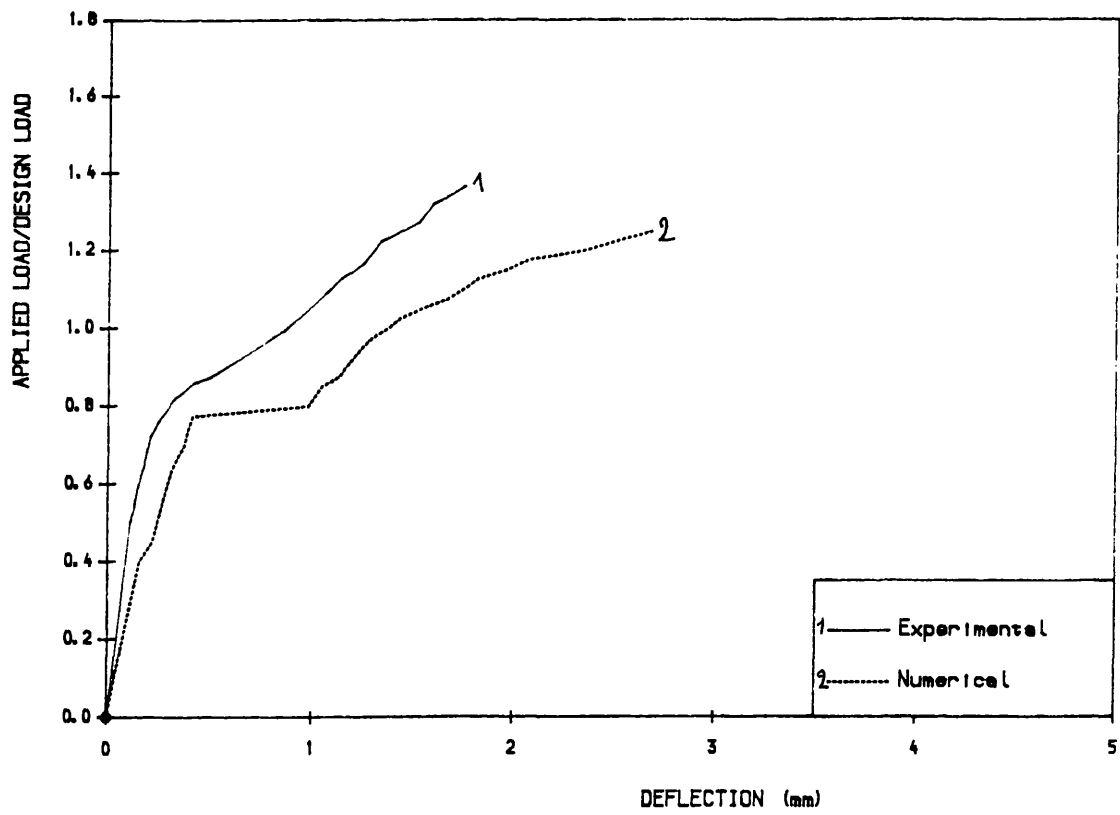


Fig. 5.33b Load— Deflection Curve. Khaskheli Beam TRGRAS3

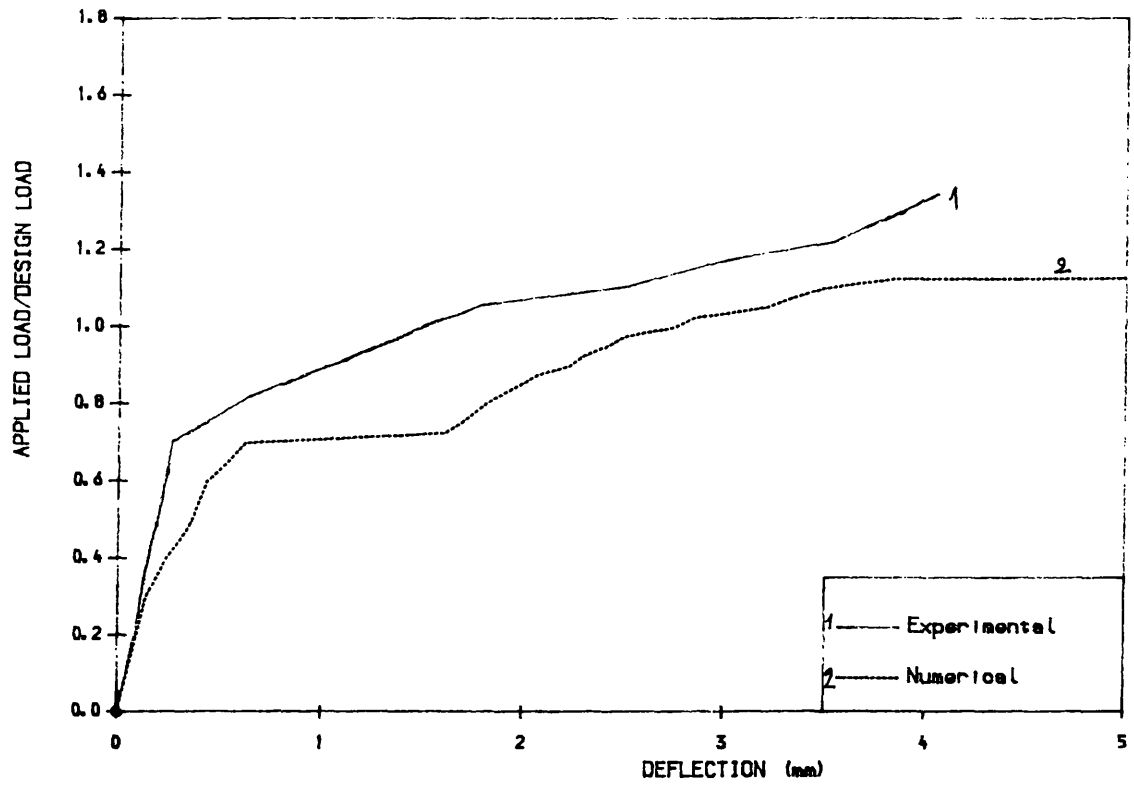


Fig. 5.34a Load- Deflection Curve. Khaskheli Beam TRGRAS4

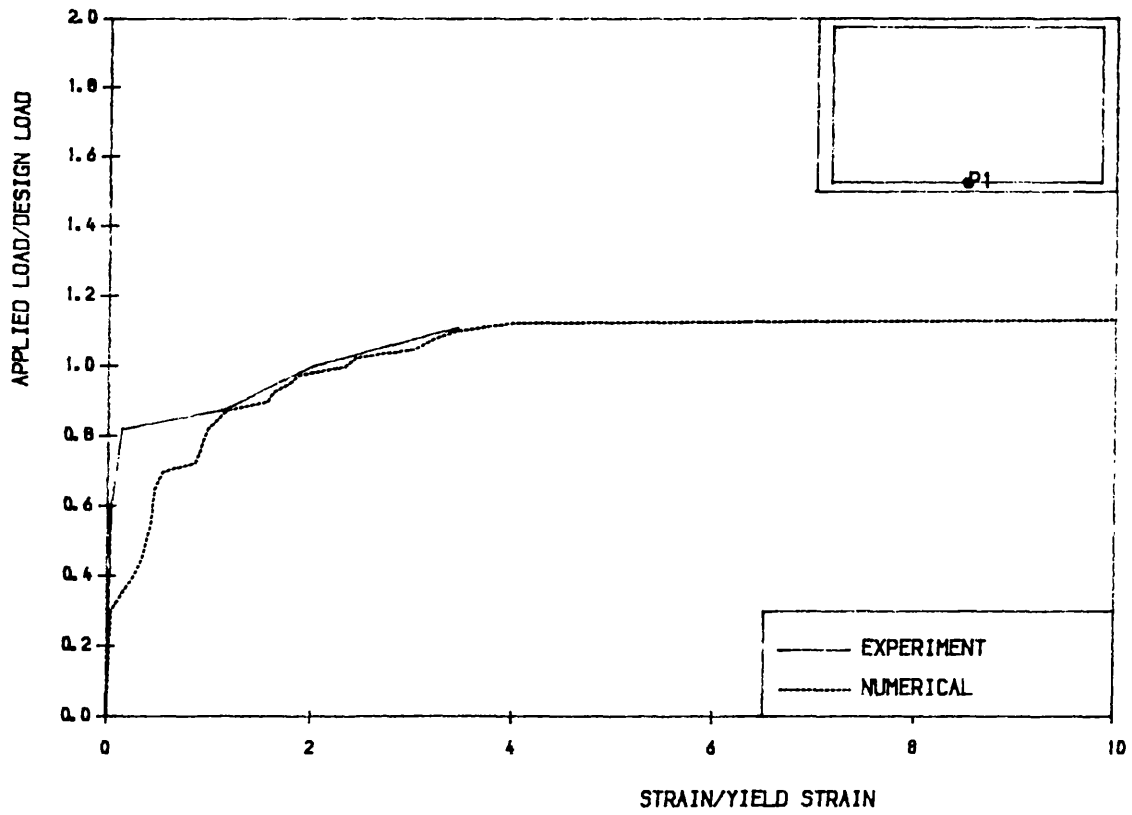


Fig. 5.34b Load- Steel Strain Curve. Khaskheli Beam TRGRAS4

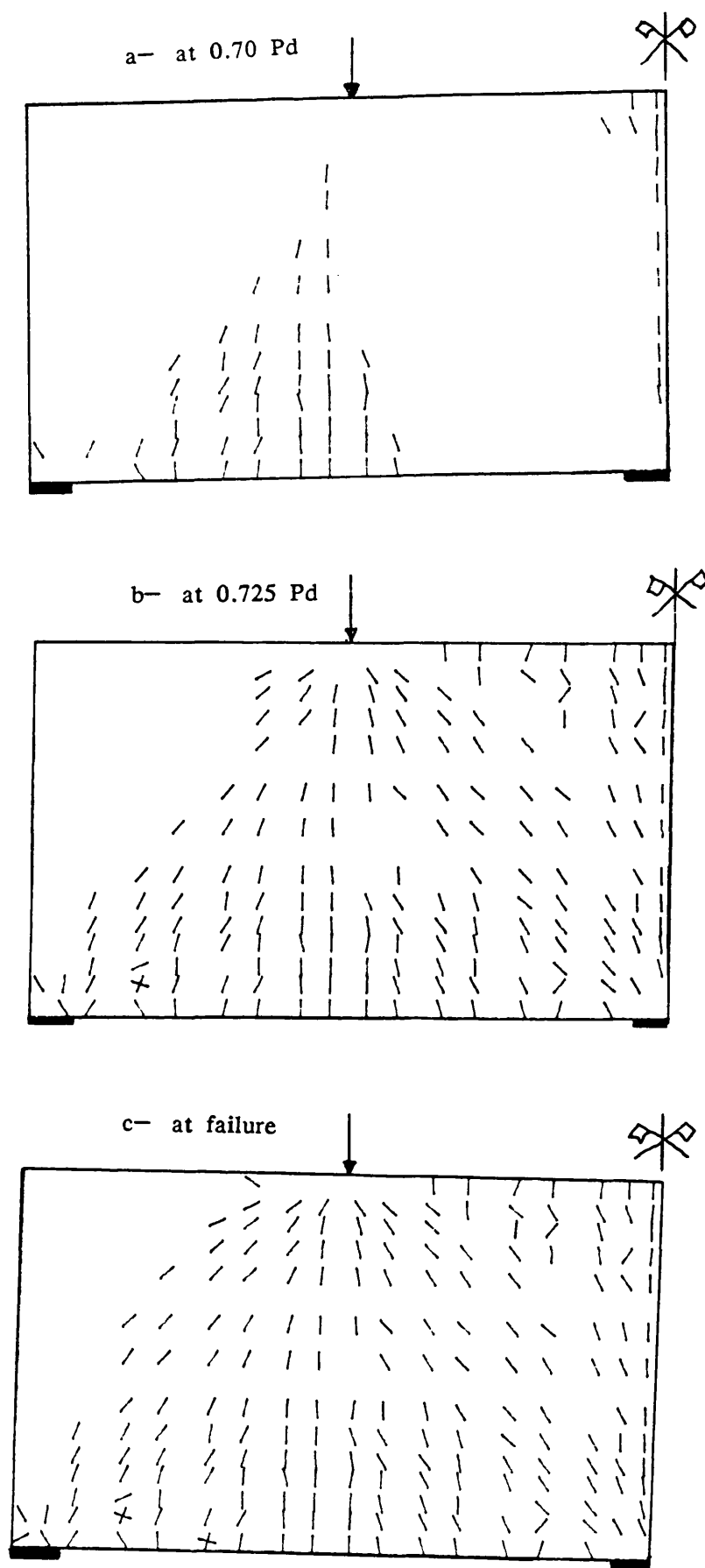


Fig. 5.35 Numerical Crack Pattern at Different Stage of Loading.

1/2 Beam TRGRAS4.

5.8.6 Gijesbers and Smit Beam:

This beam which was tested by Gijesbers and smit(112) and described by Rots et al.(114) as a challenging beam to be analysed. The beam was subjected to a uniformly distributed load, while the majority of test report in the literature has concentrated on a finite number of point loading systems. As shown in figure 5.36a, the beam was relatively small compared with large supporting end— blocks that had been added in order to fix the desired moment shear ratio. By varying the sizes a , e , and l in figure 5.36a, this moment/shear ratio as well as the slenderness of the beam could be varied. In this way a wide range of shear failure mechanism have been investigated(112), such as diagonal tension failure and shear compression failure. This beam contained both tensile and compressive reinforcement, but no stirrups. The dimensions and finite element mesh adopted are shown in figure 5.36b. The material properties of the beam were as follows:

$$\begin{aligned} E_c &= 25000 \text{ KN/mm}^2 & ; & & f_y &= 415 \text{ KN/mm}^2 \\ f_t &= 2.0 \text{ N/mm}^2 & ; & & E_s &= 210000 \text{ KN/mm}^2 \\ \nu &= 0.2 \end{aligned}$$

Since the compressive strength of concrete was not given, it was calculated from the empirical equation as given by ACI code 318–77(113).

$$E_c = 33 W^{1/2} \sqrt{f'_c} \quad 5.29$$

where W = unit weight in pounds per cubic foot and E_c and f'_c are expressed in pound per square inch.

This beam was studied by Rots et al.(114) by adopting a very sophisticated model based on plastic—fracturing model. They used 120 elements. In this analysis only 64 elements were used, as shown in figure 5.33b, and seems to give reasonable results.

The experimental result shows almost elastic behaviour up to a loading level of $q = 68 \text{ KN/m}$ when there was an abrupt loss of stiffness due to the sudden

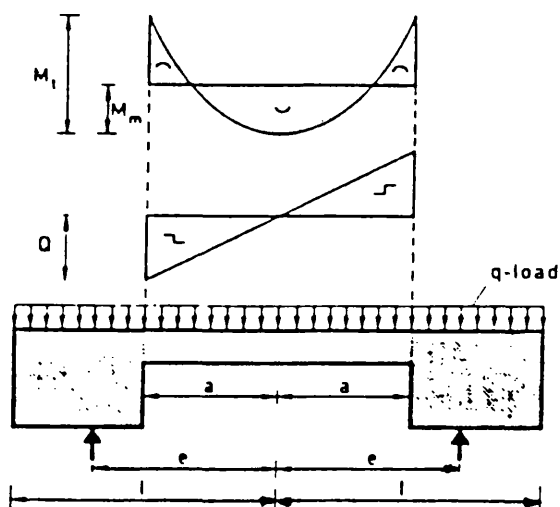
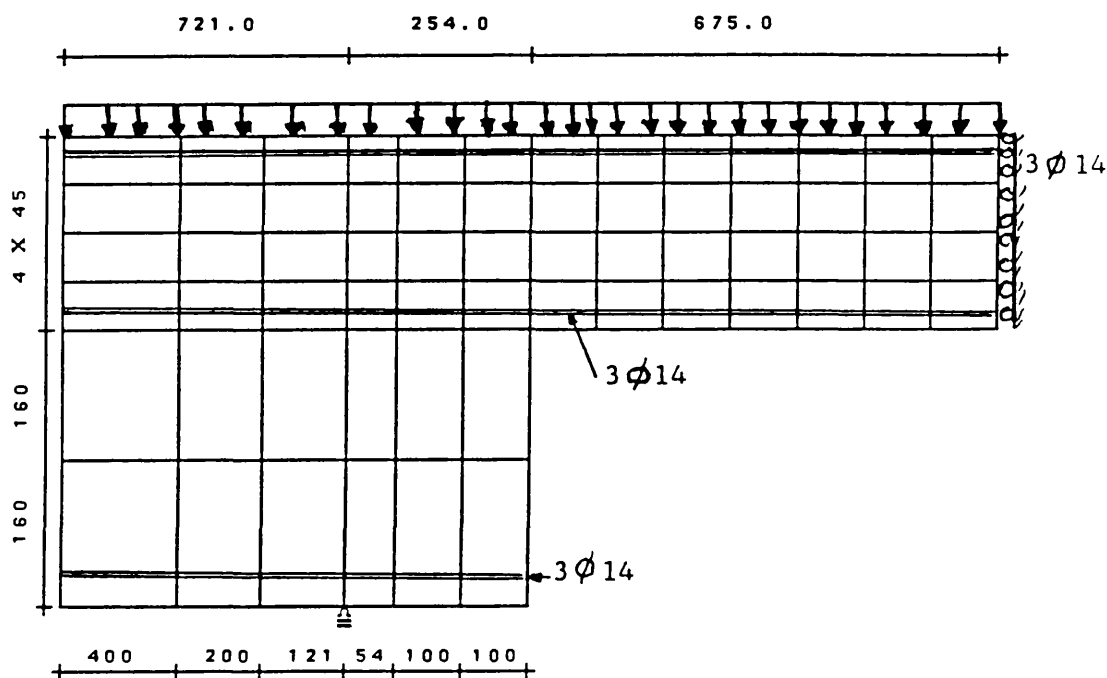
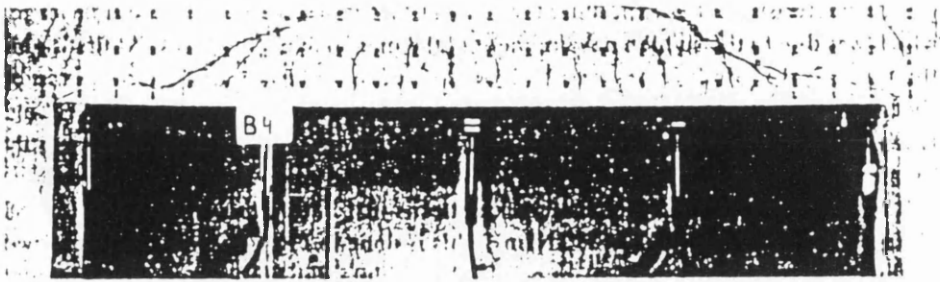


Fig. 5.36a Loading and dimension configuration.



$t = 150\text{mm}$.

Fig. 36b Finite element idealization.



Experimental
(Gijssbers & Smit, 1977)

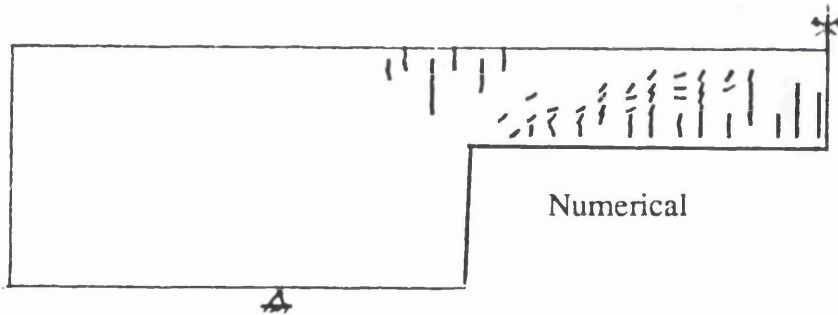
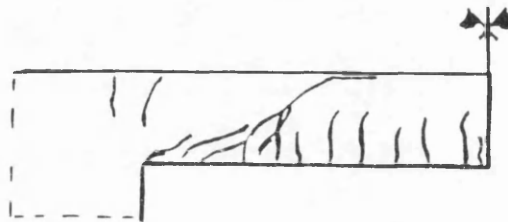


Fig. 5.37 Experimental and Numerical crack patterns
at experimental failure load $q = 75 \text{ KN/m}$

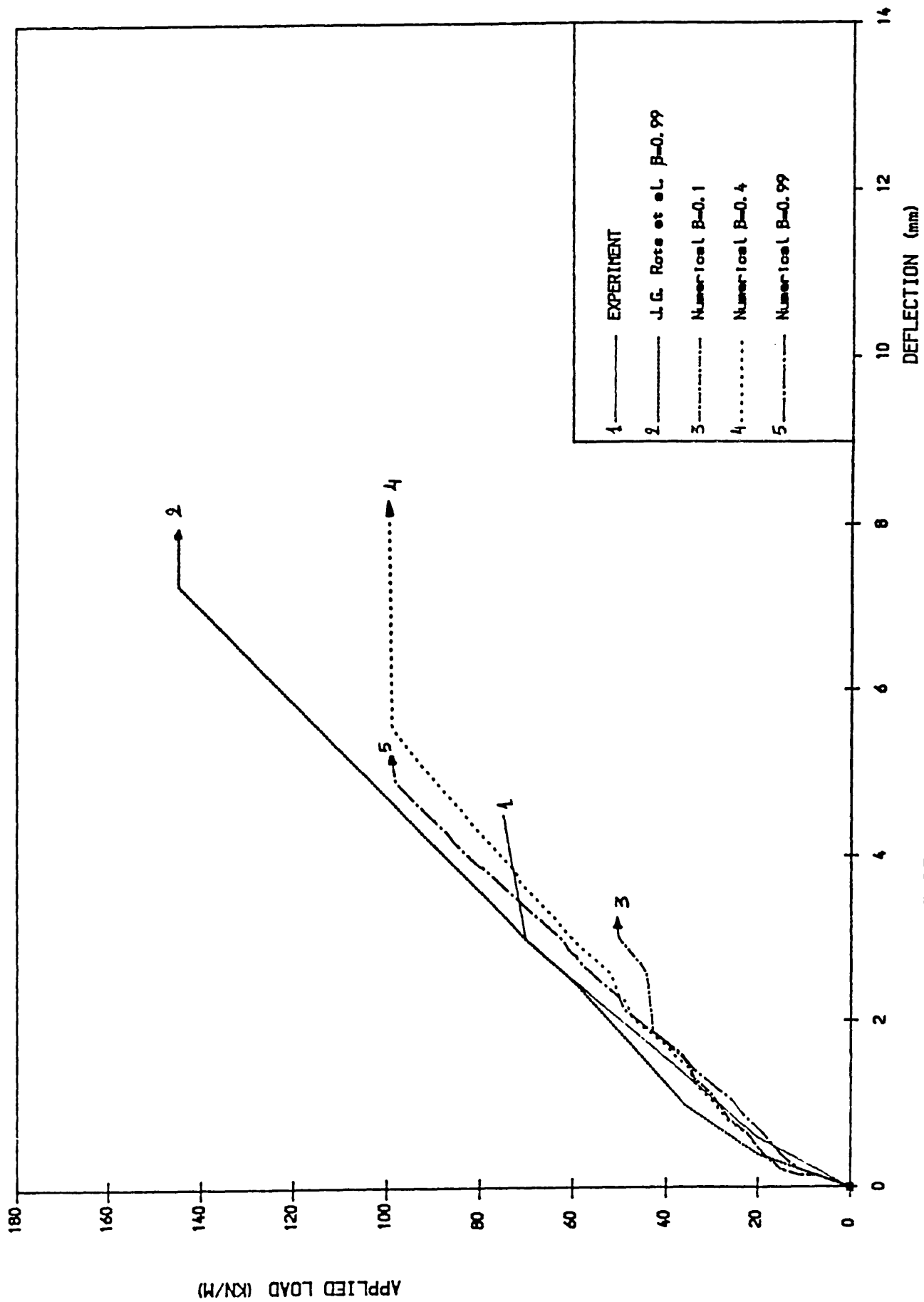


Fig. 5.38 LOAD-DEFLECTION CURVE (GIJSBERS & SMIT , 1977)

development of diagonal tension crack. Figure 5.37 shows good duplication of the numerical and experimental crack patterns at experimental failure load ($q = 75$ KN/m). Although the type of failure mechanism is reproduced quite well, it is rather disappointing that the numerical analysis does not predict well the corresponding ultimate load. Beyond the experimental ultimate load, numerically the beam behaved elastically until the numerical ultimate load. To simulate rough, smooth and almost frictionless of concrete crack surfaces, different shear retention factors ($B = 0.99, 0.4$ and 0.1) were used in the analysis. Figure 5.38 reflects the effect of the variation of the shear retention factor on the load displacement relationship. The influence of the shear retention B , up to certain values, was found to be significant for this beam. As B increased there was an increase in stiffness, but in terms of ultimate load there is no difference for B greater than 0.4 . No steel yielded until the ultimate load was reached. Experimentally no steel yielding was reported. In comparison with the numerical results presented by Rots et al.(114), the present model gives acceptable predictions.

5.9 CONCLUSIONS:

- 1— The present computational model is capable of providing a good prediction of the overall behaviour of reinforced concrete slabs and deep beams, both at working and ultimate load. The mode of failure is in general well predicted.
- 2— A mesh of 4×4 is adequate to produce acceptable results for the range of slabs used, whereas for beams an average of 7×7 can be adopted.
- 3— Tension stiffening has a significant influence on the accuracy of the predictions at working load. However as approaching the ultimate load, the predictions are stiffer. In addition, tension stiffening has a significant effect on the convergence at early cracking of the structure. In fact tension stiffening is affected by many factors such as the amount of steel, type of tension stiffening curve, type of

structure and its behaviour. So it is difficult to suggest a fixed values but in general a value of 0.5 and 10.0 for the constants C_1 and C_2 can be adopted, respectively.

4— For slabs and deep beams failing in flexure, the shear retention factor has almost no influence on the results. In general a value 0.4 for the shear retention factor at cracking strain can be used.

Chapter 6

Experimental Set-up and Instrumentation

6.1 Introduction:

The theory given in chapter 3 for the Direct Design of reinforced concrete slabs and deep beams has been verified experimentally by many research workers(43,115,79,80,81) using elastic stress field distribution. The object of this experimental investigation is to study the behaviour of reinforced concrete slabs and deep beams designed using nonelastic stress fields, at working and ultimate load. A total of six slabs and two deep beams were tested. Three square slabs were simply supported, designed using different levels of plasticity, two square slabs were simply supported with mid-column support, and one was rectangular simply supported. The deep beams were of different span-depth ratio and simply supported at their ends. Tables 6.1 and 6.2 show the geometric details of all slabs and deep beams respectively. The method of determination of plasticity levels for both slabs and deep beams are described in the next chapter.

Table 6.1 Tested slabs-designations and dimensions.

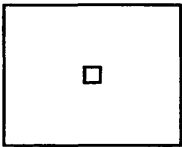
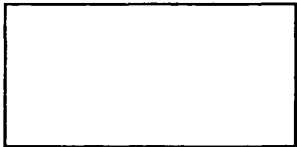
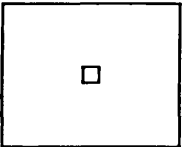
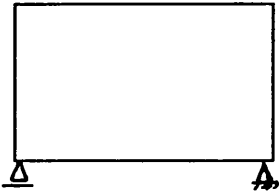
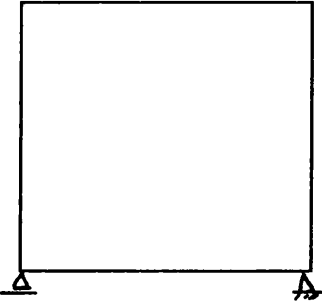
Test	Designation	Support Conditions	Dimensions mm
1	Model S.1	Square Simply Supported	2140x2140x100
2	Model S.2	//	2140x2140x100
3	Model S.3	//	2140x2140x100
4	Model S.4	// + Mid-Column 	2140x2140x100
5	Model S.5	Rectangular Simply Supported 	3140x2140x100
6	Model S.6	Square simply Supported + Mid-Col. 	2140x2140x100

Table 6.2 Tested Deep Beams-designations and dimensions.

Test	Designation	Support Conditions	Dimensions mm
1	Beam B.1		1050x500x100
2	Beam B.2		1050x900x100

6.2 Description of Experimental Parameters:

Since the design procedure gives a continuously varying reinforcement pattern, it is necessary to use large scale models, in order that the variation in steel can be properly represented. The thickness of the designed slab models were chosen to comply with the limiting span–depth ratio and as required by sections 3.2.1.1 of BS8110(1) Part 1. For all the slabs tested, a fixed span length of 2000mm is used. The other length was changed only for model S.5, having an aspect ratio of 1.5. The support conditions considered was simple support along the edges for all models. A steel column support was used in the middle of slab Models S.4 and S.6. Models S.1 and S.3 were designed using 70% and 30% plasticity level stress distribution respectively. The other models were designed using 100% plasticity level. Figure 6.1 shows the slabs dimensions, support system and loading point locations.

Two different span–depth ratios were chosen for the tested deep beams. The first beam had a ratio of 1.8 where as the second had 0.9. The beams had the same thickness of 100mm and were designed using 100% plasticity stress level.

6.3 Loading Rig:

6.3.1 Slabs:

The rig for slabs was adopted from earlier research programs(43,115) involving tests on square and rectangular reinforced slabs at a maximum dimensions of 3000mm x 2000mm. The loading rig is shown in figures 6.2. The 2000mm span was fixed but the other dimensions can be varied. The rig allows 1500mm headroom under the slab so that the bottom concrete surface of the slabs can be examined during the tests and the width of the cracks can be measured. The rig was designed to carry safely 600 KN.

Loads are applied as concentrated loads, by using loading cables passing through holes provided in the slab at the time of casting, and corresponding holes in the floor of the laboratory.

6.3.1.1 Support System:

For all slabs, a simple support system was used along their edges. This support system consisted of two mild steel flats of 12mm thick and 100mm wide separated by a steel roller of 25mm diameter as shown in figure 6.3. This support was extended over the whole length except near the corners and in the middle of two adjacent sides of the slab, where a V plates—Roller were placed to stabilize the slab on the rig. Since uplift forces were expected at the corners, which were held down using a corner support shown in figure 6.4. The uplift forces are caused by the presence of high twisting moments at the corner region. Load cells were used to measure the corner uplift forces. The corner support was designed so to provide an equivalent spherical support. A 6mm diameter high tension strength steel bar which passes through the load cell, through the hole in the slab corner and then through a set of flats and rollers system was finally anchored to the loading rig. For model S.4 and S.6 a steel column was placed under the middle of the slabs. The head of the column provided a spherical support in contact directly with the bottom concrete face of the slab. Figure 6.5 shows the column support system used.

6.3.1.2 Loading System:

Two different Systems of loading were used for applying concentrated load on the slab models They are:

1— Direct Point load.

2— Indirect point load.

6.3.1.2.1 Direct Point Load System:

This system was adopted for all slabs except for model S.5. The loads were applied by four prestressing cables symmetrically placed through four holes in the slab, as shown in figure 6.6. The cables were anchored on the top of load cells which were placed on the hydraulic jacks. The load cells were used to measure the applied load on the slabs. At the other end, the cables were anchored under the laboratory strong floor on to 60 ton Hydraulic jacks. The bottom jacks were operated by hand pumps, whereas the top ones were operated by an electrical motor pump. The hand pumps were used to adjust the load applied at each point.

6.3.1.2.2 Indirect two point load system:

This was used for Model S.5 only and the load was applied through four 30mm diameter prestressing cables passing through four holes in the slab. Each cable transmits equal load on two point of the slab by a system of simply supported spreader beams as shown in figure 6.7. A V—Roller support system was used at one end of each spreader beam, while on the other end plates—roller system was placed.

6.3.2 Deep Beams:

Figure 6.8 shows the set up for deep beams tested. The Beams were accommodated in a 10.000 KN Losenheim Universal Testing Machine. The rig was designed for a total loading capability of 2000 KN and comprised of:

1— Two Support Girders

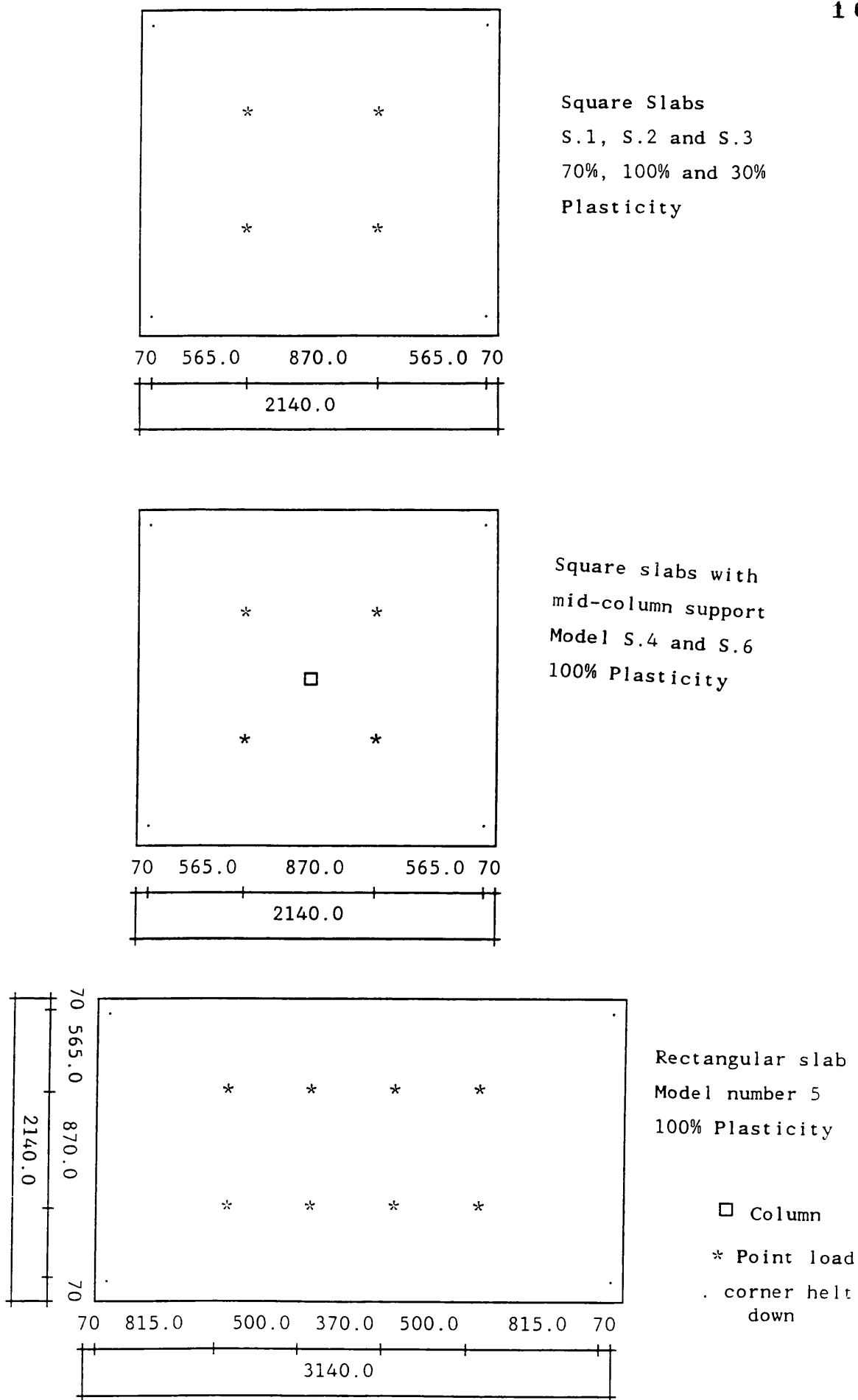


Fig. 6.1 Slabs Dimensions, Support and Loading System.

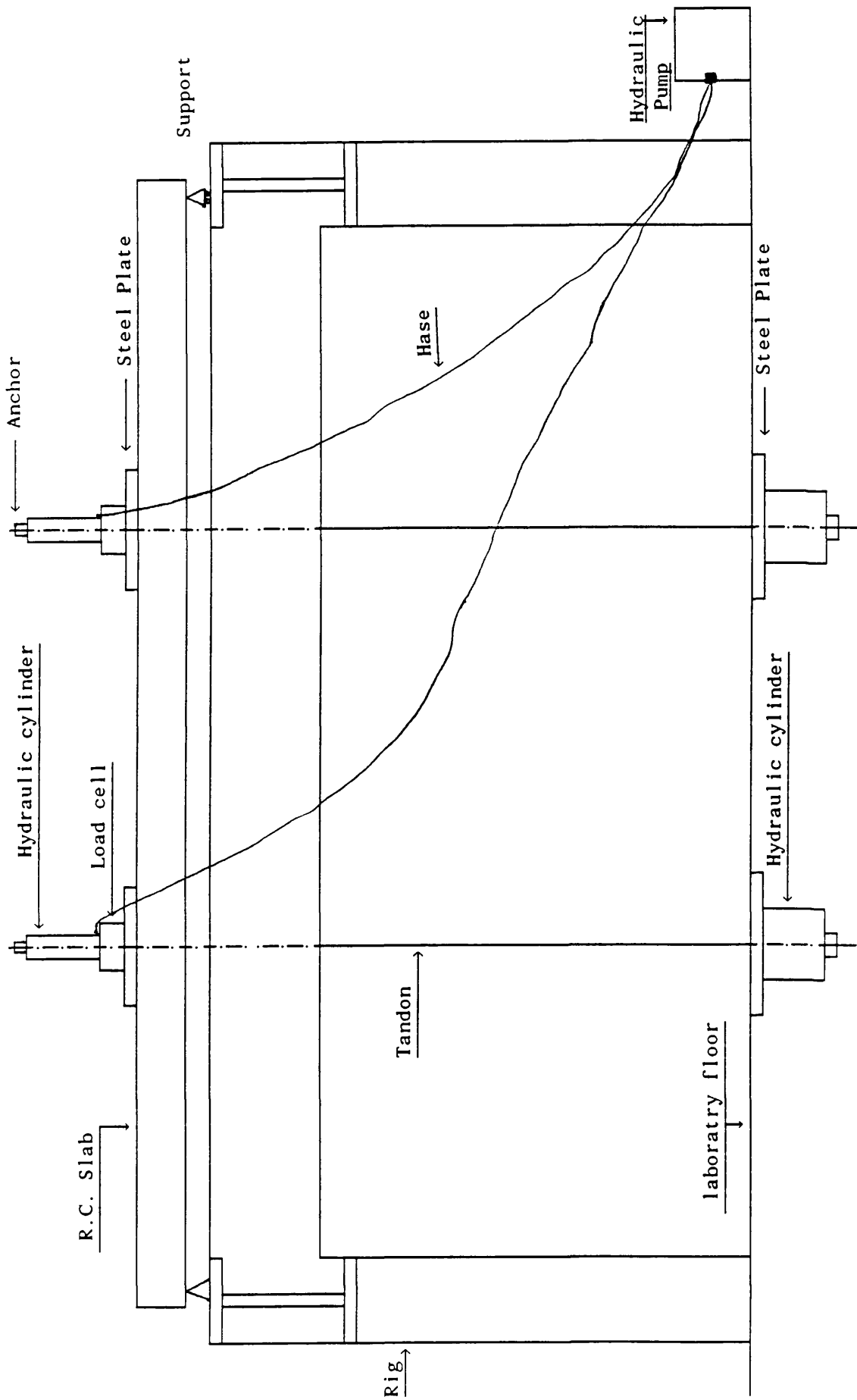


Fig. 6.2 The loading Rig for Slab Models

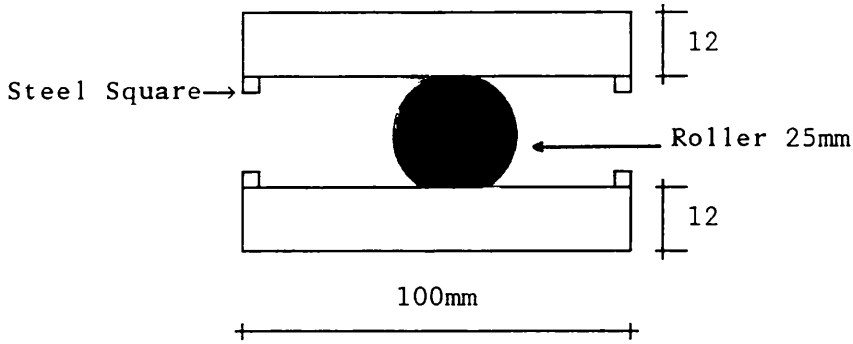


Fig. 6.3 The Edge support System (Steel Plates and Roller).

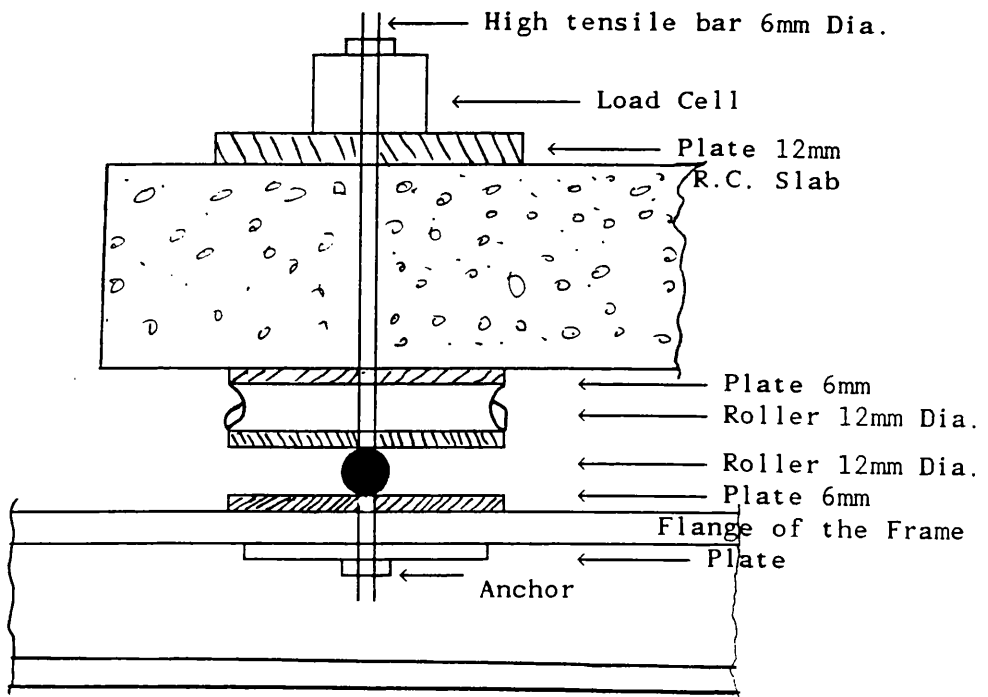


Fig. 6.4 The Corner support system.

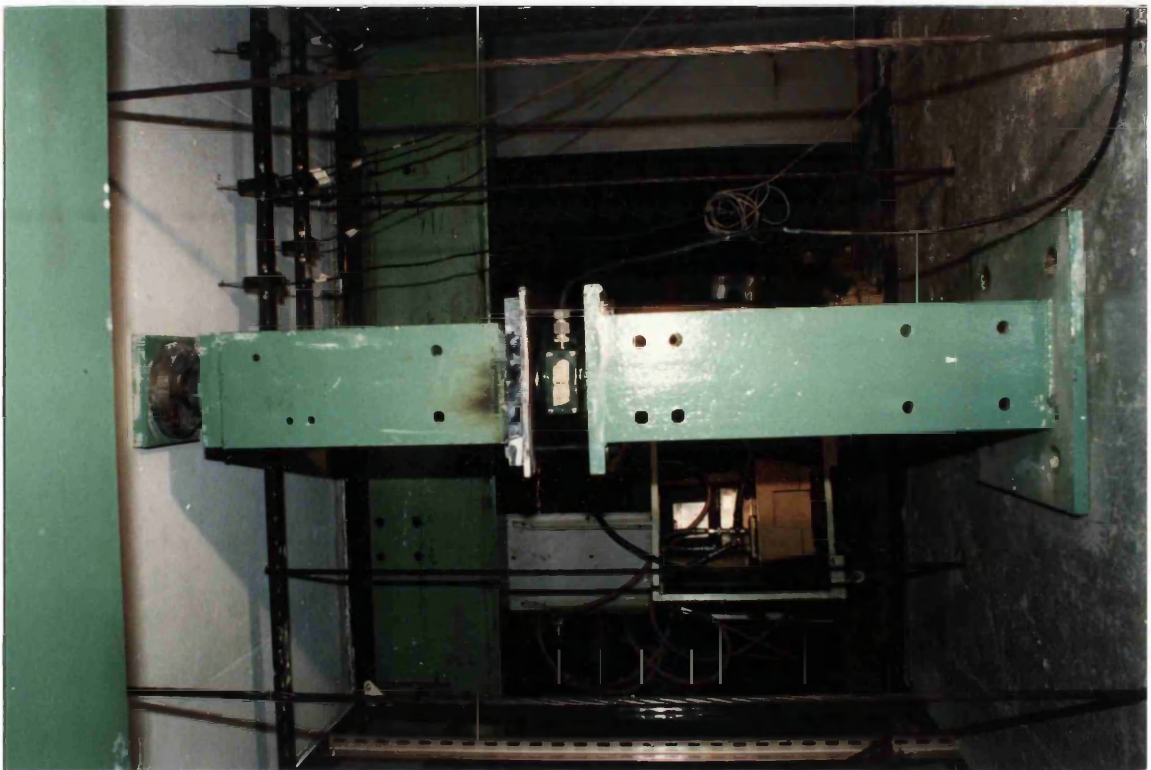
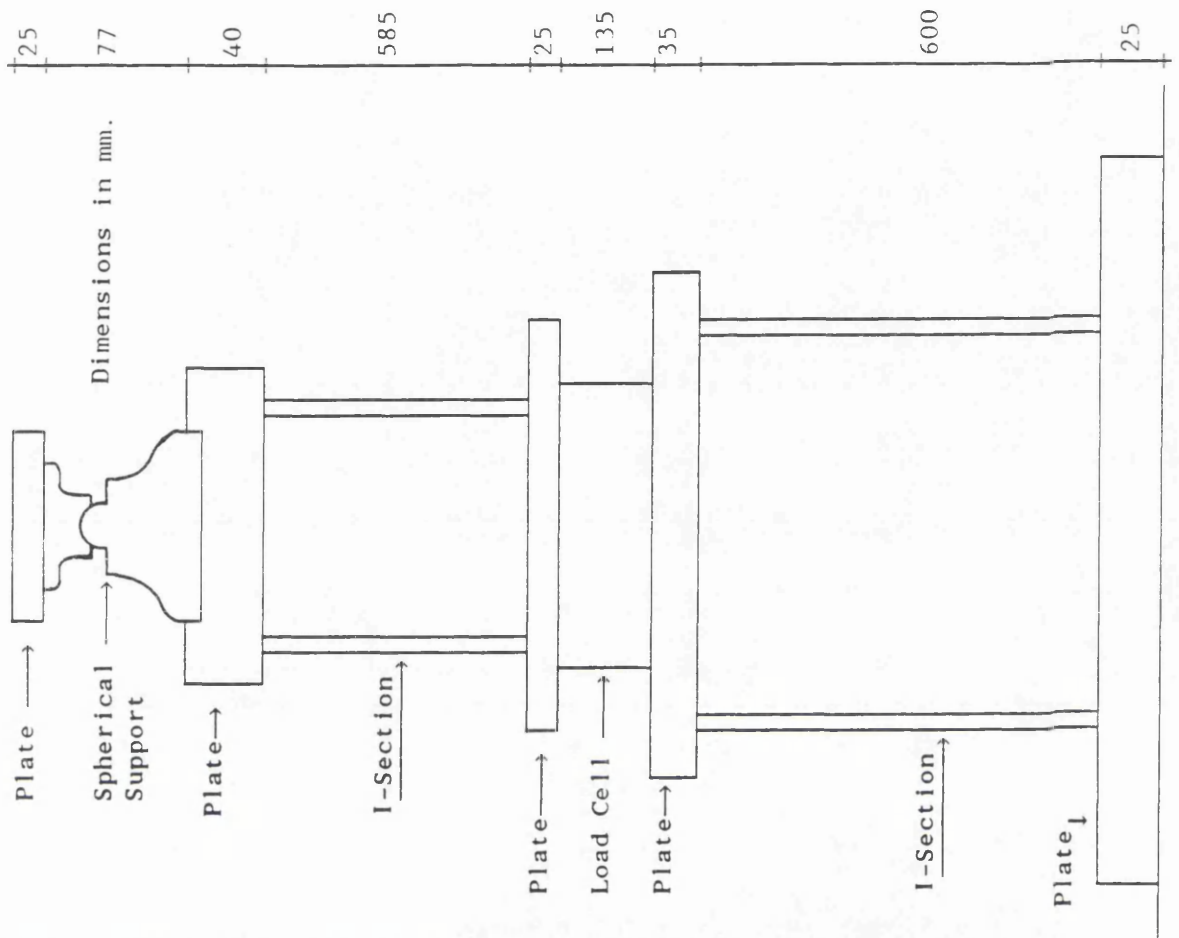


Fig. 6.5 Column support system.

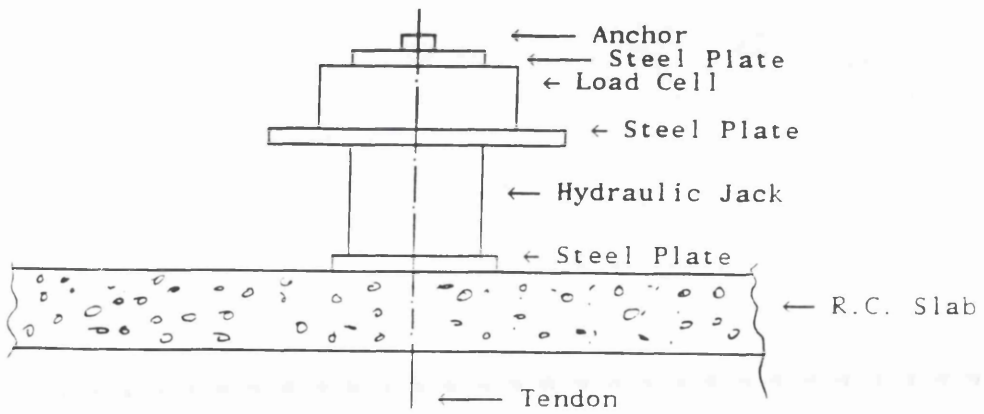
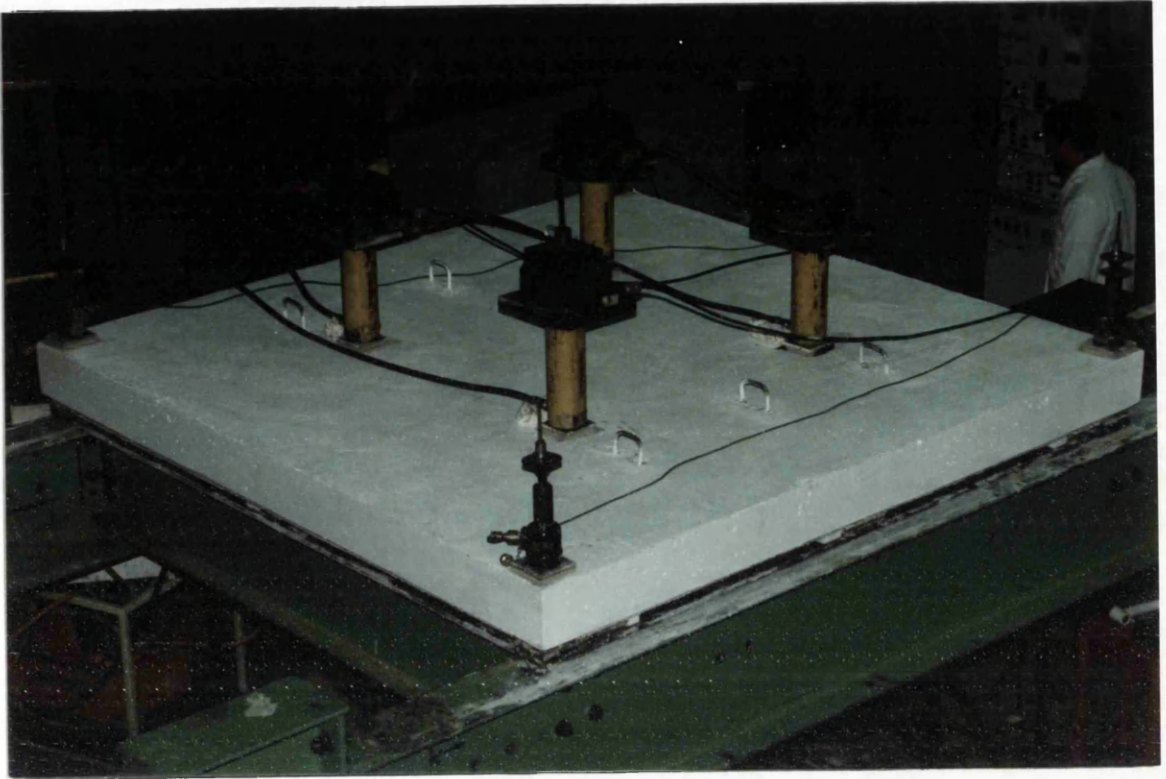


Fig. 6.6 Direct Point Load System.

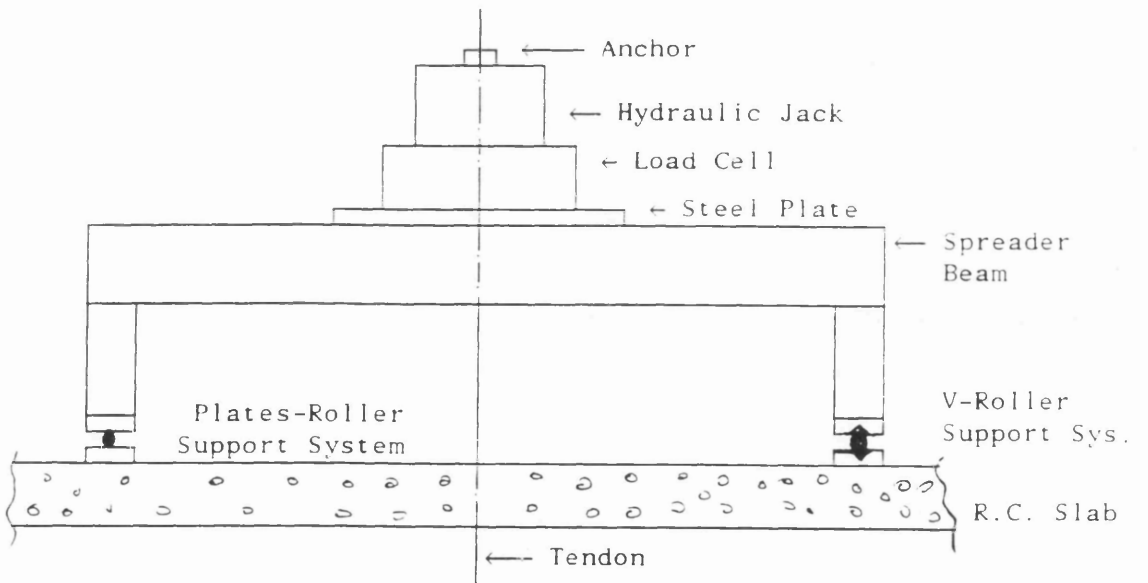
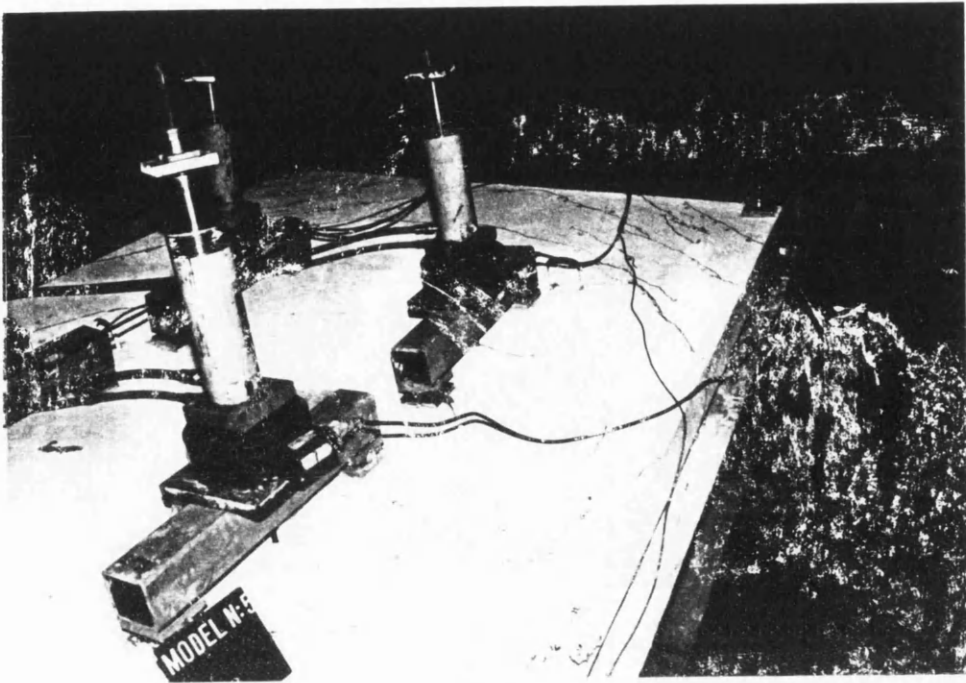


Fig. 6.7 Indirect Point Load System.

- 2– Supporting Bearings
- 3– Loading Point System
- 4– Losenhausen Platen

6.3.2.1 Support Girders:

Support girders of 250x250x16 Kg/m hollow square box cross section were used. The girders were used a previous test program(81).

6.3.2.2 Support Bearings:

The support bearings were made of mild steel. One support was provided with rollers to allow free horizontal translation and the second was made to be restrained horizontally and vertically, with allowance of rotation. The support bearing plates dimensions were 150x100x50mm and the 25 mm rollers were used. To restrain the local bursting forces, steel plates of 200x150x15mm were used, fig. 6.8.

6.3.2.3 Loading point system:

The loading point system consisted of two mild steel plates of 200x100x50mm and roller of 25mm diameter. Two mild steel plates of 200x200x15mm were used to confine the concrete under the point load.

6.3.2.3 Losenhausen Machine Platen:

The two platens of the machine were used. One of them was on the top of the machine to transmit the load on the beam, the second was in the bottom and moves only in the horizontal direction to transport the test beam under the machine. This

platen is restrained at the time of testing.

6.4 Formwork:

For all the slabs, the same formwork was used. It was adjusted as required by the dimensions of the slabs. For beams, since they were cast simultaneously, it was necessary to design two form works on one base.

The form works were made from 200mm thick polywood panels. To maintain the stability and strength of the mould during casting, 50x50mm timber battens were nailed at close spacing along the length of the mould. Prior to casting, the mould was coated in oil in order to prevent the concrete sticking to the mould.

6.5 Material:

6.5.1 Concrete:

The same concrete mix was used for all the specimens. The mix consisted of Rapid Hardening Portland Cement (RHPC), Hyndford uncrushed gravel of maximum aggregate size of 10mm and Hyndford sand grading zone 2. The mix proportions by weight were 1 : 1.48 : 2.61 (ie. cement : sand : gravel) with a water cement ratio of 0.48. The weighed quantities of cement, sand, gravel and water were mixed thoroughly in a 3 cu.ft capacity pan mixer.

When the bending of steel and cementing of strain gages on the steel was completed, the fabrication of steel reinforcement mat commenced by placing the steel bars in their required locations for both slabs and deep beams. Plastic spacers were attached to the bars, before casting at a certain intervals to ensure adequate cover to the reinforcement on both sides of the specimens.

All the specimens were cast horizontally. The holes on the models were positioned in

their right places for loading the slab and also holding down the corners of the slabs. Each model was cast in several batches and was properly compacted using a 12mm diameter poker vibrator. The vibration continued until a reasonably good compactation was achieved. The models were left for about six hours to dry in the open air of the laboratory. In addition to the main specimen, four 100x100 mm cubes and six 150x300mm cylinders were cast as control specimens from different batches. All the control specimens and the main specimen were kept under a polythene cover for the first 24 hours. The cover was removed after this period and 50% of the control specimens were cured in the water tank, whereas the remaining ones were kept under the laboratory conditions near the main specimen.

The cubes were used to determine the cube strength, two cylinders were used to determine the tensile strength and the remaining four others were used to determine modulus of elasticity of concrete.

The concrete tensile strength f_t obtained from cylinder splitting test as follows:

$$f_t = \frac{2 P}{\pi D L}$$

Where $L = 300\text{mm}$ is the length of the cylinder

$D = 150\text{mm}$ is the diameter of the cylinder

P is the ultimate load.

Average value for concrete properties for each model were calculated and are given in table 6.3.

6.5.2 Reinforcing Steel:

Figures 6.9a and 6.9b show the steel layout for slab and deep beam respectively. High yield deformed bars of 6, 8 and 10mm diameter were used. The yield stress of all different bar sizes were measured on samples taken from different batches of steel

bars using a Tinius Olsen Universal Class A testing machine, fitted with an S-type electronic extensometer. The testing procedure followed the manufacture's instruction manual. Table 6.4 shows average steel properties measured.

The yield stress of the bars was taken as the stress at which a line starting from 0.2 % strain and parallel to the initial slope of the curve intersects the stress-strain curve. Typical steel stress strain curve is presented in figure 6.10.

6.6 Instrumentation:

6.6.1 Deflections:

Deflections were measured using Linear Voltage Displacement Transducers (LVDT) at the bottom concrete surface for slabs at chosen points, and at the bottom soffit for the beams. Figure 6.10a to 6.10c show the chosen points position for slab models. The transducers, capable of measuring 50 and 70 mm, were mounted on an independently supported measuring frame. Each transducer was given an identification number and was then connected to the data logger for data processing.

Beam deflections are very small and also the plaster between the supports plates and the beam is subjected to a high stress causing extra deflections. Thus for beams the deflections must be measured with a great care.

6.6.2 Steel strains:

Strains in steel bars were measured by 6mm electrical resistance strain gages. The gages were cemented to the steel bars at a chosen points to record the strain history. Prior to the fixing of strain gages, the surface of the steel bars were prepared by filling and then smoothening with sand paper. During this process, care was taken not to remove a considerable area which would weaken the steel bars. The surface

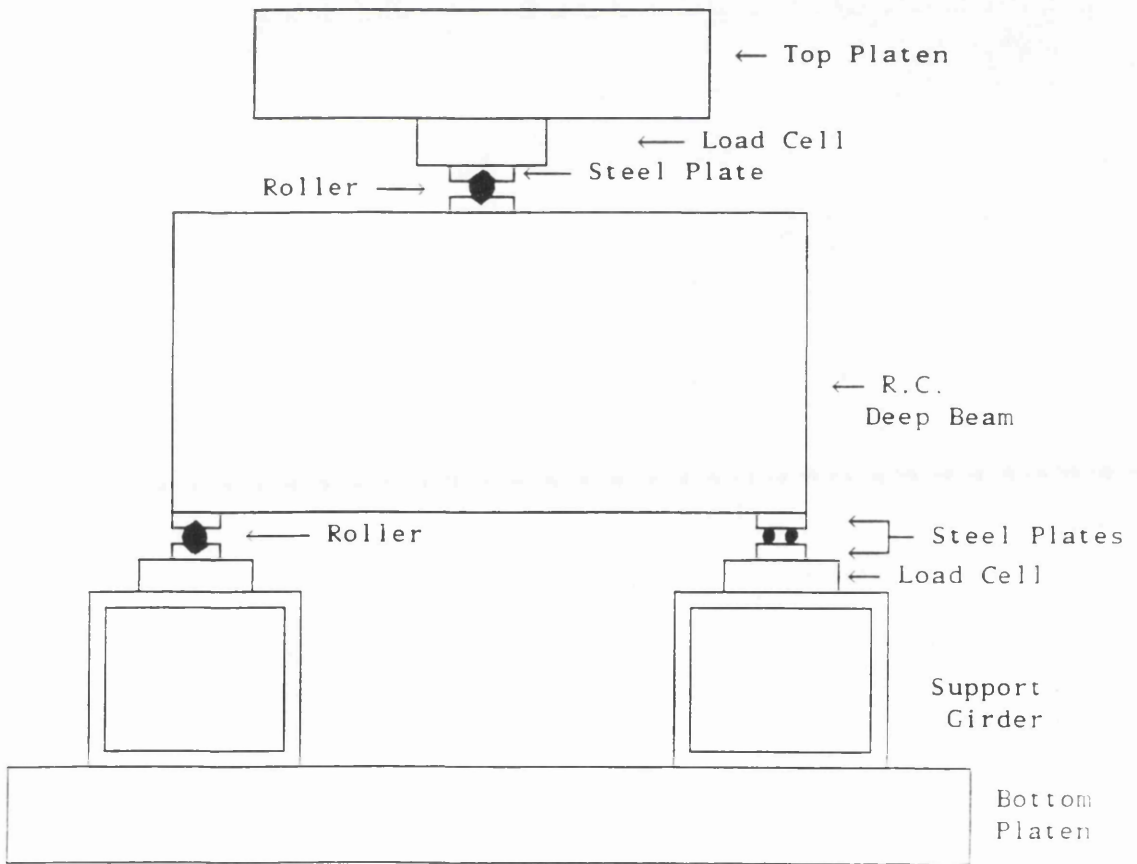
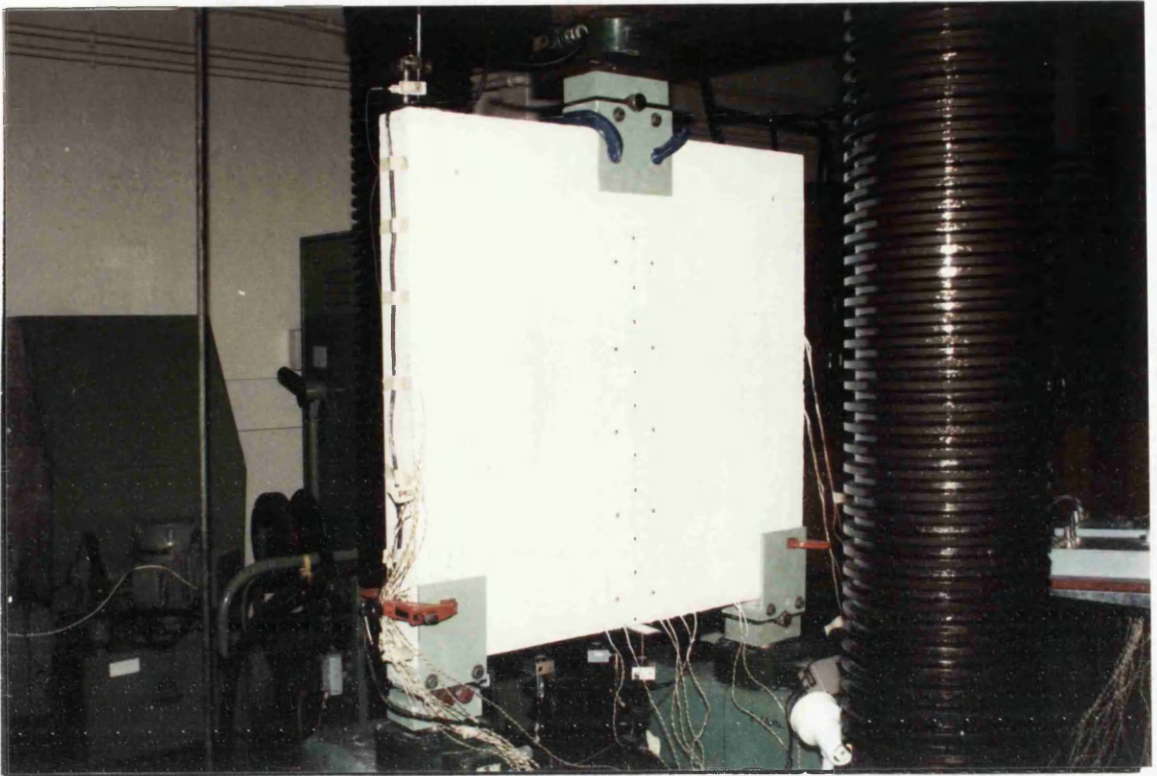


Fig. 6.8 Loading Rig for Deep Beam.

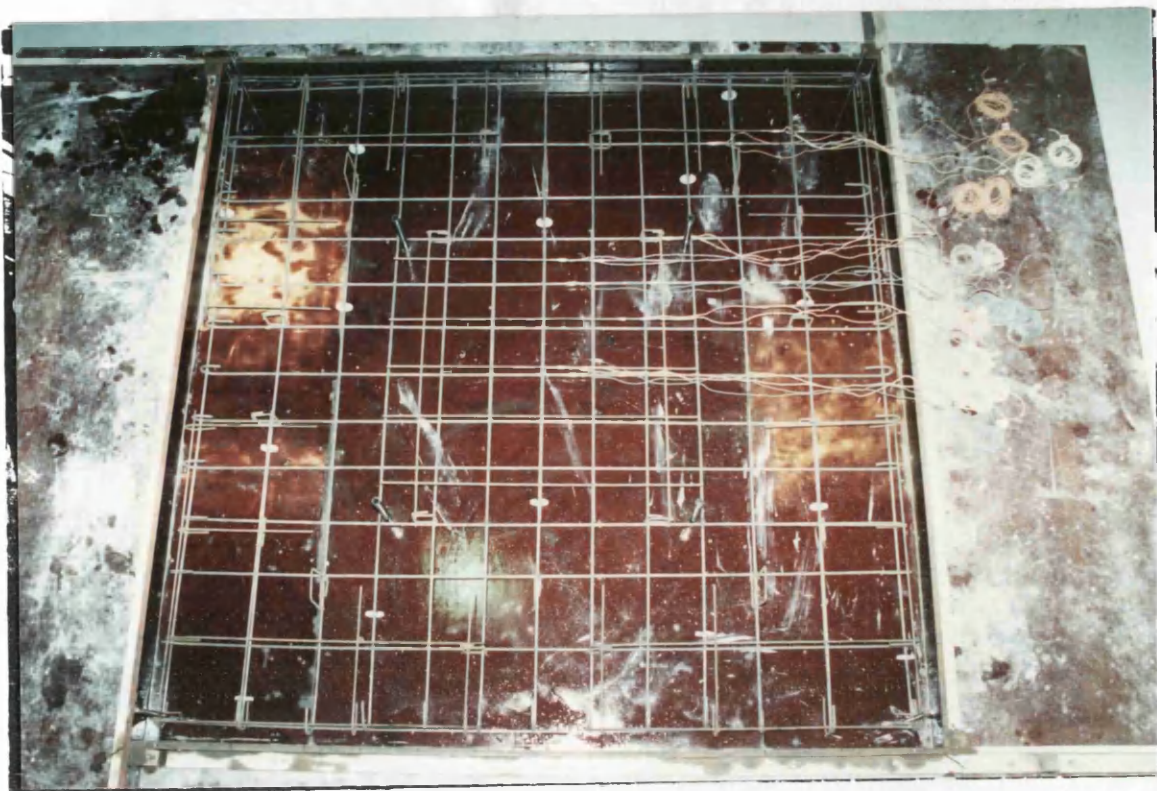


Fig. 6.9a Steel Layout - Slab Model



Fig. 6.9b Steel Layout - Beam Model

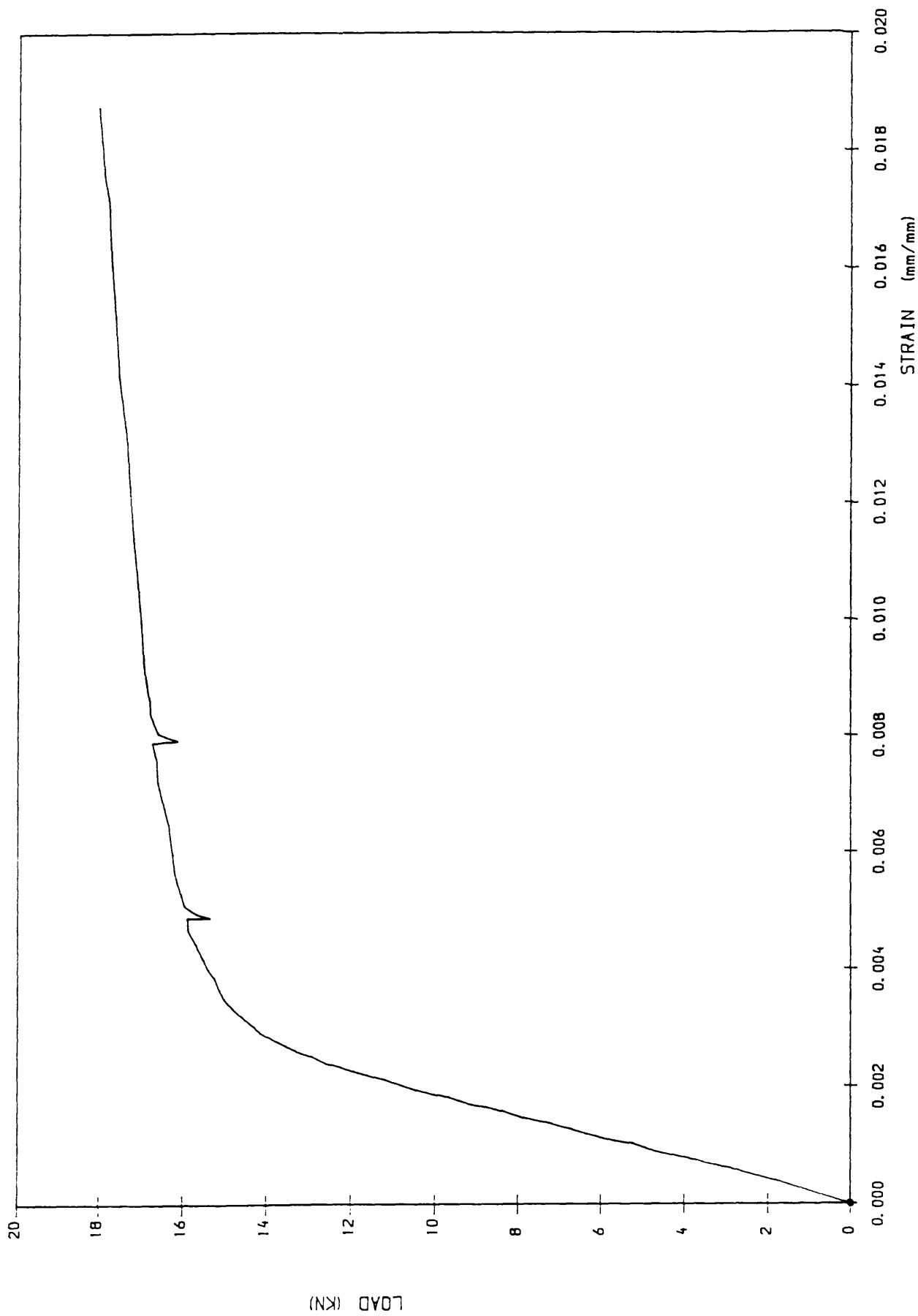


Fig 6.10 Steel Load-Strain Relationship. Bar Dia. 6mm

was then treated with M-prep conditioner A and M-Prep neutraliser 5 to remove any dirt and grease. After fixing the gage on the bar, it is checked using an voltmeter before cementing. The strain gage was protected from moisture and mechanical damage during fabrication and casting, using an air drying protective coating type M-coated and epoxy resin was applied over the gage and terminal. At all the strain gage position on a bar, a pair of strain gages were fixed on diametrically opposite sides.

6.7 Test Procedure:

When each specimen was fully cured, it was white painted. All the specimens were taken to the test rig by crane. Once the specimens were installed properly, all the strain gages, load cells and displacement transducers were connected to a 3530 Orion data logger for automatic recording. All connections were checked before testing started. Deflection transducers were checked to ensure that they were truly vertical, and they would operate properly under test. The strain gages were also checked and defective ones were immediately disconnected. The load cells were checked by applying a small load to the slab and then unloaded.

At each load increment, results were printed and saved on a floppy disc to be processed later. During testing, load displacement and load strain curves at a critical points were plotted to follow and examine the behaviour of the specimen. The concrete faces of each specimen was illuminated using powerful light sources. Crack widths were measured at each load increment using a micro-crack reader for small cracks and a crack ruler for large cracks. The cracks development were traced with a black marker at each load increment. The whole procedure was repeated until the ultimate load was reached.

Properties → Designation ↓	Design Load (KN)	f_{cu} KN/mm ²	f_t N/mm ²	E_c KN/mm ²
Model S.1	210	51.30	4.30	20.70
Model S.2	210	56.30	3.40	21.50
Model S.3	210	60.50	3.50	22.80
Model S.4	320	58.77	3.07	22.45
Model S.5	210	59.26	3.46	23.12
Model S.6	320	57.62	3.59	22.73
Beam B.1	250	58.63	3.17	23.13
Beam B.2	500	58.63	3.17	23.13

Table 6.3 Concrete Properties.

f_{cu} : Concrete Cube Strength f_t : Concrete Tensile Strength

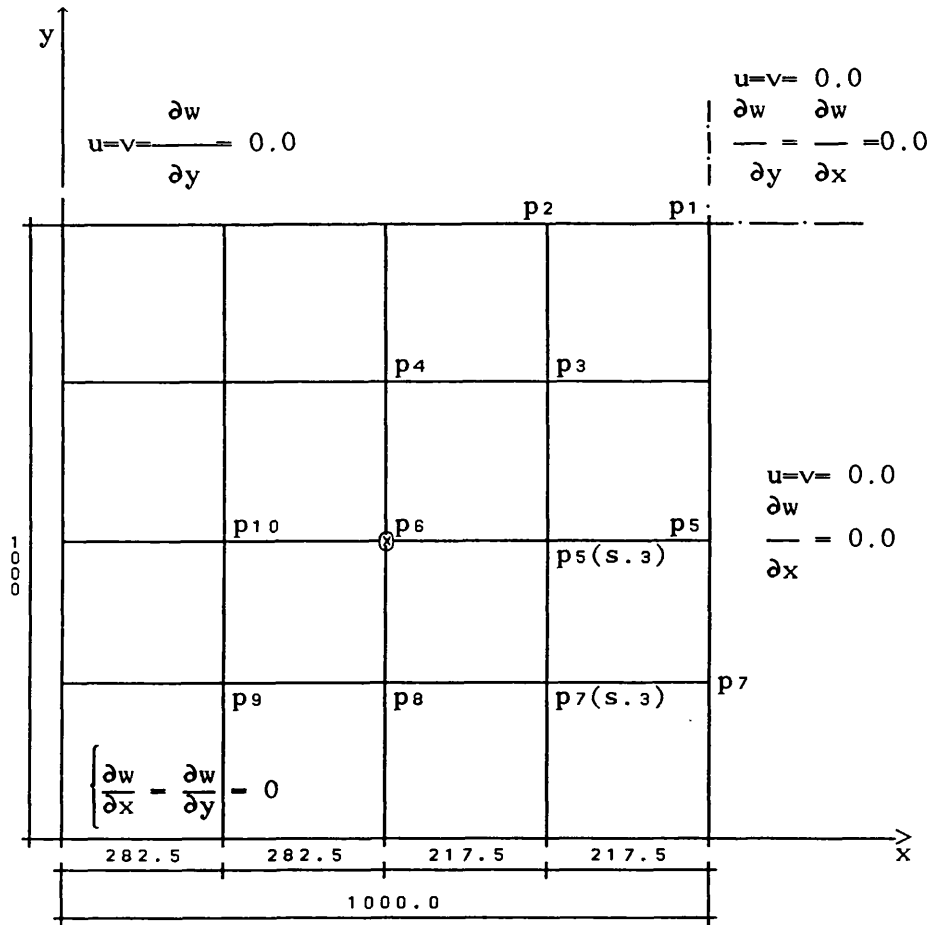
E_c : Concrete Elastic Young Modulus

Bar diameter	f_y N/mm ²	E_s KN/mm ²	ϵ_y * 10 ⁻³	H
Φ 6 mm	580.0	195.0	2.974	0.028
Φ 8 mm	477.0	186.0	2.565	0.025
Φ 10 mm	483.0	203.0	2.379	0.000

Table 6.4 Steel Properties.

f_y : Steel yield stress ϵ_s : Steel yield strain

E_s : Steel Young modulus H: Steel hardening parameter.



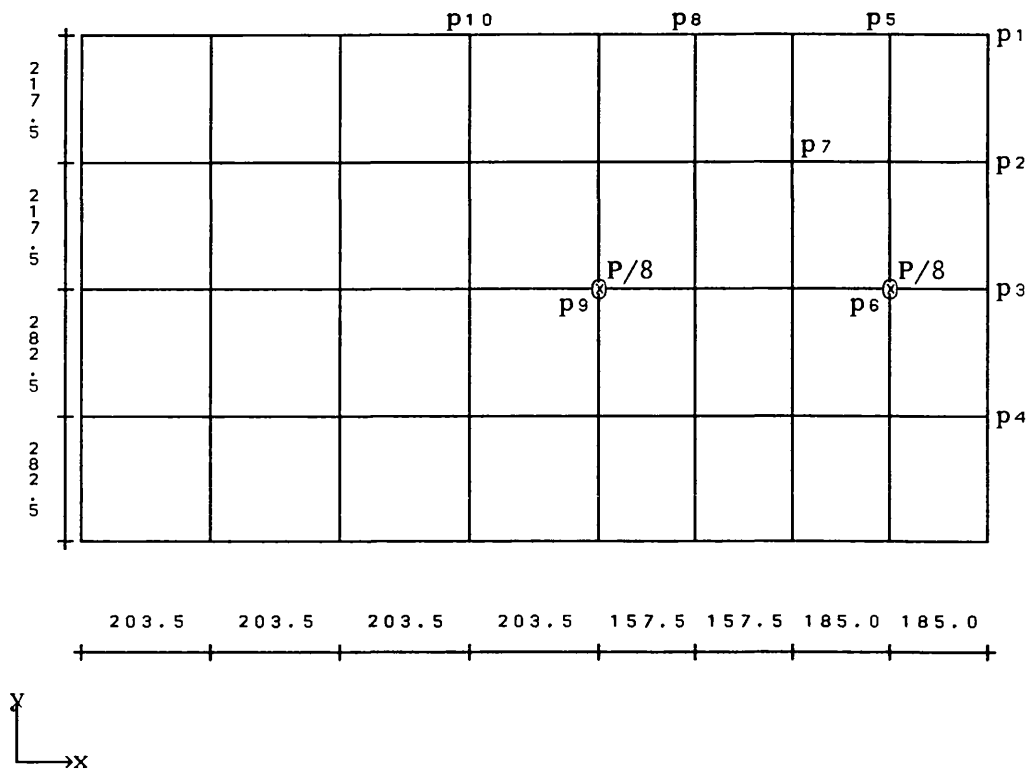
* For $x = 0.0$, $w = 0.0$ and $\frac{\partial w}{\partial x} = 0.0$

* For $y = 0.0$, $w = 0.0$ and $\frac{\partial w}{\partial y} = 0.0$

⊗ Point load = $P/4$

Fig. 6.10a Transducers Positions and Finite Element Mesh.

Quarter of slab. Models S.1, S2 and S.3



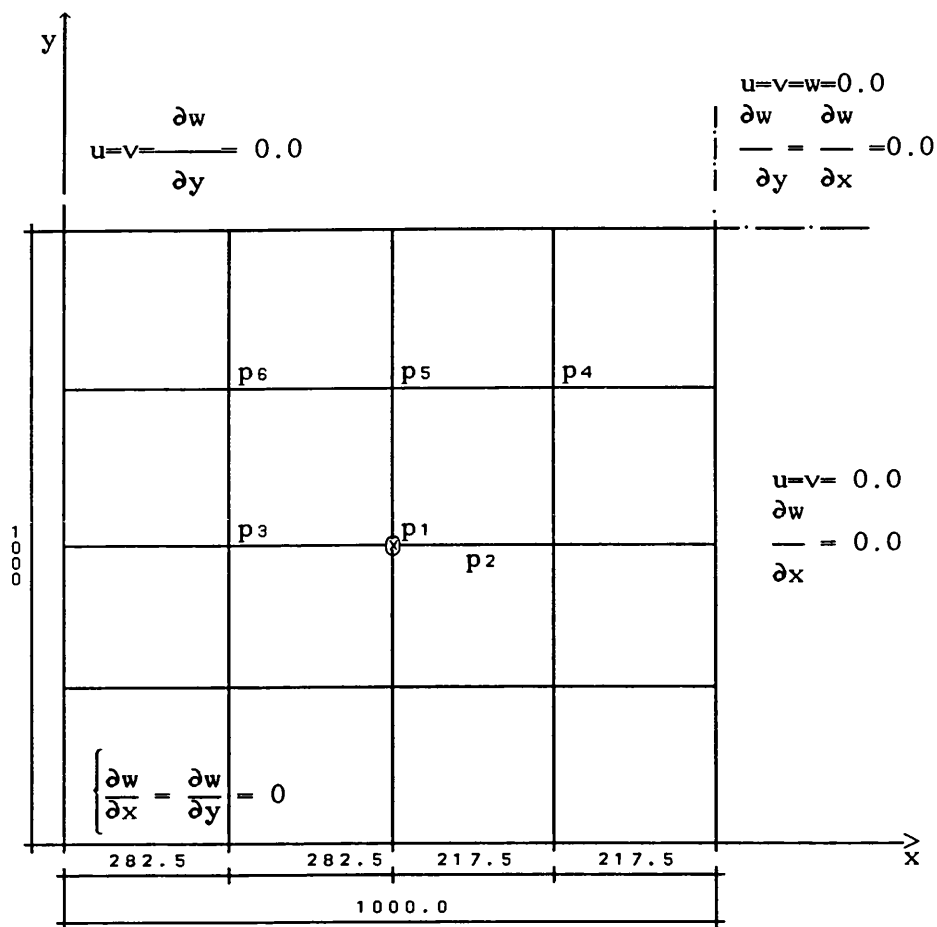
* For $x = 0.0$, $w = 0.0$ and $\frac{\partial w}{\partial x} = 0.0$

* For $y = 0.0$, $w = 0.0$ and $\frac{\partial w}{\partial y} = 0.0$

⊗ Point load = $P/8$

Fig. 6.10b Transducers Positions and Finite Element Mesh.

Quarter of slab. Models S.5



* For $x = 0.0$, $w = 0.0$ and $\frac{\partial w}{\partial x} = 0.0$

* For $y = 0.0$, $w = 0.0$ and $\frac{\partial w}{\partial y} = 0.0$

⊗ Point load = $P / 4$

Fig. 6.10c Transducers Positions and Finite Element Mesh.

Quarter of slab. Models S.4 and S.6

Chapter 7

Nonelastic Stress Fields and Design of Experimental Models

7.1 Introduction:

During the early development of analytical methods for stress analysis of structures, the assumption that the system was linearly elastic was generally accepted for nearly all structural systems. One reason for this simplified approach was that the design stresses were expected to remain well within the elastic range of the material. With the introduction of more complicated structures and experimental evidence that most structural elements dissipate energy by exhibiting nonelastic deformations, major effort was directed towards the development of analytical methods that deal with the nonelastic behaviour of structures. In the present work the use of nonelastic stress fields in the design of reinforced concrete slabs and deep beams will be examined. In particular the effect of using nonelastic stress fields on the distribution of steel reinforcement in slabs and simply supported deep beams will be studied.

7.2 Design Procedure For Slabs:

The design procedure is dependent on the nonlinear finite element Mindlin plate analysis program(5) using von Mises yield criterion. The program uses an eight node isoparametric element.

The major steps in the determination of nonelastic stress fields are as follows:

1— Treat the slab as a metallic plate, with any assumed properties and determine the elastic stress distribution (M_x , M_y , M_{xy}) under ultimate design load.

2— Determine the von Mises stress $\sqrt{(M_x^2 + M_y^2 - M_x M_y + 3M_{xy}^2)}$ at the most highly stressed point at design ultimate load and set it as plastic moment capacity M_p . ie.

$M_p = \max \text{ of } [\sqrt{(M_x^2 + M_y^2 - M_x M_y + 3M_{xy}^2)}]$ any where in the plate.

3— The material is assumed to be elasto—plastic obeying von Mises criterion and normality rule and having the plastic moment capacity of M_p . Accordingly for the fully yielded region the elastic material matrix is replaced by an elasto—plastic material matrix so that tangent stiffness matrix approach can be adopted. Figure 7.1 shows a typical load—deflection curve. As can be seen, yielding starts exactly at the applied load equal to the design ultimate load. At the start of yielding, the percentage spread of plasticity is zero and at the true ultimate load, spread of plasticity is designated as 100%.

4— Let the ultimate load be equal to $(1 + \lambda)$ design load. At any percentage of plasticity p , the stresses in equilibrium with the applied load are given by $1/(1 + p\lambda)$ of the stresses at the chosen level of plasticity percentage. The resistant moment M_x^* and M_y^* at this level of

plasticity can now be determined using Wood—Armer criterion. M_x^* and M_y^* are determined, for both top and bottom slab reinforcement using equations of chapter 3.

7.3 Design of Slab Models and Discussion:

A total of six slab models were designed using different plasticity levels. For more details reference can be made to section 6.2.

7.3.1 Models S.1, S.2 and S.3:

The slab models S.1, S.2 and S.3 were 2140mm (2000mm effective span) square simply supported slabs. One quarter of the slab was analysed using a 4x4 finite element mesh. They were designed for a total load of 210 KN, using 70, 100 and 30% of plasticity stress distribution levels. The dimensions and the loading system were described in the previous chapter in table 6.1 and figure 6.1. A typical load—deflection curve, obtained from the elastoplastic analysis, is shown in figure 7.1. This curve is used to calculate the different percentage of plasticity spread over the slab. The spread of the yielded points over the slab at different levels of plasticity are shown in figure 7.2. The plastification of the slab started in the corner and as the percentage of plasticity increases, the yield points spread towards the applied point loads. At 100% of plasticity, the whole area of the corner of the slab and the inner square between the point loads had yielded. Figure 7.3 and 7.4 show the distribution of bottom and top design moment over the slab as a function of the degree of plasticity spread. It can be seen that the bottom design moment surface peaks under the point load and in the corner at the elastic stage and tends to flatten as the degree of plasticity level increases, figure 7.3. At 100% of plasticity spread we can see that the maximum design moment peak shifted to the middle of the slab and covers a large area.

As shown in figure 7.4, at elastic level the top design moment peaks at the corner of the slab. As the percentage of plasticity reached 100%, the peak spreads along the edges and towards the point load. Also the maximum design moment decreases,

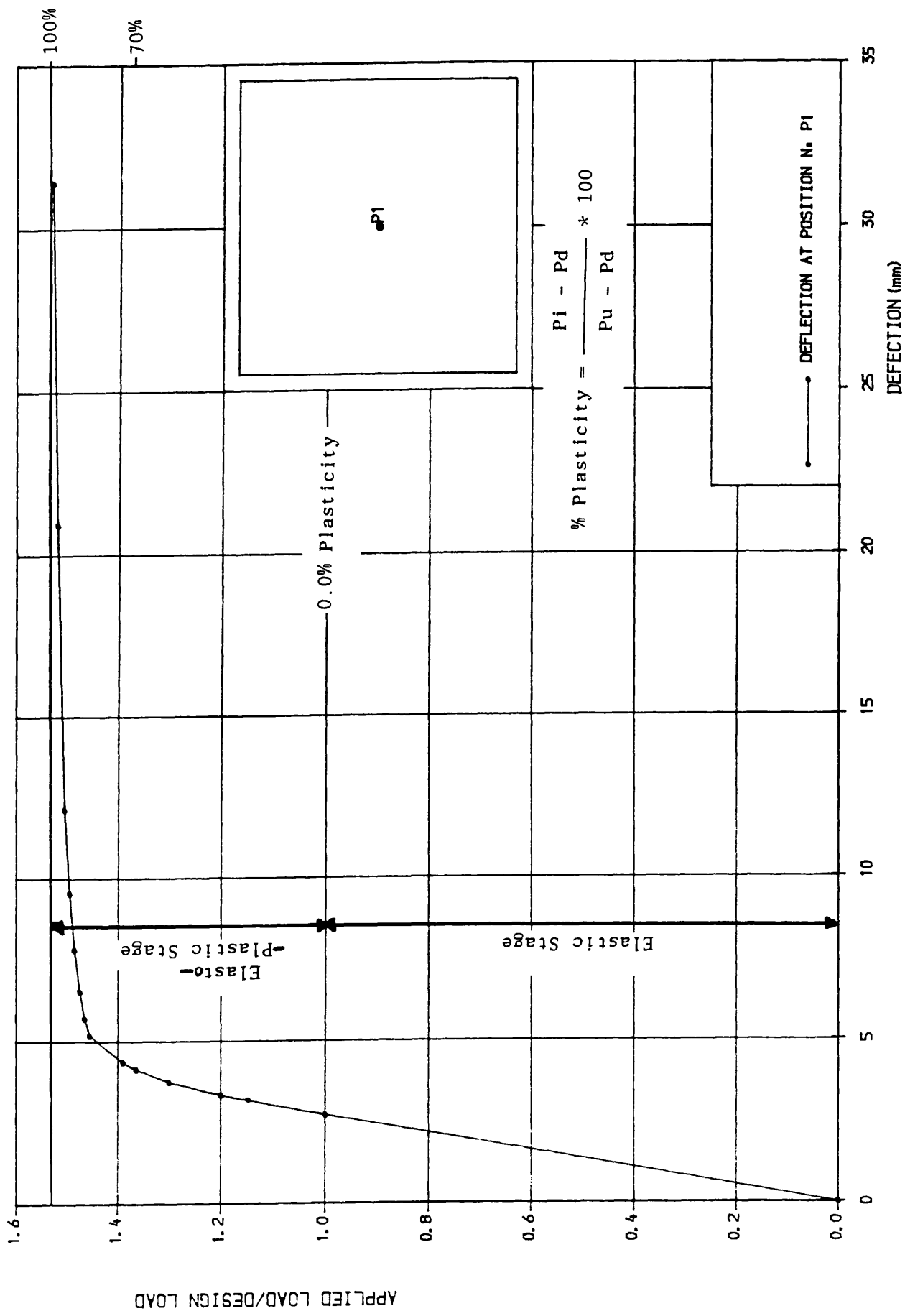


Fig. 7.1 Load Deflection Curve. Determination of Plasticity Levels.

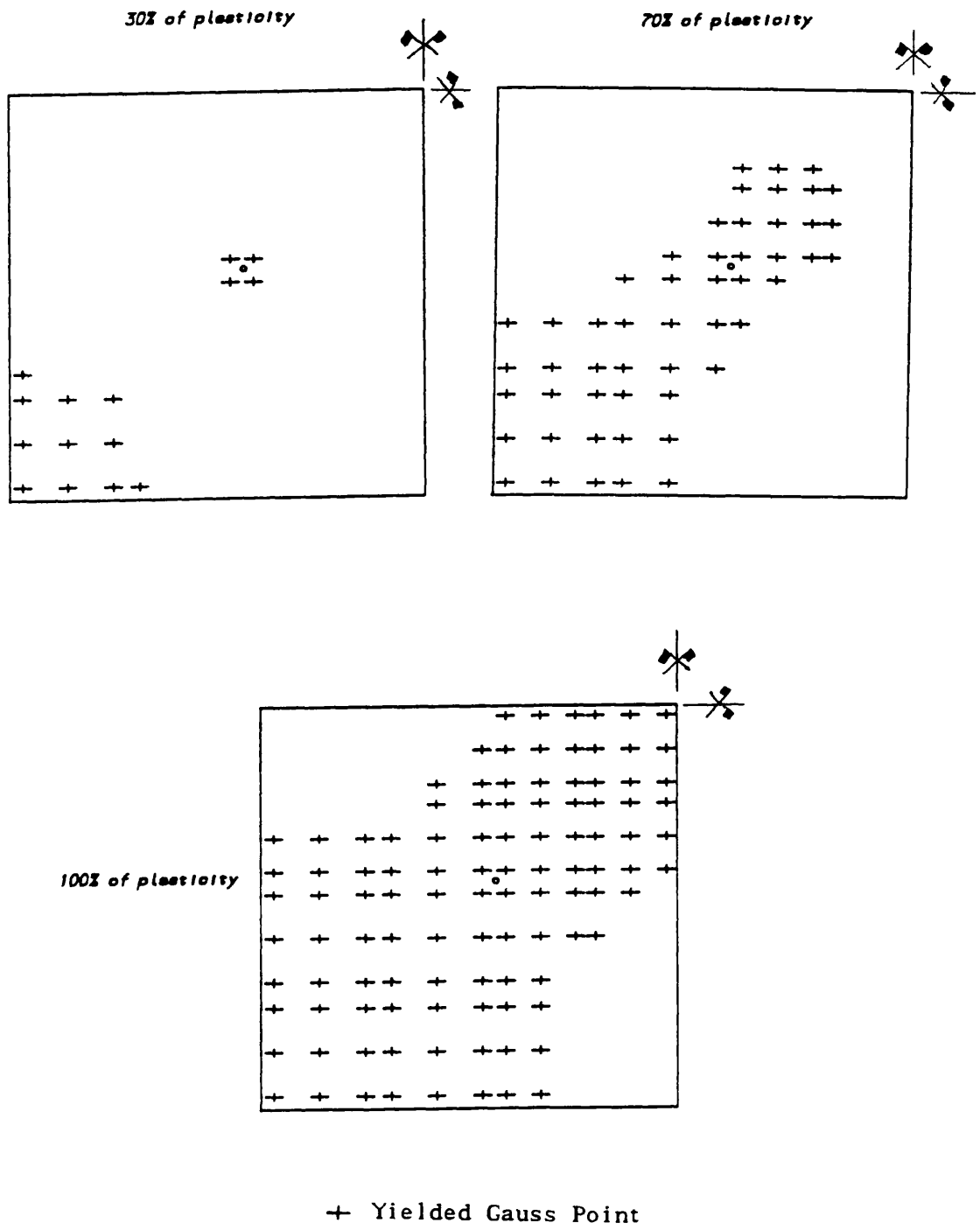
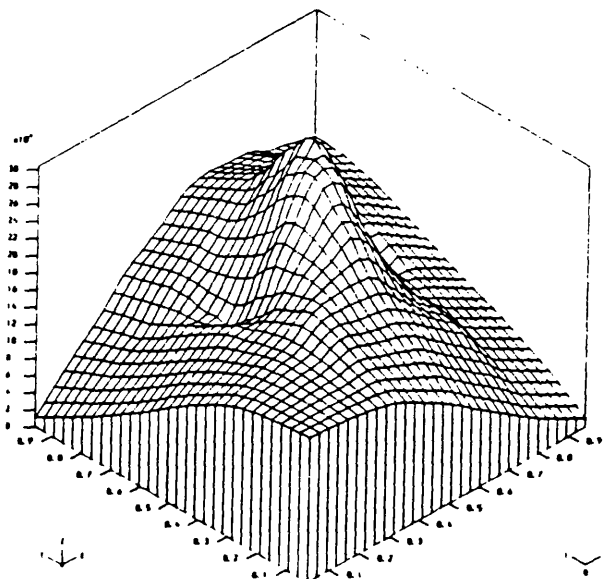
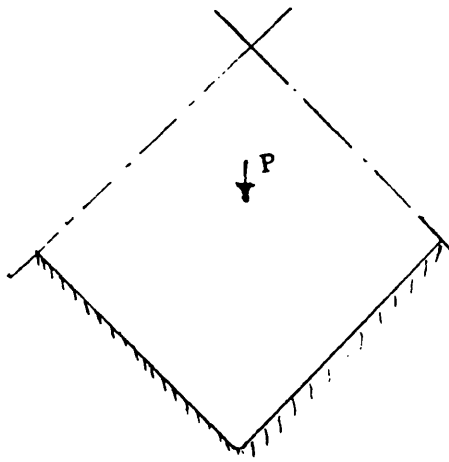
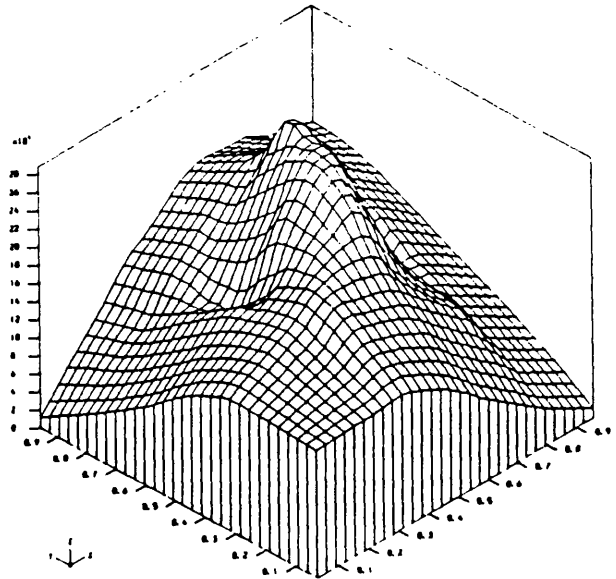


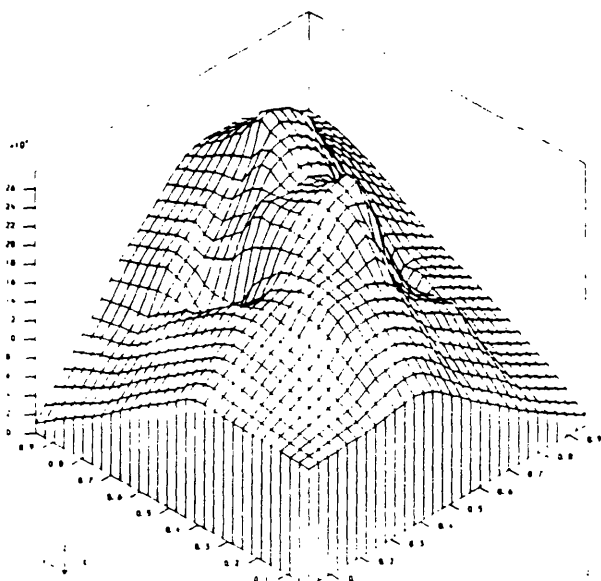
Fig. 7.2 Plasticity Spread over the Slab. (S1, S2, S3)



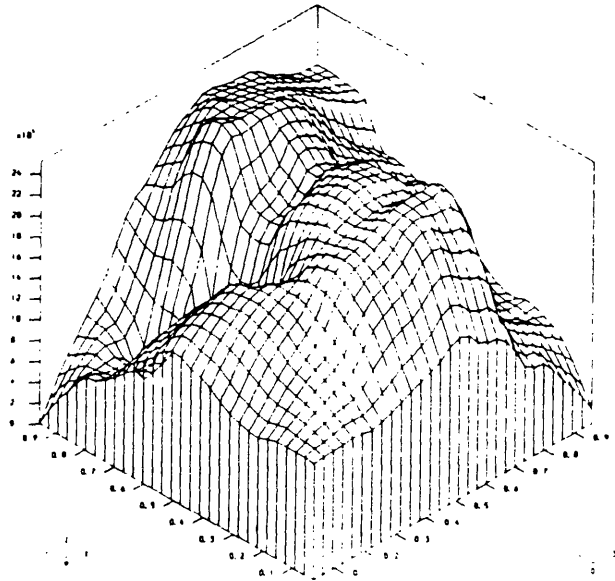
BOT. MX. (ELASTIC) 1/4 SLAB



BOT. MX. (130% PLASTICITY) 1/4 SLAB

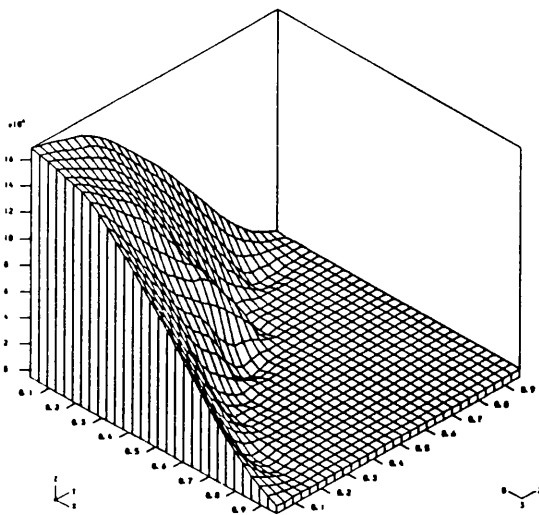
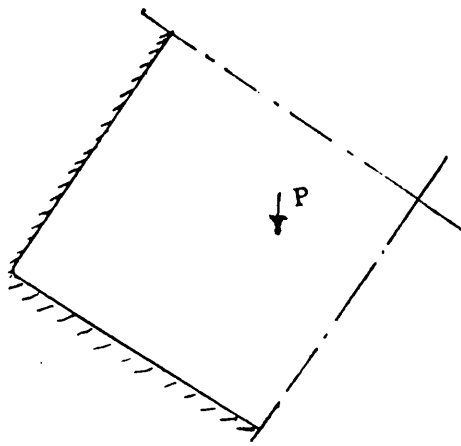


BOT. MX. (170% PLASTICITY) 1/4 SLAB

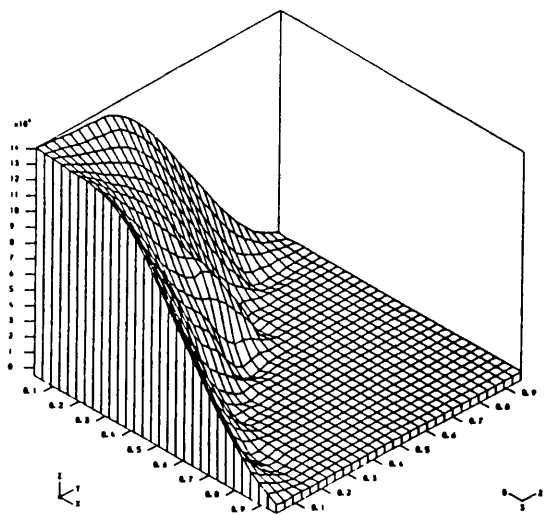


BOT. MX. (1100% PLASTICITY) 1/4 SLAB

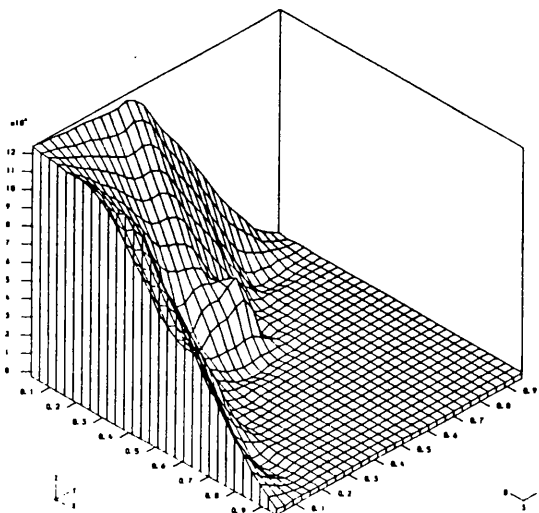
Fig. 7.3 Bottom Design moment Distribution at Different Levels of Plasticity.



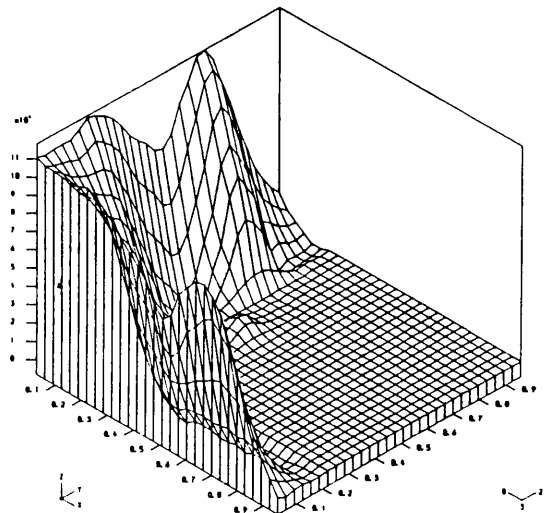
MX = (ELASTIC) 1/4 SLAB



MX = (130% PLASTICITY) 1/4 SLAB



MX = (170% PLASTICITY) 1/4 SLAB



MX = (1100% PLASTICITY) 1/4 SLAB

Fig. 7.4 Top Design Moment Distribution at Different Levels of Plasticity.

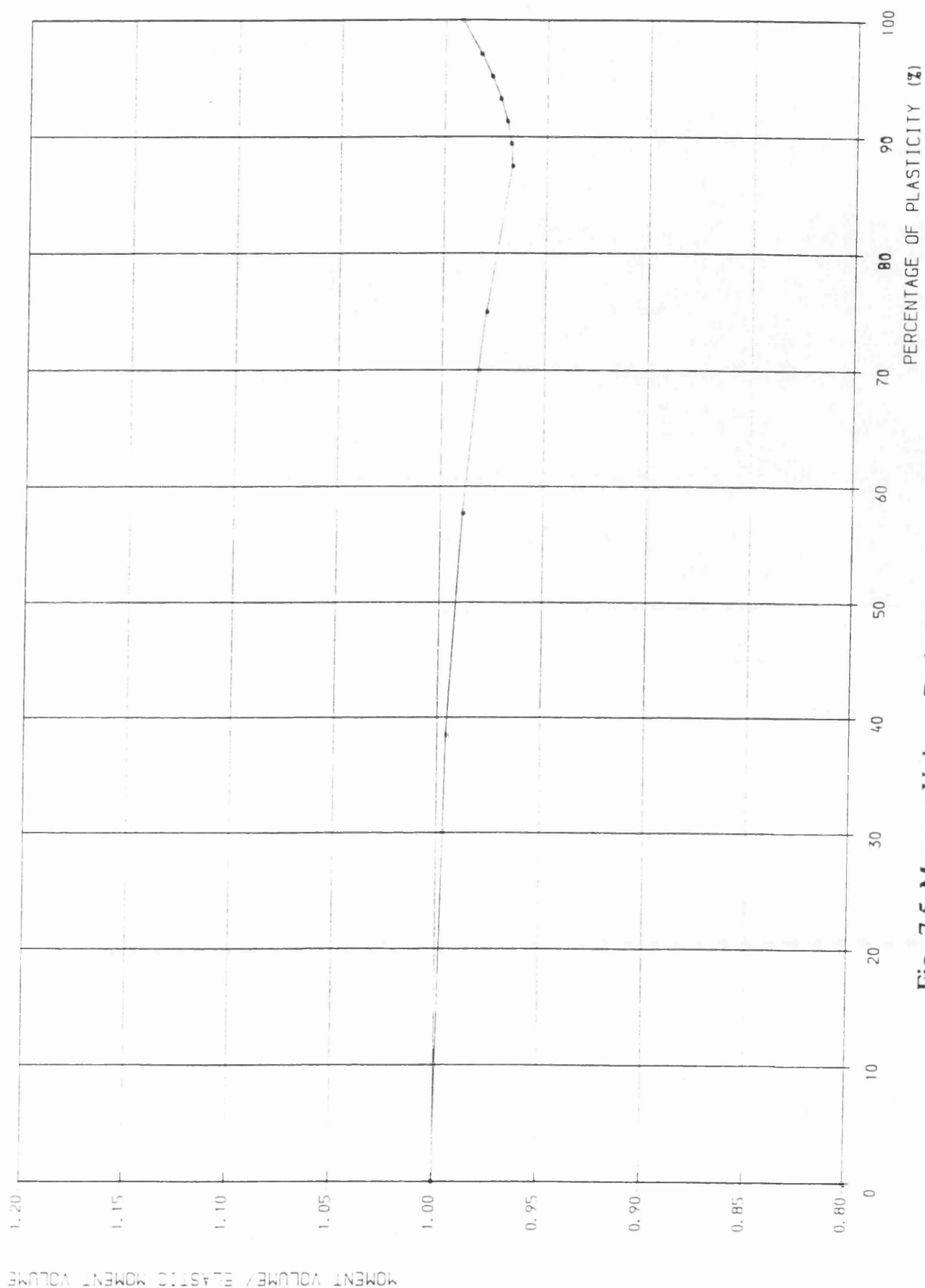


Fig. 7.5 Moment Volume Ratio-Percentage of Plasticity Curve.

Bottom steel in x direction: Provided steel
(Computed steel)

0.1300	0.3900	0.3900	0.3900
(0.1176)	(0.3104)	(0.4039)	(0.3290)
0.2600	0.3900	0.3900	0.3900
(0.1914)	(0.3365)	(0.4286)	(0.2833)
0.3000	0.3000	0.3000	0.3000
(0.2699)	(0.3931)	(0.3084)	(0.1868)
0.3000	0.3000	0.3000	0.3000
(0.2481)	(0.2920)	(0.1961)	(0.0904)

Top steel in x direction: Provided steel
(Computed steel)

0.0000	0.0000	0.0000	0.0000
(0.0061)	(0.0000)	(0.0000)	(0.0000)
0.1300	0.0000	0.0000	0.0000
(0.0440)	(0.0000)	(0.0000)	(0.0000)
0.2000	0.2000	0.0000	0.0000
(0.1307)	(0.0186)	(0.0000)	(0.0000)
0.2000	0.2000	0.2000	0.0000
(0.1903)	(0.1093)	(0.0440)	(0.0069)

Table 7.1 Numerical Required and Provided Steel Area per mm
Model S1 (70% Plasticity)

a- Bottom steel area			
0.09720	0.3609	0.4109	0.3581
(0.3770)	(0.3770)	(0.3770)	(0.3770)
0.1836	0.2848	0.3746	0.2777
(0.3770)	(0.3770)	(0.3770)	(0.3770)
0.2891	0.3595	0.3641	0.2462
(0.3770)	(0.3770)	(0.3770)	(0.3770)
0.2291	0.3313	0.3333	0.1454
(0.3770)	(0.3770)	(0.3770)	(0.3770)

b- Top steel area			
0.0315	0.0000	0.0000	0.0000
(0.0000)	(0.0000)	(0.0000)	(0.0000)
0.0591	0.0000	0.0000	0.0000
(0.0000)	(0.0000)	(0.0000)	(0.0000)
0.0755	0.0028	0.0000	0.0000
(0.1779)	(0.1779)	(0.0000)	(0.0000)
0.1577	0.0487	0.0457	0.0000
(0.1779)	(0.1779)	(0.0000)	(0.0000)

Table 7.2 Numerical Required and Provided Steel Area per mm
Model S2 (100% Plasticity)
between brackets the provided steel areas.

a- Bottom steel area per mm

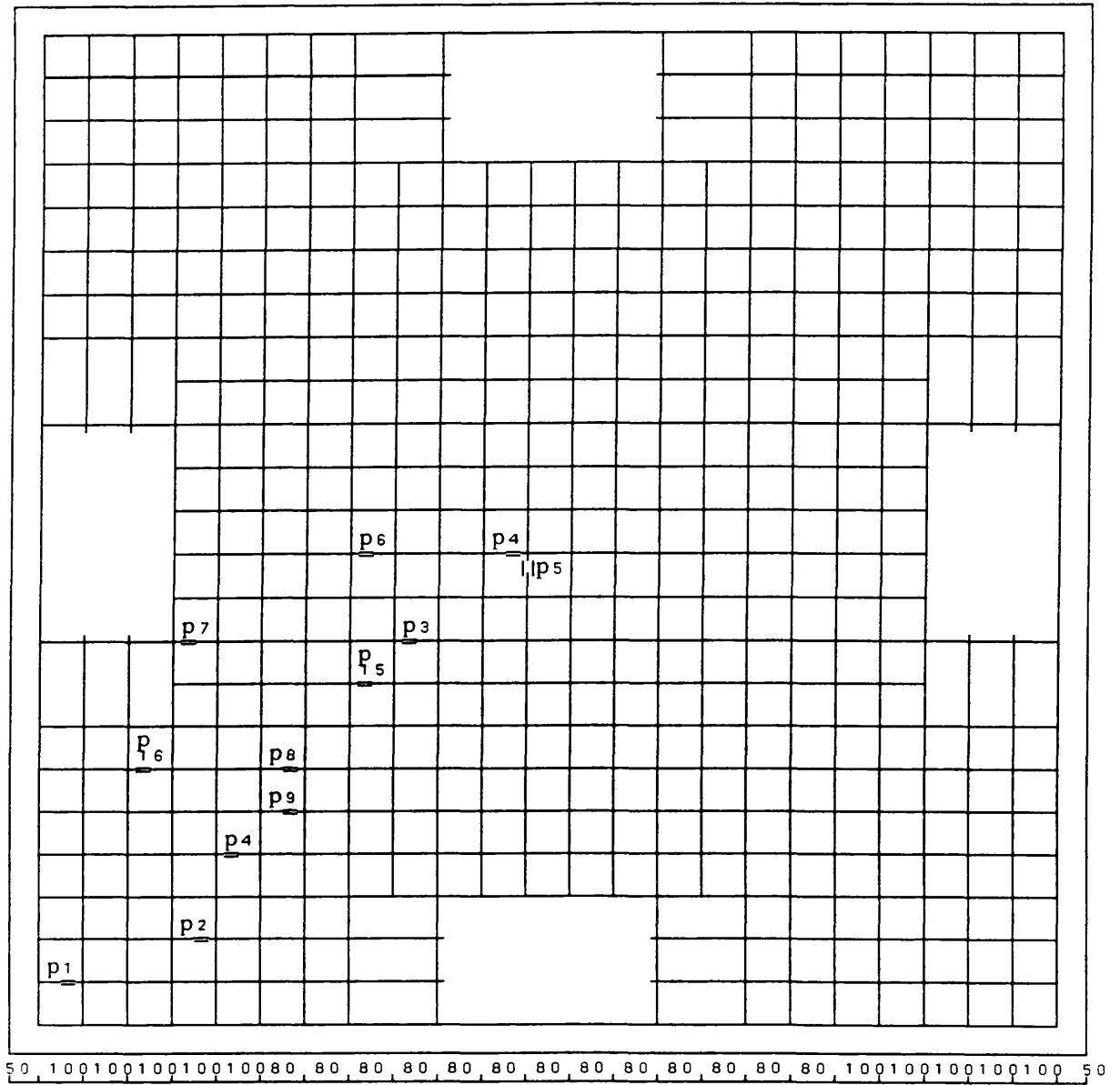
0.1130	0.2882	0.3546	0.2968
(0.3448)	(0.3448)	(0.3448)	(0.3448)
0.1895	0.3429	0.4192	0.2646
(0.4597)	(0.4597)	(0.4597)	(0.4597)
0.2770	0.3988	0.3226	0.1854
(0.3539)	(0.3539)	(0.3539)	(0.3539)
0.2838	0.2912	0.1909	0.0895
(0.3539)	(0.3539)	(0.3539)	(0.3539)

b- Top steel area per mm

0.0057	0.0000	0.0000	0.0000
(0.0000)	(0.0000)	(0.0000)	(0.0000)
0.0442	0.0000	0.0000	0.0000
(0.1799)	(0.0000)	(0.0000)	(0.0000)
0.1542	0.0350	0.0000	0.0000
(0.1779)	(0.1779)	(0.0000)	(0.0000)
0.3537	0.1404	0.0412	0.0066
(0.3558)	(0.3558)	(0.0000)	(0.0000)

**Table 7.3 Numerical Required and Provided Steel Area per mm
Model S3 (30% Plasticity)**
between brackets the provided areas.

a- Bottom steel



b- Top steel

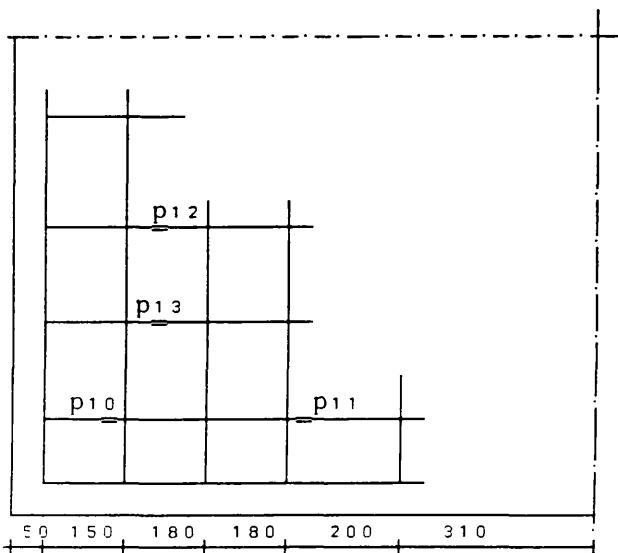
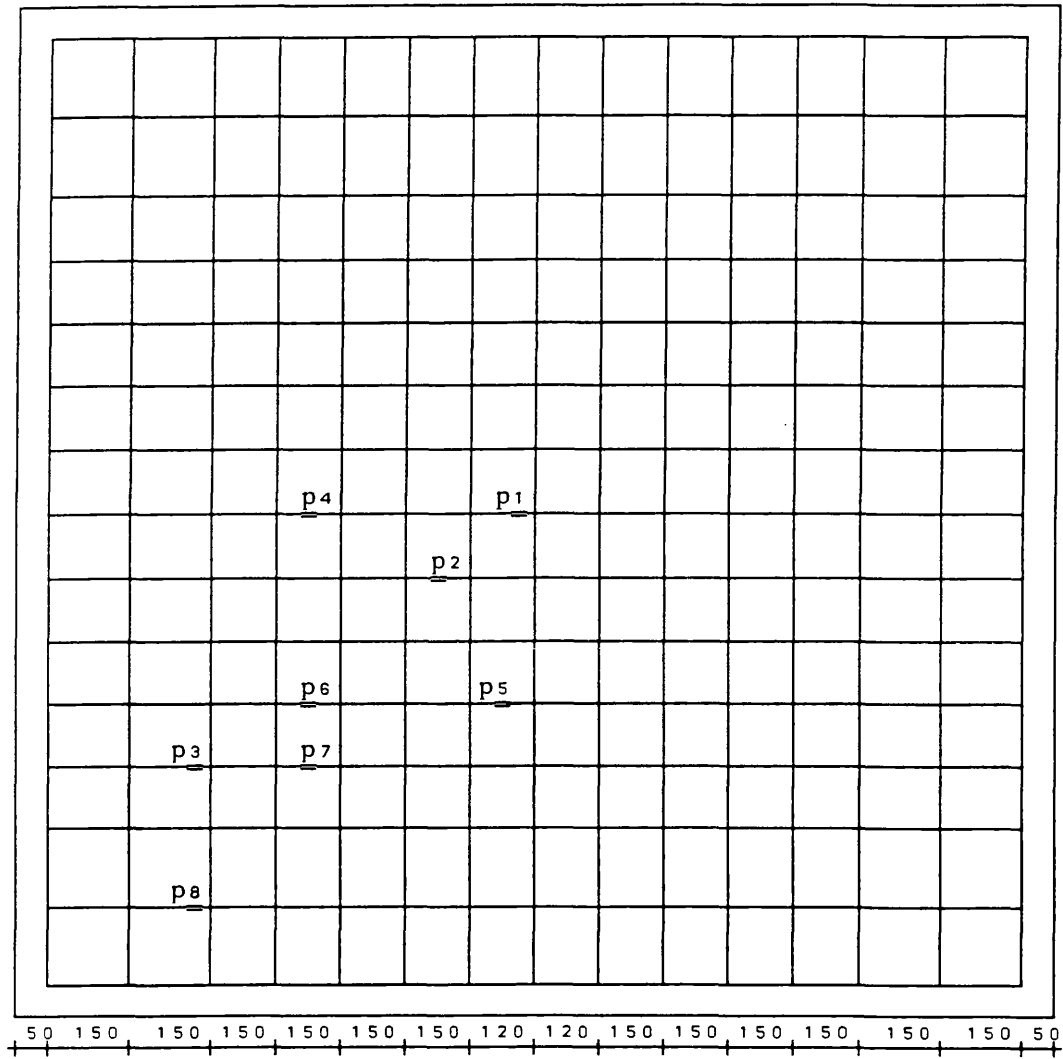


Fig. 7.6 Steel Layout for Model S1 and Strain Guage Positions.
S1 Designed Using 70% Plasticity. (All bars ϕ 6mm)

a- Bottom steel



b- Top steel

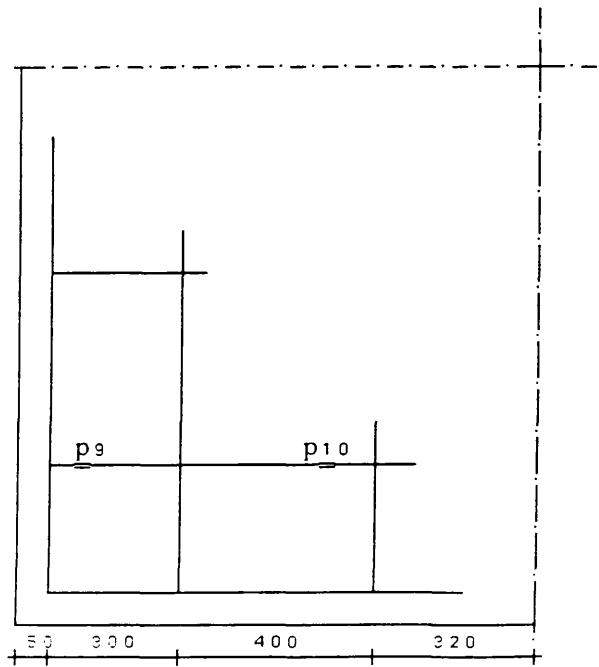
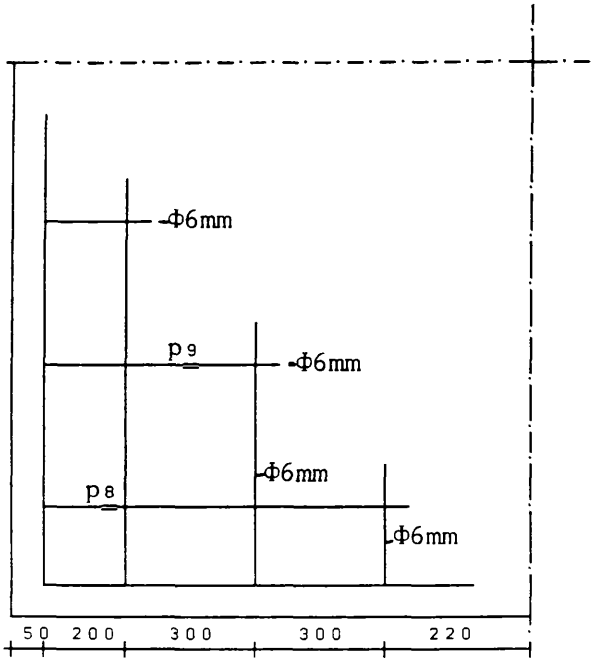
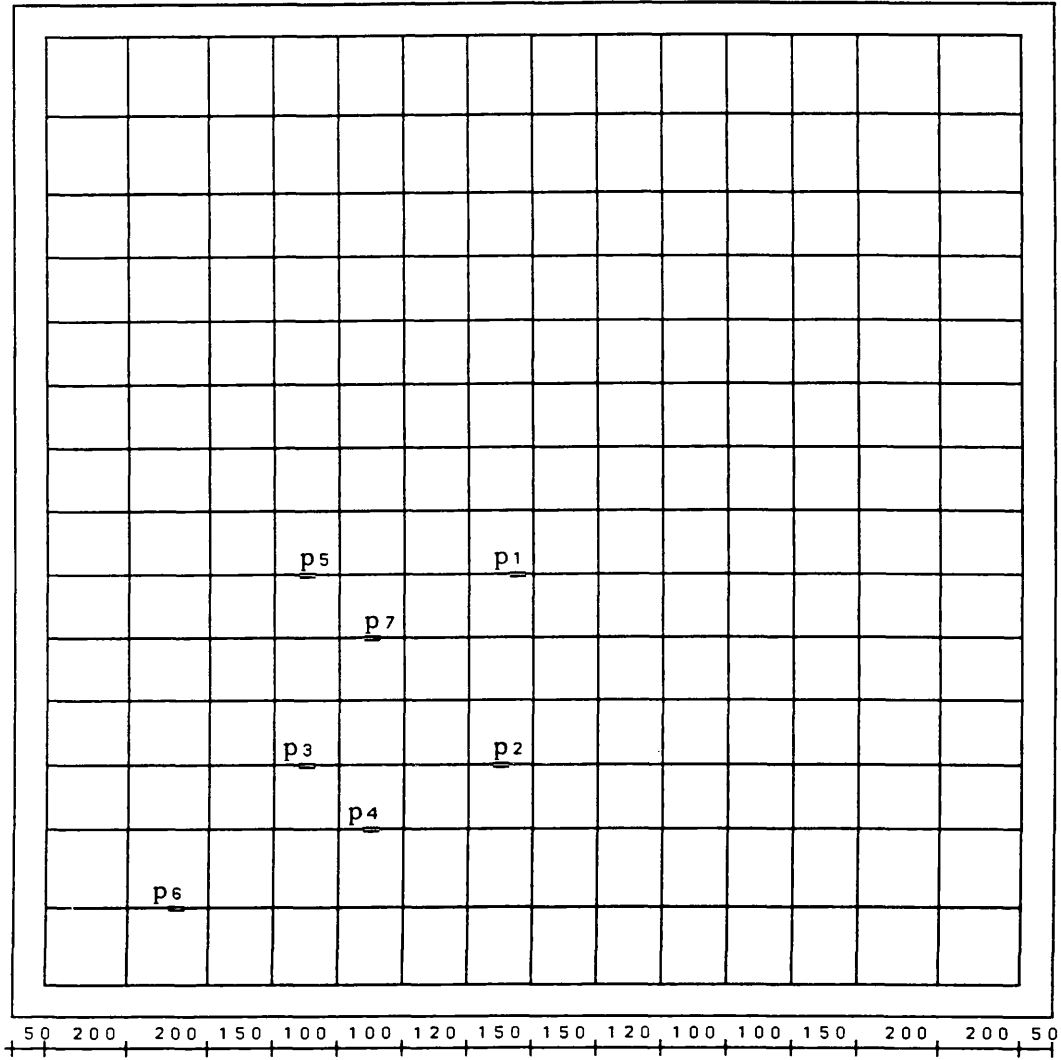


Fig. 7.7 Steel Layout for Model S2 and Strain Guage Positions.
S2 Designed Using 100% Plasticity. (All bars Φ 8mm)

a- Bottom steel



b- Top steel

Fig. 7.8 Steel Layout for Model S3 and Strain Guage Positions.
S3 Designed Using 30% Plasticity.
(All non marked bars are Φ 8mm)

for both top and bottom reinforcement, as the percentage of plasticity reached 100%, as shown in figure 7.3 and figure 7.4. Although as shown in figure 7.5 the design moment volume shows little decrease as the percentage of plasticity increases, designing using high level of plasticity leads to an economical design, since the moment peaks are smoothed out. Table 7.1, 7.2 and 7.3 show the required and the provided steel area per mm for slab models S.1, S.2 and S.3 respectively. It can be noticed that the provided steel area is greater than the required one, especially for models S.2 and S.3. The reason for this is that model S.1 was reinforced using 6 mm diameter steel bars while 8 mm diameter were used for S.2 and S.3. The steel layout for these models are presented in figure 7.6, 7.7 and 7.8 respectively.

7.3.2 Model S5:

This was a rectangular slab of overall dimension 3140mm, 2140mm and 100mm thick. The slab was designed for a total load of 210 KN, applied as eight point loads as shown in figure 6.1. The stress distribution level used in the design was the 100% of plasticity distribution. By taking advantage of symmetry only a quarter of the slab was analysed, using a 4x8 finite element mesh. The load deflection curve is illustrated in figure 7.9. The plasticity spread over the slab is shown in figure 7.10. The plastification started in the corner of the slab. At 50% of plasticity distribution figure 7.10a the yielding points start to cover the area of the corner along the long edge and under the point loads. At 100% plasticity the whole diagonal between the corner and the point along the line of the point loads had yielded. Figure 7.11 and 7.12 show the bottom and the top design moment in x direction, respectively. At the elastic stage the peak moment can be seen to be under the point loads. At 100% plasticity level there is a little smoothing out of the moment near the corner and the peaks of the loaded area. The moment volume which defines the steel volume to be used to reinforce the slab is almost constant and independent of the level of plasticity, as shown in figure 7.13.

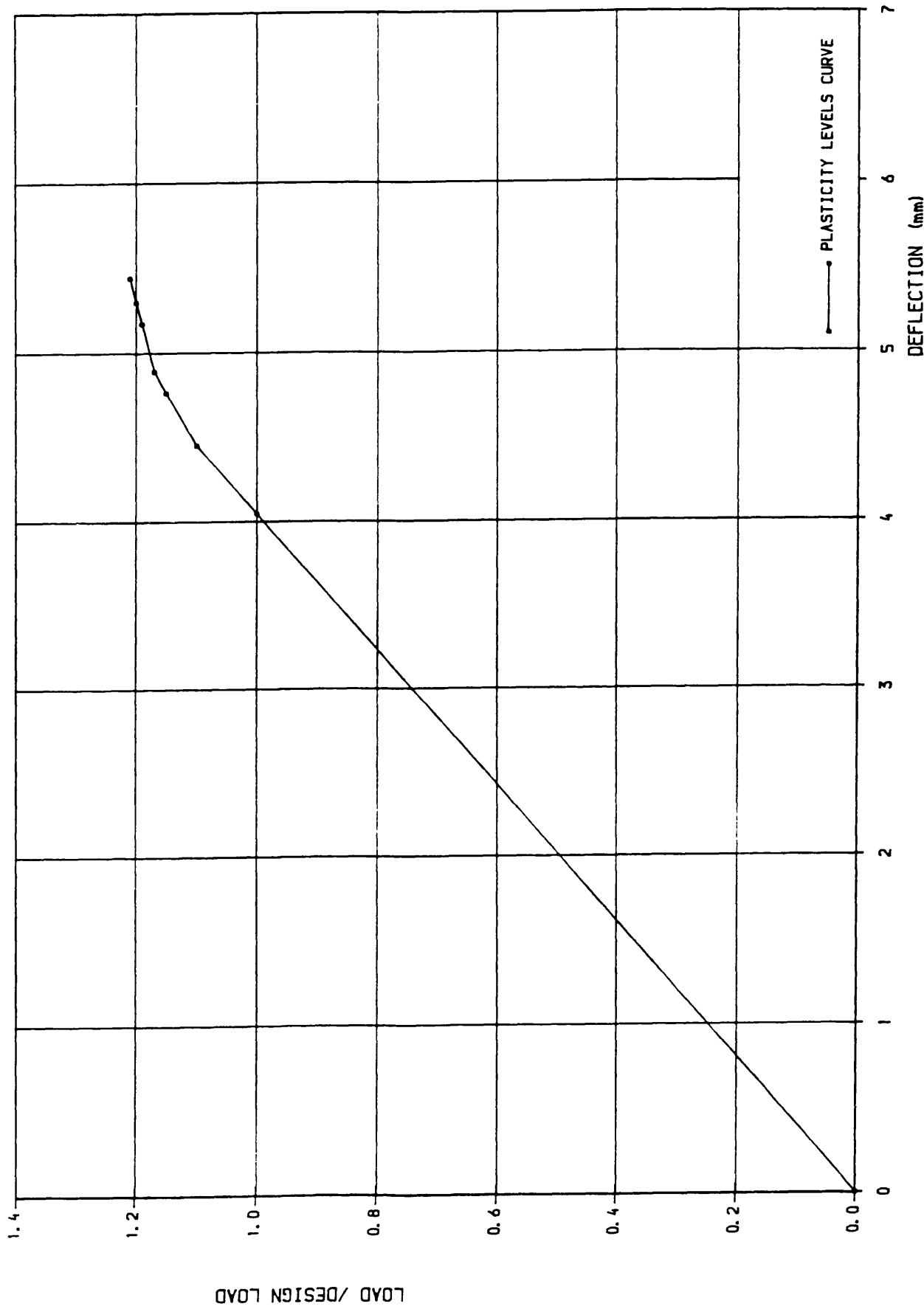
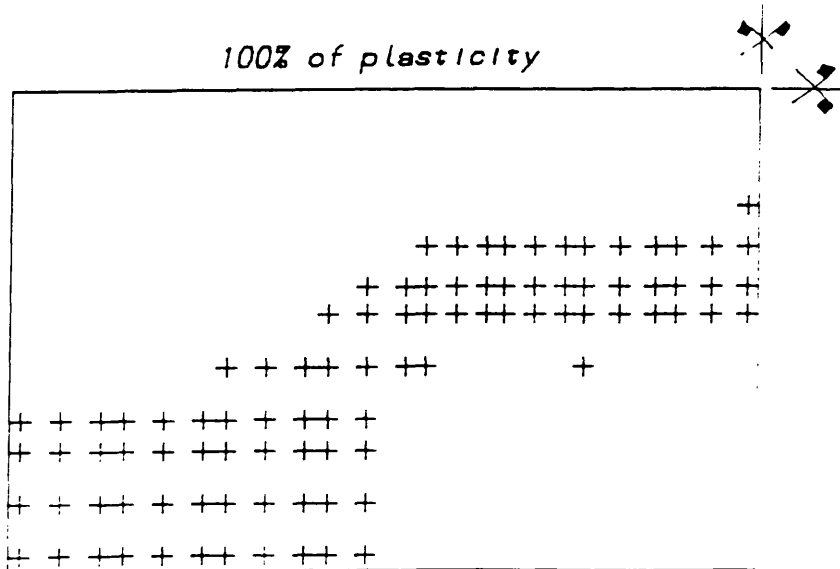
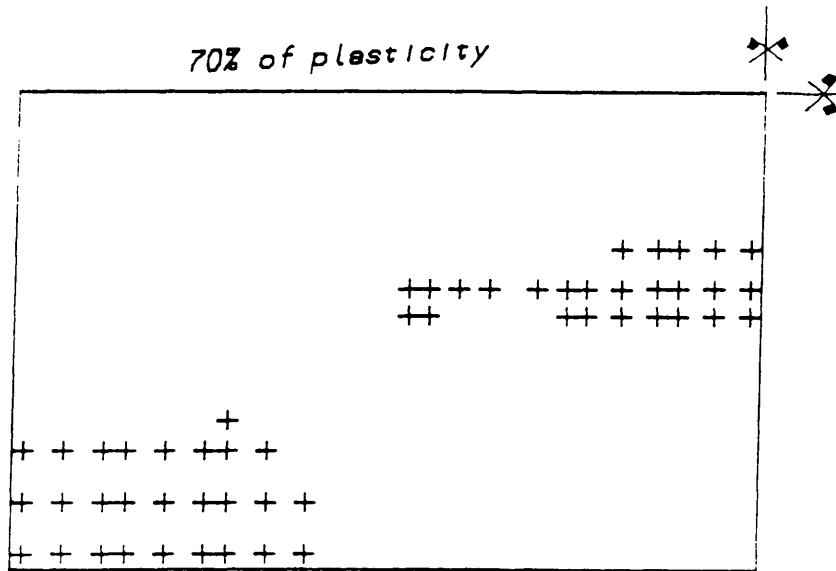
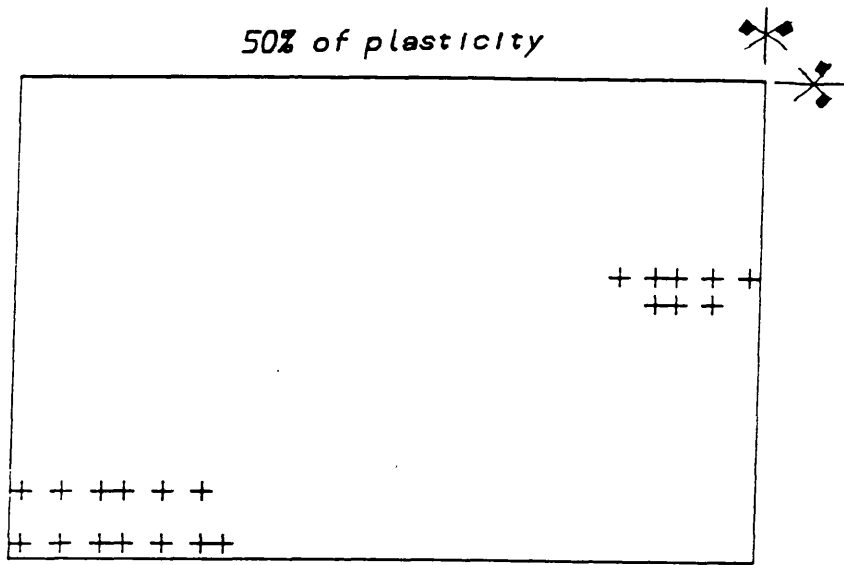


Fig. 7.9 Load deflection curve. Determination of Plasticity Levels S5.



+ Yielded Gauss Point

Fig. 7.10 Plasticity Spread over the Slab S5.

(1/4 SLAB)

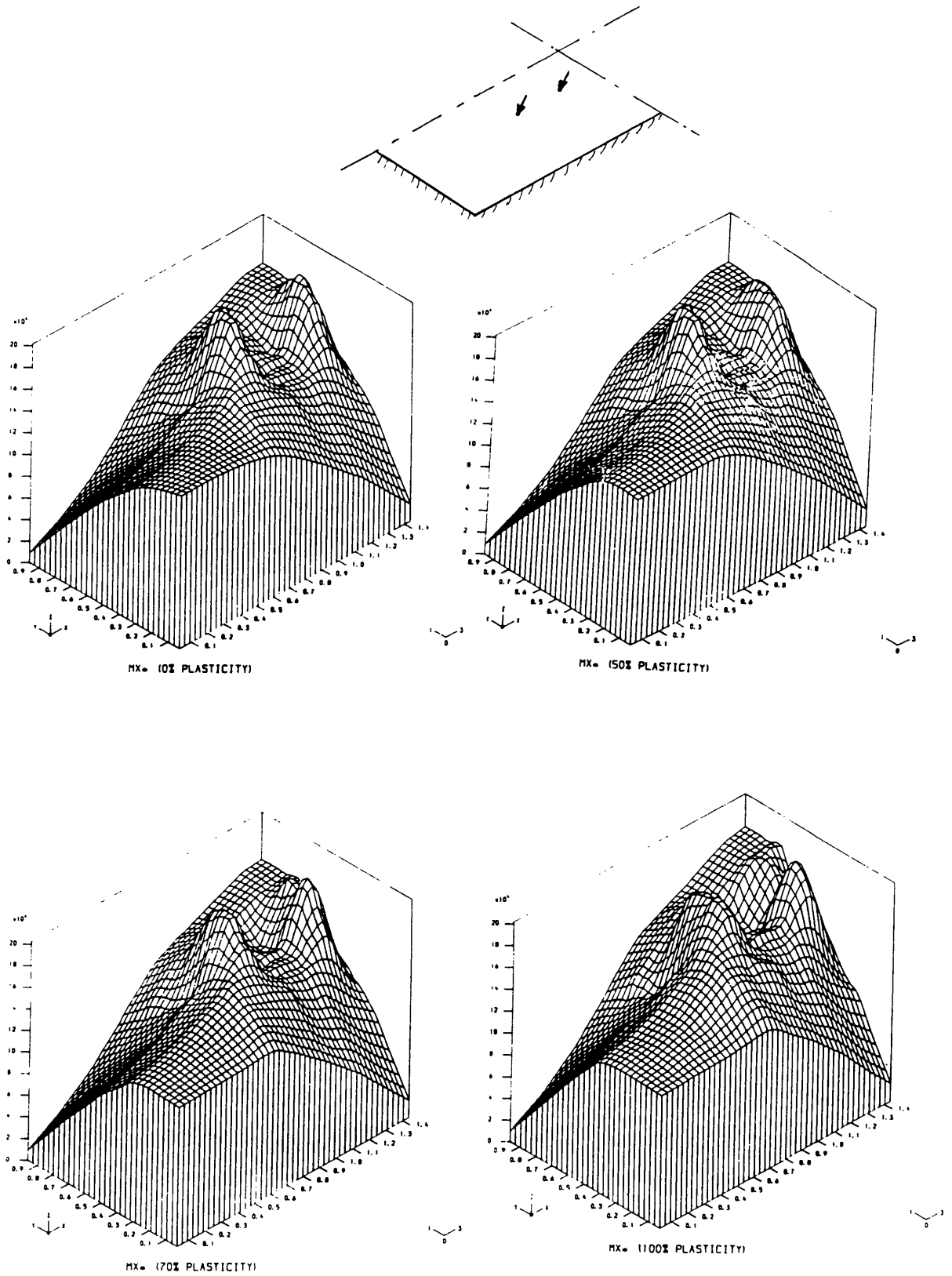


Fig. 7.11 Bottom Design Moment Distribution at Different Levels of plasticity in x Direction S5.

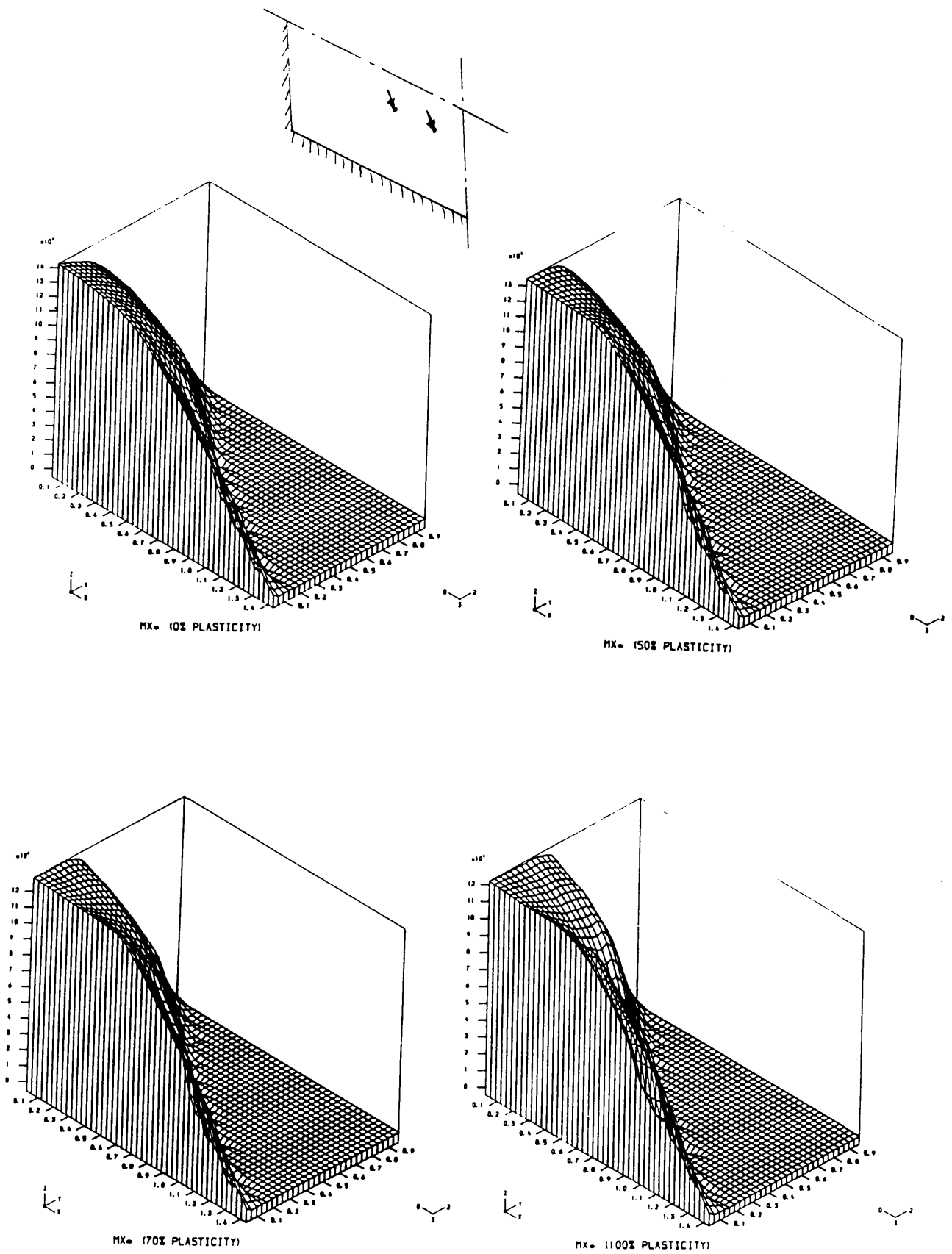


Fig. 7.12 Top Design Moment Distribution at Different Levels of Plasticity in x Direction S5.

c- Bottom Steel Area Per mm in y Direction
Numerical Required and Between Brackets the Provided

.085	.173	.246	.310	.357	.382	.389	.391
(.370)	(.370)	(.247)	(.247)	(.319)	(.478)	(.478)	(.478)
.166	.253	.338	.405	.457	.459	.432	.413
(.370)	(.370)	(.247)	(.247)	(.319)	(.478)	(.478)	(.478)
.233	.311	.388	.435	.440	.448	.422	.350
(.370)	(.370)	(.247)	(.247)	(.319)	(.478)	(.478)	(.478)
.233	.263	.284	.294	.373	.236	.191	.134
(.370)	(.370)	(.247)	(.247)	(.319)	(.478)	(.478)	(.478)

y
↑
└─x

d- Bottom Steel Area Per mm in x Direction
Numerical Required and Between Brackets the Provided

.050	.091	.136	.203	.246	.256	.282	.303
(.231)	(.231)	(.231)	(.231)	(.231)	(.231)	(.231)	(.231)
.139	.151	.248	.295	.249	.265	.280	.056
(.231)	(.231)	(.231)	(.231)	(.231)	(.231)	(.231)	(.231)
.207	.255	.260	.315	.299	.262	.279	.122
(.231)	(.356)	(.356)	(.356)	(.356)	(.356)	(.356)	(.356)
.221	.232	.249	.259	.231	.190	.153	.095
(.356)	(.356)	(.356)	(.356)	(.356)	(.356)	(.356)	(.356)

y
↑
└─x

Table 7.4 Numerical Required and Provided Steel Area per mm
Model S5 (100% Plasticity)

a- Top Steel Area Per mm in y Direction
Numerical Required and Between Brackets the Provided

.012	.00	.00	.00	.00	.00	.00	.00
(.00)	(.00)	(.00)	(.00)	(.00)	(.00)	(.00)	(.00)
.075	.008	.00	.00	.00	.00	.00	.00
(.00)	(.00)	(.00)	(.00)	(.00)	(.00)	(.00)	(.00)
.161	.079	.151	.057	.002	.00	.00	.00
(.247)	(.247)	(.00)	(.00)	(.00)	(.00)	(.00)	(.00)
.200	.167	.140	.119	.081	.045	.023	.045
(.247)	(.247)	(.247)	(.00)	(.00)	(.00)	(.00)	(.00)

y
↑
└─→x

b- Top Steel Area Per mm in x Direction
Numerical Required and Between Brackets the Provided

.240	.001	.00	.00	.00	.00	.00	.00
(.00)	(.00)	(.00)	(.00)	(.00)	(.00)	(.00)	(.00)
.107	.054	.004	.00	.00	.00	.00	.00
(.00)	(.00)	(.00)	(.00)	(.00)	(.00)	(.00)	(.00)
.190	.162	.087	.028	.007	.00	.00	.00
(.266)	(.266)	(.00)	(.00)	(.00)	(.00)	(.00)	(.00)
.212	.198	.177	.153	.119	.071	.029	.006
(.266)	(.266)	(.266)	(.00)	(.00)	(.00)	(.00)	(.00)

y
↑
└─→x

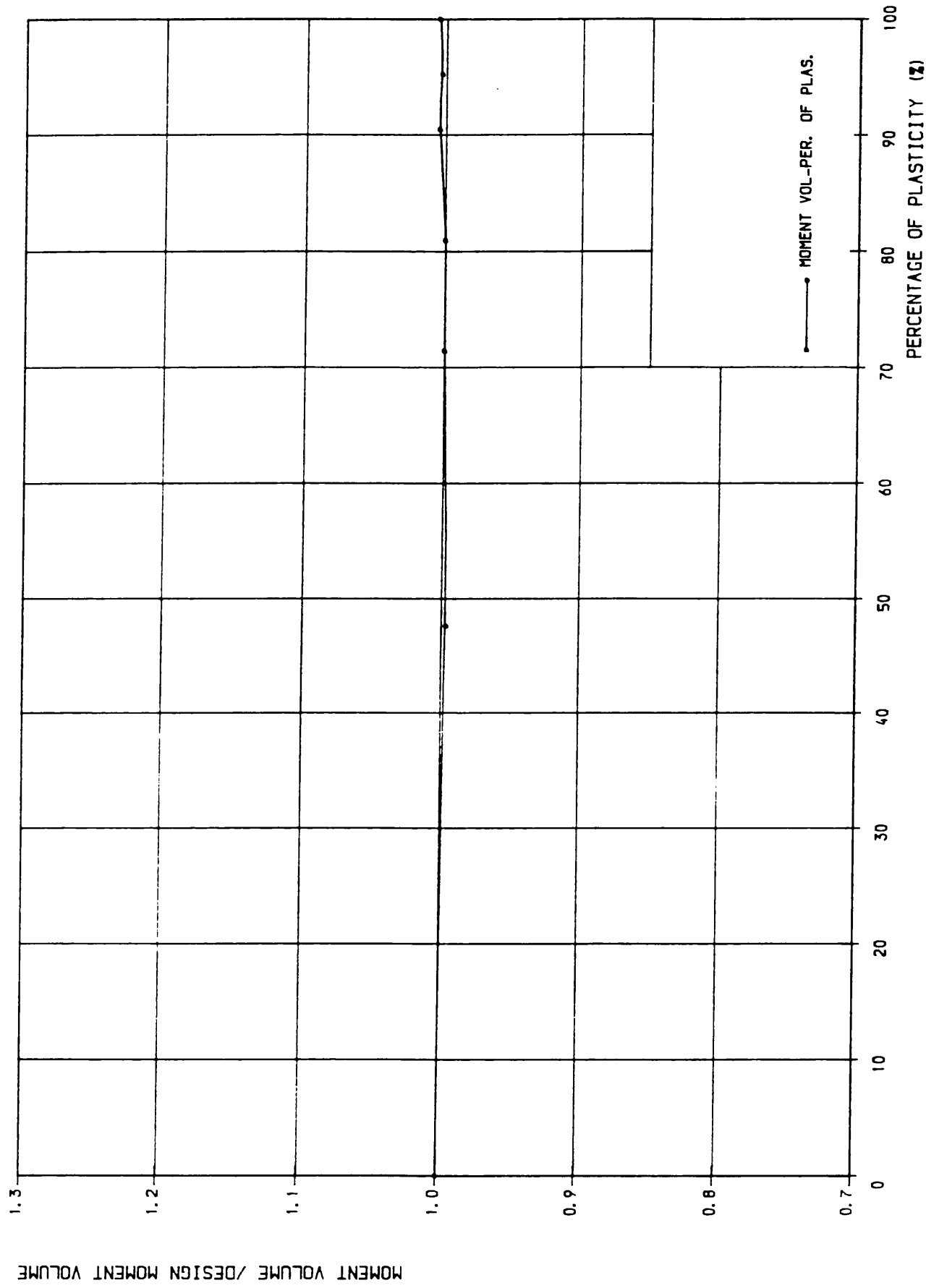


Fig. 7.13 Moment Volume Ratio-Percentage of Plasticity

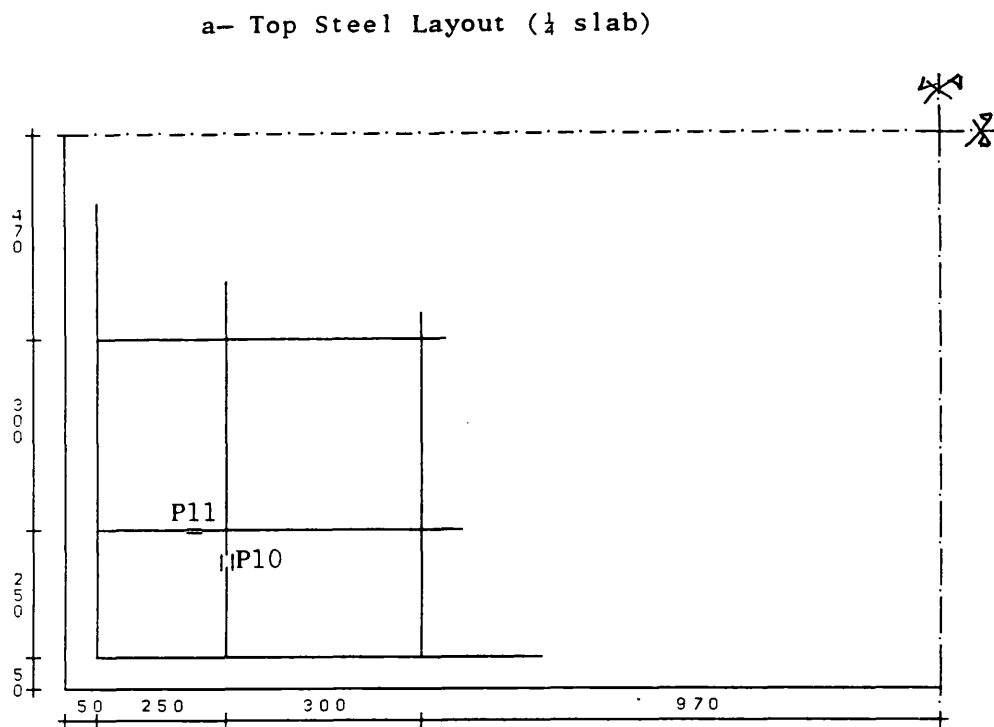
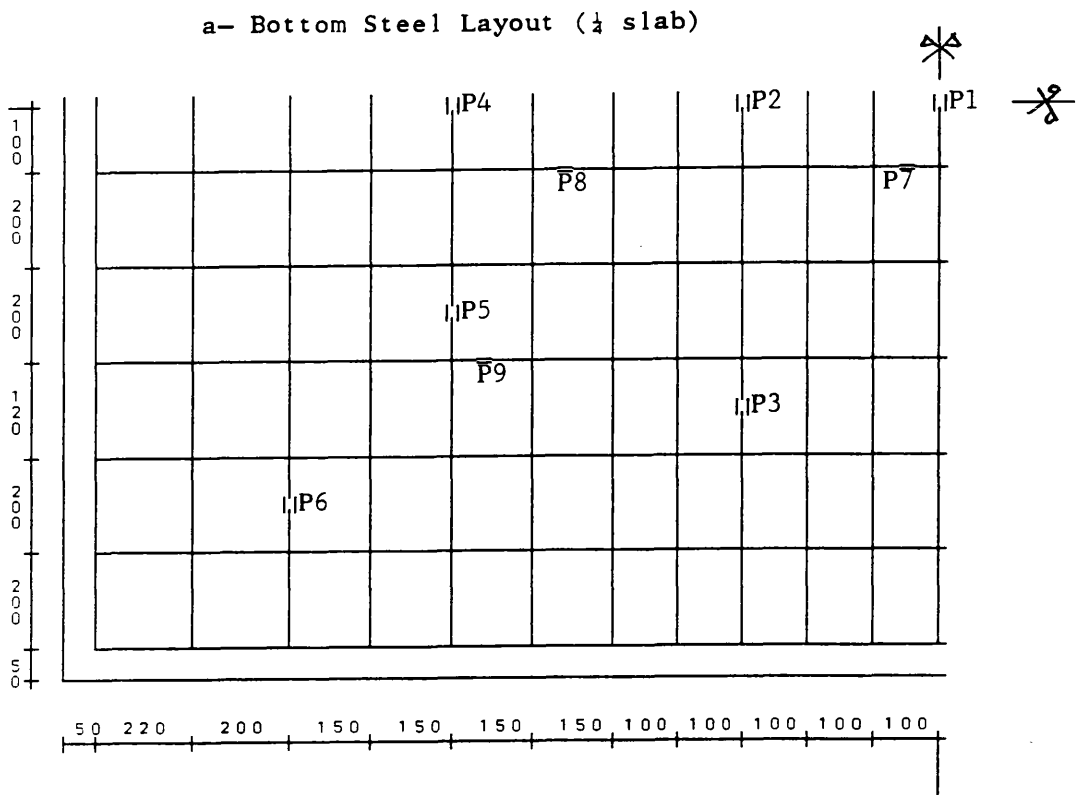


Fig. 7.14 Steel Layout for Model S5 and Strain Guage Positions.
S5 Designed Using 100% Plasticity.

(All bars diameter 8 mm)

7.3.3 Model S.4 and S.6:

These two models S.4 and S.6 were square simply supported slabs with a column support at the middle of the slab. Both slabs had the same length of 2140 mm (with a clear span of 2000mm), boundary and loading conditions, but were different in thickness. The first model was 100 mm thick while the second was 150 mm thick. The reason for increasing the thickness of S.6 is to facilitate the provision of shear links on the column. The models were designed for the same ultimate load of 320 KN using 100% of plasticity stress distribution. Dimensions and loading system were presented in table 6.1 and figure 6.1.

Generally over a column support, the moment tends to have a sharp peak. The object of these tests was to see:

- i— How far can the peak be reduced to facilitate the placing of reinforcement.
- ii— What effect this would have on the serviceability behaviour.

The slabs were designed by analysing a quarter of the slabs, using 4x4 element mesh. Tables 7.5 and 7.6 show the required and the provided steel areas. As can be seen, the ratio of the provided steel volume is greater than the theoretical required one in most cases. This is due to practical constraints. The different levels of plasticity are determined from figure 7.15 which shows the load deflection of the point where the load is applied for both models S.4 and S.6. The required moment, for both top and bottom, from which the required steel area is determined, are plotted in figures 7.16 and 7.17. Figures 7.18 presents the points which yielded at different levels of stress redistribution. The points started to yield on the column and under the point load. As the percentage of plasticity increases the yielded points cover a large area of the diagonal joining the corner to the column. The design moment distribution in figures 7.16 and 7.17 show a considerable redistribution and smoothing out of the peaks for both top and bottom design moments as the percentage of plasticity increases. Figure 7.19 represents the moment volume at different levels of plasticity. Since the thickness of the slab S.6 is greater than that of S.4, it is obvious that the required steel amount will be less for S.6 than the one for S.4. From figures 7.16 and 7.17 it can be noticed that,

at 100% of plasticity, there is an important reduction of the peak moment on the column which is redistributed to the surrounding points. The moment volume increased as the percentage of plasticity increased, figure 7.19.

Shear design:

Both slabs were checked for shear failure, using section 3.7.7 of BS8110(1) part 1. The failure zones near the column and under the point loads, for model S.4, were checked at the design load and no shear reinforcement was needed. Because the provided steel is greater than the required one as shown in table 7.5, this resulted in an ultimate load for S.4 greater than the value for which it was designed. Therefore the shear capacity of the slab near the column ^{was} reached before the slab attained its full strength flexurally. To prevent this, model S.6 was designed to resist a shear force 40% greater than the reaction of the column given by the analysis at the design load. And the shear links were provided on the column area of the slab as shown in figure 7.21. The thickness of the slab S.6 was increased to 150 mm, to facilitate the provision of shear links near the column. Under the point load no shear reinforcement was needed. The shear reinforcement was provided in the failure zone of the column as required by section 3.7.7.5 of BS8110(1).

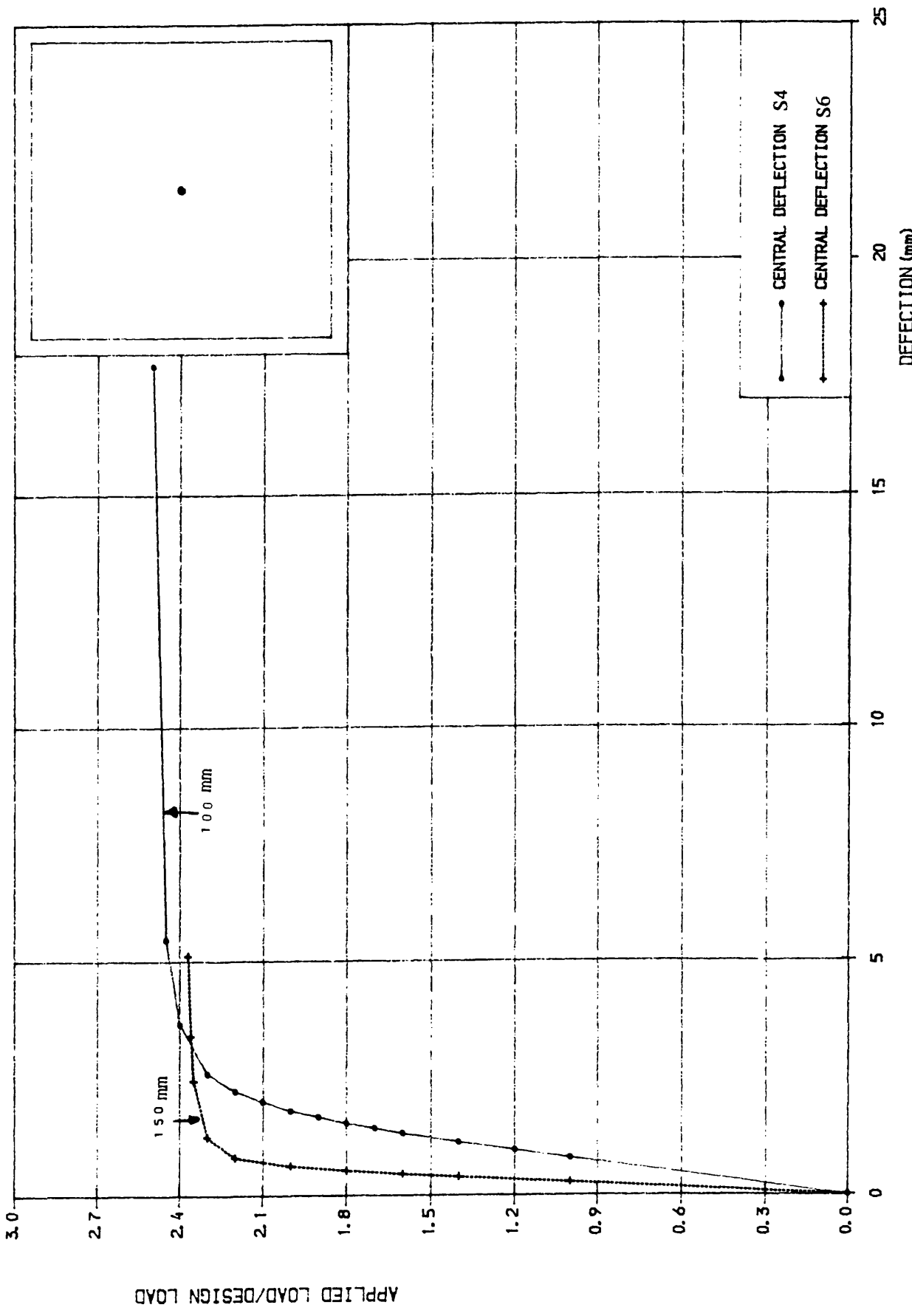


Fig. 7.15 Load Deflection Curve. Determination of Plasticity Levels.
Models S4 and S6.

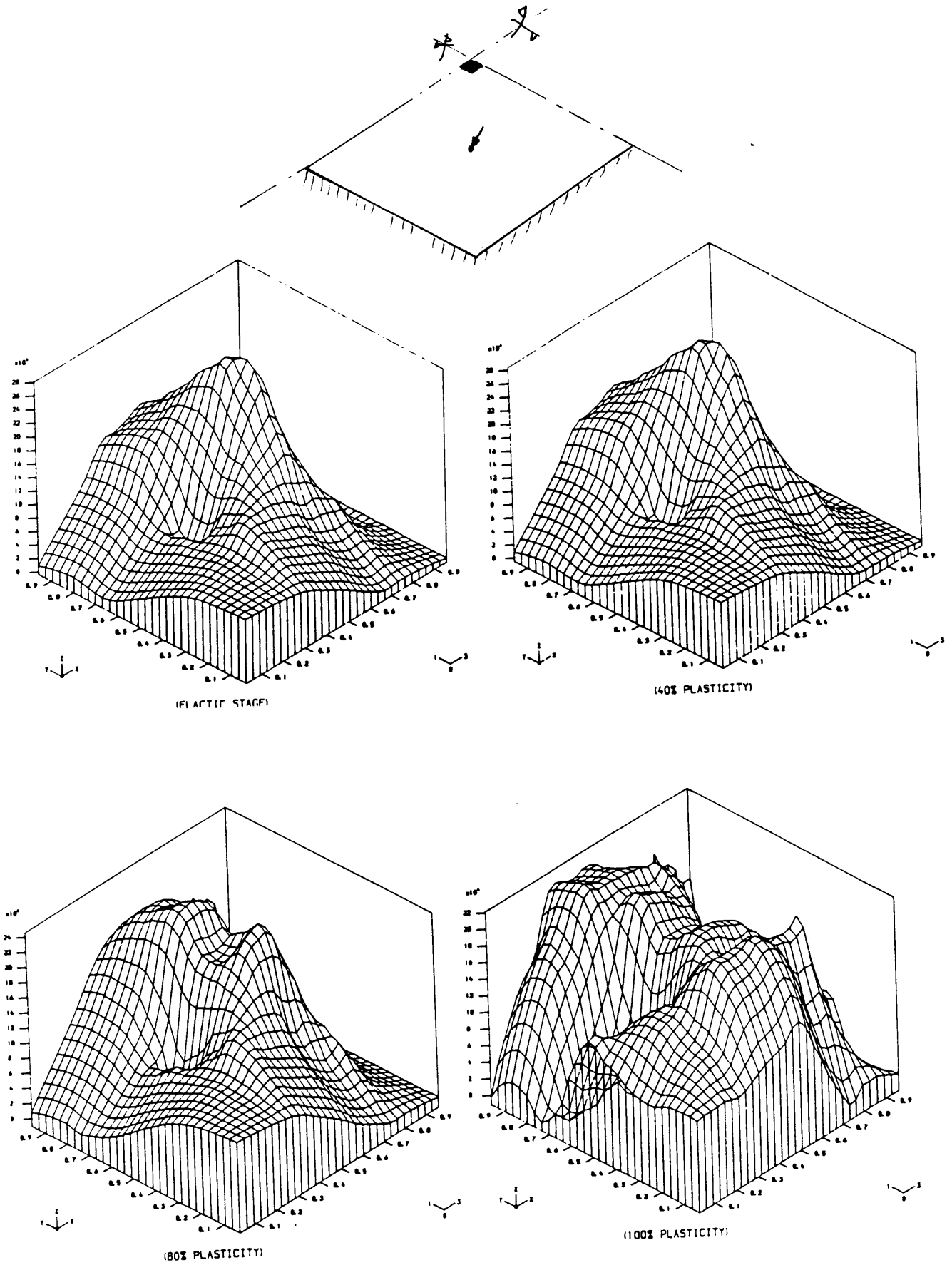


Fig. 7.16 Bottom Design Moment Distribution at Different Levels of Plasticity. Models S4 and S6.

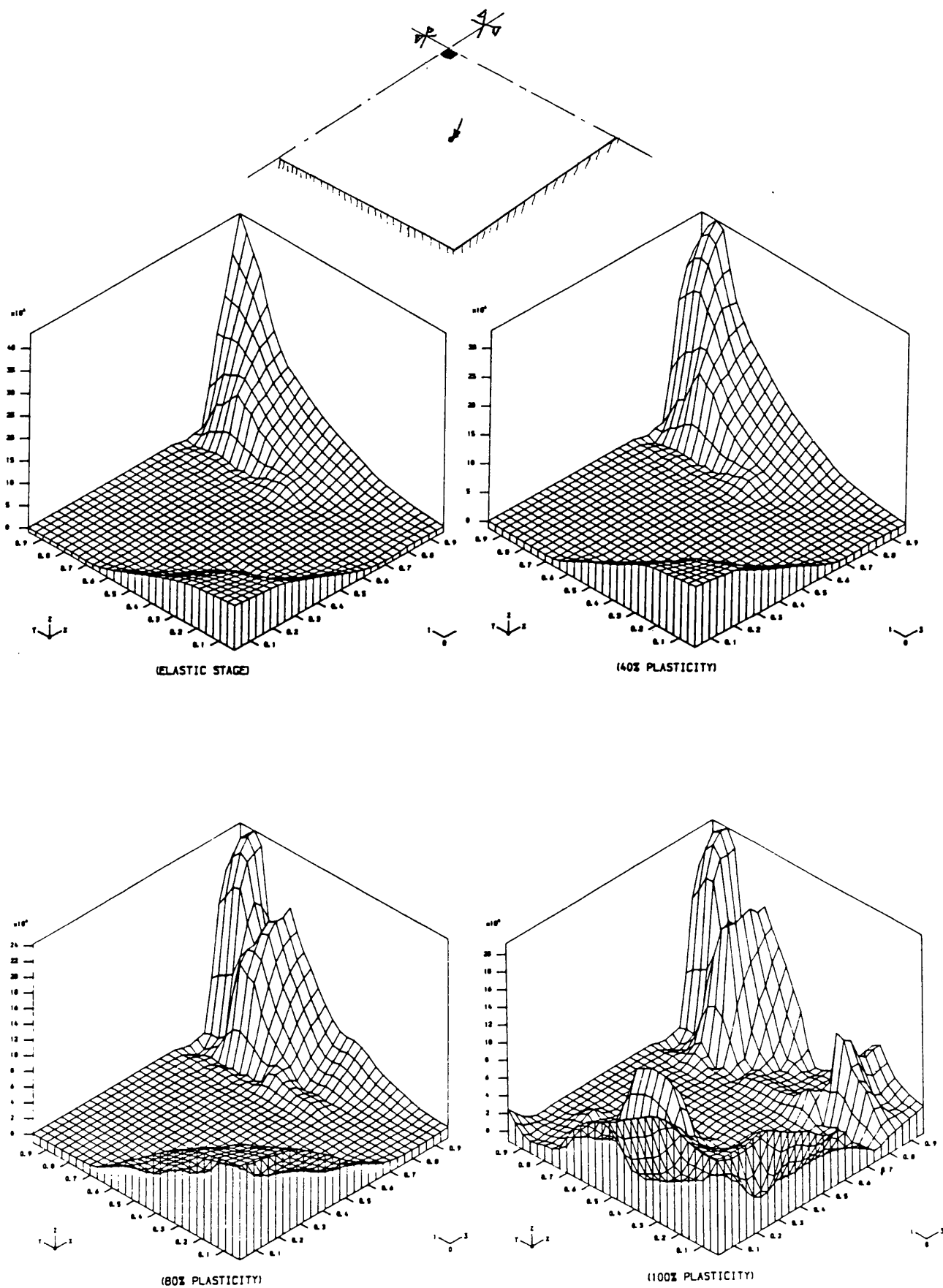
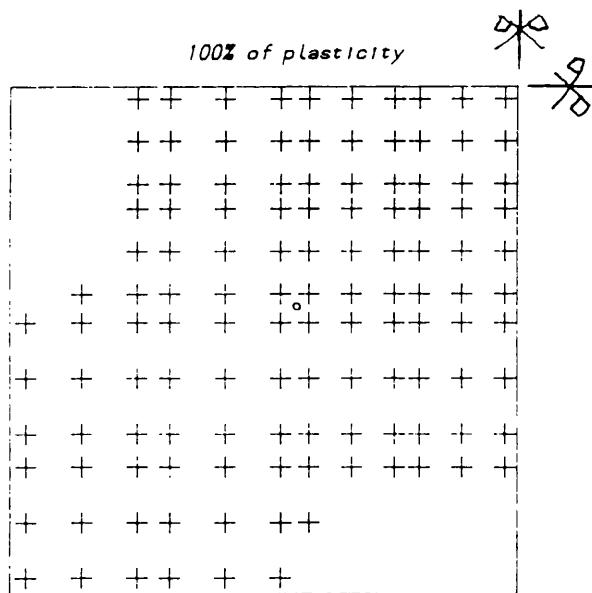
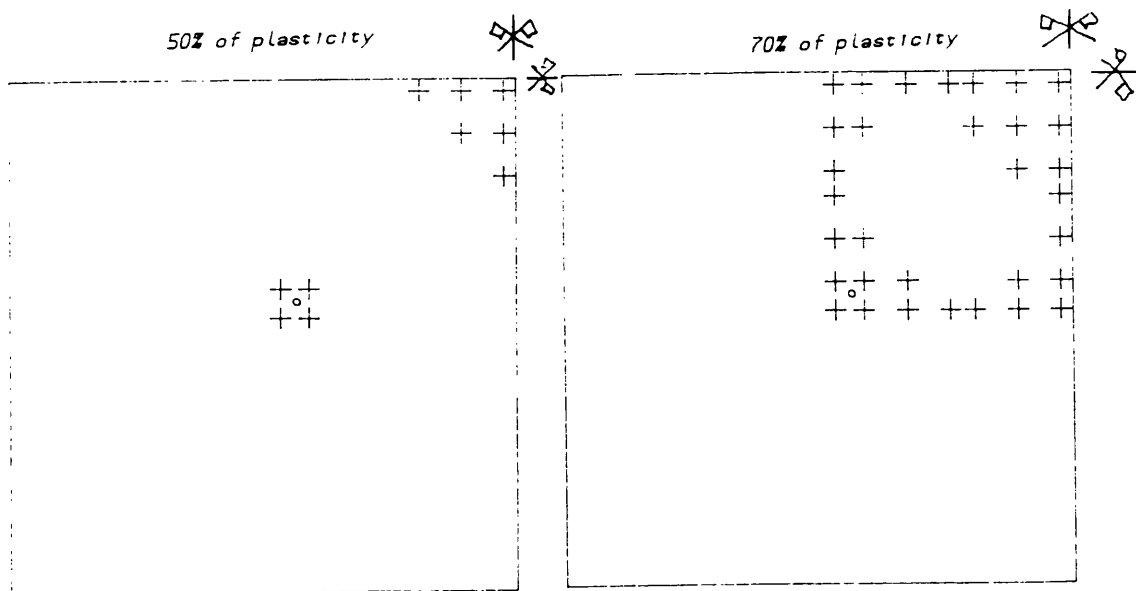


Fig. 7.17 Top Design Moment Distribution at Different Levels of Plasticity. Models S4 and S6.



+Yielded Gauss Point

Fig. 7.18 Plasticity Spread over the Slab. S4 and S6.

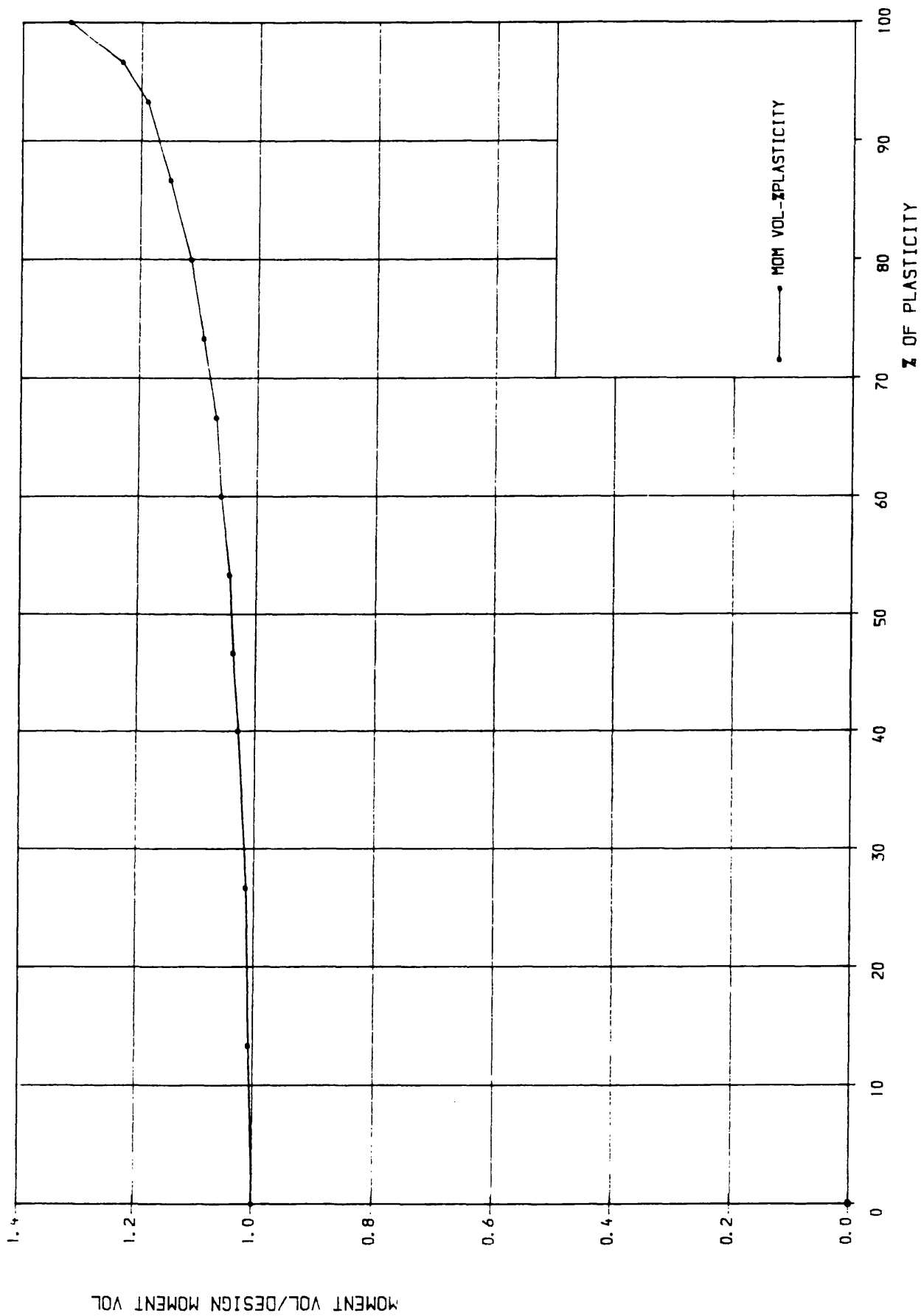


Fig. 7.19 Moment Volume Ratio-Percentage of Plasticity

a- Bottom steel area per mm

0.2888	0.2888	0.2888	0.2888
(0.0167)	(0.0367)	(0.0232)	(0.0907)
0.2888	0.2888	0.2888	0.2888
(0.0869)	(0.2766)	(0.2534)	(0.0302)
0.3558	0.3558	0.3558	0.3558
(0.2179)	(0.2844)	(0.2407)	(0.1279)
0.3558	0.3558	0.3558	0.3558
(0.2003)	(0.3139)	(0.2234)	(0.0476)

b- Top steel area per mm

0.0000	0.0000	0.3466	0.3466
(0.0097)	(0.0000)	(0.0047)	(0.1871)
0.2311	0.0000	0.2311	0.2311
(0.0383)	(0.0273)	(0.0010)	(0.1335)
0.2311	0.0000	0.0000	0.0000
(0.0560)	(0.0161)	(0.0102)	(0.0000)
0.3535	0.3558	0.3558	0.0000
(0.1413)	(0.0386)	(0.0122)	(0.0671)

Provided steel area and between brackets the theoretical required area.

Table 7.5 Numerical Required and Provided Steel Area per mm
Model S4.

a- Bottom steel area per mm

0.2311 (0.1024)	0.2311 (0.2260)	0.2311 (0.1429)	0.2311 (0.0573)
0.2311 (0.0482)	0.2311 (0.1678)	0.2311 (0.1555)	0.2311 (0.0158)
0.1779 (0.1351)	0.1779 (0.1797)	0.1779 (0.1501)	0.1779 (0.0823)
0.1779 (0.1298)	0.1779 (0.1933)	0.1779 (0.1346)	0.1779 (0.0319)

b- Top steel area per mm

0.0000 (0.0035)	0.0000 (0.0000)	0.1299 (0.0028)	0.1299 (0.1154)
0.0000 (0.0263)	0.0000 (0.0191)	0.1299 (0.0002)	0.1299 (0.0852)
0.1000 (0.0357)	0.0000 (0.0078)	0.0000 (0.0086)	0.0000 (0.0000)
0.1000 (0.0817)	0.0000 (0.0243)	0.0000 (0.0082)	0.0000 (0.0036)

Provided steel area and between brackets the theoretical required areas.

Table 7.6 Numerical Required and Provided Steel Area per mm
Model S6.

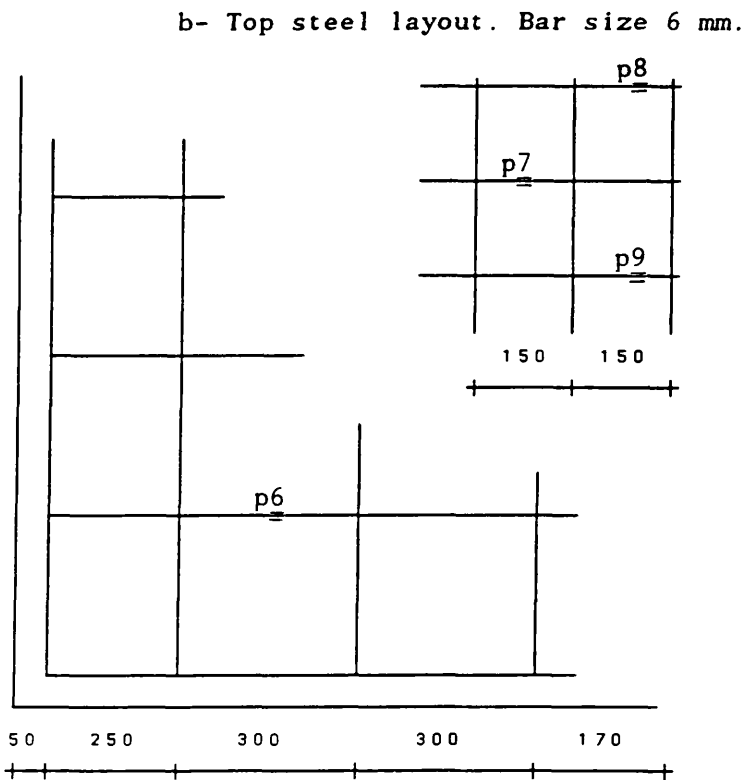
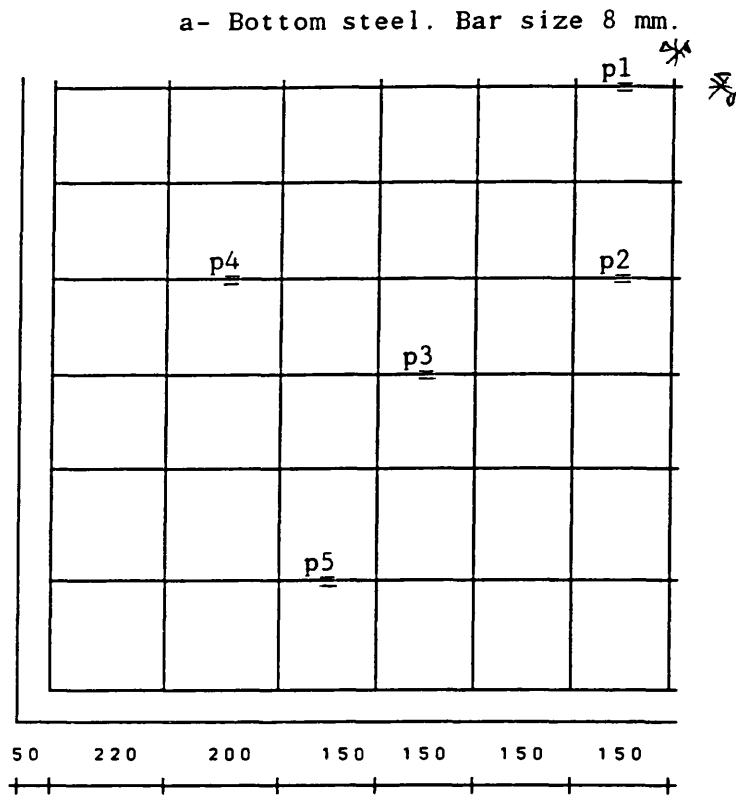
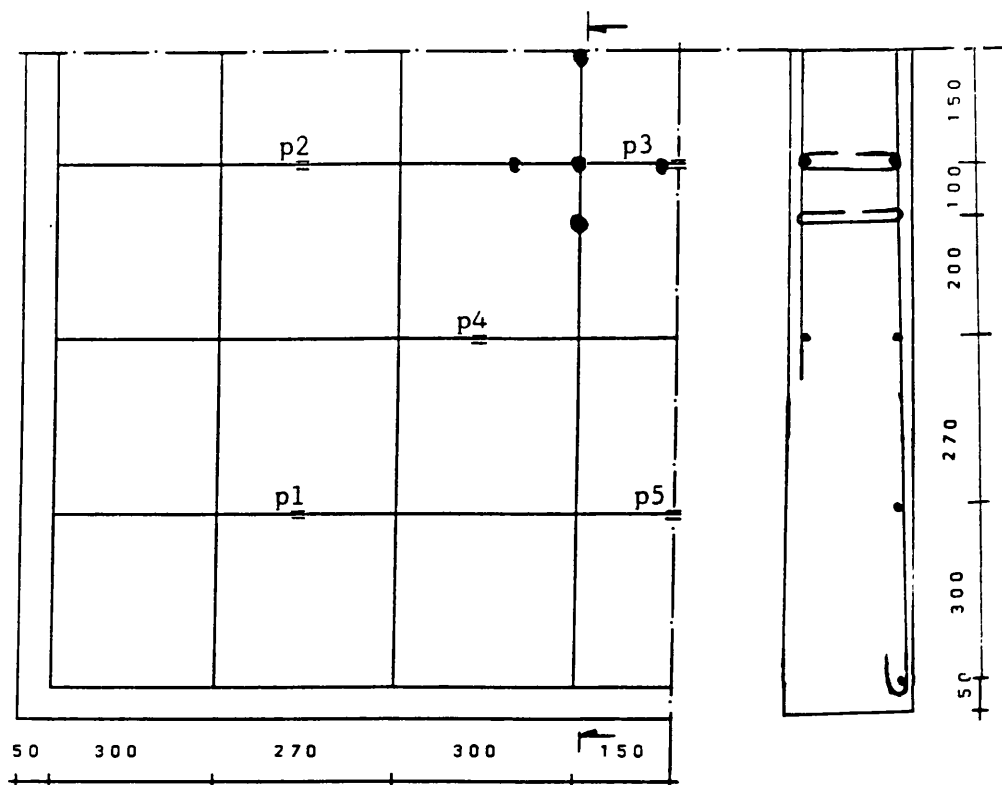
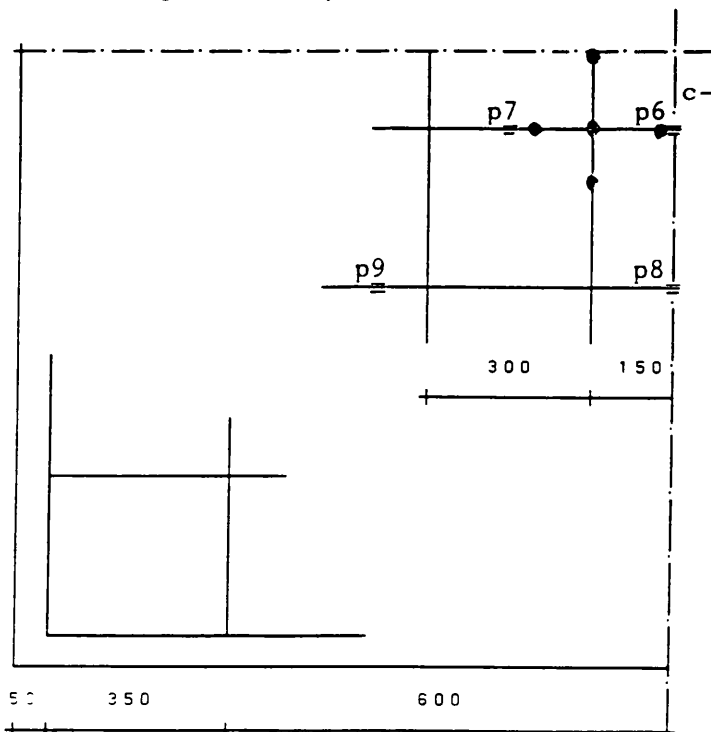


Fig. 7.20 Steel Layout for Model S4 and Strain Gauge Positions.
S4 Designed Using 100% Plasticity.

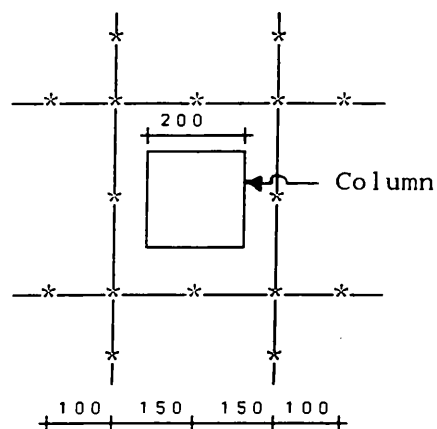
a- Bottom steel. Bar diameter size 8 mm.



b- Top steel layout. Bar diameter size 6 mm.



c- Position of shear links(*)



≡ Strain gauge position. ● Position of shear links.

Fig. 7.21 Steel Layout for Model S6 and Strain Gauge Positions.
S6 Designed Using 100% Plasticity.

7.4 Design of Deep Beams:

To obtain the stress fields at different levels of plasticity, an elastoplastic finite element inplane program (5) using von Mises criterion was adopted. The element used was isoparametric with eight nodes. For the determination of different levels of plasticity stress fields, similar approach to that of slabs was adopted as follows:

- 1— The beam was considered as a metallic member with uniform thickness obeying von Mises criterion.
- 2— At the design ultimate load the elastic stress distribution was determined from which the von Mises stress σ_0 at the most stressed point was computed and taken as yield stress of the beam material.

$$\sigma_0 = \sqrt{(\sigma_x^2 + \sigma_y^2 - \sigma_x\sigma_y + 3.0 \tau_{xy}^2)}$$

- 3— The material was assumed to behave as an elastoplastic material obeying von Mises criterion and normality rule(5). At the design ultimate load, where yielding started, plasticity percentage p was assumed to be zero. At the true ultimate load, which is assumed to be equal to $(1 + \lambda)$ of the design load, 100% of plasticity is adopted. Different levels of plasticity can be chosen between these two states. The stresses, at each plasticity level, were factored as for slabs using $1/(1 + p\lambda)$, such that the stress distribution was in equilibrium with the design load.

- 5— At each level of plasticity, using the stress σ_x , σ_y , τ_{xy} , which are in equilibrium with the design load, the required steel ratio was calculated, using rules described in chapter 3. This ratio varies from point to point and from one element to another. In order to simplify this, all the steel ratios for each element were averaged in each direction.

Although this procedure is adopted, the variation of the averaged steel ratio still varied from element to element. Since the test beams are small in comparison to the usual practical dimensions, there was little possibility of varying the steel by curtailing the steel bars. To match better the theoretical steel requirements, the

following two ways can be adopted:

- i- Choose the maximum steel ratios at each band of the beam and place the required steel through the corresponding band.
- ii- Take average steel ratios at each band, and place the steel bar accordingly.

It is clear that the first method is uneconomical but provides a safe design, since it uses higher steel areas in most regions of the structure while averaging procedure, though more economical, might give an unsafe design, since some areas of structures would be under reinforced. Because the steel is already averaged in the element, the first method was adopted.

7.4.1 Design of Support Bearings:

Many authors have reported that local failure due to point load is the most common example of premature failure in deep beams. This is because under point load, a considerable force is transmitted to the support directly through the compression strut. The concentration of the stress in these areas may become higher than the permissible allowable bearing stress. As a result many codes of practice have proposed a criteria for checking bearing capacity. Section 3.4.3 of CIRIA Guide 2(98) states that the compression stress in the contact should not exceeds $0.4 f_{cu}$ under ultimate loads. Stresses in excess of $0.8 f_{cu}$ should only be used in laboratory under special conditions with proper provision of reinforcement.

A short column design was employed, to insure that there would be no local failure using clause 3.8.4.3 in BS 8110(1) part 1, that is:

$$P = 0.4 f_{cu} A_c + 0.75 A_s f_y$$

where P is the applied force (eg. reactions or applied load). f_{cu} is the cube strength of concrete. A_c is the concrete area (eg. the area which is in contact with the plate of bearing). A_s is the required compression steel area in the bearing area and f_y is the characteristic strength of the compression reinforcement.

In fact using ^{the} direct design method a sufficient amount of steel is directly provided in the most stressed areas both in vertical and horizontal directions, figures 7.3a-d

and 7.31a–b. Lin⁽⁷⁹⁾ and Memon⁽⁸⁰⁾ reported that at the bearing point, bearing failure can also be caused by the Poisson's effect. To confine the beam areas where stress concentration is high, in this test program, the local lateral force was restrained by using metallic plates clamped to the bearing plate which is in contact with the concrete surface of the beam for both the support bearings areas and under the loading point. Figures 7.22a and 7.22b show test rig set up, the support systems and the dimensions of the test specimens.

7.4.2 Bond and anchorage:

The Direct design method assumes that the steel bars are fully bonded and anchored. This means that the strain in the reinforcement is equal to the adjacent concrete. Clause 3.12.8.3 and 3.12.8.4 of BS 8110(1) may^{be} used for checking anchorage length required. By using hooks of 180° at the end of main bars, an additional positive anchorage is provided by the presence of steel cages at the supports.

7.4.3 Beam Models Design and Discussion:

One of the main factors affecting the behaviour of deep beams and stress distribution is the span depth ratio. Dimensions and the support system, for the designed beams B.1 and B.2, are shown in figure 7.22a and 7.22b, respectively. Two different span/depth ratios were chosen. The ratio of the first beam was 1.8 and expected to behave like an ordinary beam with flexural stress being dominant. Whereas the second beam, which had a ratio of 0.9, was assumed to be heavily loaded in shear and the compression forces joining the point load and the supports. Both beams were analysed using an elastoplastic finite element inplane program, with 8x8 finite element mesh for a symmetrical half. Figure 7.22 and 7.23 show typical load–deflection relationship obtained from elastoplastic analysis. Figures 7.24 and 7.25 show the points which yielded. It can be noticed for both beams only the area near the point load and the support yielded. In comparison

with the slabs designed, beams have small area where the plastic stress capacity is reached. The ratio of steel volume at any plasticity level to the elastic steel volume is presented in figures 7.26 and 7.27. There is a little increase, in this ratio as the percentage of plasticity redistribution level increases. From the principal stress representation, figures 7.28 and 7.29, the compressive stress path, joining the point load to the support, is *very* clear and the compressive stress is of great importance as span depth ratio is decreased. The factored stress intensity was slightly affected as the percentage of plasticity increased.

Unlike slabs, deep beams show little redistribution of stresses. This is shown in figures 7.30 and 7.31 where the steel areas were not much affected by the levels of plasticity. This means that the redistribution of stresses in simply supported deep beams are not taking place as for the plate bending. Finally the steel layout and strain gage positions on steel bars, are shown in figures 7.32a and 7.32b, for both beam B.1 and beam B.2 respectively. The beams were designed using 100% plasticity stress distribution. It is clear that the direct design method gives not only the main reinforcement for beams but also the reinforcement at local areas such as under the point loads and on the supports.

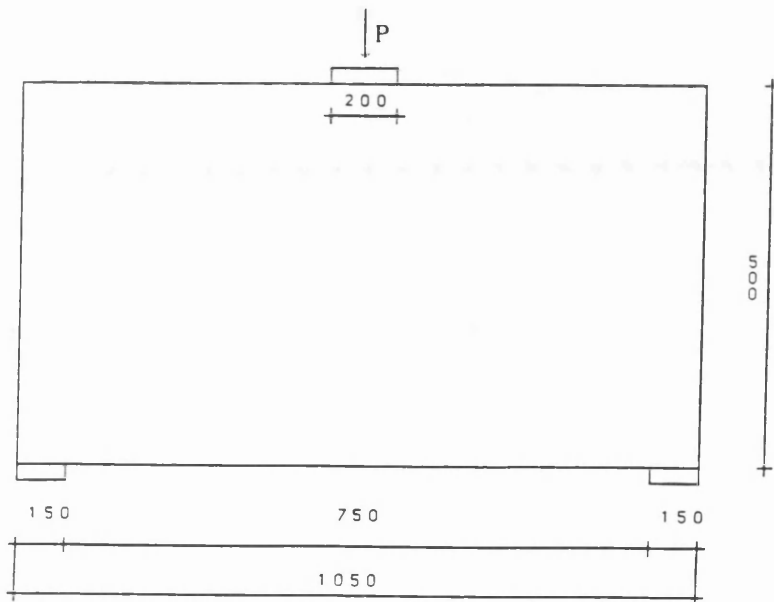
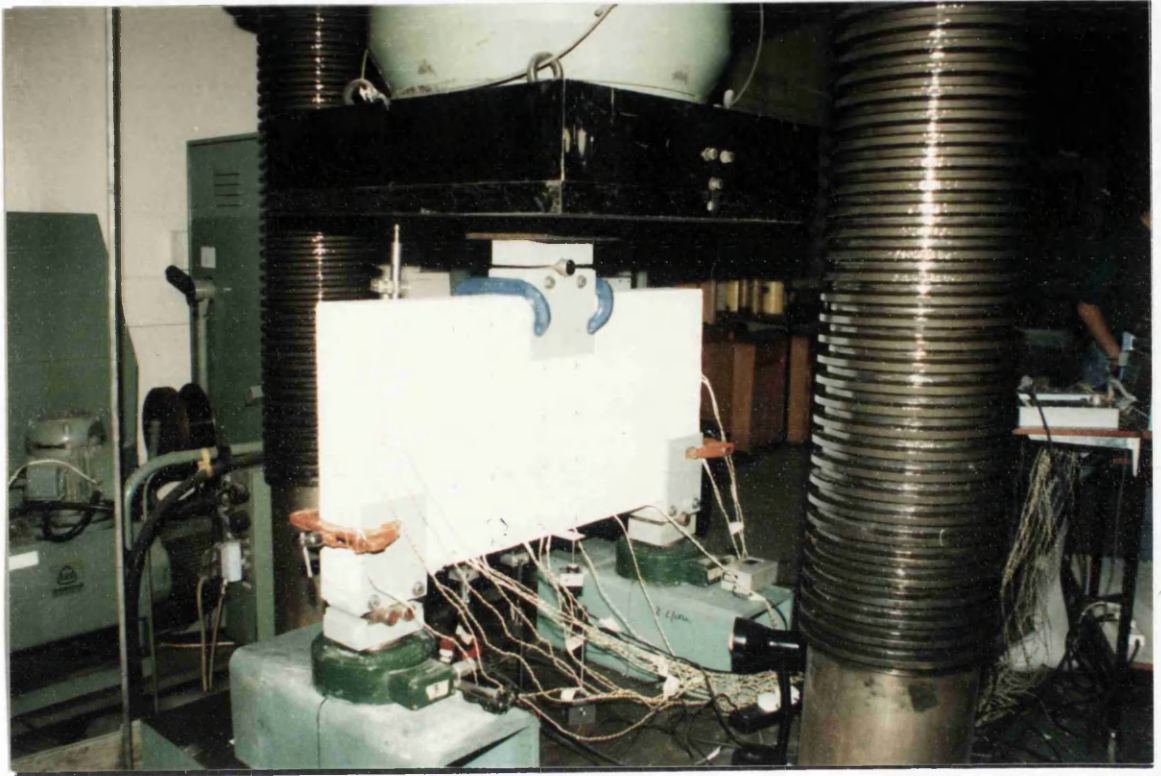


Fig. 7.22a Test Rig and Dimensions Beam 1

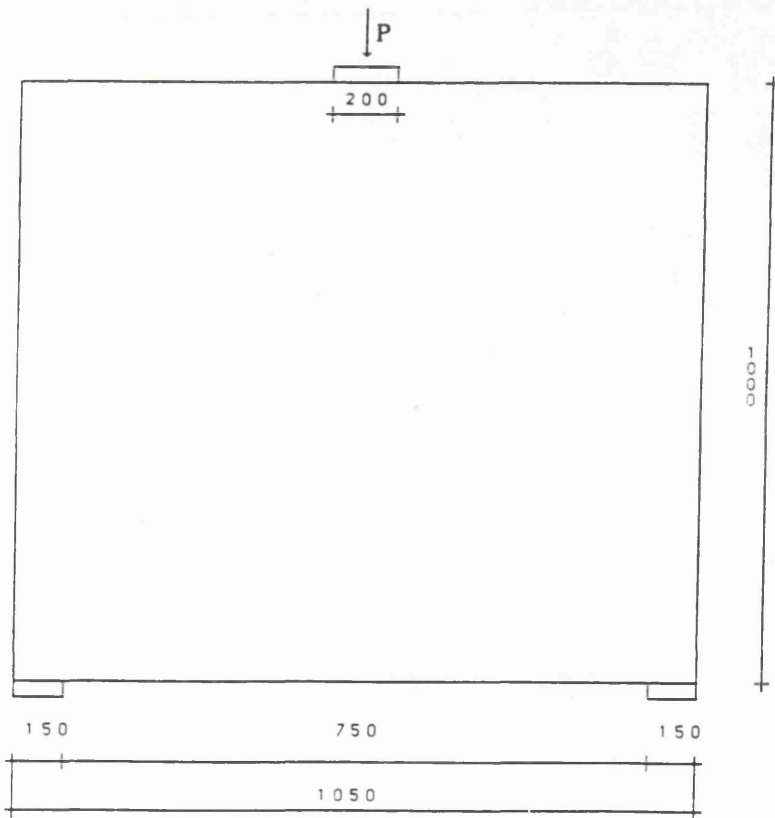
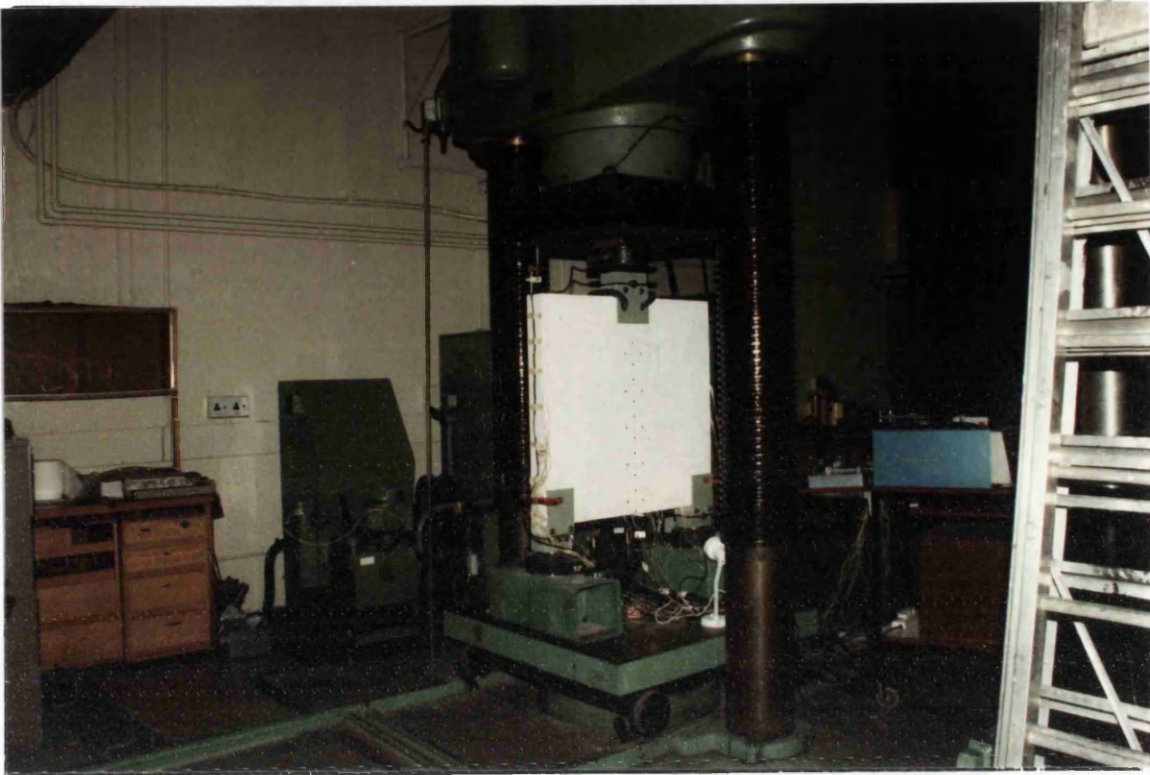


Fig. 7.22b Test Rig and Dimensions Beam 2.

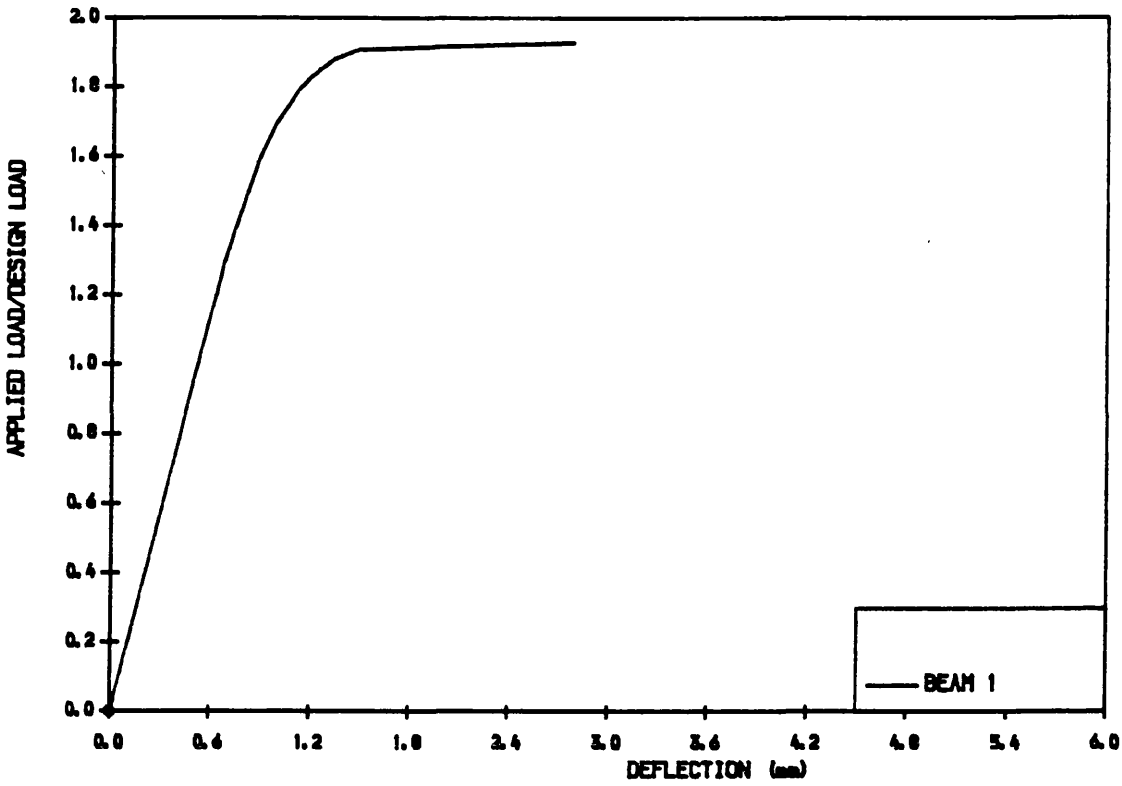


Fig. 7.23a Load Deflection Curve. Determination of Plasticity Levels.
Beam 1.

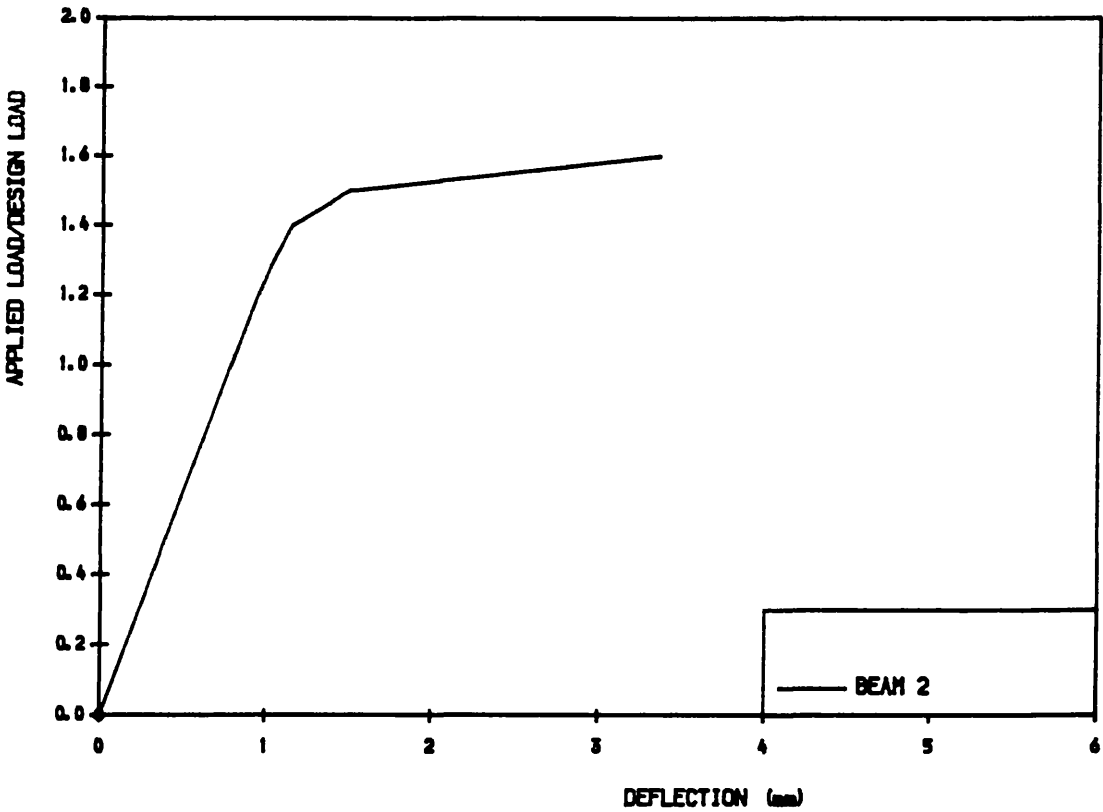


Fig. 7.23b Load Deflection Curve. Determination of Plasticity Levels.
Beam 2.

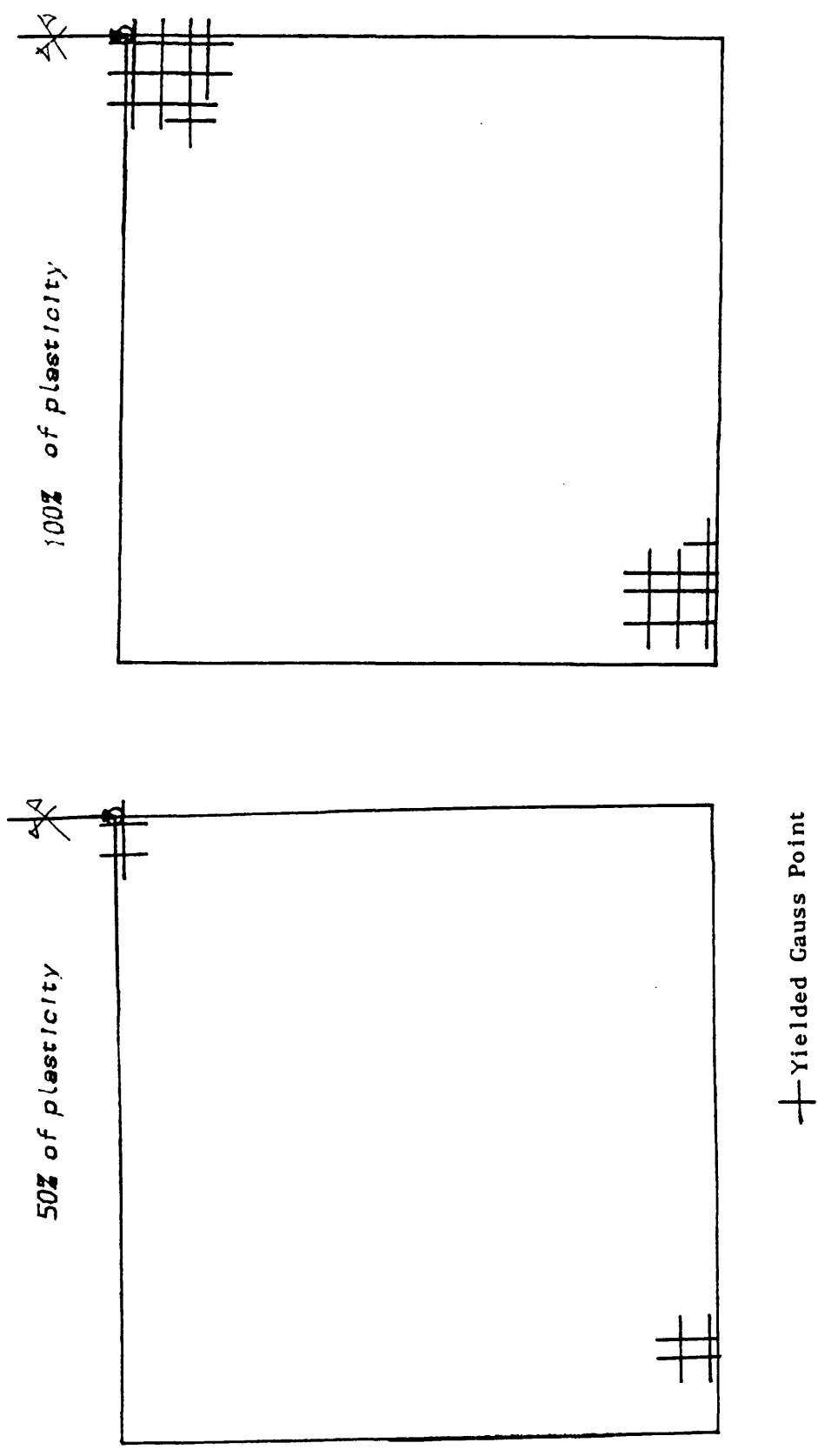


Fig. 7.24 Plasticity Spread over Beam 1.

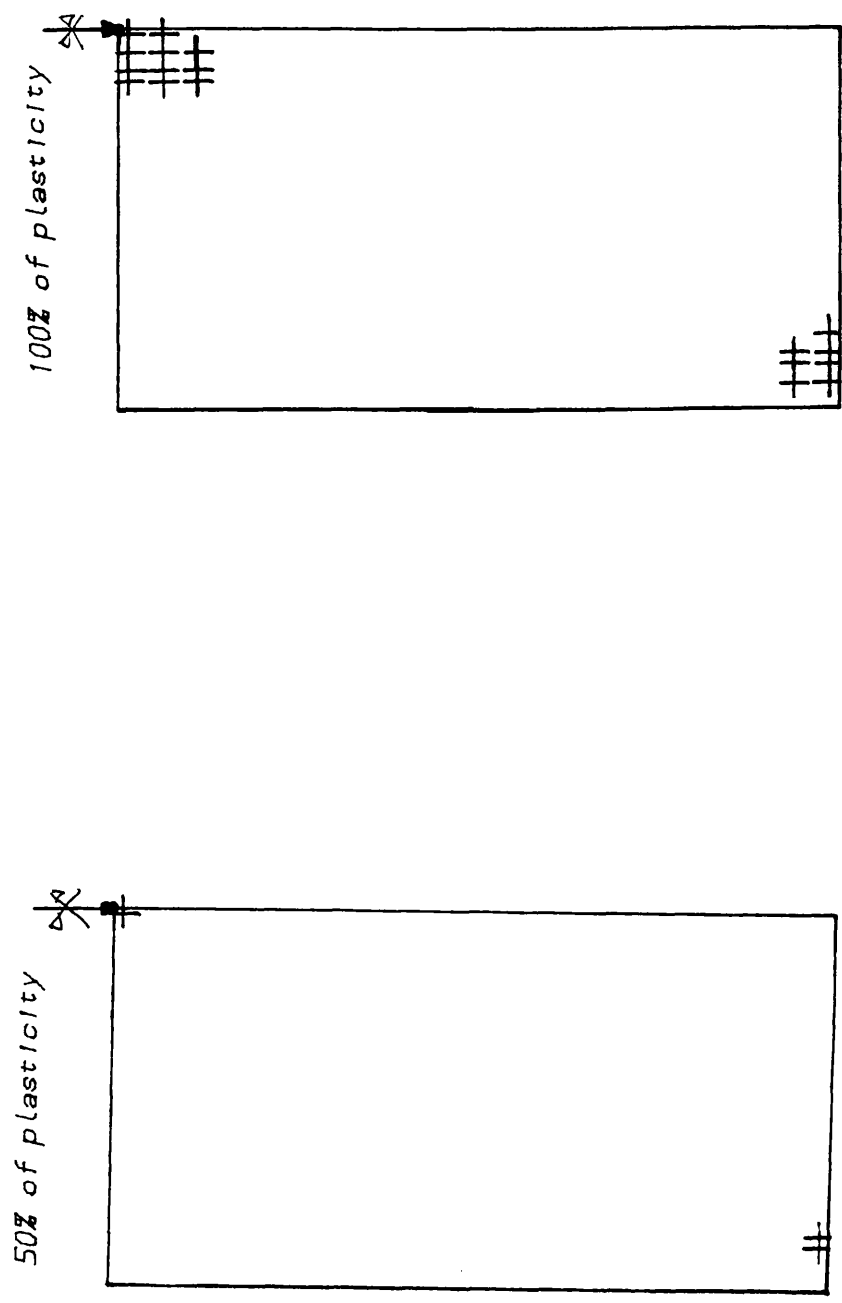


Fig. 7.25 Plasticity Spread over Beam 2.

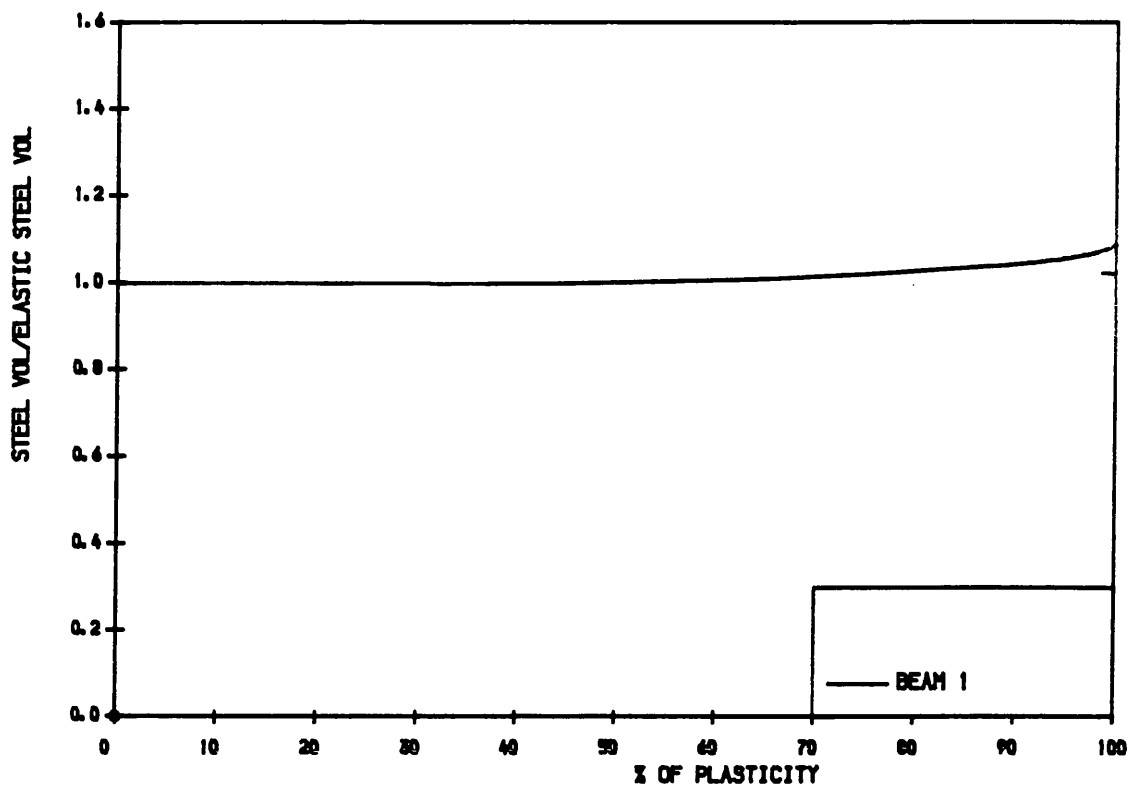


Fig. 7.26 Steel Volume Ratio-Percentage of Plasticity Beam 1.

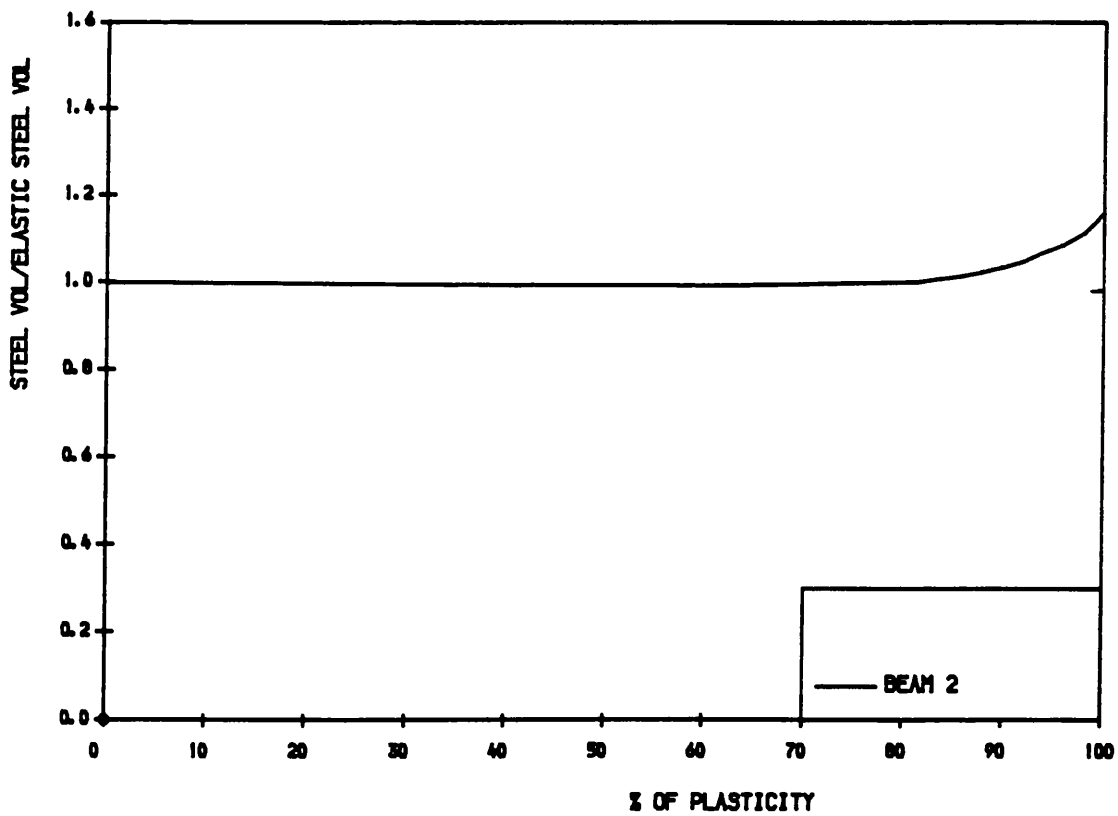


Fig. 7.27 Steel Volume Ratio-Percentage of Plasticity Beam 2.

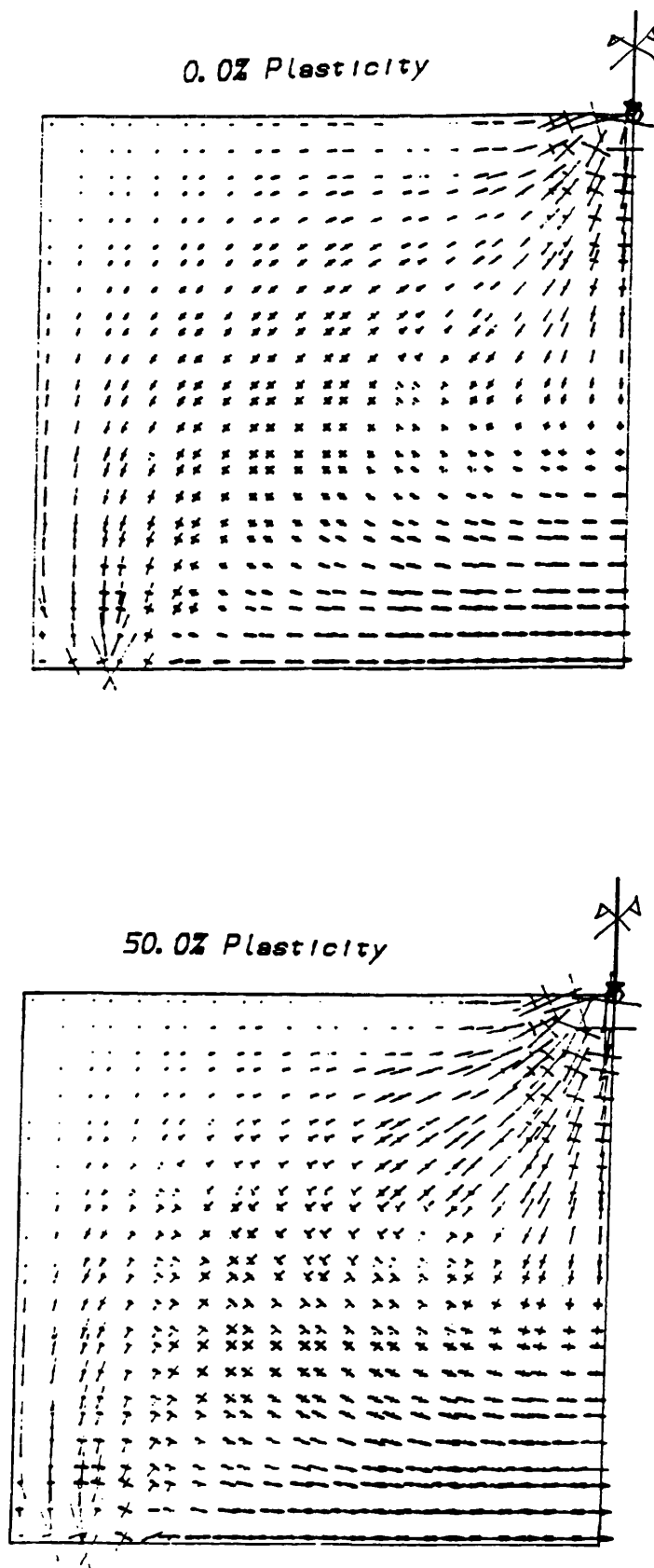
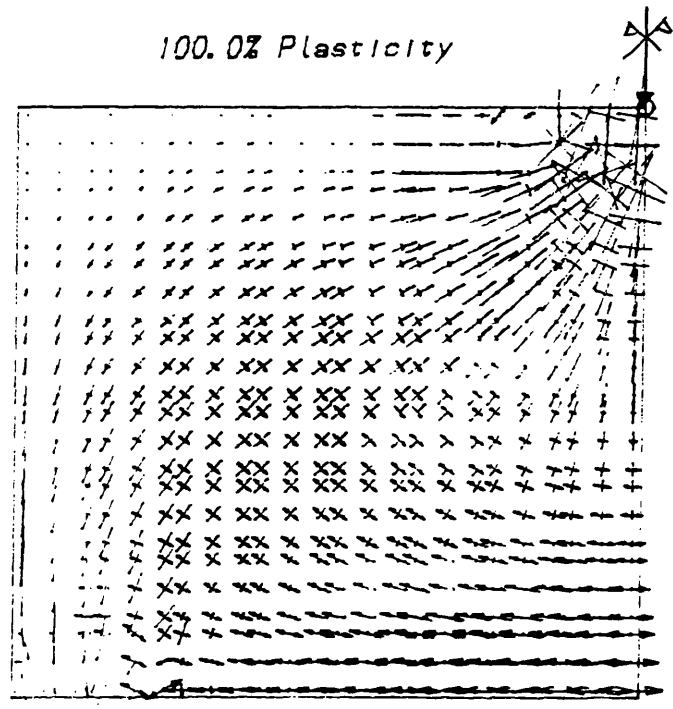


Fig. 7.28 Orientation and magnitude of principal stress at Different Levels of Plasticity Beam 1.



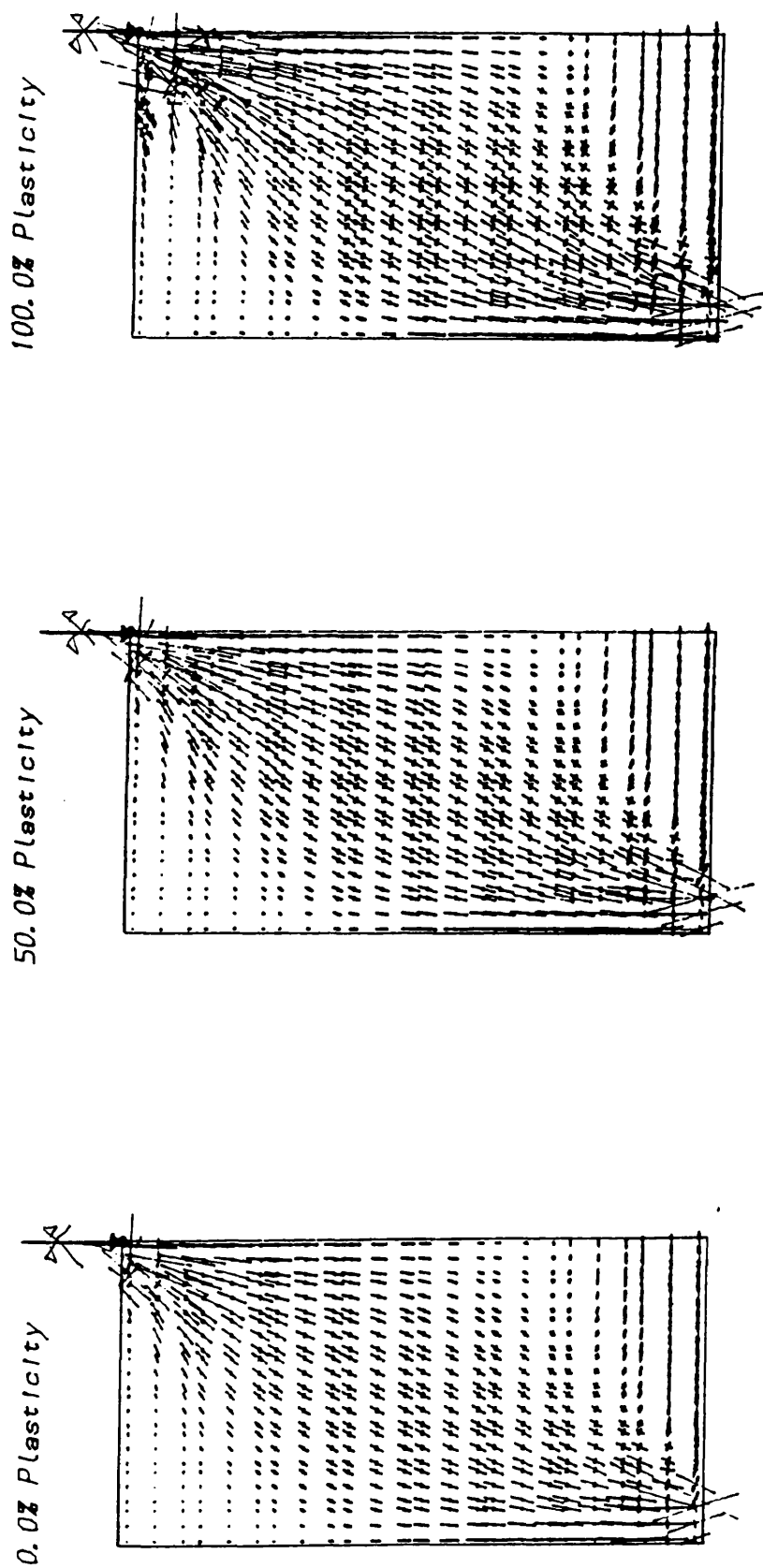


Fig. 7.29 Orientation and magnitude of principal stress at Different Levels of Plasticity Beam 2.

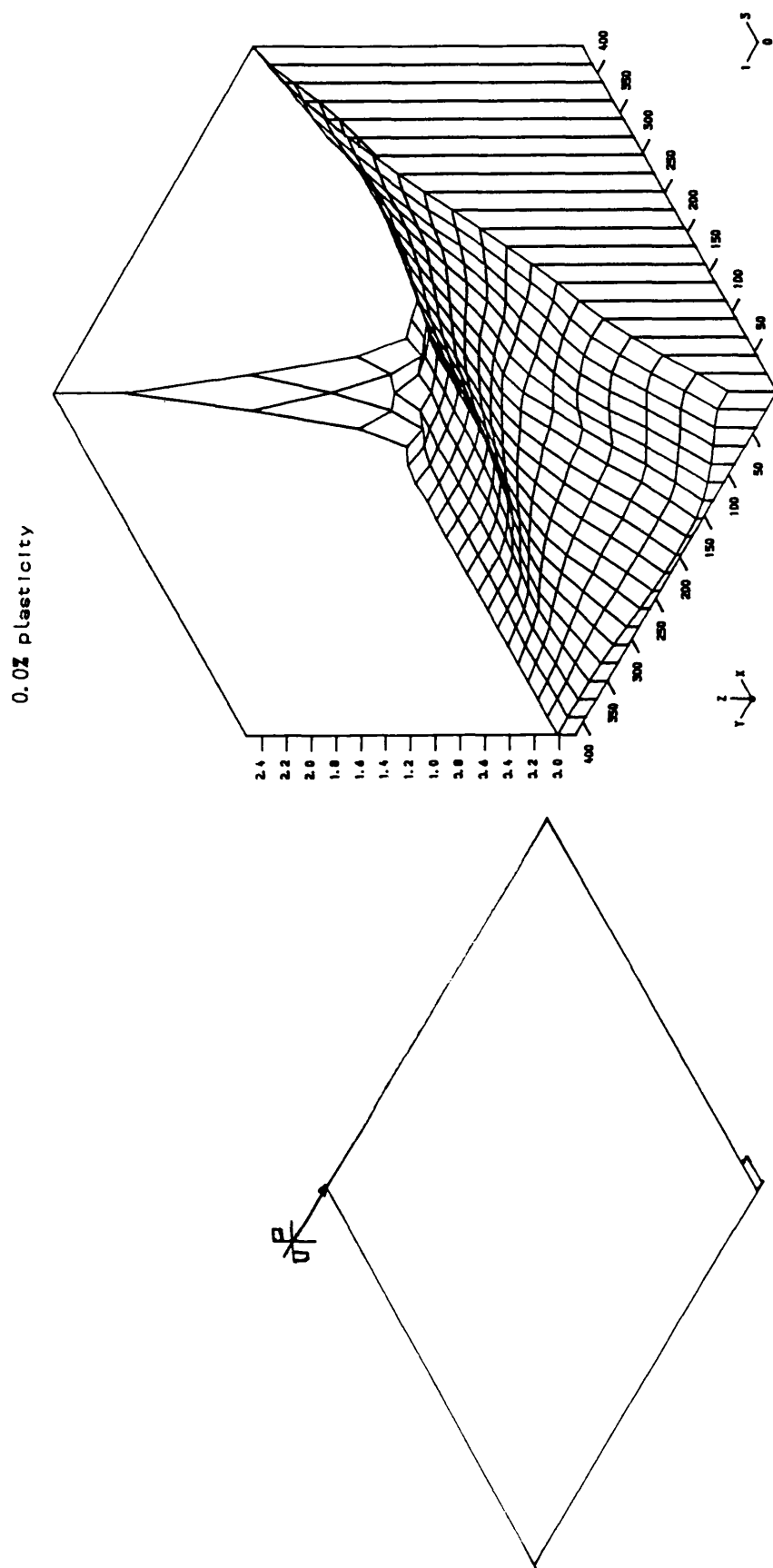
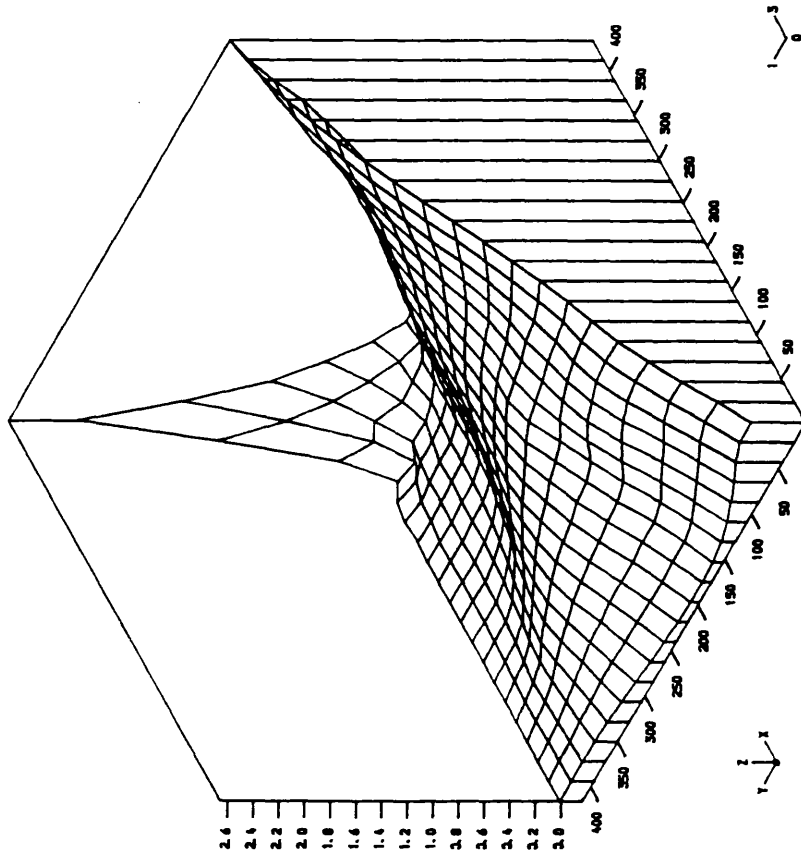
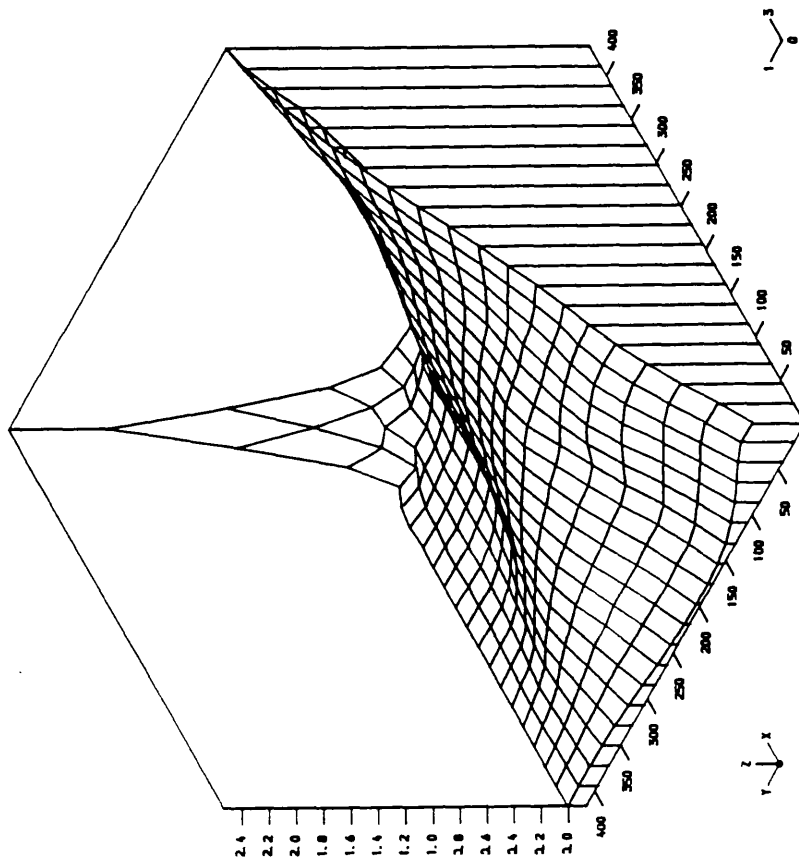


Fig. 7.30a Steel Ratio Distribution at Different Levels of Plasticity.
x Direction Beam 1.

100.0% plasticity



50.0% plasticity



Steel ratio in x direction BEAM 1

0.0% plasticity

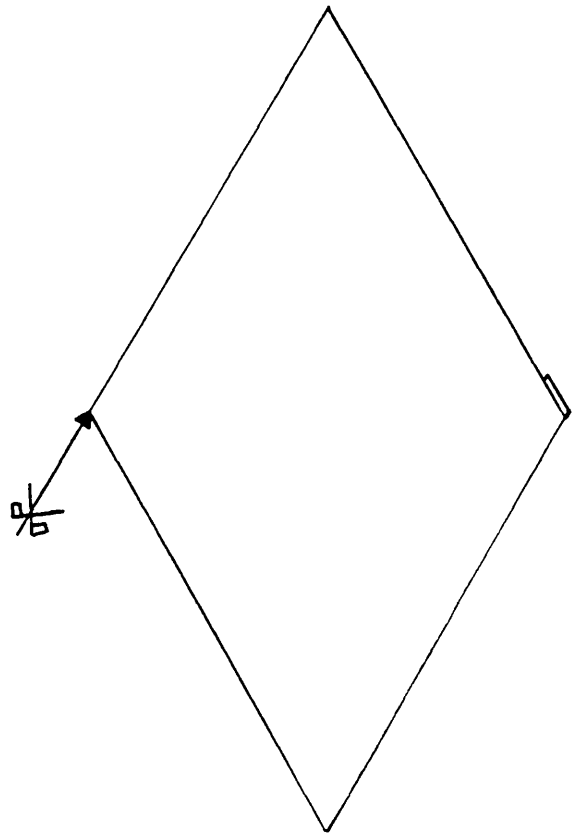
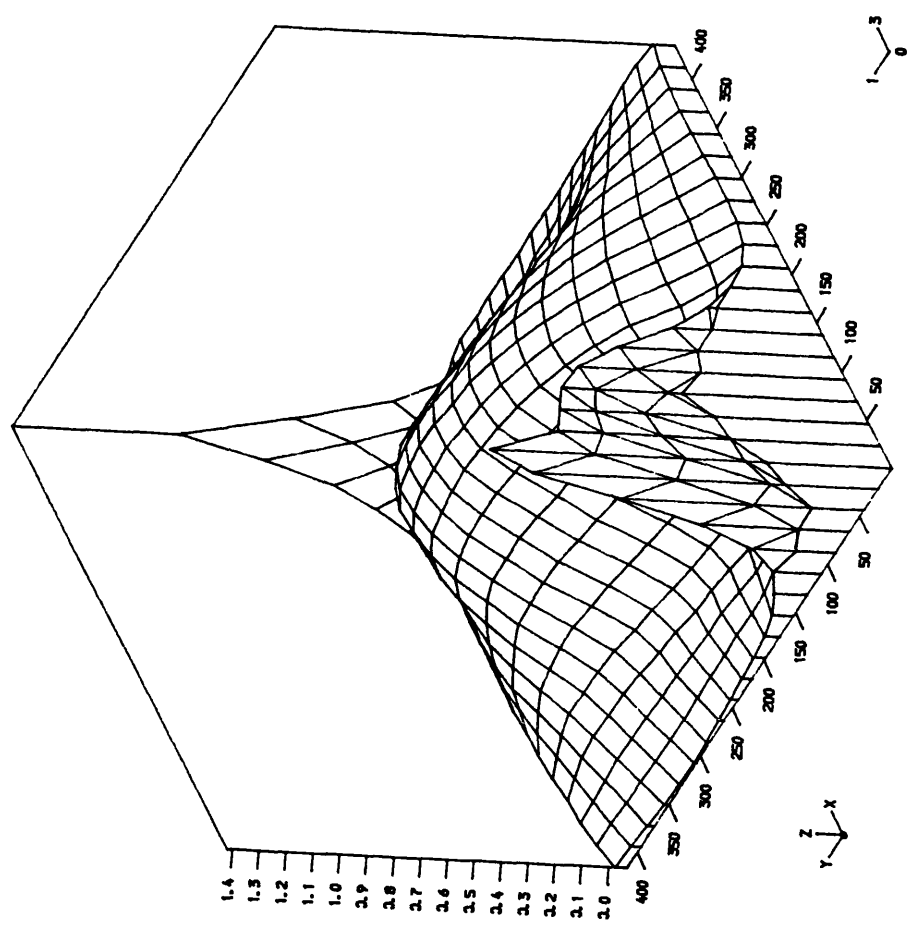
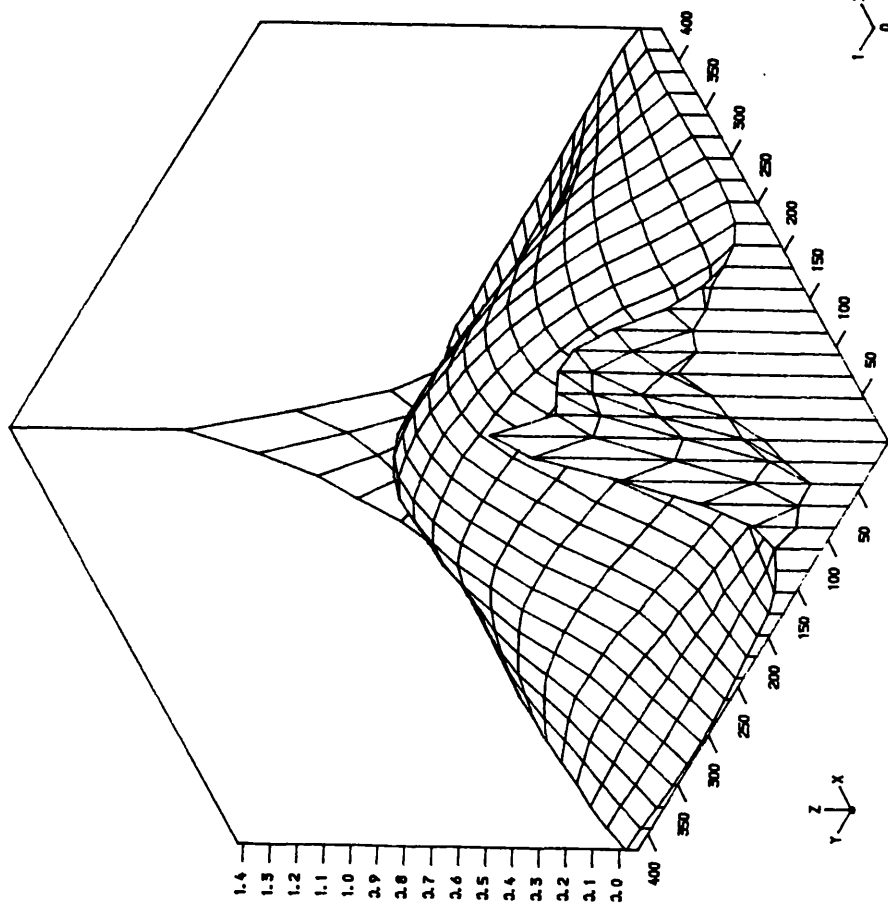
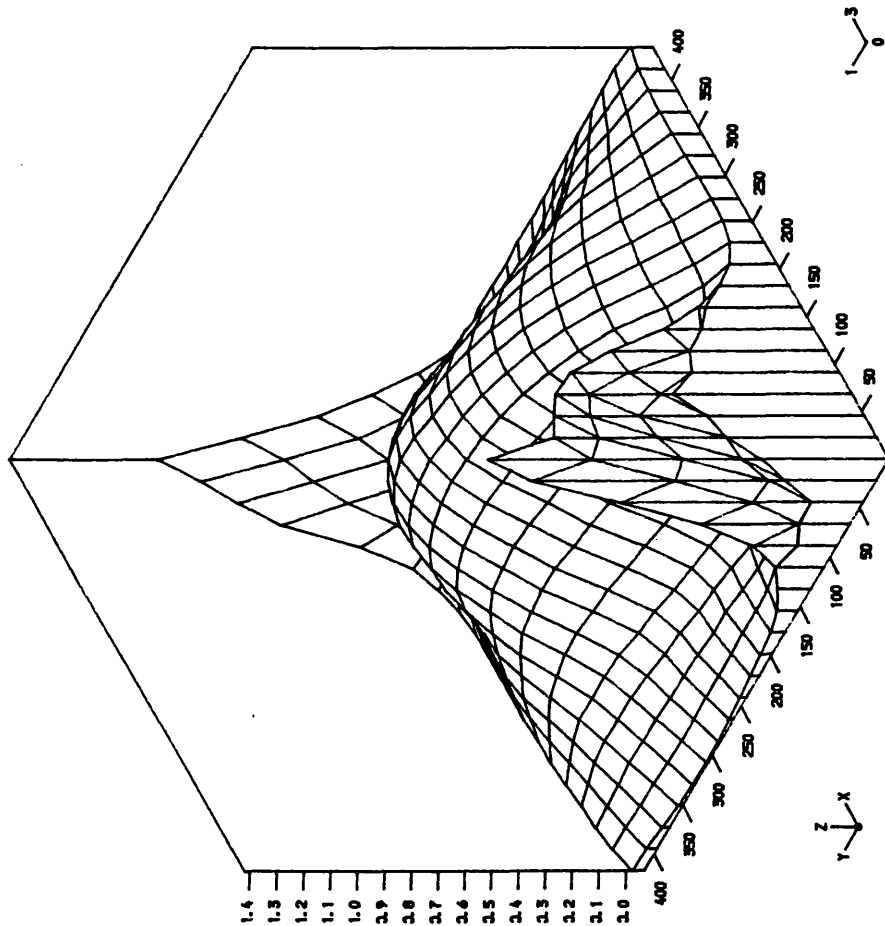


Fig. 7.30b Steel Ratio Distribution at Different Levels of Plasticity.
y Direction Beam 1.

50.0% plasticity



100.0% plasticity



Steel ratio in y direction BEAM 1

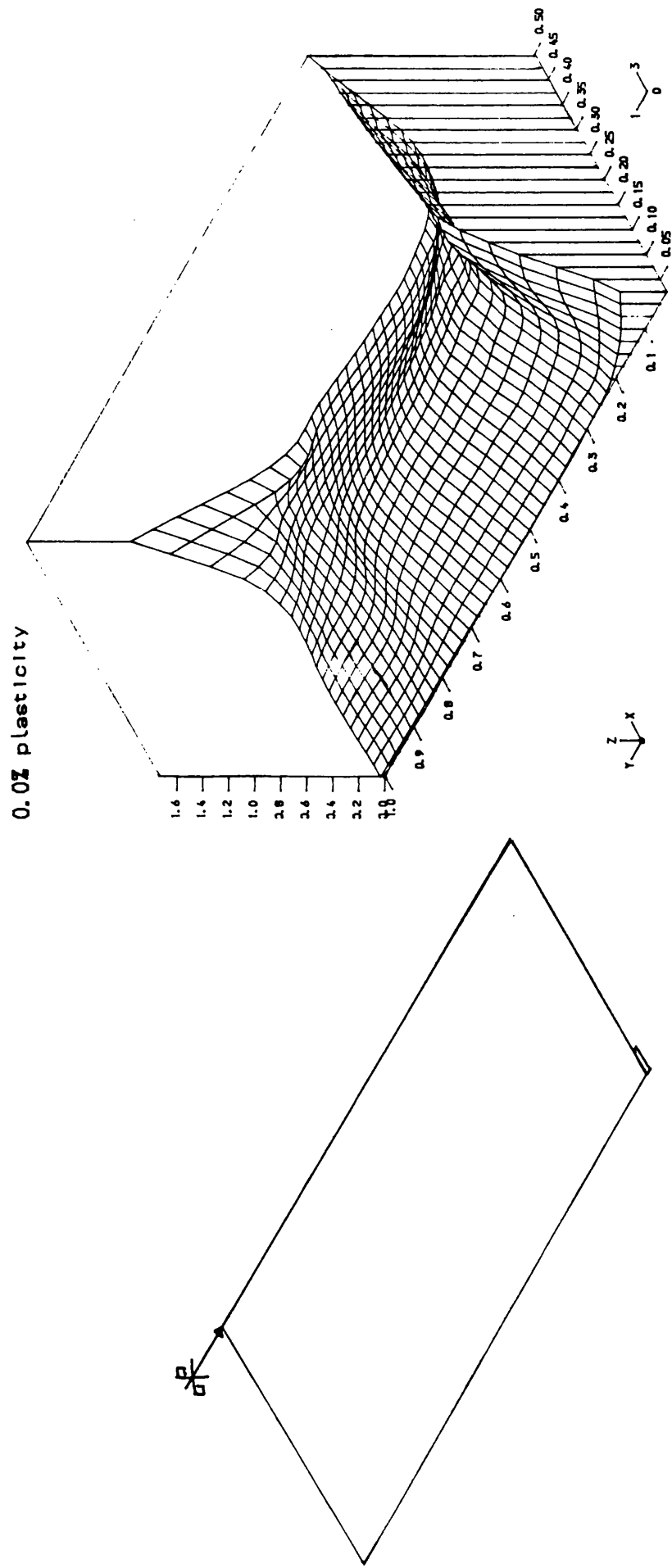
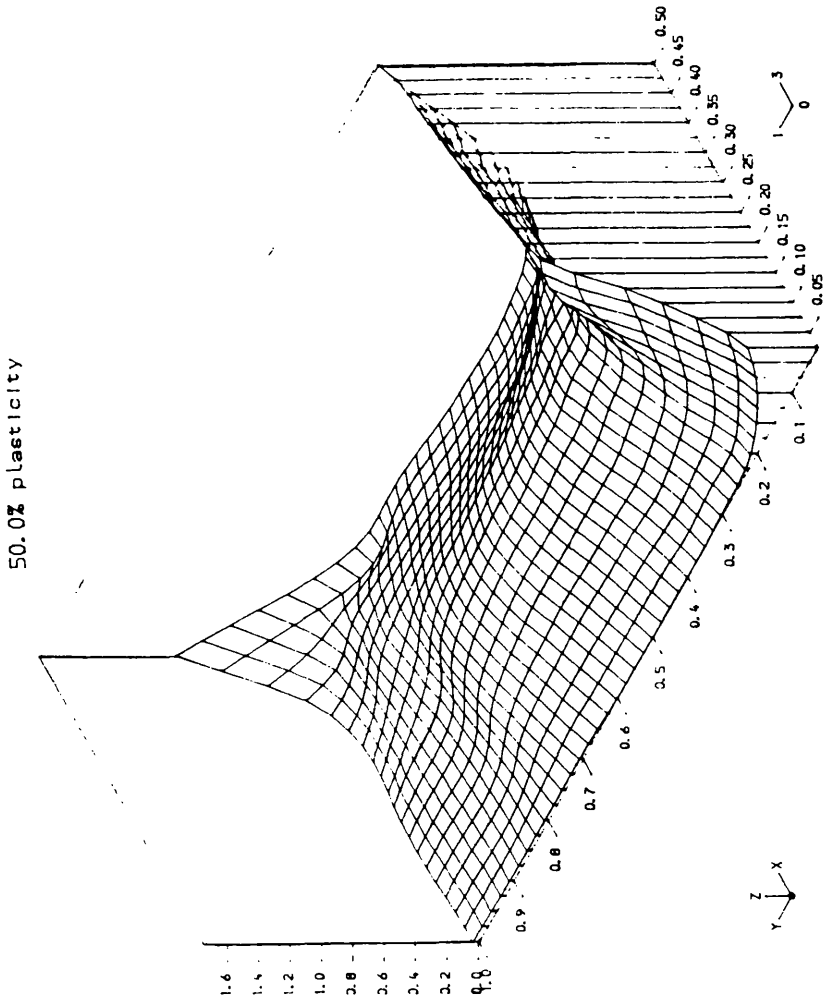
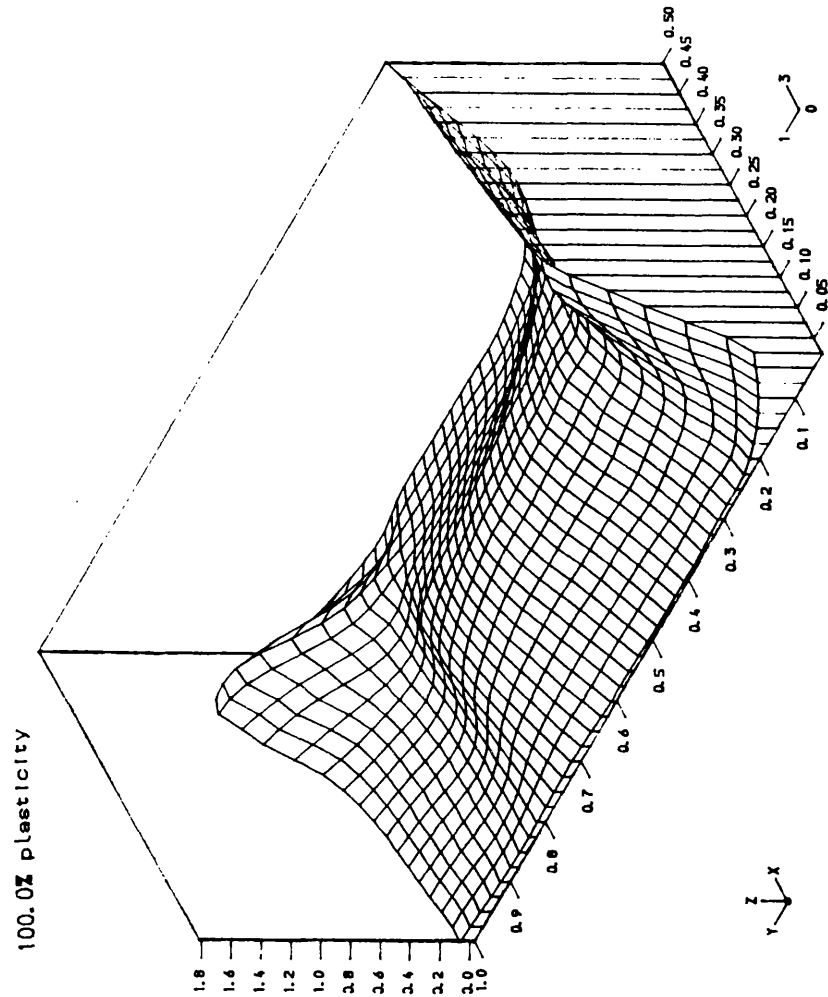


Fig. 7.30c Steel Ratio Distribution at Different Levels of Plasticity.
x Direction Beam 2.



Steel ratio in x direction BEAM 2

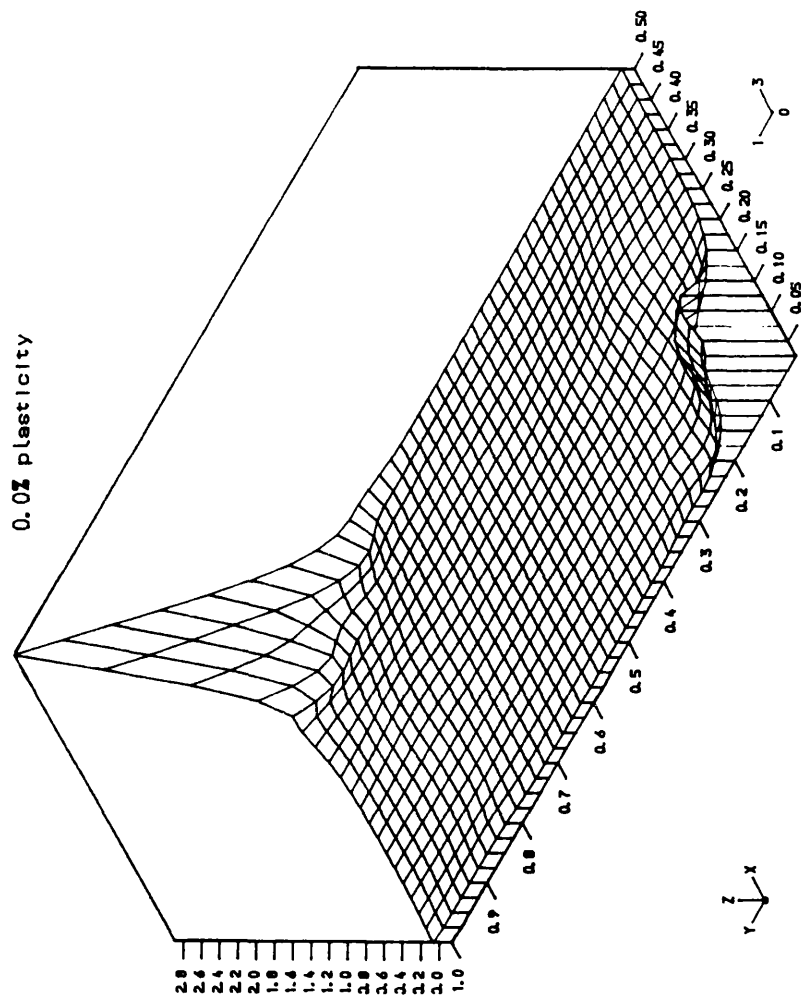
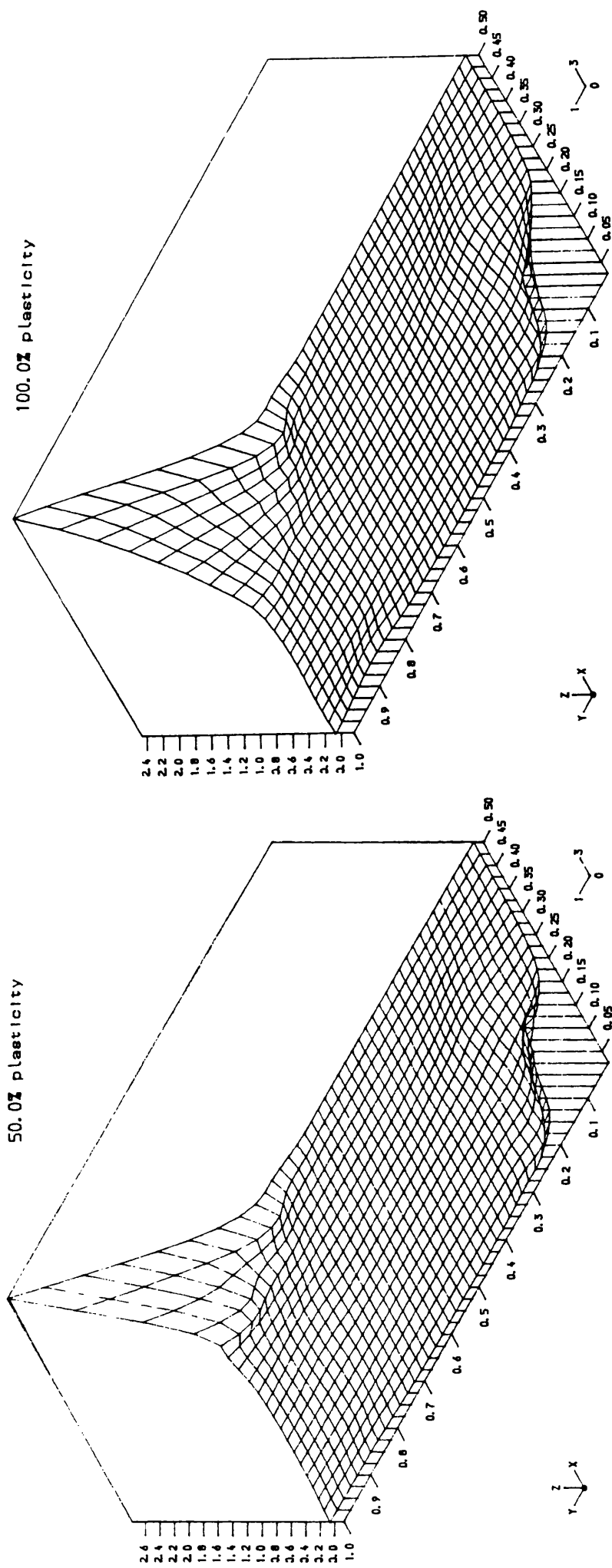
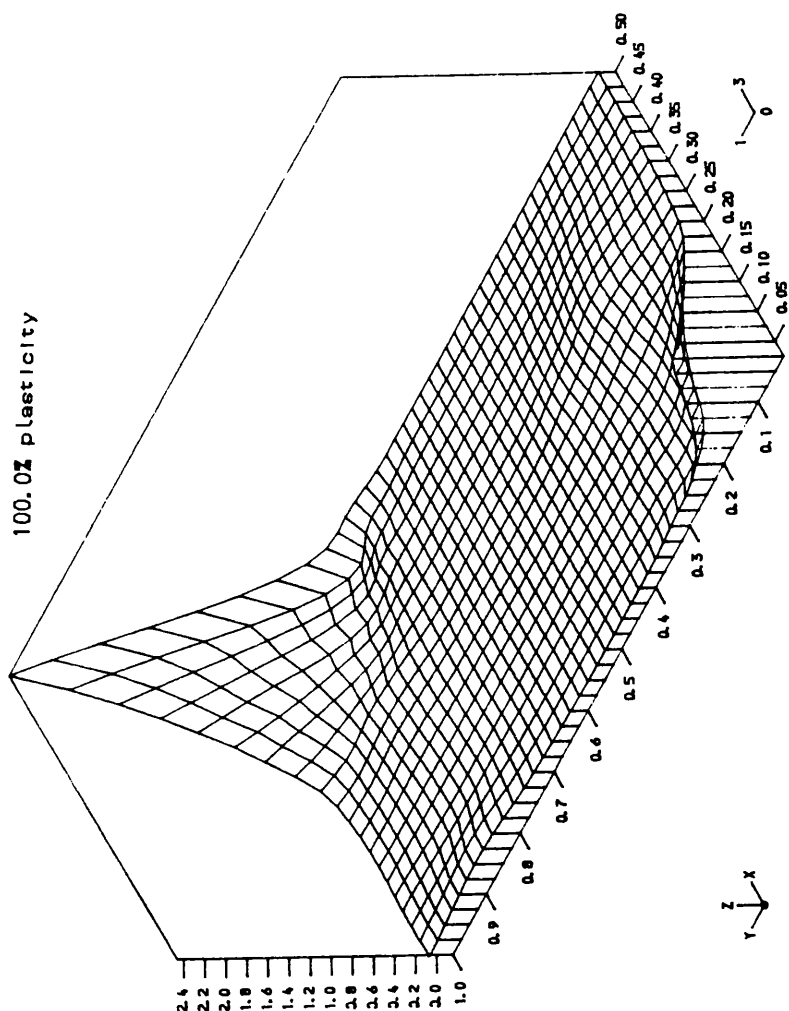


Fig. 7.30d Steel Ratio Distribution at Different Levels of Plasticity.
y Direction Beam 2.

50.0% plasticity



100.0% plasticity



BEAM 2

Steel ratio in y direction

0.0 Z Plasticity

0.01	0.00	0.00	0.00	0.00	0.00	0.00	1.94
0.01	0.04	0.05	0.04	0.00	0.06	0.23	0.76
0.04	0.07	0.03	0.00	0.00	0.00	0.00	0.01
0.01	0.12	0.25	0.28	0.24	0.16	0.01	0.00
0.08	0.25	0.24	0.16	0.09	0.09	0.09	0.00
0.00	0.12	0.38	0.54	0.57	0.43	0.07	0.00
0.09	0.40	0.50	0.49	0.47	0.49	0.40	0.11
0.00	0.08	0.40	0.60	0.63	0.44	0.07	0.00
0.09	0.49	0.73	0.77	0.80	0.84	0.77	0.48
0.00	0.03	0.35	0.60	0.61	0.42	0.08	0.00
0.12	0.56	0.93	0.98	1.07	1.16	1.15	0.95
0.00	0.00	0.29	0.55	0.55	0.39	0.12	0.00
0.30	0.81	1.02	1.13	1.35	1.52	1.60	1.53
0.00	0.04	0.30	0.43	0.40	0.30	0.14	0.01
0.50	0.94	1.11	1.38	1.70	1.97	2.16	2.23
0.81	0.77	0.27	0.16	0.15	0.12	0.08	0.02

50.0 Z Plasticity

0.01	0.00	0.00	0.00	0.00	0.00	0.00	1.80
0.01	0.04	0.05	0.05	0.04	0.07	0.30	0.80
0.04	0.07	0.03	0.00	0.00	0.00	0.00	0.14
0.01	0.12	0.25	0.28	0.24	0.16	0.01	0.00
0.08	0.25	0.24	0.15	0.09	0.08	0.09	0.00
0.00	0.12	0.38	0.54	0.57	0.43	0.07	0.00
0.09	0.40	0.50	0.48	0.47	0.49	0.41	0.11
0.00	0.08	0.40	0.61	0.64	0.45	0.07	0.00
0.09	0.49	0.73	0.77	0.80	0.84	0.77	0.48
0.00	0.03	0.35	0.61	0.62	0.43	0.08	0.00
0.12	0.56	0.93	0.98	1.07	1.16	1.16	0.95
0.00	0.00	0.29	0.56	0.55	0.39	0.12	0.00
0.30	0.81	1.02	1.13	1.35	1.53	1.61	1.53
0.00	0.04	0.30	0.43	0.40	0.30	0.15	0.01
0.50	0.94	1.12	1.38	1.71	1.98	2.17	2.24
0.81	0.77	0.27	0.16	0.15	0.13	0.08	0.02

Fig. 7.31a Theoretical Required Steel Ratio per mm Beam 1.

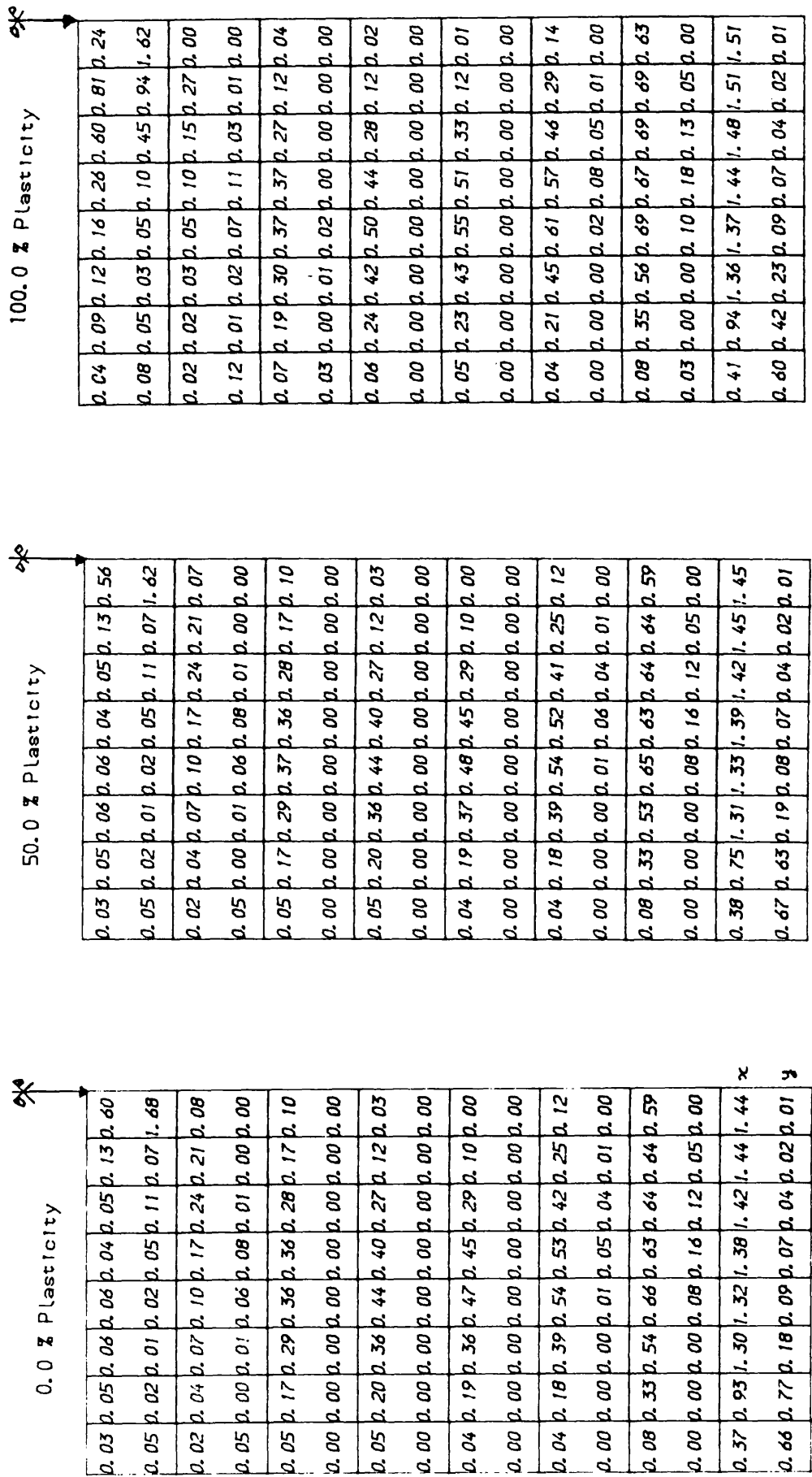


Fig. 7.31b Theoretical Required Steel Ratio per mm Beam 2.

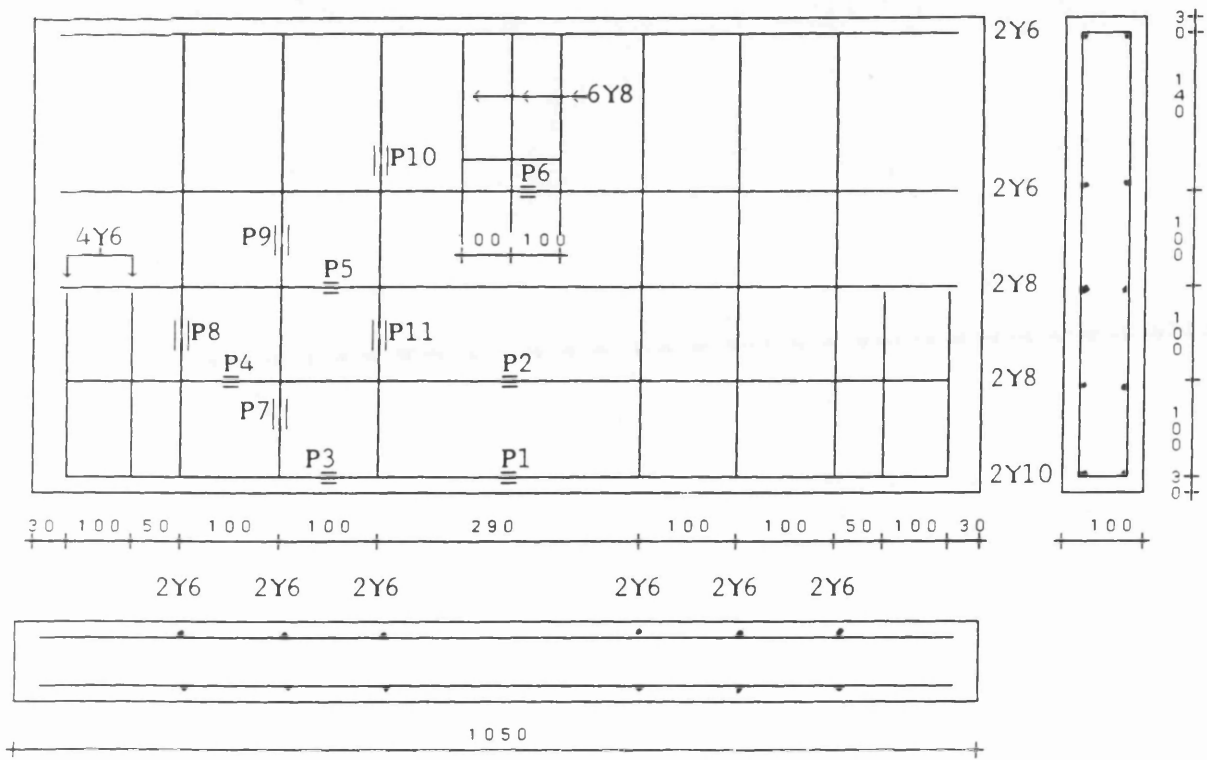


Fig. 7.32a Steel Layout and Strain Gauge Positions.
Beam 1 Designed Using 100% Plasticity.

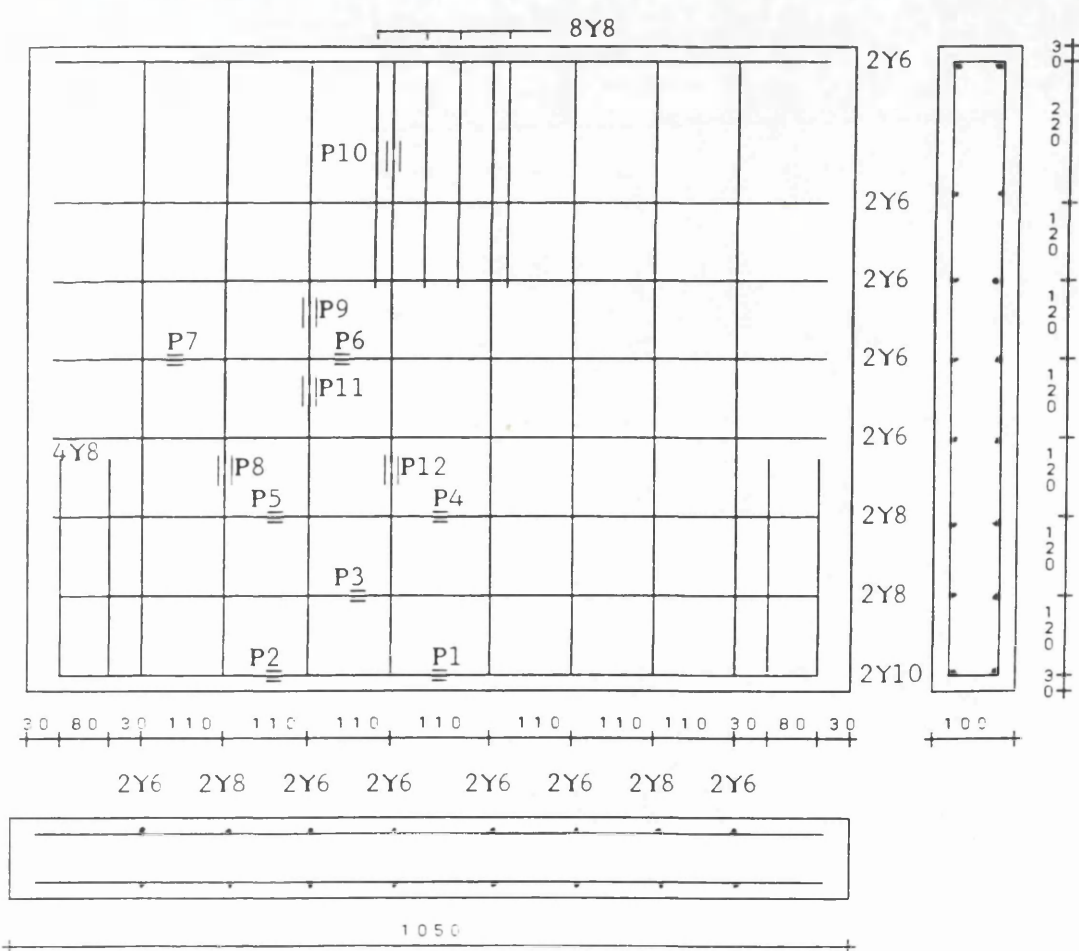
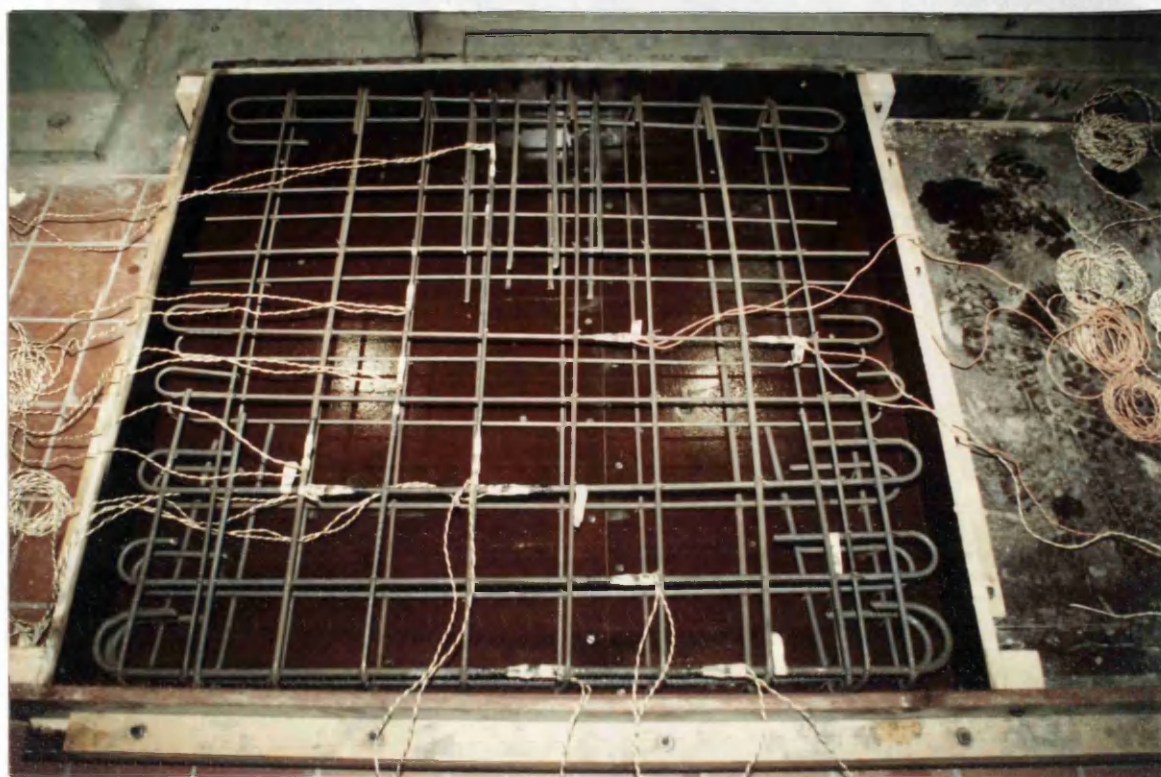


Fig. 7.32b Steel Layout and Strain Gauge Positions.
Beam 2 Designed Using 100% Plasticity.

Chapter 8

Experimental and Numerical Analysis of Slabs and Deep Beams

8.1 Introduction:

This chapter presents the test results on reinforced slabs and deep beams described in chapter seven. The purpose of the experimental investigation was mainly to explore in particular the effect on serviceability limits and ultimate behaviour, of using nonelastic stress fields in the direct design of reinforced concrete slabs and deep beams. A total of six large scale slabs and two deep beams were tested to failure, and for each test the following data were recorded:

- 1— Deflections
- 2— Steel strains
- 3— Crack development and crack widths
- 4— Ultimate load and mode of failure
- 5— Reactions.

In this chapter P_d and P_u stand for the design ultimate load and the experimental ultimate load respectively.

Taking advantage of symmetry, numerically only a quarter of slabs was analysed, using 4x4 finite element mesh for all slab models, figures 6.10a and 6.10b, except for S.5 where 4x8 element mesh was used as shown in figure 6.10c. For beam models 8x8 finite element mesh was used to analyse one half of each beam. For all slabs the first increment was 0.20 of P_d . Small increments of 0.1 P_d and 0.05 P_d was used as necessary. As approaching the design load a 0.025 of P_d was adopted. A maximum of 50 iterations was fixed at each increment and a 2x2 sampling points were used over each element. All slab models were divided in to 10 layers including the steel layers, except S.6 which was divided into 12 layers, because of its increased thickness. A 4.0 % tolerance was fixed for all analysis. A value of $\beta = 0.4$ for the shear retention is adopted while tension stiffening has been ignored.

8.2 Slab models:

8.2.1 Simply Supported Slabs:

8.2.1.1 Model S.1:

This was a simply supported square slab with corners held down. The slab was designed for a load P_d of 210 KN, using 70% level of plasticity stress field. The loading system is four direct points loads system as shown in figure 8.1. Dimensions and material properties of the slab were presented in chapter six (figure 6.1 and tables 6.3 and 6.4). The steel layout of the slab was presented in figure 7.6.

The slab was loaded in small load increments up to failure. The first and second load increments were of 0.1 of design load (P_d). The rest of increments were an average of 0.05 P_d . The first visible crack was seen under the point load at 0.42 P_d (0.37 P_u), figure 8.2. The angle of the crack was 45° . On further loading, cracks were concentrated on the diagonals of the slab, and spreading towards the middle and corners of the slab. At 0.52 P_d (0.46 P_u) the first visible crack in the

middle appeared, figure 8.3, whereas at 0.57 Pd (0.50 Pu) the cracks parallel to diagonals reached the corners. At 0.60 Pd (0.53 Pu) the yield lines had clearly developed. The limiting deflection ($\text{span}/250 = 8 \text{ mm}$) was reached at 0.62 Pd (0.55 Pu), while the crack limit width of 0.3 mm was at 0.66 Pd (0.58 Pu). Beyond this loading intensive cracking occurred represented by fast development of new cracks in a very large area of the slab surrounding the point loads and the middle of the slab (compare figure 8.2 and 8.4). Further, the old cracks were widening and very few new cracks were forming near the corners of the slab. This is mainly caused by the increase of steel strain as can be seen in figures 8.12 to 8.17. The steel yielding was observed at 0.80 Pd (0.71 Pu), under the point load, figure 8.13. At the design load a large area of the bottom of the slab concrete face was cracked, figure 8.4, and the whole steel under point loads and in the middle of the slab yielded, figures 8.12 to 8.16. At this stage of loading, the cracks were widening. A few new cracks were seen near and parallel to the edges. 1st visible crack appeared at the top of the slab at 1.08 Pd (0.95 Pu), figure 8.5. Failure occurred at 1.13 Pd (1.0 Pu) with a large crack surrounding the point loads as shown in figures 8.6 and 8.7.

Deflections:

The load—deflection curves of different points of the slab are shown in figures 8.8 to 8.11. The load—deflection curves indicate the initiation of nonlinearity near 0.25 Pd which is lower than the loading level at which the first crack was observed viz. 0.42Pd (0.37 Pu). This is probably caused by the presence of invisible micro cracks. At 0.62 Pd (0.55 Pu), the central deflection was equal to the limiting service deflection equal to $\text{span}/250 = 8 \text{ mm}$. This represents an acceptable permissible serviceability limit on deflection.

Steel strains:

The measured steel strain are shown in figures 8.12 to 8.17 for bottom steel and in figure 8.18 for top steel. In the middle and under the point loads, at the design load the whole steel has yielded. For top steel from figure 8.18, no

yielding had occurred. This is possibly caused by a lifting of the corners (the initial force in the prestressing wire holding the corner down was not sufficient). From load-strain curves for bottom steel, we can notice that the whole strain of the measured points on the steel bars indicate that steel had yielded. This means that the slab behaved in a ductile manner.

Reactions:

The reaction at the corners are shown in figure 8.19. It is clear that these reactions were primarily negligible until 0.4 Pd. At collapse load the measured corner reactions were almost 20% of the applied point load.

Cracks width:

The first crack was seen under the point load at 0.42 Pd (0.37 Pu). Service crack width limit of 0.3 mm was reached at 0.66 Pd (0.58 Pu) under the point load. At 0.90 Pd (0.80 Pu) the maximum crack width was 0.65 mm while at the middle of the slab it was 0.25 mm. At 1.05 Pd a 0.4 mm wide crack was recorded at the middle area between the point loads. The crack width which caused failure was of 1.0 mm at the top and 3.0 mm in the bottom.

Mode of failure:

It is clear that the slab behaved in a ductile manner up to the ultimate load. This can be explained by the crack pattern which had spreaded over the whole bottom face of the slab and the steel strains were several times the yield strain. At the end, the crack which caused failure, was primarily a flexural crack and which was present in the previous loading increments. It has gone through the depth of the slab with no appearance at the top of the slab. At the last increment, suddenly sliding happened along this crack. This is caused by the inability of the remaining uncracked depth of the slab to transmit the forces to the support. The main crack was inclined and joining the point load to the end anchorage of the bottom steel.

Numerical analysis:

In general good agreement is obtained between the theoretical analysis and the experimental results. The first crack appeared under the point load at 0.40 Pd, while experimentally it was seen at 0.42 Pd, figure 8.2. The cracks have the same direction as the of the experiment. Load–deflection curves are presented in figures 8.8 to 8.11. The slab shows a loss of stiffness at the first stage of cracking. Numerically, the slab reached the service limit deflection of 8mm at 0.45 Pd and experimentally at 0.62 Pd. Bottom Steel strains were in good agreement with the experimental, figure 8.12 to 8.17. The steel yielded at the same load level under the point load, figure 8.13. For top steel strains, figure 8.18, severe deviation from the experimental results can be observed. This is due to the uplift of the corners during the experimental loading. The failure took place at 1.06 the experimental failure load. Crack patterns comparison between experiment and numerical up to the failure load are presented in figures 8.2 to 8.6 for bottom slab face and in figures 8.5 and 8.6 for top slab face.

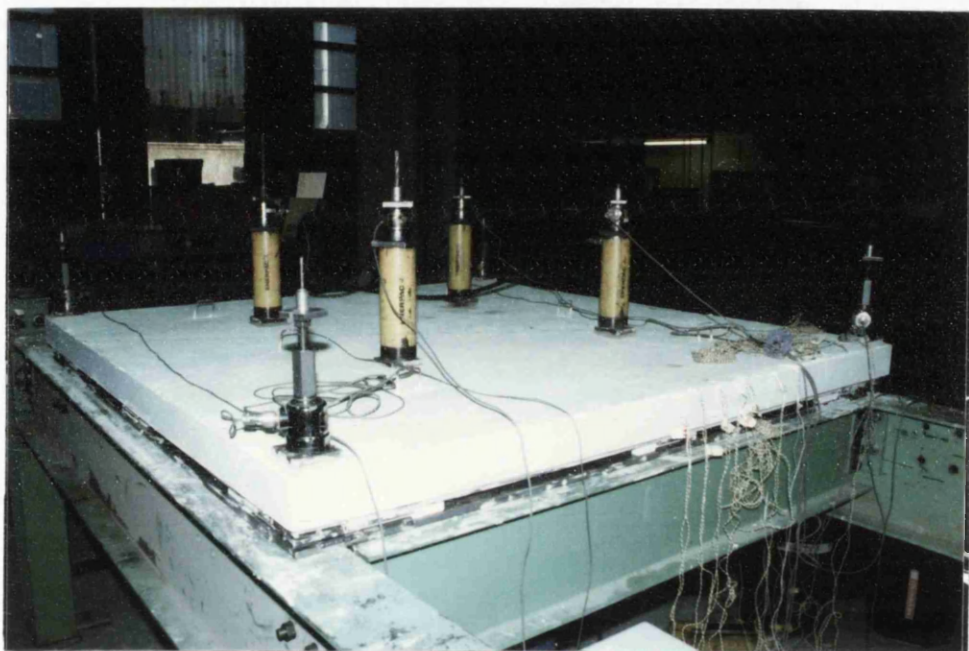
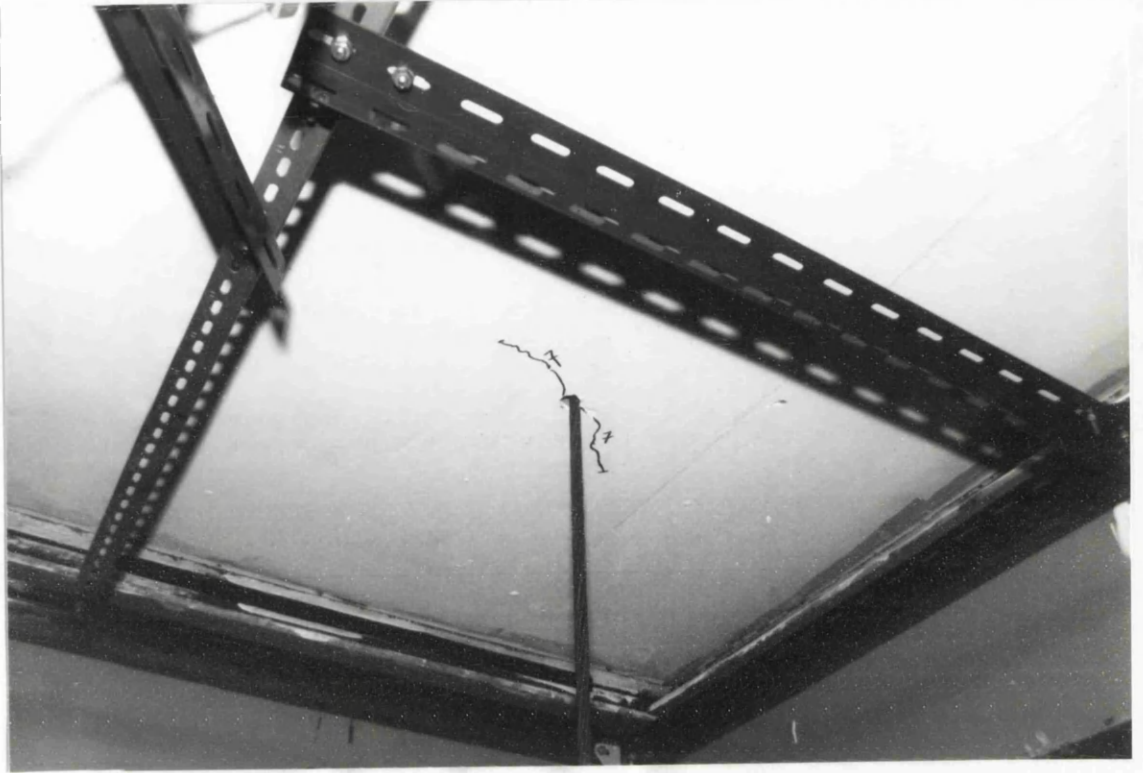


Fig. 8.1 Test setup for slab Models S.1, S.2 and S.3

a- Experimental at 0.42 Pd.



b- Numerical at 0.40 Pd 1/4 Slab

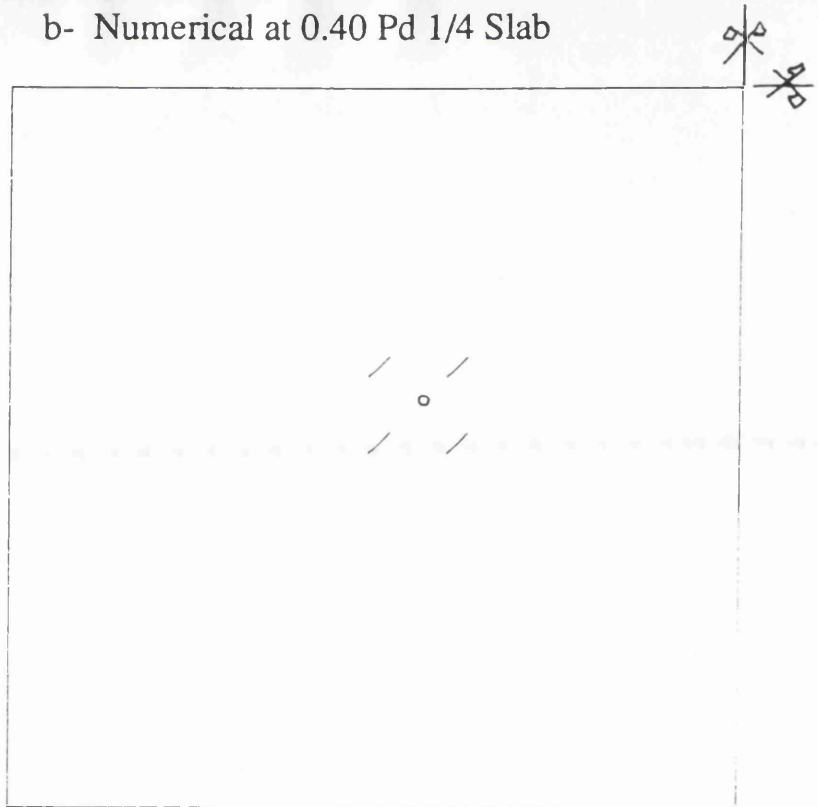
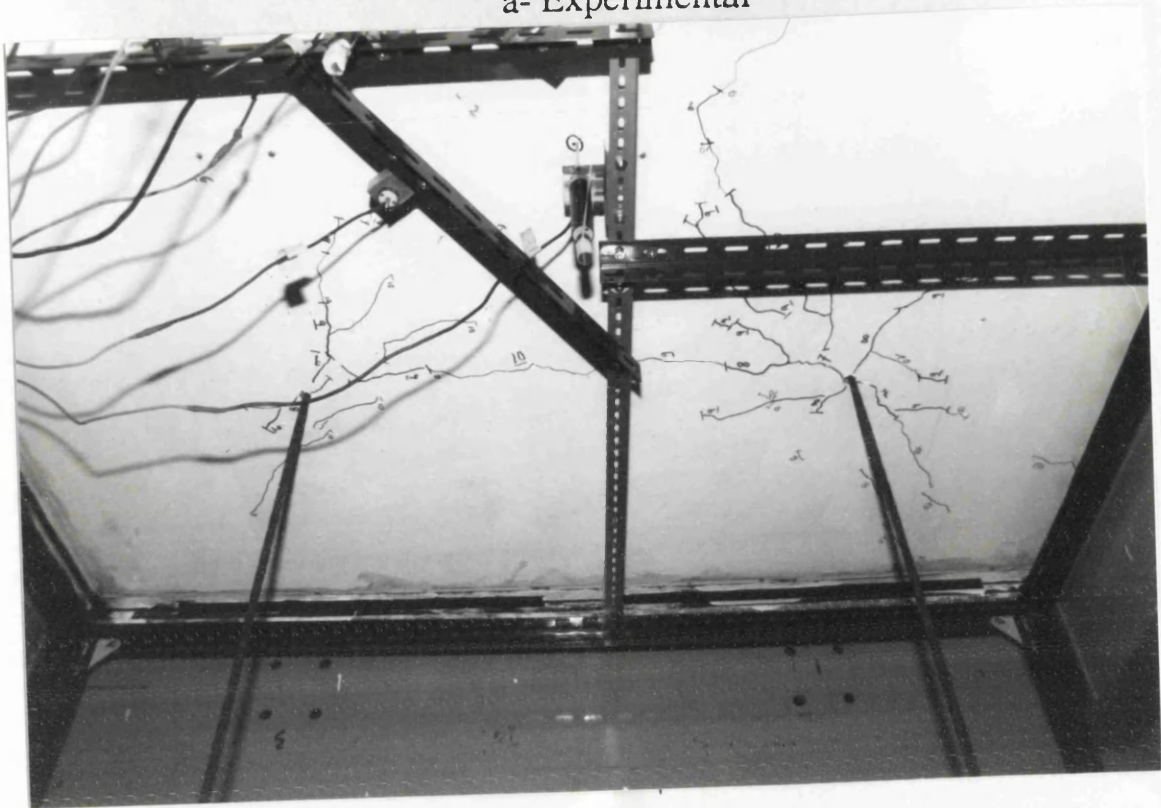


Fig. 8.2 Bottom first cracks.

a- Experimental



b- Numerical 1/4 Slab

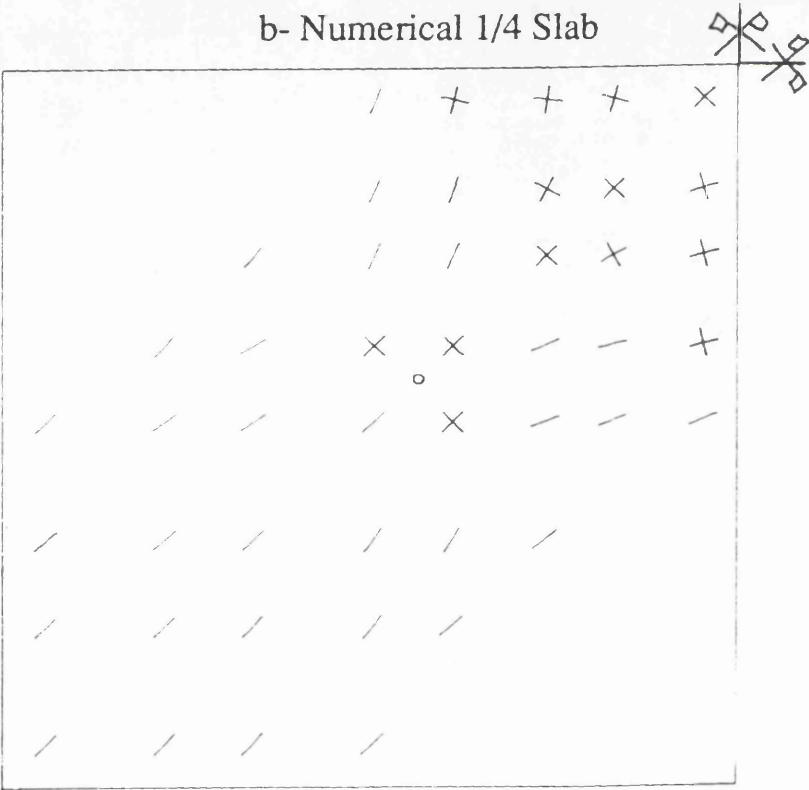
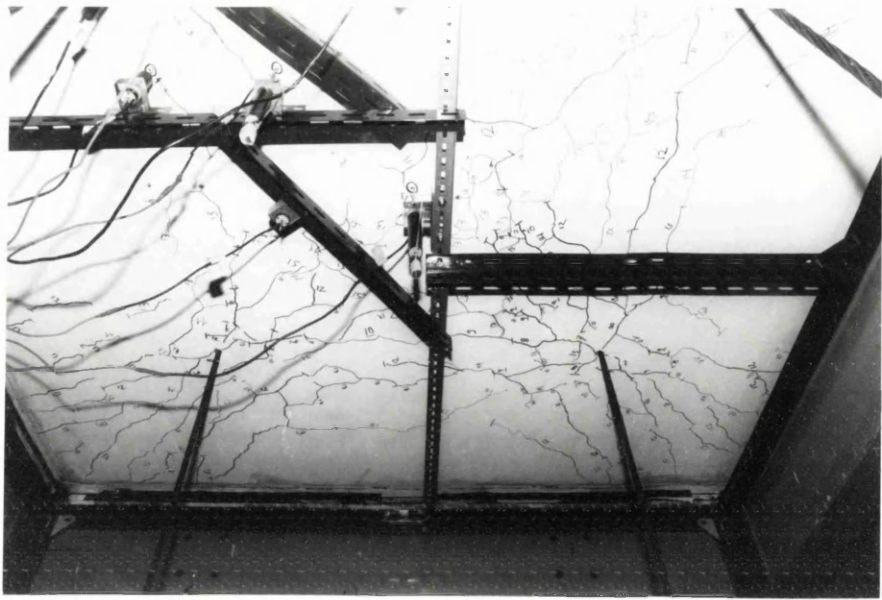


Fig. 8.3 Bottom crack pattern at 0.5Pd.

a- Experimental



b- Numerical 1/4 Slab

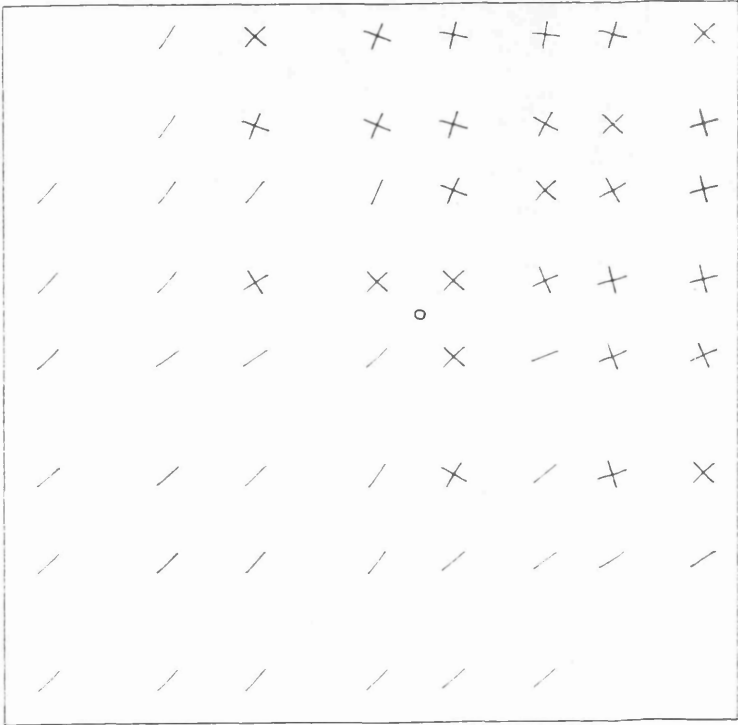
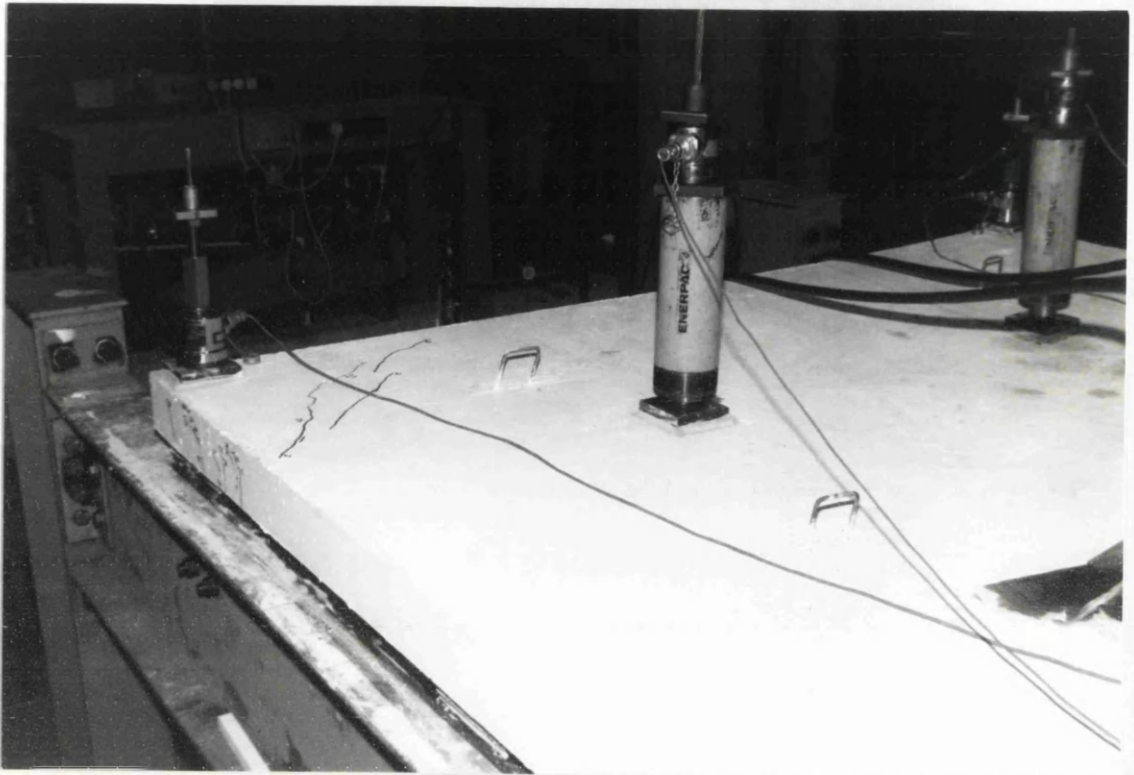


Fig. 8.4 Bottom crack pattern at design loadPd.

a- Experimental at 1.08 Pd.



b- Numerical at 1.05 Pd 1/4 Slab

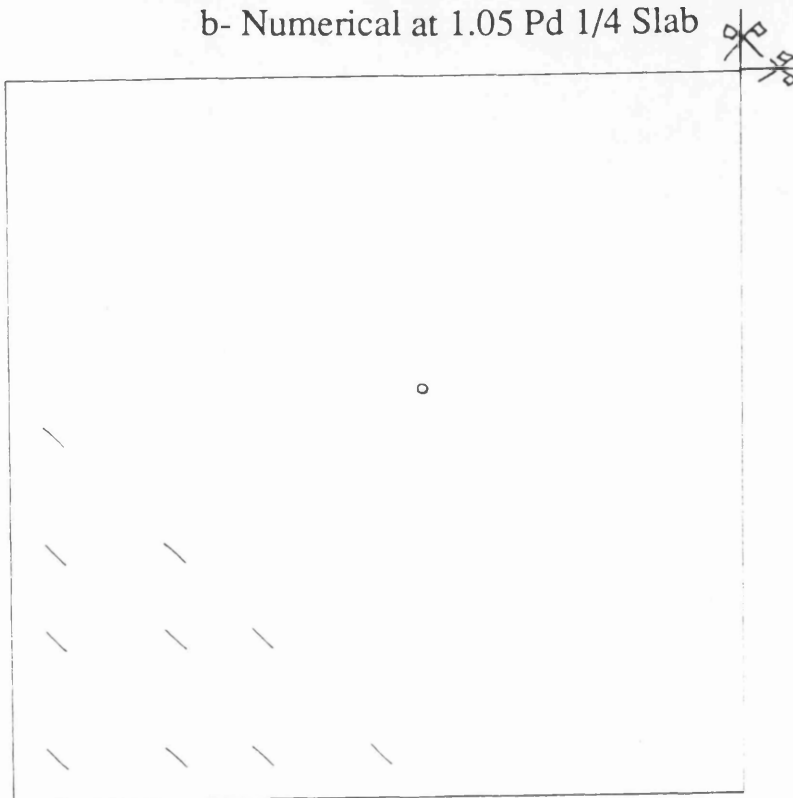
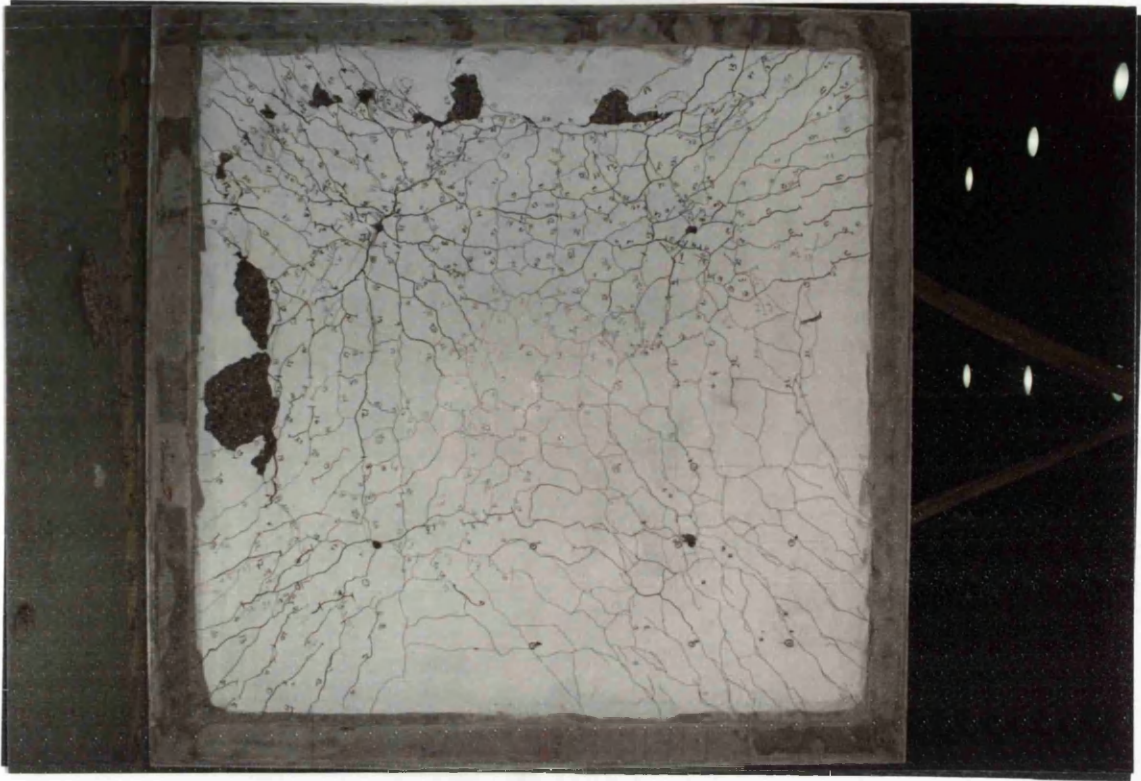


Fig. 8.5 Top crack pattern

a- Experimental



b- Numerical 1/4 Slab

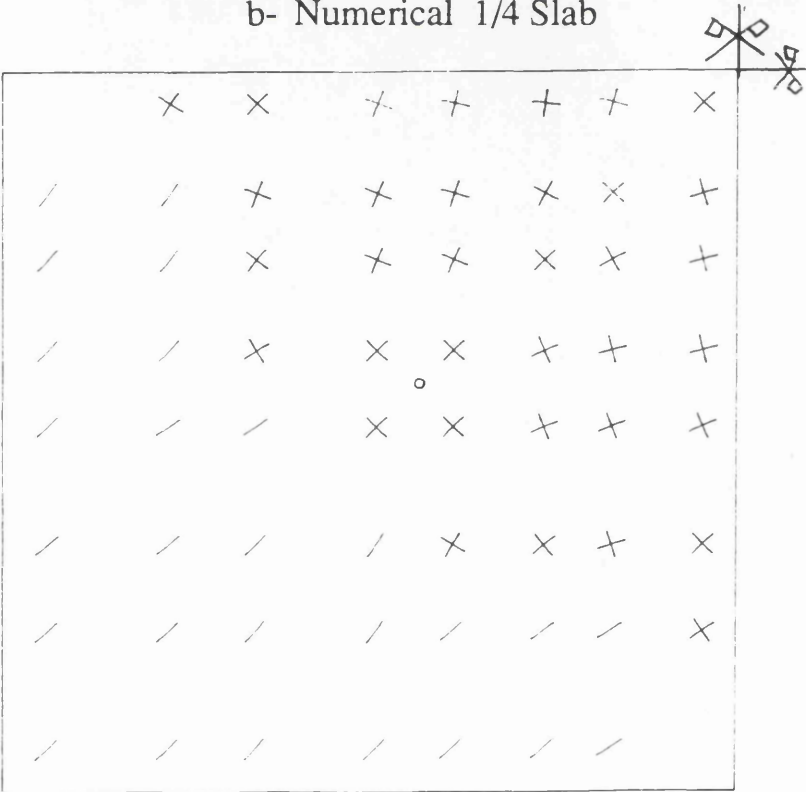
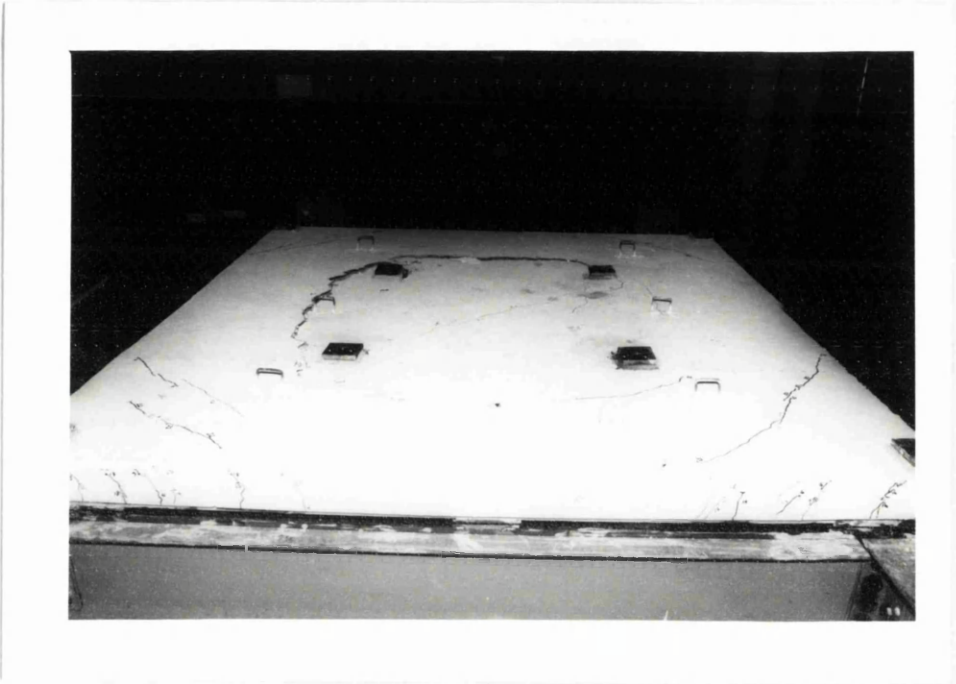


Fig. 8.6 Bottom crack pattern
at collapse load P_u .

a- Experimental



b- Numerical 1/4 Slab.

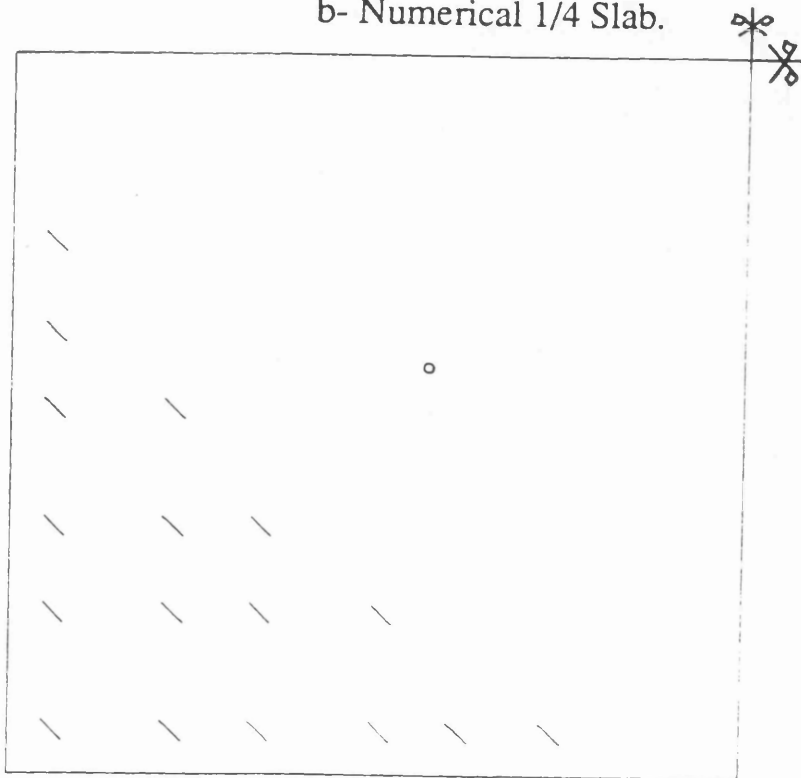


Fig. 8.7 Top crack pattern at collapse load

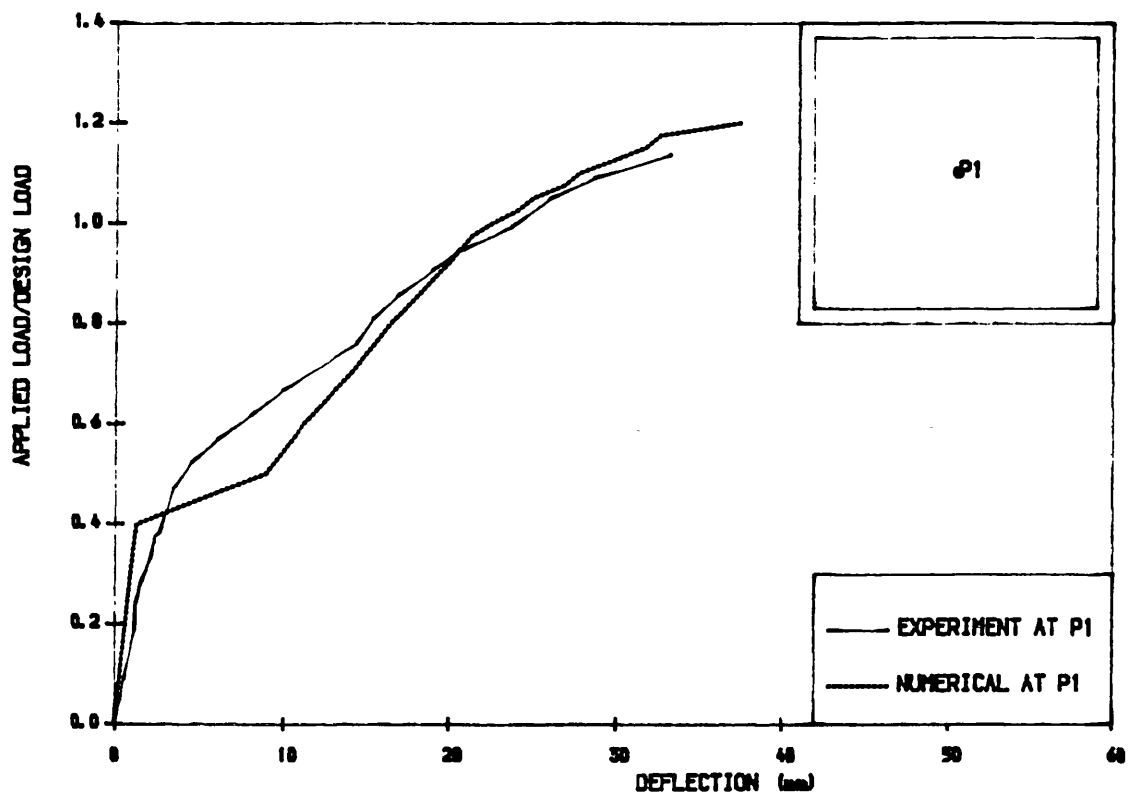


Fig. 8.8 Load-deflection curve. Central point. Model S.1

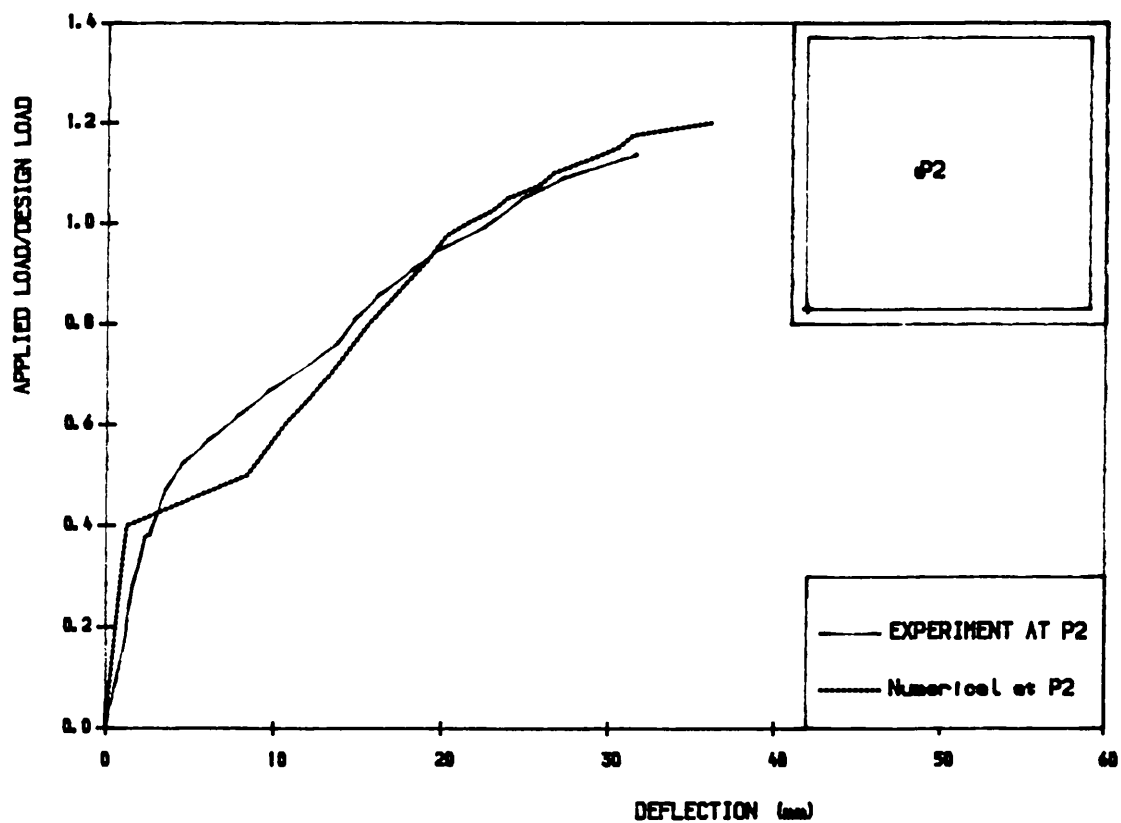


Fig. 8.9 Load-deflection curves. Model S.1

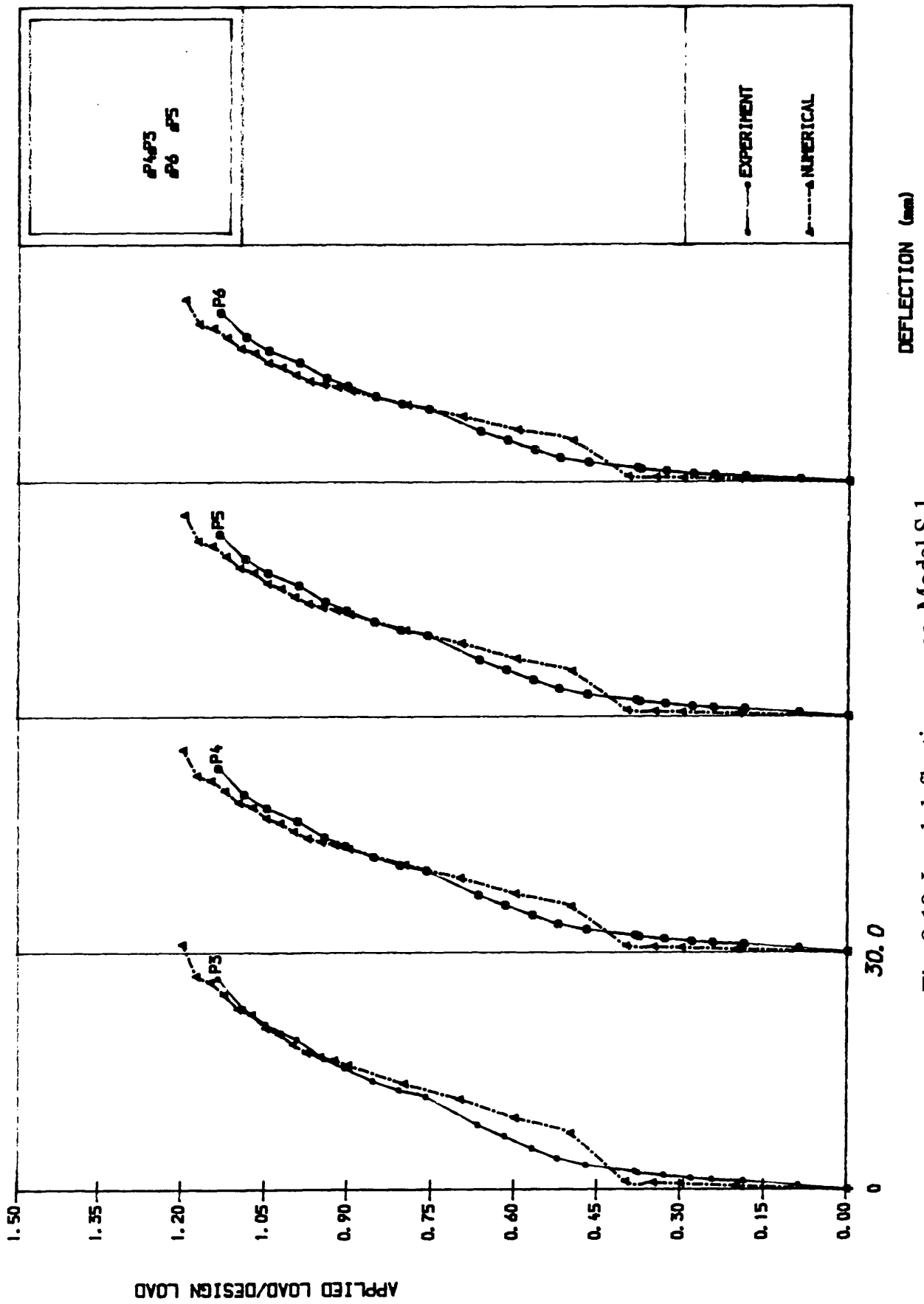


Fig. 8.10 Load-deflection curves. Model S.1

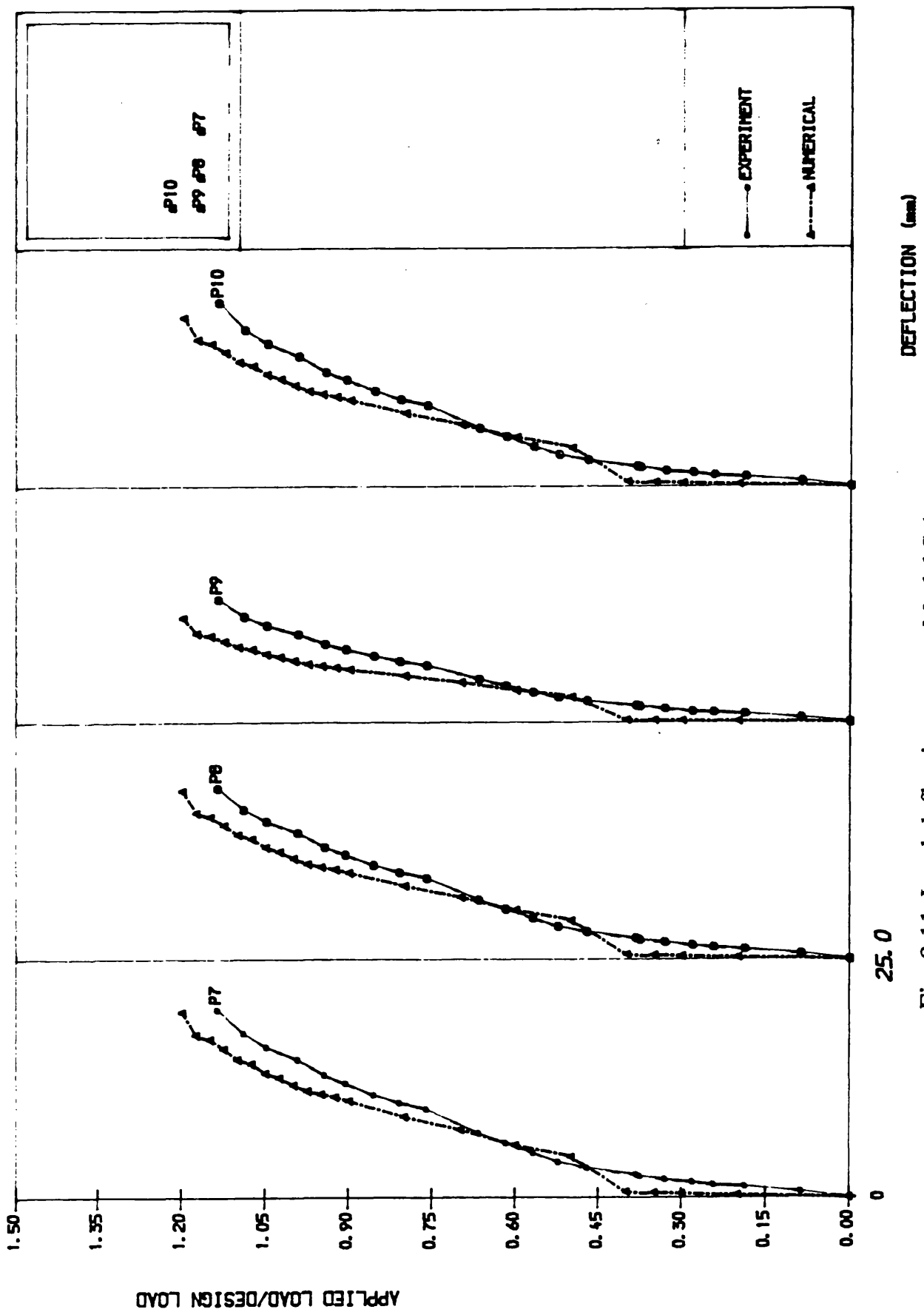


Fig. 8.11 Load-deflection curves. Model S.1

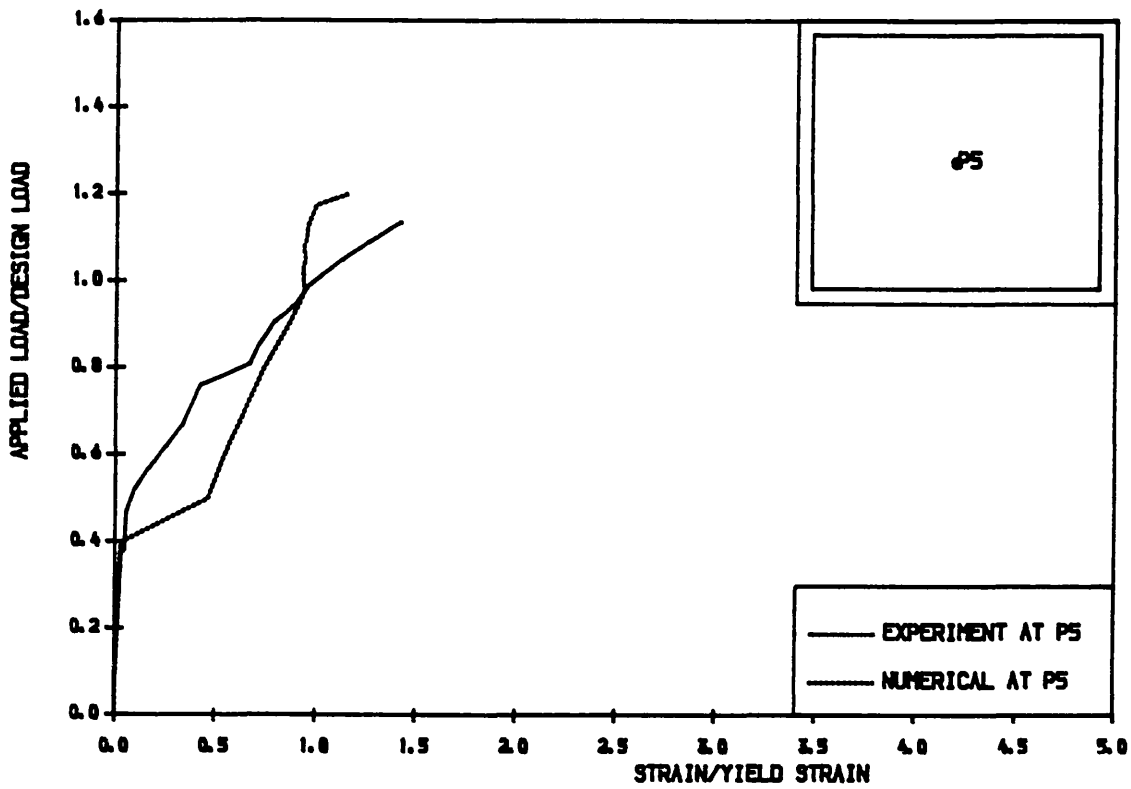


Fig. 8.12 Load-strain curve. Bottom steel Model S.1

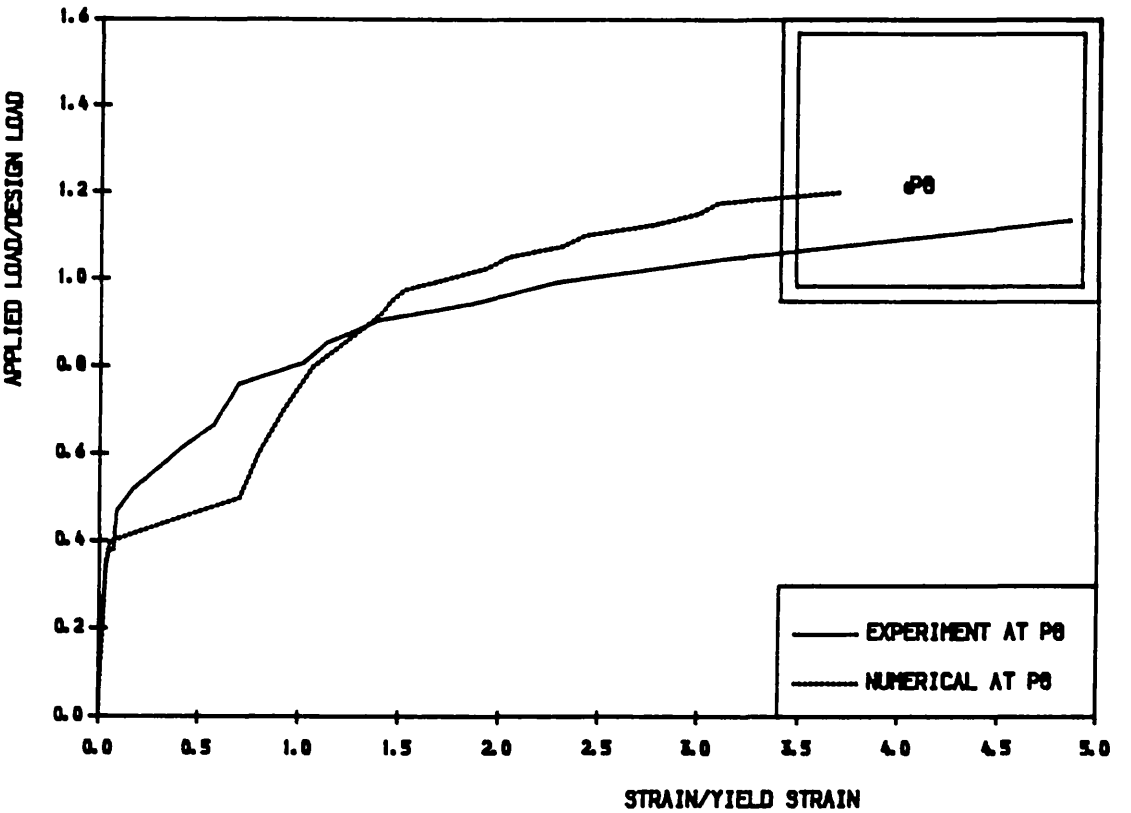


Fig. 8.13 Load-strain curve. Bottom steel Model S.1

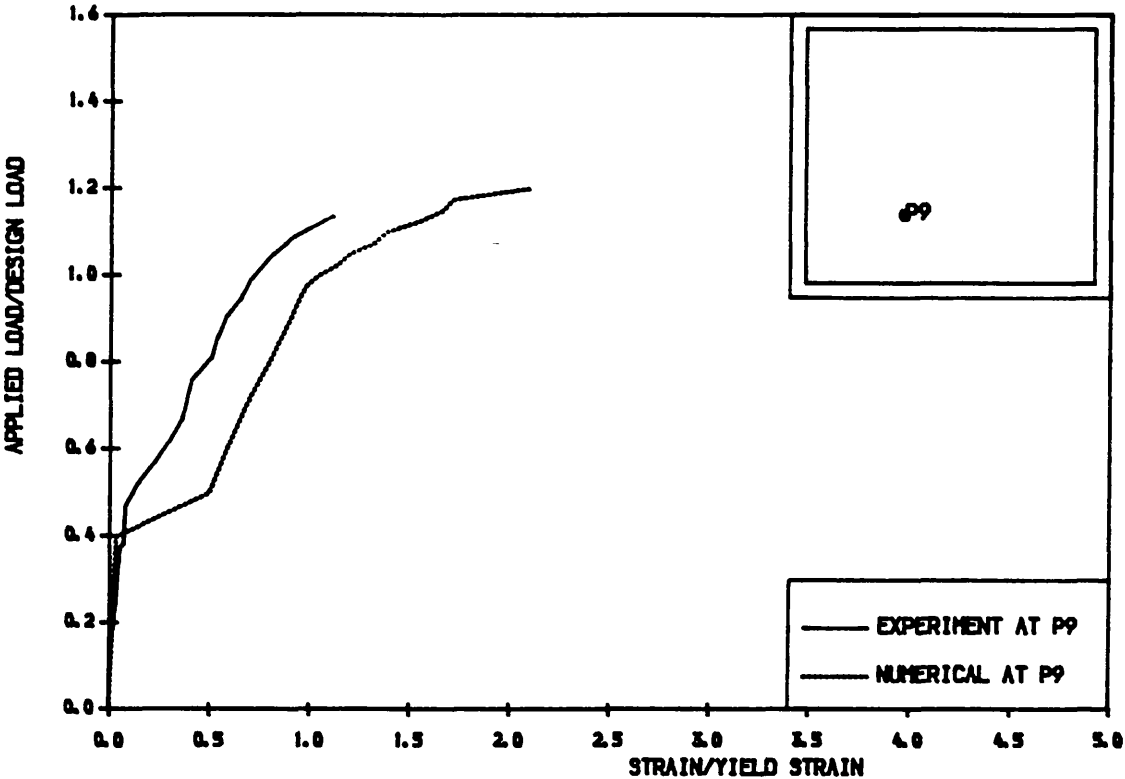


Fig. 8.14 Load-strain curve. Bottom steel Model S.1

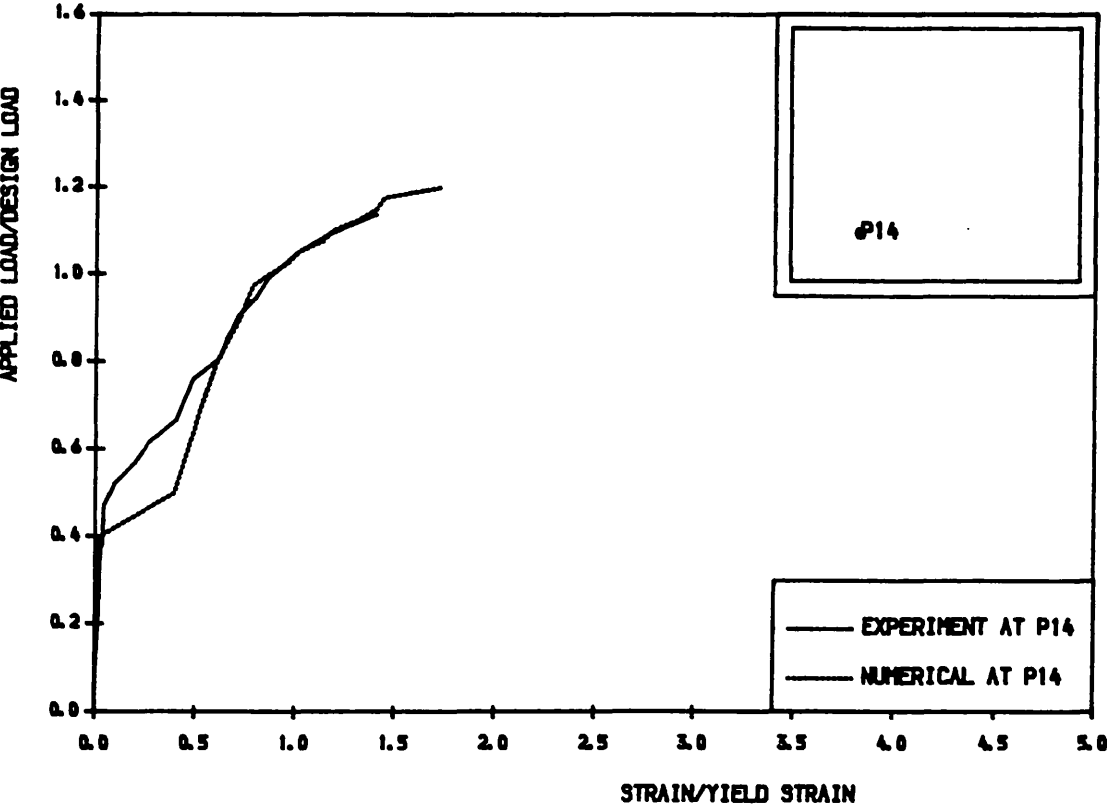
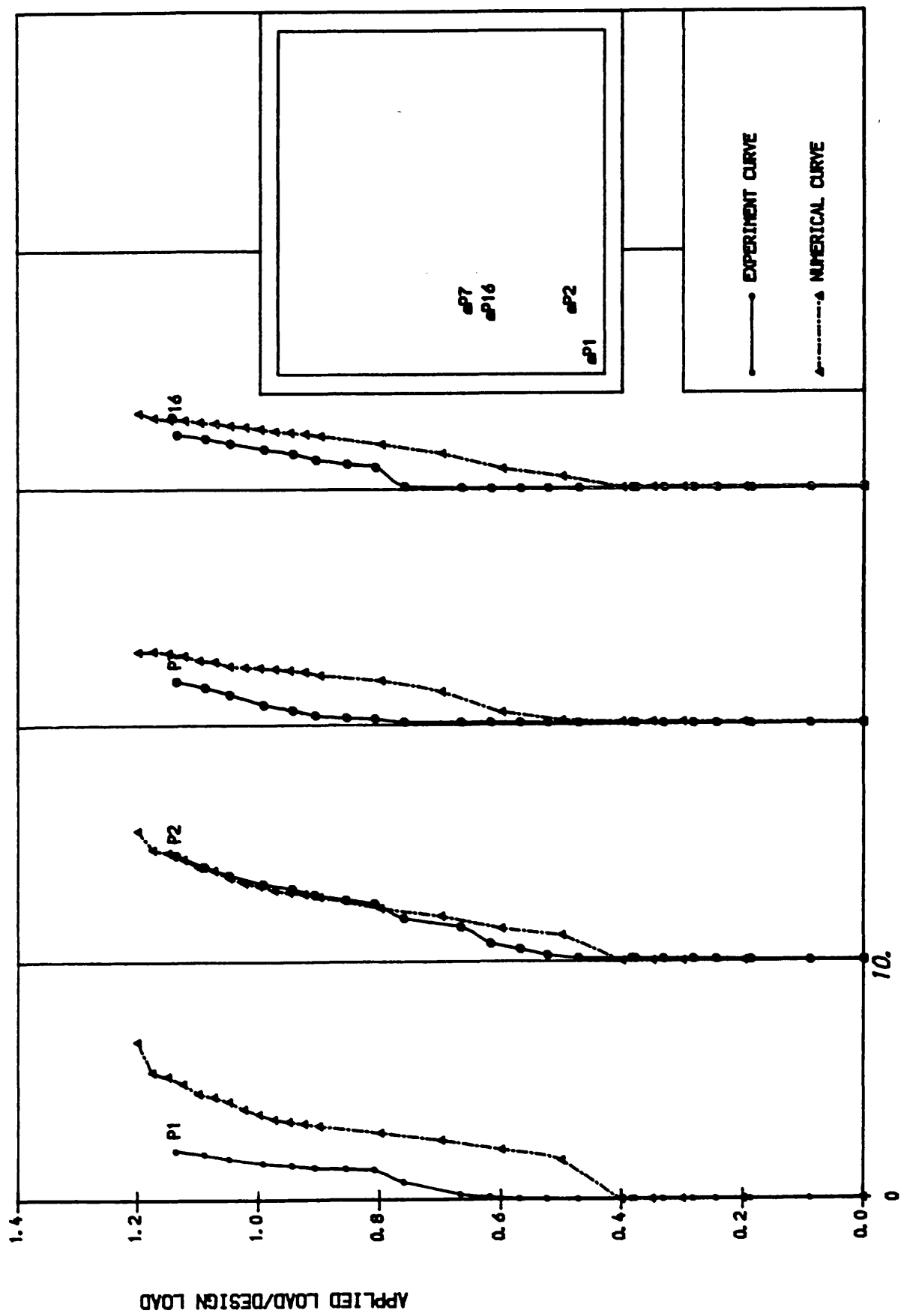


Fig. 8.15 Load-strain curve. Bottom steel Model S.1



STRAIN/YIELD STRAIN

Fig. 8.16 Load-strain curves. Bottom steel Model S.1

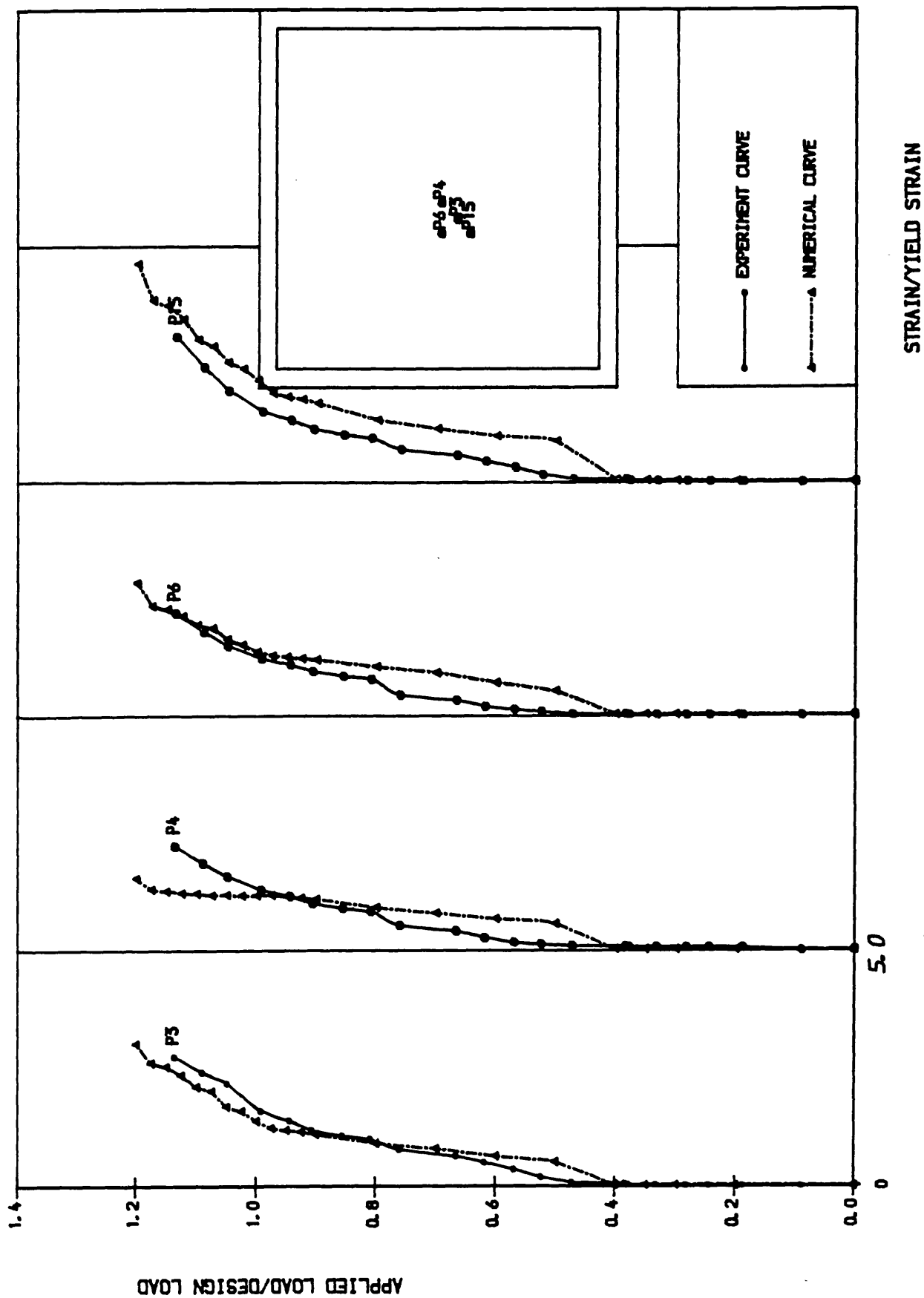


Fig. 8.17 Load-strain curves. Bottom steel Model S.1

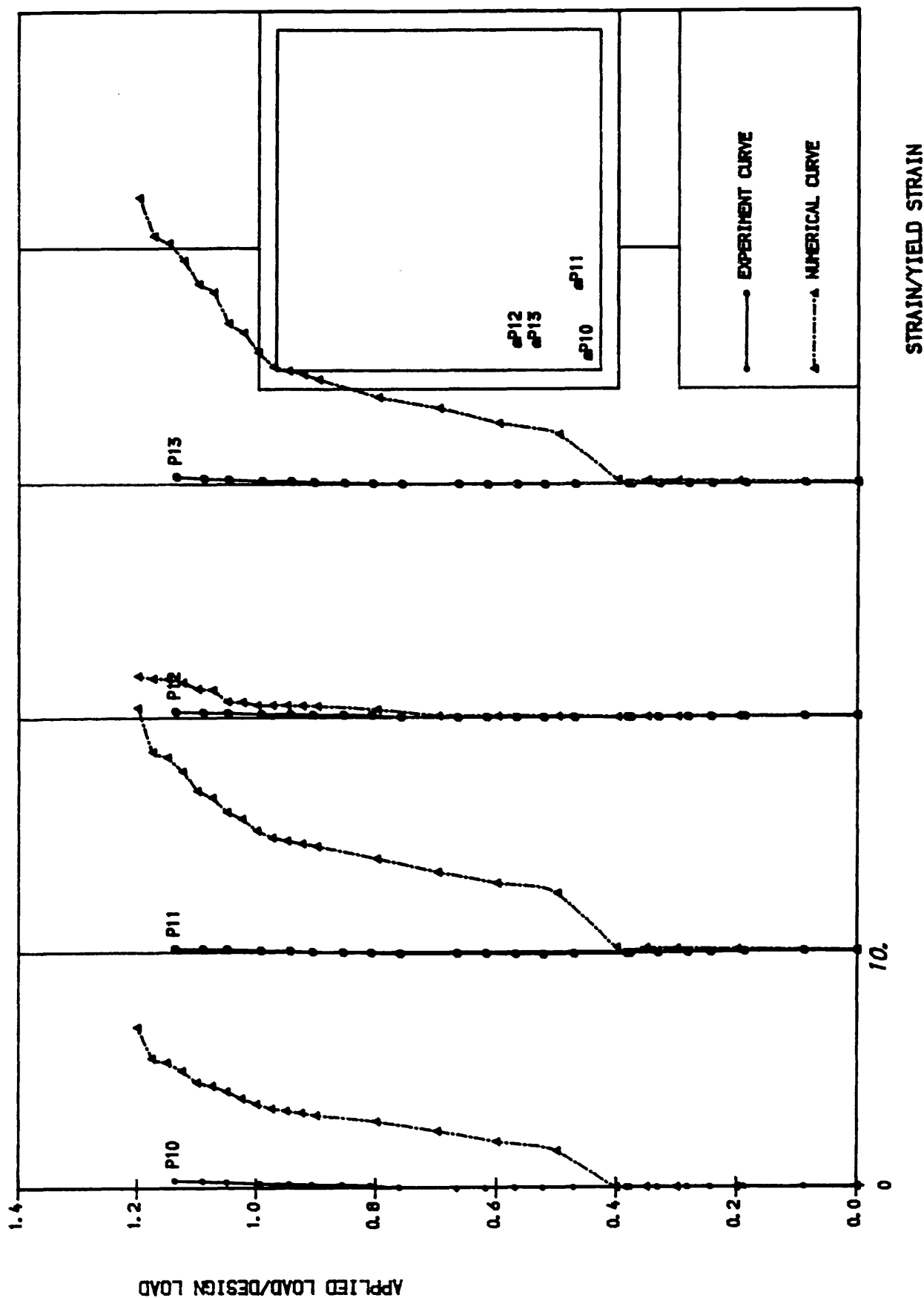


Fig. 8.18 Load-strain curves. Top steel Model S.1

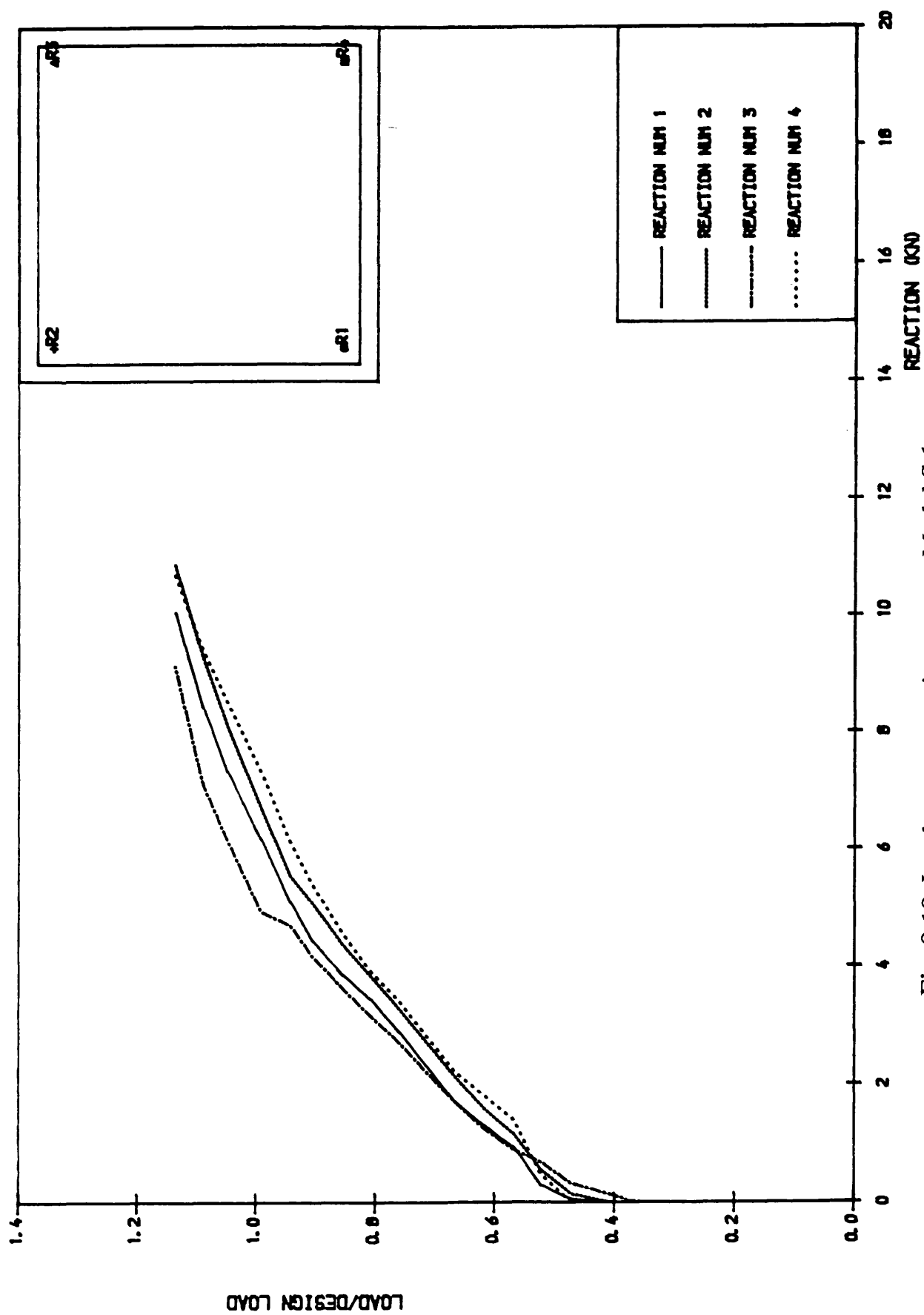


Fig. 8.19 Load-corner reaction curves. Model S.1

8.2.1.2 Model S.2:

This model had the same dimensions as model number 1 but was designed using 100% plasticity stress field. Details of the loading arrangements together with the resulting supports reaction are the same as for the previous model and are shown in figure 6.10a.

The slab was loaded up to failure using an average load increment of 0.05 of the design load ($P_d = 210 \text{ KN}$). The load–deflection curves are given in figures 8.20a to 8.20h. The first visible cracks were observed under the point loads at a load of $0.38 P_d$ ($0.29 P_u$). This early cracking had the effect of producing flexible behaviour over the slab loading history. Similar to the previous model, cracks spread over the central square defined by the loading holes and also along the diagonals between the corners and these holes. Cracks reached the corners of the slab at $0.58 P_d$ ($0.45 P_u$). The limiting crack width of 0.3 mm was reached at $0.62 P_d$ ($0.48 P_u$), while the limiting service deflection of $\text{span}/250 = 8.0 \text{ mm}$ was attained at about $0.66 P_d$ ($0.51 P_u$), figure 8.20a. At this level the crack pattern was similar to the collapse mechanism due to the formation of the yield lines. For further loading, the old cracks widened and very few new cracks, in the area limited by the four load points, opened. Figures 8.21a to 8.21f show the crack history of the slab. The crack width varied from 0.06 mm at first visible crack, to 2.0 mm at the design load, and at the collapse load the maximum crack width measured was of 6.5 mm in the area under the point load. As can be seen, the rate of increase of crack width with load is high, mainly because of the yielding of steel under the point load in a large area of the slab.

The first yielding of the steel was at $0.80 P_d$ ($0.62 P_u$) under the point load, figure 8.22f, while the top steel yielded at $0.97 P_d$ ($0.75 P_u$), figure 8.22i. At this level of loading the top corner concrete face of the slab was already cracked. Failure took place at $1.30 P_d$ ($1.0 P_u$) in a flexural manner.

Deflections:

The load–deflection curves are presented in figures 8.20a to 8.20h. From these

curves, it is clear that the nonlinearity started at 0.23 Pd (0.18 Pu) which is less than the load at the first visible crack, 0.38 Pd (0.29 Pu). The limiting deflection of span/250 was reached at 0.67 Pd (0.52 Pu), figure 8.20a. This represents an acceptable serviceability limit state deflection.

Steel Strain:

Figures 8.22a to 8.22h and 8.22i to 8.22j show the load steel strain relationship for bottom and top steel respectively. As can be seen, all the strain gage readings show that the steel reached its yielding strain and in different places of the slab the steel strain was several times the yield strain. This indicates the flexural behaviour of the slab. The first yielded point was under the point load at 0.8 Pd (0.62 Pu), figure 8.22c, while for the top steel, it was at 0.97 Pd (0.75 Pu), figure 8.22i.

Reactions:

It can be noticed that the reactions are negligible until the concrete cracked at 0.38Pd (0.30 Pu), figure 8.23. The slab corner reactions decreased while approaching the ultimate load. The maximum uplift reactions in the corners, at the penultimate load increment was 18% of the point load ($P/4$), which is 50% greater than the one for the previous slab. A maximum of 16.4 KN was recorded in one corner, while for the first slab only 11.0 KN was reached. The ultimate load of this slab was greater by 15% of the ultimate load of S.1.

Crack width:

The first crack was 0.06 mm wide at 0.38 Pd (0.29 Pu) under the point load. Crack width limit of 0.3 mm was reached at 0.62 Pd (0.48 Pu). At 0.85 Pd (0.65 Pu) the maximum crack width was 0.55 mm. At the design load the crack width was 2.0 mm. In this model the cracks are not near each other like in model S.1. This is caused by the distance between steel bars, which was greater than the one in model S.1. This model was reinforced using 8 mm diameter bars, whereas in model S.1 6 mm diameter bars were used. At the collapse load the maximum

crack width measured was of 6.5 mm.

Mode of failure:

The slab behaved in a ductile manner. This can be seen by the crack pattern over the bottom of the slab, figure 8.21c and 8.21d, and also by the maximum flexural bottom crack width which was 6.5 mm, without any crushing of top concrete slab surface. The slab failed at 1.3 Pd in a flexural mode.

Numerical Analysis:

As for the previous model, using the same finite element mesh and the same number of layers through the depth, a quarter of the slab was analysed. The first increment was of 0.2 Pd. Small increments of 0.1 of the design load was used till approaching the design load after which a value of 0.025 Pd was adopted.

The numerical first crack appeared at 0.35 Pd, while in the experiment it was seen at 0.38 Pd. Load– deflection curves, figure 8.20a to 8.22h show good agreement between experimental and numerical results. The service load deflection limit of 8.0 mm was reached at 0.55 Pd numerically and at 0.66 Pd experimentally, both at the central point, figure 20a. Load– Strain curves are presented in figures 8.22a to 8.22h for bottom steel and figures 8.22i and 8.22j for top corner steel. The bottom steel yielded at 0.80 Pd under the point load, both numerically and experimentally. At the central point, the bottom steel yielded at 1.0 Pd and 0.90 Pd in the numerical and experimental analysis respectively, figure 8.22a. Good agreement also is obtained in crack pattern development as shown in figures 8.21a to 8.21d. The numerical failure load was 0.96 the experimental one (Pu).

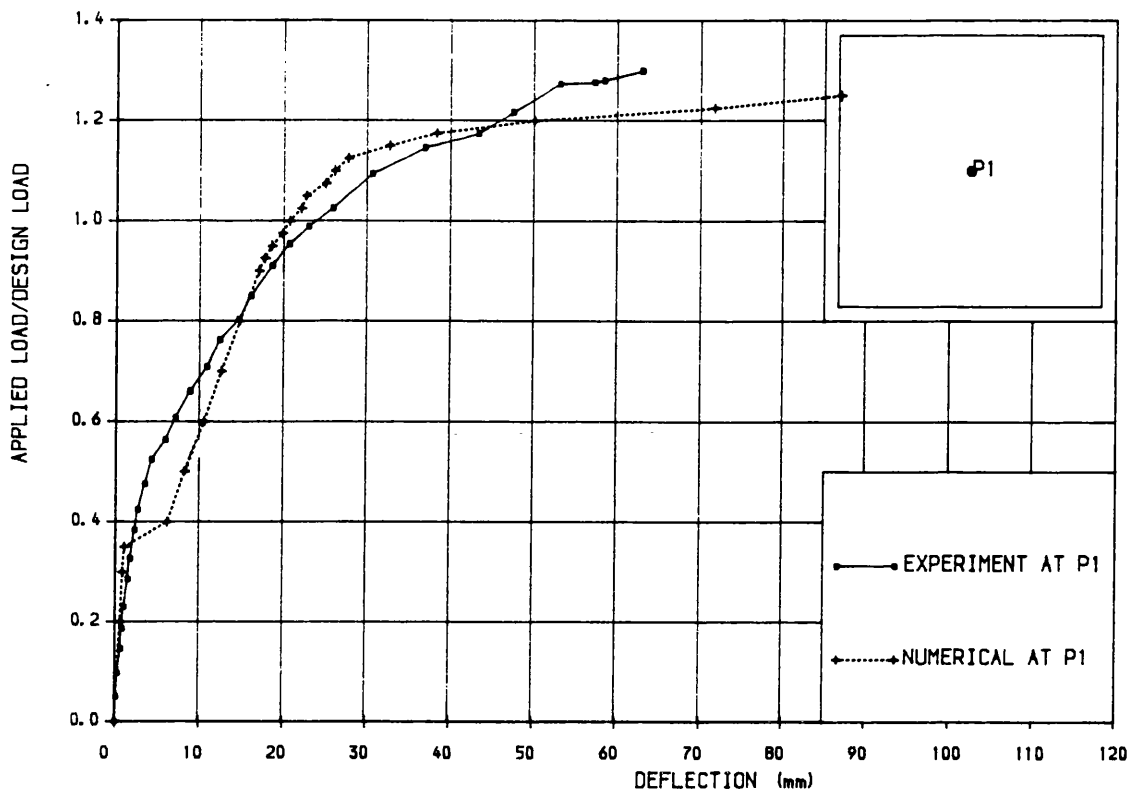


Fig. 8.20a Load-deflection curve. Model S.2

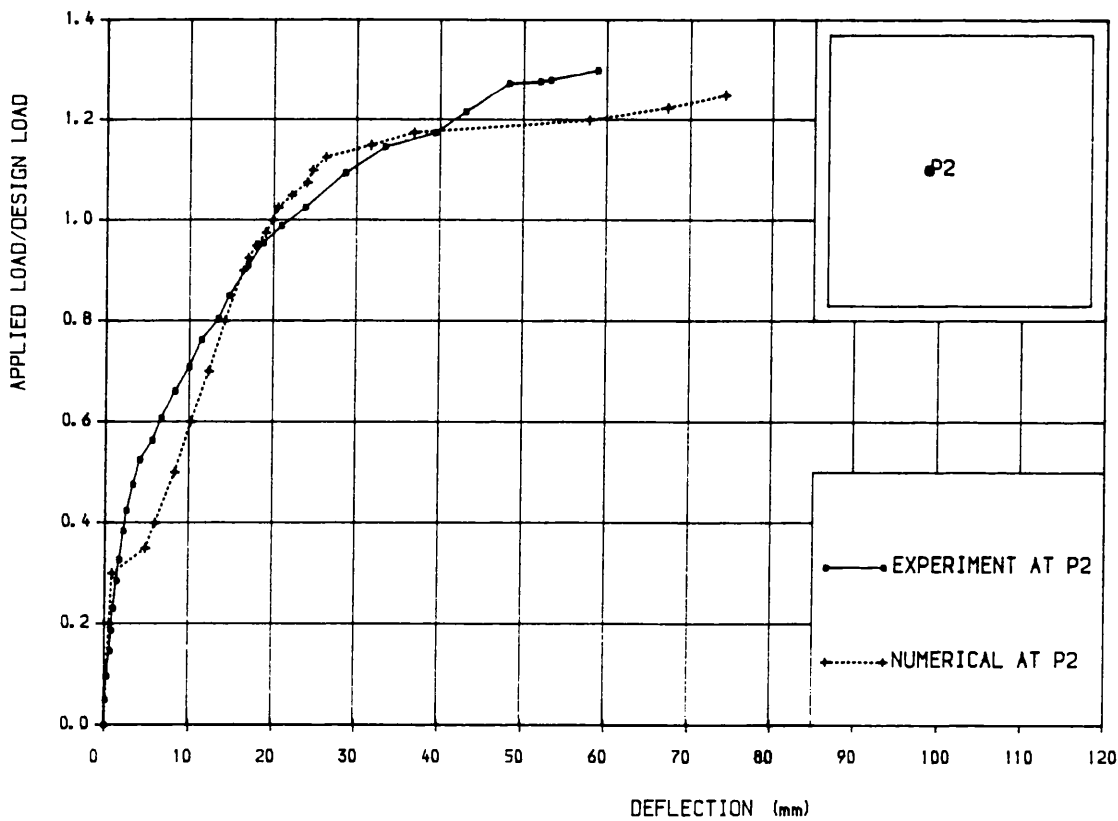


Fig. 8.20b Load-deflection curve. Model S.2

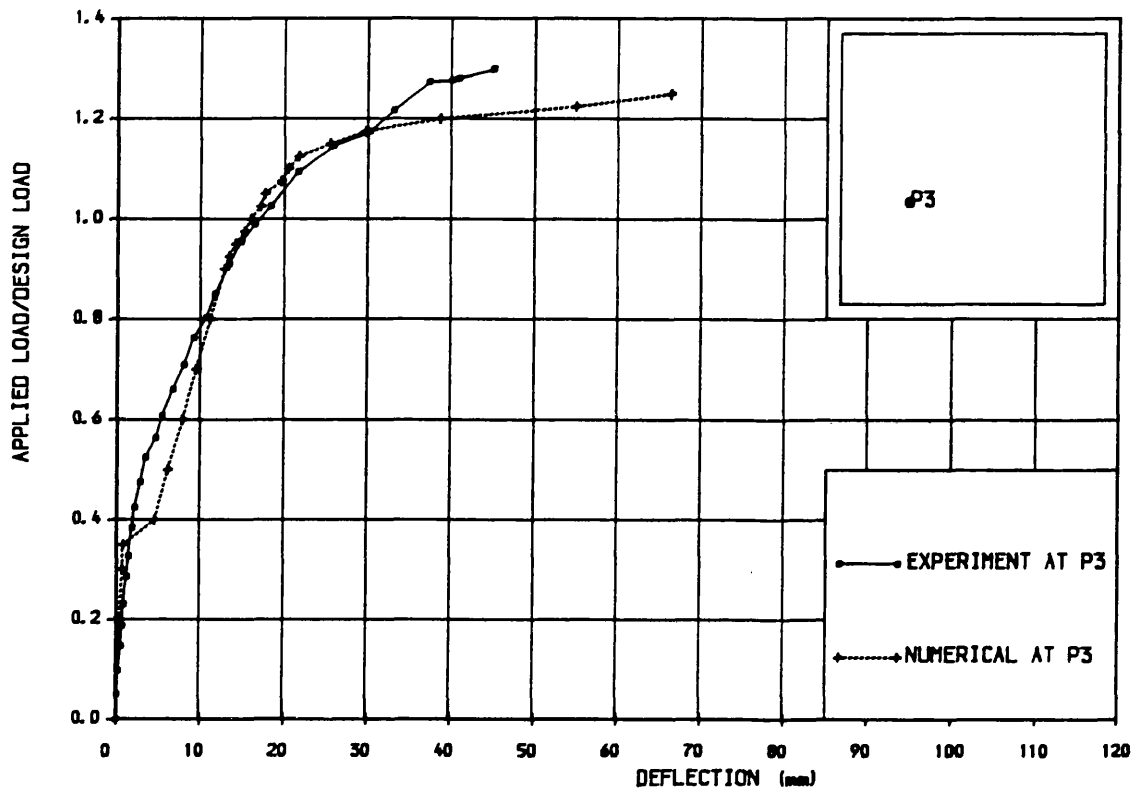


Fig. 8.20c Load-deflection curve. Model S.2

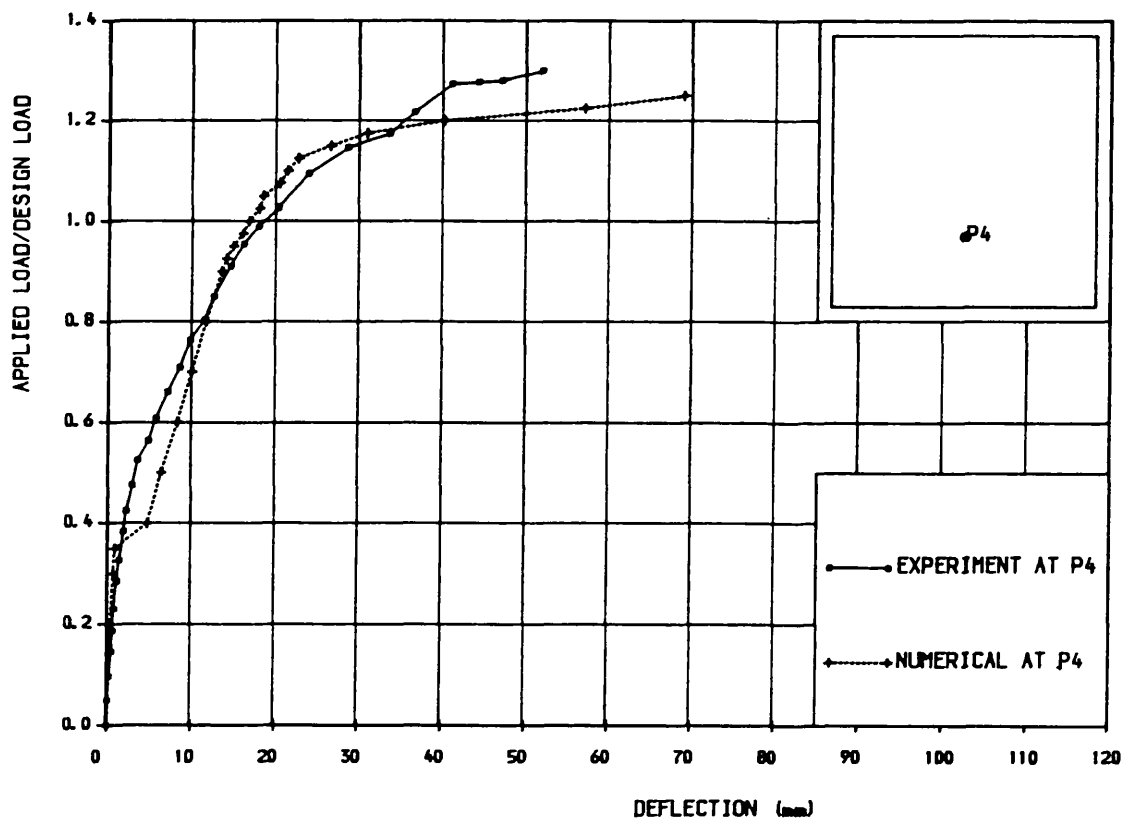


Fig. 8.20d Load-deflection curve. Model S.2

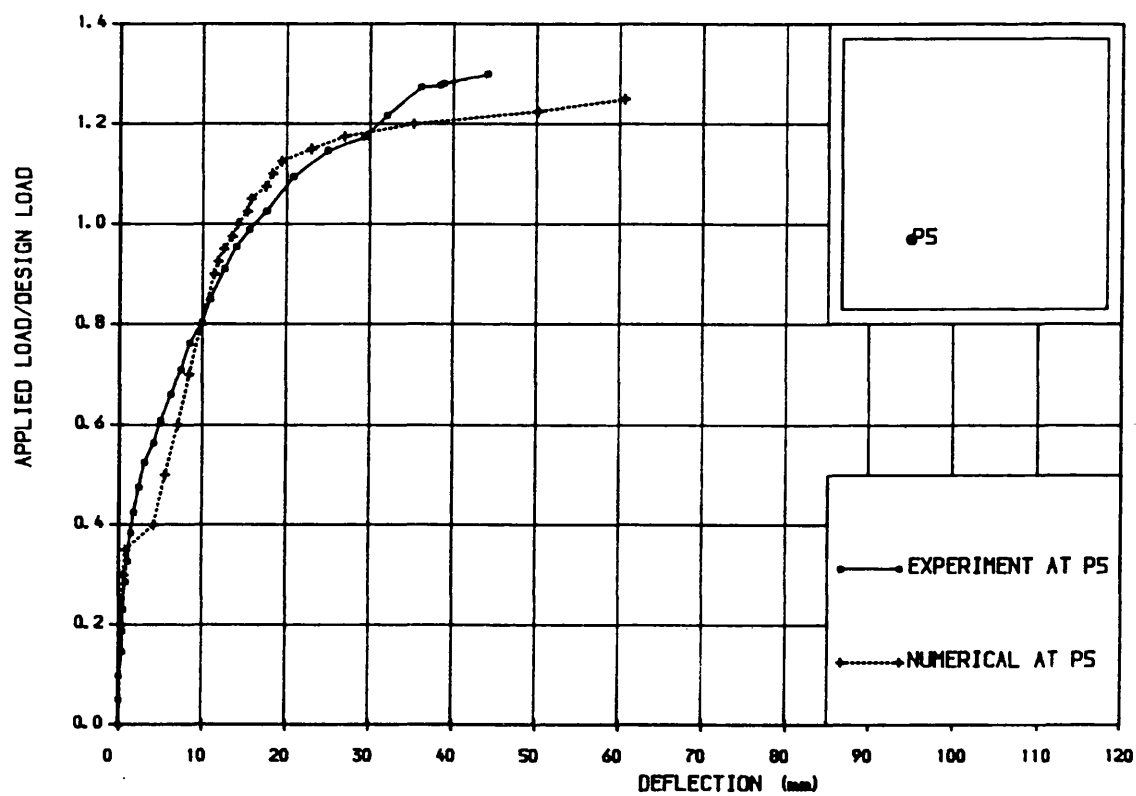


Fig. 8.20e Load-deflection curve. Model S.2

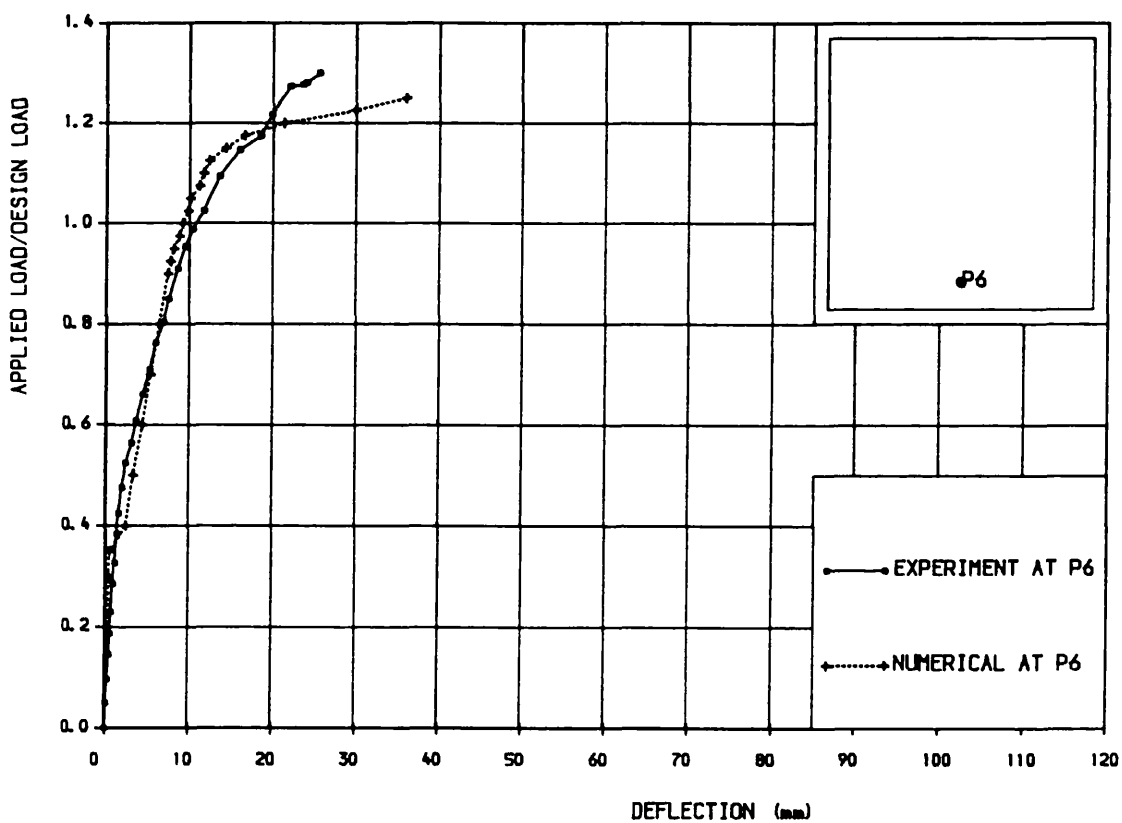


Fig. 8.20f Load-deflection curve. Model S.2

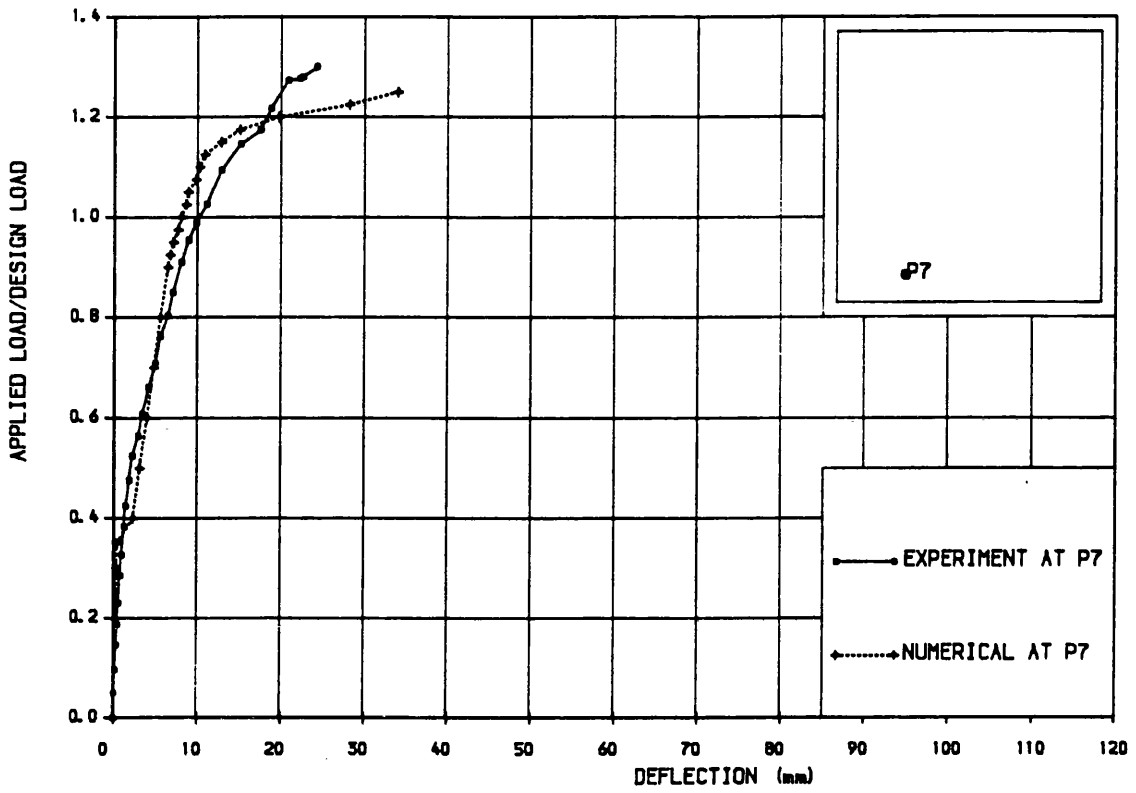


Fig. 8.20g Load-deflection curve. Model S.2

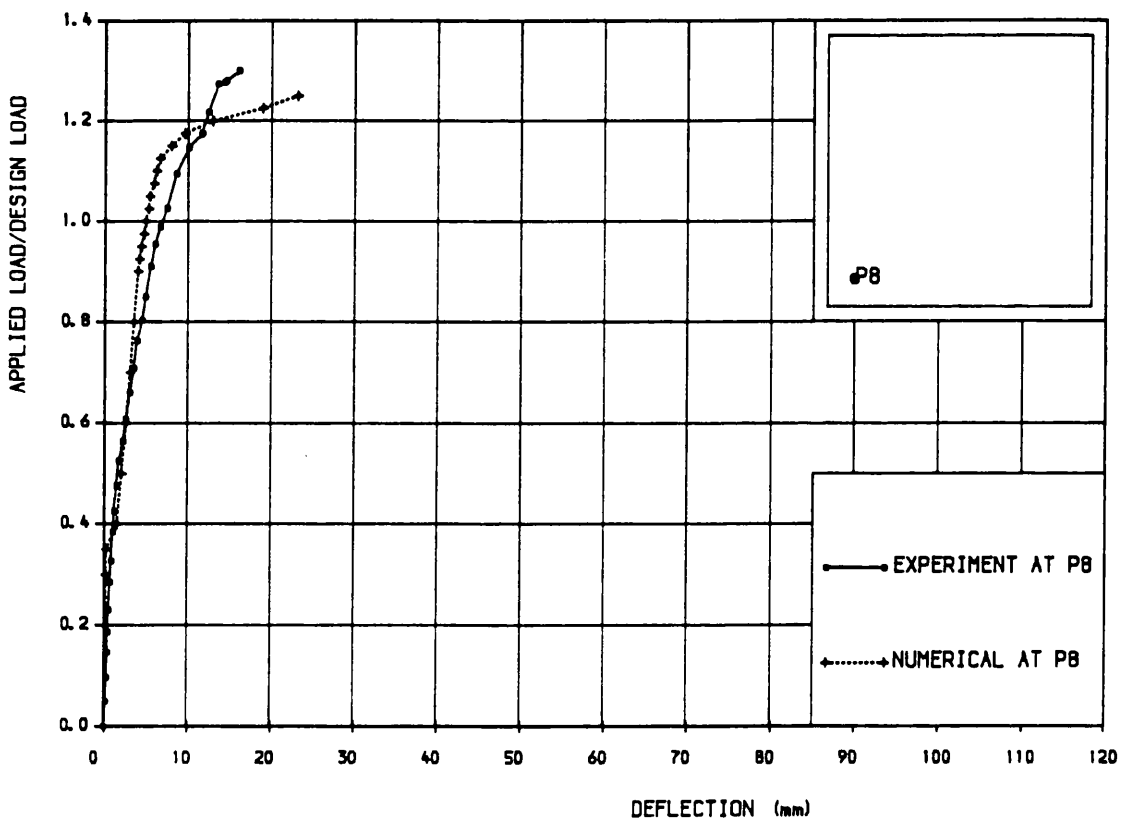


Fig. 8.20h Load-deflection curve. Model S.2

Experimental

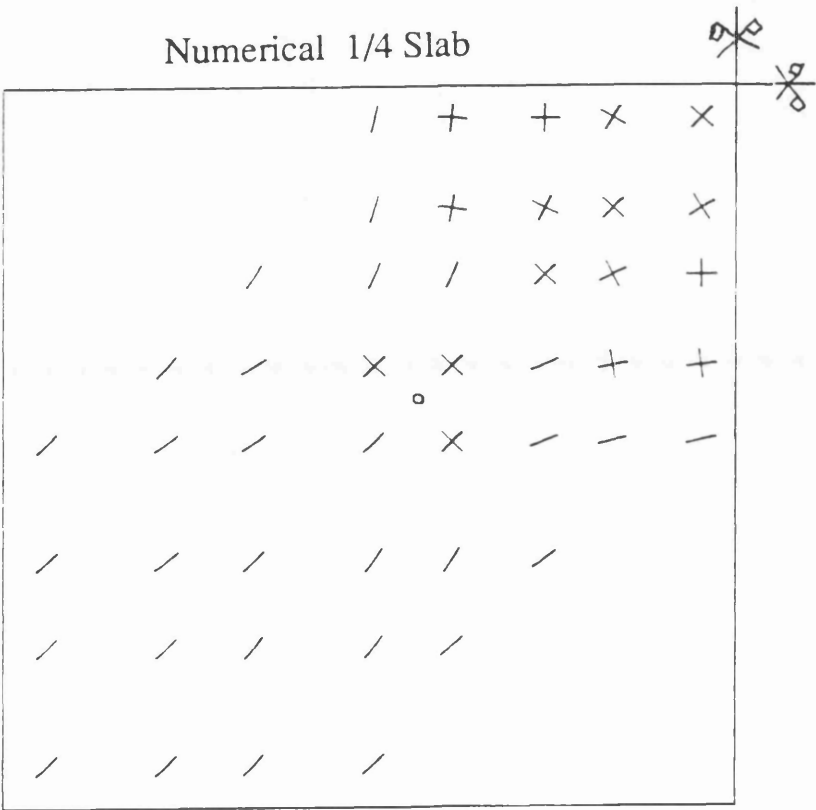
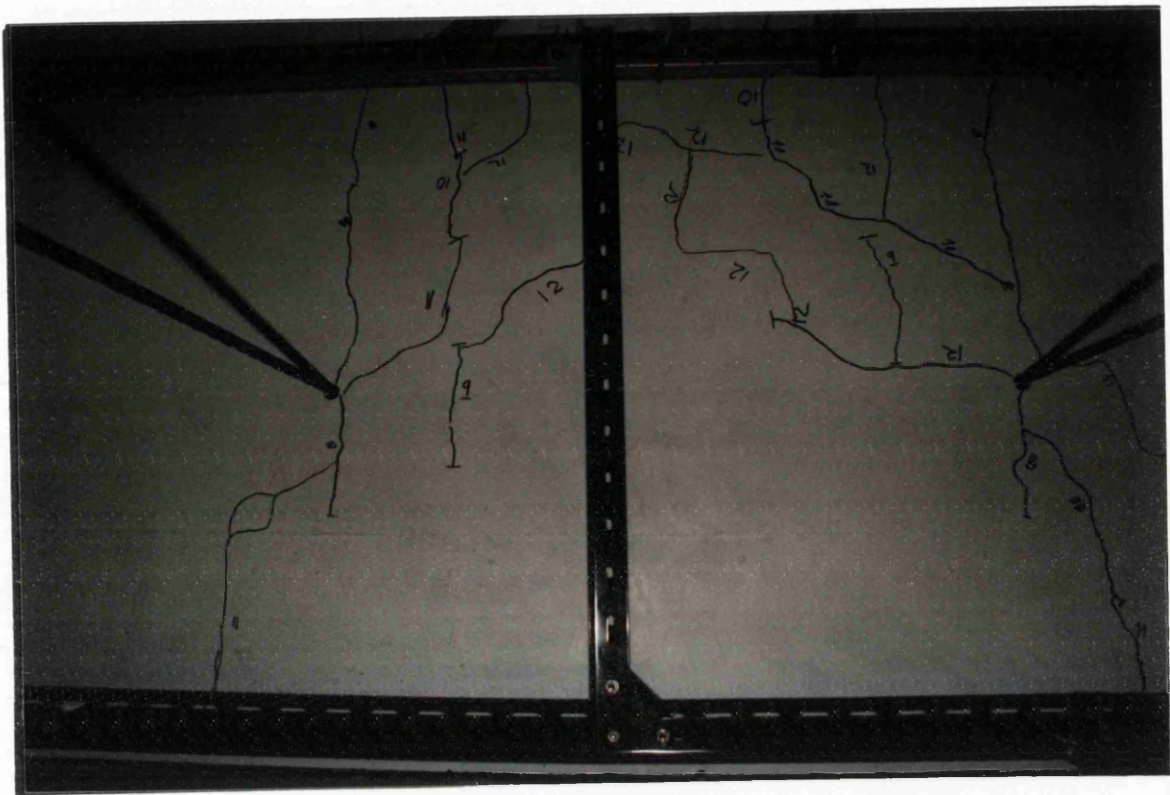
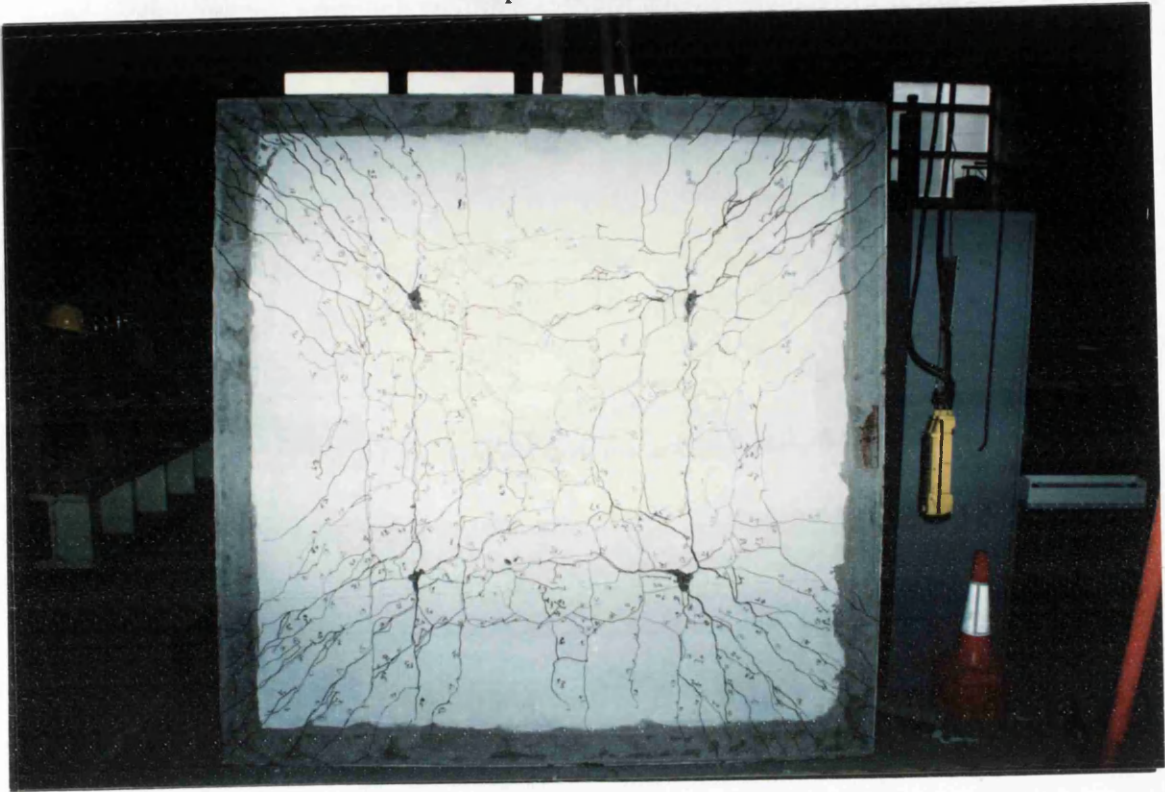


Fig. 8.21a Bottom crack pattern at 0.55 Pd
Model S.2

Experimental



Numerical 1/4 Slab

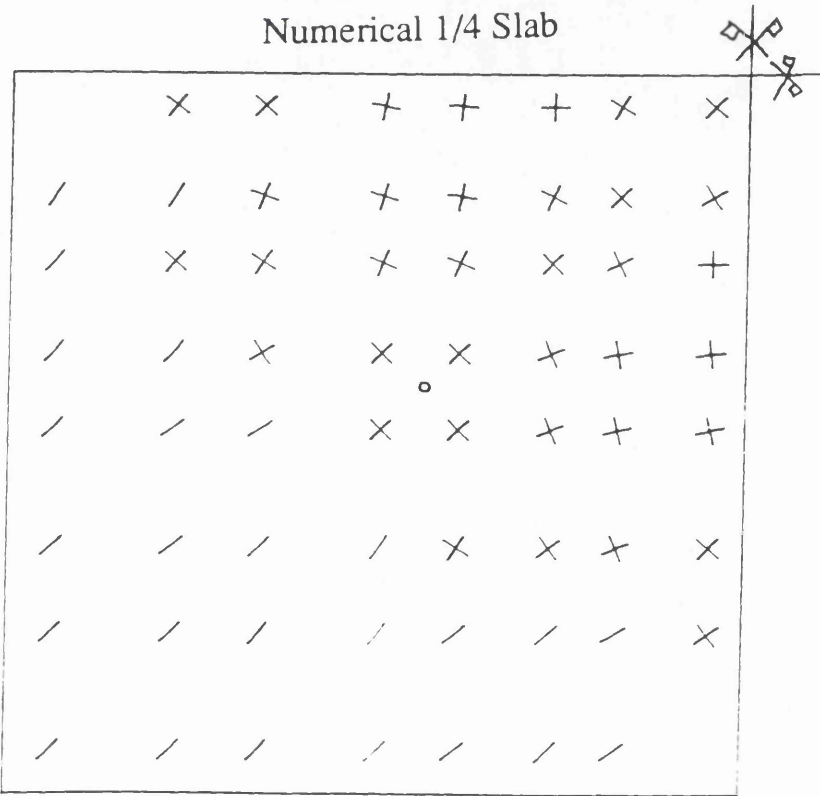
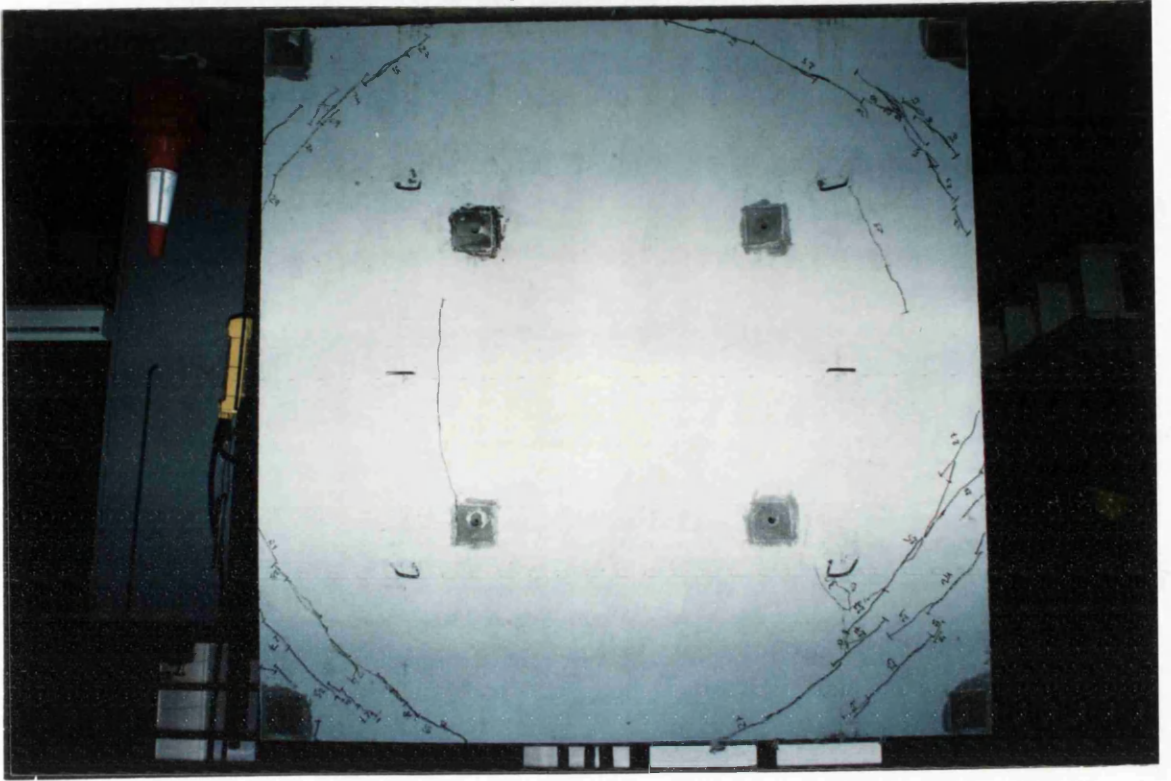


Fig. 8.21c Bottom crack pattern
at collapse load P_u . Model S.2

Experimental



Numerical 1/4 Slab

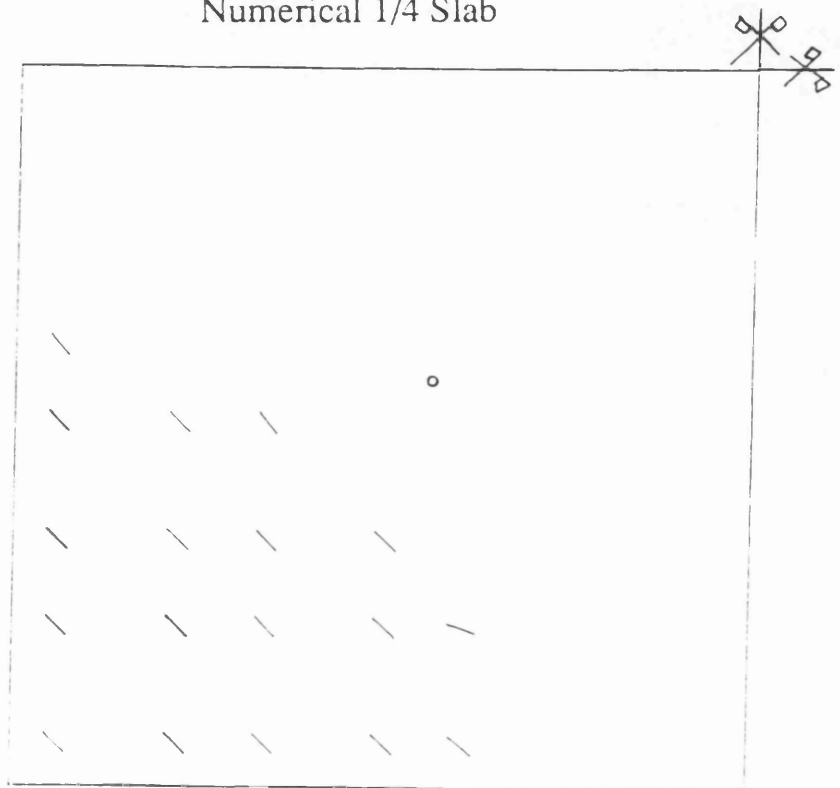


Fig. 8.21d Top crack pattern
at collapse load P_u . Model S.2

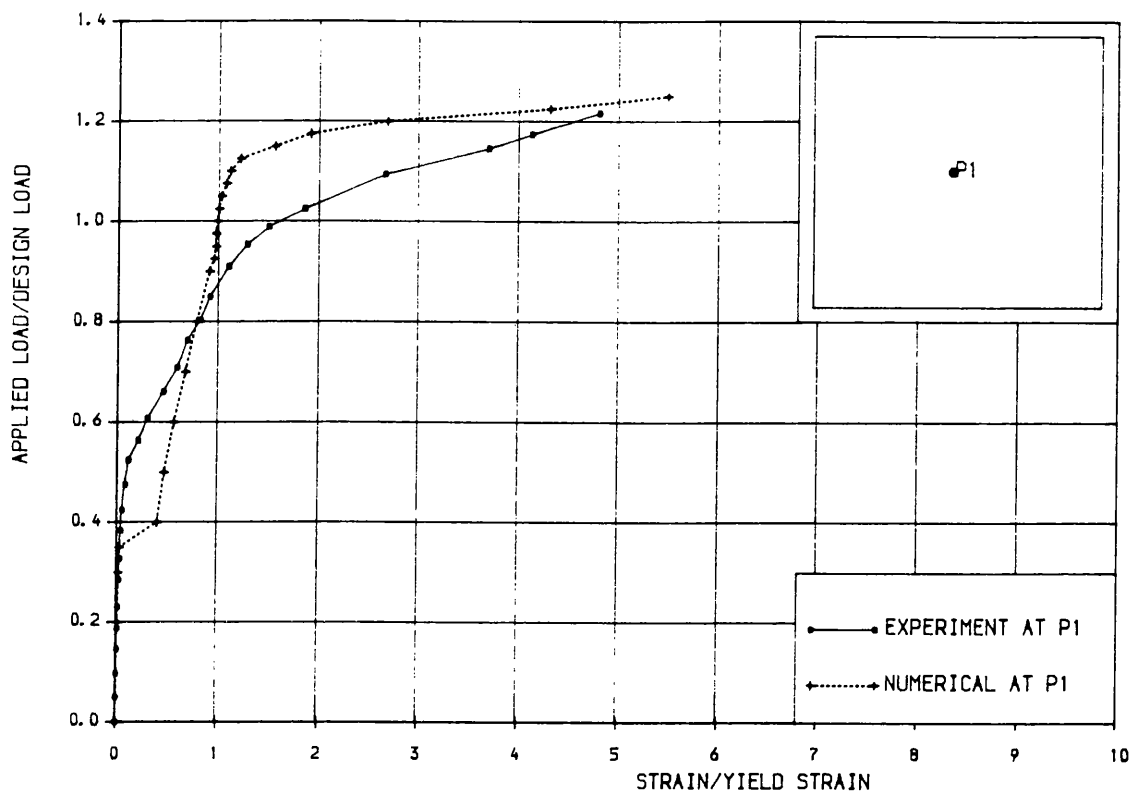


Fig. 8.22a Load-bottom steel strain curve. Model S.2

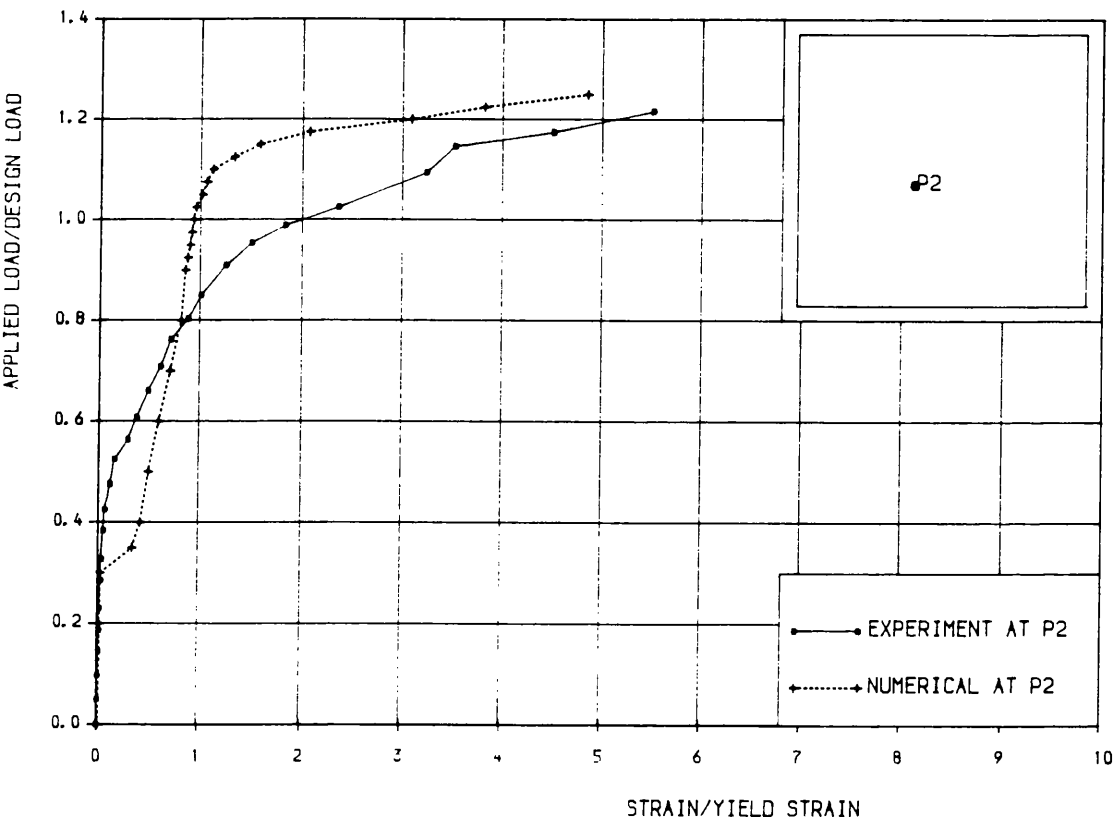


Fig. 8.22b Load-bottom steel strain curve. Model S.2

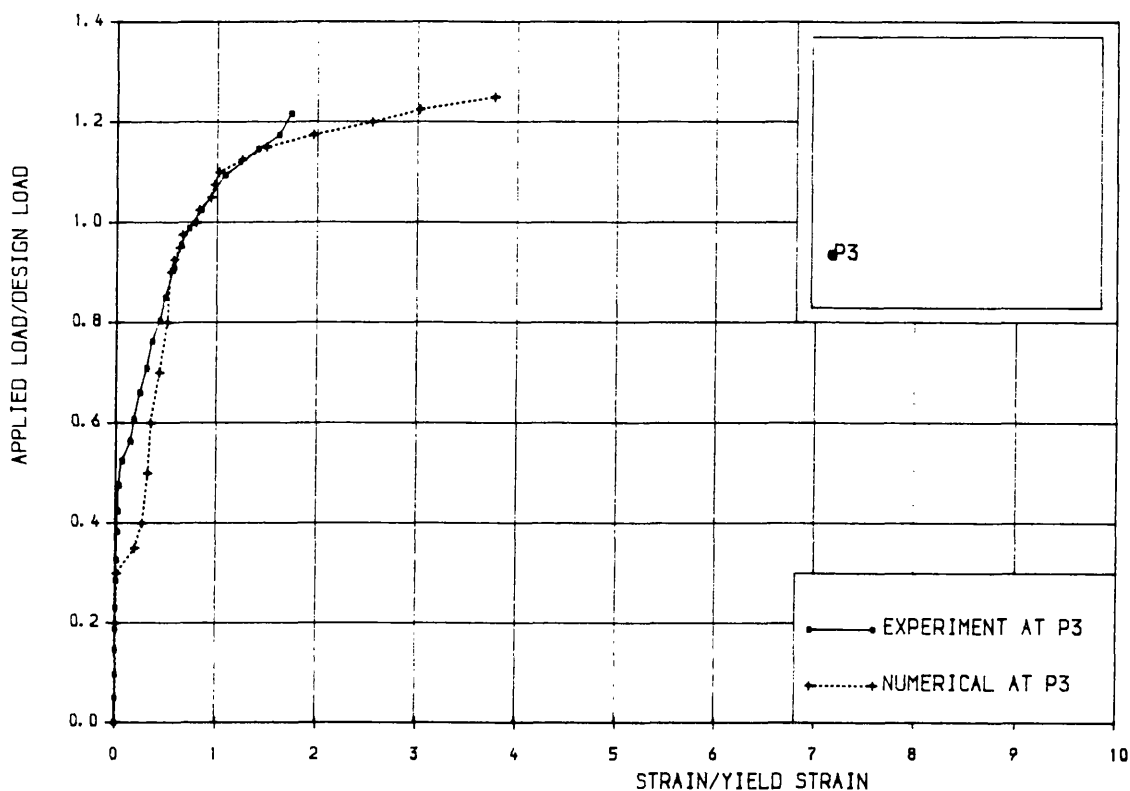


Fig. 8.22c Load-bottom steel strain curve. Model S.2

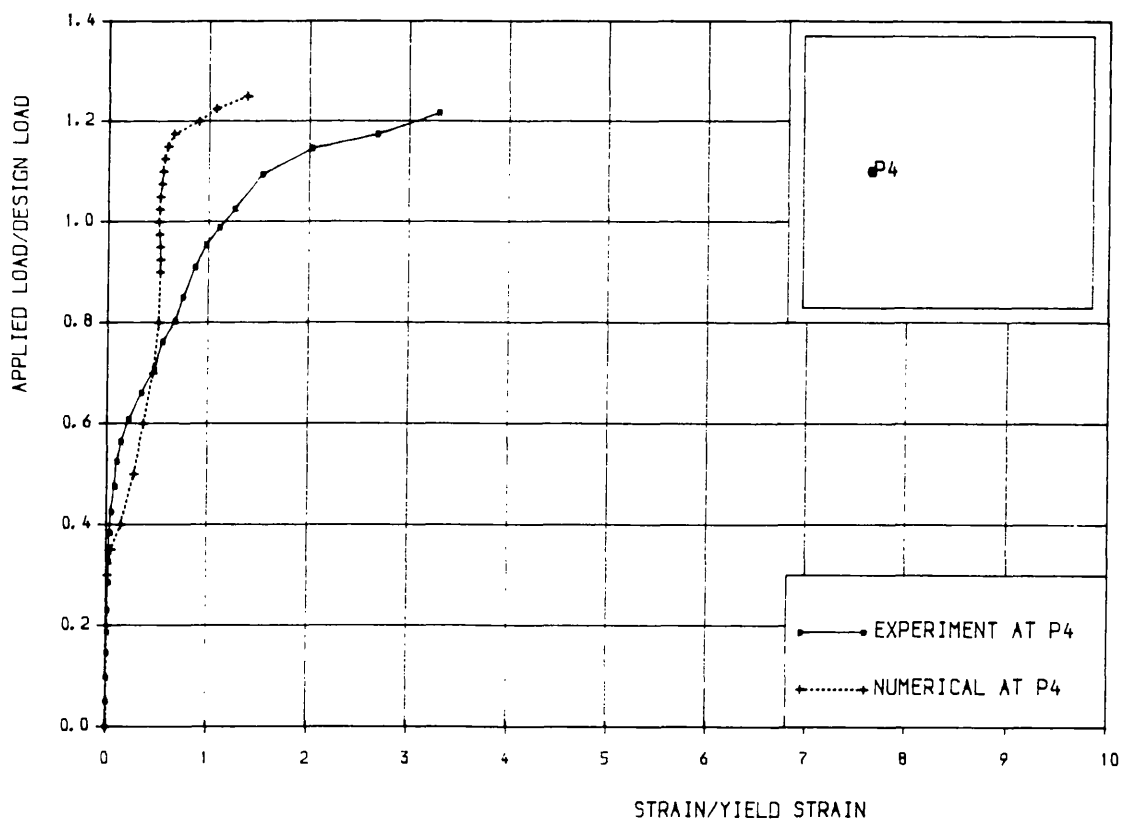


Fig. 8.22d Load-bottom steel strain curve. Model S.2

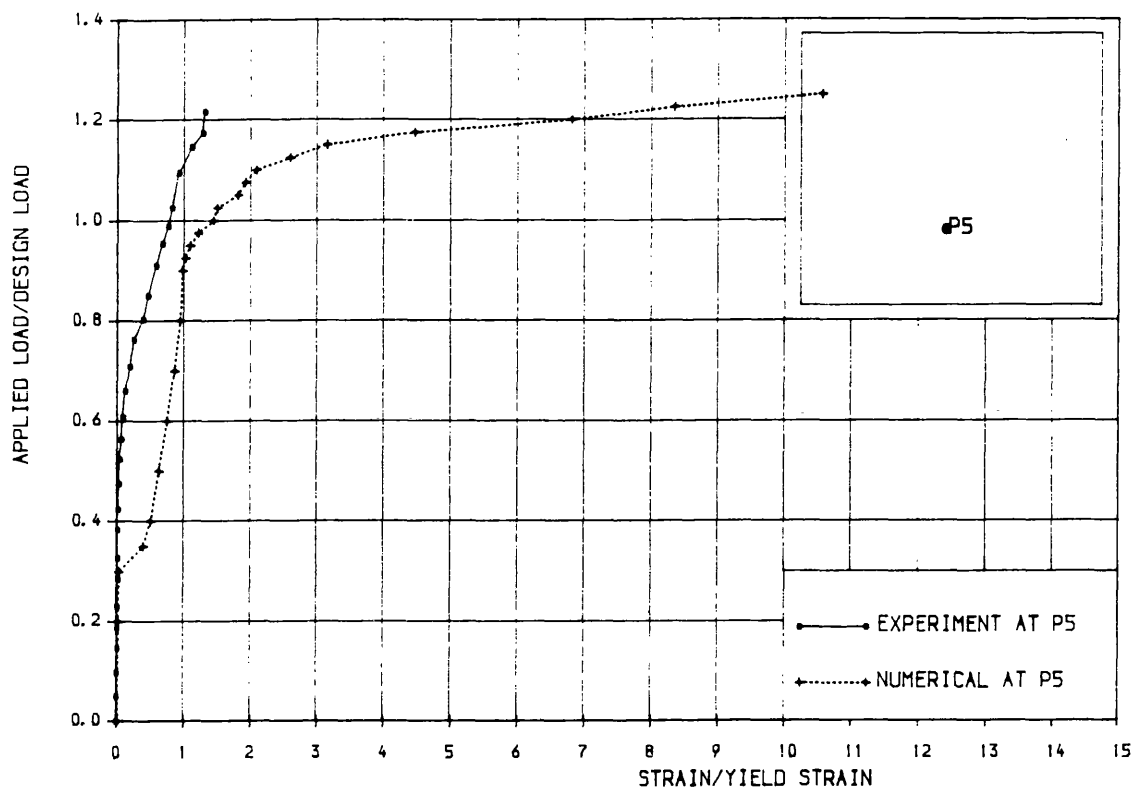


Fig. 8.22e Load-bottom steel strain curve. Model S.2

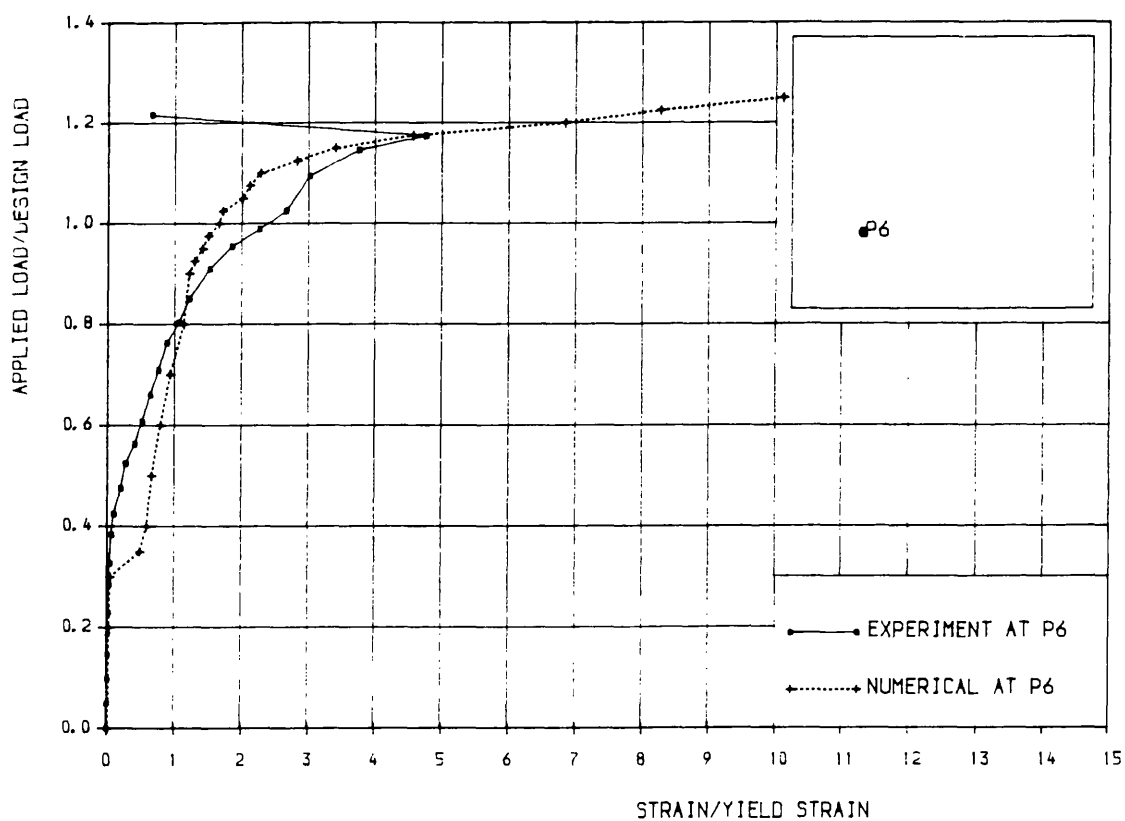


Fig. 8.22f Load-bottom steel strain curve. Model S.2

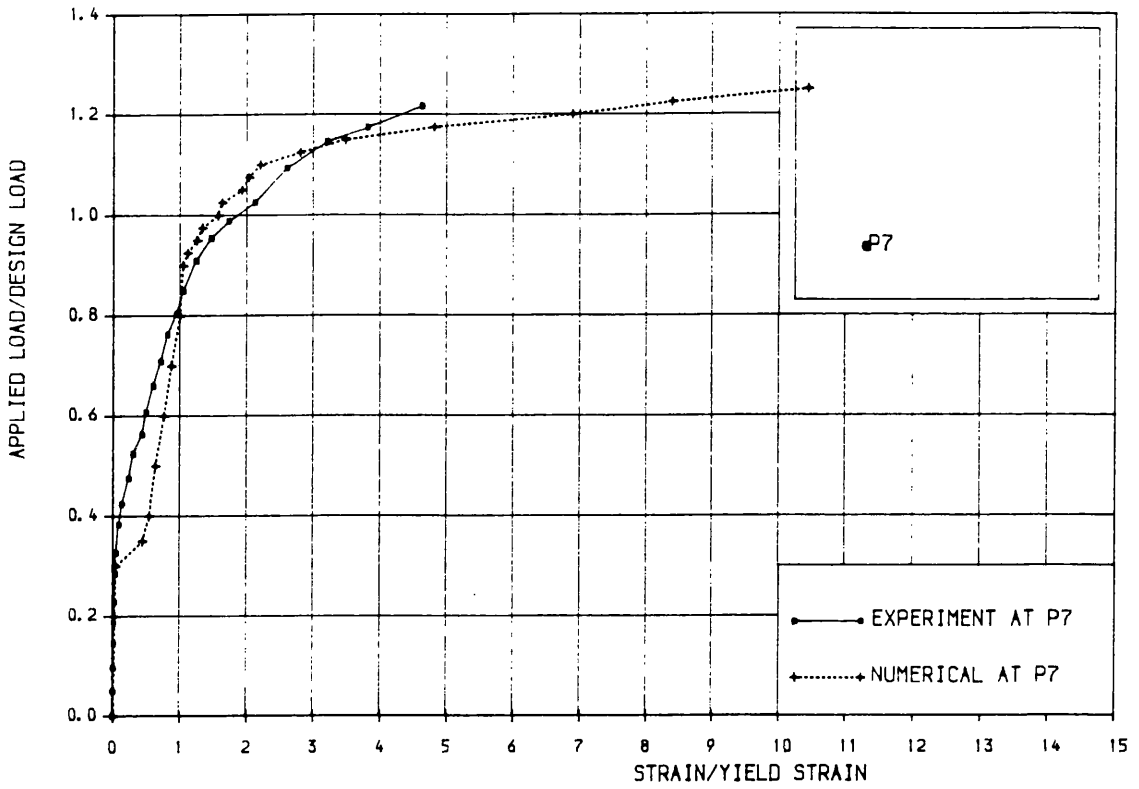


Fig. 8.22g Load-bottom steel strain curve. Model S.2

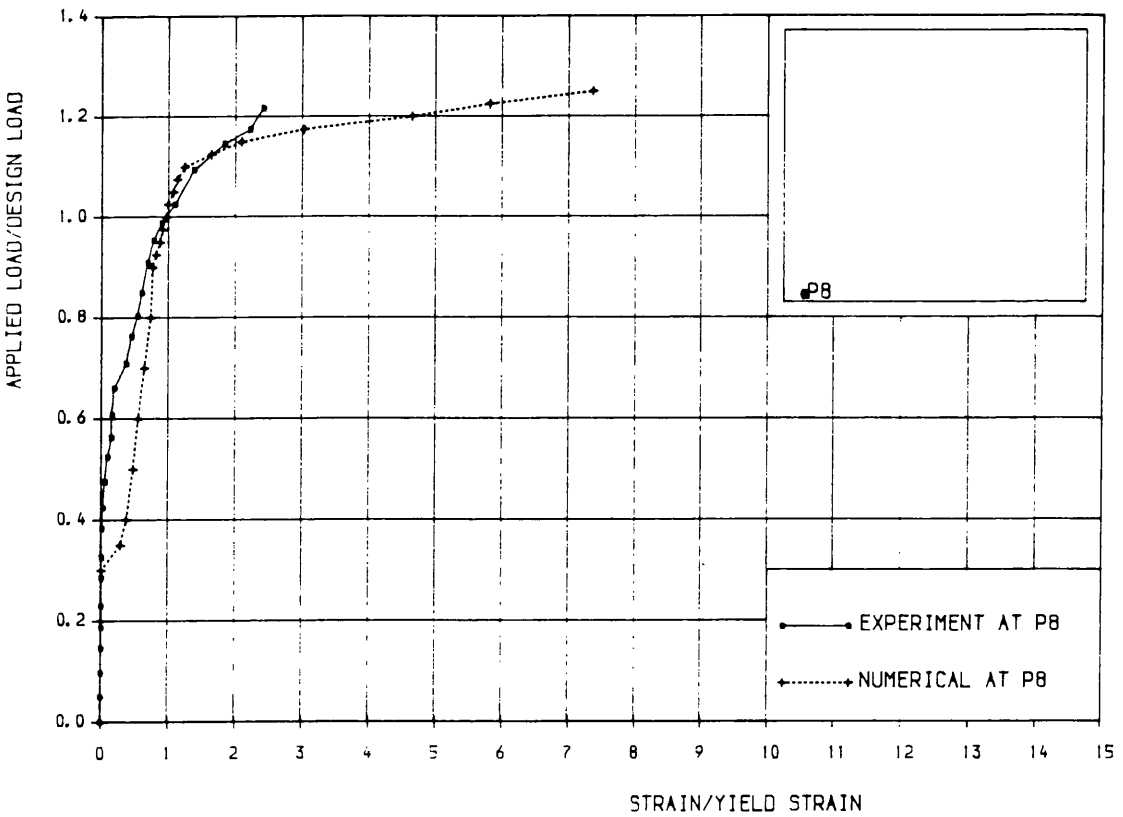


Fig. 8.22h Load-bottom steel strain curve. Model S.2

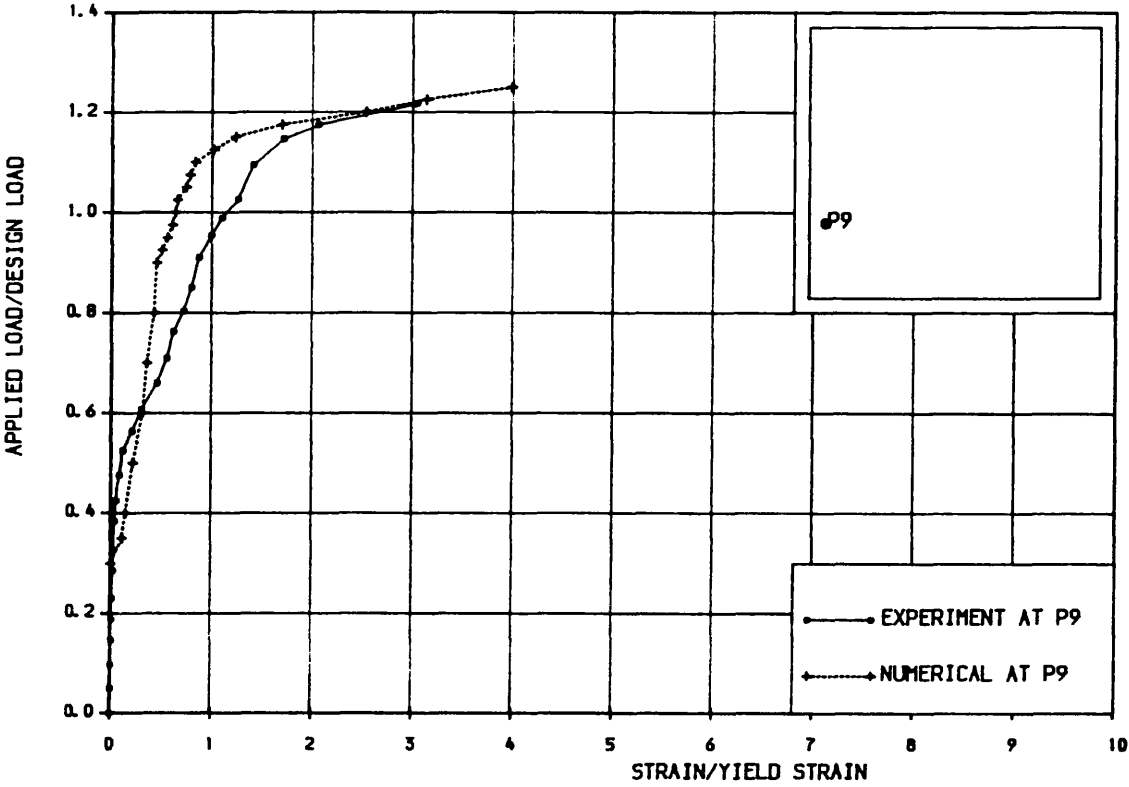


Fig. 8.22i Load-top steel strain curve. Model S.2

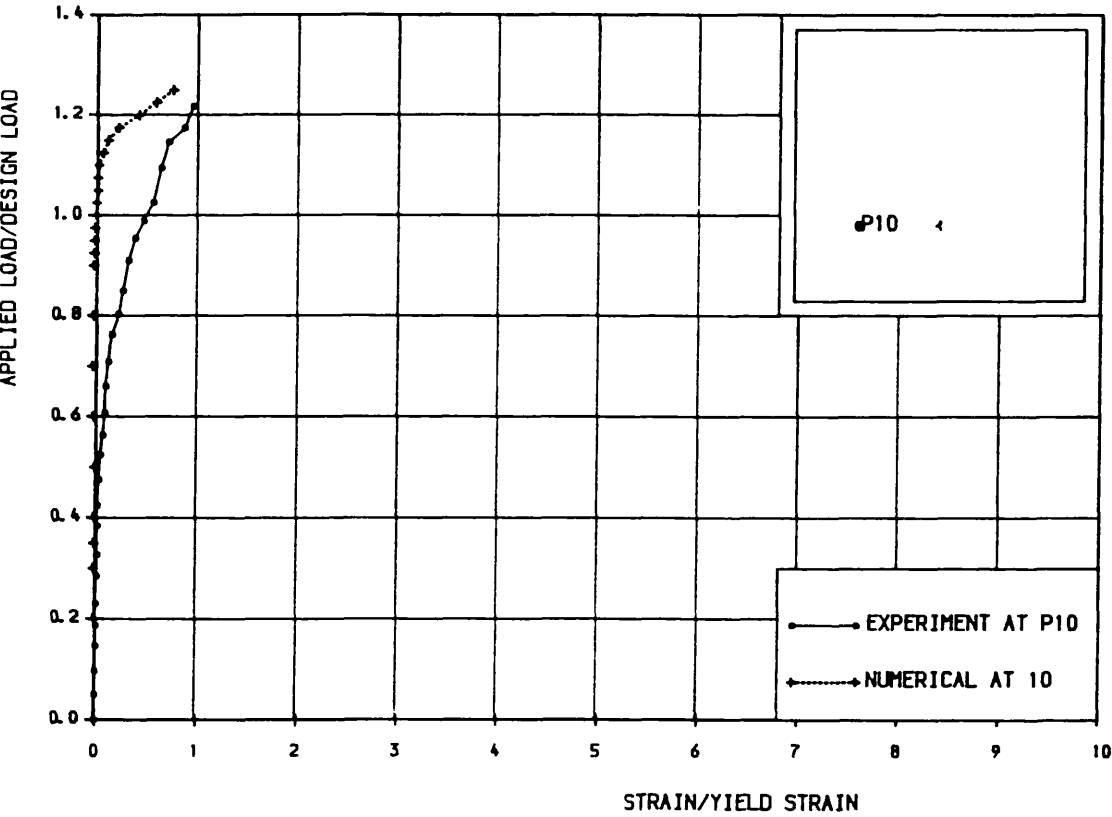


Fig. 8.22j Load-top steel strain curve. Model S.2

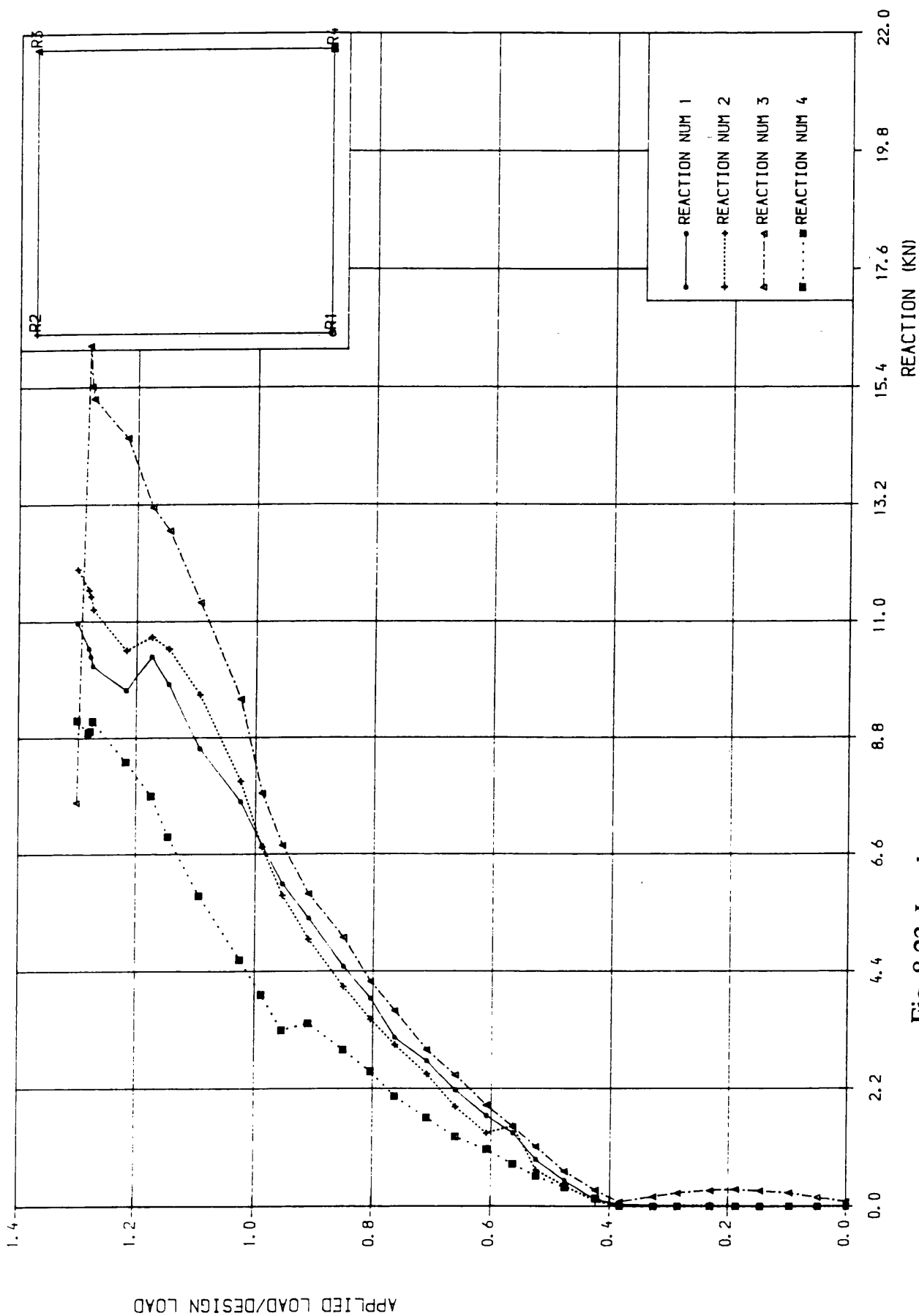


Fig. 8.23 Load-corners reaction curves. Model S.2

8.2.1.3 Model S.3:

This model was a square simply supported slab. Dimensions, loading arrangements were the same as for the previous two models. The slab was designed for the same load of 210 KN but using 30% of plasticity stress distribution.

Initially the slab was loaded in small increments of 0.1 of the design load for the first four increments. For later increments, an average of 0.05 of P_d was used. The first visible crack was observed at 0.41 P_d (0.30 P_u) under the point load at an angle of 45° and 0.03 mm wide. At 0.48 P_d (0.35 P_u) the cracks reached the middle of the slab with some cracks parallel to the lines joining two adjacent load points. The cracks reached the corner supports at 0.52 P_d (0.38 P_u) and the yield line pattern had developed, figure 8.24a. The permissible deflection $\text{span}/250 = 8$ mm and the maximum permissible crack width of 0.3 mm were reached at 0.62 P_d (0.45 P_u), figure 8.25a. At 0.66 P_d more cracks progressed towards the corners and a few new cracks were opening in the middle whereas the old ones were widening. At this level of loading the maximum crack width was 0.35 mm, on the line joining the corners to the point loads. More cracks parallel to the edges and near the point loads opened at 0.71 P_d (0.51 P_u). First yield of reinforcement was detected at 0.75 P_d (0.54 P_u) under the point load, figure 8.26c, while in the central zone at 0.95 P_d (0.69 P_u), figure 8.26a. During further load increments few new cracks appeared. The maximum crack width of 0.6 mm was attained at 0.85 P_d . Figure 8.24b shows that at the design load, cracks covered most of the central area surrounded by the points loads and the diagonal zones towards the corners. On further loading very few new cracks were forming, in contrast to the widening of the old cracks. The first crack at the top face of the slab was seen at 1.05 P_d (0.76 P_u). At this stage most of the strain gages in the bottom reinforcement indicate that steel had yielded. At 1.22 P_d more cracks opened at the top surface towards the points loads, while the maximum bottom crack width along the diagonal was of 1.5 mm. More cracks spread at the top surface at 1.30 P_d towards the point loads. The failure took

place at 1.38 Pd with new top surface cracks and the maximum crack width at the bottom face was of 5.0 mm. Figure 8.24c shows the bottom crack pattern at collapse load. The top concrete surfaces of the diagonals, between the point loads and the corners, crushed, figure 8.24d.

Deflections:

Figures 8.25a to 8.25j show the load–deflection curves of the chosen points of the slab. The load deflection relationship shows that nonlinearity started before 0.41 Pd where the first visible crack was seen. Limiting service deflection of the central point (8 mm) was reached at 0.62 Pd (0.45 Pu). This represents a low serviceability in terms of the ultimate load. The maximum deflection of the central point was of 69.12 mm, figure 8.25a.

Steel Strains:

Figures 8.26 and 8.27 represent the load–strain curves of measured points for bottom and top reinforcement respectively. The first yielding of steel occurred under the point load at 0.75 Pd (0.54 Pu), figure 8.26c. At the design load all the bottom steel points had yielded, figures 8.26. Figures 8.27 show that at collapse load top steel did not yield.

Crack width:

The first crack appeared at 0.41 Pd (0.30 Pu) in the bottom surface under the point load. The service limit crack width of 0.3 mm was reached at 0.62 Pd (0.45 Pu). A maximum crack width was 0.85 mm at the design load, while at collapse load a 5.0 mm wide crack was recorded. Crack pattern for both bottom and top concrete faces are presented in figures 8.24a to 8.24d.

Reactions:

It is clear from figure 8.28 that the reactions at the corners were negligible until the bottom concrete surface cracked, at 0.41 Pd. A maximum reaction of 15.9 KN was recorded which is 3% less than the one of S.2 although the ultimate

load of this model was 6% greater than the ultimate load of slab S.2.

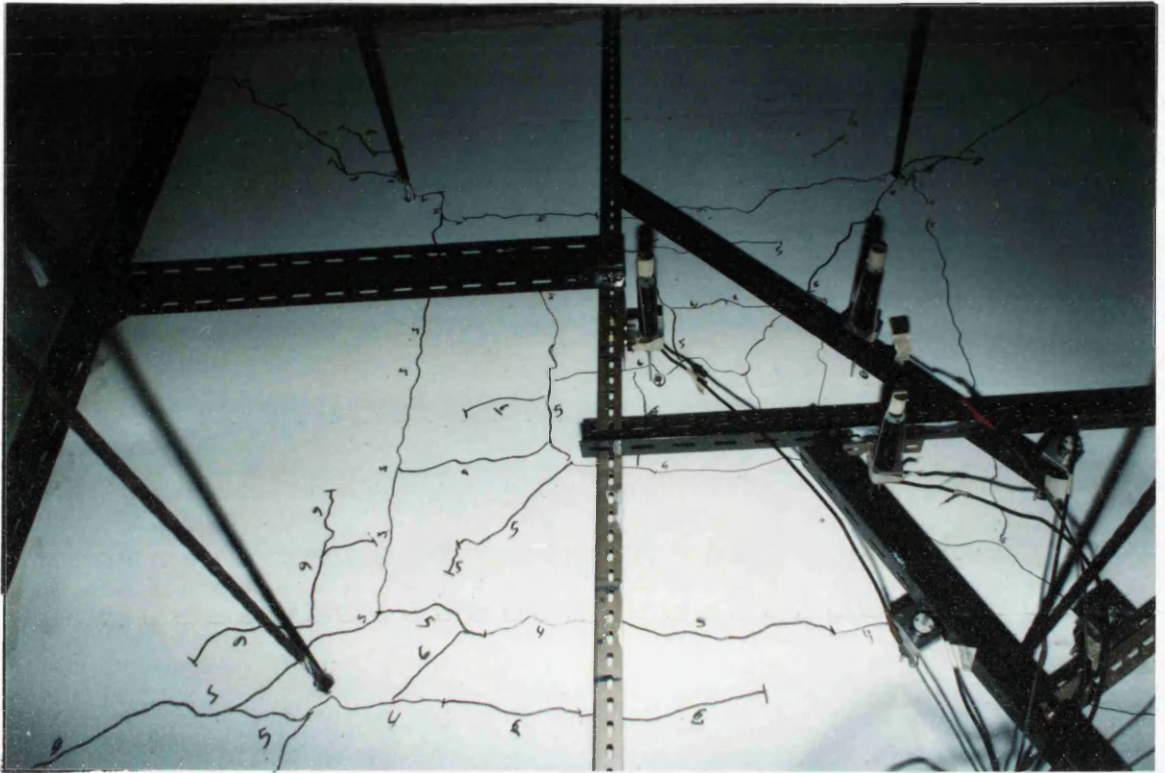
Mode of failure:

From the steel strains, and crack pattern and width it can be seen that the slab behaved in a ductile manner. The slab failed flexurally at 1.38 Pd. A little concrete crushing of the top diagonal between the point load and the corner can be seen in figure 8.24d.

Numerical analysis:

Good agreement can be seen with the experimental results as shown in figures 8.25a–j for load–deflection curves and figures 8.26 and 8.27 for load–strain curves, for both bottom and top steel, respectively. The serviceability load limit deflection of 8mm was reached at 0.5 Pd numerically while in the experiment it was reached at 0.62 Pd. The steel yielded at the same level of loading at 0.75 Pd under the point load as shown in figure 8.26c. While approaching the ultimate load the numerical values of both deflection and strain prediction were larger than the experimental results. Good agreement was obtained for crack patterns at different load stages as shown in figures 8.24a to 8.24d. Both numerically and experimentally the slab failed flexurally. The numerical failure load was 0.94 the experimental one.

Experimental



Numerical 1/4 Slab

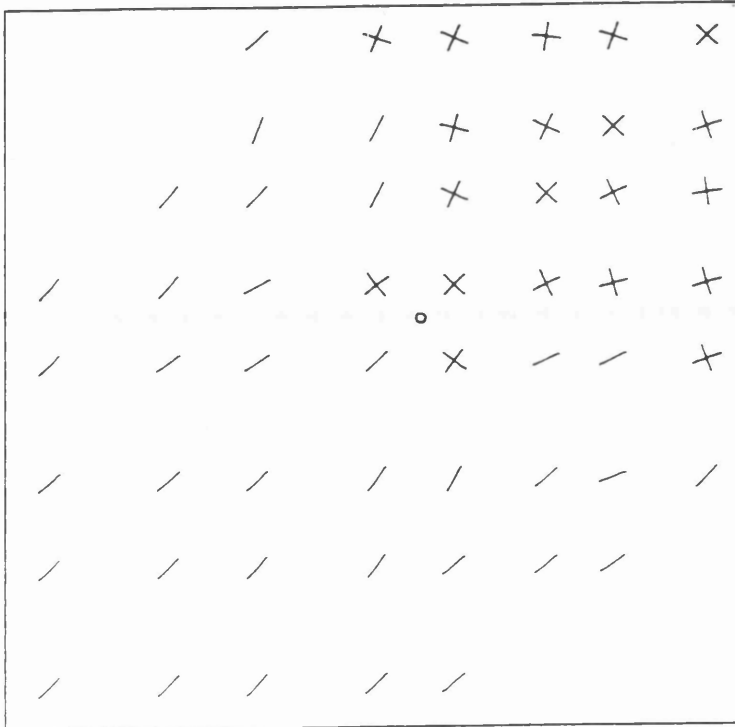
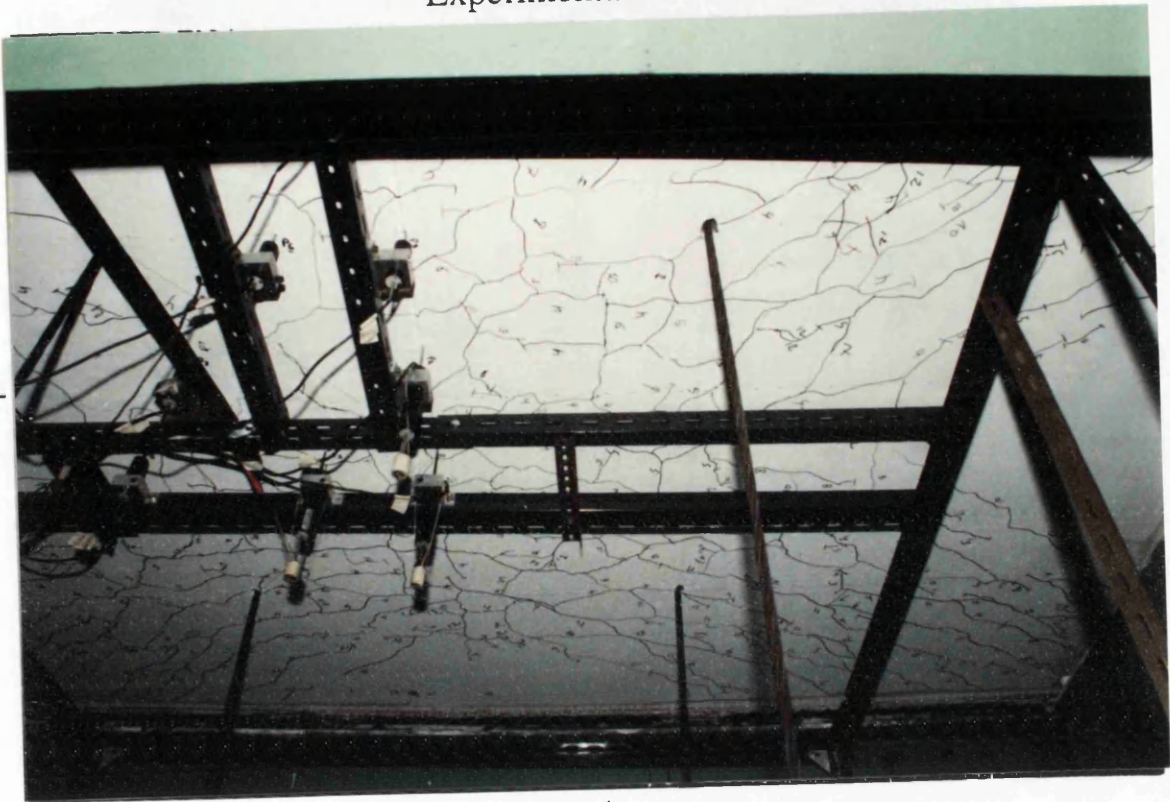


Fig. 8.24a Bottom crack pattern at 0.5 Pd
Model S.3

Experimental



Numerical 1/4 Slab

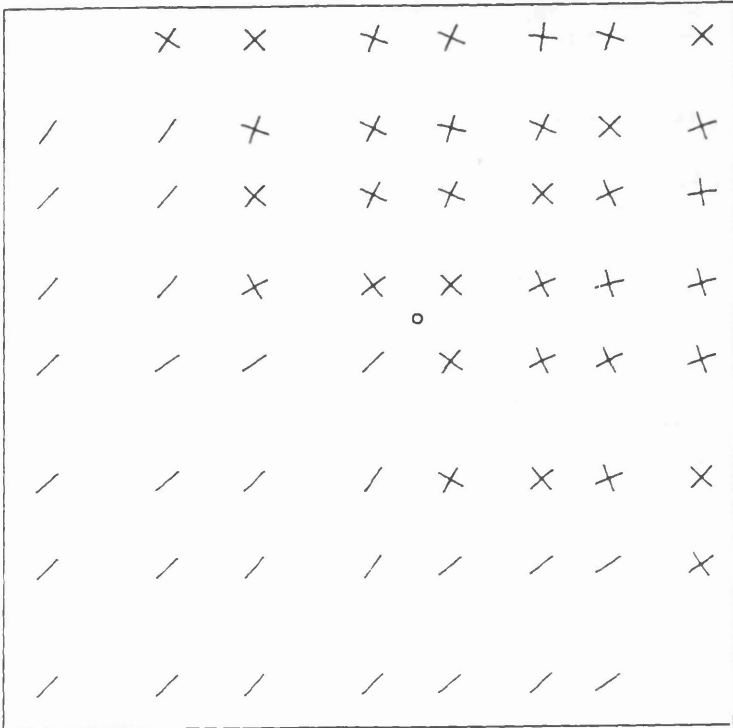
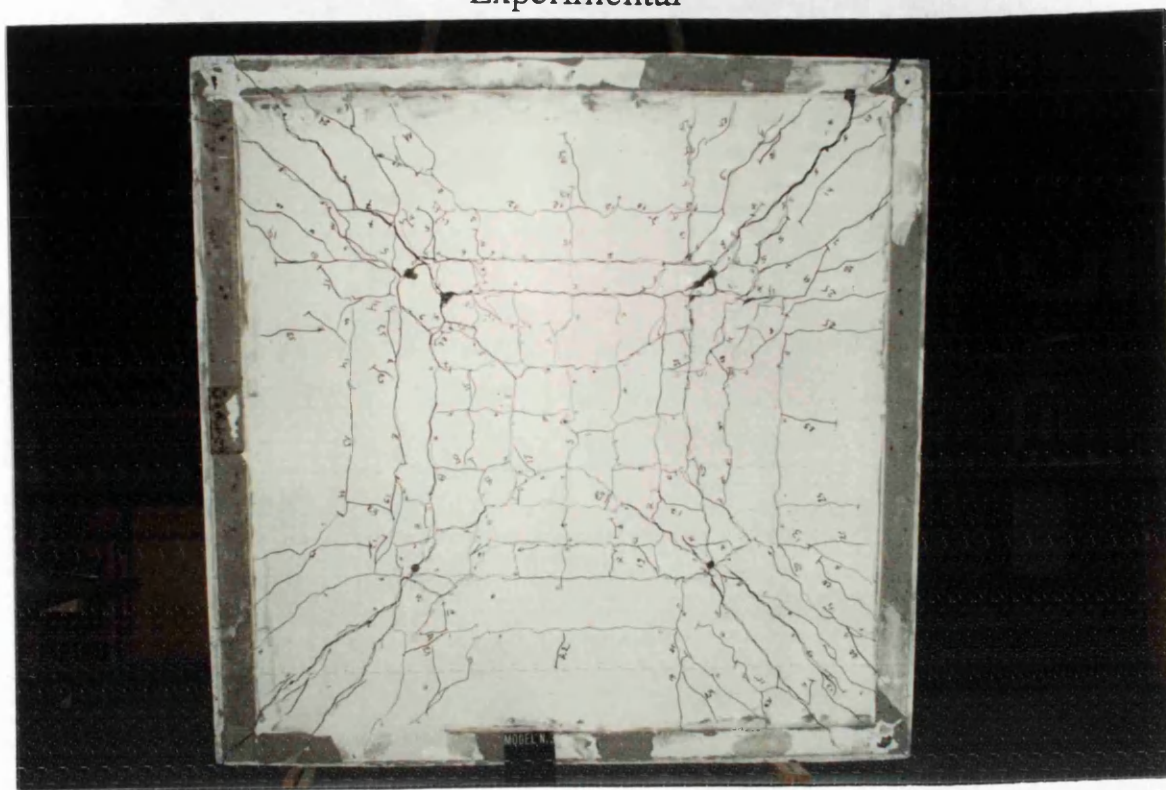


Fig. 8.24b Bottom crack pattern at design load Pd. Model S.3

Experimental



Numerical 1/4 Slab

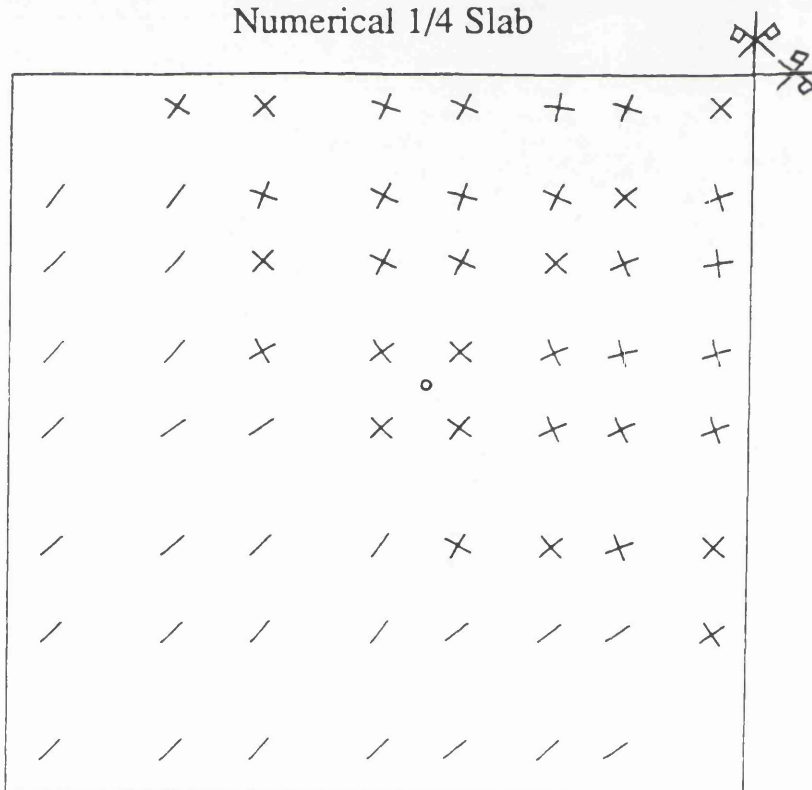
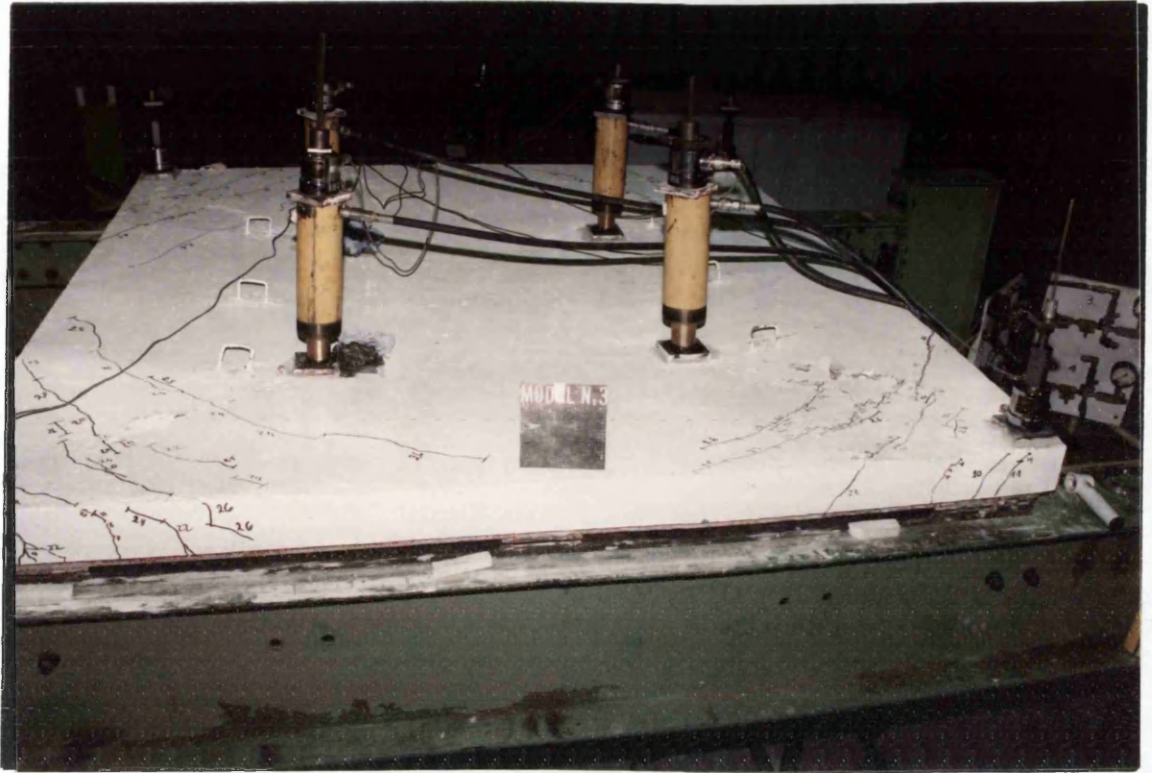


Fig. 8.24c Bottom crack pattern
at collapse load P_u . Model S.3

Experimental



Numerical 1/4 Slab

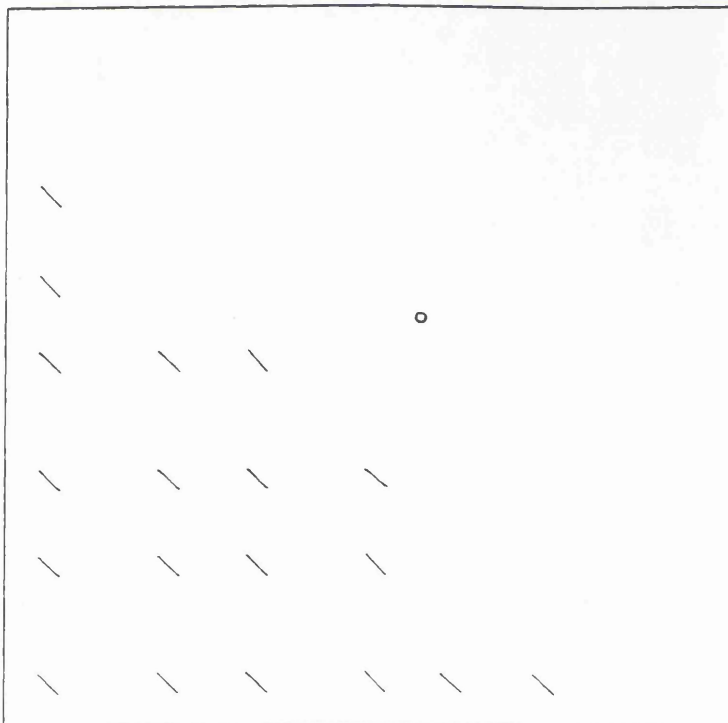


Fig. 8.24d Top crack pattern
at collapse load P_u . Model S.3

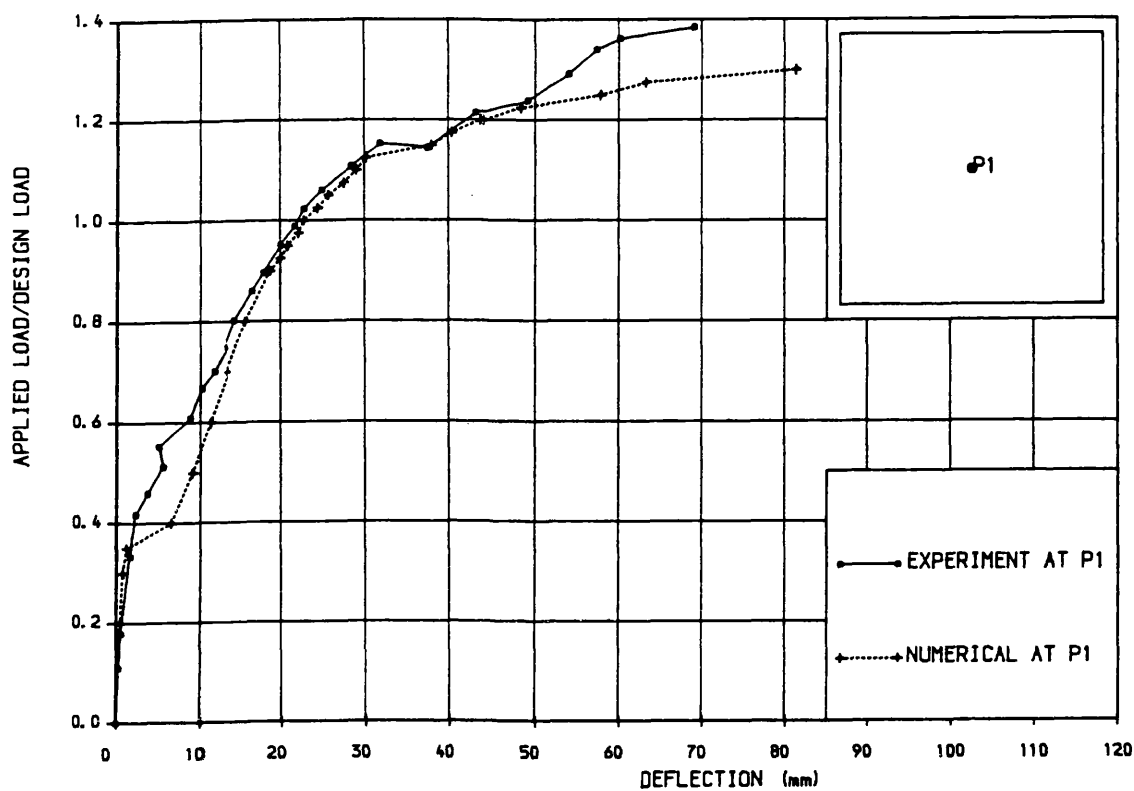


Fig. 8.25a Load-deflection curve. Model S.3

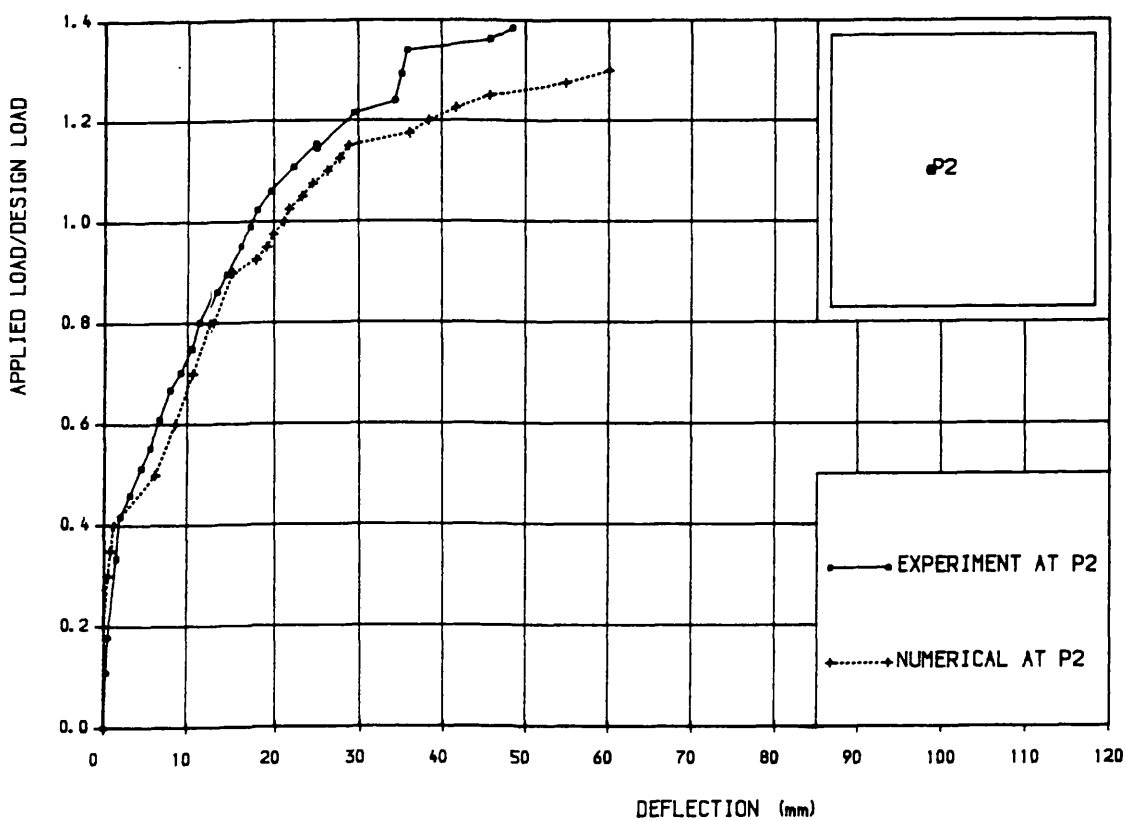


Fig. 8.25b Load-deflection curve. Model S.3

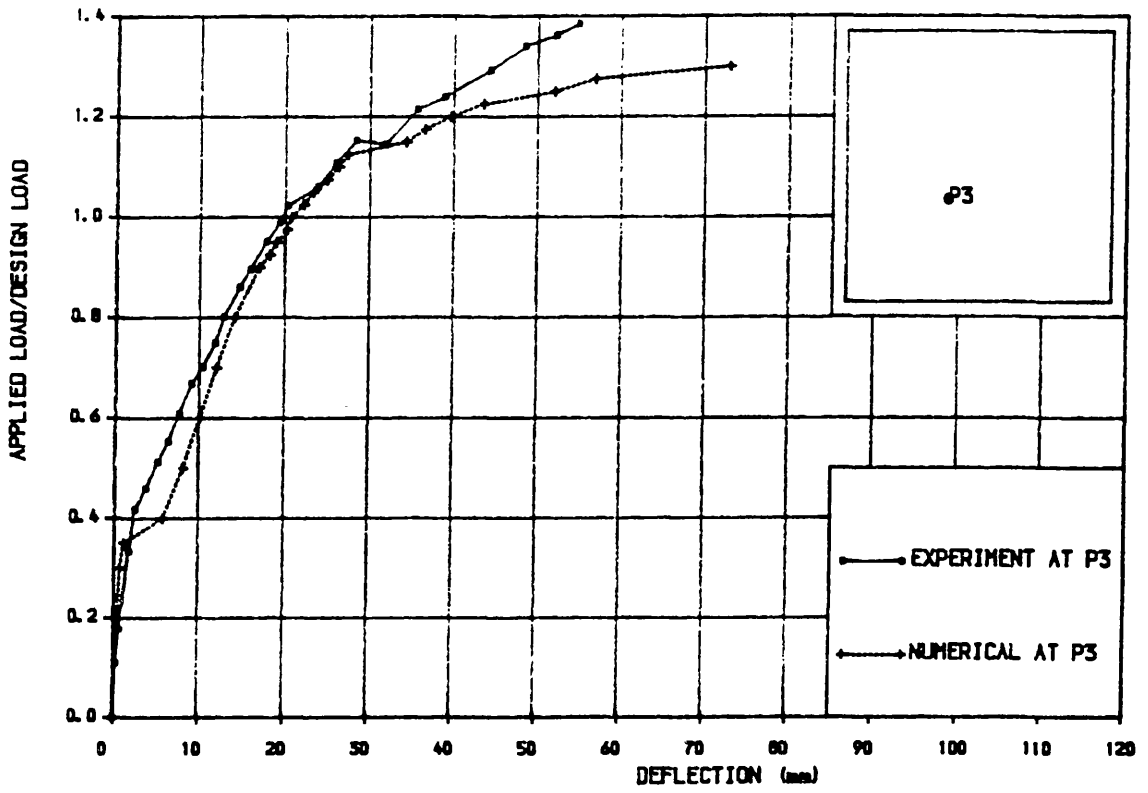


Fig. 8.25c Load-deflection curve. Model S.3

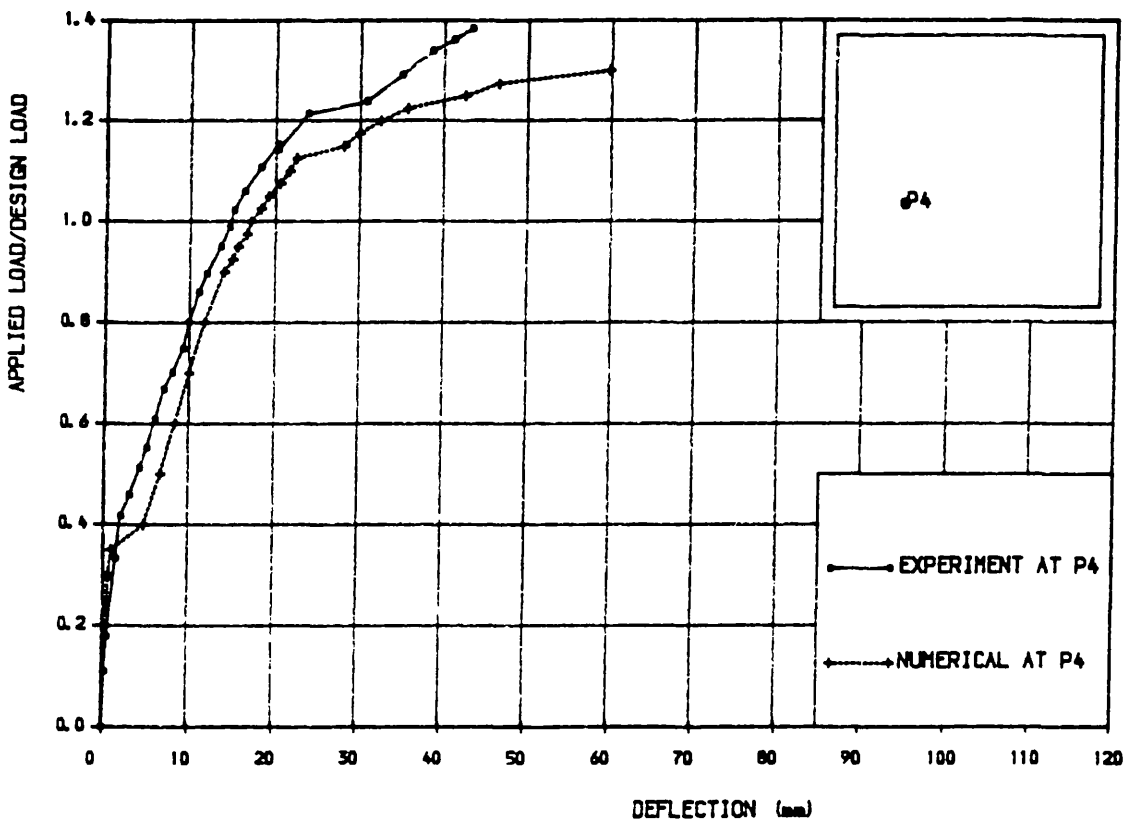


Fig. 8.25d Load-deflection curve. Model S.3

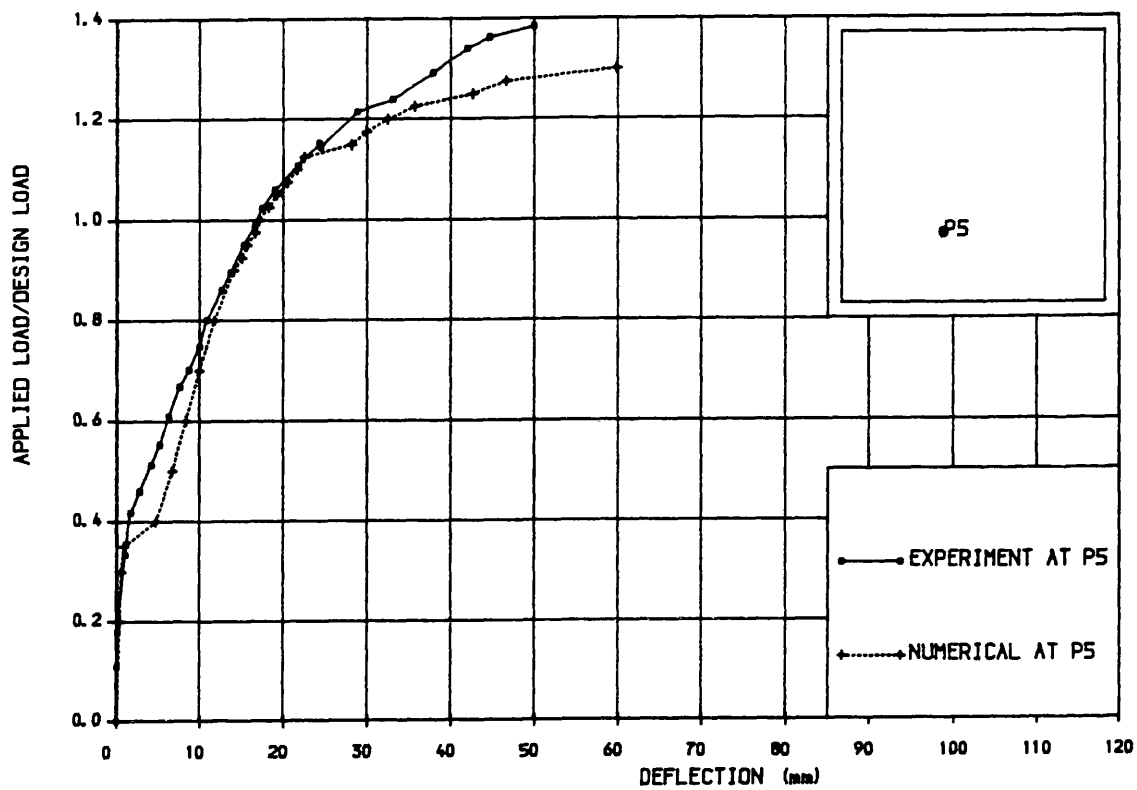


Fig. 8.25e Load-deflection curve. Model S.3

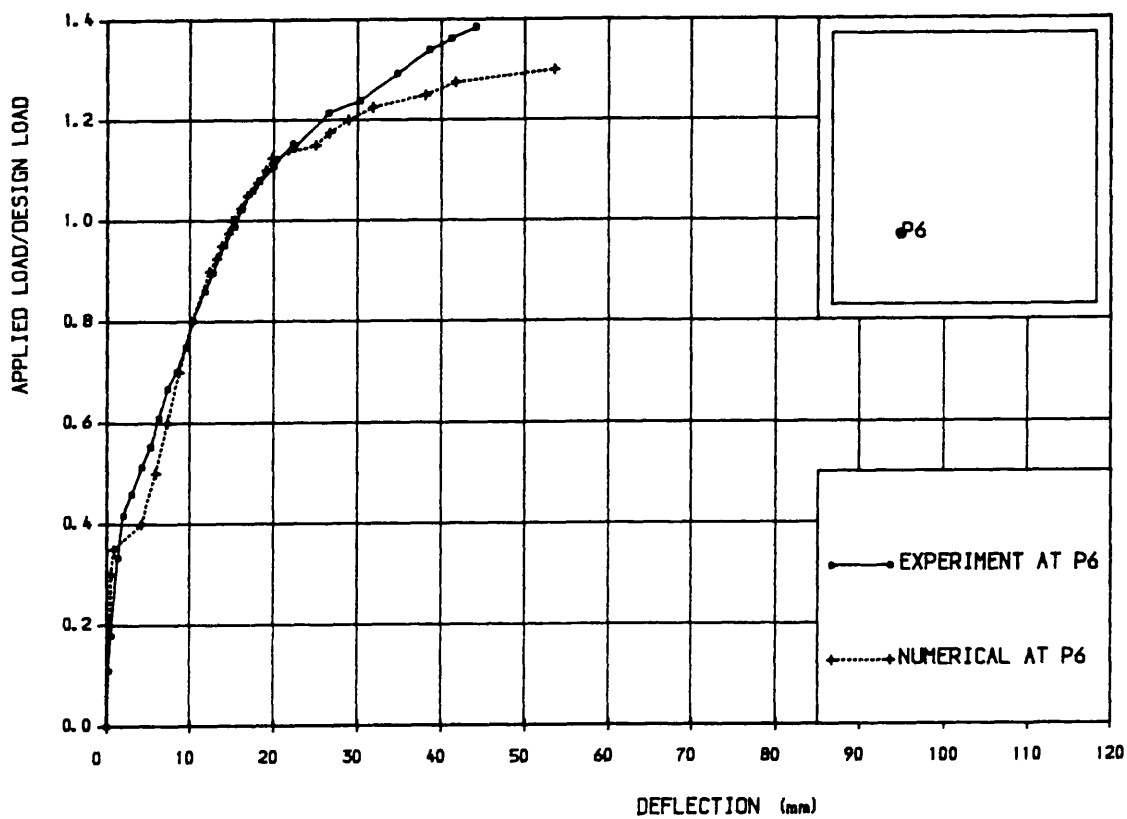


Fig. 8.25f Load-deflection curve. Model S.3

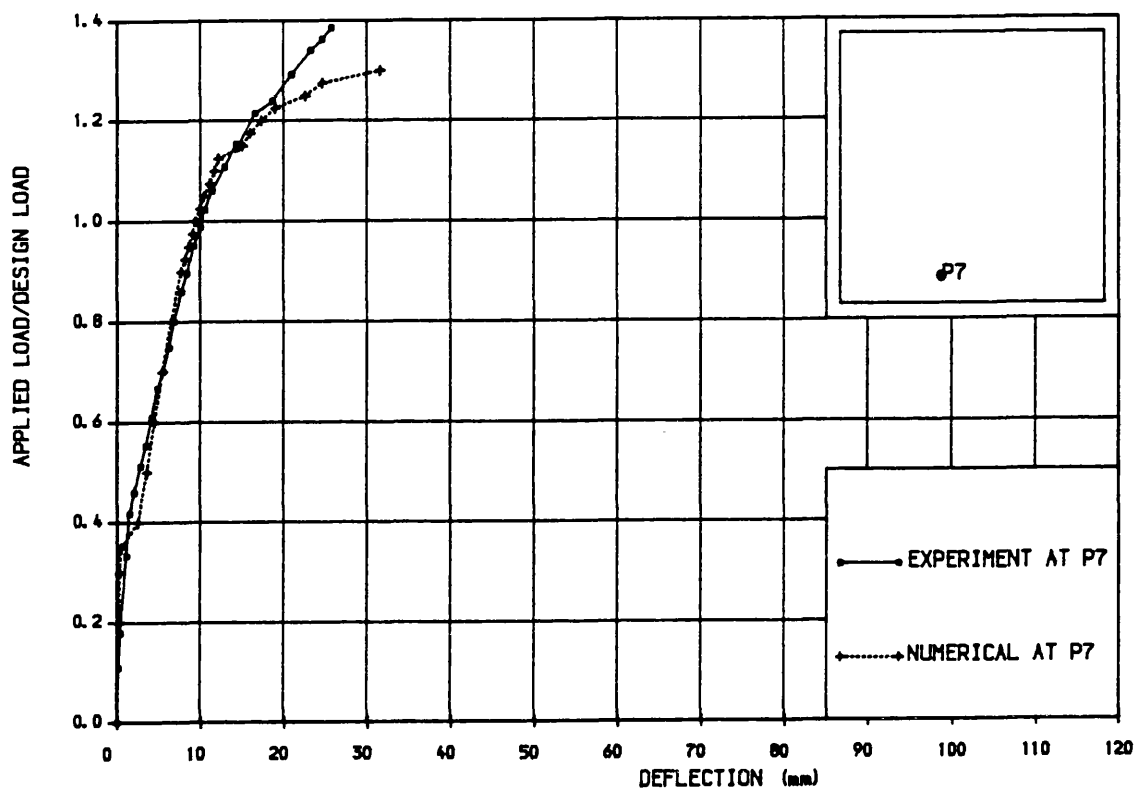


Fig. 8.25g Load-deflection curve. Model S.3

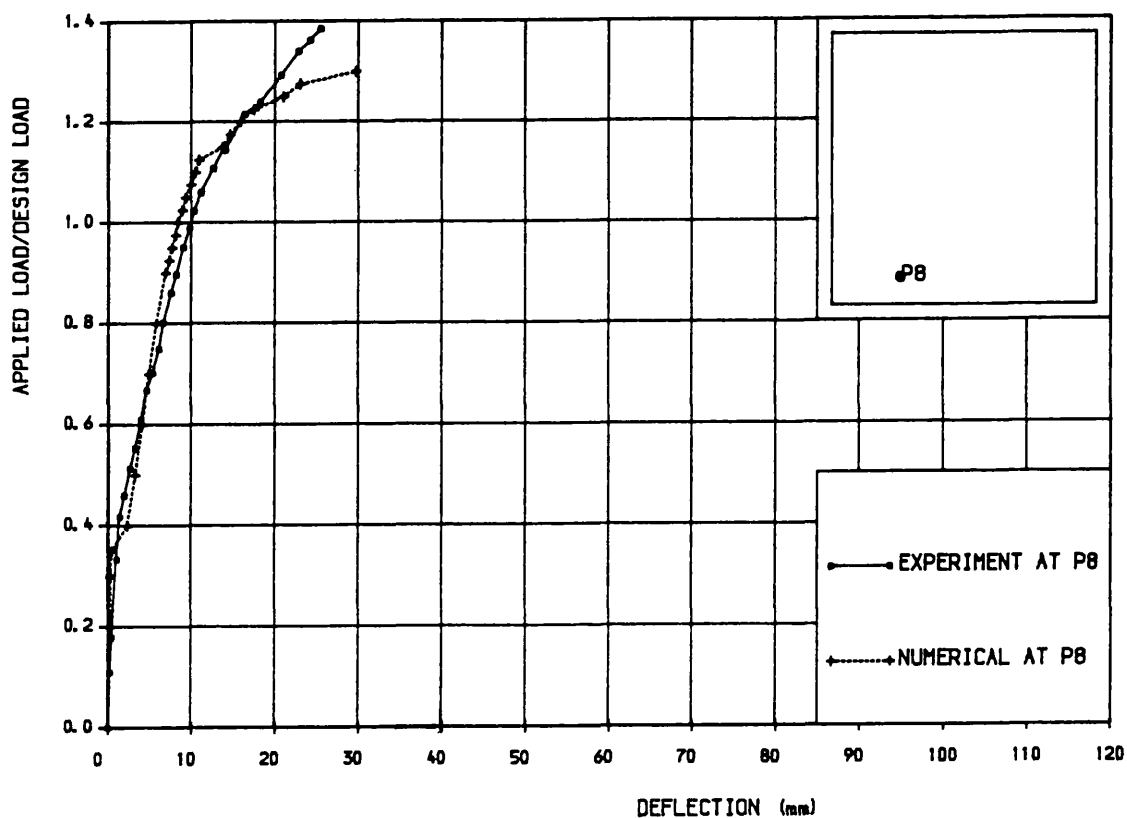


Fig. 8.25h Load-deflection curve. Model S.3

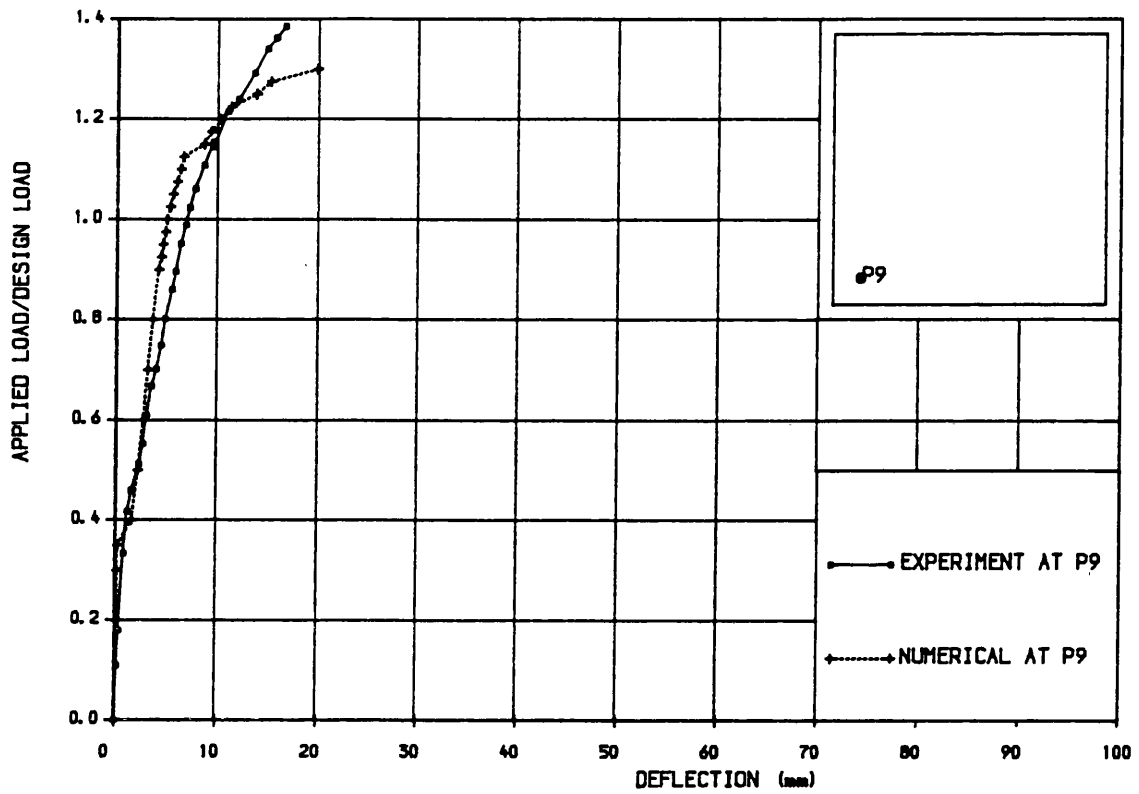


Fig. 8.25i Load-deflection curve. Model S.3

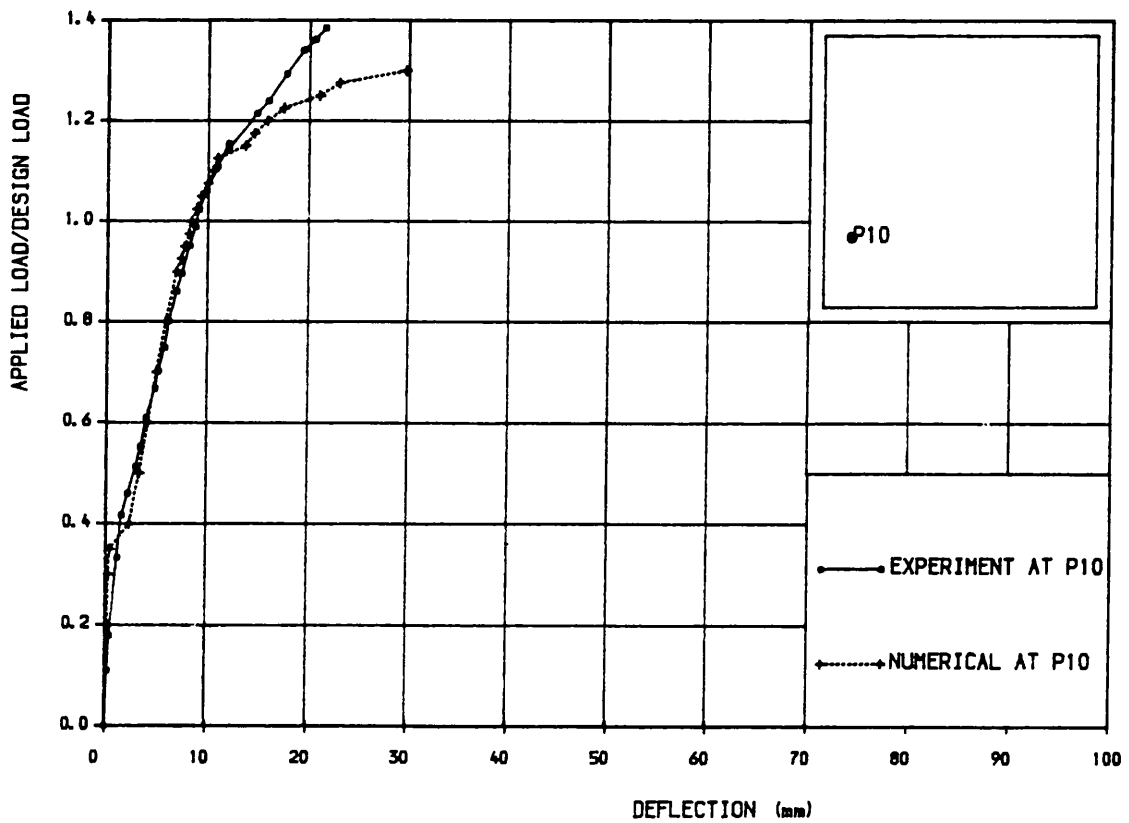


Fig. 8.25j Load-deflection curve. Model S.3

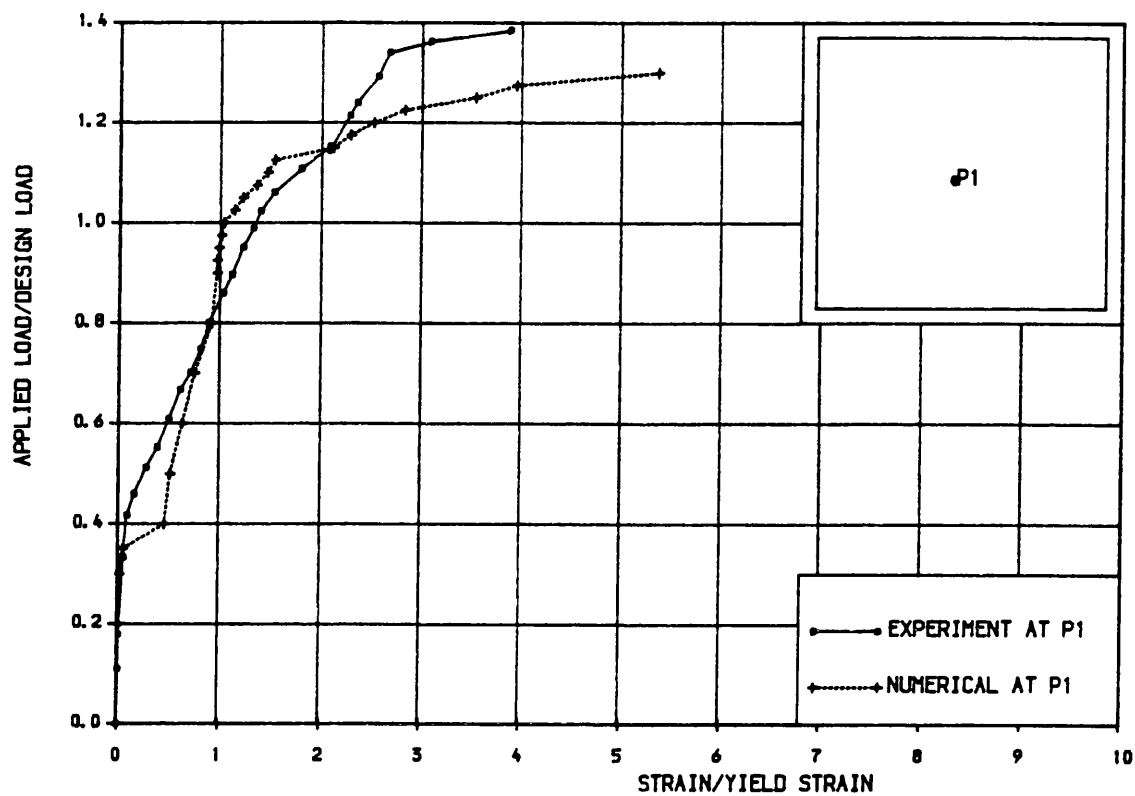


Fig. 8.26a Load-bottom steel strain curve. Model S.3

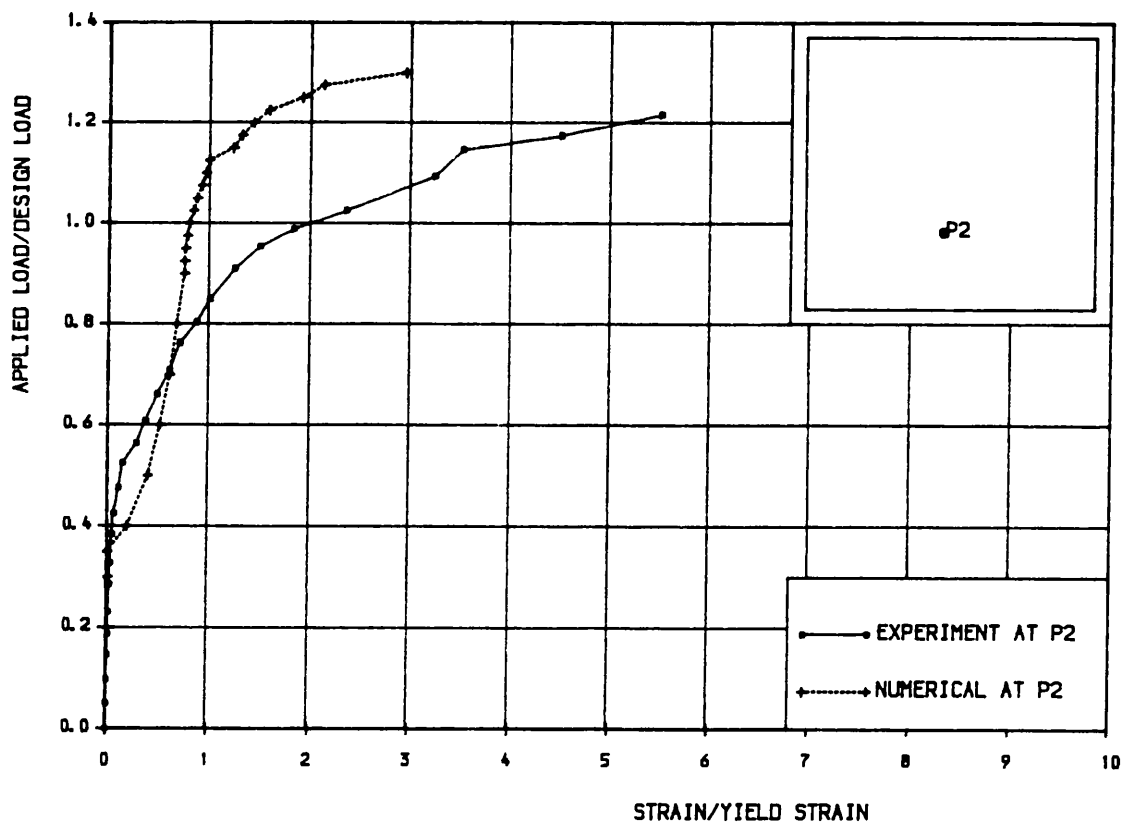


Fig. 8.26b Load-bottom steel strain curve. Model S.3

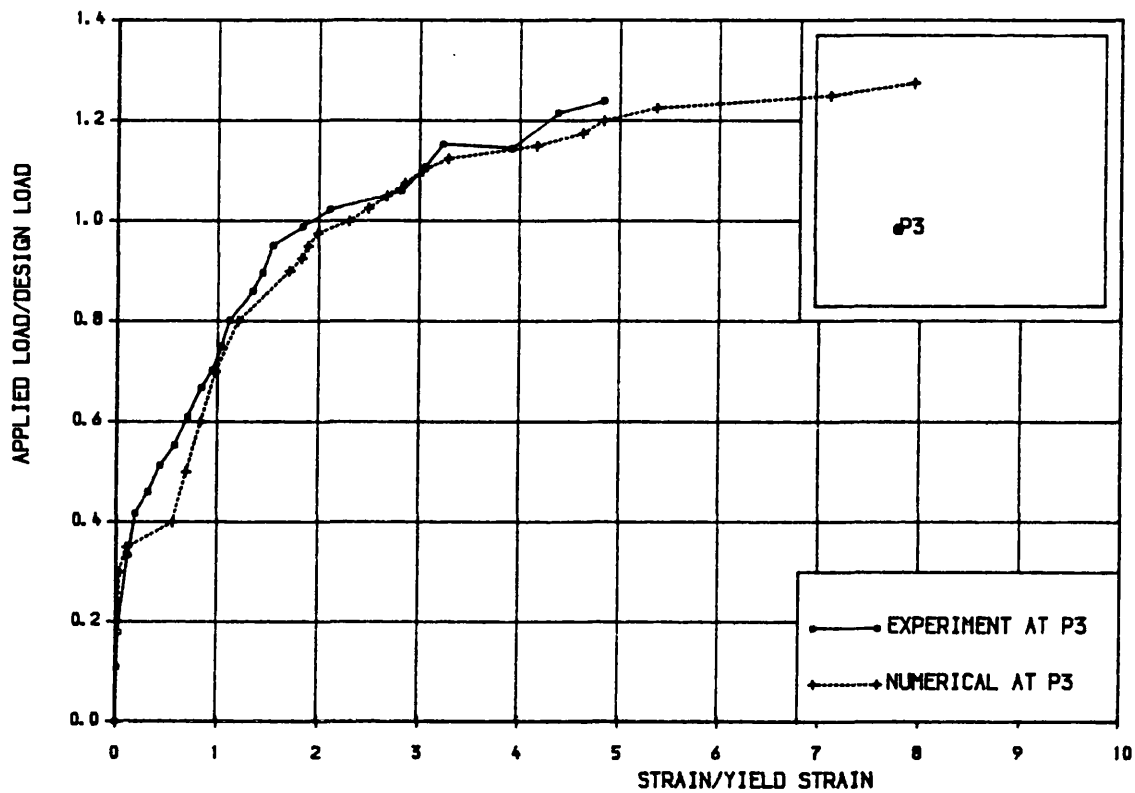


Fig. 8.26c Load-bottom steel strain curve. Model S.3

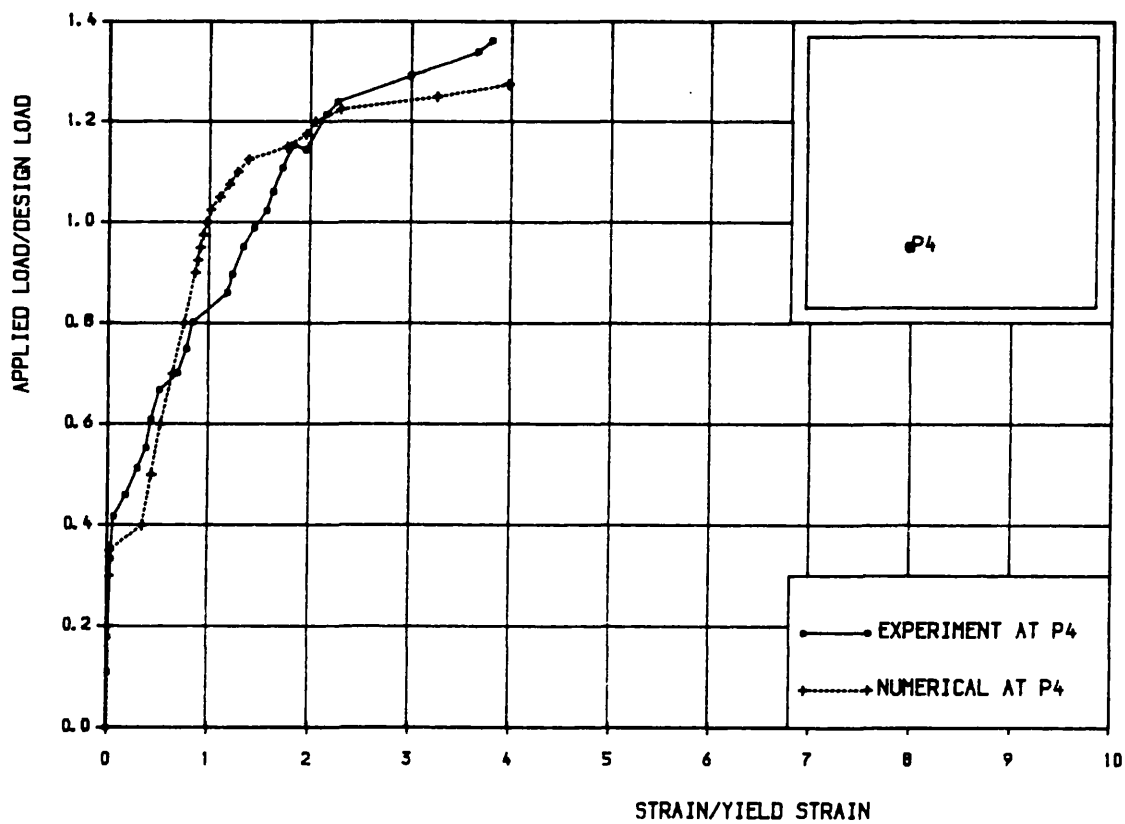


Fig. 8.26d Load-bottom steel strain curve. Model S.3

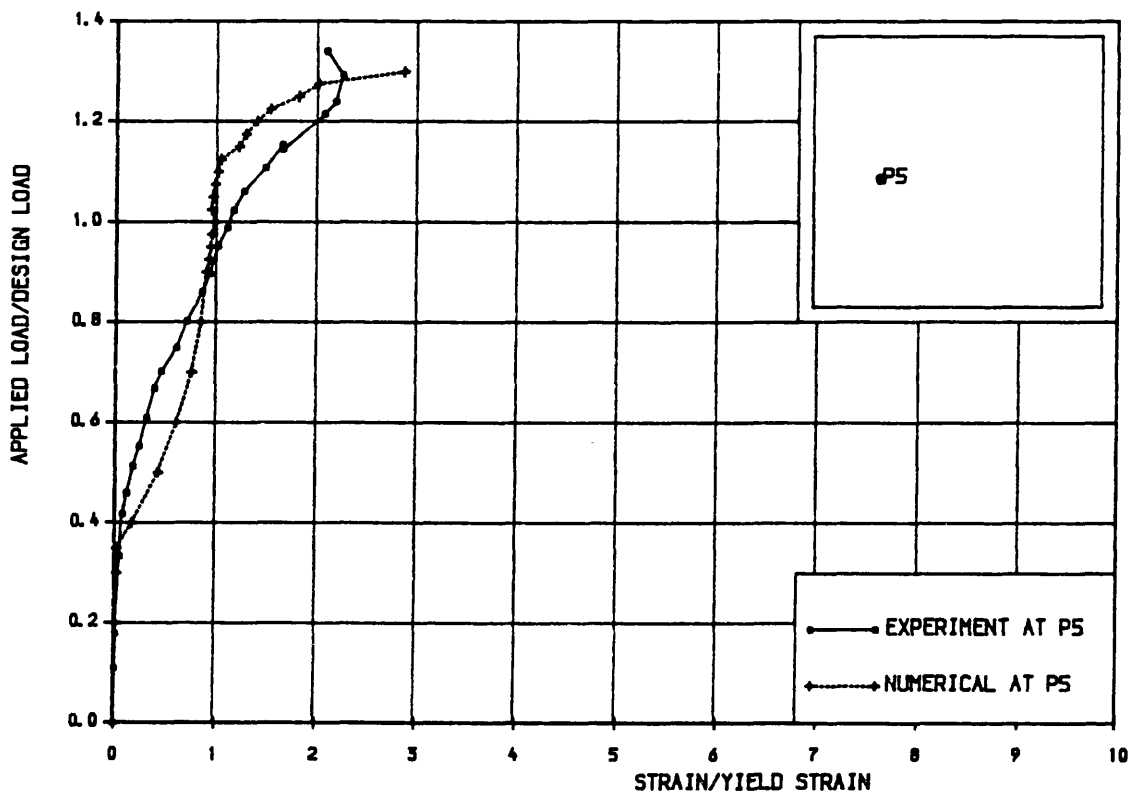


Fig. 8.26e Load-bottom steel strain curve. Model S.3

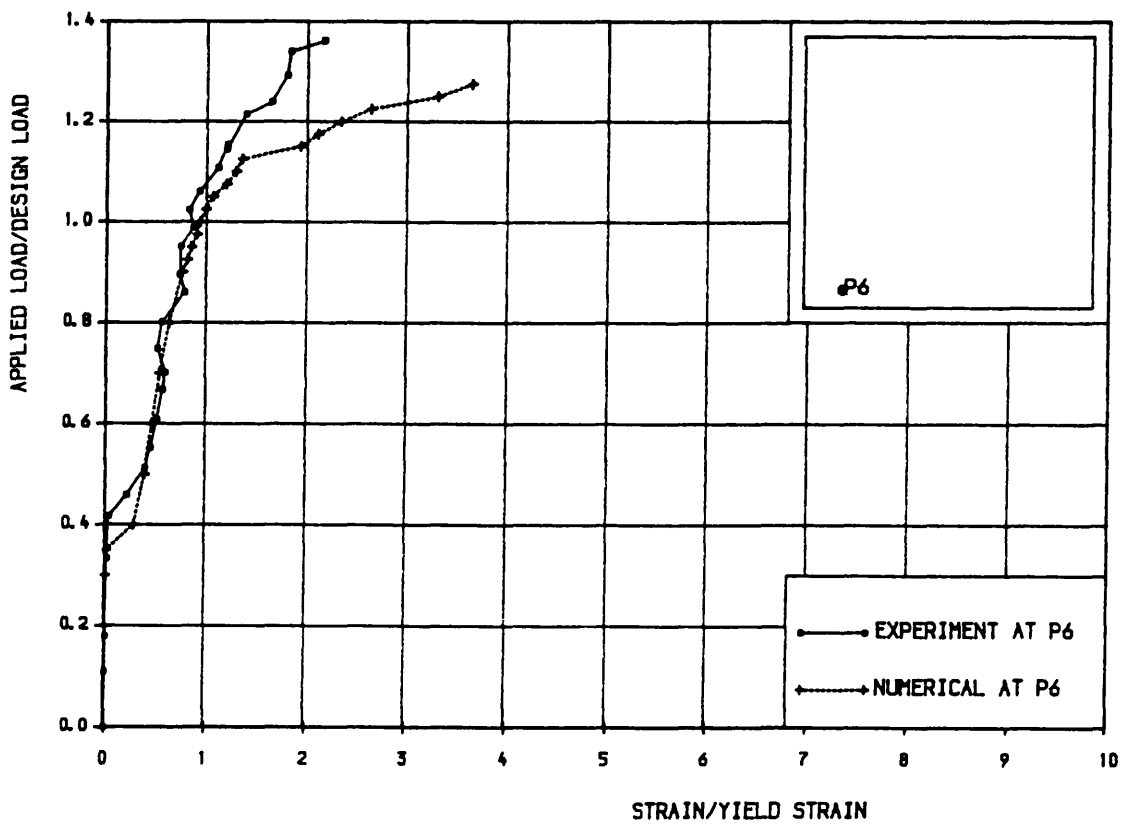


Fig. 8.26f Load-bottom steel strain curve. Model S.3

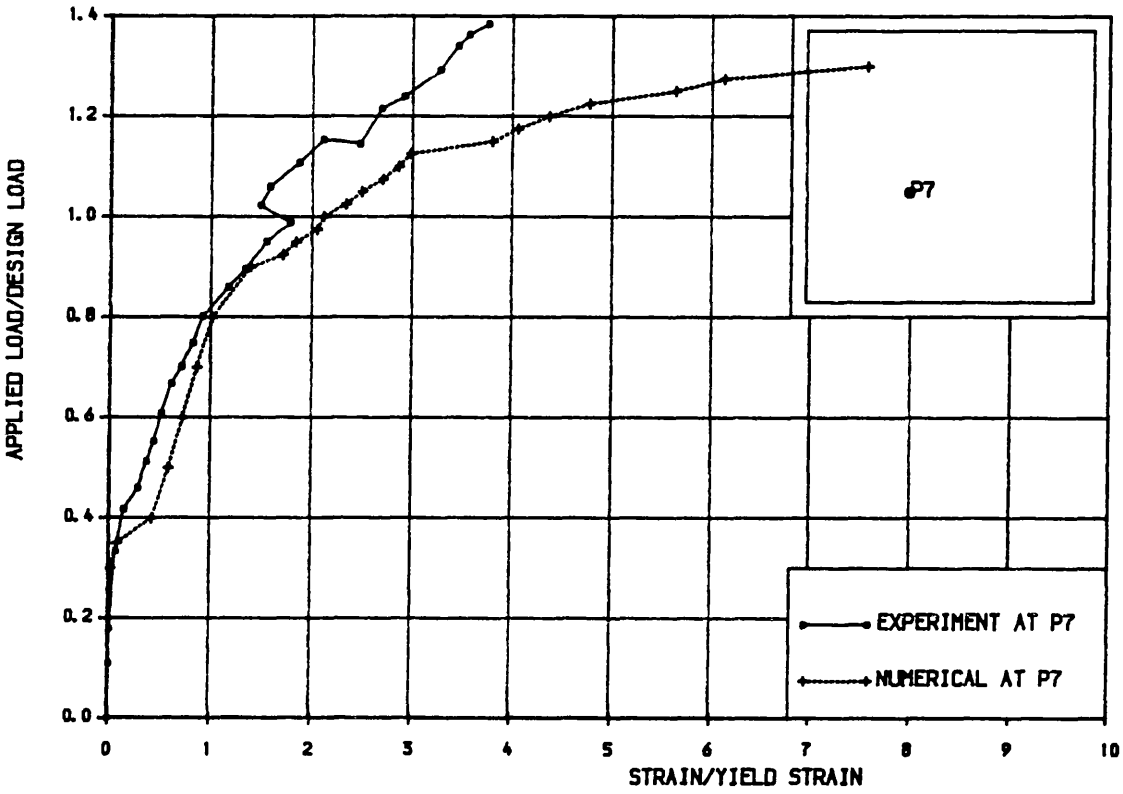


Fig. 8.26g Load-bottom steel strain curve. Model S.3

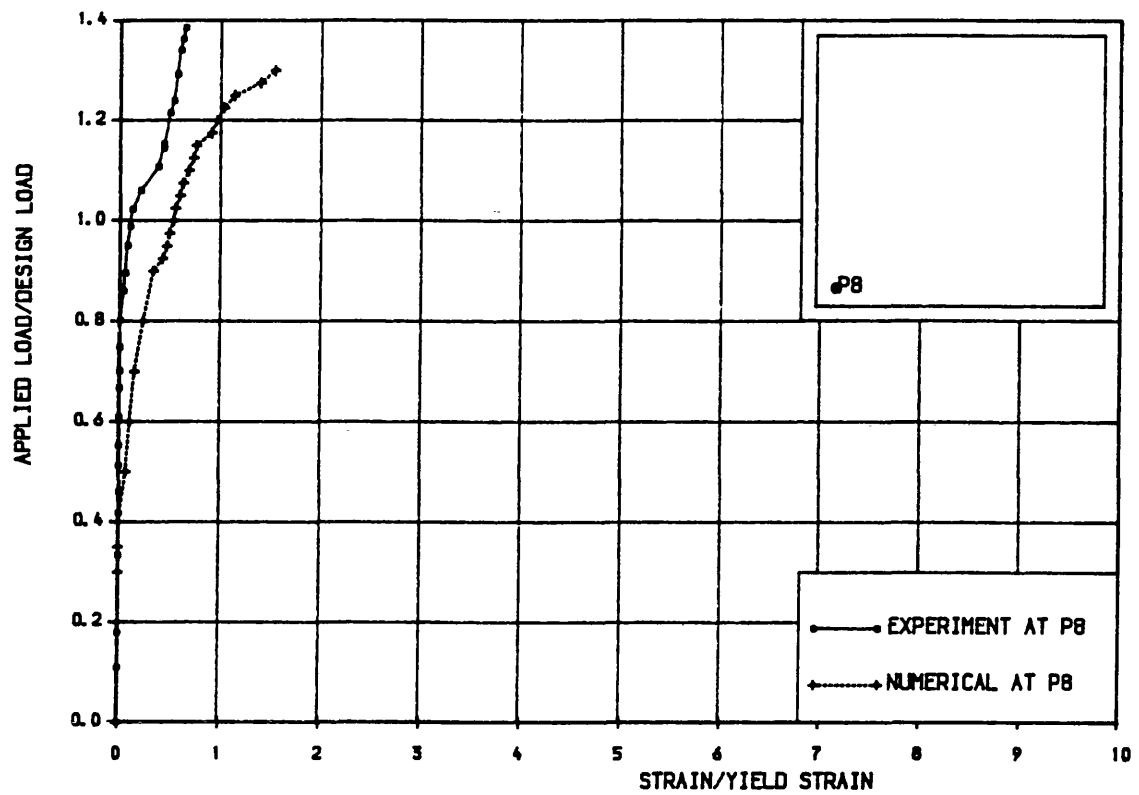


Fig. 8.27a Load-top steel strain curve. Model S.3

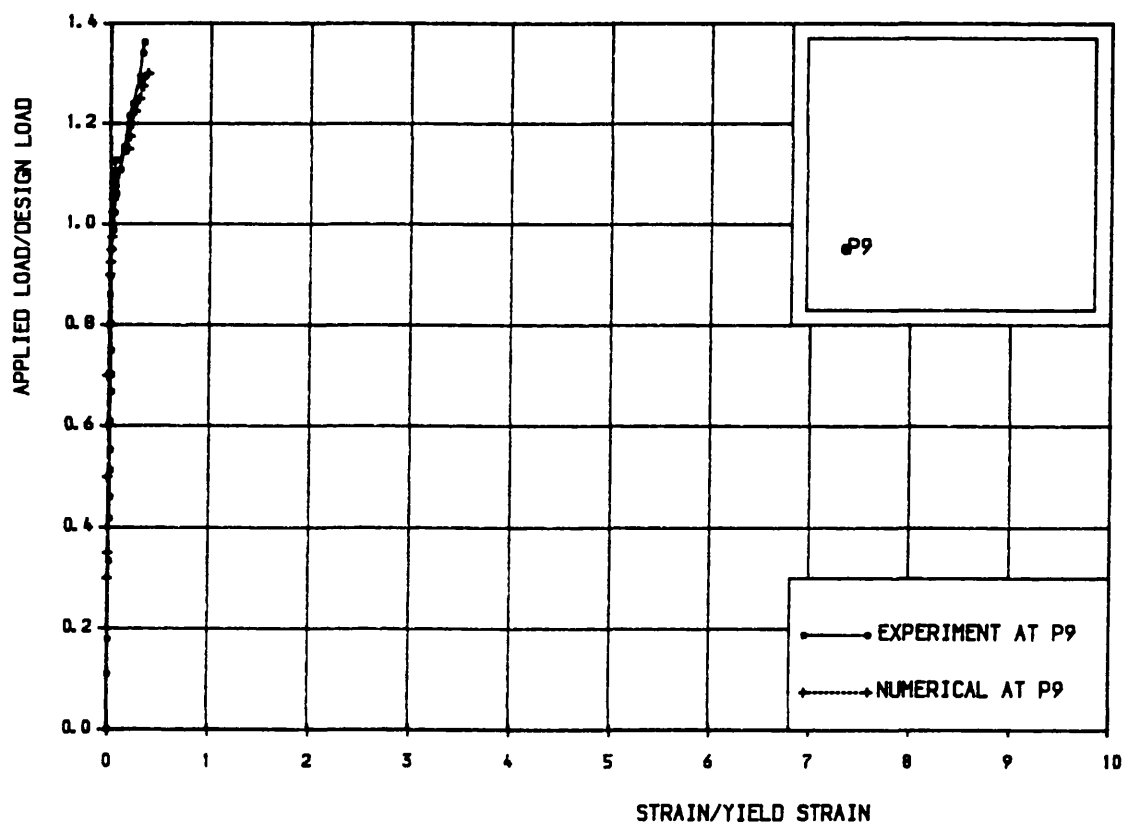


Fig. 8.27b Load-top steel strain curve. Model S.3

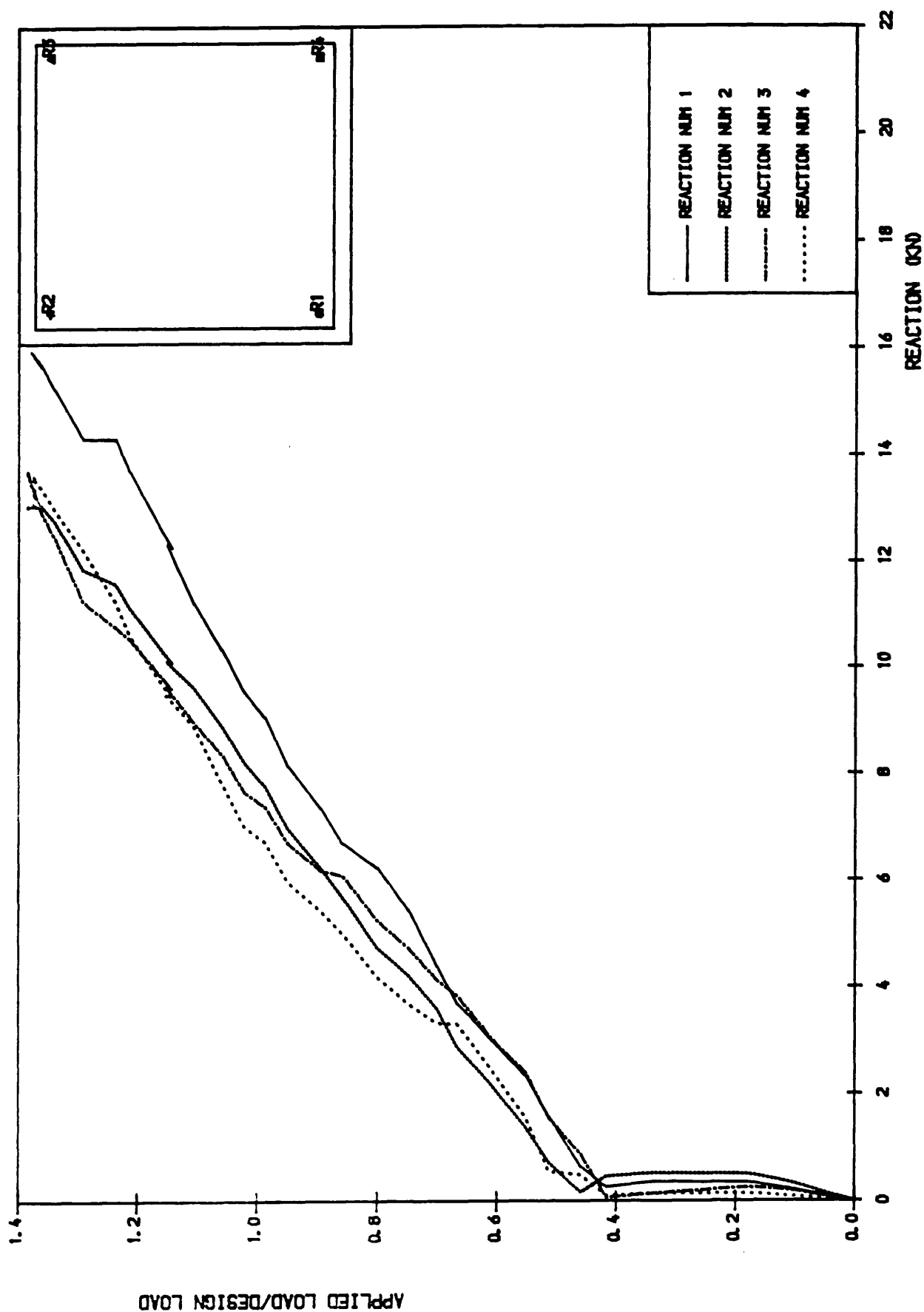


Fig. 8.28 Load-comers reaction curves. Model S.3

8.2.1.4 Comparison of Models(S.1, S.2 and S.3):

These three models S.1, S.2 and S.3 were designed using 70, 100 and 30% of plasticity stress distribution. Figure 8.29 and 8.30 show respectively load–deflection curves and load–strain curves. Table 8.2 shows the main observations from test results of these models and Hago(115)'s model N. 3. It was shown(9) that the behaviour of the slabs, up to the design load were independent of the stress field used in the design. At the collapse load for model S.3, the top concrete surface of the diagonal joining the corners and the point loads was crushed, figure 8.24d. This is mainly due to the concentration of the steel under the point load. The numerical moment curvature curves of these models are presented in figures 8.31. It can be noticed that using 100% plasticity in the design, the slab S.2 behaved in a more ductile manner as can be seen also from load–strain curves in figure 8.30. The ductility ratio δ , as defined in figure 8.31, is equal 1.0, 3.0 and 2.0 for S.1, S.2 and S.3 respectively. Although the models were designed for a design load P_d , because of practical constraints one is forced to use more steel than required. Table 8.1 shows the ratio of the provided steel volume to the numerical required steel volume. Because of the increased area of steel provided, the ultimate experimental load P_u is greater than the ultimate design load P_d . Using 70% plasticity level stress field in design, the ultimate load is less than for the other two models S.2 and S.3. This is mainly due to the fact that for this model, the difference between the required and provided steel is less than for other two models.

Tab. 8.1 Steel volume ratio (Provided steel/Num. required steel)

Models & Steel Bar Diameters $\Phi \downarrow$	Bottom	Top	Total
30% plasticity Φ 8 mm	1.39	1.58	1.44
70% Plasticity Φ 6 mm	1.09	1.61	1.21
100% plasticity Φ 8 mm	1.30	1.82	1.42

Table 8.2: Comparison between the designed models using different stress fields. Pd is the ultimate design load.
Pd is the experimental ultimate load.

Model → Facts ↓	HAGO's Model N: 3 Elastic str. field	Model S.3 30% Plastic. Stress field	Model S.1 70% Plastic. Stress field	Model S.2 100% Plastic Stress field
First visible crack at bottom face	0.38 Pd	0.41 Pd	0.42 Pd	0.38 Pd
Width of the first Crack	0.04 mm	0.03 mm	0.03 mm	0.06 mm
Location of this first crack	Under point load	Under point load	Under point load	Under point load
Direction of this first crack	45°	45°	45°	45°
Service deflection limit (span/250)	0.72 Pd 0.62 Pu	0.62 Pd 0.45 Pu	0.62 Pd 0.55 Pu	0.66 Pd 0.51 Pu
Service crack limit width (0.3 mm)	0.67 Pd 0.57 Pd	0.62 Pd 0.45 Pu	0.66 Pd 0.58 Pu	0.62 Pd 0.48 Pu
Location of this crack	—	Diagon. near point load	Diagon. near point load	Diagon. near point load
Apperance of yield line pattern	—	0.58 Pd	0.60 Pd	0.67 Pd
First yielding of bottom steel	1.0 Pd 0.86 Pd	0.75 Pd 0.54 Pu	0.80 Pd 0.71 Pu	0.80 Pd 0.62 Pu
Location of this yielding	Middle+Under point load	Under the point load	Under the point load	Under the point load
Yielding of top steel	No yielding	No yielding	No yielding	0.97 Pd 0.75 Pu
Failure took at	Pu=1.16 Pd	Pu=1.38 Pd	Pu=1.13 Pd	Pu=1.30 Pd
Mode of failure	Flexural	Flexural	Flexural	Flexural
Maximum central deflection	50.00 mm	69.12 mm	34.00 mm	64.00 mm
Maximum crack width at failure	—	5.0 mm	3.0 mm	6.5 mm

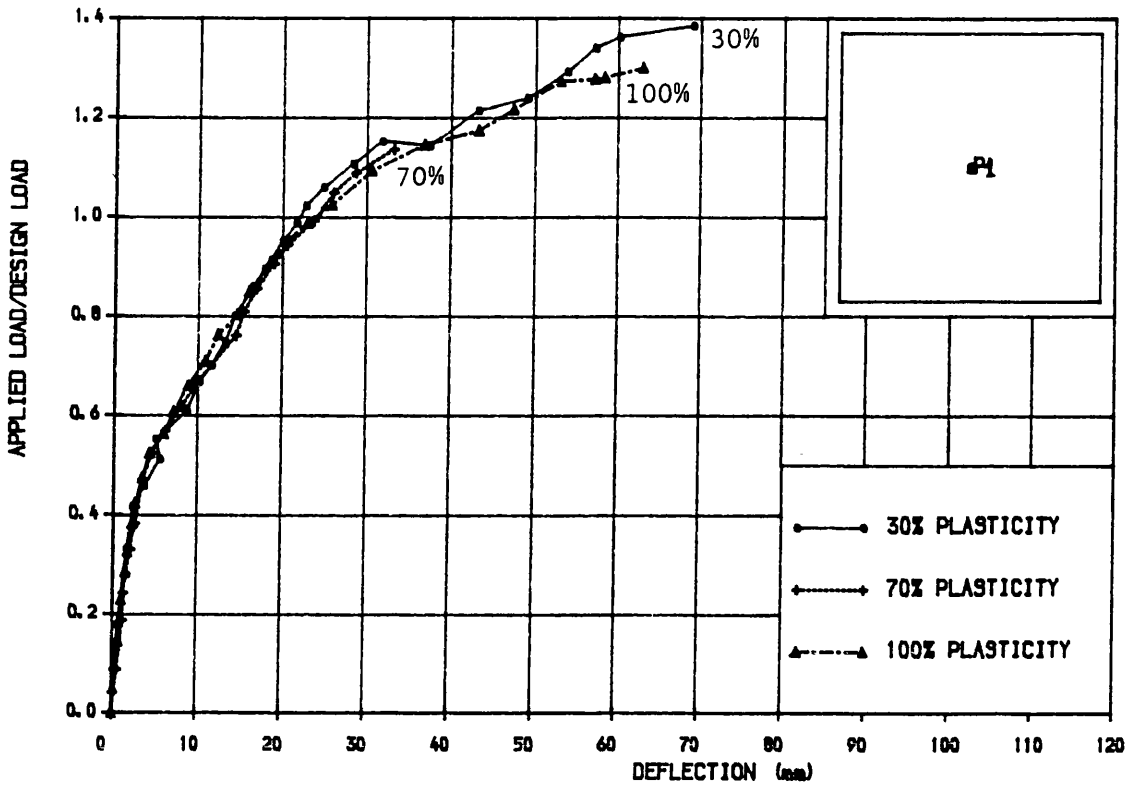


Fig. 8.29 Experimental load-deflection curves. Comparison of Models S.1(70%), S.2(100%) and S.3(30%)

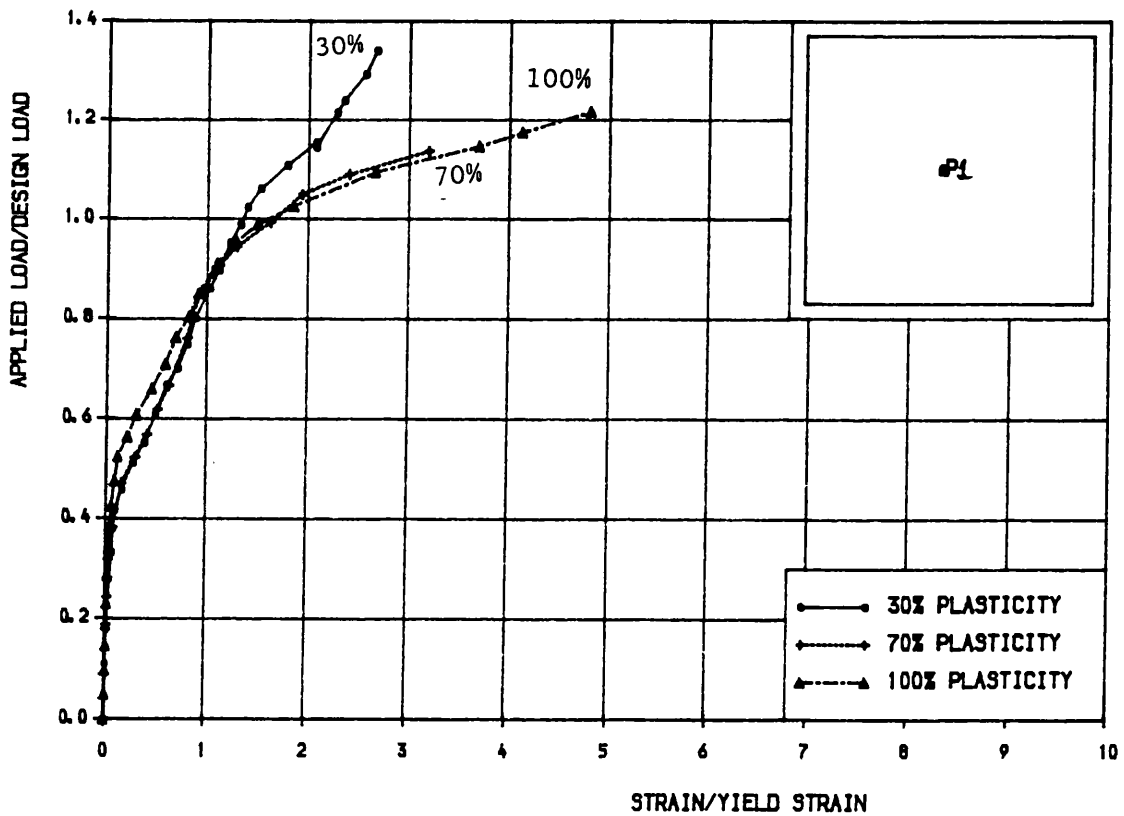


Fig. 8.30 Experimental load-Bottom steel strain curves. Comparison of Models S.1(70%), S.2(100%) and S.3(30%)

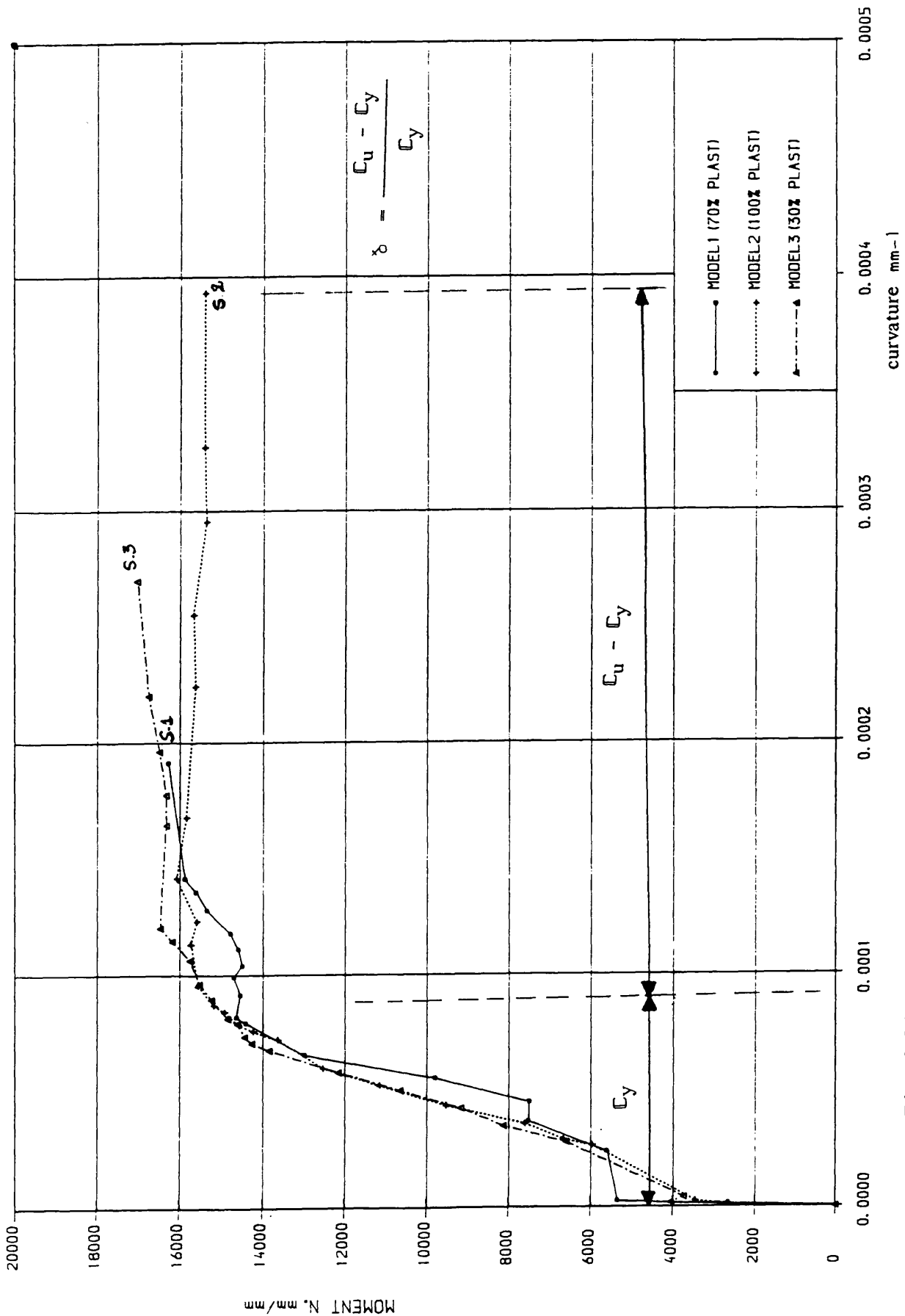


Fig. 8.31 Numerical moment curvature curves. Comparison of Models S.1(70%), S.2(100%) and S.3(30%)

8.2.1.5 Model S.5:

This model is a rectangular simply supported slab 3000 x 2000 mm and 100 mm thickness, designed for a total load P_d equal to 210 KN using 100% plasticity level. Full details of the slab were shown in figure 6.1. Material properties of concrete and steel reinforcement were presented in table 6.3 and 6.4 respectively. The steel layout for top and bottom layers were shown in figure 7.14. This slab was loaded using an indirect two point load system of four spreader beam, resulting in an eight point load, figure 8.32a.

The first cracks were observed suddenly over a large area under the point loads at 0.38 P_d (0.26 P_u). The maximum width of these cracks was of 0.15 mm in the middle of the line joining the loading holes. Figure 8.36a shows the crack pattern at the cracking load. Cracks reached the corners of the slab at 0.48 P_d (0.32 P_u). The service load deflection limit of span/250 was reached at 0.58 P_d (0.39 P_u) and the yield line pattern was clear and the maximum crack width was 0.25 mm. The cracks start to join each other in the short direction of the slab at 0.61 P_d (0.41 P_u) and the service load crack width limit of 0.3 mm was reached under the point loads. At 0.84 P_d (0.56 P_u) no new cracks were noticed but old cracks were widened to reach a maximum width of 0.4 mm. The steel yielded at this level of loading in the central area of the slab. Beyond this load, few new cracks were forming while the old ones were widening. This is mainly caused by the yielding of steel. The first cracks at the top surface were observed at 1.0 P_d (0.67 P_u). The maximum bottom crack width of 0.5 mm was under the inner point loads, whereas in the middle of the slab a width of 0.45 mm was measured. With increasing loads a few new bottom cracks formed and new top cracks opened rather than the widening of the existing cracks. At 1.25 P_d (0.84 P_u) the maximum crack width under the point loads was of 2.0 mm, while in the central area of the slab a 1.1 mm wide crack was registered. As loading increased, the width of the cracks under the point load increased, however in the central area of the slab the maximum crack width was almost constant, while new cracks were forming near the edges. The top corner steel yielded at 1.40 P_d (0.94 P_u), figure

8.35a. The slab failed in a flexural manner at 1.48 Pd.

Deflection:

Figures 8.33a to 8.33d show the load–deflection curves at different positions of the slab. Nonlinearity started at the cracking load of 0.38 Pd. The limiting service deflection of span/250 (8.0 mm) was reached at 0.58 Pd (0.39 Pu), figure 8.33a, which presents unacceptable service deflection in term of experimental ultimate load.

Steel Strains:

Figures 8.34 and 8.35 show the steel strain of the measured points, for both top and bottom steel respectively. The bottom steel yielded at 0.84 Pd (0.56 Pu) in the central area, figures 8.33a and 8.34b. At the design load (0.67 Pu) the measured steel strains were above yield strain. The top steel yielded at 1.40 Pd (0.94 Pu), figure 8.35a. At failure the strain of the bottom steel was several times the steel yield strain.

Crack Width:

The first crack appeared in the bottom face of the slab at 0.38 Pd (0.26 Pu) with a maximum width of 0.15 mm. The service crack limit width of 0.3 mm was reached at 0.61 Pd (0.41 Pu). At failure the maximum crack width of 5.5 mm was measured near the holes of the loading wires.

Reactions:

The corner up lift reactions were negligible up to the cracking load of 0.38 Pd (0.26 Pu), figure 8.37. Beyond this load, the reactions increased almost linearly with load. A maximum corner reaction of 25% of the measured load on one spreader beam (ie. $0.25 P/4$), was measured.

Mode of Failure:

From the crack patterns, load–deflection and steel strain curves, the slab

behaved and failed flexurally in a ductile manner. The failure took place at 1.48 Pd, which is greater than the load for which the slab was initially designed. This is mainly caused by the provided steel amount which was greater than the required one, table 8.3, because of practical constraints that the steel provided can not match the exact required steel amount.

Tab. 8.3 Steel volume ratio (Provided steel/Num. required steel)
Model S.5

Steel	Bottom		Top	
Direction	X	Y	X	Y
Steel Volume Ratio Provided	1.36	1.16	1.41	1.65
Required				

Numerical Comparison:

The first crack opened under the point loads as shown in figure 8.36b at 0.35 Pd. The bottom steel yielded at almost the same load as in the experiment, figures 8.34a and 8.34b. In contrast the top steel yielded earlier than in the experiment, figure 8.35a and 8.35b. Near the failure load, the slab is less stiff than the experimental values, but in general good agreement was obtained between the numerical and the experimental results. A good comparison also can be seen in the crack patterns at failure load in figures 8.36b for the bottom face and 8.36c for the top one.

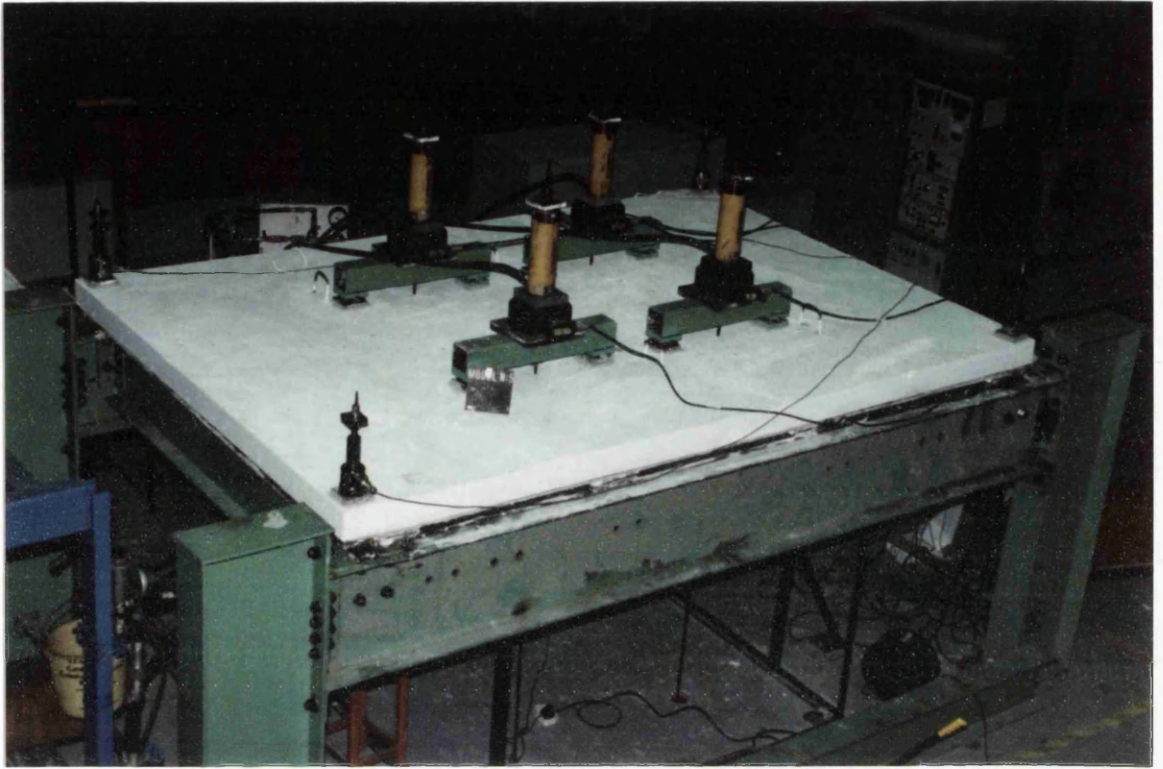


Fig. 8.32 Loading arrangement. Model S.5

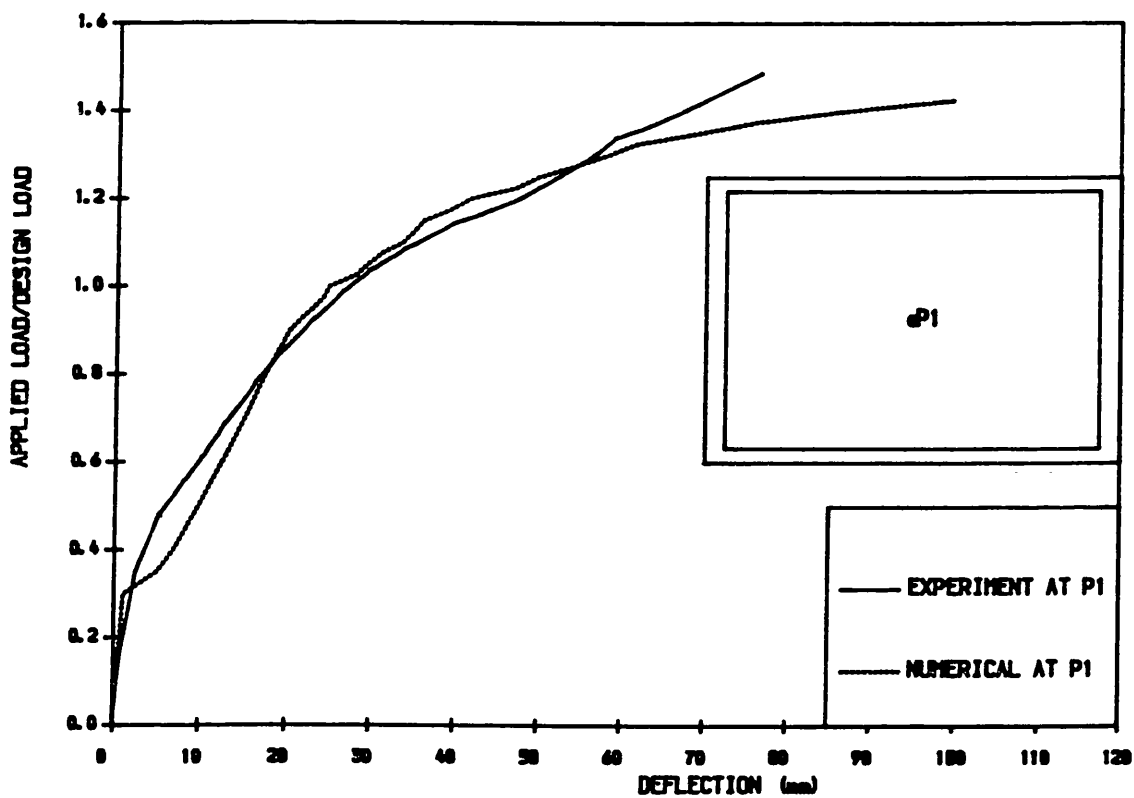


Fig. 8.33a Load-deflection curve. Model S.5

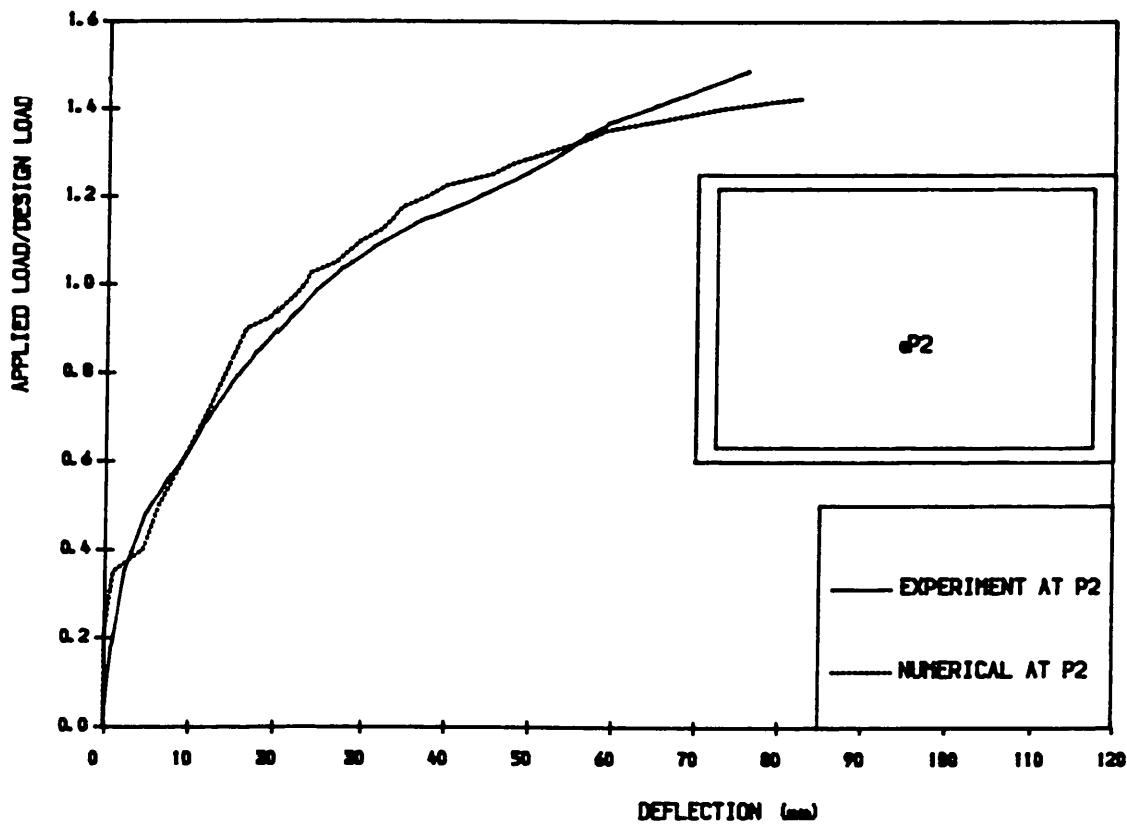


Fig. 8.33b Load-deflection curve. Model S.5

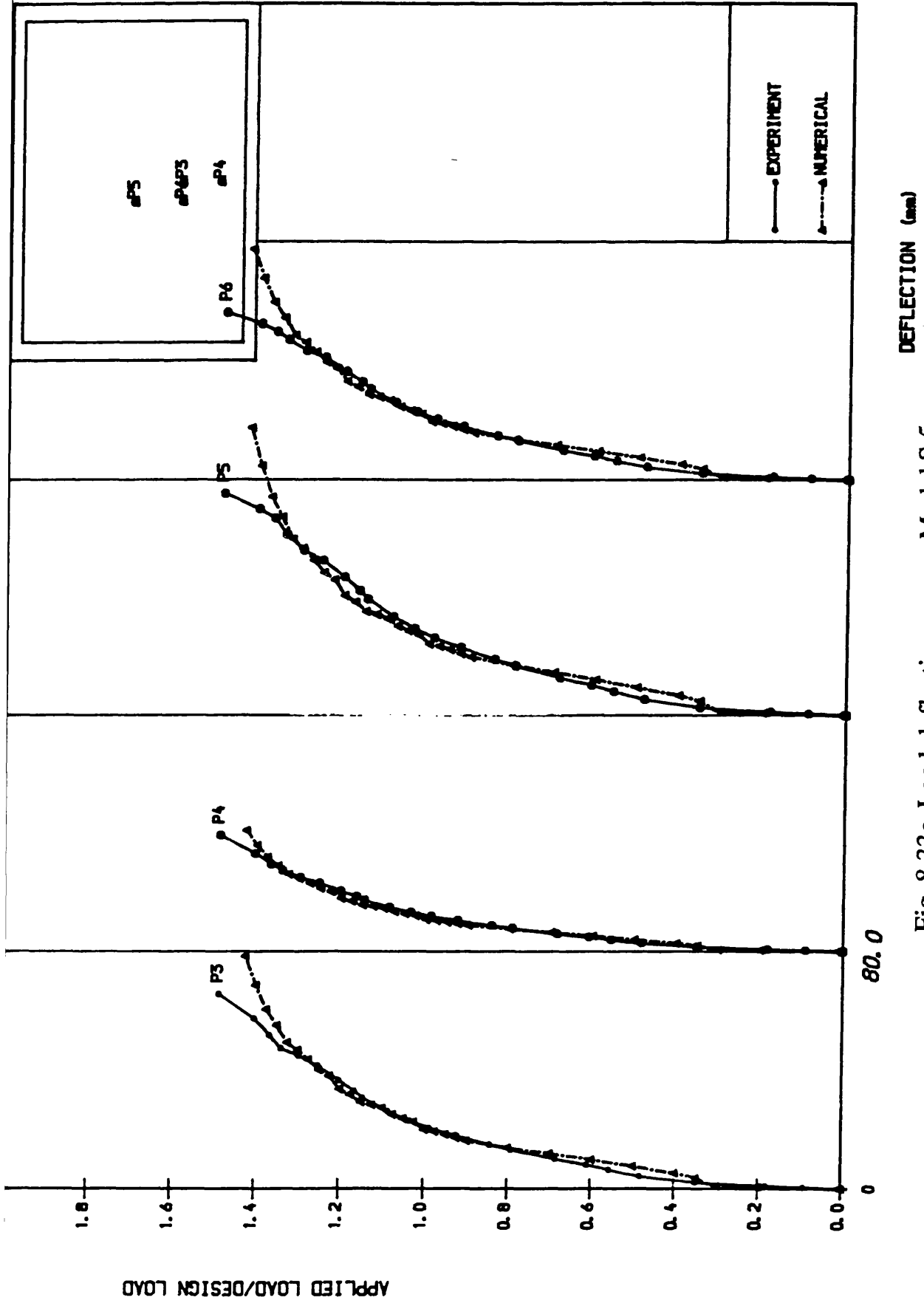


Fig. 8.33c Load-deflection curves. Model S.5

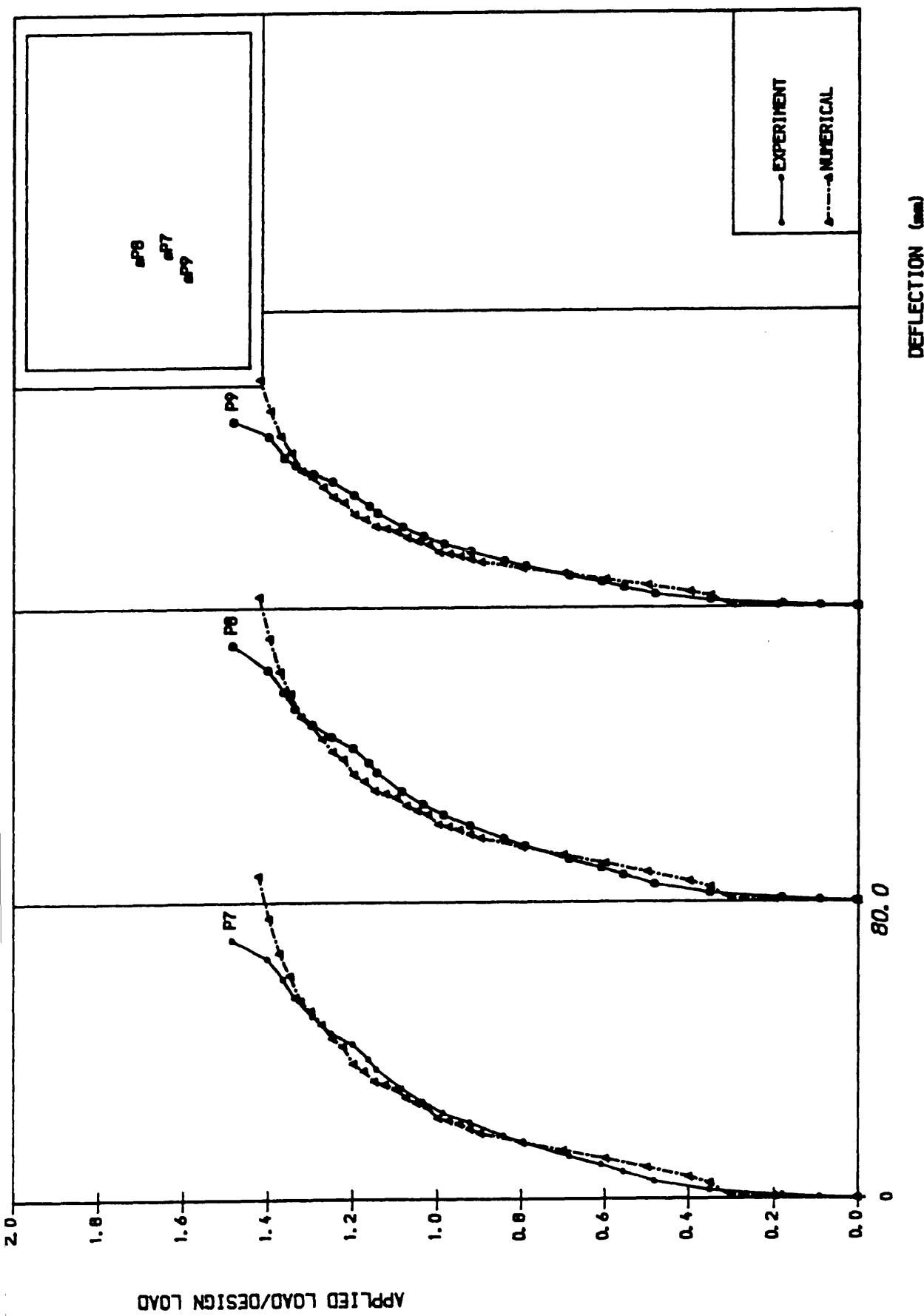


Fig. 8.33d Load-deflection curves. Model S.5

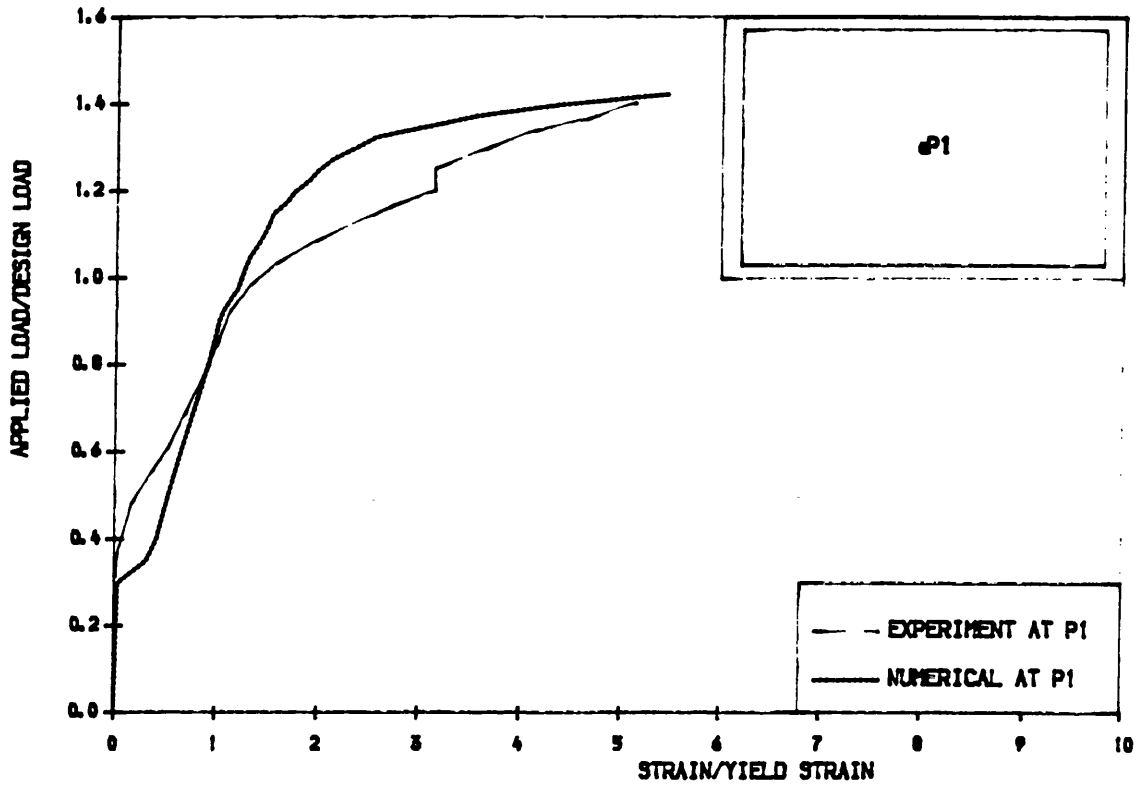


Fig. 8.34a Load-strain curve. Bottom steel in the short span direction.
Model S.5

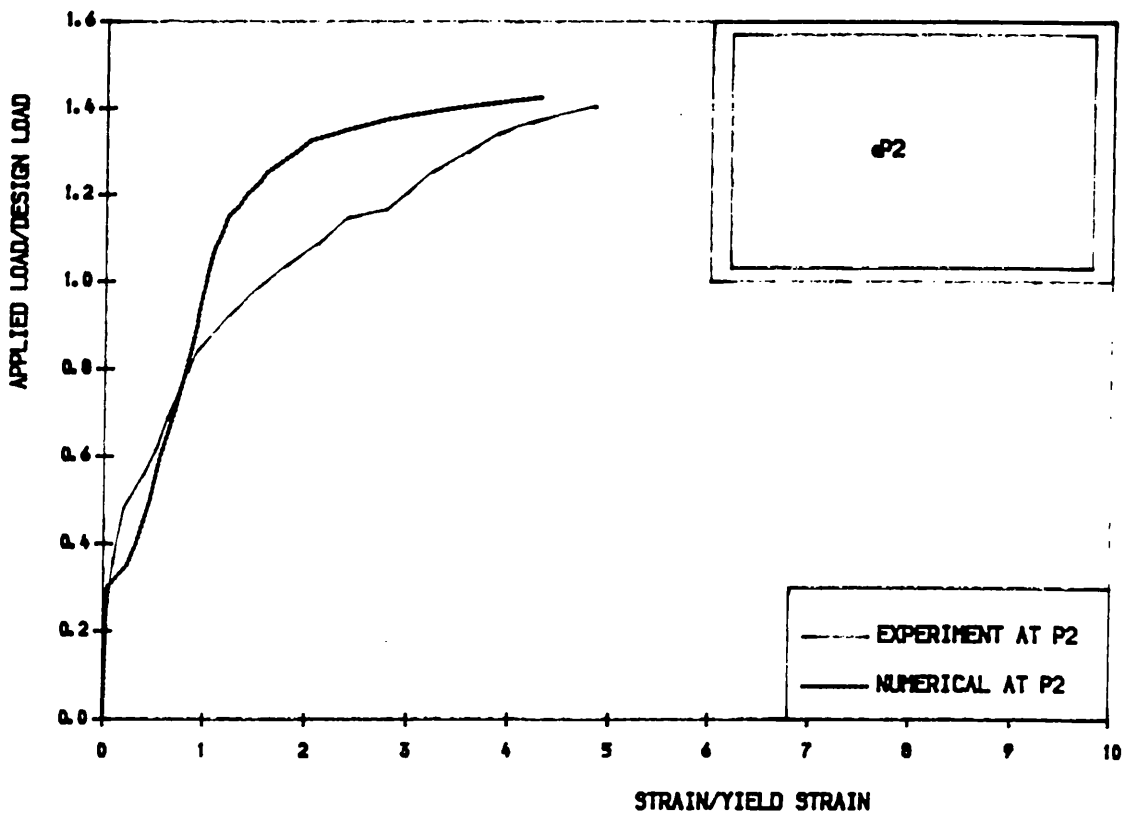


Fig. 8.34b Load-strain curve. Bottom steel in the short span direction.
Model S.5

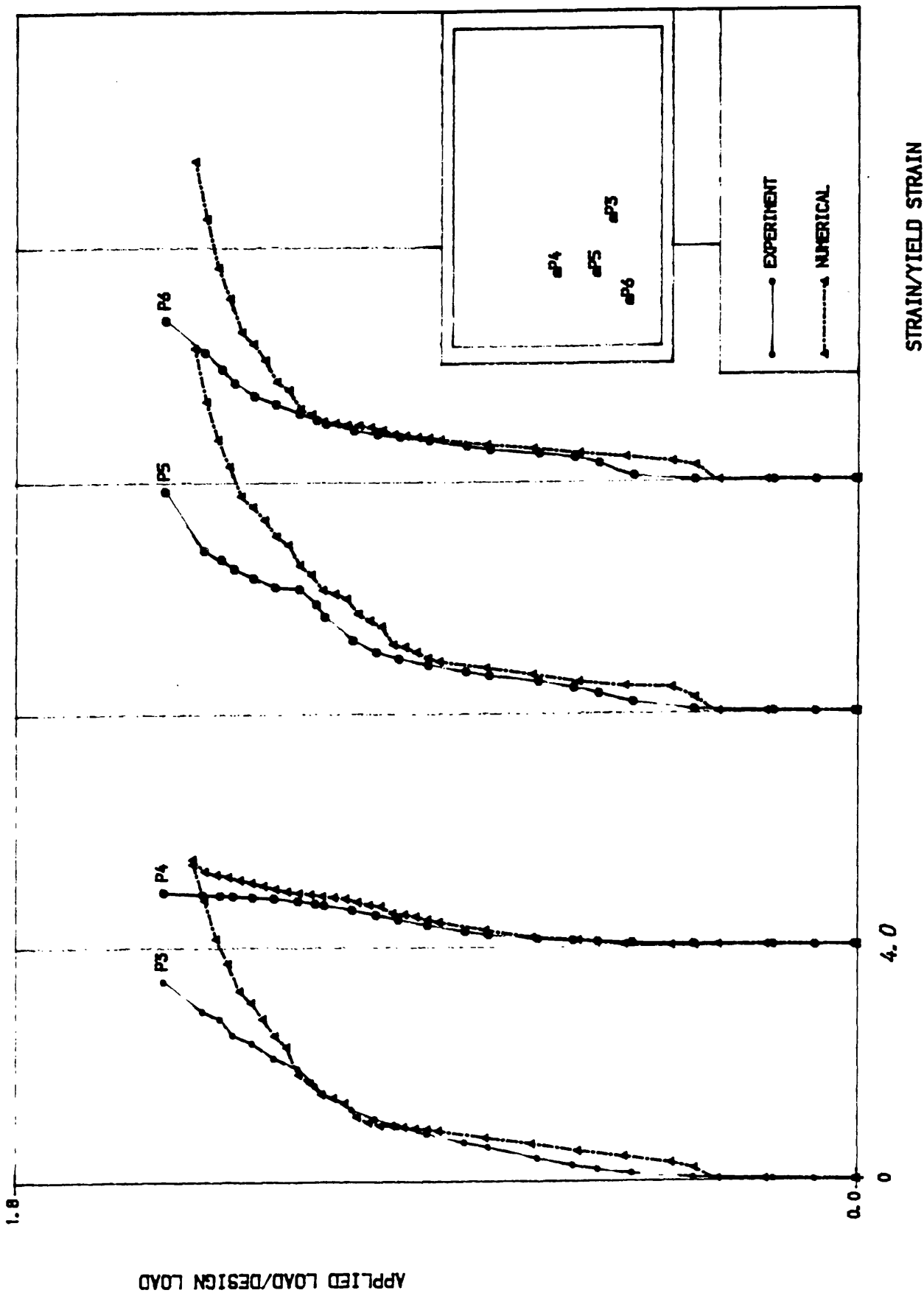


Fig. 8.34c Load-strain curves. Bottom steel in the short span direction. Model S.5

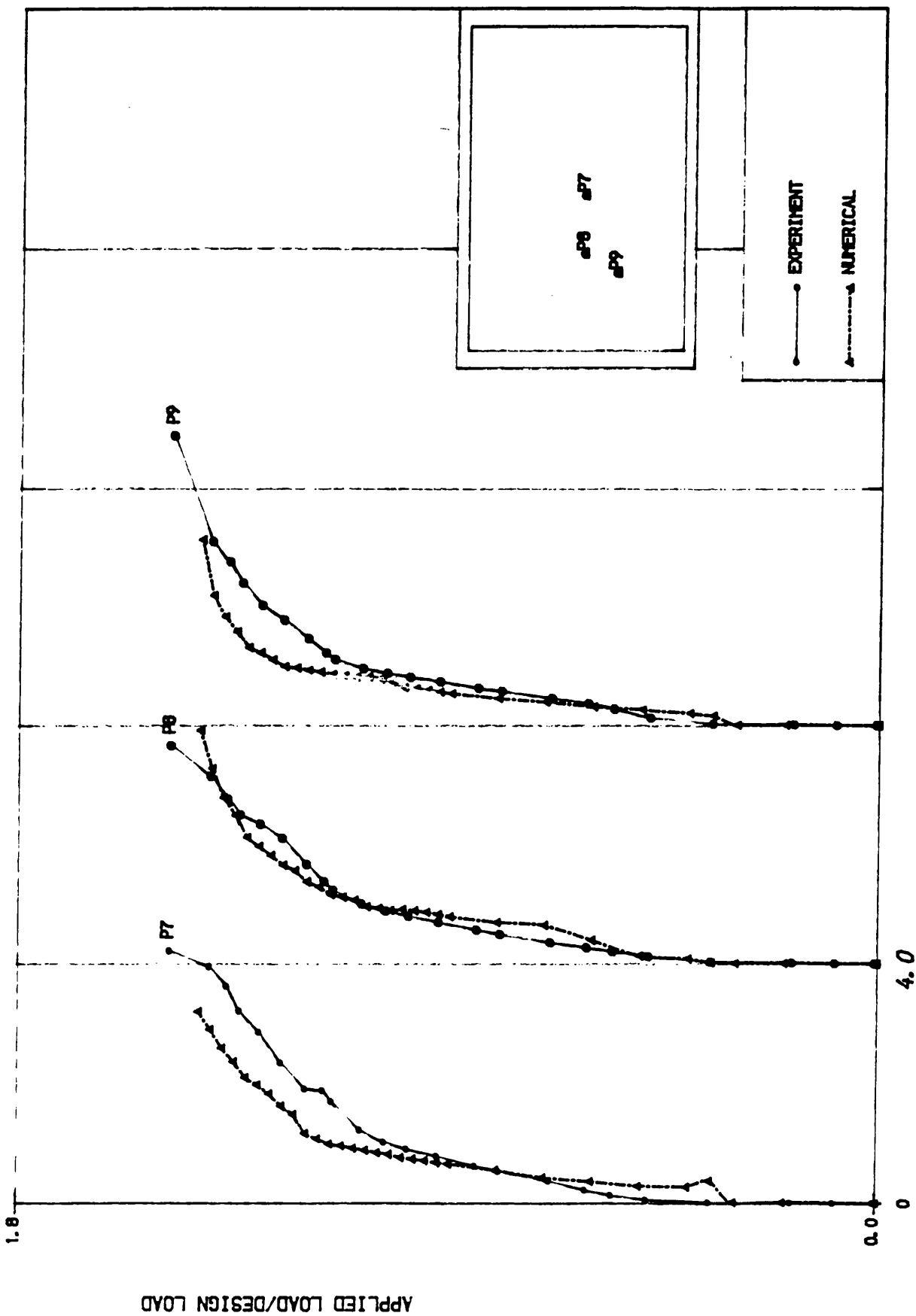


Fig. 8.34d Load-strain curves. Bottom steel in the long span direction. Model S.5

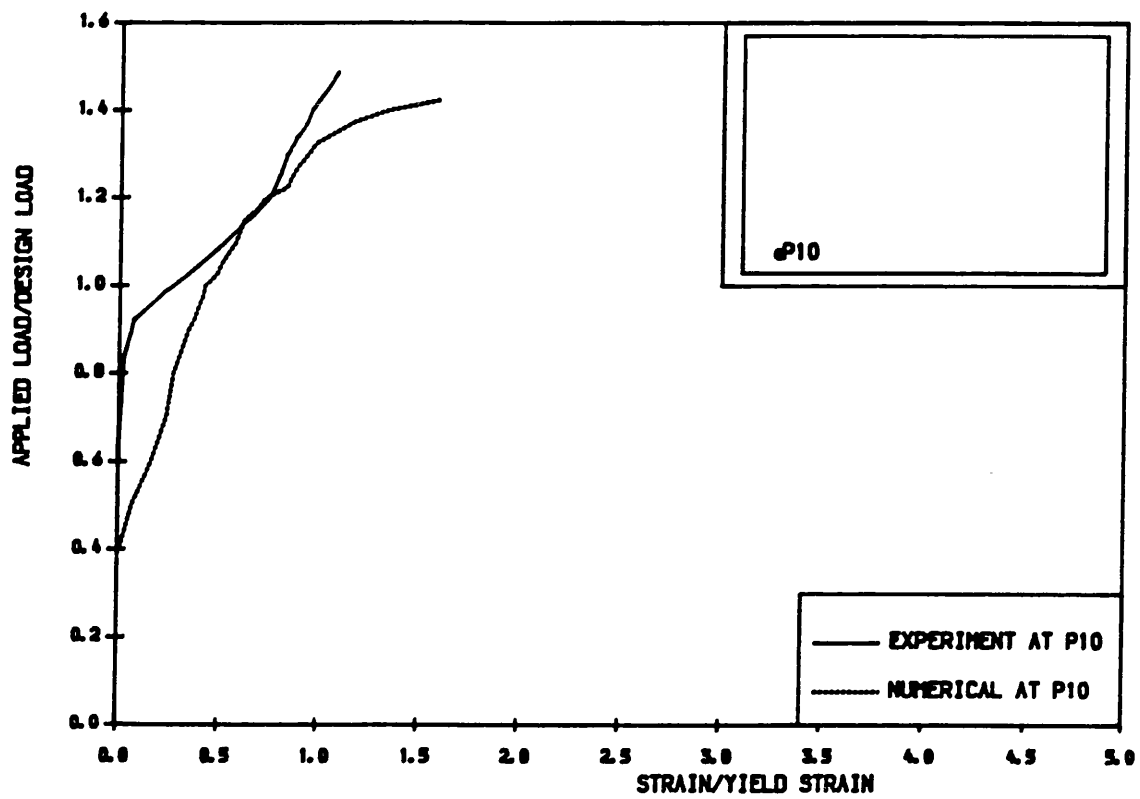


Fig. 8.35a Load-strain curve. Top steel in the short span direction.
Model S.5

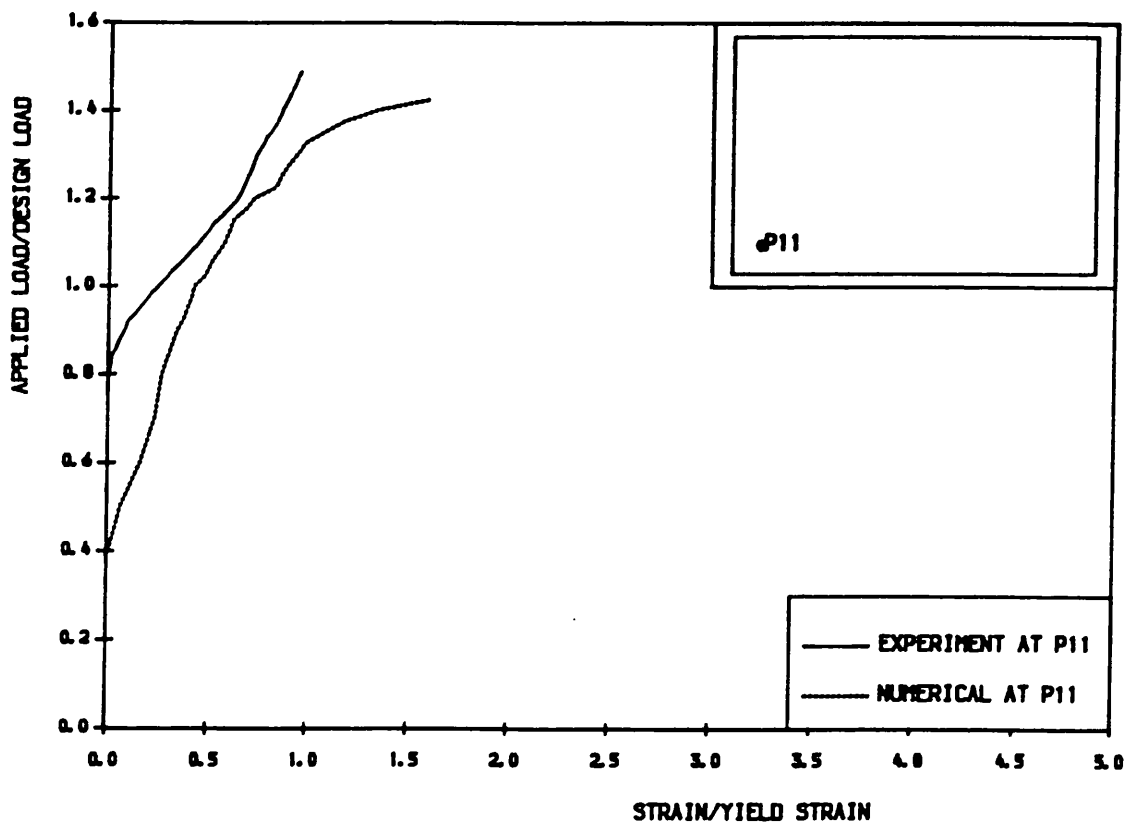


Fig. 8.35b Load-strain curve. Top steel in the long span direction.
Model S.5



Experimental at 0.38 Pd

Numerical at 0.35 Pd 1/4 Slab

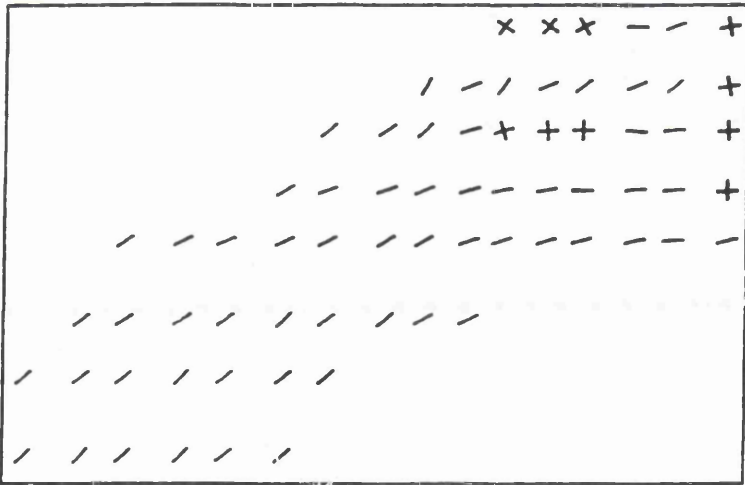


Fig. 8.36a First appearance of cracks at bottom face. Model S.5

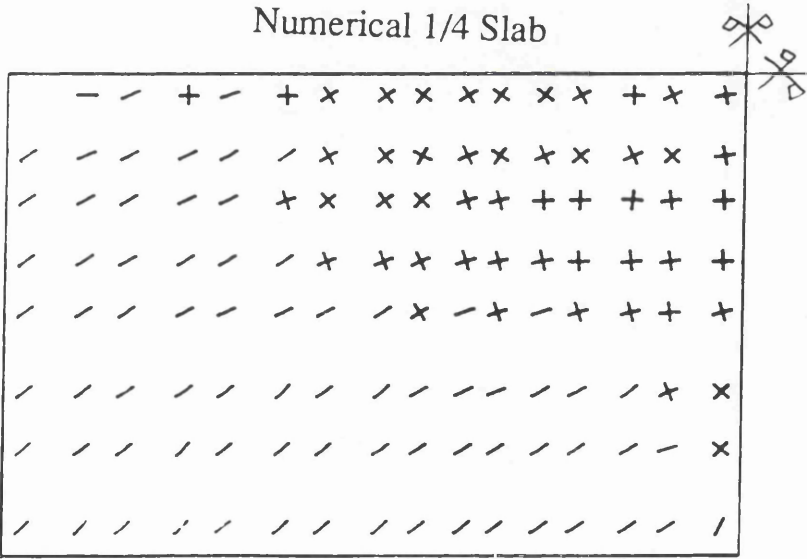
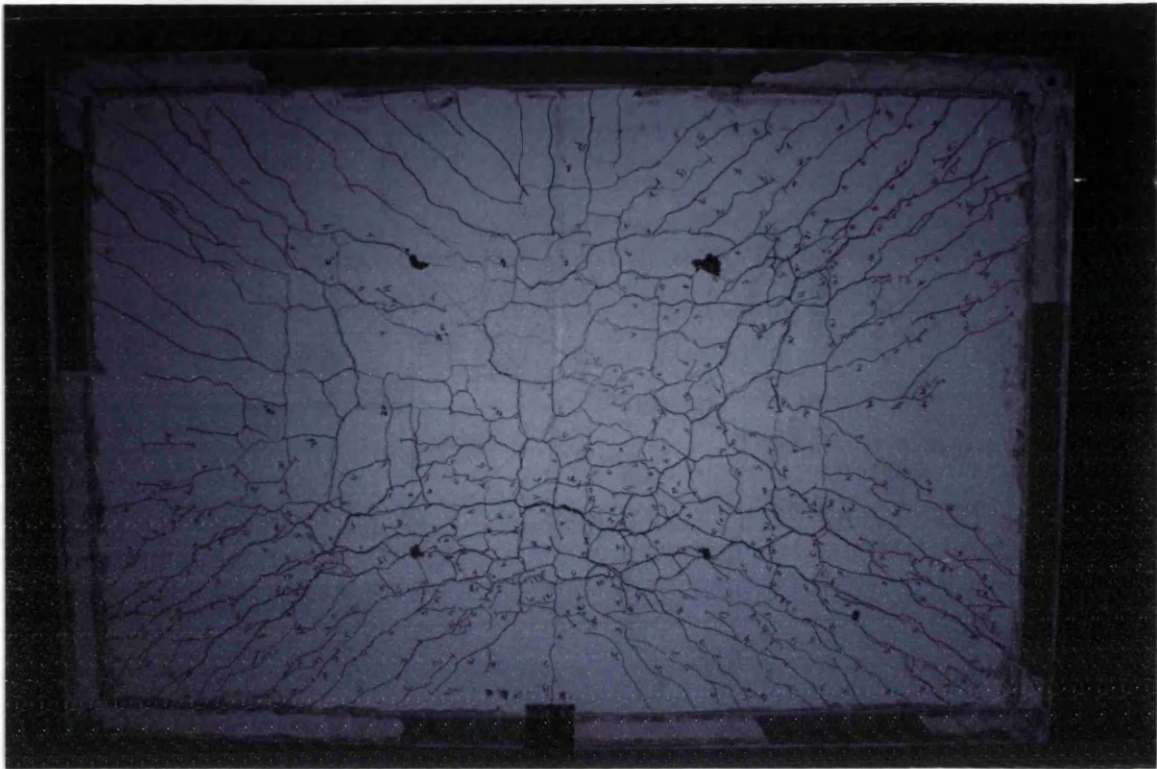


Fig. 8.36b Bottom experimental and numerical crack pattern at collapse load.
Model S.5

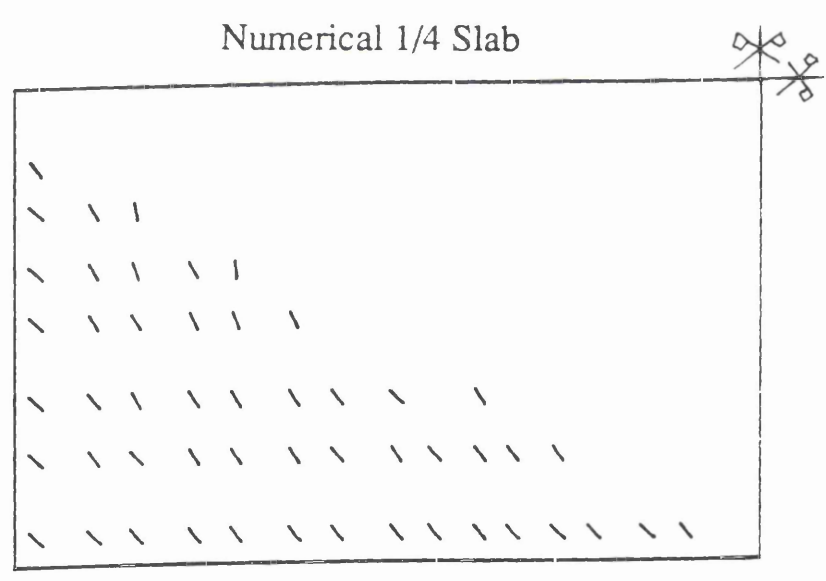
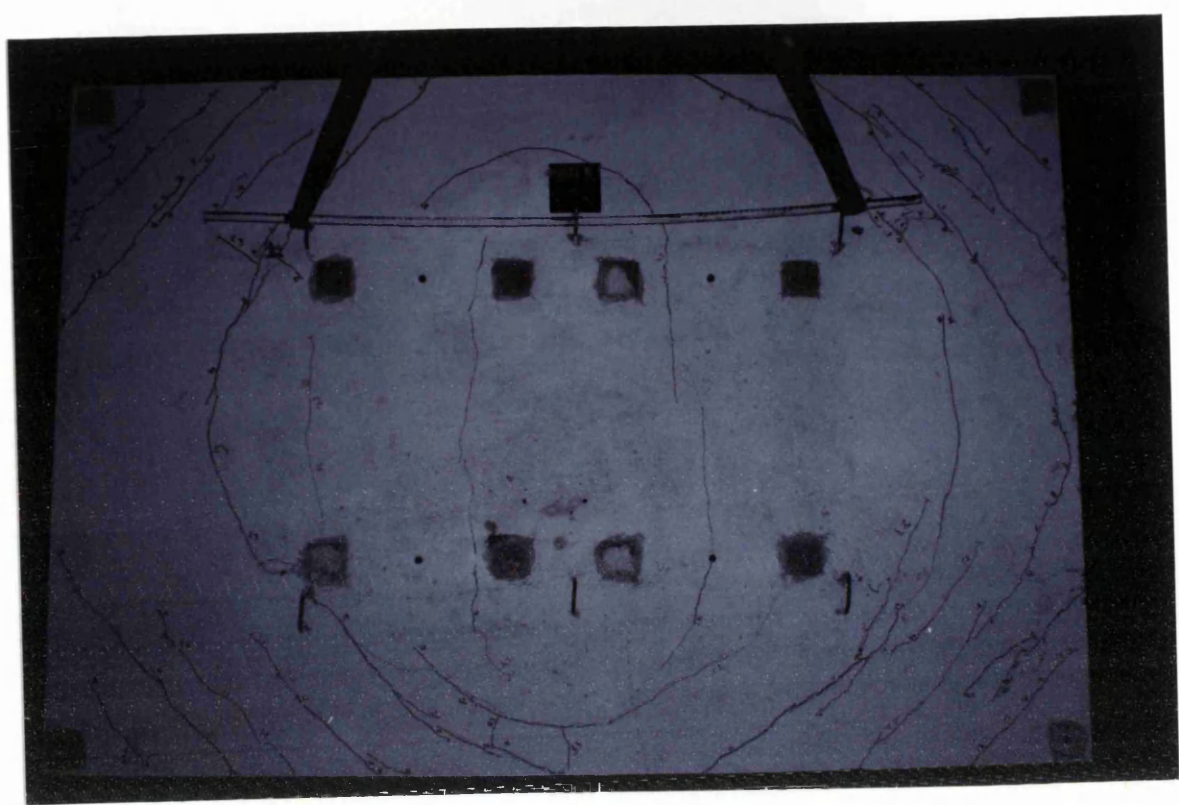


Fig. 8.36c Top experimental and numerical crack pattern at collapse load.
Model S.5

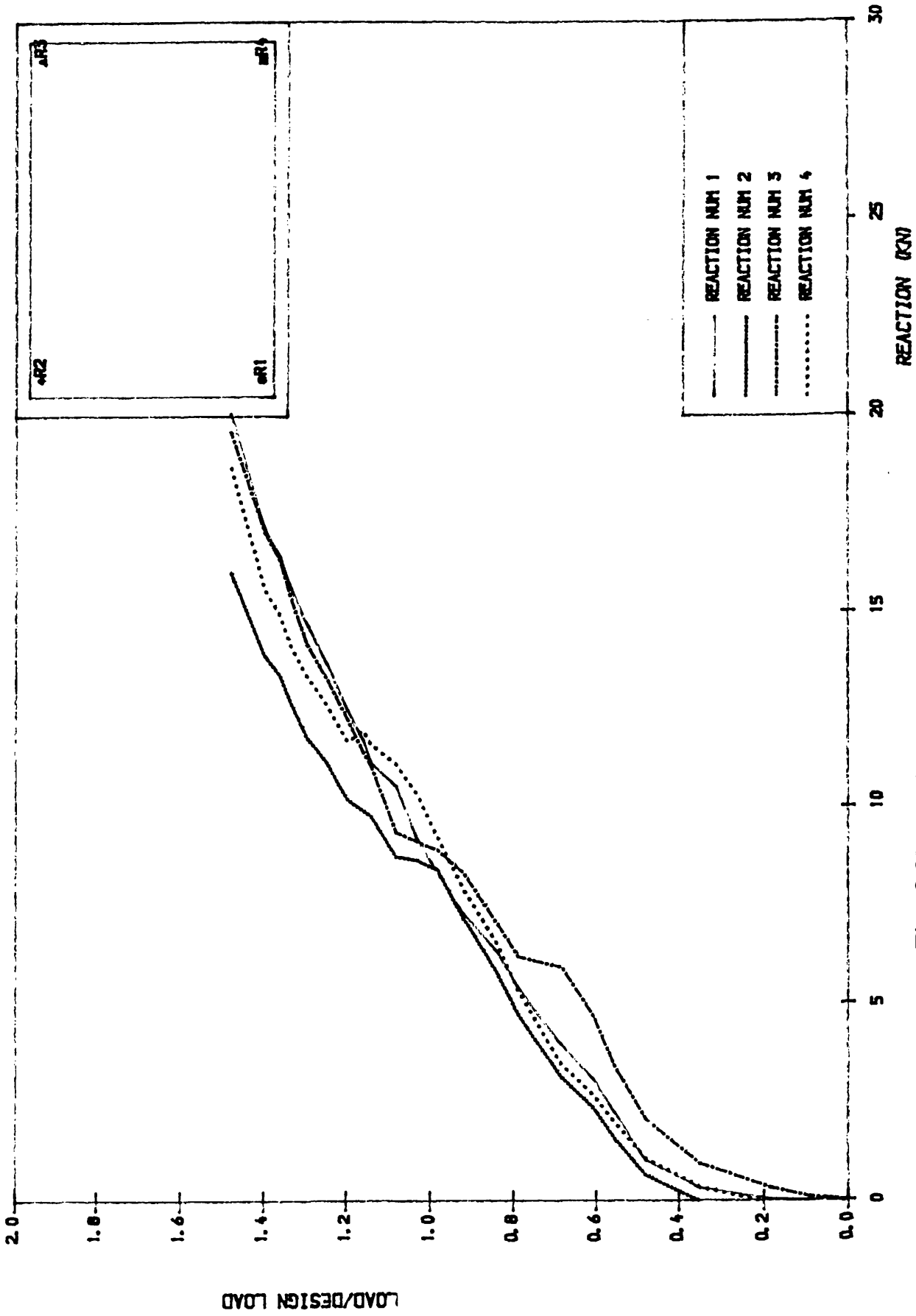


Fig. 8.37 Load-corner reations curves. Model S.5

8.2.2 Simply Supported Slabs with a Column Support in the Middle:

Two models S.4 and S.6 consisted of two square simply supported slabs with a mid-column support, figures 8.38a– b. These models have all dimensions same as the first three models, except that the thickness of model S.6 was 150 mm. These models were designed for the same ultimate load of 320 KN using 100% of plasticity level. The material properties can be found in tables 6.3 and 6.4. The steel layout of the models were presented in the previous chapter in figures 7.20 and 7.21 for model S.4 and S.6, respectively. The aim of testing this models is to explore the stress smoothening possible over the column supports in flat slab type of structures.

8.2.2.1 Model S.4:

The first load increment was of 0.2 of the design load (P_d), after which small increments on an average of 0.05 P_d was adopted. The first visible crack occurred at 0.48 P_d (0.33 P_u) under the point load and was 0.1 mm wide. At this level the cracks spread slowly to the surrounding area under the point load. At 0.62 P_d (0.43 P_u) the maximum crack width was of 0.15 mm. The first crack at the top concrete surface appeared on the column at 0.75 P_d (0.52 P_u). This crack was 0.2 mm wide. The cracks at slab edge started to appear at this level of loading and the cracks surrounded all the four point loads and along the diagonals towards the corners of the bottom face. The maximum crack width reached the serviceability load limit of 0.3 mm at 0.78 P_d (0.54 P_u). Additional cracks towards the corners at the bottom face developed at 0.88 P_d (0.61 P_u). At this level no new cracks appeared at the top face while the width of the old main cracks continued to increase. At 0.94 P_d (0.65 P_u) the permissible deflection limit of $\text{span}/250 = 4.0$ mm was reached under the point load. Since the slab was supported by a mid-column, the span was taken as the distance from the column to the edge support of the slab. At this level of loading, the old cracks were

widening and a few new cracks were forming so that the maximum crack width at the top slab surface was 0.4 mm. The top cracks were perpendicular to the edge supports and formed a cross dividing the top face of the slab into four uncracked regions. At the design load, almost the whole region under the point loads and in the corners had cracked on the bottom face.

The top steel over the column yielded at 1.15 Pd (0.80 Pu), figure 8.40b, whereas the bottom steel yielded under the point load at 1.20 Pd (0.83 Pu), figure 8.40a.

Up to the ultimate load the old cracks were widening at an increasing rate but very few new cracks were forming. At 1.38 Pd (0.96 Pu) the maximum width of cracks at the top face and the bottom face were 3.5 and 1.5 mm respectively. As loading increased, noise of concrete cracking could be heard. Suddenly at 1.44 Pd the whole area between the point loads lifted by almost 15.0 mm, making a big noise and the total load dropped sharply. The punching crack was inclined to the plane of the slab as shown in figure 8.41c. Because of practical constraints, the steel provided is greater than the theoretically required one as shown in table 8.4, thus it resulted in the ultimate load being greater than the design load ($P_u = 1.44$ Pd). Unfortunately the shear strength of the slab was lower than this value. Hence the slab failed in punching shear.

Deflections:

Figures 8.39a–c present the load–deflections curves up to the ultimate load. Nonlinearity started at 0.6 Pd (0.28 Pu), but the cracks were not visible at this stage. The limiting service load–deflection was reached, under the point load, at 0.94 Pd (0.65 Pu) and this represent an acceptable serviceability limit state of deflection. The maximum deflection of the slab was of 13.8 mm under the point load.

Steel strains:

The load–strain curves for both the bottom and the top steel are shown in figures 8.40a to 8.40d. It is clear that the steel was behaving linearly up to the cracking load at the critical points. The top steel yielded on the column at 1.15

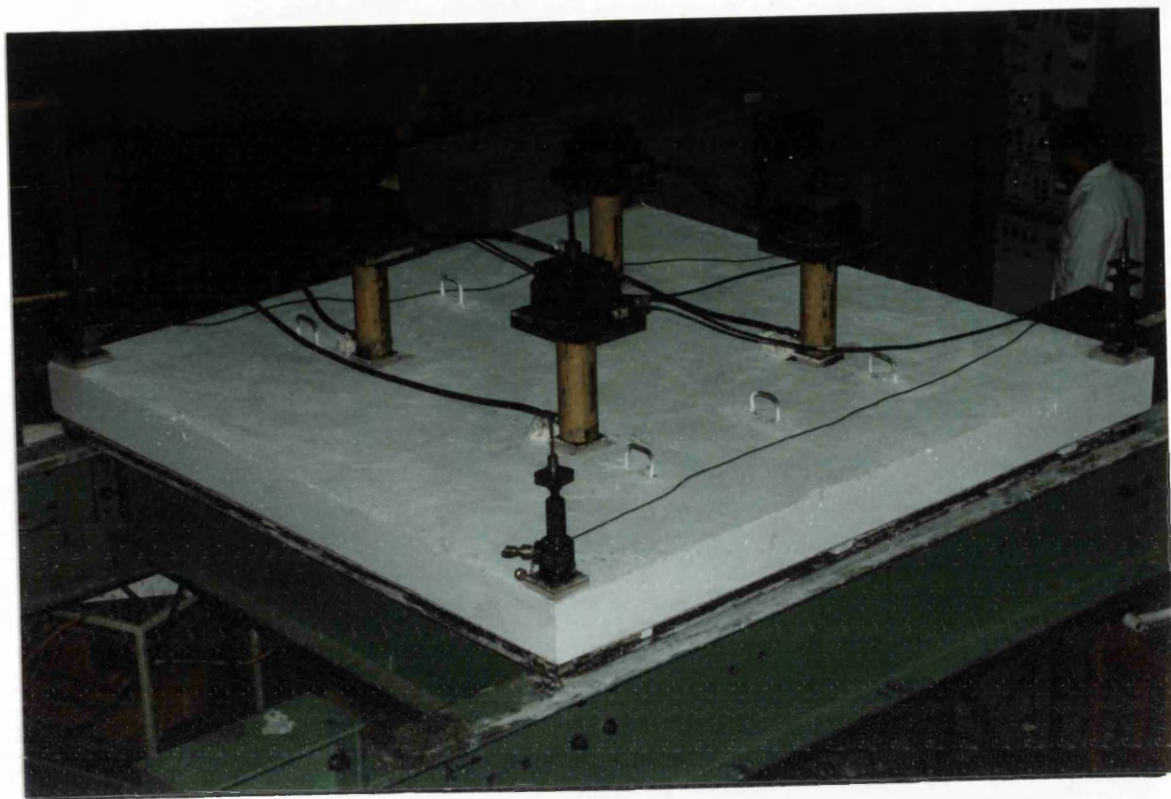


Fig. 8.38a Loading arrangement. Model S.4 and S.6

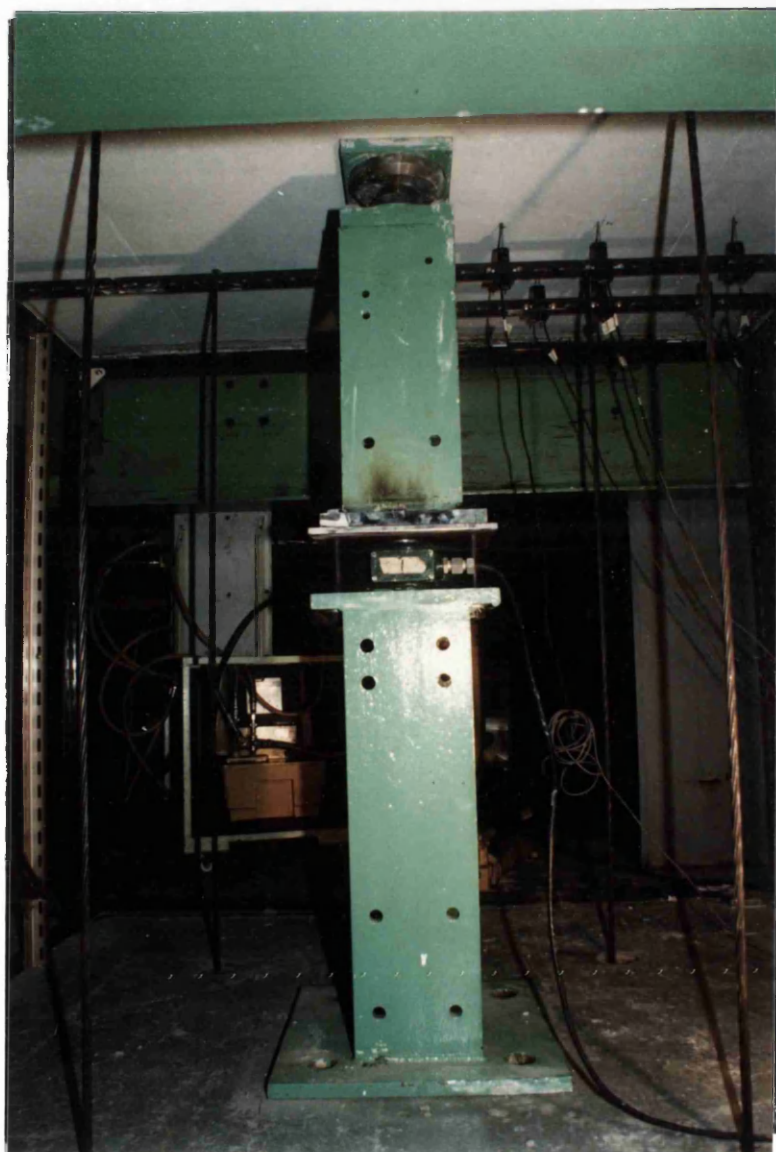


Fig. 8.38b Column-slab connection.

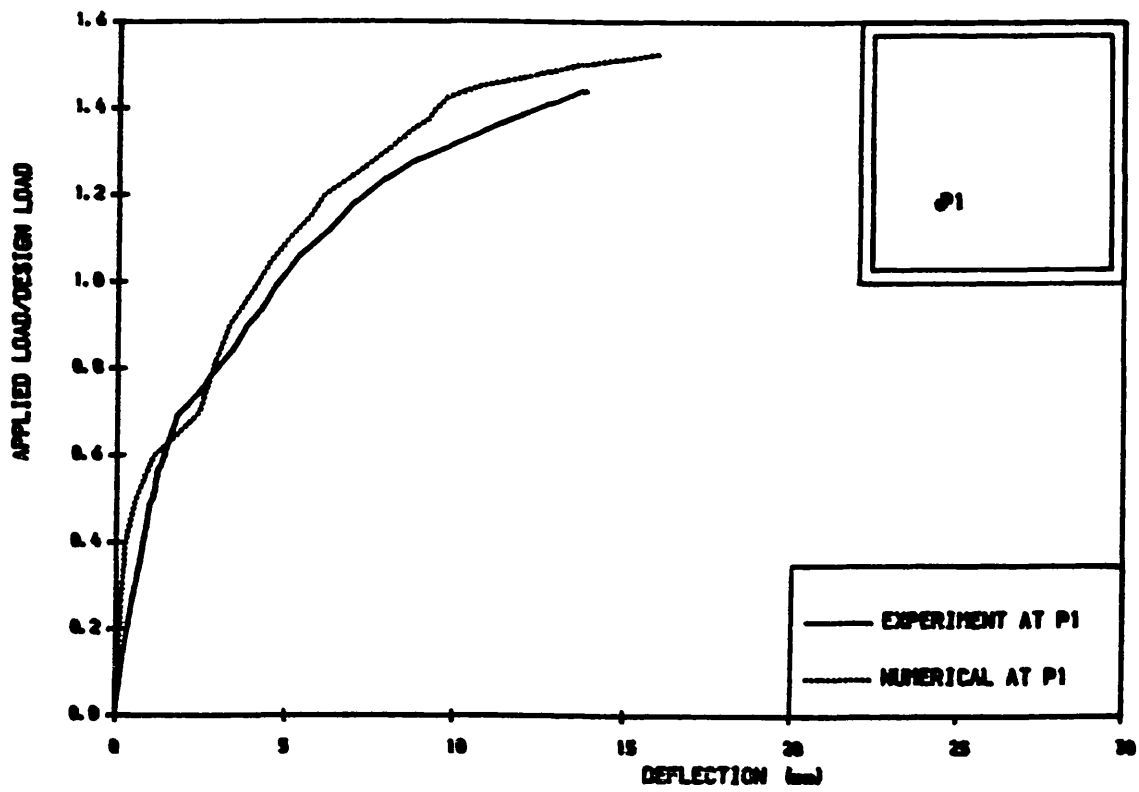


Fig. 8.39a Load-deflection curve. Model S.4

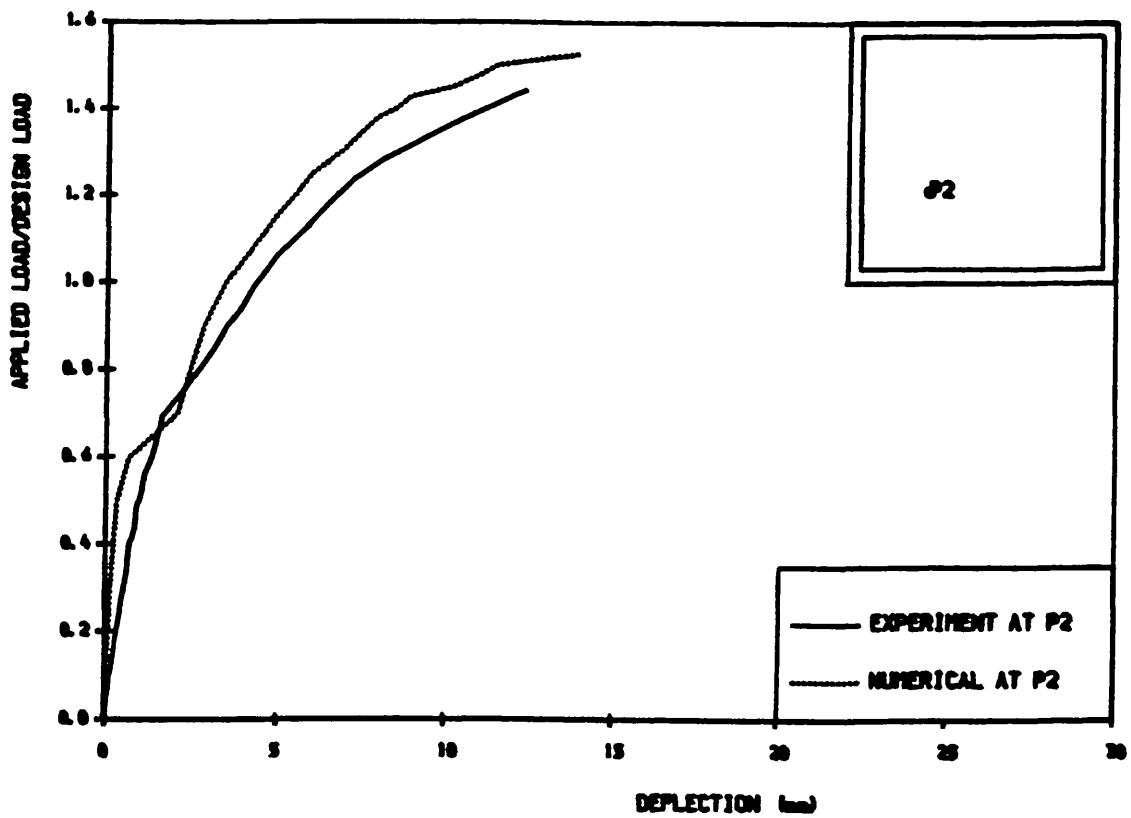


Fig. 8.39b Load-deflection curve. Model S.4

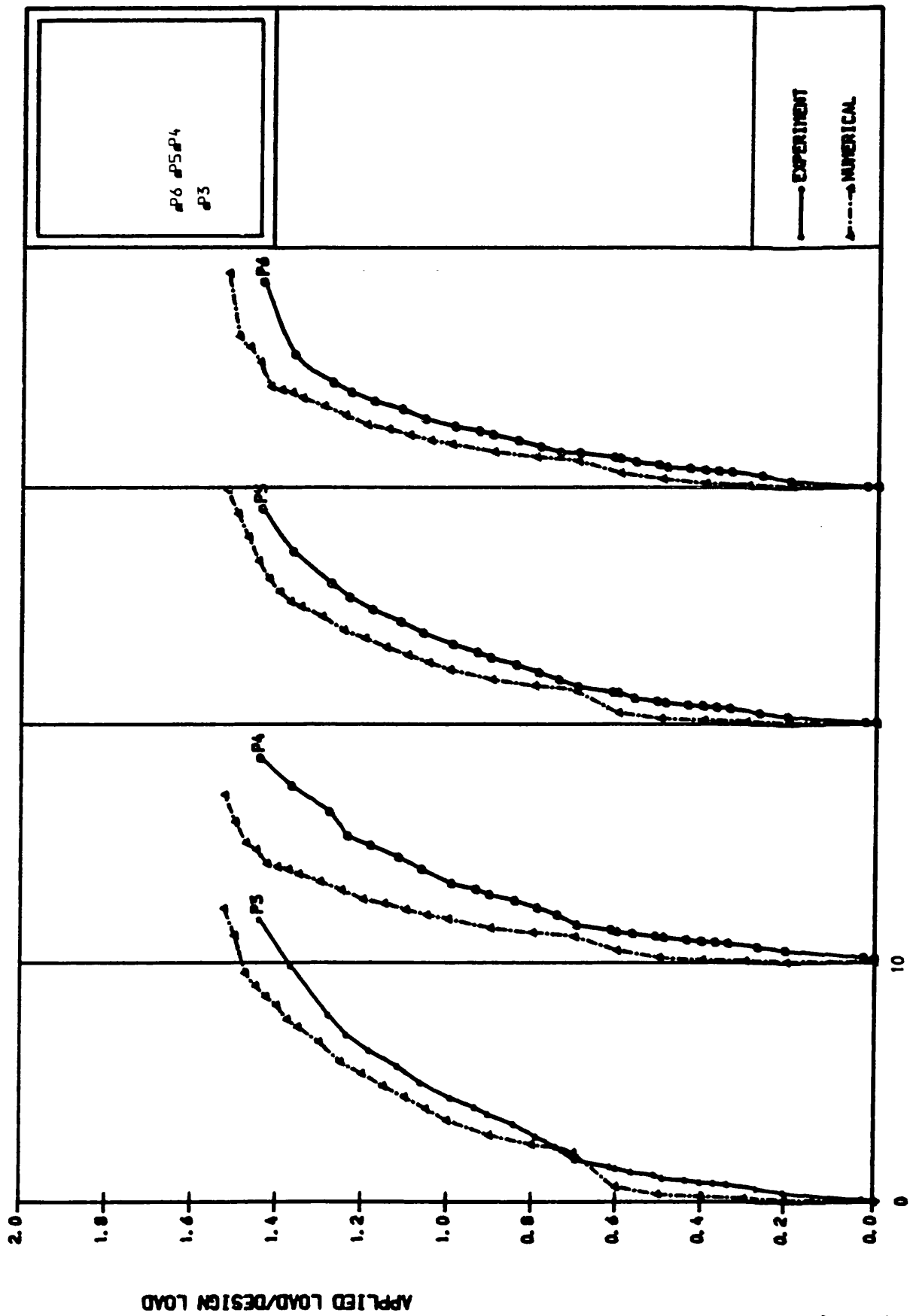


Fig. 8.39c Load-deflection curves. Model S.4

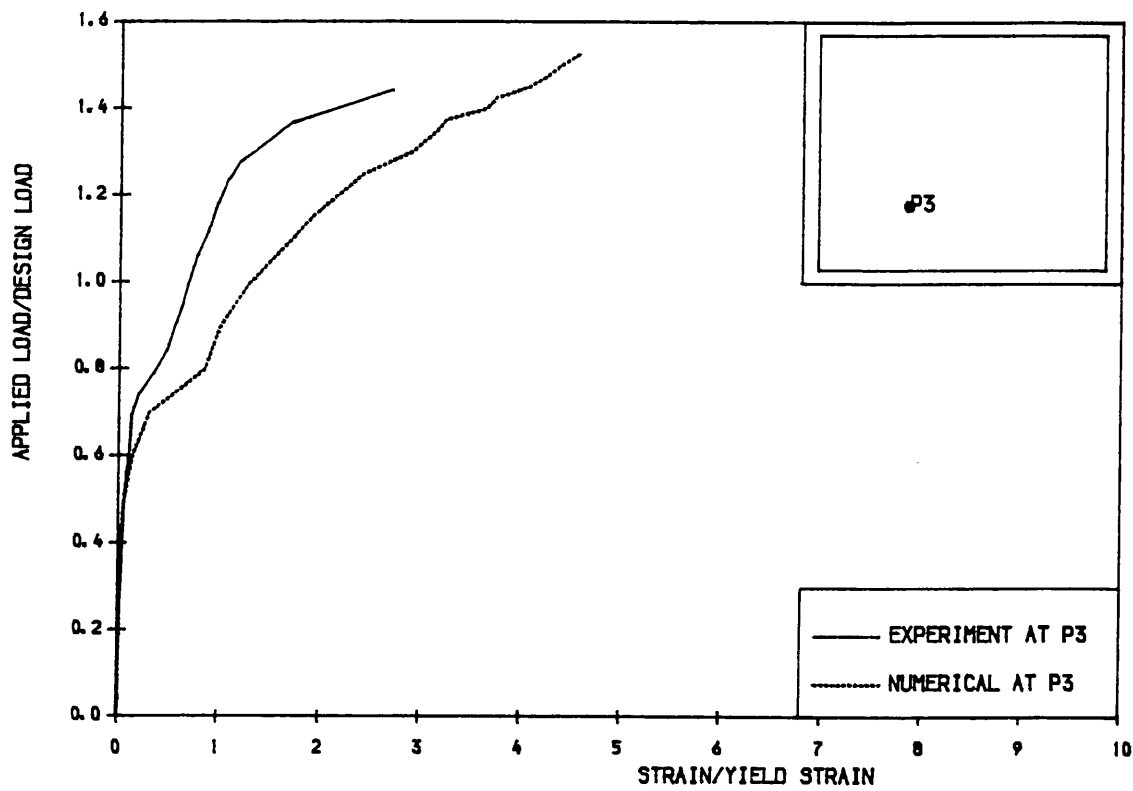


Fig. 8.40a Load-strain curve. Bottom steel. Model S.4

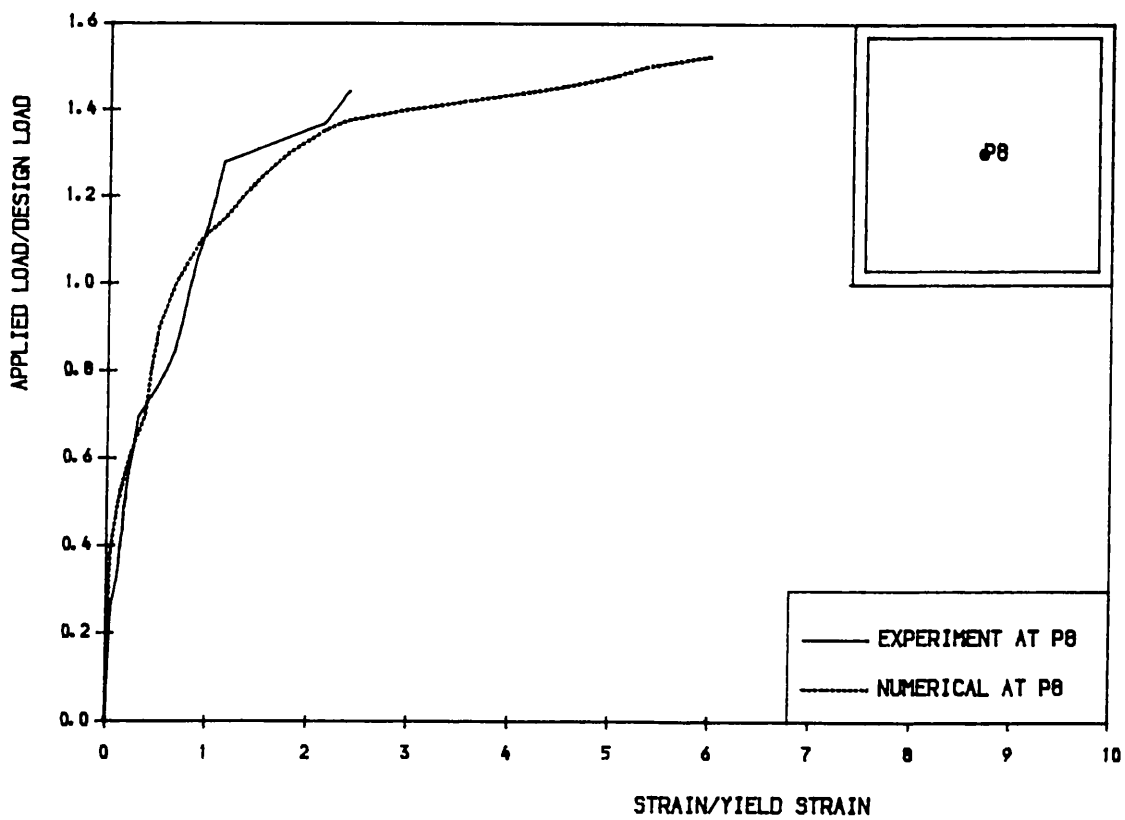


Fig. 8.40b Load-strain curve. Top steel. Model S.4

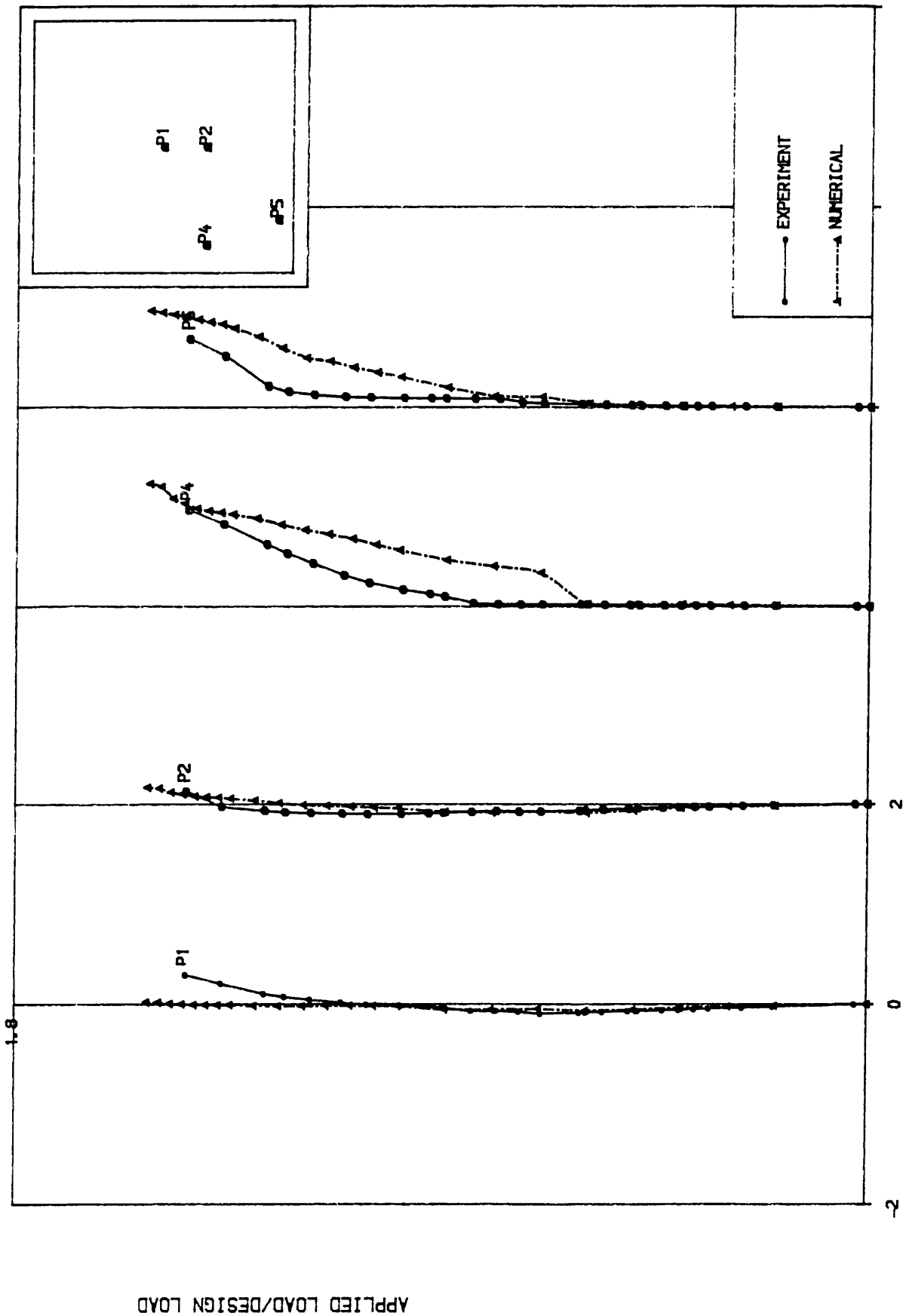


Fig. 8.40c Load-strain curves. Bottom steel. Model S.4

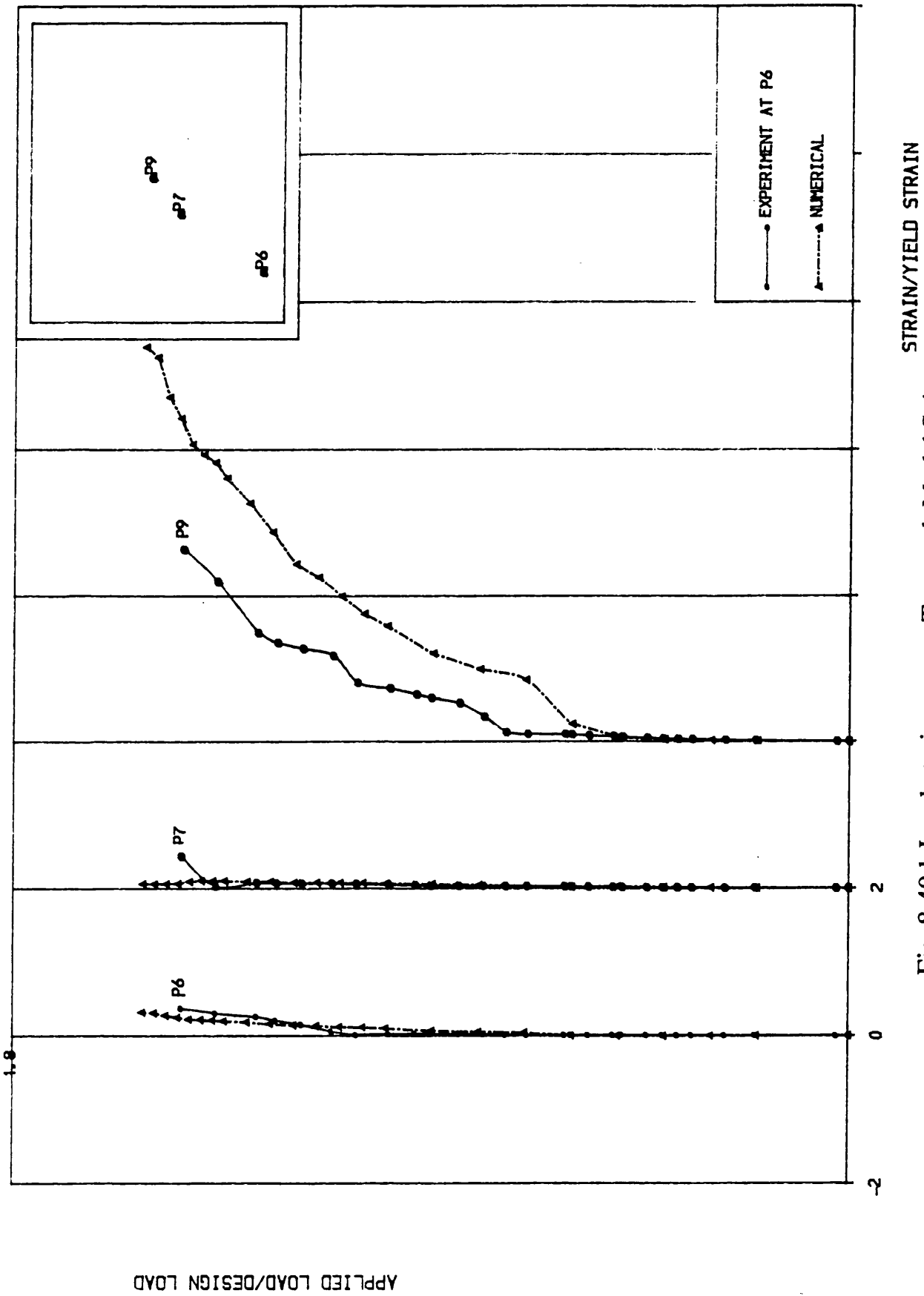
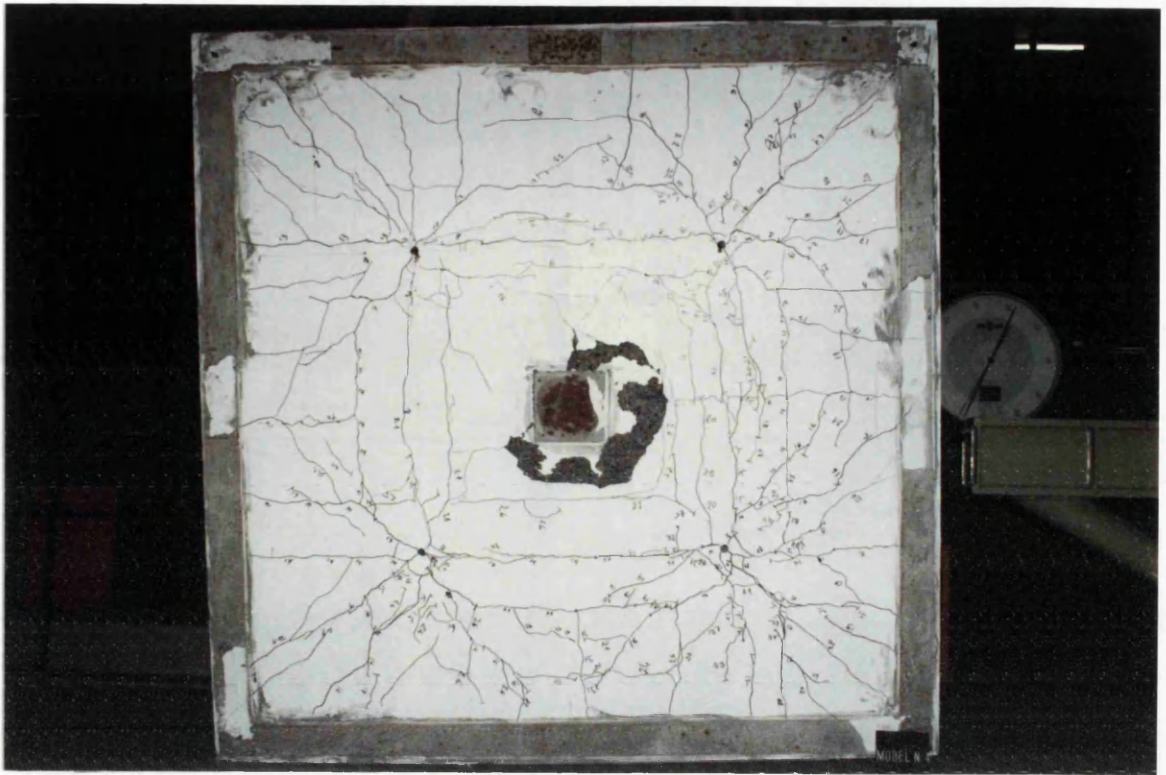


Fig. 8.40d Load-strain curves. Top steel. Model S.4



Numerical 1/4 Slab

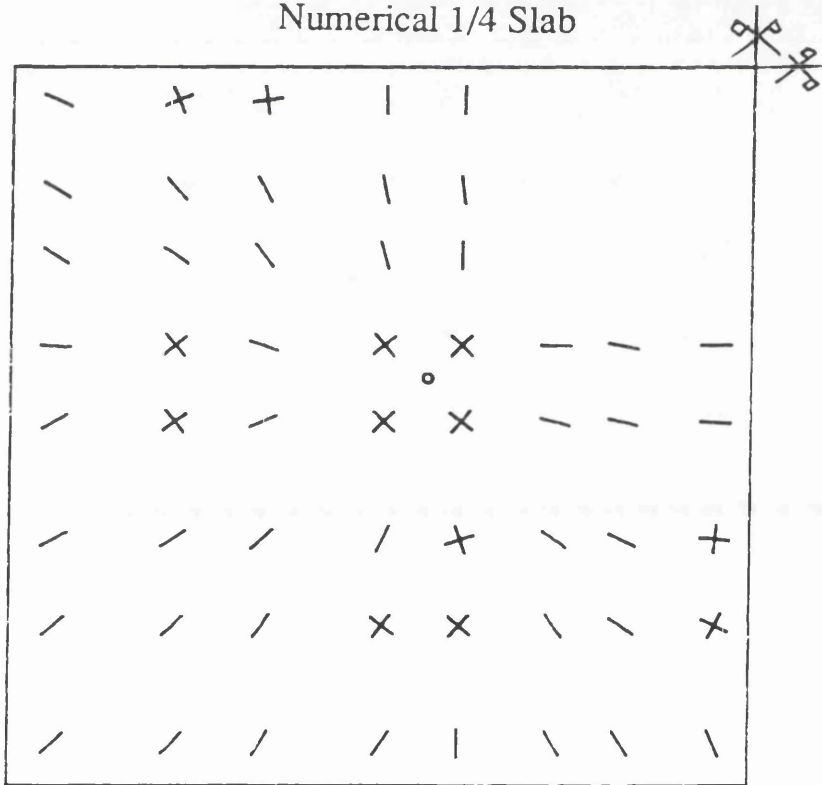


Fig. 8.41a Bottom experimental and numerical crack pattern at collapse load.
Model S.4

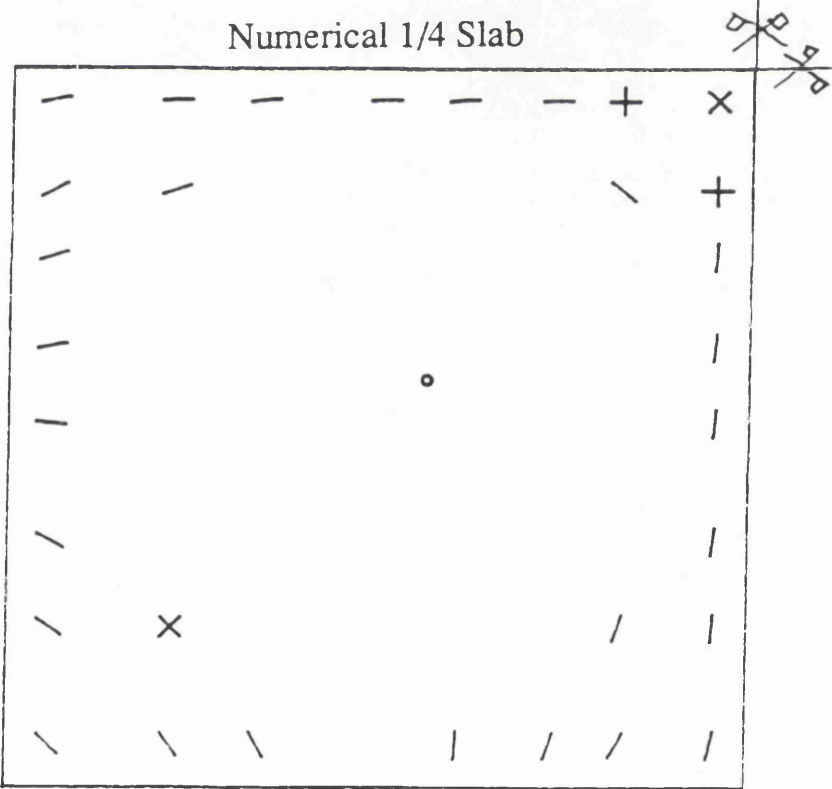
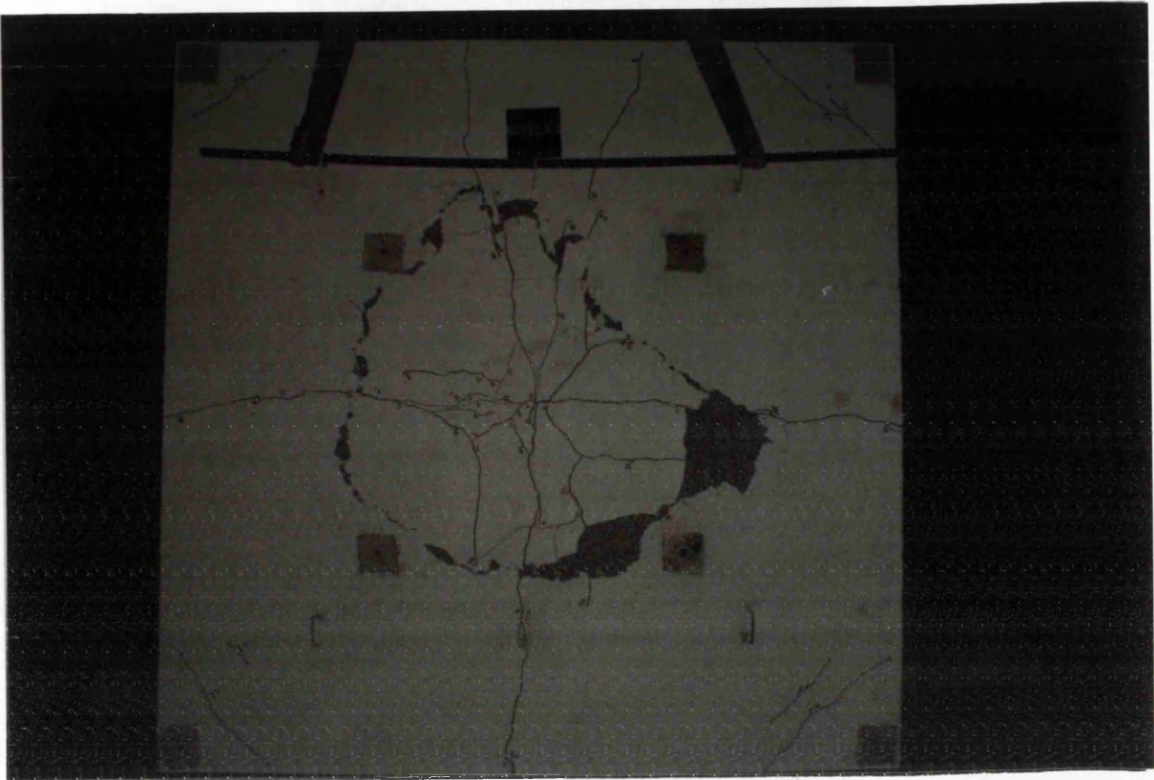
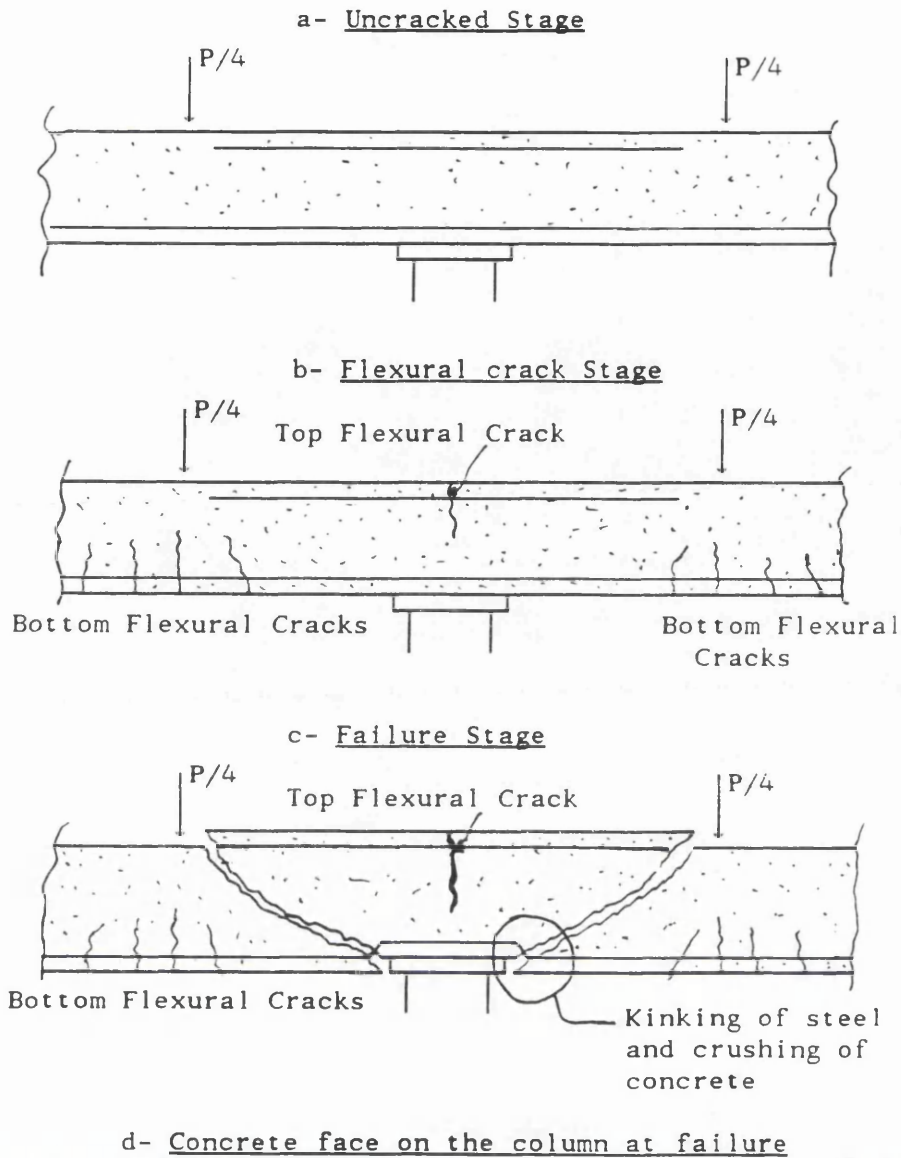


Fig. 8.41b Top experimental and numerical crack pattern at collapse load.
Model S.4

Fig. 8.41c Slab behaviour stages. Model S.4



Pd (0.80 Pu), figure 8.40b, whereas the bottom steel yielded under the point load at 1.2 Pd (0.83 Pu), figure 8.40a.

Crack width:

At 0.48 Pd (0.33 Pu) the first crack was seen under the point load and was 0.1 mm wide, whereas for top concrete surface the crack appeared at 0.75 Pd (0.52 Pu). The limiting service crack width of 0.3 mm was reached at 0.78 Pd (0.54 Pu) under the point load. The top crack widened at a faster rate than the bottom one so that at collapse load the maximum crack width at the top was 4.5 mm, while at the bottom it was only 3.0 mm. Figures 8.41a and 8.41b show the crack pattern for both top and bottom surfaces after failure of the slab.

Mode of failure:

Figure 8.41c explains the stages which the slab passed through until failure. Before the ultimate load was reached the steel strain shows that the steel yielded under the point load for bottom steel, figure 8.40a, and on the column for top steel, figure 8.40b. From crack pattern it can be seen that the bottom face of the slab was covered by flexural cracks. The failure was in punching shear at a load of 1.44 Pd. The failure was mainly caused by the shear strength of the slab reached before the flexural strength was exhausted, because the provided flexural steel was greater than the required one.

8.2.2.2 Model S.6:

The first visible crack occurred at 1.06 Pd (0.66 Pu) under the point load. The width of this crack was of 0.05 mm. As loading continued, a few new long cracks opened so that at 1.25 Pd (0.77 Pu) the cracks reached the corners. The first crack on the top face of the slab was seen at this level of loading on the column. At 1.31 Pd (0.81 Pu) the crack parallel to the edges joined the four point loads to each other forming an inner square at the bottom face of the slab. Also at this loading level the bottom cracks joined each loading point to its

nearest corner of the slab. At this load increment the service load crack width limit was reached under the point load. At 1.35 Pd (0.84 Pu) the maximum crack width at the top face was 0.75 mm, whereas at the bottom face it was 0.8 mm. As the load cell controlling the mid-column reaction, was not properly connected, at 1.40 Pd (0.87 Pu) the slab was unloaded. Before unloading no steel had yielded. The connection of the load cell was repaired and the slab was reloaded at an average loading increment of 0.1 Pd until the loading level reached in the previous loading cycle, after which an average of 0.05 Pd was adopted. At 1.40 Pd (0.87 Pu) the steel yielded both at the top and bottom near the column support and under the point load respectively, while at this level of the first loading history the steel did not yield. This may be due to the transfer of the forces taken previously by the uncracked concrete to the steel in the second loading history because, at critical points, most of the concrete had already cracked. After the steel yielded, the crack width increased rapidly so that at 1.5 Pd (0.93 Pu) the maximum crack widths at the top and bottom face were of 3.0 mm and 1.5 mm respectively. The maximum crack width of 4.0 mm was reached at the top face at 1.56 Pd (0.97 Pu), while at the bottom face it was 3.0 mm. At this stage the deflection of the slab increased rapidly, figures 8.42a–c and some crack opening noise was heard. At 1.60 Pd (0.99 Pu) the old cracks were widening rapidly and a few new cracks appeared near the column at the bottom face and also the crack which caused failure at the next load increment was seen at the top face only on one side of the column. The maximum crack width was of 5.0 mm and 4.0 mm at top and bottom faces respectively. The failure took place at 1.61 Pd with the lifting of a large part of the slab area on the column and between the point loads in a conical shape, figure 8.45c. The loading was dropping slowly. This is due to the presence of shear reinforcement. The presence of shear reinforcement had a significant effect on the punching shear strength of the slab and on the failure mode, so that this slab S.6 showed a more ductile failure. This can be seen from load–deflection of figures 8.42a to 8.42c. Because this model is thicker than S.4 it was expected that it will not have a deflection greater than that of model S.4. In this model almost at all the points where strain

was measured, steel had yielded, figures 8.39a–c and 8.40a–c, and the strain was several times the yielding strain.

The punching crack formed between the point of application of the loads and the mid–column support as in model S.4. Figure 8.45c shows different stages of the slab up to failure, which took place by combination of punching and flexure at 1.61 Pd.

Deflections:

The load–deflection curves are shown in figures 8.42a to 8.42c. It can be noticed that a slight nonlinearity started beyond the design load where the cracking started. Because the percentage of steel is very small, therefore after cracking of a large area of the slab, its stiffness decreased sharply. At 1.4 Pd (0.87 Pu) the limiting service load deflection was reached. This represents an acceptable serviceability level in terms of the ultimate load.

Steel strains:

The steel load–strain curves are shown in figures 8.43a–c and 8.44a–c for bottom and top steel respectively. The first yielding of steel, both top on the column and bottom under the point load, was detected at 1.40 Pd (0.87 Pu). The corner top steel yielded at 1.60 Pd (0.99 Pu). Most measured steel strains show the steel had yielded in most parts of the slab.

Crack width:

The first crack occurred on the bottom face under the point load at 1.06 Pd (0.66 Pu). At 1.31 Pd (0.81 Pu) the limiting service load crack width of 0.3 mm was reached. After the yielding of steel, the crack widened at an increasing rate especially at the top face. The crack pattern for both the top and the bottom face are presented in figures 8.12a and 8.12b.

Column Reaction:

The variation of the central reaction with load is presented in figure 8.46 and

was linear up to the collapse load. The maximum reaction at failure load was 20% greater than the reaction used in the design of the shear capacity of the slab on the column. The shear reinforcement for the slab was designed using BS8110(1).

Mode of failure:

It was expected that the maximum deflection of this model will be much less than that of model S.4, because S.6 is 150 mm thick while S.4 is of 100 mm thick. Model number S.4 did not fail in a true ductile manner, this can^{be} seen from the maximum deflection at collapse load. For the first model S.4 the deflection was 13.8 mm while for S.6 a value of 23.0 mm was recorded. The experimental ultimate load was greater than the one designed for. This is mainly due to the provided steel which was greater than the required one, table 8.4. It was confirmed by Marzouk and Hussein(44) that as the slab depth increases, slab stiffness increases, and ductility decreases. In contrast here model S.6, because of the presence of shear links in the column area, behaved in a more ductile manner than S.4. This explains the importance of shear links in the ductility demand for such structures. The presence of the shear links near the column region for model S.6 also enhanced its strength, although the volume of the provided steel to the required one was less than that for model S.4. Also from figures 8.41c and 8.45c it can be seen that the concrete at the bottom face near the column head in slab S.4 suffered serious damage. This was caused by the push out of the concrete surrounding the bottom flexural steel bars, which was not the case in slab S.6, where shear links restrained the bottom and the top horizontal steel together. This did not allow the horizontal steel to push out the concrete cover of the bars. Despite the fact that the method of design does not account directly for the vertical shear strength, the experimental results of these two slabs give a satisfactory behaviour both at service load and at the ultimate load.

Numerical analysis:

Model S.4 and S.6 were analysed using finite element mesh shown in figure 6.10b. The slab S.4 was divided into 10 layers four of which were steel wherever it is present, whereas for the slab S.6 a 12 layers were taken to represent the 150mm concrete thickness and steel layers.

The first increment was of 0.2 Pd and it was reduced to 0.1 Pd up to the design load after which it was reduced further to 0.05 Pd. For S.6 the first load increment was 0.3 Pd and reduced to 0.1 Pd until 0.7 Pd. Afterwards the load increment was reduced further to 0.05 Pd until the design load after which 0.025 Pd was applied until failure load was reached. For slab model S.4 the first crack was detected under the point load at 0.4 Pd. A good agreement between the numerical and the experimental values for the load–deflection curves figure 8.39a–c, load–strain curves figure 8.40a–d and crack pattern 8.41a–b was obtained. Acceptable results were obtained for model S.6 also in terms of load–deflections figures 8.42a–c, load steel strains figures 8.43 and 8.44 for bottom and top steel respectively. The crack pattern comparison between the observed and computed at failure load, for both bottom and top faces of the slab S.6 respectively, gave good agreement. Good agreement, between the experiment and the numerical results, can be seen also for the mid–column reaction as shown in figure 8.46. Both slabs failed numerically in a flexural manner. For S.6 all measured steel strains at the bottom exceeded the yield strain both experimentally and numerically. Whereas for S.4 numerically the slab failed flexurally while experimentally it can be seen that the slab can carry more load if it did not fail in shear. Table 8.5 summarizes the comparison between numerical and experimental results. The numerical early cracking lead to early yielding of steel in comparison to experiment especially in model S.6 where the ratio of steel area to the concrete depth is much smaller than in S.4.

Tab. 8.4 Steel volume ratio (Provided steel/Num. required steel)
Model S.4 and S.6

Model	Steel Ratio Provided/Required	
	Bottom	Top
Model S.4	1.94	1.86
Model S.6	1.67	1.71

Table 8.5 Experimental and Numerical Results Comparison.
Slab S.1 and S.2.

Model → Facts ↓	Slab S.4		Slab S.6	
	Experim.	Numerical	Experim.	Numerical
First visible crack at the bottom face	0.48 Pd 0.33 Pu	0.50 Pd	1.06 Pd 0.66 Pu	0.75 Pd
Width of this Crack	0.1 mm	-	0.05 mm	-
Location of this Crack	Under the point load	Under the point load	Under the point load	Under the point Load
First visible crack at the top face	0.75 Pd 0.52 Pu	0.70 Pd	1.25 Pd 0.77 Pu	0.80 Pd
Width of this Crack	0.2 mm	-	-	-
Location of this Crack	On the Column	On the Column	On the Column	On the Column
Service Crack width limit	0.78 Pd 0.54 Pu	-	1.31 Pd 0.82 Pu	-
Service deflection limit	0.94 Pd 0.65 Pu	1.0 Pd	1.40 Pd 0.87 Pd	1.15 Pd
1 st yielding of top steel on the column	1.15 Pd 0.80 Pu	1.25 Pd	1.40 Pd 0.87 Pu	0.9 Pd
1 st yielding of bottom steel under Poin. Loa.	1.20 Pd 0.83 Pu	0.90 Pd	1.40 Pd 0.87 Pu	0.80 Pd
Failure took place at	1.44 Pd	1.525 Pd	1.61 Pd	1.575 Pd
Mode of failure	Shear	Flexural	Shear + Flexural	Flexural

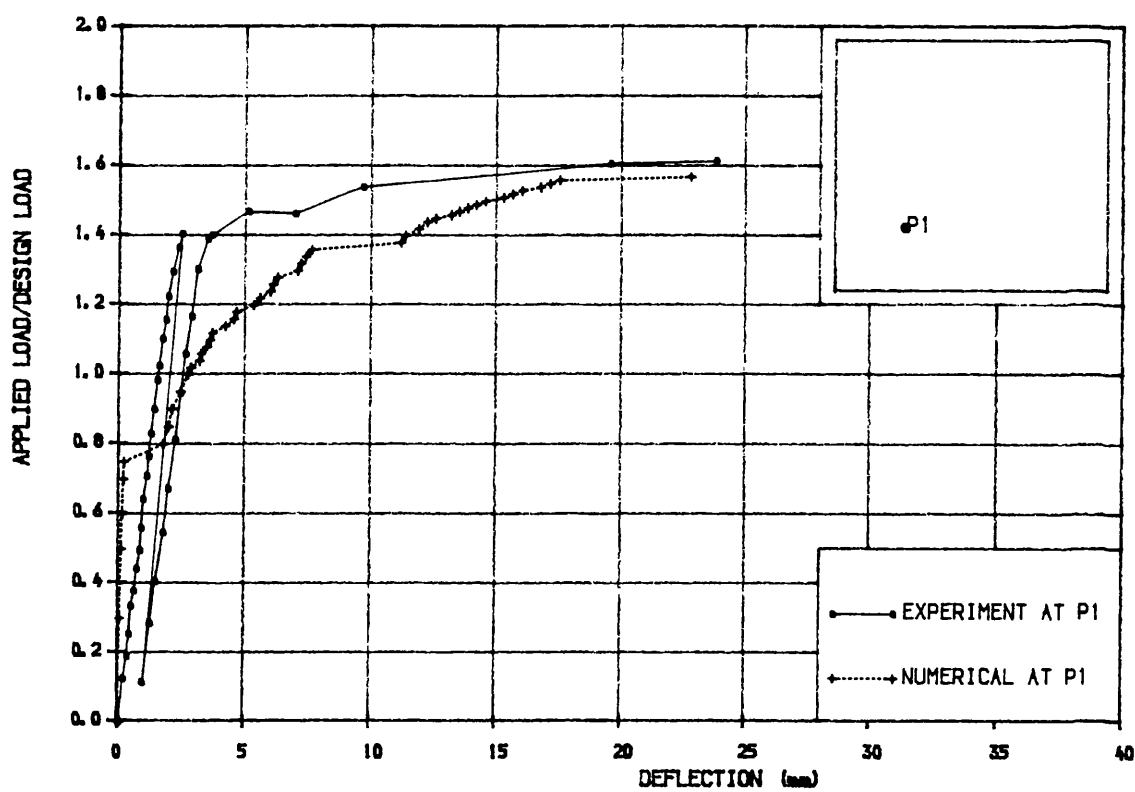


Fig. 8.42a Load-deflection curve. Model S.6

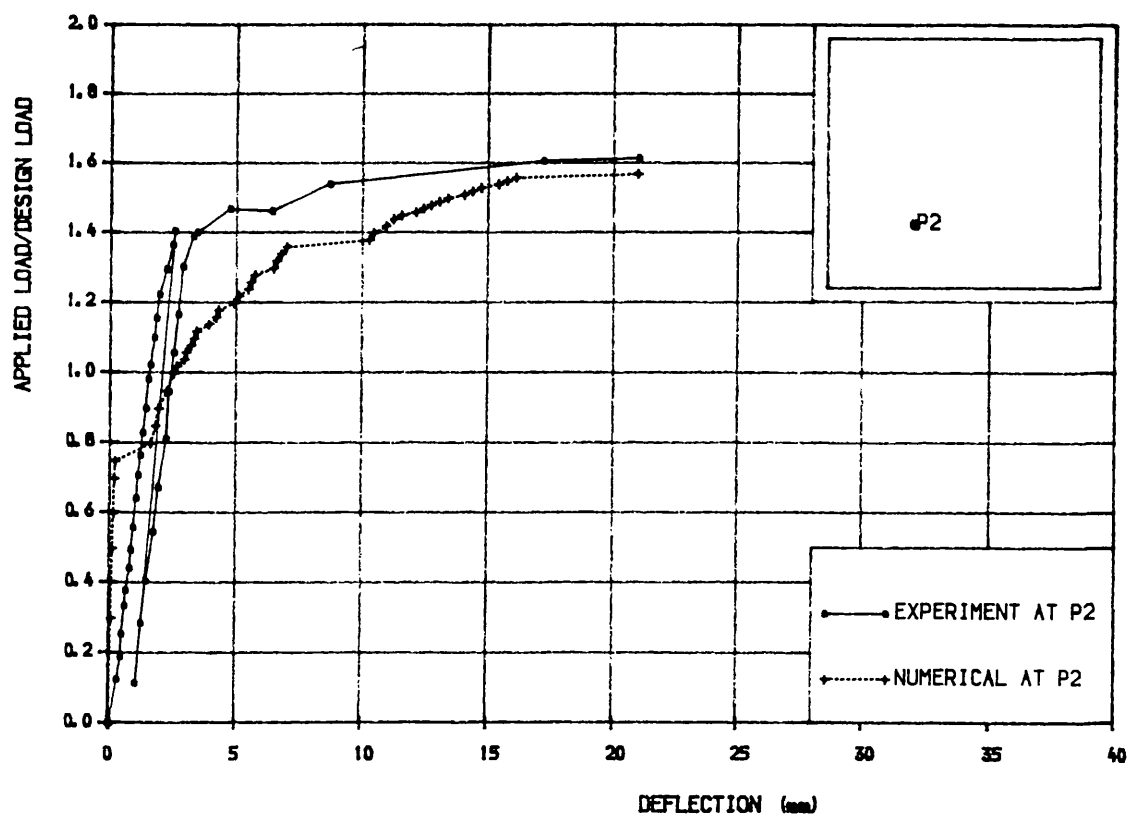


Fig. 8.42b Load-deflection curve. Model S.6

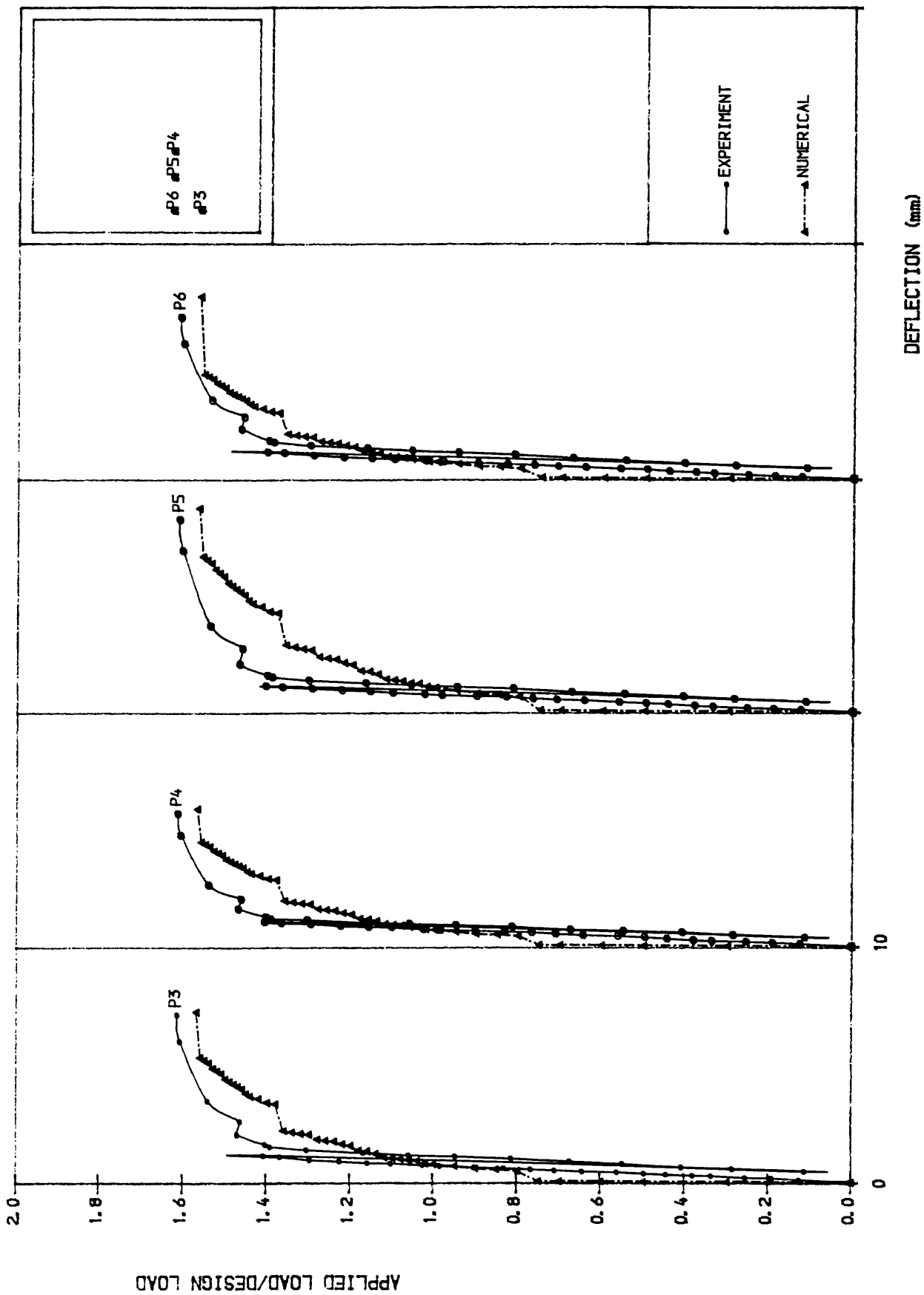


Fig. 8.42c Load-deflection curves. Model S.6

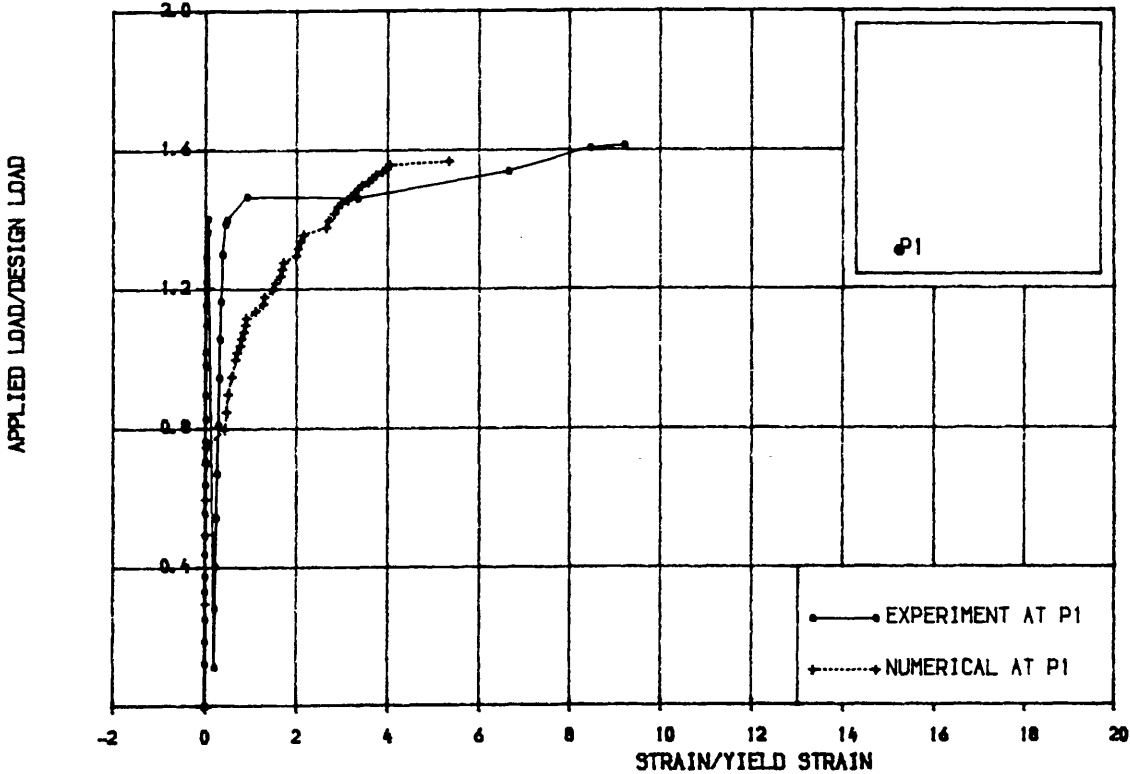


Fig. 8.43a Load-strain curve. Bottom steel. Model S.6

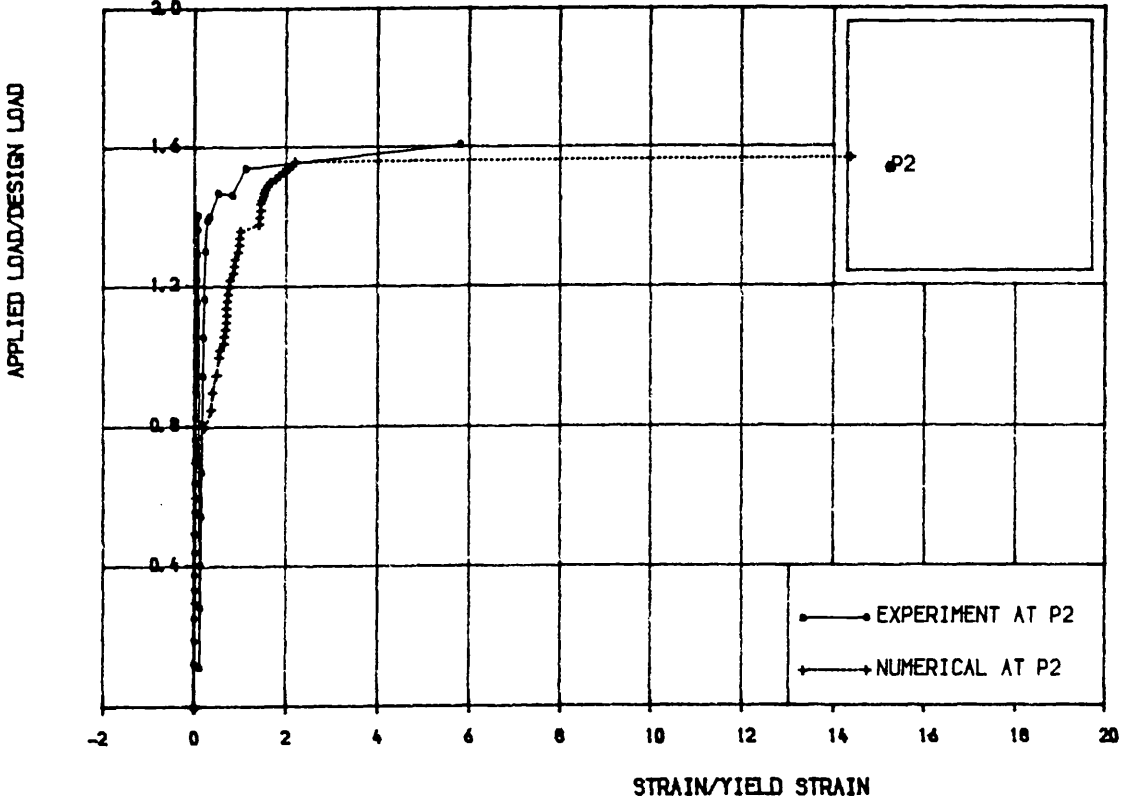


Fig. 8.43b Load-strain curve. Bottom steel. Model S.6

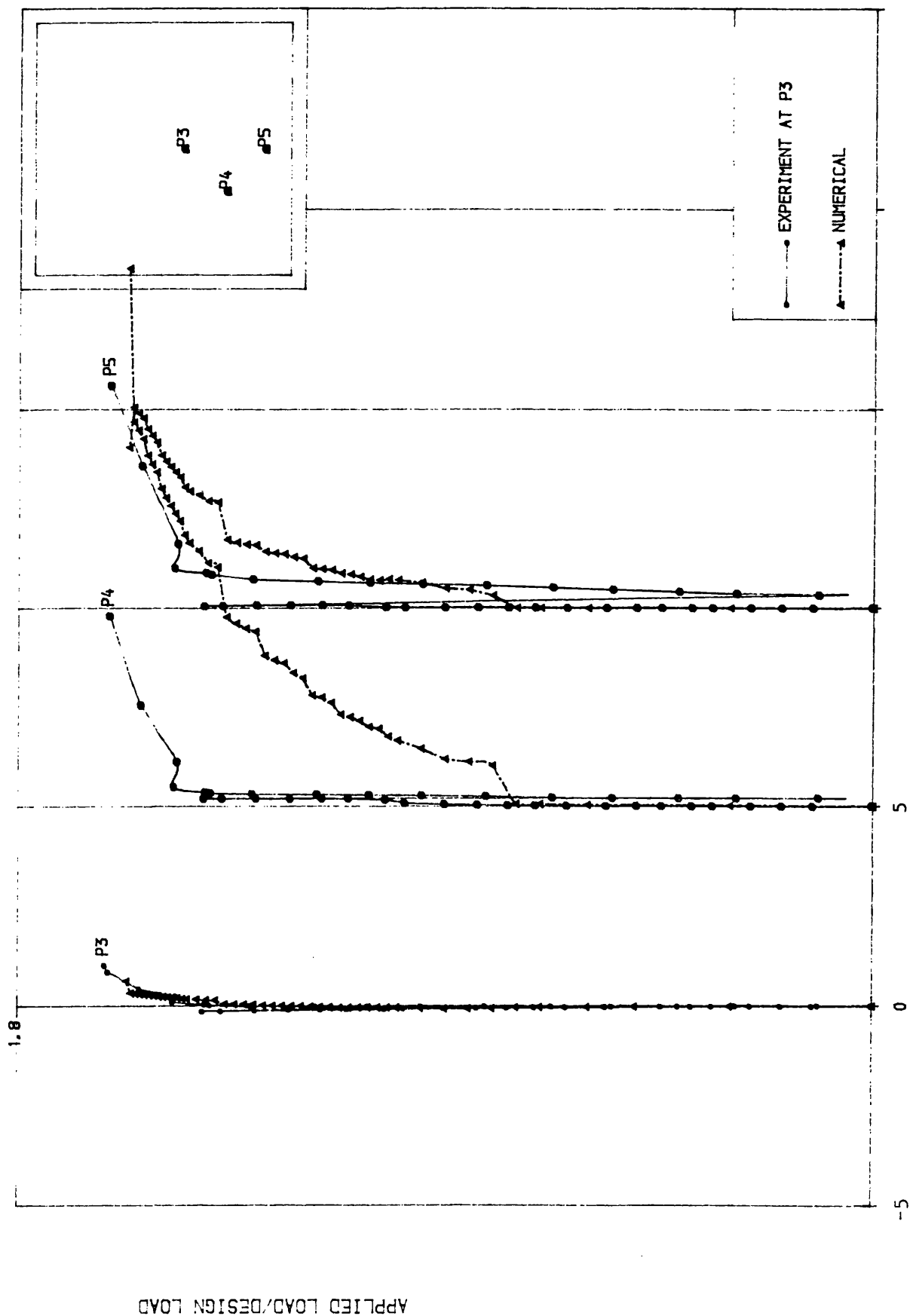


Fig. 8.43c Load-strain curves. Bottom steel. Model S.6

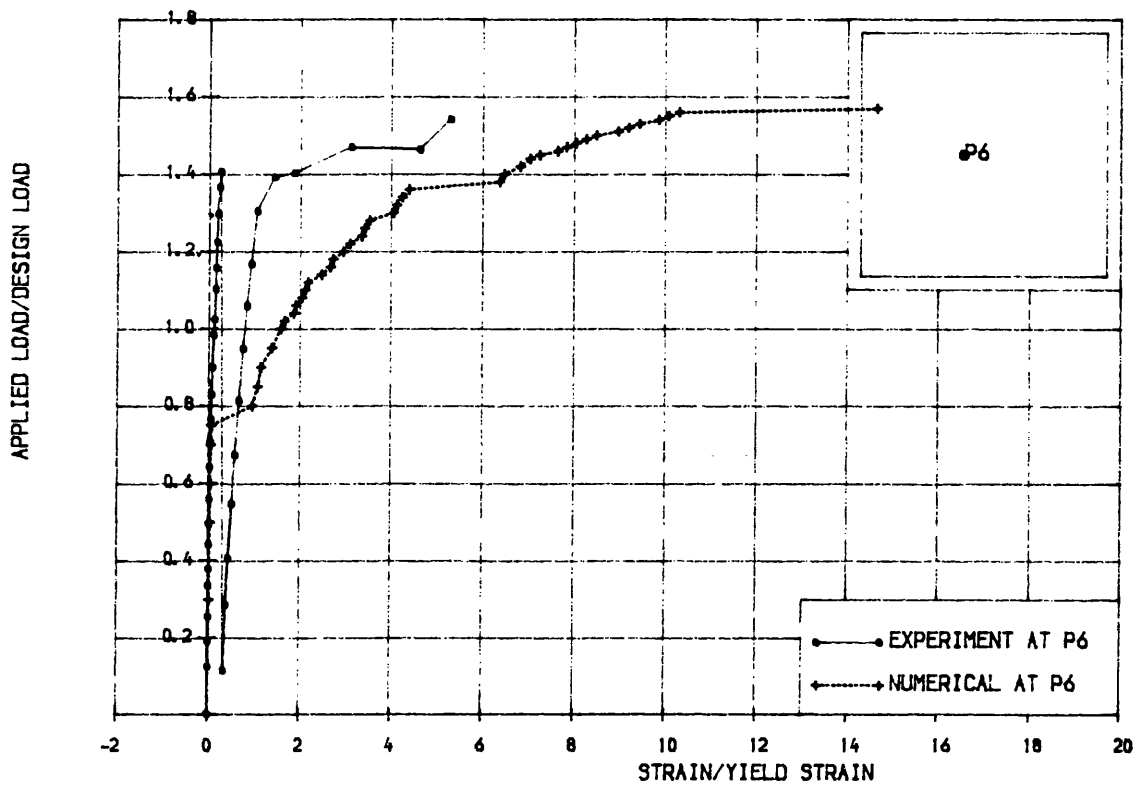


Fig. 8.44a Load-strain curve. Top steel. Model S.6

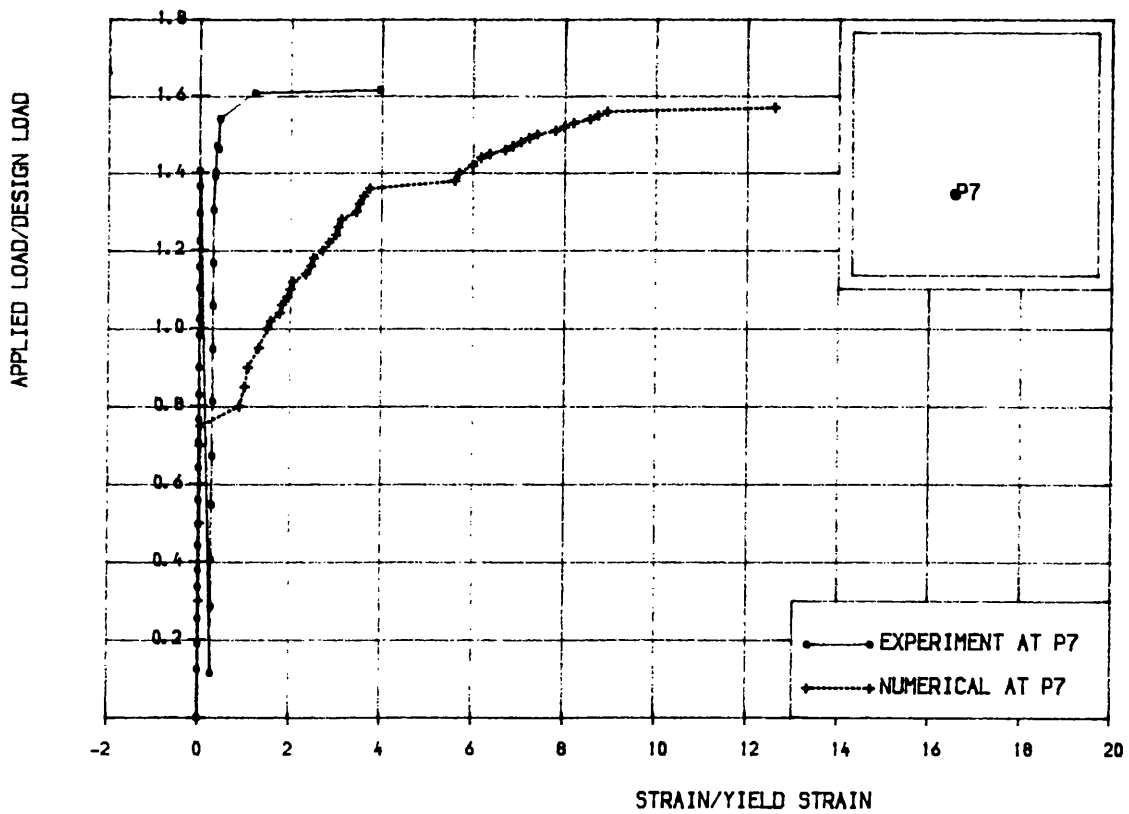
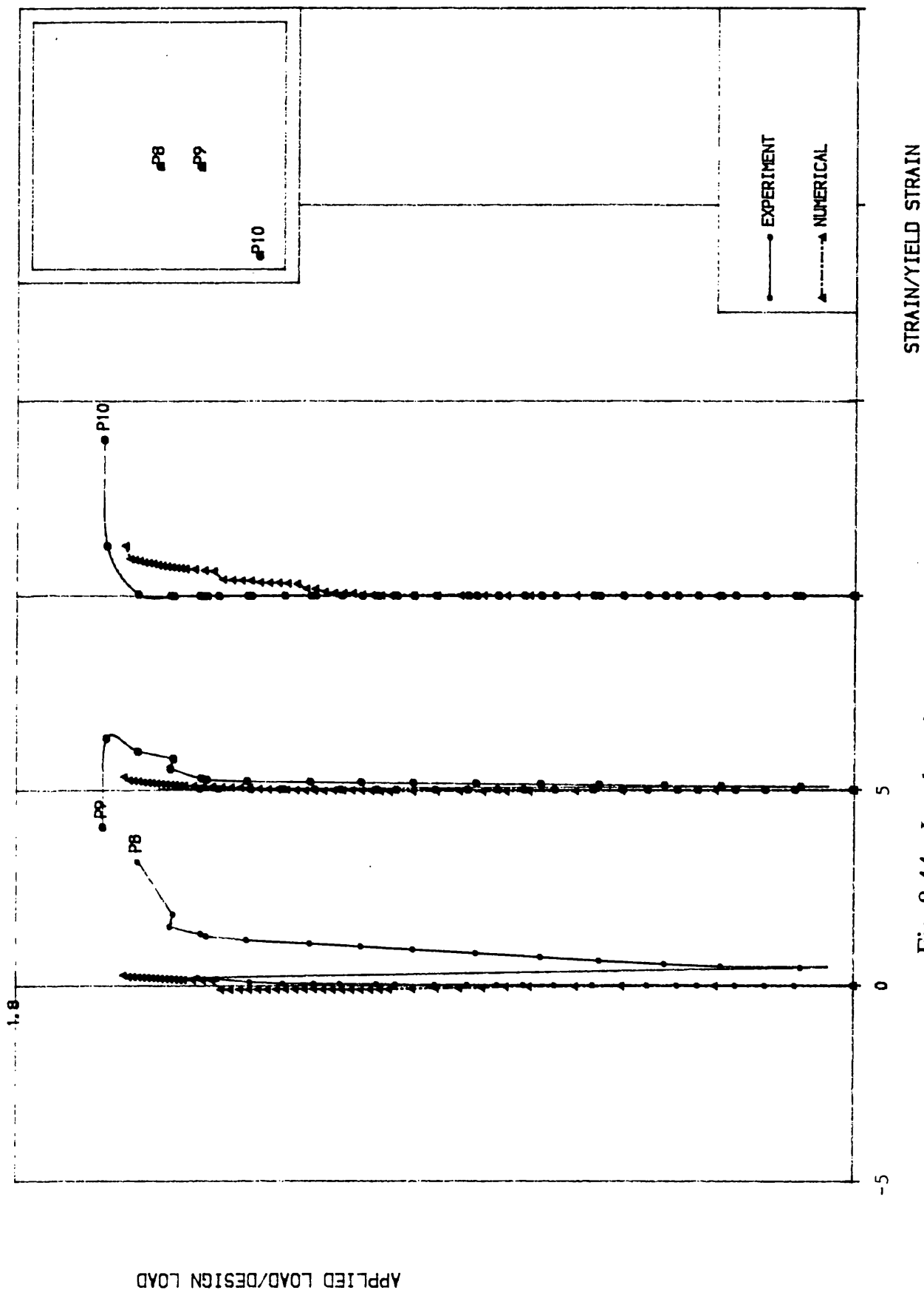


Fig. 8.44b Load-strain curve. Top steel. Model S.6



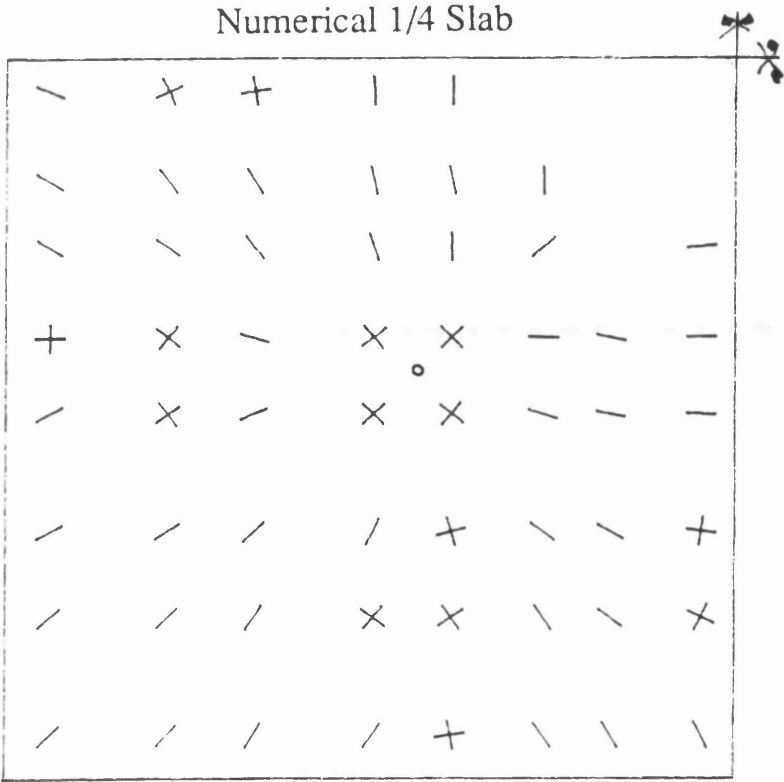
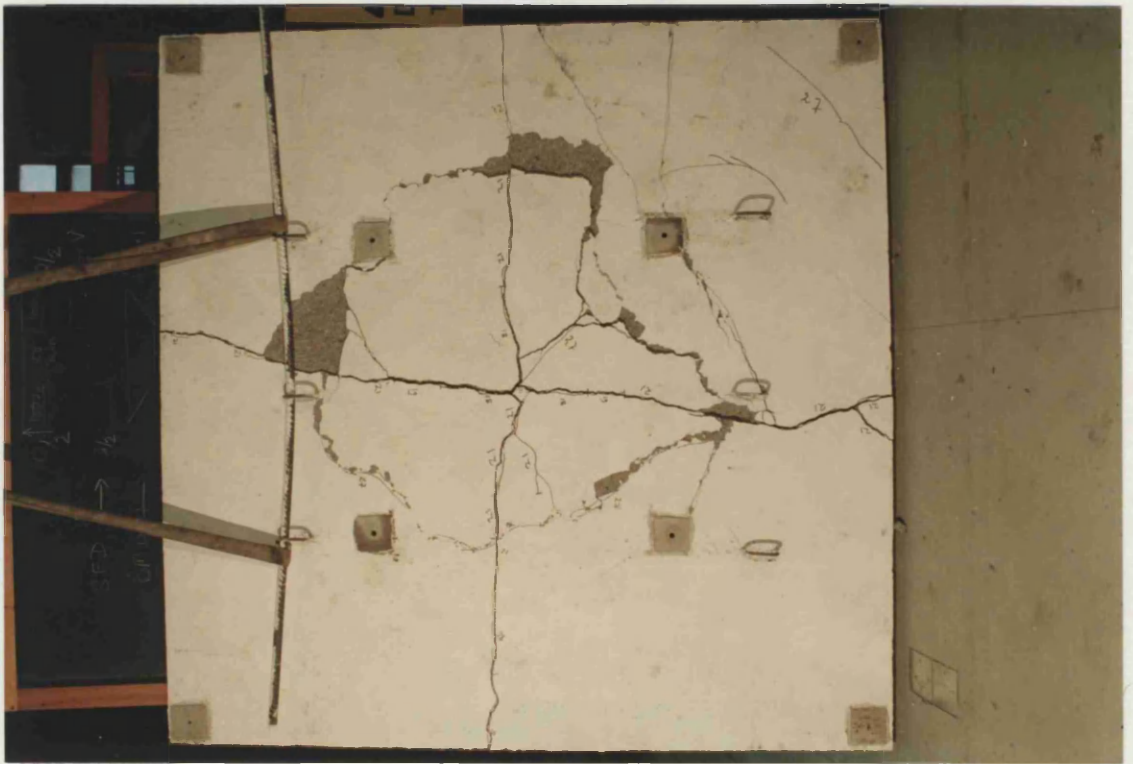


Fig. 8.45a Bottom experimental and numerical crack pattern at collapse load.
Model S.6

Fig. 8.45c Slab behaviour stages. Model S.6



Bottom Flexural Cracks

Numerical 1/4 Slab

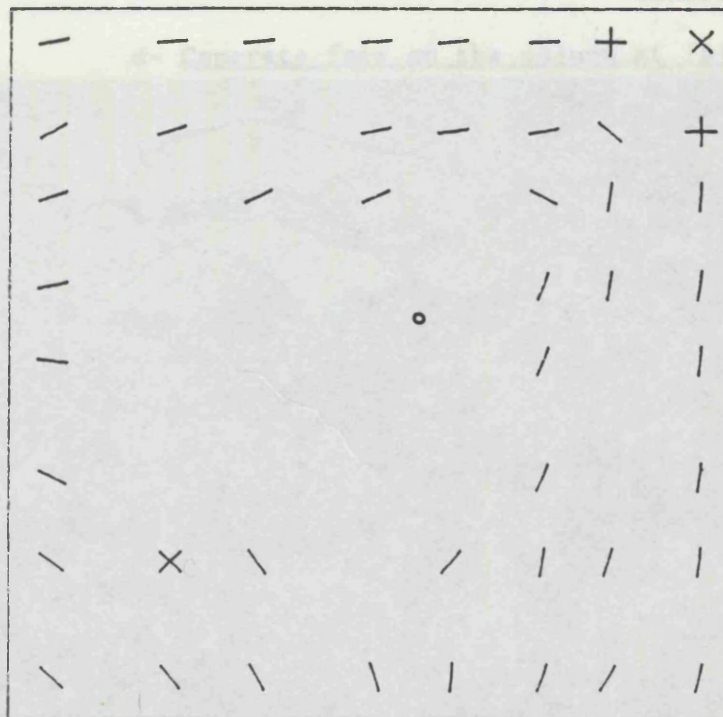
Kinking of steel
and crushing of
concrete

Fig. 8.45b Top experimental and numerical crack pattern at collapse load.
Model S.6

Fig. 8.45c Slab behaviour stages. Model S.6

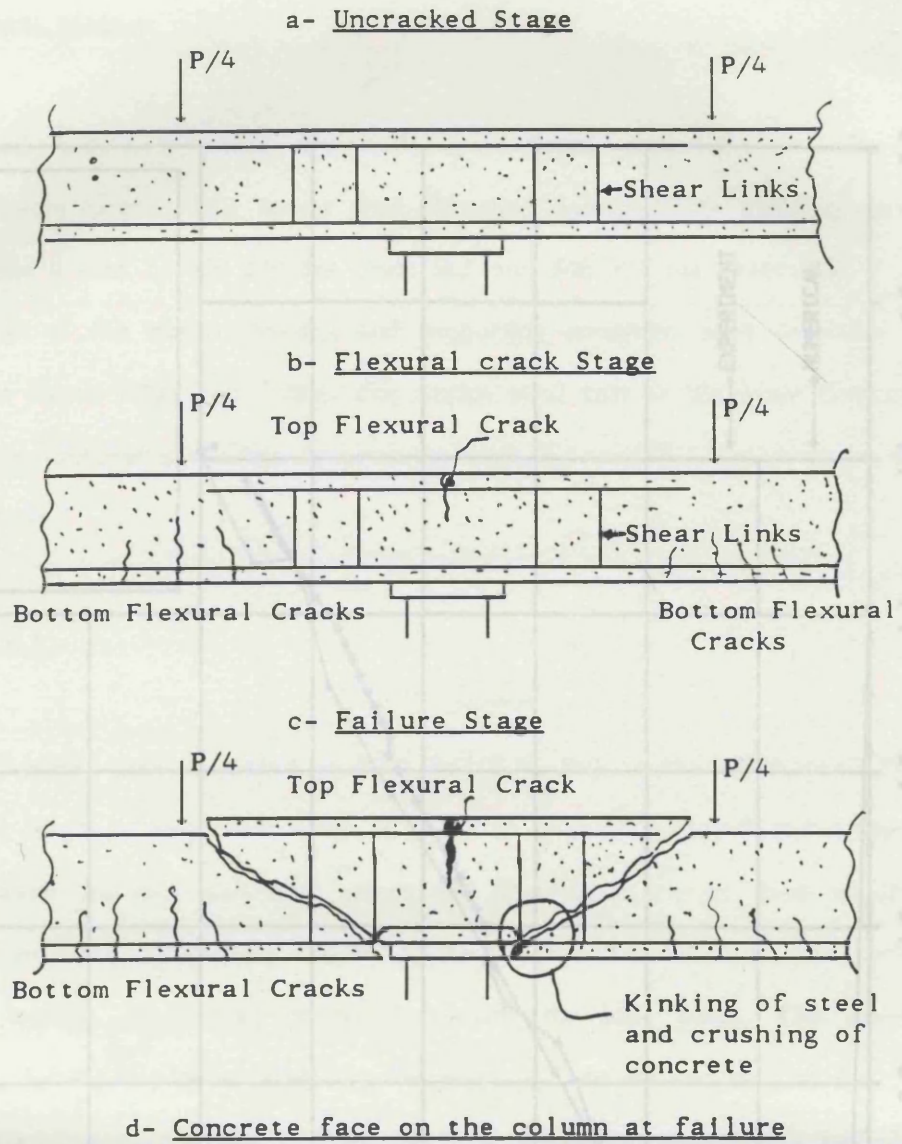


Fig. 8.46 Load-mid-column reaction curve. Model S.6

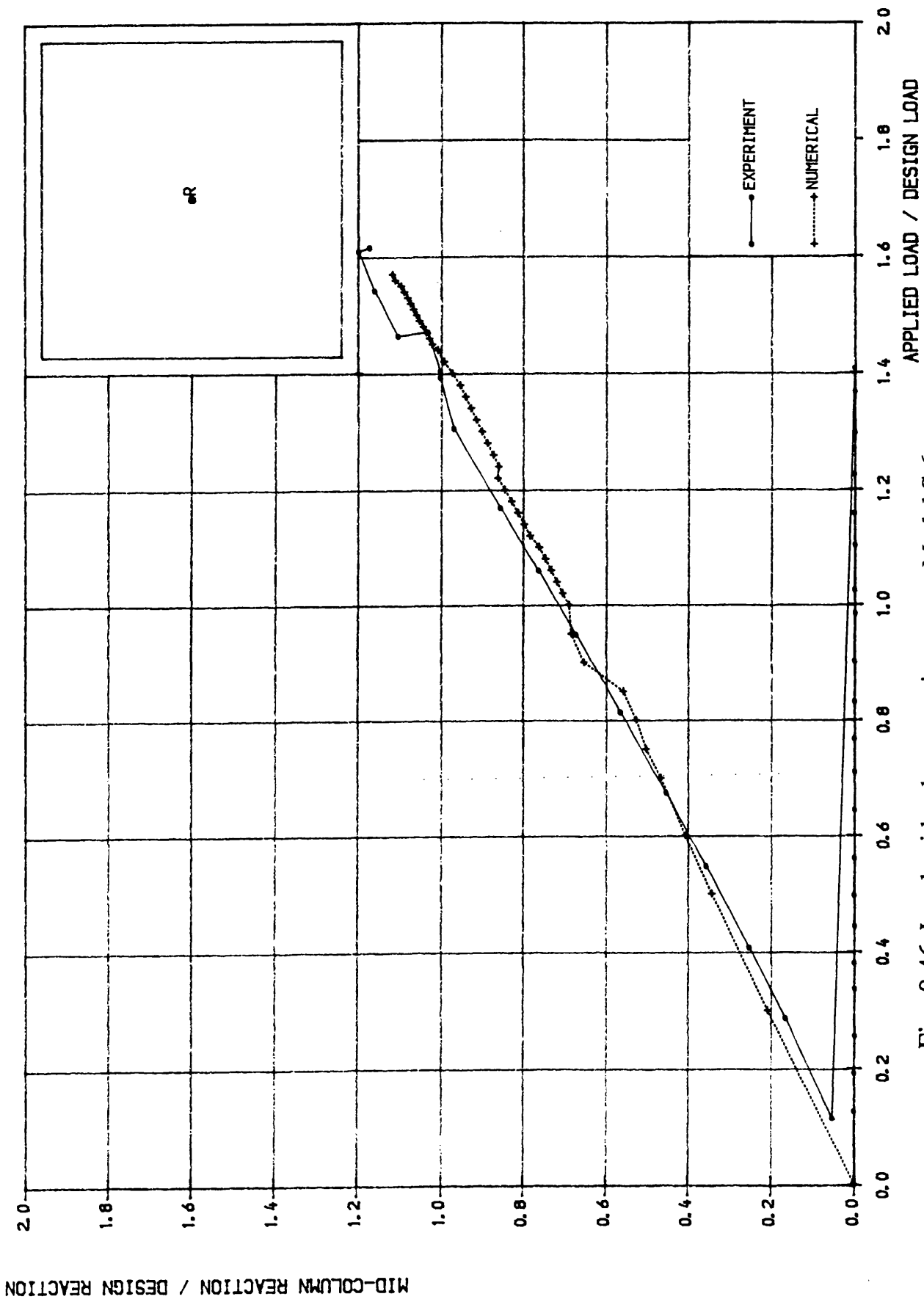


Fig. 8.46 Load-mid.column reation curve, Model S.6

8.3 Deep Beam Models:

Two deep beams B.1 and B.2 with span depth ratio of 1.8 and 0.9 respectively, were tested. The beams were designed, using 100% plasticity stress distribution, for a load of 250 KN for beam B.1 and 500 KN for beam B.2.

The dimension of the beams, loading and supporting condition were presented in chapter seven figure 7.22a and 7.22b. The beams were cast at the same time and have the same material properties as given in table 6.3 and 6.4 for concrete and steel respectively.

8.3.1 Beam B.1:

The first visible crack appeared at 0.15 Pd (0.33 Pu) at the mid-span. They were flexural cracks of maximum width of 0.1 mm. Figures 8.47a–d and 8.48a–d respectively show the load–deflection curves and load–strain curves, from which it can be observed that nonlinearity started before the first visible crack. On further increase in loading, the cracks propagate towards the load point. The inclined shear cracks, joining the point load and the supports, opened suddenly at 0.87 Pd (0.40 Pu). The maximum width of these cracks at this level was of 0.15 mm. The service load crack width limit of 0.3 mm was reached on the inclined shear crack at the mid-shear span, at 1.13 Pd (0.52 Pu). Beyond this stage of loading the old cracks were widening and very few new cracks were opening. At 1.32 Pd (0.61 Pu) the flexural steel yielded at the bottom mid-span of the beam, figure 8.48a, and the flexural cracks reached the point load, figure 8.49a. Up to 1.98 Pd (0.91 Pu) the maximum crack width was measured on the diagonal joining the point load and the supports. At 2.05 Pd (0.94 Pu) the maximum crack width of 2.5 mm at the mid-span was measured. The widening of the flexural cracks was increased beyond this level of loading, such that at 2.16 Pd (0.99 Pu) the maximum crack width was of 4.0 mm. At this loading stage all the measured horizontal steel strains reached the yield strain.

Collapse took place, at Pu equal 545 KN ($P_u = 2.18 P_d$), by a combination of

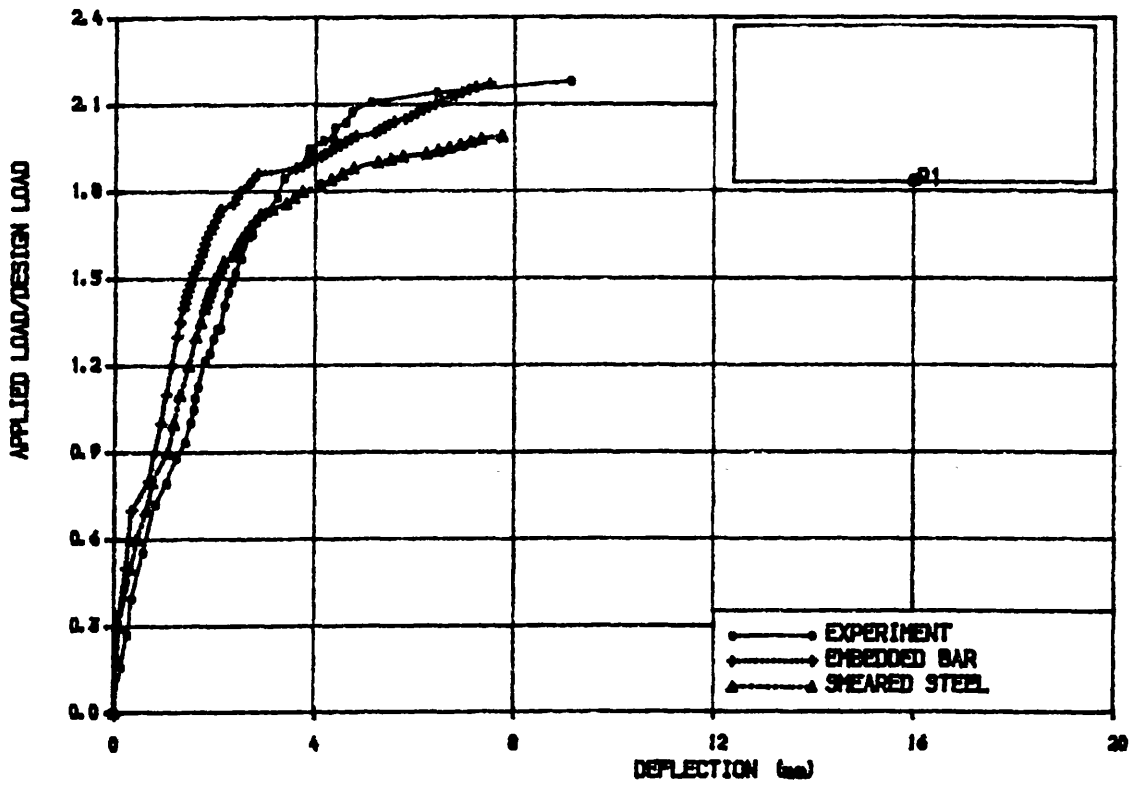


Fig. 8.47a Load-deflection curve. Beam B.1

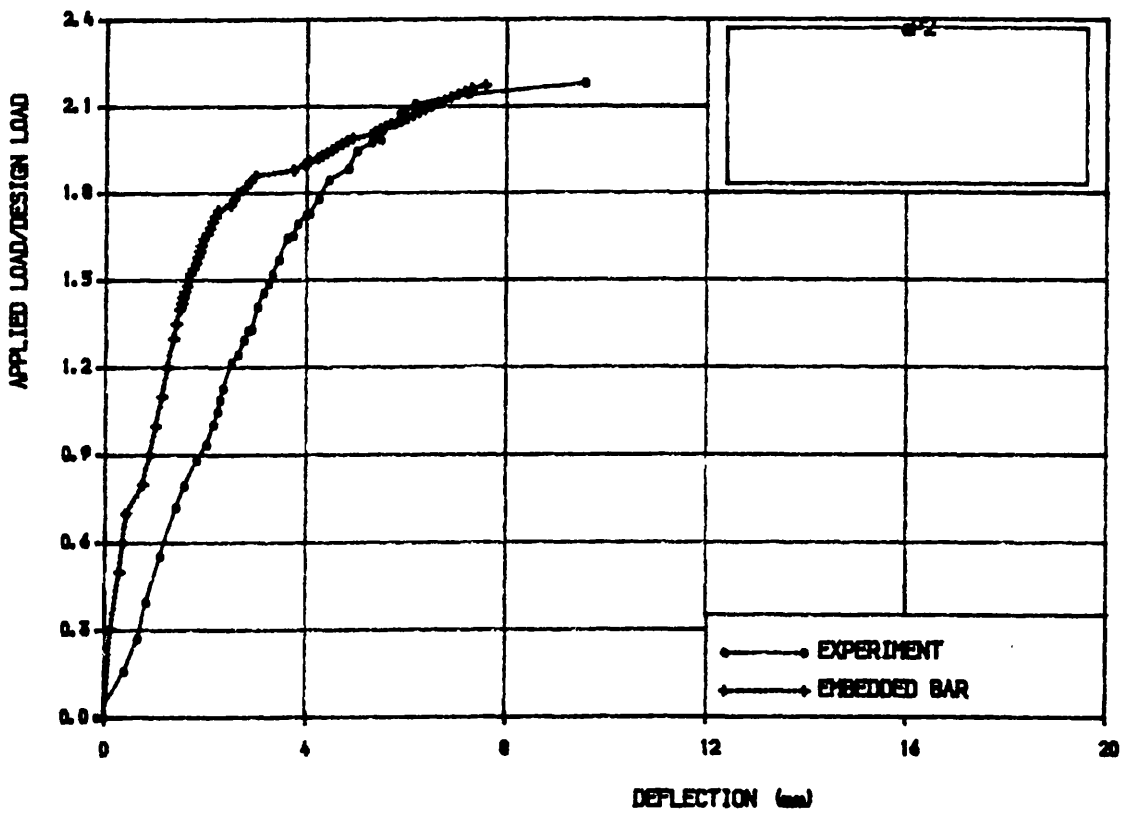


Fig. 8.47b Load-deflection curve. Beam B.1

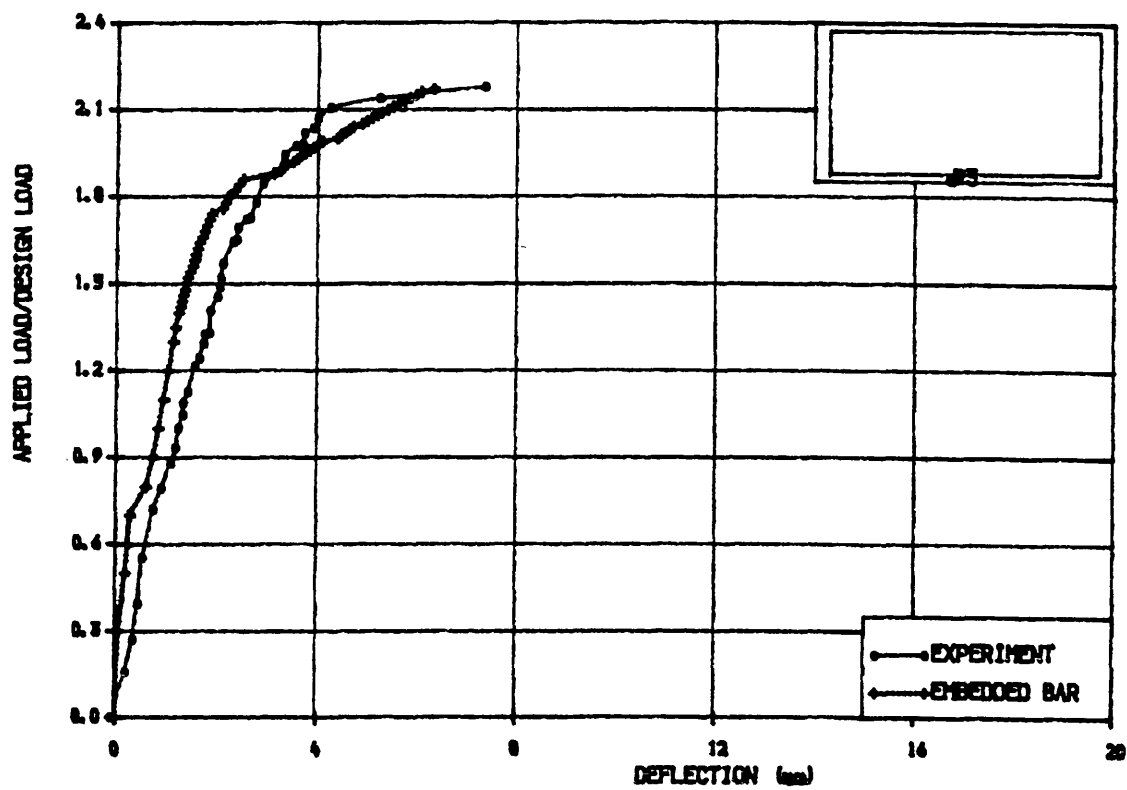


Fig. 8.47c Load-deflection curves. Beam B.1

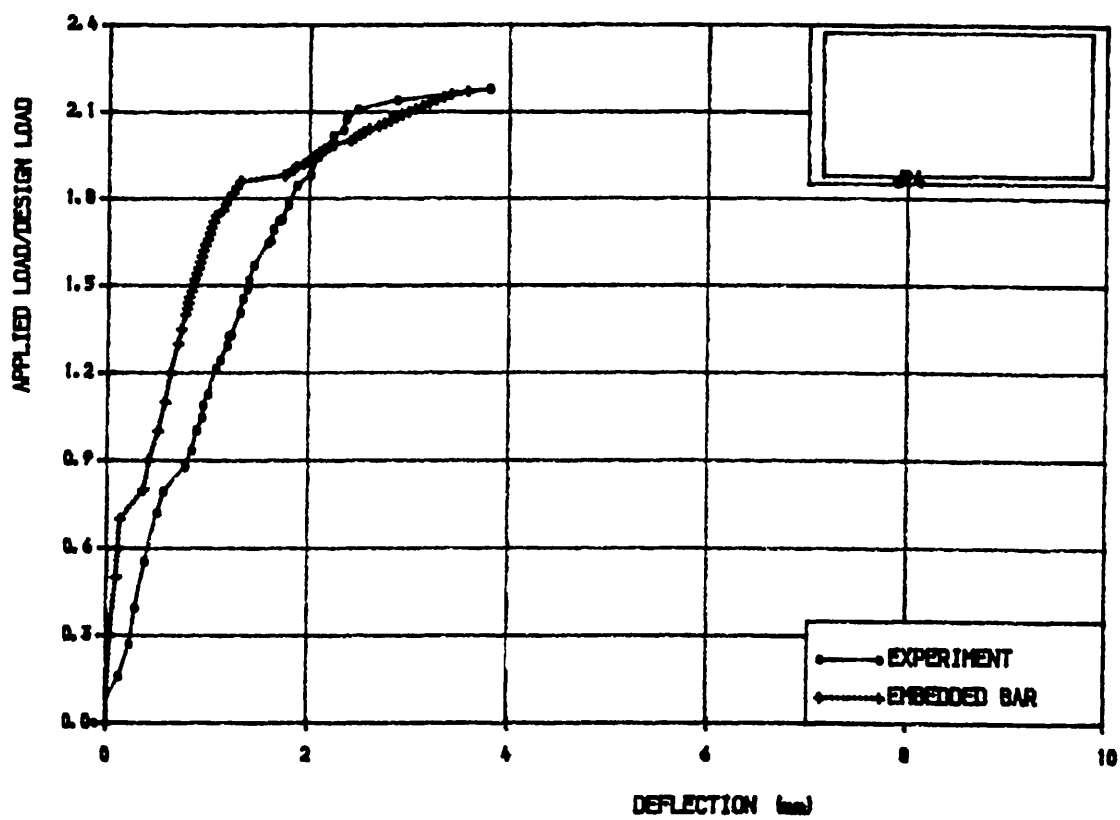


Fig. 8.47d Load-deflection curves. Beam B.1

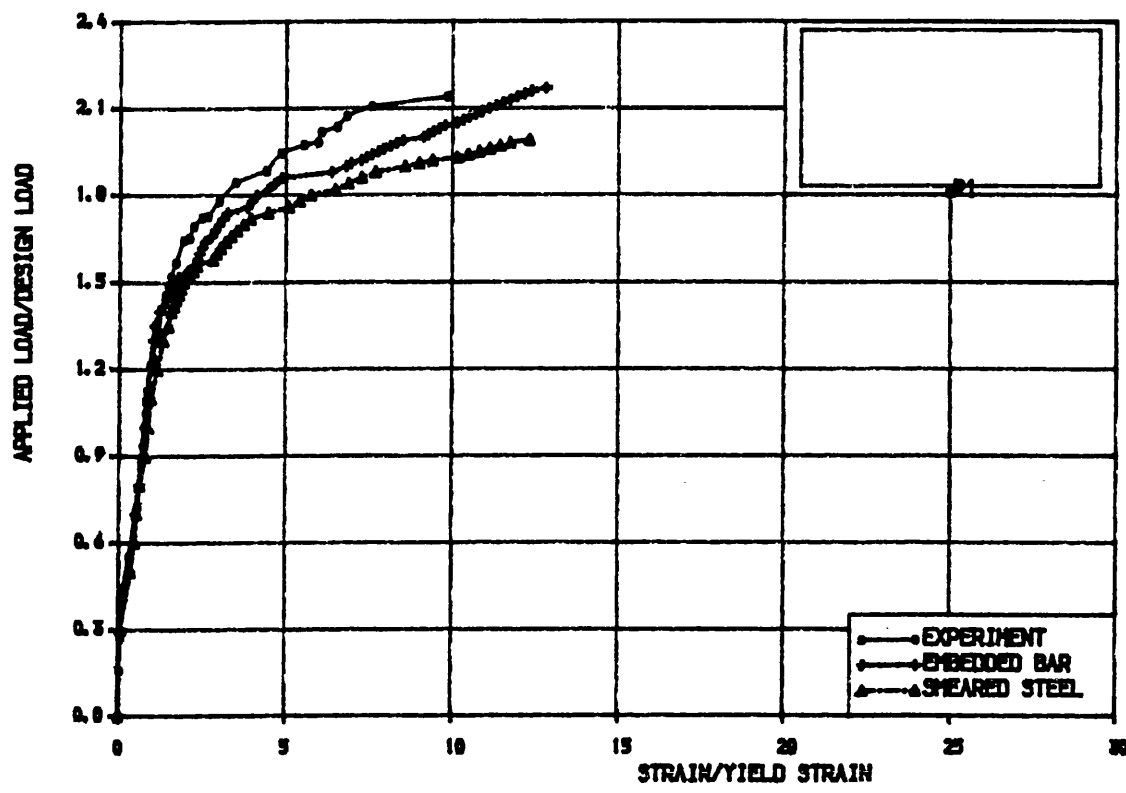


Fig. 8.48a Load-horizontal steel strain curve. Beam B.1

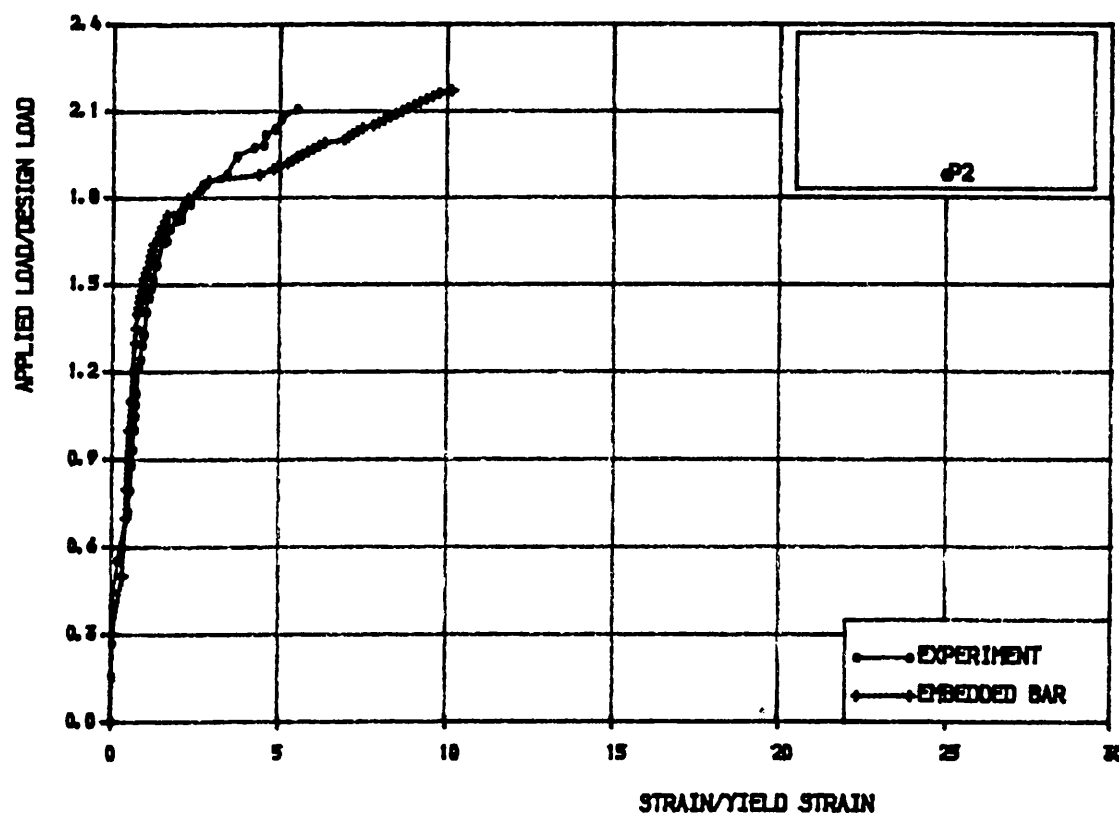


Fig. 8.48b Load-horizontal steel strain curve. Beam B.1

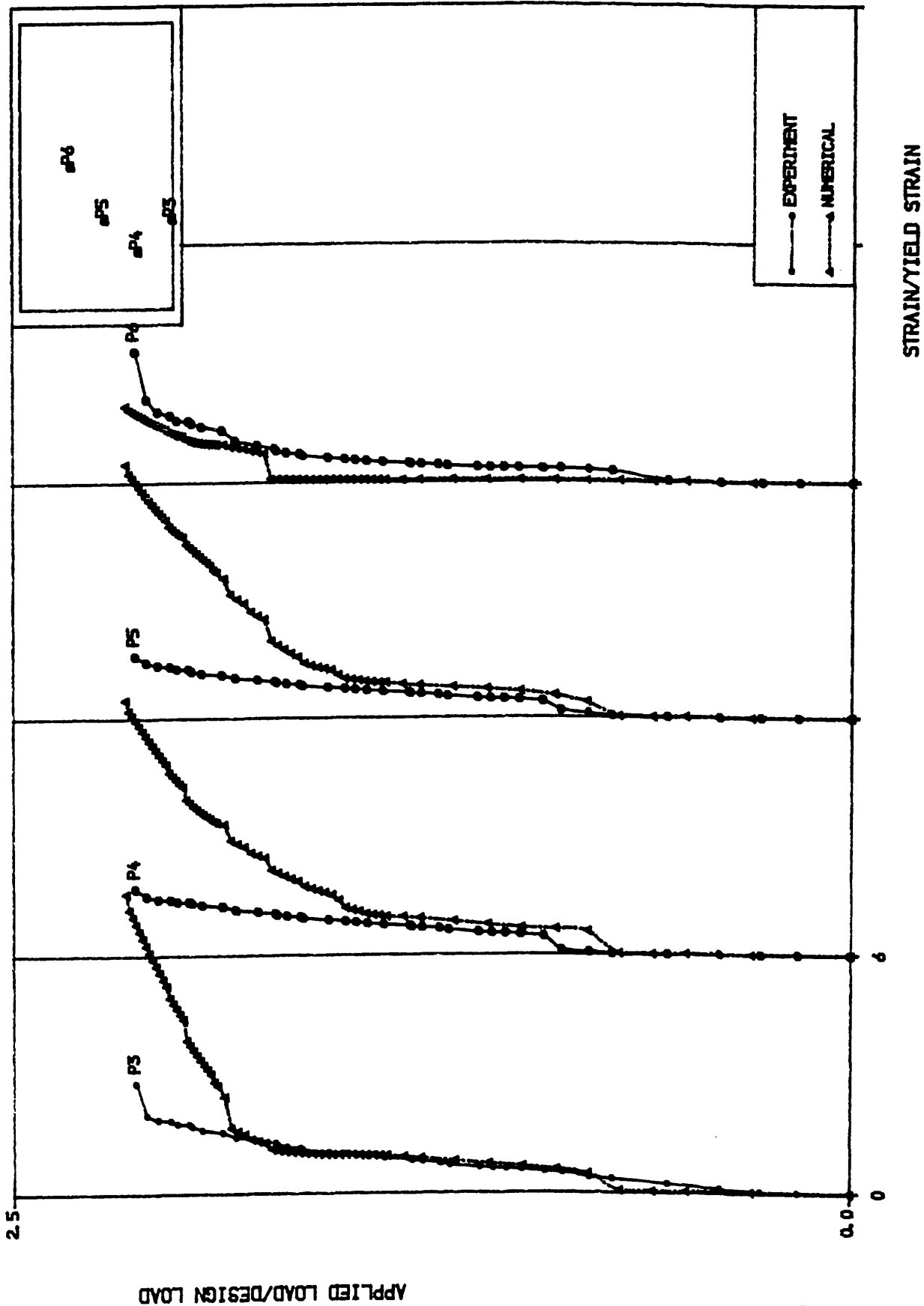


Fig. 8.48c Load-horizontal steel strain curves. Beam B.1

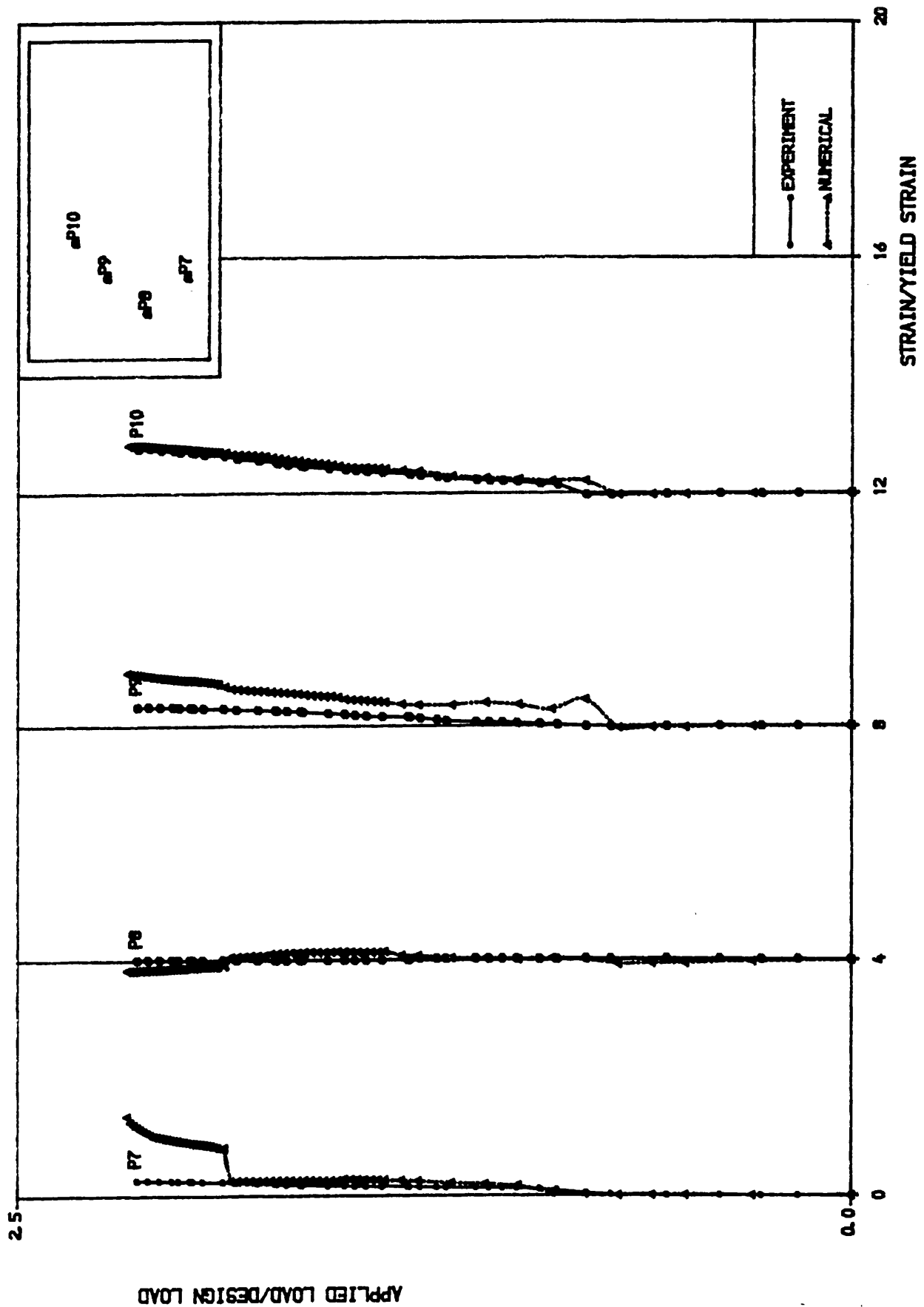
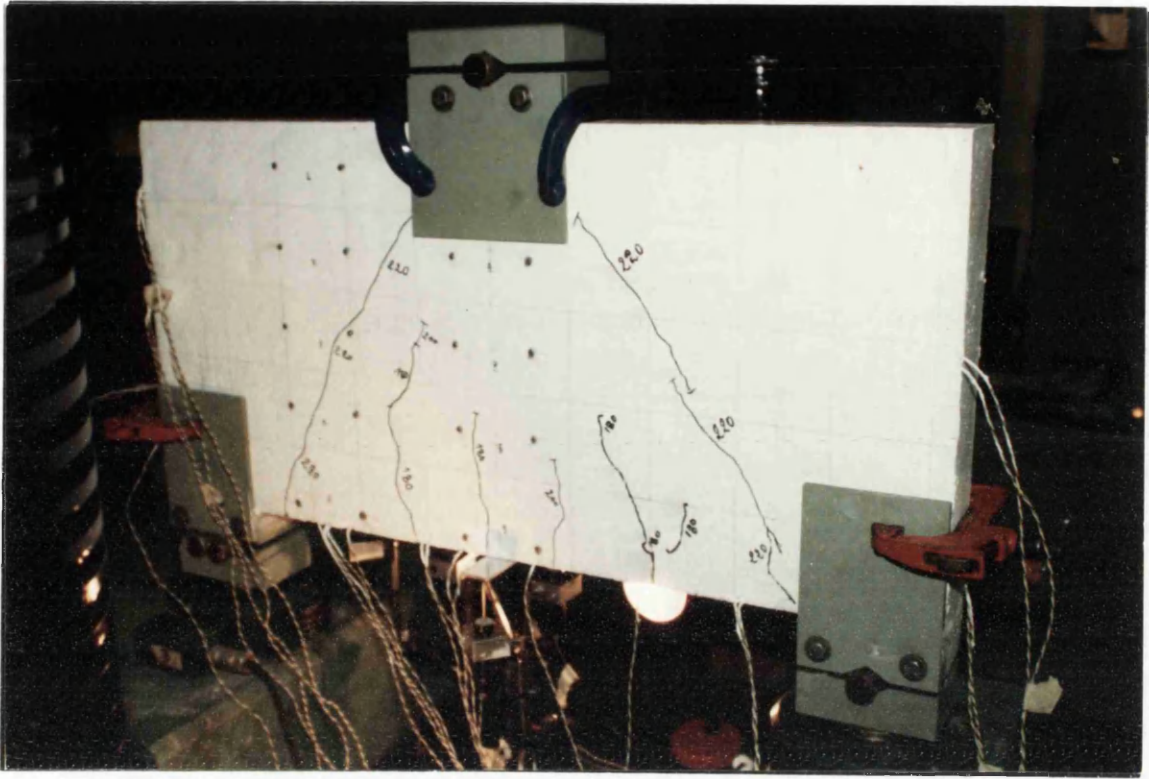


Fig. 8.48d Load-vertical steel strain curves. Beam B.1



Numerical 1/2 Beam

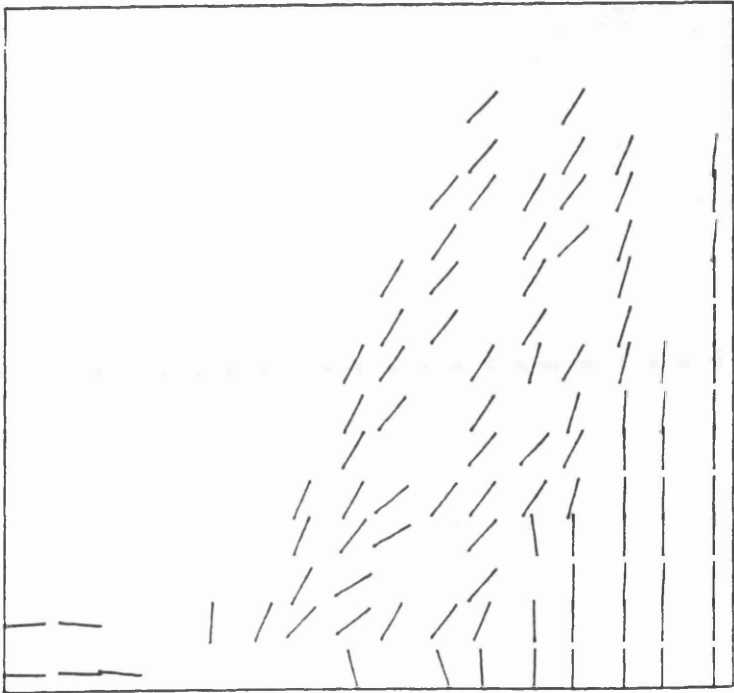


Fig. 8.49a Experimental and numerical crack pattern at 250 KN.
Beam B.1



Numerical 1/2 Beam

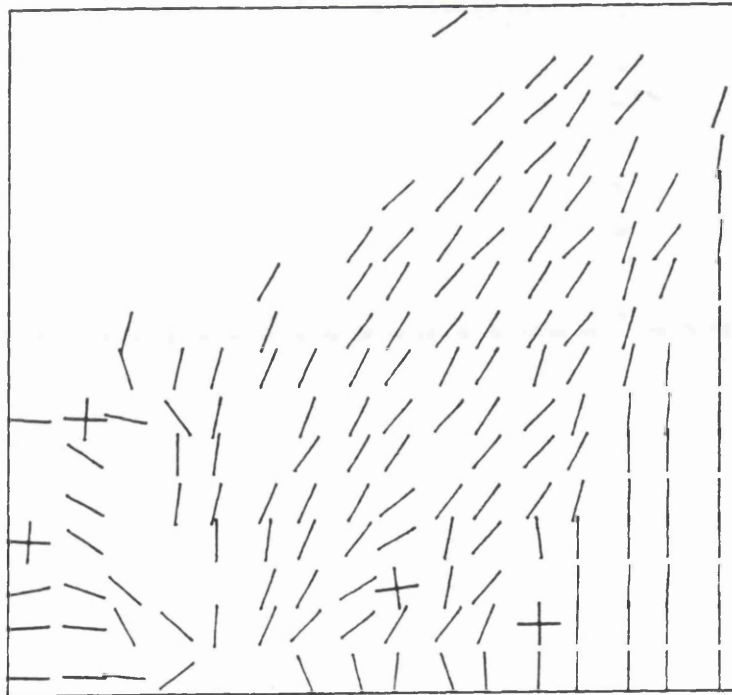


Fig. 8.49b Experimental and numerical crack pattern at collapse load.
Beam B.1

flexural and diagonal compression failure with a maximum crack width at mid span of 6.5 mm. At the inclined diagonal crack a 5.0 mm width was measured. The crack pattern at the collapse load is shown in figures 8.49b and it is clear that the cracks covered most parts of the beam. The ultimate load is mainly affected by the fact that the provided steel is greater than the numerical required one as will be discussed later.

8.3.2 Beam B.2:

The beam was loaded with an average increment of 0.1 Pd. The first visible crack appeared at 0.49 Pd (0.185 Pu). It was a vertical flexural crack at mid-span and measuring 0.05mm. Up to 0.89 Pd (0.33 Pu) there was a continuation of the flexural cracks at the mid-span, and formation of additional flexural cracks at the bottom mid-shear span. The maximum crack width was 0.1 mm. Like beam B.1 beam B.2 also developed little flexural cracks in the mid-span at the first stage of loading. As the load increases these cracks continue to propagate towards the point load, while their width is almost insensitive to the applied load at this initial stage. At this level of loading the maximum crack width was 0.15 mm. The service load crack width limit of 0.3 mm reached at 1.37 Pd (0.51 Pu). The first yielding of steel was measured on the horizontal bar at the bottom of the mid-span of the beam at 1.78 Pd (0.66 Pu), figure 8.51a. Beyond this level the width of the flexural crack increased quickly so that at 1.89 Pd (0.70 Pu) it was 0.45 mm. The most significant event during loading history of this beam is the development of long diagonal inclined shear crack which occurred suddenly at 1.99 Pd (0.74 Pu). This crack was accompanied by a loud bang. It joined the point load and the support. Before this shear crack opened, the triangular flexural concrete area between the mid-shear spans and the point load had cracked. At this stage of loading the deflection increased. Figures 8.50a and 8.50b illustrate that after the yielding of steel and the formation the shear inclined cracks the stiffness of the beam was reduced. This can be seen more clearly in figures 8.51a and 8.51b where the load-strain curves, of the horizontal steel bar

at the soffit of the beam, are presented. The maximum crack width of 0.60 mm was measured at $2.18 P_d$ ($0.81 P_u$), whereas at the diagonal of the crack width was only 0.5 mm. At this loading level the vertical steel yielded under the point load, figure 8.52c(P10). Most of the measured strains in the vertical steel was compression at the early loading history. After cracking of a large area of the beam, most these points were under tension, figure 8.52a to 8.52c. As well as the load increased the speed of the widening of the flexural cracks increased, so that at $2.59 P_d$ ($0.96 P_u$) the maximum flexural crack was 1.75 mm. At this stage a 0.70 mm wide crack at the diagonal was recorded. Failure took place at 1350 KN which is 2.70 times the design load P_d . The maximum crack width was of 4.0 mm and 1.5 mm at the bottom near mid-span and at the inclined crack respectively. Figures 14a and 14b show the crack patterns at the design load and at ultimate load respectively. From the crack width and the flexural steel strain it can be seen that the beam failed flexurally. A little local crushing of concrete under the point load was seen.

Numerical Analysis:

The beams were analysed using a nonlinear inplane analysis program. By assuming symmetry, a symmetrical half of the beams was analysed using 8x8 element mesh. The steel reinforcement is assumed to be elasto-plastic with allowance for strain hardening. Two steel models were used in the analysis of beam B.1, smeared and embedded formulations. The prediction of the ultimate load is better when using the embedded bar, figure 8.74a.

In figure 8.50a, from the beginning of loading, a little loss of stiffness can be noticed in the experimental curve. This is may be due to squeeze of the plaster between the support plates and the beam. The load-strain curves figure 8.51a-c shows better correlation between experimental and numerical results. The crack patterns comparison at the design load and at the experimental collapse load are presented in figures 8.53 and 8.54 respectively. The main results are summarized in table 8.6. In general good agreement between the experimental and the numerical results is indicated.

Table 8.6 Experimental and Numerical Results Comparison.
Beam B.1 and B.2.

Beam → Facts↓	Beam B. 1		Beam B.2	
	Experim.	Numerical	Experim.	Numerical
First visible Crack	0.33 Pu	0.23 Pu	0.185 Pu	0.25 Pu
Width of the Crack	0.1 mm	-	0.05 mm	-
Location of this first Crack	Mid-span	Mid-span	Mid-span	Mid-span
Service Crack width limit	0.52 Pu	-	0.51 Pu	-
1 st yielding of horizontal Steel	0.61 Pu	0.59 Pu	0.66 Pu	0.58 Pu
1 st yielding of vertical steel	At failure	At failure	No yield.	No yield.
Failure took place at	545 KN	550 KN	1350 KN	1320 KN
Maximum crack width at failure	6.5 mm	-	4.0 mm	-

Figure 8.55a and 8.55b illustrates the theoretical required and the provided steel ratio for beam B.1 and B.2 respectively. It is clear that the provided steel is higher than the theoretically required one. The ultimate load is affected by the provided steel, which is greater than the numerical required one.

The vertical steel ratio in the mid-shear span of beam B.2 is greater than the required one, figure 8.55b. This excess helped the beam to behave flexurally, although, because of its span depth ratio, it was expected to fail in shear. This confirms Rogowski's statement that an increase in the vertical web reinforcement leads to a ductile failure of deep beams(62).

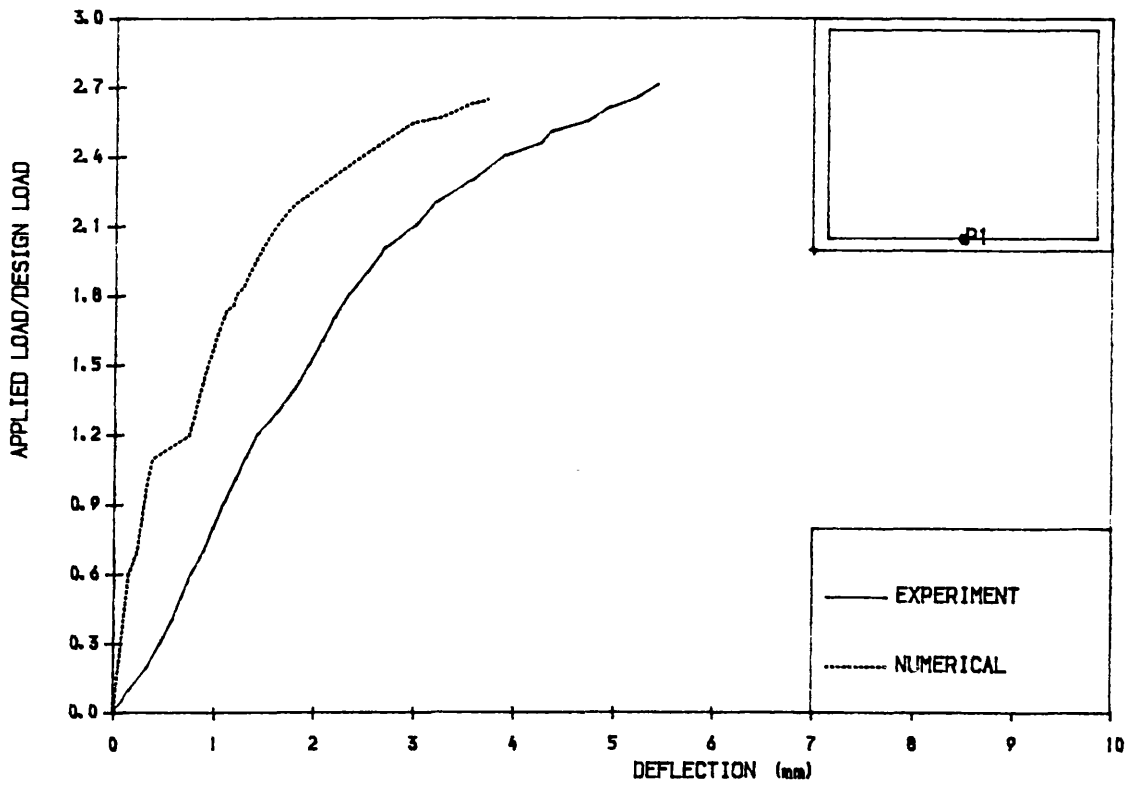


Fig. 8.50a Load-deflection curve. Beam B.2

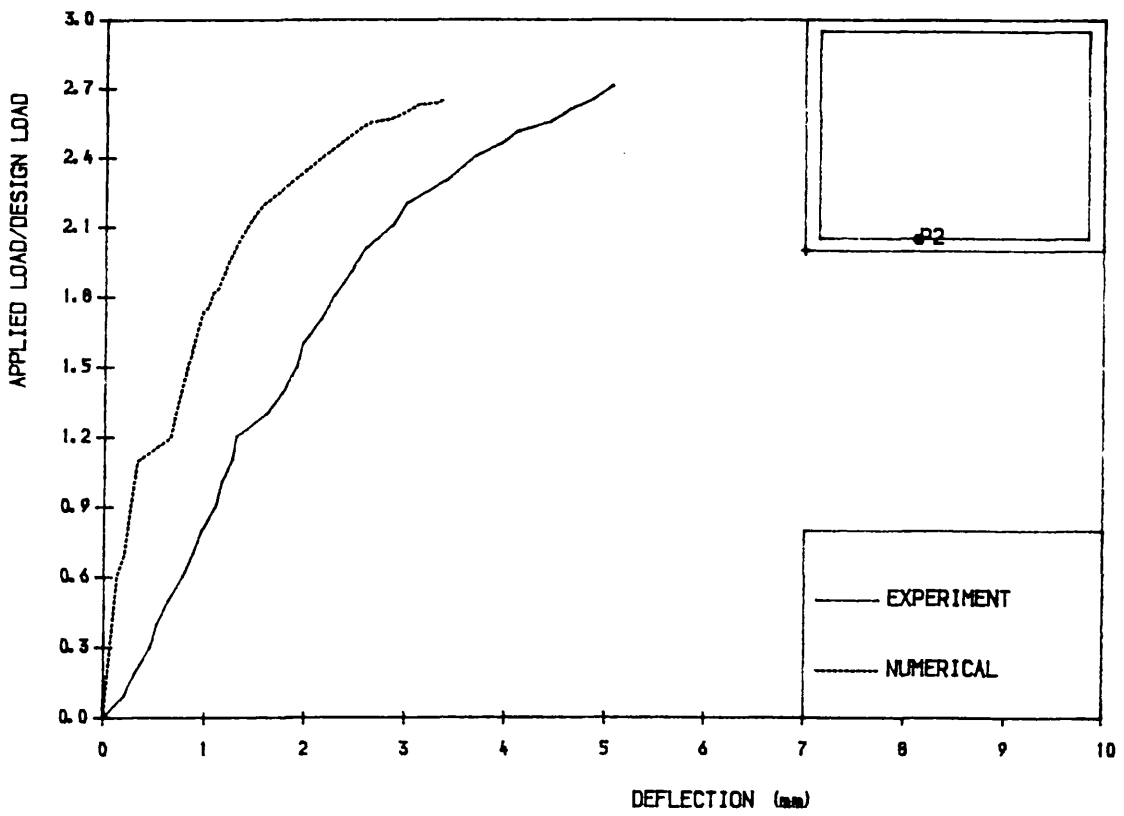


Fig. 8.50b Load-deflection curve. Beam B.2

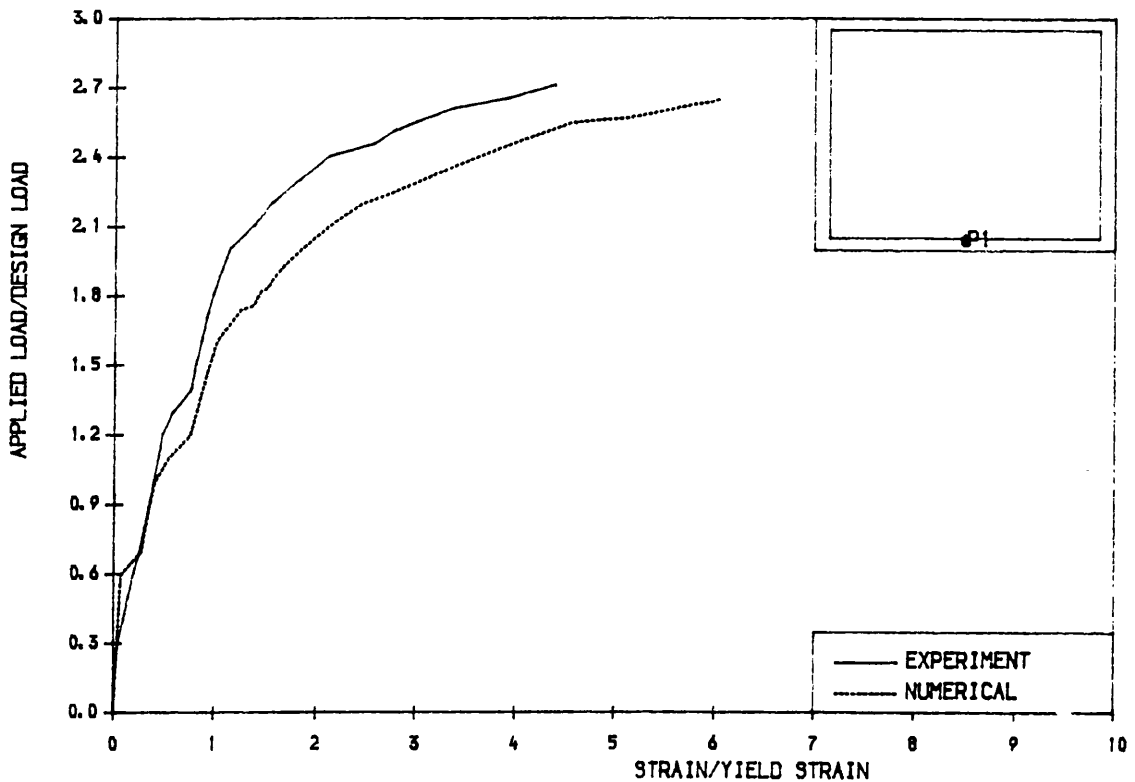


Fig. 8.51a Load-horizontal steel strain curve. Beam B.2

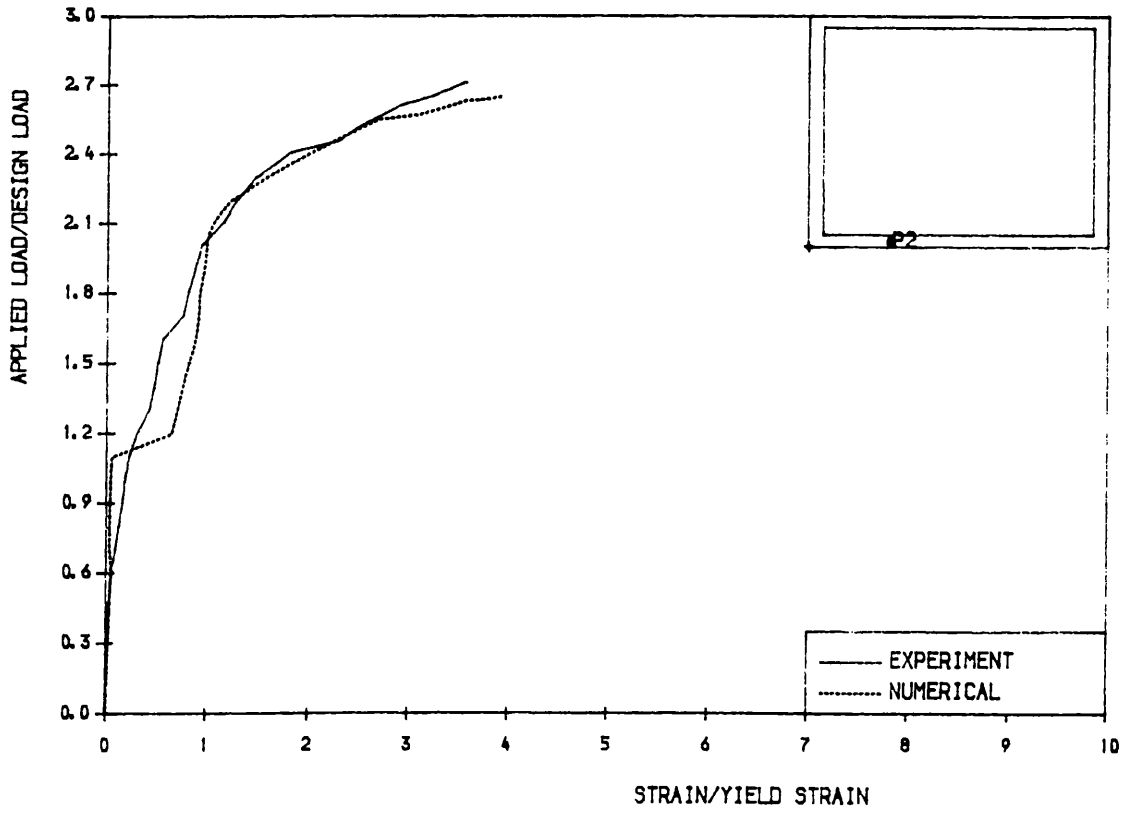


Fig. 8.51b Load-horizontal steel strain curve. Beam B.2

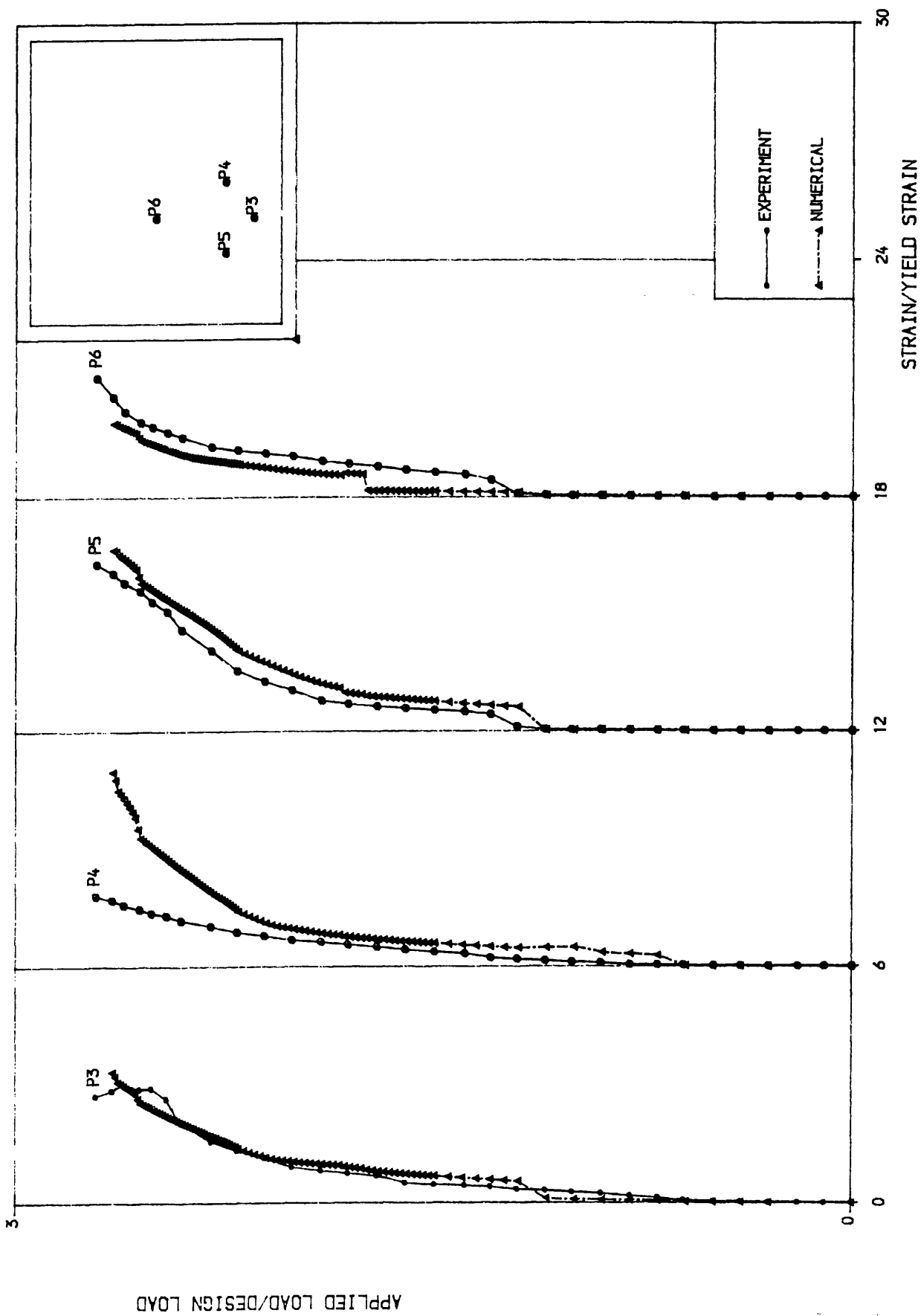


Fig. 8.51c Load-horizontal steel strain curves. Beam B.2

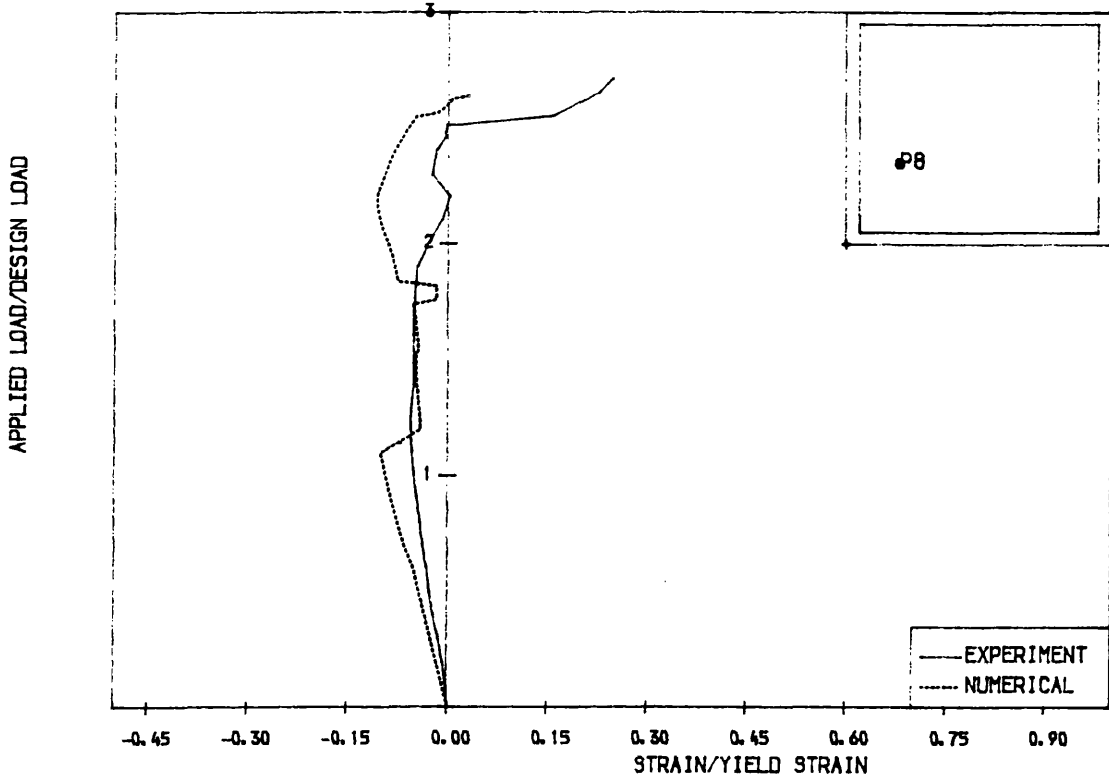


Fig. 8.52a Load-vertical steel strain curve.

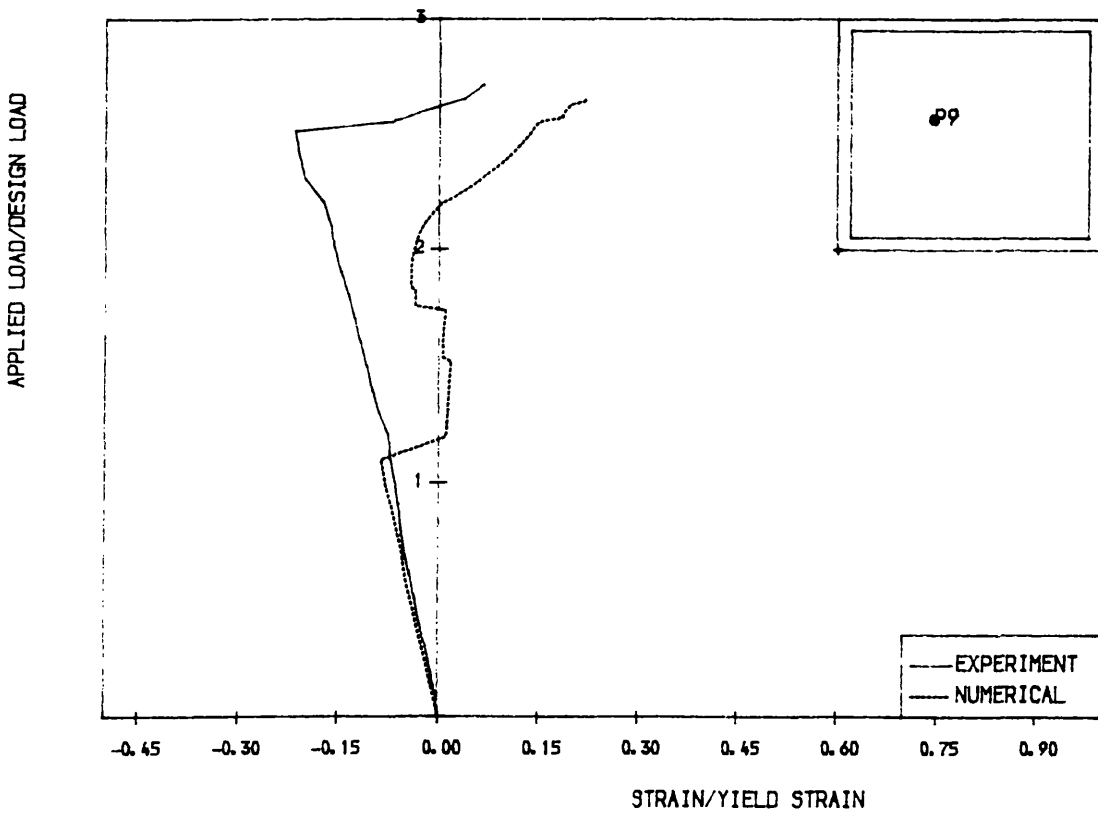


Fig. 8.52b Load-vertical steel strain curve.

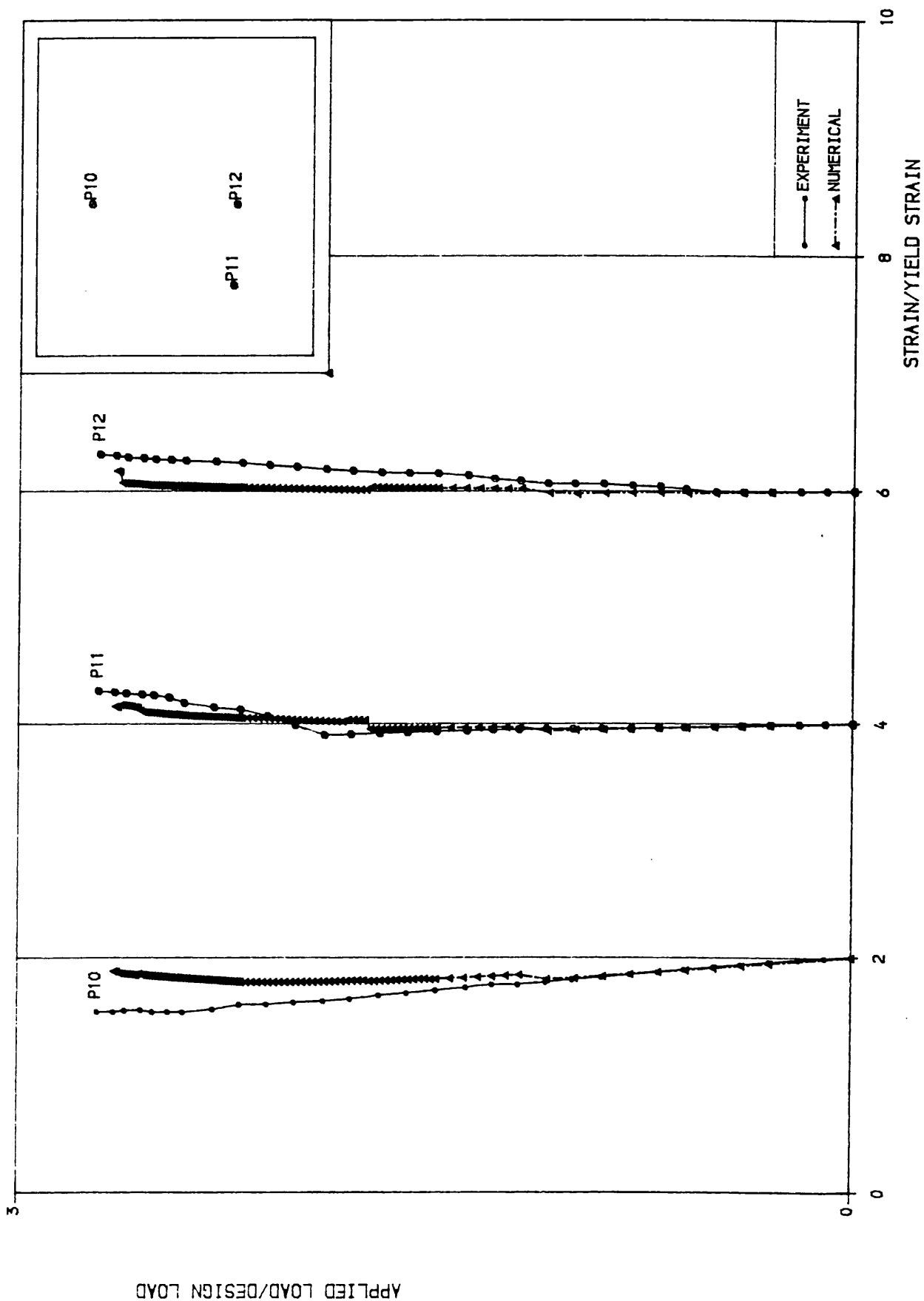
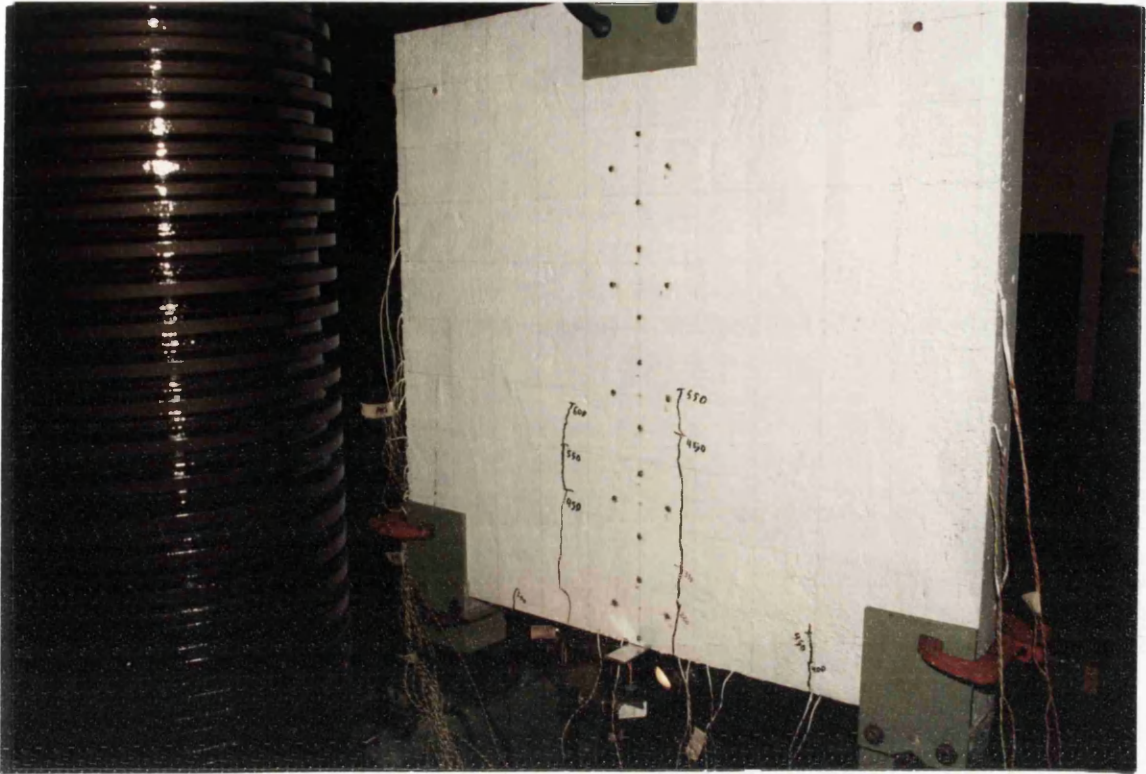


Fig. 8.52c Load-vertical steel strain curves.



Numerical 1/2 Beam

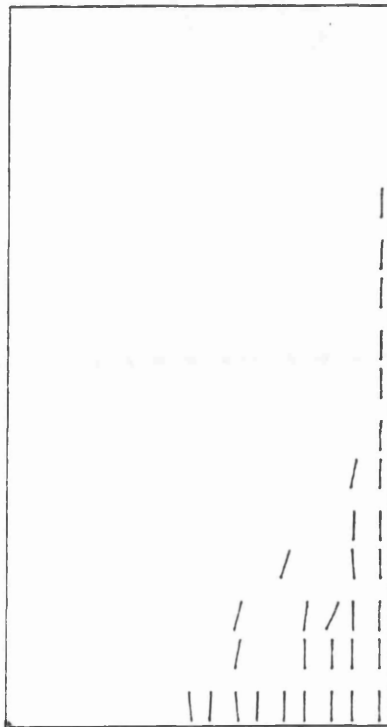


Fig. 8.53a Experimental and numerical crack pattern at 500 KN.
Beam B.2

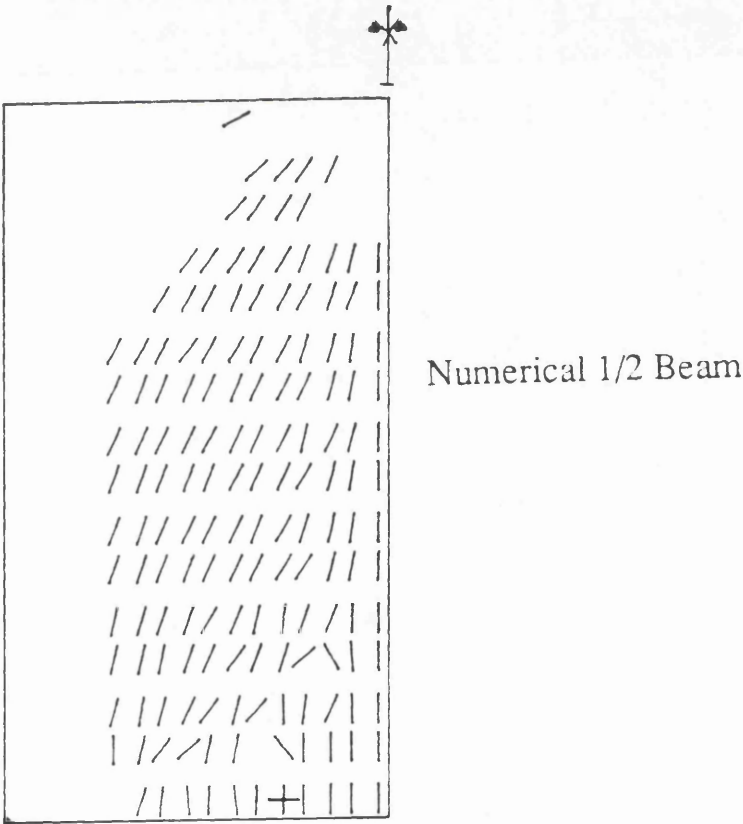
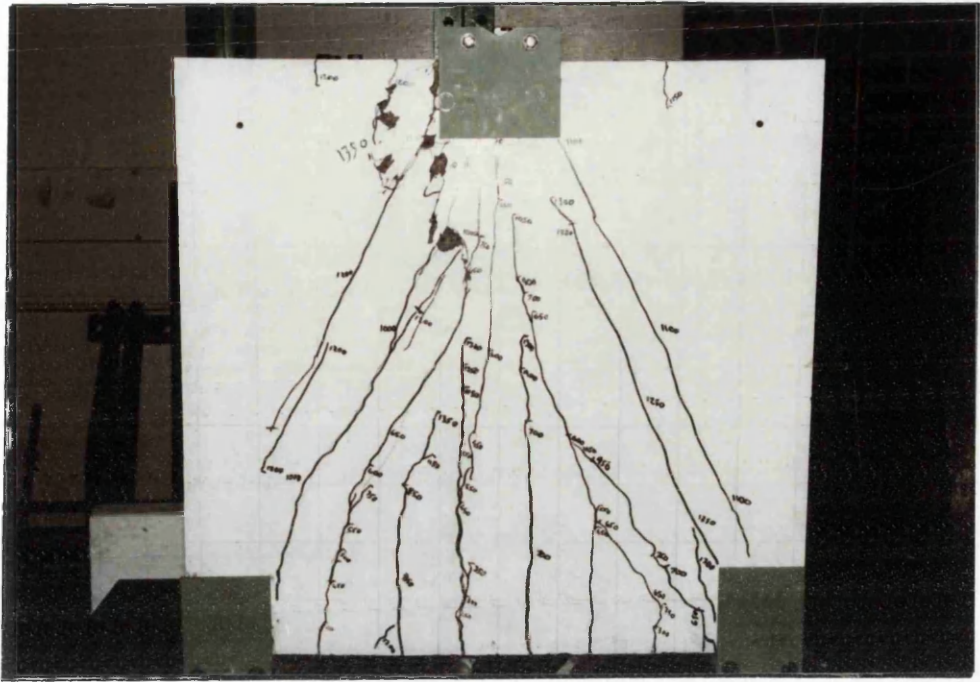


Fig. 8.54 Experimental and numerical crack pattern at collapse load.
Beam B.2

x direction.

0.01	0.00	0.00	0.00	0.00	0.00	0.00	0.00	2.12
0.90	0.90	0.90	0.90	0.90	0.90	0.90	0.90	0.90
0.04	0.07	0.02	0.00	0.00	0.00	0.00	0.00	0.59
0.00	0.00	0.00	0.00	0.00	0.00	0.00	0.00	0.00
0.08	0.24	0.22	0.12	0.05	0.05	0.06	0.01	0.01
0.45	0.45	0.45	0.45	0.45	0.45	0.45	0.45	0.45
0.09	0.40	0.48	0.46	0.43	0.45	0.41	0.10	0.10
0.45	0.45	0.45	0.45	0.45	0.45	0.45	0.45	0.45
0.09	0.49	0.72	0.76	0.80	0.85	0.79	0.49	0.49
1.07	1.07	1.07	1.07	1.07	1.07	1.07	1.07	1.07
0.12	0.57	0.94	0.99	1.10	1.20	1.20	0.99	0.99
1.07	1.07	1.07	1.07	1.07	1.07	1.07	1.07	1.07
0.30	0.82	1.04	1.16	1.40	1.59	1.68	1.60	1.60
1.07	1.07	1.07	1.07	1.07	1.07	1.07	1.07	1.07
0.50	0.94	1.13	1.41	1.76	2.06	2.27	2.35	2.35
2.51	2.51	2.51	2.51	2.51	2.51	2.51	2.51	2.51

y direction

0.01	0.04	0.05	0.05	0.05	0.14	0.61	0.86
0.00	0.00	0.87	0.43	0.43	0.87	0.75	0.75
0.01	0.12	0.24	0.26	0.23	0.15	0.10	0.27
0.00	0.00	0.87	0.43	0.43	0.87	0.75	0.75
0.00	0.13	0.38	0.55	0.57	0.45	0.13	0.00
0.00	0.00	0.87	0.43	0.43	0.87	0.00	0.00
0.00	0.09	0.42	0.64	0.70	0.52	0.10	0.00
0.00	0.00	0.87	0.43	0.43	0.87	0.00	0.00
0.00	0.04	0.38	0.65	0.68	0.48	0.10	0.00
0.00	0.00	0.87	0.43	0.43	0.87	0.00	0.00
0.00	0.00	0.32	0.59	0.60	0.43	0.14	0.00
0.00	0.00	0.87	0.43	0.43	0.87	0.00	0.00
0.00	0.04	0.32	0.46	0.43	0.33	0.16	0.01
0.81	0.81	0.87	0.43	0.43	0.87	0.00	0.00
0.81	0.77	0.27	0.17	0.16	0.14	0.09	0.02
0.81	0.81	0.87	0.43	0.43	0.87	0.00	0.00

Fig. 8.55a Theoretical Required & Provided Steel Ratio

Beam B.1

[illegible]

Fig. 8.55b Theoretical Required & Provided Steel Ratio

Beam B.2

Chapter 9

Analysis of Reinforced Concrete Slabs and Deep Beams Assuming Reinforced Concrete as an Elasto-plastic Material

9.1 Introduction:

In the analysis of reinforced concrete structures, it is important to consider the effect of material behaviour. This was carried out in the previous chapters, by using a detailed nonlinear analysis finite element program. Such an analysis gives realistic evaluation of deflections, stresses and strains over the whole range of loading up to failure. In general, such an analysis is research rather than practical analysis orientated. A designer is particularly concerned to find out the ultimate load of a given structure, without going into too many details. The main objective of this study is to develop a simple way to predict the ultimate load for any structure which can be classified as being a plate bending or an inplane problem. This chapter outlines the steps in the development of such finite element programs. The program's predictions are compared with the experimental and the detailed nonlinear finite element results.

9.2 Program Content:

The programs used for this study were originally written by Hinton and Owen(5) for plate bending and inplane problems using von Mises and Tresca yield criteria, which closely approximate metals behaviour. For these programs, the yield criteria, presented in chapter three for plate bending and inplane problems are implemented, with additional developed yield criteria for mixed state of stress for inplane structures. For plate bending problems, reduction factors Φ_1 and Φ_2 are

proposed to improve deflection prediction, which were stiff when using the original Branson's(31) equation.

9.2.1 Mathematical Formulation of the Yield Criteria:

In essence, plastic behaviour is characterised by an irreversible straining which is not time dependent and which can only be sustained once a certain level of stress has been reached. In this section a summary of the basis assumptions and the associated theoretical expressions, are presented.

The yield criteria determines the stress level at which plastic deformation begins. In order to formulate a theory which models elasto– plastic material deformation three requirements have to be met:

- i– Under elastic conditions an explicit relationship between stress and strain must be formulated to describe material behaviour.
- ii– A postulation of yield criterion defining the stress state to commence plastic flow.
- iii– A relationship between stress and strain increment must be developed for post yield behaviour. In this range the deformation is made up of both elastic and plastic components as follows:

$$d\epsilon = d\epsilon_e + d\epsilon_p \quad 9.1$$

$$\text{with } d\epsilon = \begin{bmatrix} d\epsilon_x \\ d\epsilon_y \\ d\epsilon_{xy} \end{bmatrix}$$

Where $d\epsilon$ is the total incremental strain, $d\epsilon_e$ represents the elastic component of the strain given by:

$$d\epsilon_e = [D]^{-1} d\sigma \quad 9.2$$

$$\text{with } d\sigma = \begin{bmatrix} d\sigma_x \\ d\sigma_y \\ d\sigma_{xy} \end{bmatrix}$$

and $d\epsilon_p$ represents the plastic component. $[D]$ is the elasticity matrix of the material. σ can be moments (M) or stresses. In order to derive the relationship between the plastic strain increment $d\epsilon_p$ and the stress increment $d\sigma$, it is assumed that the material obeys normality rule. This rule states that the incremental strain, is in the direction normal to the yield surface at the point considered, and is given by:

$$d\epsilon_p = d\lambda \begin{bmatrix} \frac{\partial F}{\partial \sigma_x} \\ \frac{\partial F}{\partial \sigma_y} \\ \frac{\partial F}{\partial \sigma_{xy}} \end{bmatrix} \quad 9.16$$

Where F is the yield criterion function and $d\lambda$ is a proportionality constant termed the plastic multiplier. Using equations 9.1, 9.2 and 9.3 the complete incremental relationship between stress and strain for elasto-plastic deformation is as follows:

$$d\epsilon = [D]^{-1} d\sigma + d\lambda \frac{\partial F}{\partial \sigma} \quad 9.4$$

By definition:

$$\left[\frac{\partial F}{\partial \sigma} \right] = a^T = \left[\frac{\partial F}{\partial \sigma_x}, \frac{\partial F}{\partial \sigma_y}, \frac{\partial F}{\partial \sigma_{xy}} \right]$$

which is called the flow vector.

$$\therefore d\epsilon = [D]^{-1} d\sigma + d\lambda a \quad 9.5$$

The yield function in general can be written in term of stress which governs the expression for the yield surface as follows:

$$F(\sigma) = 0.0 \quad 9.6$$

Differentiating equation 9.6 we get:

$$dF = \frac{\partial F}{\partial \sigma_x} d\sigma_x + \frac{\partial F}{\partial \sigma_y} d\sigma_y + \frac{\partial F}{\partial \sigma_{xy}} d\sigma_{xy} = 0.0 \quad 9.7$$

We know that $a^T = \frac{\partial F}{\partial \sigma}$ by definition, thus:

$$a^T d\sigma = 0.0 \quad 9.8$$

By multiplying both sides of equation 9.4 by $a^T D$ and eliminating $a^T d\sigma$ using equation 9.8 we obtain the following expression:

$$\begin{aligned} a^T D d\epsilon &= a^T D [D]^{-1} d\sigma + a^T D d\lambda a \\ a^T D d\epsilon &= a^T D d\lambda a \end{aligned} \quad 9.10$$

thus:

$$d\lambda = \frac{a^T D d\epsilon}{a^T D a} \quad 9.11$$

Then by substituting equation 9.11 into 9.4 we obtain:

$$d\sigma = D_{ep} d\epsilon \quad 9.12$$

with:

$$D_{ep} = D - \frac{D a a^T D}{a^T D a} \quad 9.13$$

9.2.2 Yield Criteria for Reinforced Concrete Plates:

i- Yield functions:

As described in chapter three, the yield criteria for reinforced concrete slabs can be expressed as:

$$F1 = - (M_x^{*b} - M_x)(M_y^{*b} - M_y) + M_{xy}^2 = 0.0 \quad 9.14$$

$$F2 = - (M_x^{*t} + M_x)(M_y^{*t} + M_y) + M_{xy}^2 = 0.0 \quad 9.15$$

F1 and F2 are the yield functions for bottom and top steel respectively. They are presented graphically in figure 9.1. (M_x^* , M_y^*) are the resistant moments developed by reinforced member in x and y directions respectively. Superscripts ^b and ^t stand for bottom and top steel respectively. M_x , M_y and M_{xy} are the moments resulting from the applied loads.

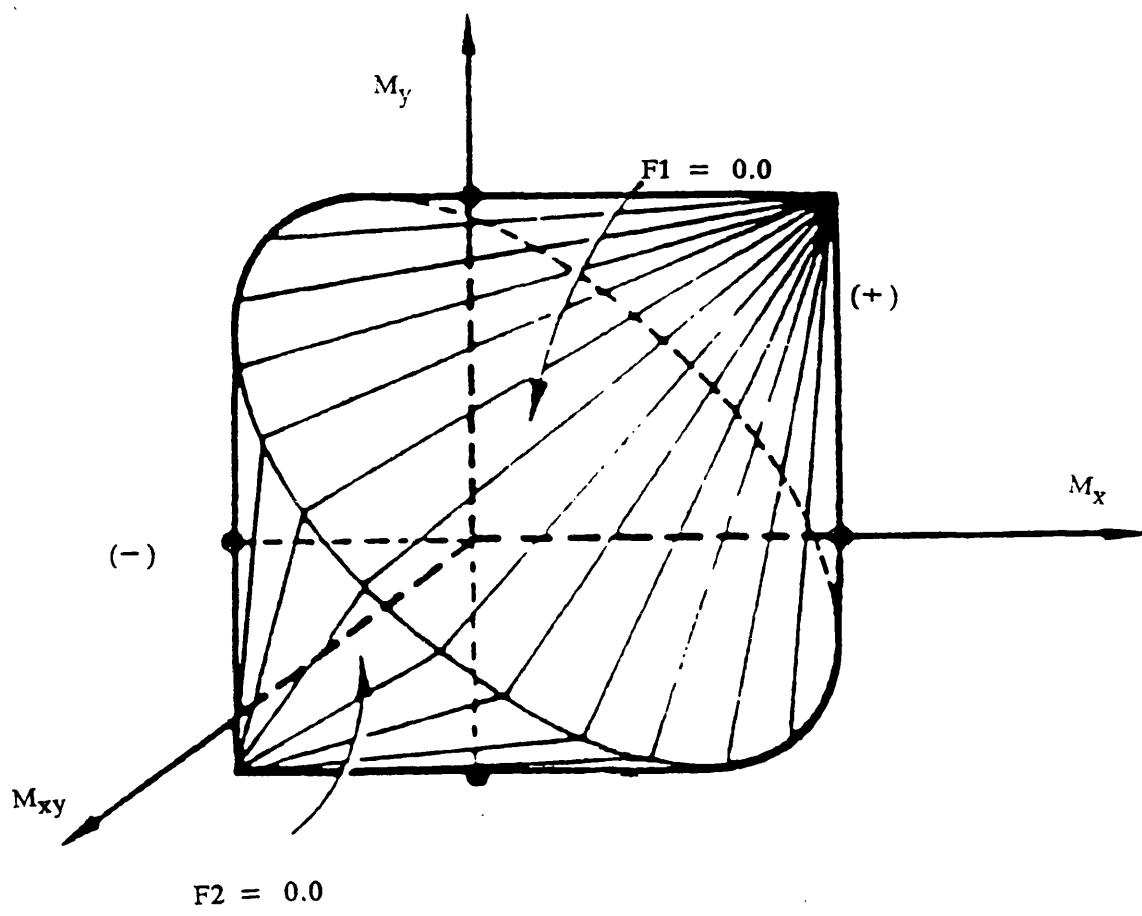
ii- Flow vectors:

Bottom steel:

$$a_b = \begin{bmatrix} \frac{\partial F1}{\partial M_x} \\ \frac{\partial F1}{\partial M_y} \\ \frac{\partial F1}{\partial M_{xy}} \end{bmatrix} = \begin{bmatrix} M_y^{*b} - M_y \\ M_x^{*b} - M_x \\ 2.0 M_{xy} \end{bmatrix} \quad 9.16$$

Top steel:

$$a_t = \begin{bmatrix} \frac{\partial F2}{\partial M_x} \\ \frac{\partial F2}{\partial M_y} \\ \frac{\partial F2}{\partial M_{xy}} \end{bmatrix} = \begin{bmatrix} - M_y^{*t} + M_y \\ - M_x^{*t} + M_x \\ 2.0 M_{xy} \end{bmatrix} \quad 9.17$$



F1 and F2 are the yield functions for plate bending.
 (+) Bottom steel yield surface and (-) Top steel yield surface.

Fig. 9.1 Yield Surfaces in The Three Dimensional Space of Stresses

9.2.3 Yield Criteria for Reinforced Concrete Inplane Problems:

i- Yield functions:

In chapter three section 3.2.3.1 the following equilibrium equations were presented:

$$\sigma_x = \sigma_1 \cos^2 \theta + \sigma_2 \sin^2 \theta + \sigma_{xs} \quad 9.18a$$

$$\sigma_y = \sigma_1 \sin^2 \theta + \sigma_2 \cos^2 \theta + \sigma_{ys} \quad 9.18b$$

$$\tau_{xy} = (\sigma_2 - \sigma_1) \cos \theta \sin \theta \quad 9.18c$$

Where σ_x , σ_y and τ_{xy} are the stresses resulting from the applied loads. σ_{xs} and σ_{ys} are stresses carried by steel, with $-\sigma_x^* \leq \sigma_{xs} \leq \sigma_x^*$ and $-\sigma_y^* \leq \sigma_{ys} \leq \sigma_y^*$. (σ_x^*, σ_y^*) are the resistant stresses developed by reinforcement in x and y directions respectively. They are taken in this chapter as numerical values (positive). σ_1 and σ_2 are principal stresses in concrete, with values limited to $-f_c \leq \sigma_1 \leq 0$ and $-f_c \leq \sigma_2 \leq 0$. f_c is the compressive strength of concrete (positive). Table 9.1 shows the possible stresses cases on steel and concrete.

Table 9.1 Possible cases of stresses on steel and Concrete

σ_{xs}	σ_{ys}	σ_1	σ_2	Case
+	+	0	-	1
+	+	-	$-f_c$	7
+	-	0	-	3
+	-	-	$-f_c$	5
-	+	0	-	4
-	+	-	$-f_c$	6
-	-	0	-	8
-	-	-	$-f_c$	2

From equilibrium equations 9.18 the yield criterion for each case can be derived as follows:

Case 1: In this case both in x and y direction the steel is under tension. The maximum tensile stresses which can be carried by tensile steel are σ_x^* and σ_y^* in x and y direction respectively. The stresses in the concrete can take this values $\sigma_1 = 0$ and $-f_c \leq \sigma_2 \leq 0$. Therefore equations 9.18 can be written as follows:

$$\sigma_x = \sigma_2 \sin^2 \theta + \sigma_x^* \quad 9.19a$$

$$\sigma_y = \sigma_2 \cos^2 \theta + \sigma_y^* \quad 9.19b$$

$$\tau_{xy} = \sigma_2 \cos \theta \sin \theta \quad 9.19c$$

Thus the yield criterion:

$$F1 = -(\sigma_x - \sigma_x^*)(\sigma_y - \sigma_y^*) + \tau_{xy}^2 = 0.0 \quad 9.20$$

Case 2: In this case the steel in both x and y direction is under compression with maximum stresses $-\sigma_x^*$ and $-\sigma_y^*$ respectively and the concrete is subjected to $-f_c \leq \sigma_1 \leq 0$ and $\sigma_2 = -f_c$. The yield criteria can be written as:

$$F2 = -(\sigma_x + f_c + \sigma_x^*)(\sigma_y + f_c + \sigma_y^*) + \tau_{xy}^2 = 0.0 \quad 9.21$$

Nielsen(74) concluded that, if only small degree of reinforcement is used, then the yield criteria of equations 9.20 and 9.21 can be used, without considering the cases of the mixed stress fields. However in practice the reinforcement in the critical areas might not be small. Thus in the present work the mixed stress field was taken into account as follows.

Case 3: The steel in x direction is under tension and y direction is under compression with the principal stresses in concrete $\sigma_1 = 0.0$ and $-f_c \leq \sigma_2 \leq 0$.

Equations 9.18 can be written as follows:

$$\sigma_x = \sigma_2 \sin^2 \theta + \sigma_x^* \quad 9.22a$$

$$\sigma_y = \sigma_2 \cos^2 \theta - \sigma_y^* \quad 9.22b$$

$$\tau_{xy} = \sigma_2 \cos \theta \sin \theta \quad 9.22c$$

Thus the yield function of this case can be written as:

$$F3 = - (\sigma_x - \sigma_x^*)(\sigma_y + \sigma_y^*) + \tau_{xy}^2 = 0.0 \quad 9.23$$

Case 4: In the same manner when steel in y direction under tension and x direct is under compression but with $\sigma_1 = 0.0$ and $-f_c \leq \sigma_2 \leq 0$.

$$F4 = - (\sigma_x + \sigma_x^*)(\sigma_y - \sigma_y^*) + \tau_{xy}^2 = 0.0 \quad 9.24$$

Case 5: In this case steel in y direction is under compression and in x direction is under tension. The principal stresses in concrete are: $-f_c \leq \sigma_1 \leq 0$ and $\sigma_2 = -f_c$, thus equations 9.18 can be presented as:

$$\sigma_x = \sigma_1 \cos^2 \theta - f_c \sin^2 \theta + \sigma_x^* \quad 9.25a$$

$$\sigma_y = \sigma_1 \sin^2 \theta - f_c \cos^2 \theta - \sigma_y^* \quad 9.25b$$

$$\tau_{xy} = (f_c - \sigma_1) \cos \theta \sin \theta \quad 9.25c$$

The corresponding yield function is:

$$F5 = - (\sigma_x + f_c + \sigma_x^*)(\sigma_y + f_c - \sigma_y^*) + \tau_{xy}^2 = 0.0 \quad 9.25d$$

Case 6: In the same manner if steel in y direction is under compression and steel in x direction is under tension, with the principal stresses in concrete having the following values $-f_c \leq \sigma_1 \leq 0$ and $\sigma_2 = -f_c$. The yield function can be written as:

$$F6 = -(\sigma_x + f_c - \sigma_x^*)(\sigma_y + f_c + \sigma_y^*) + \tau_{xy}^2 = 0.0 \quad 9.26$$

Case 7: If steel in both x and y direction is under tension and the principal stresses in concrete having the following values $\sigma_1 = 0.0$ and $-f_c \leq \sigma_2 \leq 0$. Then the yield function of this case can be written as:

$$F7 = -(\sigma_x + f_c - \sigma_x^*)(\sigma_y + f_c - \sigma_y^*) + \tau_{xy}^2 = 0.0 \quad 9.27$$

Case 8: If steel in both x and y direction is under compression and the principal stresses in concrete having the following values $\sigma_1 = 0.0$ and $-f_c \leq \sigma_2 \leq 0$. Then the yield function of this case can be written as follows:

$$F8 = -(\sigma_x + \sigma_x^*)(\sigma_y + \sigma_y^*) + \tau_{xy}^2 = 0.0 \quad 9.28$$

ii- Flow vectors:

Case 1:

$$a = \begin{bmatrix} \frac{\partial F1}{\partial \sigma_x} \\ \frac{\partial F1}{\partial \sigma_y} \\ \frac{\partial F1}{\partial \sigma_{xy}} \end{bmatrix} = \begin{bmatrix} -(\sigma_y^* - \sigma_y) \\ -(\sigma_x^* - \sigma_x) \\ 2.0 \tau_{xy} \end{bmatrix} \quad 9.29a$$

Case 2:

$$a = \begin{bmatrix} \frac{\partial F2}{\partial \sigma_x} \\ \frac{\partial F2}{\partial \sigma_y} \\ \frac{\partial F2}{\partial \tau_{xy}} \end{bmatrix} = \begin{bmatrix} -(\sigma_y^* + f_c + \sigma_y) \\ -(\sigma_x^* + f_c + \sigma_x) \\ 2.0 \tau_{xy} \end{bmatrix} \quad 9.29b$$

In the same manner the flow vector can be obtained for the remaining cases.

9.2.4 Yielding Condition and Stress Reduction Factor:

If the generated resistance in any one direction x or y or both directions are exceeded, then yielding is considered to have occurred. The stress level must be brought on the yield surface allowing plastic flow to occur. A reduction factor ψ was adopted to correct the stresses.

i- Computation of iterative stress reduction factor ψ for plate bending:

At the $(i-1)^{th}$ iteration, let the state of the stress (M_x, M_y, M_{xy}) level be inside or on the yield surface. By adding the incremental stress (dM_x, dM_y, dM_{xy}) of the i^{th} incremental if yielding occurred, the stress must be brought on the yield surface by multiplying the present iterative stress by the reduction factor ψ so that the stresses are on the yield surface figure 9.2, which means $F1$ is equal to zero ($F1 = 0.0$). Thus:

$$F1 = - \left[M_x^{*b} - (M_x + \psi dM_x) \right] \left[M_y^{*b} - (M_y + \psi dM_y) \right] + \left[(M_{xy} + \psi dM_{xy}) \right]^2 = 0.0 \quad 9.30$$

Equation 9.30 can be written in the form:

$$F1 - A\psi^2 + B\psi + C = 0.0$$

9.31

with:

$$A = dM_x dM_y + dM_{xy}^2$$

$$B = - (M_x^{*b} - M_x) dM_y - (M_y^{*b} - M_y) dM_x + 2.0 (M_{xy}) dM_{xy}$$

$$C = (M_x^{*b} - M_x) (M_y^{*b} - M_y) + M_{xy}^2$$

Equation 9.31 is a quadratic equation and ψ is given by:

$$\psi_{1,2} = \frac{-B \pm \sqrt{B^2 - 4AC}}{2A} \quad 9.32$$

$$1.0 \geq \psi \geq 0.0.$$

The same procedure was adopted for F2 in equation 9.15 to compute the reduction factor if the yielding occurs in top steel. Thus the following expressions for top steel were obtained:

$$A = - dM_x dM_y + dM_{xy}^2$$

$$B = - (M_x^{*t} + M_x) dM_y - (M_y^{*t} + M_y) dM_x + 2.0 M_{xy} dM_{xy}$$

$$C = (M_x^{*t} - M_x) (M_y^{*t} - M_y) + M_{xy}^2$$

If both bottom and top steel yield, then the stresses are reduced so that they are brought onto the yield surface. In general the lowest value of ψ obtained from bottom or top yielding is used to govern the reduction. The remaining portion of the stresses, that is $(1-\psi) (dM_x, dM_y, dM_{xy})$, are applied as iterative stresses.

ii- Computation of iterative stress reduction factor ψ for inplane problem:

In the same manner as for slabs, when yielding occurs the stresses must be brought onto the yield surface. If yielding occurs in case 1, the iterative stresses are reduced as follows:

$$-[\sigma_x^* - (\sigma_x + \psi d\sigma_x)] [\sigma_y^* - (\sigma_y + \psi d\sigma_y)] + (\tau_{xy} + \psi d\tau_{xy})^2 = 0.0$$

After some rearrangements the above equation can be written in the following expression:

$$F1 = A\psi^2 + B\psi + C = 0.0 \quad 9.33$$

with:

$$A = - (d\sigma_x d\sigma_y - d\tau_{xy}^2)$$

$$B = - (\sigma_x^* - \sigma_x) d\sigma_y - (\sigma_y^* - \sigma_y) d\sigma_x + 2.0 \tau_{xy} d\tau_{xy}$$

$$C = - (\sigma_x^* - \sigma_x)(\sigma_y^* - \sigma_y) + \tau_{xy}^2$$

The solution of equation 9.33 is given by the same expression of equation 9.32.

The same procedure was adopted for the remaining cases.

9.2.5 Yielding and Plastic Flow:

At each Gaussian integration point the stress and strain quantities are calculated. During a load increment a Gauss point of an element in a structure can behave partly elastically and partly plastically. Thus for any load increment it is necessary to determine what portion of the stress increment for which the behaviour is elastic and the remaining part which produces plastic deformation and then adjust the stress and strain terms until yield criterion is satisfied. In this program the following procedure is adopted:

i- The applied load at the i^{th} iteration are either the incremental applied load or the residual forces resulting from previous iteration $i-1$. This forces give rise to displacement increment $d\delta_i$ and strain $d\epsilon_i$.

ii- By assuming elastic behaviour, the incremental stress $d\sigma_e^i$ is calculated ($d\sigma_e^i = D d\epsilon_i$) and then the total stress at each Gauss point is $\sigma_e^i = \sigma^{i-1} + d\sigma_e^i$, where σ^{i-1} is the stress of the iteration $i-1$ and supposed to be inside or on the yield surface. The material properties matrix D can be variable at each increment as will be explained later.

iii- Check if yielding occurred in one or both directions in the current iteration. If no yielding occurred then continue the same procedure for other Gauss points. If yielding occurred then compute the portion of the total stress which satisfies the yield criterion as $\sigma^{i-1} + \psi d\sigma_e^i$ and the remaining portion of the stress, that is $(1-\psi) d\sigma_e^i$ must be eliminated by bringing the point A in figure 9.2 on the yield surface by allowing plastic deformation to occur. The total stress σ^i is calculated in the same manner as presented by Hinton and Owen(5), as follows:

$$\begin{aligned} \text{since } d\epsilon_p &= d\lambda a, \therefore D d\epsilon_p = d\lambda D a \\ \sigma^i &= \sigma^{i-1} + d\sigma_e^i - d\lambda D a. \end{aligned} \quad 9.34$$

9.3 Numerical Applications and Comparisons:

The aim of this section is to compare the results of the finite programs assuming the material as an elasto-plastic material with the experimental and the layer program predictions. The main object is to investigate the ultimate load predictions, so that if on a wide range of experimental problems the present programs can give an accurate and economical (time wise) prediction, then the model can be used in the prediction of similar problems in the design offices without going into detailed nonlinearity parameters of reinforced concrete component, such as cracking of concrete and yielding of steel etc which are time consuming. An attempt is made to get a reasonable prediction of deflections for plate bending, using Branson(31) equation by introducing two reduction factors ϕ_1 and ϕ_2 to reduce the stiffness of the plate.

9.3.1 Plate Bending:

In this program the thickness of the slab can be taken as constant or variable

depending on the moment applied. For the variation of the thickness the so called Branson(31) equation was adopted to calculate the effective second moment of area as follows:

$$I_{eff} = (M_{cr}/M)^3 I_g + [1-(M_{cr}/M)^3] I_{cr} \quad 9.35$$

where I_{eff} is the effective second moment of area, I_g is the second moment of area of gross concrete section, I_{cr} is the second moment of area of a cracked section, M_{cr} is the cracking moment of concrete section and M the applied moment in the appropriate direction. M is calculated, for both direction x and y , from the applied moments M_x , M_y and M_{xy} using equations presented in chapter three for plate bending problems, so that the torsional moment M_{xy} are directly accounted.

The results obtained using equation 9.35, as will be shown, gives stiff prediction in the deflection for all the models analysed. Therefore, two reduction factors ϕ_1 and ϕ_2 were suggested as follows:

$$I'_{eff} = \phi_1 (M_{cr}/M)^3 I_g + \phi_2 [1-(M_{cr}/M)^3] I_{cr} \quad 9.36$$

Where $0 \leq \phi_1 \leq 1$ and $0 \leq \phi_2 \leq 1$

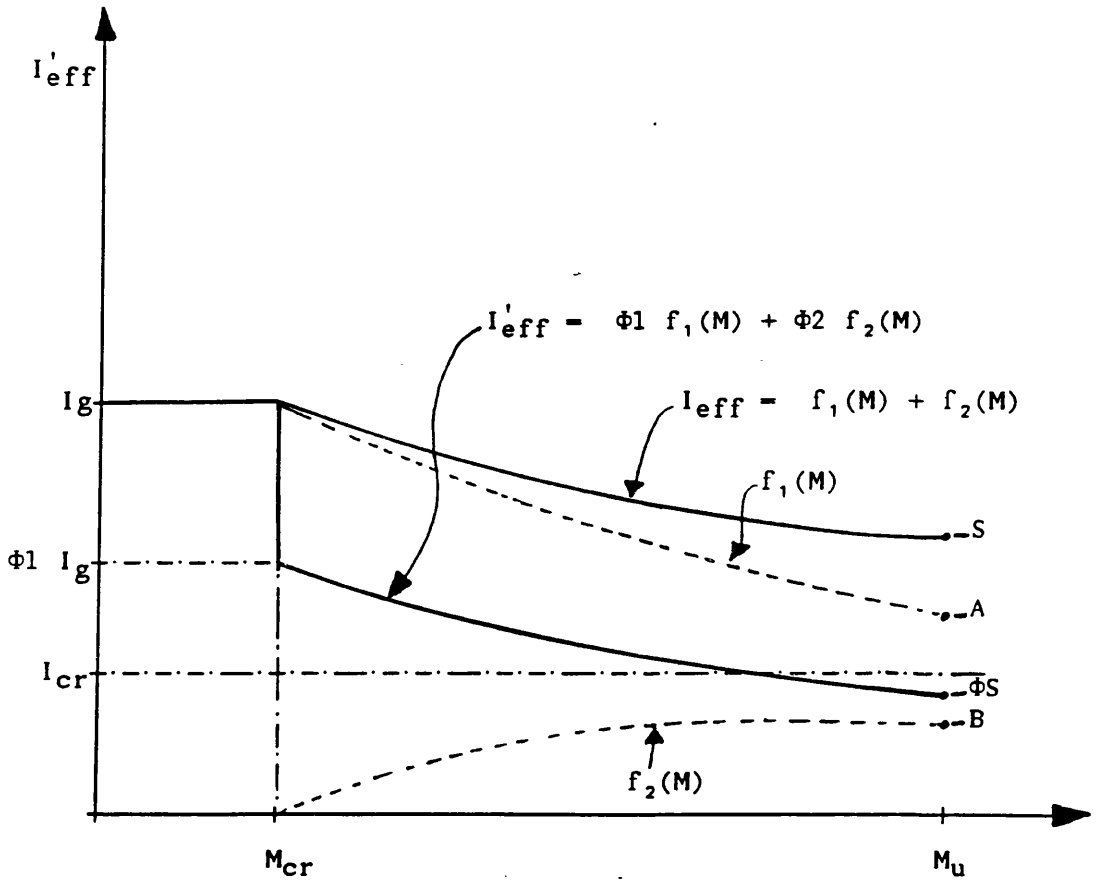
I'_{eff} can always be divided into two functions as follows:

$$I'_{eff} = \phi_1 f_1(M) + \phi_2 f_2(M) \quad 9.37$$

with :

$$f_1(M) = (M_{cr}/M)^3 I_g \quad \text{and} \quad f_2(M) = [1-(M_{cr}/M)^3] I_{cr}$$

The graphical presentation of these functions are presented in figure 9.3. If $\phi_1 = \phi_2 = 1$, I'_{eff} will have the same value as I_{eff} . If $M < M_{cr}$, I'_{eff} is equal to I_g , thus the thickness is equal to the non cracked thickness of the slab. If $M > M_{cr}$ then the thickness is calculated as follows:



$$A = (M_{cr}/M_u)^3 I_g$$

$$B = [1 - (M_{cr}/M_u)^3] I_{cr}$$

$$S = A + B$$

$$\phi S = \phi_1 A + \phi_2 B$$

$$I_{eff} = (M_{cr}/M)^3 I_g + [1 - (M_{cr}/M)^3] I_{cr}$$

$$I'_{eff} = \phi_1 (M_{cr}/M)^3 I_g + \phi_2 [1 - (M_{cr}/M)^3] I_{cr}$$

Fig. 9.3 Graphical Representation of I_{eff} and I'_{eff}

$$I'_{eff} = \phi_1 (M_{cr}/M)^3 I_g + \phi_2 [1 - (M_{cr}/M)^3] I_{cr} - (b h_p^3)/12 \quad 9.38$$

where b is unit width and h_p is the pseudo-thickness which will be used for the calculation of stiffness D in equation 9.13.

In order to have confidence in the accuracy of the results obtained from the finite element programs, a sensitivity study was carried out on the finite element mesh size and the tolerance. Slab model S.1 was chosen to perform this study. A 3*3 Gauss integration rule was used over each element. The element stiffness were computed at the first iteration of the first increment and at second iteration of the other increments if convergence was not obtained in the first iteration. In this sensitivity study equation 9.38 was used to calculate the pseudo-thickness of the slab with $\phi_1 = \phi_2 = 1$. The same criterion of equation 4.41 in chapter four, which is based on a tolerance value of the residual forces, was used. Using different values of tolerance of 5, 4, 3, 2 and 1% gives no difference in the results as presented in figure 9.4a in terms of the ultimate load. Also from figure 9.4b it can be seen that there is little difference in the ultimate load using different mesh sizes. It can be concluded that a tolerance value of 4% can be adopted and a 4*4 finite element mesh can be used. In comparison with the layer program, this program gives an economic prediction in terms of time costs. When using 4*4 finite element mesh with layer analysis it is found that the overall solution is almost four times the time cost when using the present program.

Four slabs, with different support and loading systems, were analysed. Two of the slabs have 100mm thickness, another with 150mm and McNeice(116) slab which has 44.4mm thickness. Three of the slabs were chosen from the previous experimental program. They are models S.1, S.2 and S.6 which were square simply supported at the edges, with S.6 having a column support at the middle of the slab. The material properties, the dimensions and the support systems can be found in chapter six, while the steel reinforcement distribution can be found in chapter seven. Their experimental and numerical results are presented in chapter eight. The

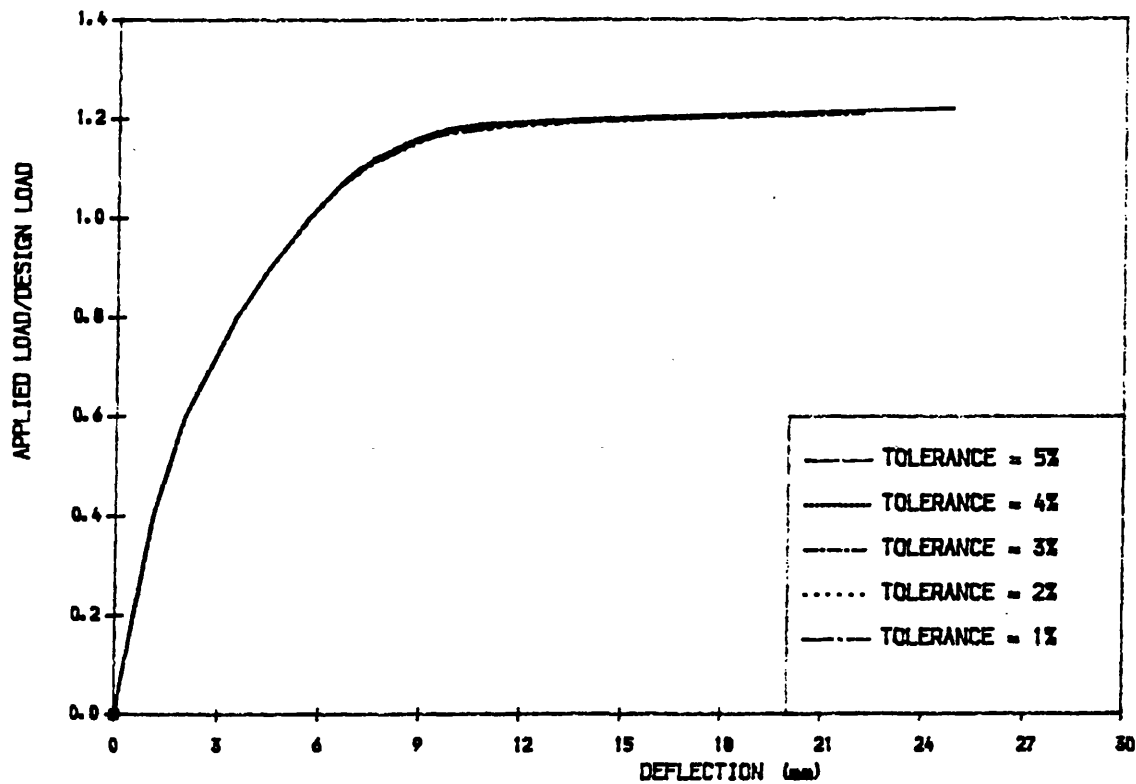


Fig. 9.4a Load- Deflection Curves. Different Tolerance Values

Model S.1

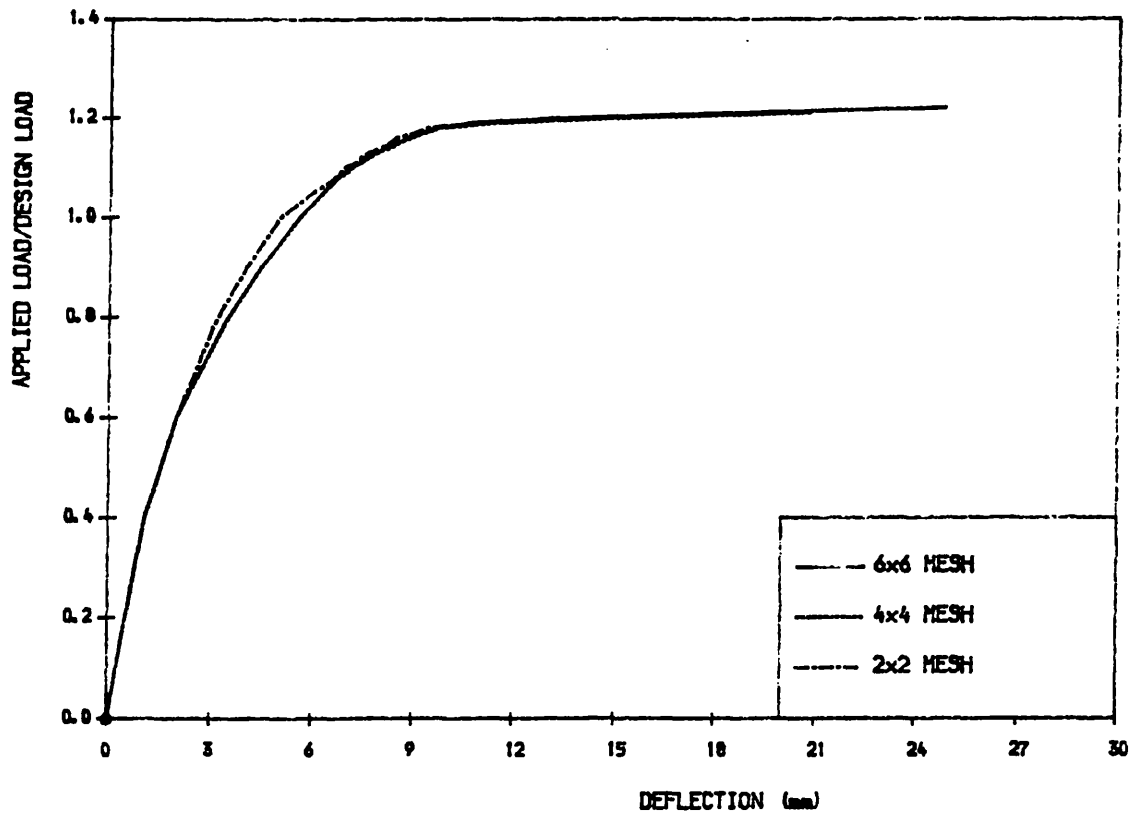


Fig. 9.4b Load- Deflection Curves. Different Finite Element Meshes

Model S.1

fifth slab is McNeice corner supported slab(116). The present result for this slab is also compared with the results obtained from the detailed layer program in chapter five.

In terms of deflection, as mentioned previously, the slabs are very stiff when Branson's equation 9.35 is used. In the first instance the object of this program is to give the designer roughly an idea of the ultimate load with minimum computational effort. But it seems that, when the reduction factors ϕ_1 and ϕ_2 were introduced, the predicted deflections are reasonable when compared with the experimental ones. Figure 9.5 shows the comparison of load deflection curves, of the central point, for experimental and numerical results both of layer program and the present elasto-plastic program for model S.1. In the present program different values of ϕ_1 and ϕ_2 were used. It can be noticed that the variation of the reduction constants have a little effect on the ultimate load. However, the experimental deflections are considerably affected when the constant ϕ_1 and ϕ_2 are decreased. The best deflection comparison with the experimental values is obtained when $\phi_1 = 0.2$ and $\phi_2 = 0.2$ for both slabs S.1 and S.2 in figure 9.5 and 9.6. In general, ϕ_1 governs the stiffness of the slab at working load while ϕ_2 governs the stiffness of the slab when approaching the ultimate load. This can be seen in figure 9.5 for the curves corresponding for $\phi_1 = 0.2$ and $\phi_1 = 0.1$ when ϕ_2 was held constant to 0.2. Table 9.2 summarizes the results for all the models. The numerical ultimate load of the present elasto-plastic program, for model S.1 as shown in figure 9.5, is of 1.07 of the experimental ultimate load, while the layer prediction was of 1.04 of the experimental ultimate load. Figure 9.6 shows the load deflection curves, of the central point for Slab S.2 where the prediction by the present program of the ultimate load is 0.93 of the experimental ultimate load. Figure 9.7a shows that the ultimate load predicted by the present program is 0.80 of the experimental ultimate load for slab S.6. The ultimate load prediction, in figure 9.7b, using elasto-plastic program for McNeice(116) slab is 1.07 of the experimental ultimate load, while layer prediction are 1.10 Pu. From table 9.2, it can be seen that the steel percentage has an effect on the constants ϕ_1 and ϕ_2

which give the best comparison. S.1 and S.2 have almost the same steel percentage in both top and bottom steel, therefore the same values of the reduction factors ϕ_1 and ϕ_2 gives the best comparison with the experimental results. It is believed that the support, loading system and the thickness of the slab may have also an effect on the choice of the reduction constants. It is suggested that further investigation on a large number of slabs with different steel ratios and different support, loading systems and thicknesses, so that an appropriate conclusion on the choice of the reduction factors can be achieved. Figures 9.8 and 9.9 show the comparison of yielded points for layer and elastoplastic programs for bottom and top steel, at the numerical ultimate load for S.1, respectively. It can be seen that the yielded points formed the yield line pattern known for such shape of the slabs and loading and support systems and the yielded regions are almost the same.

Table 9.2 Slabs Results Comparison.

Slab	Reinforcement % (Average)		Best Result with		$\frac{P_{uN}}{P_u}$	$\frac{P_{uL}}{P_u}$
	Bottom	Top	$\phi_1 =$	$\phi_2 =$		
S.1 t=100mm	0.32	0.18	0.2	0.2	1.07	1.04
S.2 t=100mm	0.38	0.18	0.2	0.2	0.93	0.95
S.6 t=150mm	0.13	0.07	0.2	0.2	0.80	0.96
McNeice t=44.45mm	0.64	0.00	0.7	0.6	1.07	1.10

P_u Experimental ultimate load. P_{uN} Elastoplastic program ultimate load

P_{uL} Layer program ultimate load. t Thickness of the slab.

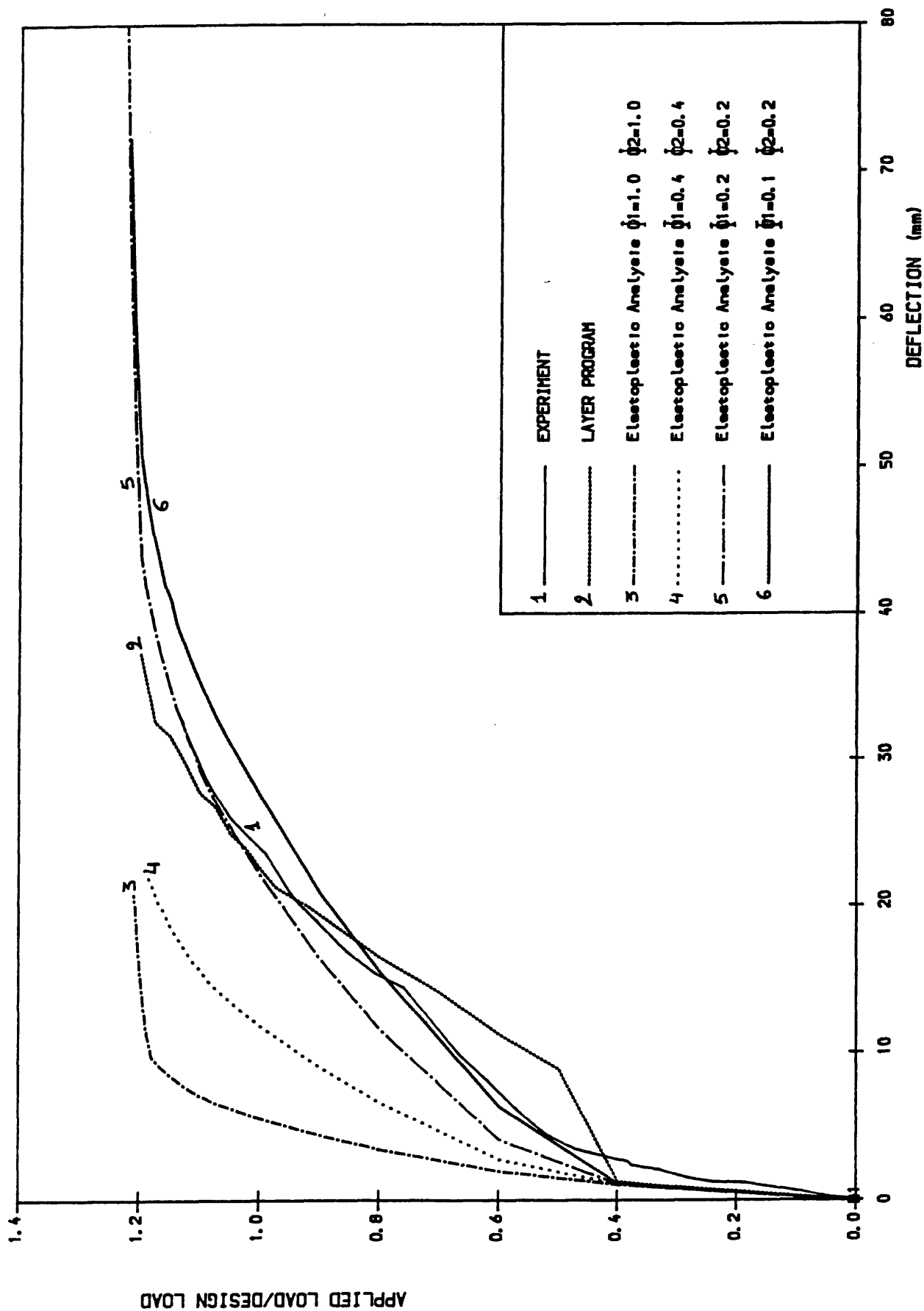


Fig. 9.5 Load-Deflection Curves at Central Point. Model S.1.

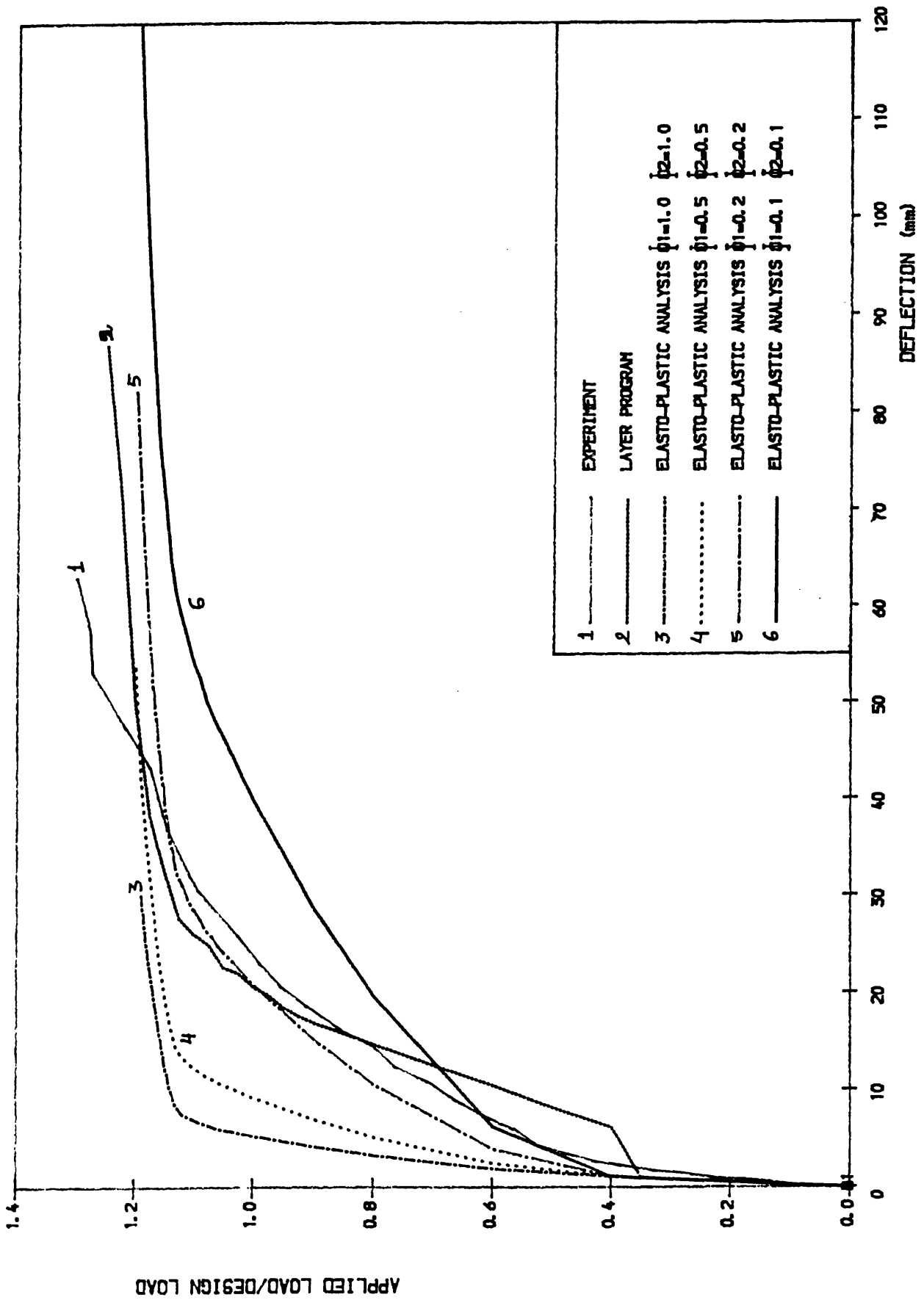


Fig. 9.6 Load-Deflection Curves at Central Point. Model S.2

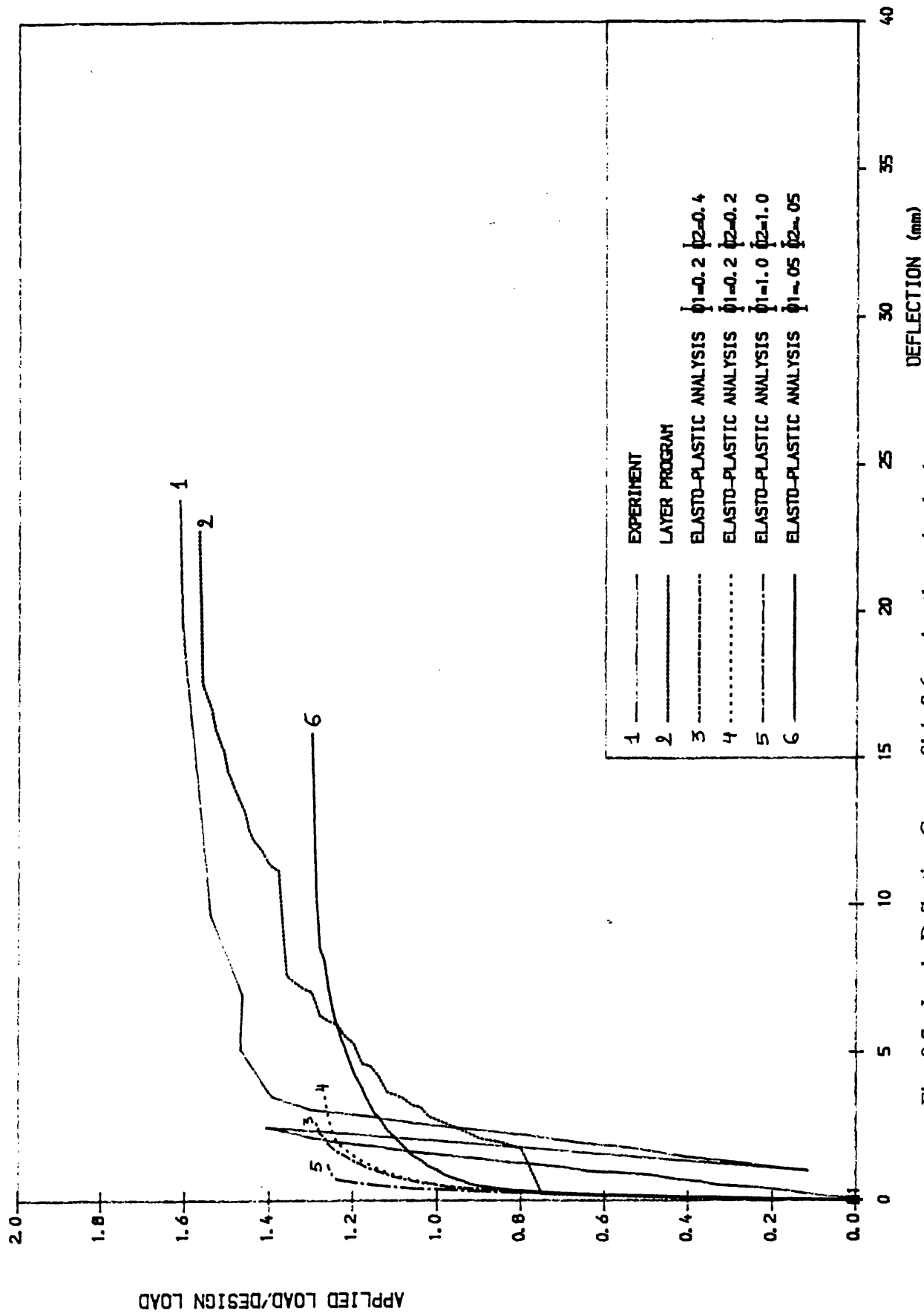


Fig. 9.7a Load-Deflection Curves. Slab S.6 under the point load.

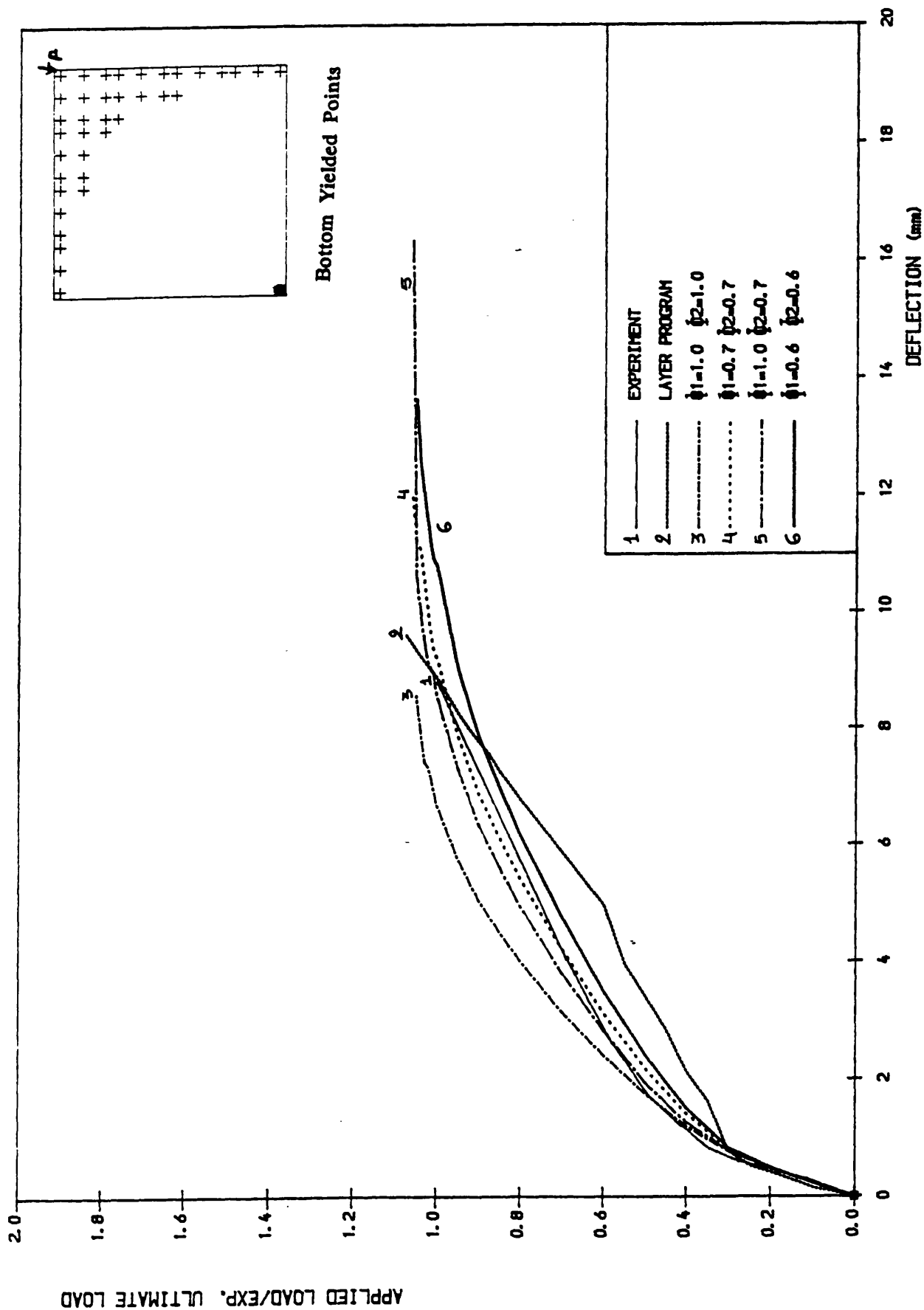


Fig. 9.7b Load-Deflection Curves. McNeice Slab Corner Supported.

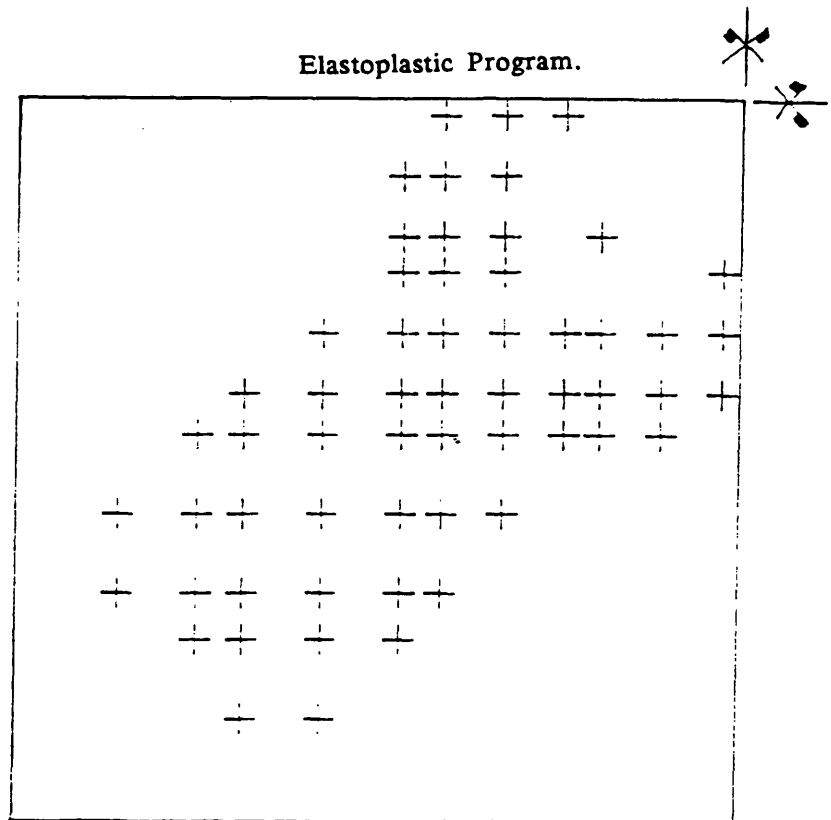
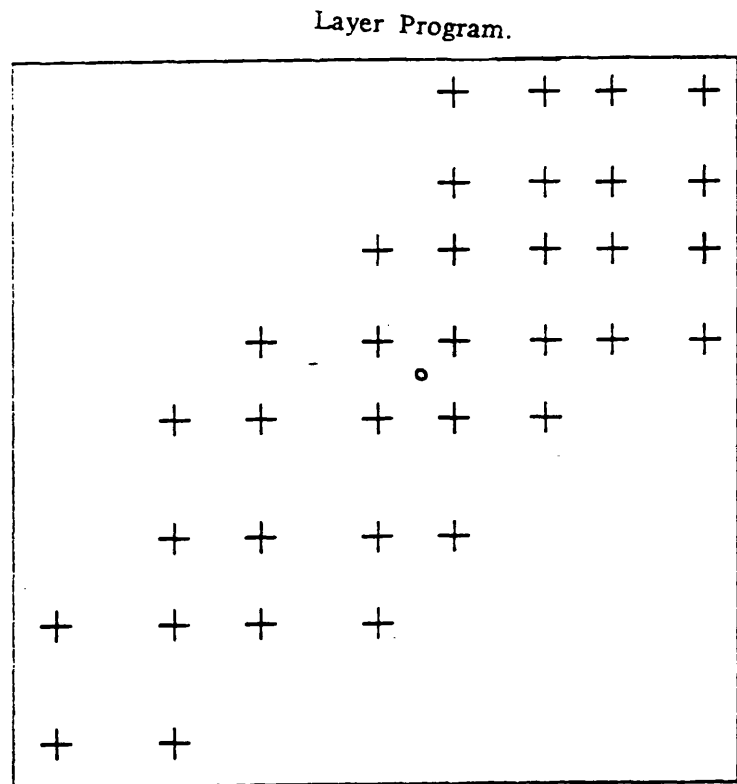


Fig. 9.8 Bottom Steel Yielded Points at Ultimate Load.

Slab S.1

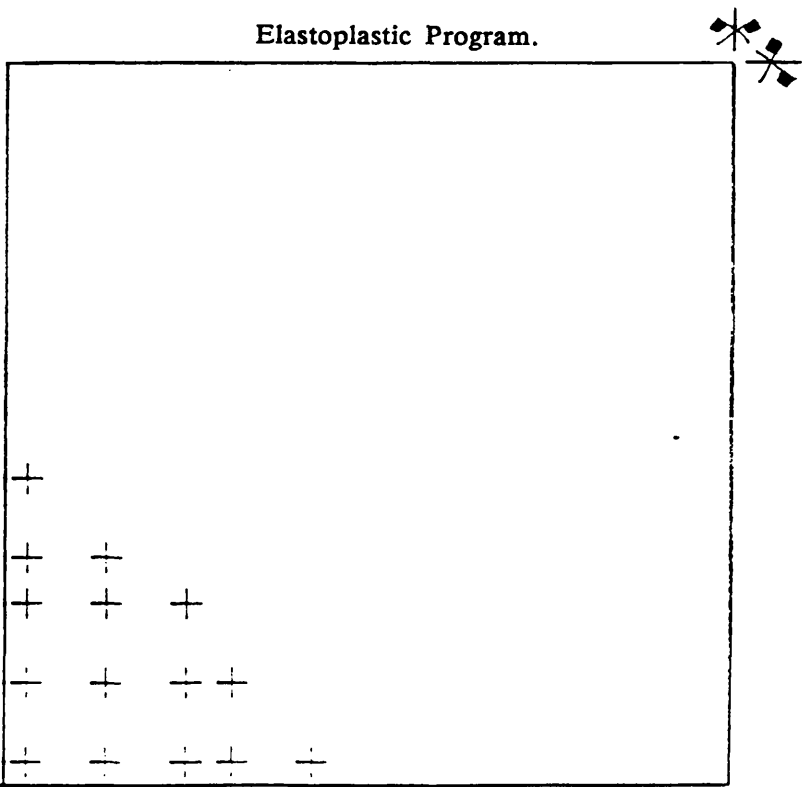
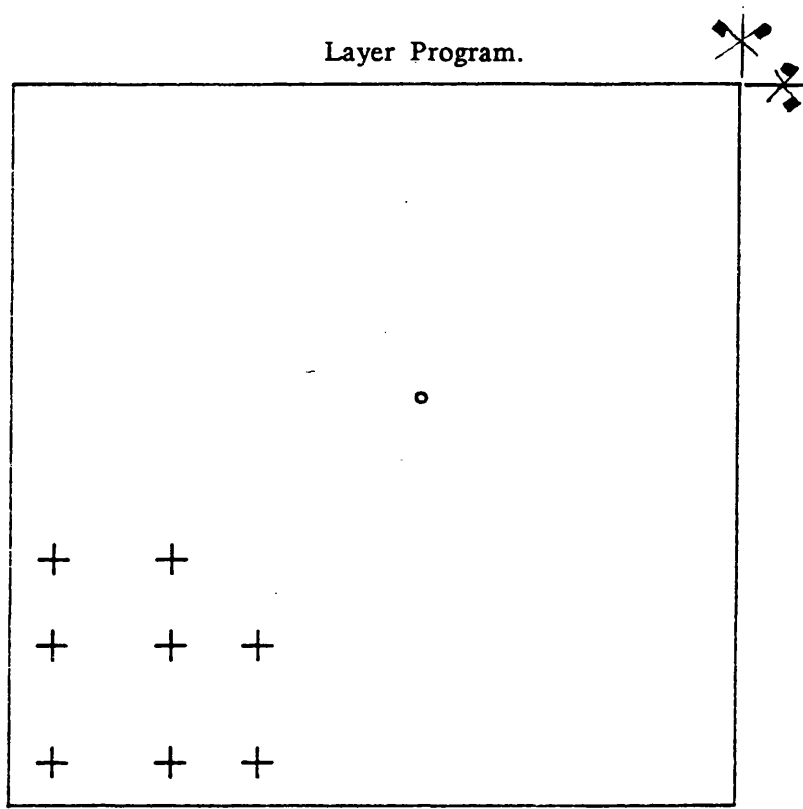


Fig. 9.9 Top Steel Yielded Points at Ultimate Load.

Slab S.1

9.3.2 Inplane Problem:

In the case of inplane problem, three deep beams were chosen to test the comparison of the present program predictions with the experiment and layer program. The first two beams were the ones tested in the present work and had different span/depth ratios. The third Beam is Khaskheli's Transfer Girder TRGRAS1 of two spans, which was analysed in chapter 5 using layer program. The beams were analysed using 8x8 finite element mesh with 3x3 Gauss point integration. The tolerance value was fixed at 4% throughout the analysis. The results show encouraging prediction of the ultimate load, although the beams show high stiffness. Figure 9.10 shows load-deflections comparisons for beams B.1. As can be seen both layer prediction and the present program gives very stiff deflection predictions. The first yielding is detected at 0.55 of the experimental ultimate load for beam B.1 at the same location as in the experimental results viz. at the mid-span of the beam. The first experimental yielding of steel for this beam was at 0.61 Pu, while in the layer program prediction the steel was yielded at 0.59 Pu. For beam B.2 the first yielding was detected at 0.52 Pu, 0.58 Pu and 0.66 Pu in the elastoplastic program, layer program and the experiment respectively. The ultimate load was also well predicted and was 1.01 of the experimental ultimate load, while layer predictions was almost of 1.0 of the experimental ultimate load. For beam B.2 and Khaskheli's TRGRAS1, the load-deflection predictions are presented in figures 9.11 and 9.12 respectively. The ultimate load prediction of the present program for the beam B.2 is 0.96 of the experimental ultimate load, while layer program prediction was 0.98 Pu. The ultimate load of Khaskheli's Beam is better predicted in the present elastoplastic program as shown in figure 9.12. The deflections are less in the present prediction which is mainly due to the fact that there is no loss of concrete stiffness when the stresses in the concrete reach their tensile strength. Thus it is important to allow cracks in concrete to open, so that stiffness of the structure can be reduced, which will result in a reasonable deflections comparison with the experiment. In terms of

time for computations, when analysing beam B.1, the present program computing time cost was 70% of the time used by layer program. Figure 9.13 and 9.14 show the points yielded in both present program analysis and layer analysis for beams B.1 and B.2 respectively. In layer program the steel was considered as embedded individual bars while in the present elastoplastic program a smeared model was adopted. In general it can be seen that regions of yielding over the beams are almost the same in both programs results at different load levels. It should be appreciated that the treatment of reinforced concrete as an elastoplastic material assumes a certain uniform distribution of steel in the element. This means that structures where it is not reasonable to assume smeared representation can not be handled by the elastoplastic analysis described in this chapter.

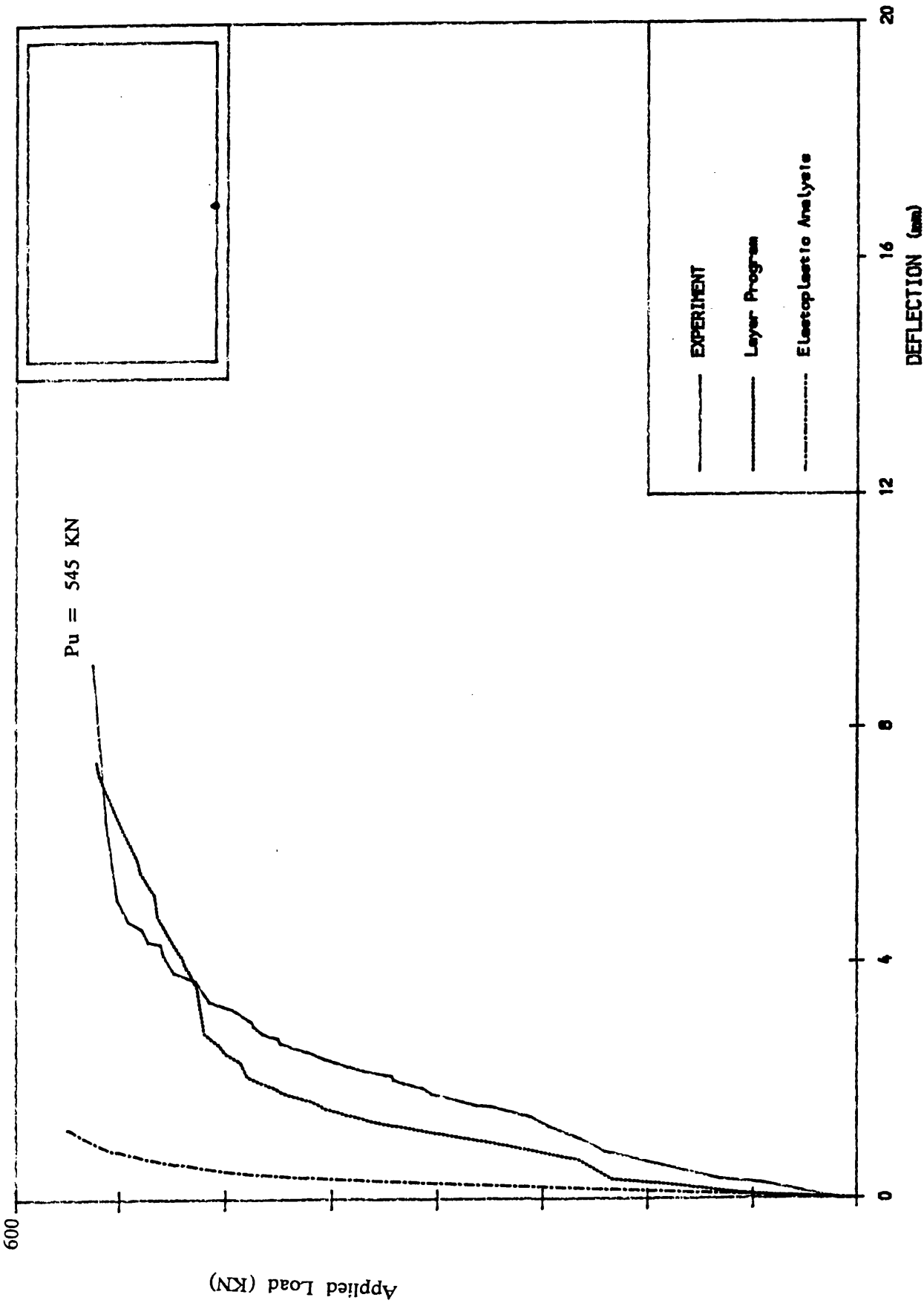


Fig. 9.10 Load-Deflection Curves. Beam B.1 at mid-span

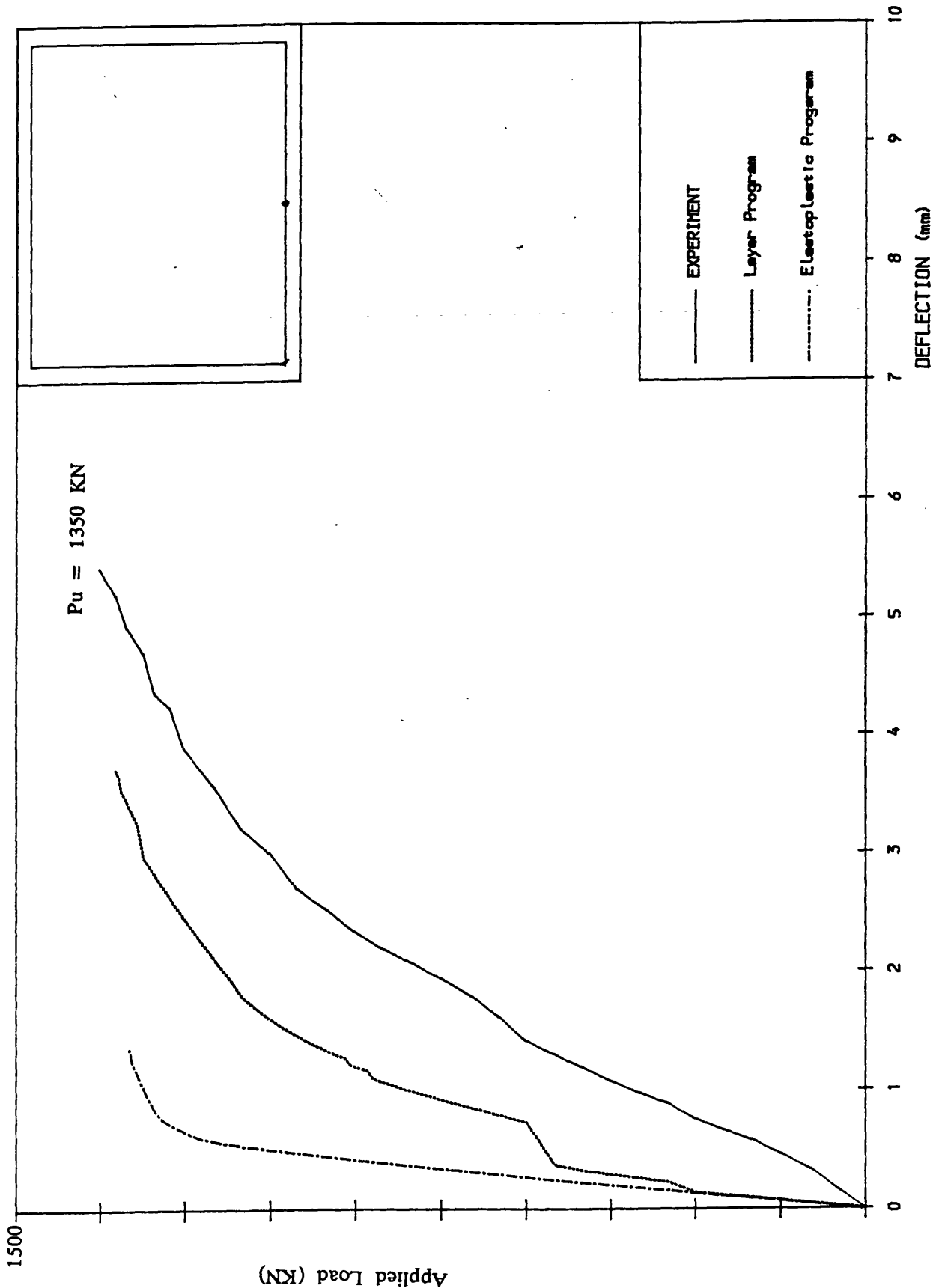


Fig. 9.11 Load-Deflection Curves. Beam B.2 at mid-span

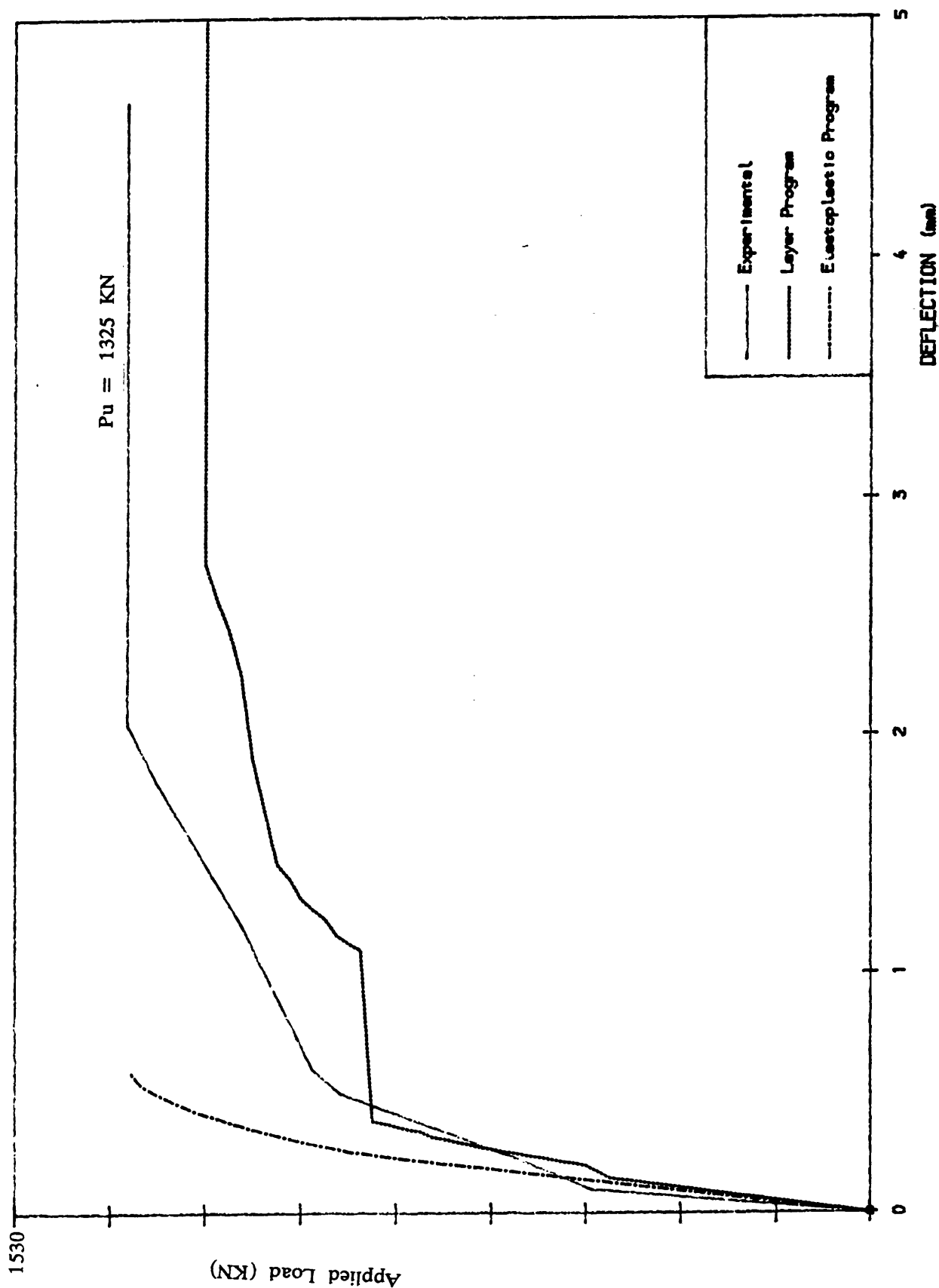


Fig. 9.12 Load-Deflection Curves. Khaskheli Beam 1 at mid-span.

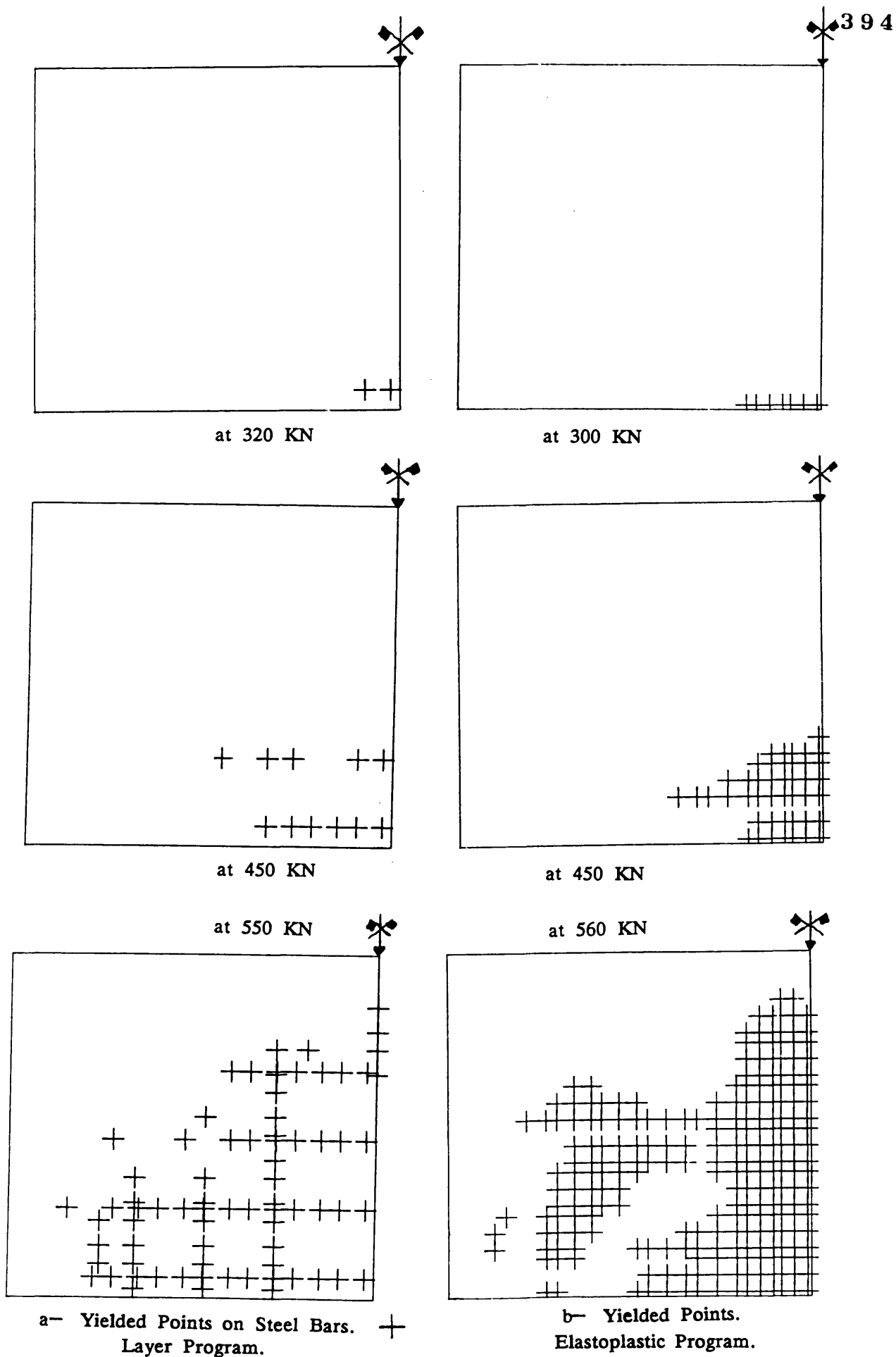


Fig. 9.13 Yielding Points Comparison at Different Loading Levels.

Beam B.1

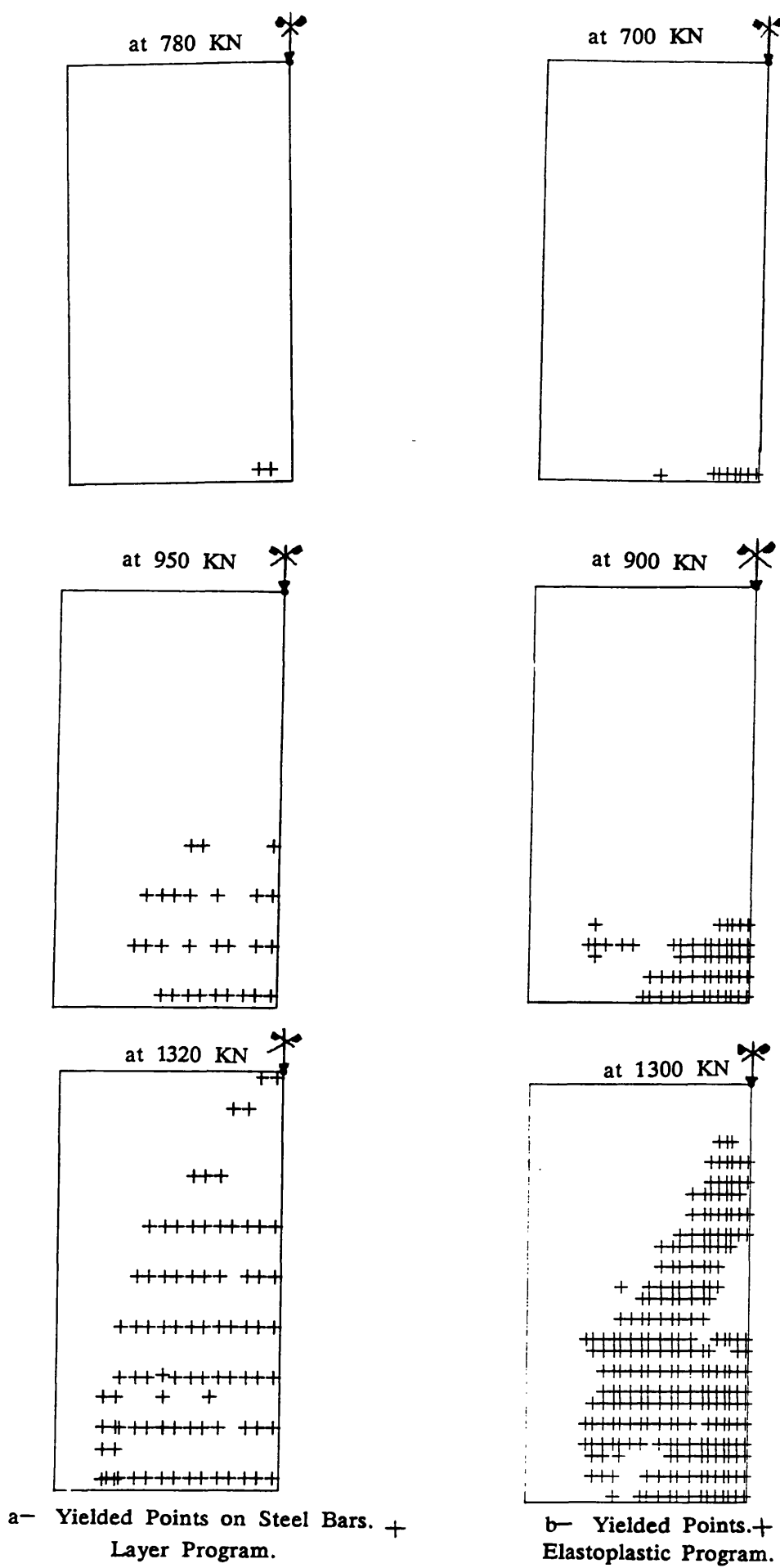


Fig. 9.14 Yielding Points Comparison at Different Loading Levels.

Beam B.2

Conclusions and Suggestions for Further Work

10.1 Conclusions:

From the theoretical analysis and experimental investigation reported in this thesis, the following conclusions can be drawn.

1— The use of nonelastic stress fields in the direct design of reinforced concrete slabs and deep beams leads to a satisfactory behaviour both at service and ultimate loads.

2— The use of nonelastic stress fields in the design of slabs has great practical advantage in the distribution of the design moments M_x^* and M_y^* over the slab in a more uniform way than when pure elastic stress field is used. This means congestion of reinforcement is avoided in the critical areas. In this way, in practice a desirable layout of steel is obtained with minimum intervention by the designer.

3— The use of nonelastic stress fields in the design of slabs may result in an economical design, since the design moments at the critical areas are reduced by redistribution of stresses to the neighbouring areas which are less stressed. This results in less steel reinforcement because there is saving in steel cut offs and lap lengths.

4— Unlike slabs, simply supported deep beams show little stress redistribution as the percentage of plasticity increases. It can thus be concluded that the use of elastic stress field is sufficient.

5— More stress redistribution takes place in simply supported slabs with mid-column

support than in simply supported slabs. Direct design method using stress distribution at high level of plasticity can be used for slabs with mid column support provided that a separate check for shear strength using BS8110 is performed.

6- Using ^{the} direct design method in the design of deep beams leads to an acceptable provision of steel reinforcement at the bearings and under the point loads.

7- Reinforced concrete deep beams are sensitive to the amount of steel provided. An increase in the vertical shear reinforcement leads to ductile failure.

8- The numerical model adopted is capable of providing acceptable predictions at working and ultimate loads for both reinforced concrete slabs and deep beams failing in different modes. From the number of models tested numerically it can be concluded that the model gives a very close lower bound solution.

9- Large variation in shear retention factor has almost no influence on the deflections and the ultimate load of slabs and deep beams failing in flexure, so that for a large number of models analysed a value of $B = 0.4$ gives acceptable results.

10- The embedded individual bar model for steel finite element representation has a significant effect on the ultimate load of deep beams. However for slab models, as expected, it seems that there is no difference in the results between the individual embedded and the smeared model.

11- Finite element programs, analysing reinforced concrete plate bending and inplane concrete as an elastoplastic material were developed. The prediction of the ultimate load are satisfactory, while for beams the deflection predictions are very stiff. The programs are much cheaper to use than the layer analysis programs.

12- The proposed reduction factors ϕ_1 and ϕ_2 have a significant effect in

improving the deflection predictions. In general $\phi_1 = 0.2$ and $\phi_2 = 0.2$ can be adopted. An important advantage of these two reduction factors is that they do not affect the ultimate load.

13— Mixed stress field yield equation for reinforced concrete inplane structures are developed and implemented in a finite element program. The ultimate load of the beams analysed, are well predicted, whereas the deflection prediction is stiff. A method needs to be developed for allowing for cracking of concrete.

10.2 Suggestion for future work:

1— The work presented in this thesis was concentrated only on two dimensional plate bending and inplane problems using nonelastic stress fields. It is worth while to investigate the possibility of using elastic and nonelastic stress fields in the design of reinforced concrete members of three dimensions under arbitrary stress fields as presented by Baker(117).

2— Most slabs supported on columns fail either by shear or by combination of flexure and shear. The numerical analysis of slabs in this work neglected the steel contribution in the vertical shear capacity of the slab. It will be useful to investigate the possibility of detecting shear failure of slabs subjected to such complicated phenomenon using 3— D analysis.

3— Only orthogonal steel was considered in the present investigation, whereas skew reinforcement is encountered in practice and may lead to a more economical design(43,81). Hence, it would be useful if the work could be extended to skew reinforcement cases.

4— Slabs and deep beams are often encountered in practice with openings to allow for access. It would be useful to investigate the stress redistributions on such

structures and their behaviour, when designed using high plasticity stress fields.

5- The predicted stiffness of the deep beams analysed by the elastoplastic program is stiff. It is important to allow for cracks to open so that the results in terms of deflection are better predicted.

6- More investigation is needed, on a large number of existing data of slabs with different boundary conditions, loading systems, percentage of steel and thicknesses, so that the classification of an appropriate reduction factors Φ_1 and Φ_2 can be suggested.

7- Most ultimate load predictions of the elastoplastic program for plate bending are lower than the experimental ultimate loads. It is worth while to allow for the effect of hardening of steel on the resistant moment, so that the yield surfaces can expand which will result in a numerical ultimate load greater than the present given ones.

8- In practice, many structures are in the state of combined bending and inplane forces. Therefore an extension of the present work to account for the effect of membrane forces will be useful in practice.

- 1- BS8110 Part 1 and 2,
Structural Use of Concrete,
British Standards Institution, 1985.

- 2- Zienkiewicz, O.C.
The Finite Element Methods,
McGraw Hill, 4th Edition, 1989, London.

- 3- Cook, R.D.
Concepts and Applications of Finite Element Analysis.
Willey, 2nd Edition, 1981, New York.

- 4- Nath, B.
Fundamental of Finite Elements for Engineers.
The Athone Press of the University of London, 1974.

- 5- Owen, D.R.J., and Hinton, E.
Finite Element in Plasticity, Theory and Applications.
Pineridge Press Limited, 1980, Swansea, U.K.

- 6- Bhatt, P.
Programming the Matrix Analysis of Skeletal Structures,
John Willey & Sons, Chichester 1986.

- 7- Ngo, D., and Scordellis, A.C.
Finite Element Analysis of Reinforced Concrete Beams.
J. Amer. Con. Inst., Vol. 64, 1967, pp. 152-163.

- 8- Buyukozturk, O. and Shareef, S.S.
Constitutive Modelling of Concrete in Finite Element Analysis,
Computers and Structures, Vol. 21, No. 3, pp. 581-610. 1985.

- 9- Bhatt, P. and Bensalem, A.
Behaviour of Reinforced Concrete Slabs Designed using Nonelastic Stress Fields,
Computational Methods and Experimental Mesurments, CMEM/91, Edited By
A. Sousa, C.A. Brebbia and C.M. Carlomagno, Computational Mechanics
Publications and Elsevier, 1991, pp. 471-480.

- 10— Popvics, S.A.
A Review of Stress—Strain Relationships for Concrete,
J. Amer. Con. Inst., Vol. 67, No. 3, 1970, pp. 243—248.

- 11— Hughes, B.P., and Chapman, G.P.
The Complete Stress—Strain Curve for Concrete in Direct Tension,
RILEM Bull. 30, (1966), pp. 95—97.

- 12— Chen, A.C.T. and Chen, W.F
Constitutive Equations and Punch Indentation of Concrete.
J. Eng. Mech. Div., ASCE, Vol. 101, No EM6, Dec. 1975, pp.889—906.

- 13— Benredouane, M.
Direct Design of Reinforced Concrete Slabs Using Nonelastic Stress Fields,
Msc. Thesis, 1988, Glasgow University.

- 14— Bhatt, P. and Benredouane, M.
Nonelastic Stress Fields and Direct Design of Reinforced Concrete Slabs,
Numerical Methods in Engineering: Theory and Application, Ed. Pande and
Middleton, J., Vol. 1, pp. 67—77, Elsevier, 1990.

- 15— Nelissen L.J.M.
Biaxial Testing of Normal Concrete,
Heron (Delft), Vol. 18, No. 1, 1972.

- 16— Tasuji, M.E., Slate, F.O., and Nilson, A.H.
Stress Strain Response and Fracture of Concrete in Biaxial Loading.
J. Amer. Concr. Inst., Vol. 75, No. 7, July 1978, pp. 306—312.

- 17— Kupfer, H., Hilsdorf and Rusch, H.
Behaviour of concrete Biaxial Stresses,
J. Amer. Concr. Inst., Vol. 66 No. 8, August 1969, pp. 656—666.

- 18— Valinas, K.C.
A Theory of Viscoplasticity Without a Yield Surface. Theory and Application,
'Archives of Mechanics' Vol. 23, No. 4, 1991, pp. 517—551.

- 19— Bazant, Z.P. and Bhat, P.D.
Endochronic Theory of Inelasticity and Failure of Concrete,
J. Eng. Mech. Div. Proc. of the ASCE, Vol. 102, No. 4, 1976, pp. 701—722.

- 20— Bazant, Z.P. and Bhat, P.D.
Prediction of Hyteresis of Reinforced Concrete Members,
Journal of the Structural Division, ASCE, Vol. 103, No. 1, 1977, pp. 153–167.
- 21— Reddy, D.V. and Gopal, K.R.
Computational Modelling of Reinforced Concrete Structures.
Edited By Hinton and Owen, Pineridge Press Ltd, 1986, pp. 155–186.
- 22— ASCE Committee on Concrete and Masonry Structure
A State of the Art Report on Finite Element Analysis of Reinforced Concrete Structures, 1981.
- 23— Chen, W.F.
Plasticity in Reinforced Concrete Structures,
McGraw Hill Book Company, New York, 1982
- 24— Hinton, E. and Owen, D.R.J.
Computational Modelling of Reinforced Concrete Structures,
Peneridge Press Ltd. 1986.
- 25— Elfgren, L.
Fracture Mechanics of Concrete Structures, From Theory to Application,
RILEM Report—Chapman and Hall Ltd. 1989.
- 26— Cervenka, V. and Gestle, K.H.
Inelastic Analysis of Reinforced Concrete Panels, Proceedings of International Association for Bridge and Structural Engineering, Vol. 31, Part 2, 1971.
- 27— Suidan, M. and Schnobrich, W.C.
Finite Element Analysis of Reinforced Concrete.
Journal of Structural Division, ASCE, Vol. 99, ST10, 1973, pp. 2109–2122.
- 28— Buyukozturk, O.
Nonlinear Analysis of Reinforced Concrete Structures,
Computers and Structures, Vol. 7, 1977, pp. 149–156.
- 29— Vermeer, P.A. and de Borst, R.
Nonassociated Plasticity for Soils, Concrete and Rock,
Heron, Delft University, Vol. 29, No. 3, pp. 1–64, 1984.

- 30- Han, D.J. and Chen, W.F.
Constitutive Modelling in Analysis of Concrete Structures,
J. Eng. Mech. Div. ASCE, Vol. 112, No. 3, 1986
- 31- Branson D.E.
Deformation of Concrete Structures,
McGraw-Hill, 1977, New York
- 32- Andenaes, E., Gerstle, K. and Ko, H.Y.
Response of Mortar and Concrete to Biaxial Compression,
J. Eng. Mech. Div., ASCE, Vol. 103(3), pp. 515-525, 1977.
- 33- Bazant, Z.P. and Kim, S.S.
Plastic-Fracturing theory of concrete.
J. Eng. Mech. Div., ASCE, Vol. 105, No. EM3, pp. 407-428, 1979.
- 34- Hiroshi, Y. and Setsuro, N.
Analysis of Reinforced Concrete Walls by Plastic-fracturing Theory.
US-Japan proceedings, 1985, pp. 204-213.
- 35- Rashid, Y.R.
Analysis of Prestressed Concrete Pressure Vessels, Nuclear Engineering and
Design, Vol. 7, No. 4, April 1968, pp. 334-344.
- 36- Al-Manaseer, A.A.
A Nonlinear Finite Element Study of Reinforced Concrete Beams,
Ph.D. Thesis, 1983, Glasgow University.
- 37- Al-Mahaidi, R.S.H.
Nonlinear Finite Element Analysis of Concrete Deep Members.
Report No. 79-1, Cornell University, January 1979.
- 38- Rots, J.G.
Smeared crack approach. Fracture Mechanics of Concrete Structures. Edited by
L. Elfgren 1989 RILEM, pp. 138-146.
- 39- Crisfield, M.A.
Snap-through and snap-back response in concrete structures and the danger of
under-integration, Int. J. Num. Meth. Engng, Vol. 22(3), 1986, pp. 751-768.

- 40- Bazant, Z.P. and Cedolin, L.
Fracture Mechanics of Reinforced Concrete.
J. Eng. Mech. Div, ASCE, Vol. 106, No. EM6, 1980, pp. 1287-1306.
- 41- Collins, M.P., Vecchio F.J., and Mehlhorn, G.
An International Competition to Predict the Response of R.C. Panels.
Canadian Jour. of Civil Engineering Vol. 12, 1985, pp. 624-644.
- 42- Joh^harry, T.
Elasto-plastic Analysis of Concrete Structures Using Finite Elements.
Ph.D. Thesis, University of Strathclyde, May 1979.
- 43- Abdel Hafez, L.M.
Direct Design of Reinforced Concrete Skew Slabs,
Ph.D. Thesis, University of Glasgow, 1986.
- 44- Marzouk, H. and Hussein, A.
Experimental Investigation on the Behavior of High-Strength Concrete Slabs,
J. Amer. Con. Inst., Nov-Dec 1991, Vol. 88, No. 6, pp.701-713
- 45- Saenz, I.P.
Discussion of 'Equation of the stress-strain Curve of Concrete' By Desayi, P.
and Krishnan, S., J. Amer. Con. Inst., Vol. 61, No. 9, Sep. 1964,
pp. 1129-1235.
- 46- Liu, T.C.Y, Nilson, A.H. and Slate, F.O.
Stress-Strain Response and Fracture of Concrete in Uniaxial and Biaxial
Compression, J. Amer. Con. Inst., Vol. 69, No. 5, May 1972, pp. 291-295.
- 47- Bell, J.C. and Elms, D.G.
Finite Element Approach to Post-Elastic Slab Behaviour,
ACI Special Publications, SP30-15, March 1971, pp. 325-344.
- 48- Chen, W.F. and Teng, E.C.
Constitutive Models for Concrete, J. Eng. Mech. Div., Proc. of the ASCE,
Vol. 106, No. EM1, Feb. 1979, pp. 1-19.
- 49- Vecchio, F. and Collins, M.P.
The Response of Reinforced Concrete to Inplane Shear and Normal Stress.
Publ. No. 82-03, Dep. Civ. Eng. Toronto University, 1982.

- 50- Soroushian, P., Obaseki, K. and Choi, K.B.
Analysis of Aggregate Interlock Behaviour at Cracks in Reinforced Concrete.
Magazine of Concrete Research, Vol. 40, No. 192, March 1988, pp. 43- 49.
- 51- Millar, S.G. and Jonson, R.P.
Shear Transfer in Cracked Reinforced Concrete,
Magazine of Concrete Research, Vol. 37, No, 130, pp.3-15, 1985.
- 52- Johnston, D.W. and Zia, P.
Analysis of Dowel Action. Journal of the Structural Division Proc. of the
ASCE , Vol. 97, No. ST5, 1971, pp. 1611-1630.
- 53- Hand, F.R., Peckhold, D.A. and Schnobrich, W.C.
Nonlinear Layered Analysis of Reinforced Concrete Plates and Shells. J. the
Str. Div., Proc. of the ASCE, Vol. 99, No. ST7, July 1973, pp.1491-1505.
- 54- Cedolin, L. and Deipoli, S.
Finite Element Studies of Shear Critical Reinforced Concrete Beams.
J. Eng. Mech. Div., Proc. of the ASCE, Vol. 103, No. EM3, June 1972,
pp. 359-410.
- 55- Scanlon, A. and Murray, D.W.
Time Dependent Reinforced Concrete Slab Deflections, J. of the Str. Div.,
Proc. of the ASCE, Vol. 100, No. ST9, 1974, pp. 1911-1924.
- 56- Clark, L.A. and Speirs, D.M.
Tension Stiffening in Reinforced Concrete Beams and Slabs Under Short Term
loads, Tech. Report 42.521, Cement and Concrete Association, London, 1978.
- 57- Nielsen, M.P. and Braestrup, M.W.
Shear Strength of Prestressed Concrete Beams without Web- Reinforcement,
Magazine of Concrete Research, Vol. 30, No. 104, Sept 1978.
- 58- Braestrup, M.W.
Shear Strength Prediction- Plastic Method, In Reinforced Concrete Deep
Beams, Ed. by F.K. Kong, Blackie and Son Ltd, 1990, UK.
- 59- Hillerborg, A.
Strip Method of Design, A View Point Publication,
Slough, 1975.

- 60— Bhatt, P.
Discussion on 'An Upper— bound Rigid— plastic Solution for the Shear Failure of Concrete Beams without Shear Reinforcement', Magazine of concrete research, Vol. 34, No. 119, June 1982.
- 61— Chen, G.W.
Plastic Analysis of Shear in Beams, Deep Beams and Corbels,
Technical University of Denmark, Dept of Strl Engng, Report R237, 1988.
- 62— Rogowski, D.M., MacGregor, J.G. and Ong, S.S.
Tests on reinforced concrete deep beams.
J. Amer. Con. Inst., Vol. 83, No. 4 : 614, 1986.
- 63— Hughes, B.P.
Limit State Theory for Reinforced Concrete Design,
Pitman Publishing Ltd. London 3rd Edition 1980.
- 64— Save, M.
A Consistent Limit— analysis Theory for Reinforced Concrete Slabs,
Magazine of Concrete Research, Vol.19, No. 58, March 1967, pp 3–12.
- 65— Hillerborg, A.
Reinforcement of Slabs and Shells Designed According to the Theory of Elasticity. Betong, 1953, 38(2), pp. 101–109.
- 66— Lenschow, R. and Sozen, M.A.
A Yield Criterion for Reinforced Concrete Slabs,
J. Amer. Con. Inst. Title No. 64–27, May 1967, pp. 266–273.
- 67— Cardenas, A.E. and Sozen, M.A.
Flexural Yield Capacity of Slabs,
J. Amer. Con. Inst., February 1973, pp. 124–126.
- 68— Jain, S.C. and Kennedy, J.B.
Yield Criterion For Reinforced Concrete Slabs, Journal of the Structural Division, Proc. of the ASCE, Vol. 100, No. St3, March 1974, pp. 631–644.
- 69— Hago A.W. and Bhatt, P.
Direct Design of Reinforced Concrete Slabs,
J. Amer. Con. Inst., Nov– Dec 1986, No. 6, Vol. 83, pp. 916–924.

- 70- Bhatt, P., Abdel Hafiz, L.M. and Green, D.R.
Direct Design of Reinforced Concrete Skew Slabs,
Computers and Structures Vol. 30, No. 3, pp. 477-488, 1988.
- 71- Wood, R.H.
The Reinforcement of Slabs in Accordance with a Pre-determined Field
of Moments, Concrete Vol. 2, February 1968, pp. 69-75.
- 72- Armer, G.S.T.
Discussion of Ref. 71,
Concrete Vol. 2, August 1968, pp. 319-320.
- 73- Nielsen, M.P.
Yield Condition for Reinforced Concrete Shells in the Membrane State,
Nonclassical Shell Problems, IASS Symposium Warsaw 1963, Editor W. OLSAK,
Amsterdam, North Holland Publishing Co, 1964, pp.1030-1038.
- 74- Nielsen, M.P.
Limit Analysis and Concrete Plasticity,
Prentice Hall, New Jersey, 1984.
- 75- Morley, C.T.
Optimum Reinforcement of Concrete Slabs Against Combination of Moments
and Membrane Forces, Magazine of Concrete Research. Vol. 22, N. 72,
Sept. 1970, pp. 155-162.
- 76- Subedi, N.K.
Design of Reinforced Concrete Sections Subjected to Membrane Forces.
The Structural Engineer, Vol. 53, N. 7. July 1975, pp. 289-292.
- 77- Jensen, B.J.
Lines of discontinuity for displacements in the theory of plasticity of plain
concrete. Magazine of Concrete Research, Vol.27, N.92, September 1975,
pp. 143-150.
- 78- Clark, L.A.
The Provision of Tension and Compression Reinforcement to Resist Inplane
Forces, Magazine of Concrete Research, Vol. 28, No. 94, March 1976.

- 79— Lin, C.K.
Ultimate Strength Design of Deep beams,
Msc. Thesis, University of Glasgow 1979.
- 80— Memon, G.H.
Ultimate Strength of Perforated Deep Beams,
Msc. Thesis, University of Glasgow 1979.
- 81— Khaskheli, G.B.
Direct Design of Reinforced Concrete Transfer Girders,
PhD. Thesis, University of Glasgow 1989.
- 82— Kemp, K.O.
The yield criterion for Orthotropically Reinforced Concrete Slabs,
International Journal of Mechanical Sciences, Vol. 7, 1965, pp 737–746.
- 83— Morley C.T. and Gulvanessian, H.
Optimum Reinforcement of Concrete Slab Elements.
Proc. Instn. Civ. Engrs. Part 2, 1977, 63, June, pp. 441–454.
- 84— Brøndum—Nielsen, T.
Optimum Design of Reinforced Concrete Shells and Slabs. Technical University
of Denmark, Structural Research Laboratory, 1974—Report, R44, 190–200.
- 85— Kong, F.K. and Chemrouk, M.
Reinforced Concrete Deep beams. In Reinforced Concrete Deep Beams,
Ed. by F.K. Kong, Blackie and Son Ltd, 1990.
- 86— Crisfield, M.A.
A Fast Incremental/Iterative Solution Procedure that Handles Snap Through.
Computers and Structures, Vol. 13, pp. 56–62, 1981.
- 87— Crisfield, M.A.
An Arc—length Method Including Line Searches and Accelerations.
Int. Jour. of Num. Meth. in Eng., Vol. 19, pp. 1269–1289, 1983
- 88— Bellini, P.X. and Chulya, A.
An Improved Automatic Incremental Algorithm for the Efficient Solution of
Nonlinear Finite Element Equations. Computers and Structures, Vol. 26,
No.1–2, pp. 99–110, 1987.

- 89— Cheung Y.K. and Chan, H.C.
Finite Element Analysis, In Reinforced Concrete Deep Beams,
Editor Kong, F.K., Blackie, Glasgow—London, 1990.
- 90— Timoshenko, S., Woinowsky—Krieger, S.
Theory of Plates and Shells,
McGraw—Hill Book Company, 1959.
- 91— Timoshenko, S., and Goodier, J.N.
Theory of Elasticity,
McGraw—Hill Book Company, 3rd ed. 1970.
- 92— Cheng, D.H., and Pei, M.L.
Continuous Deep Beams, Proc. of the ASCE, Vol.80, Separate No. 450,
June 1954, pp. 450—1—450—17
- 93— Bhatt, P.
Deep Beams on Statically Indeterminate Supports, J. of the Eng. Mec. Div.,
Proc. of the ASCE, Vol. 99, No.EM4, 1973, pp.793—802.
- 94— Kaar, D.H.,
Stress in Centrally loaded Deep Beams, Proc. of the Society for Experimental
Stress Analysis (SESA), Vol.15, No.1, 1975, pp.77—84.
- 95— CP110— 1972
The Structural Use of concrete,
British Standards Institution, London, 1972
- 96— Kong, F.K., Garcia R.C., Paine, J.M., Wang, H.H.A and Chemrouk, M.
Instability and Buckling of Reinforced Concrete Deep Beams,
The Structural Engineer, Vol.66, part2, 1986, pp. 28—37.
- 97— Kong, F.K., Robins, P.J., Singh, A. and Sharp, G.R.
Shear Analysis and Design of Reinforced Concrete Deep Beams,
The Structural Engineer, Vol. 50, No. 10, october 1972, pp. 405—413.
- 98— CIRIA Guide 2
The Design of Deep Beams in Reinforced Concrete, Ove Arup & Partners and
Construction Industry Research and Information Association, London 1977.

- 99— Jones, L.L. and Wood, R.H.
Yield Line Analysis of Slabs,
Thames and Hudson London, 1967.
- 100— Wegmuller, A.W.
Elasto— plastic Finite Element Analysis of Plates, Technical Notes TN99, Proc.
of the Inst. of Civ. Engrs, Vol. 57(2), pp. 535— 543, Sept. 1974.
- 102— Cope, R.G. and Rao, P.V.
Nonlinear Finite Element Analysis of Concrete Slabs Structures,
Proc. of the Inst. of Civ. Engrs, Vol. 63, Part 2, pp. 159— 179, 1977.
- 103— Phillips, D.V. and Zienkiewicz, O.C.
Finite Element Nonlinear Analysis of Concrete Structures,
Proc. of the Inst. of Civ. Engrs, Vol. 61, Part 2, March 1976.
- 104— Chang, T.Y., Tanigushi, H. and Chen, W.F.
Nonlinear Finite Element Analysis of Reinforced Concrete Panels.
ASCE Journal of Structural Engineering, Vol.113, No. 1, January 1987.
- 105— Elwi, A.E. and Hrudey, M.T.
Finite Element Model for Curved Embedded Reinforcement,
ASCE Journal of Engineering Mechanics, Vol. 115, No. 4, April 1989.
- 106— Phillips, D.V. and Wu, Z.P.
An Oriented Embedded Bar Formulation with Bond— Slip, Numerical Methods
in Engineering: Theory and Application, Ed. Pande and Middleton, J., Vol. 1,
pp. 320— 328, Elsevier, 1990.
- 107— Bazant, Z.P. and Cedolin, L.
Blunt Crack Band Propagation in Finite Element Analysis, J. of Eng. Mech.
Div, Proc. of the ASCE, Vol. 105, No. EM2, Apr. 1979, pp. 297— 315.
- 108— Regan, P.E. and Yu, C.W.
Limit State Design of Structural Concrete,
Chatto and Windus, London, 1973.
- 109— Cope, R.J. and Rao, P.V.
Nonlinear Finite Element Analysis of Concrete Slab Structures.
Proc. Inst. Civ. Engrs, Patr 2, Mar. 1977, vol. 63, pp. 159— 179.

- 110— Yüzügüllü, o. and Schnobrich, W.C.,
A Numerical Procedure for the Determination of the Behavior of a Shear
Wall Frame System, J. Amer. Con. Inst., Vol. 70, July 1973.
- 111— Vicchio, F. and Collins, M.P.
Stress—Strain Characteristics of Reinforce Concrete in Pure Shear, Inter.
Assoc. for Bridge and Struct. Engng Colloquium, Delft, 1981 pp. 211—225.
- 112— Gijesbers, F.B.J. and Smit, C.L.
Resultaten van de eerste serie dawaars Karachtproeven, Report No. BI77—128,
Institute TNO For Building Material and Building Structures, Rijswijk (1977).
- 113— ACI (318—77) Building Code Requirements for Reinforced Concrete,
ACI Committee 318, American Concrete Institute, Detroit, 1977, pp.113.
- 114— Rots, J.G., Nauta, P., Kusters, G.M.A. and Blaauwendraad, J.
Smeared Crack Approach and Fracture Localisation in Concrete.
Heron, Vol.30, No.1, 1985, Delft, Netherlands.
- 115— Hago, A.W.
Direct Design of Reinforced Concrete Slabs,
PhD Thesis, Glasgow University, 1982.
- 116— Jofret J.C. and McNeice, G.M.
Finite Element Analysis of R.C. Slabs, J. of the Str. Div., Proc. of the
ASCE, Vol.97, No.ST3, March 1971, pp785—806.
- 117— Baker, G.
On the Yiled Condition and Optimum Pointwise Reinforcement for Fracturing
Continua, Research Report No. CE102, Department of Civil Engineering,
University of Queensland, May 1989.
- 118— Stewart, E.G. and Watt, D.J.
Shear Failure of Prestressed Concrete Beams.
Bsc Project Report, 1981, Civ. Engng Dept, Glasgow University.